Journal of
Marine Science and Engineering

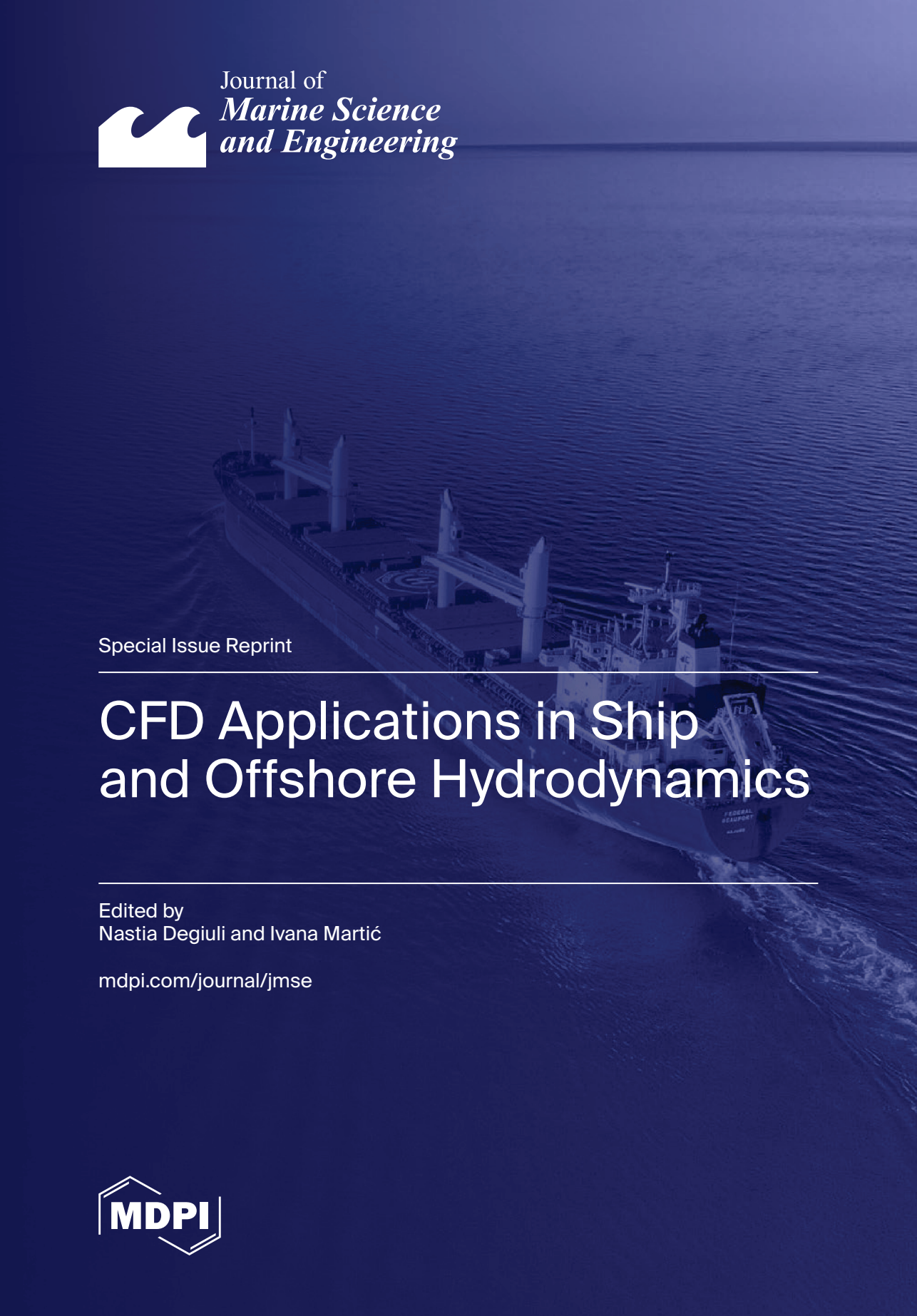

Special Issue Reprint

CFD Applications in Ship and Offshore Hydrodynamics

Edited by
Nastia Degiuli and Ivana Martić

mdpi.com/journal/jmse

MDPI

CFD Applications in Ship and Offshore Hydrodynamics

CFD Applications in Ship and Offshore Hydrodynamics

Guest Editors

Nastia Degiuli
Ivana Martić

MDPI

Basel • Beijing • Wuhan • Barcelona • Belgrade • Novi Sad • Cluj • Manchester

Guest Editors

Nastia Degiuli
Faculty of Mechanical Engineering and Naval Architecture
University of Zagreb
Zagreb
Croatia

Ivana Martić
Faculty of Mechanical Engineering and Naval Architecture
University of Zagreb
Zagreb
Croatia

Editorial Office
MDPI AG
Grosspeteranlage 5
4052 Basel, Switzerland

This is a reprint of the Special Issue, published open access by the journal *Journal of Marine Science and Engineering* (ISSN 2077-1312), freely accessible at: https://www.mdpi.com/journal/jmse/special_issues/EX406YTZL0.

For citation purposes, cite each article independently as indicated on the article page online and as indicated below:

Lastname, A.A.; Lastname, B.B. Article Title. *Journal Name* **Year**, *Volume Number*, Page Range.

ISBN 978-3-7258-2887-6 (Hbk)
ISBN 978-3-7258-2888-3 (PDF)
https://doi.org/10.3390/books978-3-7258-2888-3

Cover image courtesy of Chris Pagan

Contents

About the Editors

Nastia Degiuli

Nastia Degiuli graduated in Naval Architecture from the Faculty of Mechanical Engineering and Naval Architecture, University of Zagreb, where she also completed her MSc and PhD degrees. Currently, she holds the position of Full Professor with tenure and Head of Chair of Ship Hydrodynamics at the same institution. Her main research interests focus on numerical and experimental hydrodynamics and marine renewable energy. She has contributed to numerous internationally and domestically collaborative projects. Nastia Degiuli is the author of more than 120 papers, including papers in highly ranked international journals, conference proceedings, and book chapters. She is currently serving as the Editor-in-Chief for *Brodogradnja: An International Journal of Naval Architecture and Ocean Engineering for Research and Development*. She is a member of the Society of Naval Architects and Marine Engineers (SNAME) and the Croatian Academy of Engineering.

Ivana Martić

Ivana Martić graduated in Naval Architecture from the Faculty of Mechanical Engineering and Naval Architecture, University of Zagreb, where she also completed her PhD degree. She is currently a Postdoctoral Researcher at the same institution and serves as the Head of the Laboratory for Computational and Experimental Ship Hydrodynamics. Her main research interests focus on numerical and experimental hydrodynamics and marine renewable energy. Ivana Martić has authored over 70 publications, including papers in highly ranked international journals, conference proceedings, and book chapters. She is currently serving as the Associate Editor for *Brodogradnja: An International Journal of Naval Architecture and Ocean Engineering for Research and Development*. In recognition of her contributions to the field, she received the prestigious "Vera Johanides" Young Scientist Award for 2023 from the Croatian Academy of Engineering.

Preface

Computational Fluid Dynamics (CFD) methods are becoming an increasingly reliable and indispensable tool in the field of ship and offshore hydrodynamics. These methods offer several significant advantages over traditional experimental approaches. In addition to being time-efficient and cost-effective, CFD provides detailed insights into local flow characteristics, enabling a more comprehensive understanding of fluid behavior. Furthermore, CFD facilitates the analysis of various design alternatives under a wide range of operational conditions, leading to robust, efficient, and economically viable solutions. This capability is essential for optimizing the hydrodynamic performance of ships and offshore structures, ensuring enhanced operational efficiency, safety, and reliability. Since the overall performance of ships and offshore structures, as well as their environmental footprint, significantly depends on their hydrodynamic characteristics, the rapid and accurate assessment of such characteristics is of utmost importance.

Nastia Degiuli and Ivana Martić
Guest Editors

Journal of
Marine Science and Engineering

MDPI

Editorial

CFD Applications in Ship and Offshore Hydrodynamics

Nastia Degiuli * and Ivana Martić

Faculty of Mechanical Engineering and Naval Architecture, University of Zagreb, Ivana Lučića 5, 10000 Zagreb, Croatia; ivana.martic@fsb.unizg.hr
* Correspondence: nastia.degiuli@fsb.unizg.hr

Computational Fluid Dynamics (CFD) is an emerging field that is rapidly gaining popularity across various industries, including shipbuilding and offshore industry, primarily due to the continuous advancements in computational power. As hardware capabilities improve, it allows researchers and engineers to perform more complex simulations with higher fidelity, which leads to more accurate predictions of fluid behavior in different environments. Moreover, the ability to simulate realistic conditions without the need for extensive physical prototyping not only accelerates the design process but also reduces costs significantly. As industries strive for efficiency and sustainability, the application of CFD is likely to expand even further, making it an indispensable tool in engineering and scientific research.

The book *CFD Applications in Ship and Offshore Hydrodynamics* comprises sixteen contributions [1–16] to this Special Issue, which were published in 2023 and 2024. This collection aims to provide a comprehensive overview of the successful applications of CFD based on the potential and viscous fluid flow in the field of ship and offshore hydrodynamics.

Bašić et al. [1] performed a numerical analysis of the natural vibrations of both a segmented and a monohull barge, aiming to assess the effects of hydrodynamic damping on their dynamic responses. This was achieved by coupling fluid and structural solvers through modal analysis. The effect of water flow around and between the barge segments on hydrodynamic damping was examined by conducting free-decay test simulations using the Unsteady Reynolds-Averaged Navier–Stokes (URANS) equations. An efficient weak coupling method was introduced, which transfers the results from the flow solver onto the structure, represented by its mode shapes at each time step. The proposed coupling approach for capturing the unsteady deformation of the structure, by integrating the mode shapes over time, proves to be both stable and considerably faster than approaches that require resolving the entire structure at every time step. The validation of the results concerning damping and added mass effects demonstrated the method's feasibility in simulating the vibrations of complex ships and floating structures. The contraction and expansion of gaps lead to significant pressure gradients, resulting in localized elevations of the free surface. Furthermore, the formation of additional vortices and an increase in wall shear enhance the hydrodynamic damping effect in segmented floating structures when compared to their monohull counterparts.

Sulovsky et al. [2] conducted a comparative study using two numerical tools to estimate ship motions and added resistance in waves. The tools evaluated were the following: a commercial seakeeping code, Wasim by Det Norske Veritas (DNV); a weakly nonlinear potential flow solver based on the Rankine panel method; and the open-source viscous flow solver, OpenFOAM. This study focused on 6750 TEU and KRISO containership (KCS) models in regular head waves, both with and without forward speed. The numerical results were validated against experimental data. For the 6750 TEU containership model, the two solvers produced different trends in the heave motion. Specifically, the heave amplitude predicted by the potential flow solver was significantly smaller for large wave heights compared to that predicted by the viscous flow solver. The pitch motion was also underestimated by the potential flow solver. The authors concluded that the heave motion

Citation: Degiuli, N.; Martić, I. CFD Applications in Ship and Offshore Hydrodynamics. *J. Mar. Sci. Eng.* **2024**, *12*, 1926. https://doi.org/10.3390/jmse12111926

Received: 22 October 2024
Accepted: 24 October 2024
Published: 28 October 2024

could be underestimated with the potential flow solver, especially for increasingly steep waves. While viscous flow solvers demonstrated better accuracy in comparison to the experimental data, this study highlighted the importance of grid resolution, particularly for the KCS model. The discrepancies between numerical and experimental results at lower wave heights were attributed to an insufficient number of cells per wave height, underscoring the need for careful grid refinement in viscous flow simulations.

Martić et al. [3] developed a neural network-based model for predicting the added resistance coefficient of container ships in regular head waves, with wave frequencies ranging from 0.1 to 1.5 rad/s. This approach addresses the limitations posed by the scarcity of experimental data across various incoming wave frequencies. Unlike traditional hydrodynamic calculations, the proposed model does not require a 3D model of the ship hull and relies solely on the main ship particulars, making it suitable for preliminary ship design. The training data for the neural network were generated using numerical simulations based on the Boundary Integral Element Method (BIEM) for various container ship hull forms. These numerically obtained results were validated against experimental data for three benchmark container ships. The dataset was categorized into three classes according to ship length, and the expressions for the prediction of added resistance coefficient were formulated for each class with ship characteristics and speed as inputs.

Grlj et al. [4] investigated the influence of various numerical parameters on total resistance, wave patterns, and ship motions in numerical simulations at both model- and full scale. The investigated parameters included the choice of turbulence model and discretization schemes for convection, gradient, and temporal terms in the governing equations. The numerical model was based on the Reynolds-Averaged Navier–Stokes (RANS) equations, discretized using the Finite Volume Method (FVM). The Volume of Fluid (VOF) method was used to track the free surface, and the Grid Convergence Index (GCI) method was employed for the verification study. The results indicated that the choice of discretization scheme for the temporal term had no significant effect on the median total resistance. Additionally, the first-order scheme provided faster convergence in numerical simulations at the full scale. This finding suggests that a lower-order temporal discretization can be a practical choice for full-scale simulations, without compromising accuracy in predicting resistance. By decomposing the total resistance into frictional and pressure components, it was shown that frictional resistance is largely unaffected by the choice of discretization schemes for the convection, gradient, and temporal terms. In contrast, the pressure resistance is influenced by these schemes, with higher values observed when a first-order scheme is used for convection and gradient discretization.

Martić et al. [5] conducted a numerical study to assess the impact of shallow water on the total resistance of a solar catamaran, using an unsteady viscous fluid model based on the RANS equations. A mesh morphing algorithm was employed to account for ship motions under shallow water conditions. Simulations were performed for both deep water and limited depths, corresponding to h/T ratios of 7.6, 4, and 2, at two different speeds. The results revealed that at an operational speed of 5.5 knots, the catamaran's total resistance increased significantly with decreasing water depth, leading to considerable sinkage. However, the shallow water did not noticeably affect the trim of the catamaran in this particular scenario. Reducing the speed by 1.5 knots led to a significant decrease in both total resistance and sinkage. Analysis of the velocity magnitude at the symmetry plane of the demihull showed that the maximum velocity between the catamaran and the bottom was approximately 30% lower when the speed decreased from 5.5 to 4 knots, indicating a significant reduction in hydrodynamic effects associated with shallow water conditions.

Lee et al. [6] investigated the added resistance performance of ships under various wave conditions using CFD, considering different constraint conditions. The authors compared the added resistance coefficient and Response Amplitude Operators (RAOs) of the target ship using different modeling approaches: a 2-DOF (degree of freedom) captive model (allowing free heave and pitch) and a 3-DOF model (allowing free heave, roll, and pitch). Additionally, a soft spring system and a free-running model were employed

to simulate 6-DOF conditions. The 6-DOF soft-mooring system was modeled through spring coupling in the Dynamic Fluid Body Interaction (DFBI) framework. The 6-DOF implementation method used in the experiment was successfully reproduced through CFD. The simulations revealed variations in added resistance performance and motion response based on different constraint conditions and testing methods. Additionally, it was demonstrated that the flow distribution around the hull can change significantly in oblique wave conditions.

He et al. [7] conducted a numerical investigation into the effects of leading-edge tubercles on a three-dimensional flapping foil with enabled rolling and pitching motions. To replicate the natural flapping motion of humpback whales, appropriate spanwise flexibility was included, and the angle of attack profile was analyzed in a representative section influenced by this flexibility. The motion of the flexible foils was decomposed into rigid motion and flexible deflection using sliding mesh and dynamic mesh methods, respectively. The authors evaluated the hydrodynamic performance of the flexible flapping foils by solving the URANS equations. They assessed the effects of leading-edge tubercles with varying amplitudes and wavelengths under conditions of high propulsive efficiency. The sharpest tubercle shape exhibited a maximum efficiency loss of 19.4%. The results indicated that leading-edge tubercles are better suited for foils engaged in steady or quasi-steady motions, such as propellers and turbines.

Zheku et al. [8] evaluated the applicability and reliability of RANS solvers in predicting the hydrodynamic forces and moments of an underwater vehicle for the case of the DARPA SUBOFF model. The authors examined five different configurations across pure drift tests, rudder tests, and pure rotation in both vertical and horizontal planes. The results from the horizontal and vertical drift and rotation cases demonstrated overall good agreement with experimental data. In the bare hull configuration, two streamwise vortices were found to significantly influence the nonlinearities observed in the drifting attitudes in the absence of stern appendages. Notably, the stall of the sail for the bare hull with sail configuration occurred numerically earlier than in experiments, approximately at 10 degrees, which may have contributed to discrepancies in the longitudinal force. The authors concluded that the proposed numerical methodology effectively assesses both the linear stability and controllability characteristics of the underwater vehicle in relation to its maneuvering capabilities.

Jiang et al. [9] introduced a data-driven approach to predict ship motions, addressing the limitations of existing methods that often focus on single application scenarios and lack generalization capability. This model combines machine learning techniques with potential flow theory to improve forecasting accuracy and expand applicability. Initially, extensive numerical simulations were performed for the KCS model across various sea states and wave angles, utilizing overset grid technology. The resulting motion and wave elevation data were then used to train a Bidirectional Long Short-Term Memory (BiLSTM) network. To forecast the pitch and heave under unknown conditions, multiple pre-trained node models were selected, and the Golden Jackal Optimization Algorithm (GJO) was used to compute the regression coefficients for each model. The Dynamic Model Averaging (DMA) was then calculated to account for the diversity of sea conditions and ship motion states, resulting in more comprehensive and reliable predictions. By leveraging data from each node's conditions, the model is better suited to handle the complexities of ship motion in diverse sea states.

Paneer et al. [10] developed a Fluid–Structure Interaction (FSI) model by combining the mode superposition method with the Lagrangian Differencing Dynamics (LDD) method in a two-way partitioned weak coupling or explicit coupling approach. The LDD method allows for large time steps with lower computational costs while maintaining second-order accuracy, making it particularly well suited for complex transient problems due to its ability to work directly on meshes. By integrating the mode superposition method with LDD, the model calculates structural deformation under fluid loads using pre-calculated mode shapes and natural frequencies derived from modal analysis. This approach enables fluid-

induced structural deformation to be weakly coupled into the flow solver, with deformation obtained via direct integration. The flow particles and structural vertices were advected in Lagrangian coordinates, resulting in Lagrangian–Lagrangian coupling in space and weak or explicit coupling in time. This methodology ensures a more accurate representation of fluid–structure interactions in ship and offshore hydrodynamics.

Matsuda and Katsui [11] conducted numerical simulations of the flow around the Ryuko-maru tanker at both model and full-scale Reynolds numbers using the Reynolds Stress Model (RSM). They compared the Reynolds stress distribution obtained from the model-scale computations with experimental measurements to evaluate the RSM performance. Additionally, full-scale numerical simulations were carried out, accounting for the influence of hull surface roughness, and the resulting wake distributions were compared with actual ship measurements. The impact of hull surface roughness was incorporated using a wall function methodology that included a sand-grain roughness function and explored an appropriate roughness length scale based on empirical wake distribution data. The authors concluded that considering computational costs, the RSM combined with the linear pressure strain correlation (LPS) or the linear pressure strain correlation model with two layers (LPST) is recommended for achieving highly accurate predictions near the hull in the numerical simulations for full-scale ships.

Begović et al. [12] validated the LincoSim platform, a web-based virtual towing tank that facilitates automated and standardized CFD data sampling for calm water conditions based on a planing powerboat model at speeds of up to 40 knots. The numerical simulations in calm water were conducted over a range of Froude numbers from 0.3 to 2.0, expanding upon previous publications utilizing the LincoSim virtual towing tank. The average percentage differences between experimental fluid dynamics (EFD) and CFD data across the entire speed range were 1.84%, 6.87%, and 6.94% for resistance, dynamic trim, and sinkage, respectively. These results affirm the robustness of the standardized and automated CFD modeling for calm water conditions, even at high Froude numbers. Visual observations of wetted length and spray length on the chine demonstrate that CFD simulations accurately capture the underlying phenomena. As part of their ongoing work, the authors presented results from seakeeping analyses, illustrating that automated CFD simulations can align closely with experimental data while highlighting the complex nonlinear hull–wave interactions of planing crafts.

Ye et al. [13] proposed a new design for a seismic survey vessel, specifically optimized for shallow-water marine resource exploration and safety, based on the existing deep-water seismic survey vessel. To assess the impact of ship type, water depth, and speed on sinkage and trim, a comparative analysis was performed across infinite, medium, and shallow water depths. The results demonstrated that the new design exhibited lower trim and sinkage compared to the original vessel, ensuring no grounding risk within the operational speed range. Furthermore, an analysis of the resistance in shallow water under both constrained and free conditions revealed that changes in the vessel's attitude significantly affect resistance. This study revealed that adopting a specific trim by the stern can reduce resistance, enhancing the vessel's efficiency during shallow-water operations.

Vasilev et al. [14] developed a software tool for trim optimization for practical engineering applications. The trim optimization process was divided into seven key phases as follows: (1) creating a 3D representation of the ship, i.e., the digital twin that includes detailed modeling of the hull, rudder, and propeller, with the goal of faithfully capturing the ship characteristics; (2) first-level verification, which involves comparing hydrostatic data with the data given in the *Trim & Stability* booklet for various drafts; (3) determination of the propeller characteristics by performing the numerical simulations of the open water test; (4) second-level verification involving the conduction of the CFD simulations of the self-propulsion test; (5) trim optimization at a certain draft and speed using CFD simulations; (6) determination of a mathematical model for assessing the optimal trim, ship speed, engine (brake) power, daily fuel consumption, and propeller rate of revolutions; (7) programming an application based on the conducted analyses. In the trim optimization

study, data obtained from CFD analysis, including brake power, daily fuel oil consumption, and propeller rate of revolutions, served as output variables for training an artificial neural network (ANN), while the input variables included draft, speed, trim, and displacement. The model's applicability was demonstrated using a Ro-Ro ship case study.

Li et al. [15] conducted a study on the hydrodynamic performance of a complex-shaped Unmanned Underwater Vehicle (UUV) and developed a method aimed at optimizing the geometry to achieve stable motion control while reducing energy consumption. The simulation results indicate that the proposed design schemes result in an 18% reduction in drag in the surge direction and a 32% reduction in the heave direction. The authors highlighted that adopting a convex shape for the buoyancy blocks significantly reduces the pressure at the front end and minimizes the volume of flow separations at the rear end, leading to a notable decrease in drag from the tail. To support the simulation of underwater operation scenarios, an underwater simulation platform for the vehicle has been developed using the Robot Operating System (ROS). This platform replicates the underwater environment and external disturbances while integrating various sensors for perception within the simulated environment. It offers a comprehensive framework for validating algorithms across different types of underwater vehicles, enabling more accurate and realistic testing.

Tian et al. [16] presented a three-dimensional simplified inflow model for a ship's damaged side bulkheads, employing the shear stress transport (SST) *k*-epsilon turbulence model and the VOF method within the STAR-CCM+ software package. Additionally, this study establishes the relationship between the water intake discharge coefficient and various parameters, including the shape of the damaged opening, its area, characteristic dimensions, and the depth of the center, using the control variable method to analyze their influence. Based on the numerical calculation results, two sets of semi-empirical formulas for the discharge coefficient of ship-side damage are derived using the Π theorem and the polynomial fitting method. Both methods demonstrate good fitting accuracy and effectiveness.

Author Contributions: Conceptualization, N.D. and I.M.; writing—original draft preparation, N.D. and I.M.; writing—review and editing, N.D. and I.M.; supervision, N.D.; project administration, N.D. and I.M.; funding acquisition, N.D. All authors have read and agreed to the published version of the manuscript.

Funding: The editors were supported by the Croatian Science Foundation, under project IP-2020-02-8568.

Institutional Review Board Statement: Not applicable.

Informed Consent Statement: Not applicable.

Data Availability Statement: Not applicable.

Acknowledgments: The Editors wish to express sincere gratitude to all the authors and reviewers.

Conflicts of Interest: The authors declare no conflicts of interest.

References

1. Bašić, J.; Degiuli, N.; Malenica, Š. Insight into Hydrodynamic Damping of a Segmented Barge Using Numerical Free-Decay Tests. *J. Mar. Sci. Eng.* **2023**, *11*, 581. [CrossRef]
2. Sulovsky, I.; Hauteclocque, G.; Greco, M.; Prpić-Oršić, J. Comparative Study of Potential Flow and CFD in the Assessment of Seakeeping and Added Resistance of Ships. *J. Mar. Sci. Eng.* **2023**, *11*, 641. [CrossRef]
3. Martić, I.; Degiuli, N.; Grlj, C. Prediction of Added Resistance of Container Ships in Regular Head Waves Using an Artificial Neural Network. *J. Mar. Sci. Eng.* **2023**, *11*, 1293. [CrossRef]
4. Grlj, C.; Degiuli, N.; Martić, I. The Impact of Numerical Parameters on the Resistance Characteristics of a Container Ship at the Model and Full Scale. *J. Mar. Sci. Eng.* **2023**, *11*, 1672. [CrossRef]
5. Martić, I.; Degiuli, N.; Borčić, K.; Grlj, C. Numerical Assessment of the Resistance of a Solar Catamaran in Shallow Water. *J. Mar. Sci. Eng.* **2023**, *11*, 1706. [CrossRef]
6. Lee, S.; Hwang, S.; Kim, H.; Hyun, Y.; Lee, S.; Paik, K. A Numerical Study on the Hydrodynamic Performance of a Tanker in Bow Sea Conditions Depending on Restraint Conditions. *J. Mar. Sci. Eng.* **2023**, *11*, 1726. [CrossRef]

7. He, R.; Wang, X.; Li, J.; Liu, X.; Song, B. Effects of Leading-Edge Tubercles on Three-Dimensional Flapping Foils. *J. Mar. Sci. Eng.* **2023**, *11*, 1882. [CrossRef]
8. Zheku, V.; Villa, D.; Piaggio, B.; Gaggero, S.; Viviani, M. Assessment of Numerical Captive Model Tests for Underwater Vehicles: The DARPA SUB-OFF Test Case. *J. Mar. Sci. Eng.* **2023**, *11*, 2325. [CrossRef]
9. Jiang, Z.; Ma, Y.; Li, W. A Data-Driven Method for Ship Motion Forecast. *J. Mar. Sci. Eng.* **2024**, *12*, 291. [CrossRef]
10. Paneer, M.; Bašić, J.; Sedlar, D.; Lozina, Ž.; Degiuli, N.; Peng, C. Fluid Structure Interaction Using Modal Superposition and Lagrangian CFD. *J. Mar. Sci. Eng.* **2024**, *12*, 318. [CrossRef]
11. Matsuda, S.; Katsui, T. Ship Flow of the Ryuko-maru Calculated by the Reynolds Stress Model Using the Roughness Function at the Full Scale. *J. Mar. Sci. Eng.* **2024**, *12*, 783. [CrossRef]
12. Begovic, E.; Bertorello, C.; Ponzini, R.; Salvadore, F. Planing Hull Hydrodynamic Performance Prediction Using LincoSim Virtual Towing Tank. *J. Mar. Sci. Eng.* **2024**, *12*, 794. [CrossRef]
13. Ye, Z.; Su, S.; Wu, Y.; Guo, F.; Liu, H.; Cheng, Q. Research on Hull Form Design and Numerical Simulation of Sinkage and Trim for a New Shallow-Water Seismic Survey Vessel. *J. Mar. Sci. Eng.* **2024**, *12*, 1205. [CrossRef]
14. Vasilev, M.; Kalajdžić, M.; Ivković, I. CFD-Powered Ship Trim Optimization: Integrating ANN for User-Friendly Software Tool Development. *J. Mar. Sci. Eng.* **2024**, *12*, 1265. [CrossRef]
15. Li, X.; Zhang, D.; Zhao, M.; Wang, X.; Shen, Y. Hydrodynamic Analysis and Drag-Reduction Design of an Unmanned Underwater Vehicle Based on Computational Fluid Dynamics. *J. Mar. Sci. Eng.* **2024**, *12*, 1388. [CrossRef]
16. Tian, S.; Peng, F.; Wang, Z.; Li, J. Numerical Study of Discharge Coefficients for Side-Damaged Compartments. *J. Mar. Sci. Eng.* **2024**, *12*, 1502. [CrossRef]

Journal of
Marine Science and Engineering

MDPI

Article

Insight into Hydrodynamic Damping of a Segmented Barge Using Numerical Free-Decay Tests

Josip Bašić [1], Nastia Degiuli [2,*] and Šime Malenica [3]

[1] Faculty of Electrical Engineering, Mechanical Engineering and Naval Architecture, University of Split, R. Boškovića 32, 21000 Split, Croatia
[2] Faculty of Mechanical Engineering and Naval Architecture, University of Zagreb, Ivana Lucica 5, 10000 Zagreb, Croatia
[3] Bureau Veritas, Research Department, 67/71 Boulevard du Château, 92200 Neuilly-sur-Seine, France
* Correspondence: nastia.degiuli@fsb.hr

Abstract: Natural vibrations of a segmented and a monohull barge are analysed to compare influences of hydrodynamic damping on the dynamic responses of two different models. The influence of water flow around and between barge segments on hydrodynamic damping was investigated by simulating free-decay tests using a URANS method. Fluid forces were fed into the modal solver, which allows for efficient deformation of the structure without full resolution of structural equations. Verification of the coupled solver was performed by reproducing the model experiments of a segmented barge. Comparison of segmented and monohull results clarified the impact of gaps between barge segments, i.e., how the energy dissipates because of large pressure gradients within and around gaps, and additional free-surface movement. This insight of higher damping should be taken into account for model tests of segmented floating structures, such as wave-energy-converting systems.

Keywords: segmented barge; hydrodynamic damping; modal analysis; CFD; FSI

Citation: Bašić, J.; Degiuli, N.; Malenica, Š. Insight into Hydrodynamic Damping of a Segmented Barge Using Numerical Free-Decay Tests. *J. Mar. Sci. Eng.* **2023**, *11*, 581. https://doi.org/10.3390/jmse11030581

Academic Editor: Kostas Belibassakis

Received: 17 February 2023
Revised: 3 March 2023
Accepted: 6 March 2023
Published: 8 March 2023

1. Introduction

In unsuitable environmental conditions, i.e., sea state, heading and speed, highly nonlinear loads occur on the ship's hull and cause significant vibrations and noise, which are transmitted along the hull's structure [1]. In rough seas, the ship's bow and stern may occasionally emerge from a wave and re-enter the wave with a heavy impact or a slam [2] as the hull structure encounters the water, developing high hydrodynamic loads that produce significant vibrations. Ship-hull vibration is a major contributor to fatigue-crack growth [3,4], and structural vibrations radiate noise [5]. It is of importance to determine the vibration level of a ship in the design stage. This urgency is caused by the increasing propulsion power and very large sizes of ships. The damping is the dissipation of the energy during a vibration cycle, and it is a key parameter in resonance phenomena that influences the amplitude of harmonic vibrations and the number of significant vibration cycles in the case of transient vibrations, for example. The damping in lightly damped vibrations can be overlooked in the determination of the system's natural frequencies, but it will have a large effect on the vibration response around the natural frequencies; i.e., the excitation at resonance is only equilibrated by damping. The damping of structural systems and ships in particular is weak. Except when extremely close to resonance, the vibratory amplitude is approximately independent of damping [6]. The total damping associated with overall ship hull vibration is generally considered to be a combination of the structural damping (e.g., steel hysteresis effects), cargo damping (e.g., cargoes of grain) and hydrodynamic damping (viscous and wave damping). Hydrodynamic damping is frequency-dependent and approaches zero for high and very low frequencies. Viscous hydrodynamic damping is often nonlinear and caused by bilge keels, skin friction, vortices, etc. Water impacts that occur on the flat stern as a consequence of violent vibration may actually contribute as a

nonlinear damping due to antisymmetric loading [7]. In general, the effect of wave creation is disregarded, but it must be considered for vibrations with low frequencies [8]. Typically, an overall constant damping coefficient of around 1.5% of the critical damping is employed as a preliminary estimate [9,10].

In this study, the hydroelastic response of a floating object was simulated numerically by coupling two solvers: a fluid dynamics solver and a structural solver. In the literature, different kinds of methodologies have been established for the two-way fluid–structure interaction (FSI). Fully coupled (monolithic) techniques incorporate both the fluid and the structure equations, while relying on a single solver for the coupled system [11]. Classical CFD solutions are constructed mostly on Eulerian reference systems, thereby connecting the structural equations based on the Lagrangian reference system results in the matrices for structure systems more rigid than those for fluid systems. Solving equations using a unified method for large-scale problems is therefore computationally intensive. Using two independent solvers, partitioned methods solve the structure and fluid equations on two separate grids. In order to map the surface loads from the CFD grid to the structure grid and the displacement field from the structure grid to the CFD grid, a communication method must be established at the interface between the grids [12]. Displacement of the CFD grid's boundary necessitates careful manipulation of the surrounding nodes without tangling or twisting the cells or remeshing the deformed region. There have been successful attempts at using partitioned methods by coupling them with potential flow theory [13–15], directly coupling structure solvers with the CFD solver [16,17] and by using the boundary-integral equation method [18].

In this paper, weak coupling of the unsteady RANS-VOF solver with the reduced-order modal approach is considered, which enables rapid simulation of flexible floating structures for known vibration-mode shapes and their natural frequencies [19] that can be obtained by analytical, experimental, or numerical analysis. Fast, unsteady simulation in the time domain can give an insight into the structural response to any kind of external loads. The coupling was established in FineMarine CFD software based on modal simulations performed using NASTRAN solver. We focus on the determination of the hydrodynamic damping in the case of a flexible barge that is vertically freely vibrating, based on an extensively documented experiment [20] that was rendered in Figure 1. In comparison to realistic monohull ship models, the modal damping ratios for this segmented vibrating structure were found to be unusually high in comparison to regular floating structures. This phenomenon is caused by the influence of the barge gaps on the hydrodynamics. Therefore, numerical simulations were performed for the segmented structure and the monohull structure in order to clarify the impact of the gaps between pontoons on the hydrodynamic response of the floating structure. A CFD approach was used that was similar to those applied in [16,21]. The aims of the investigation were twofold: to show that weak coupling of a validated RANS solver and stable modal solver is quick and accurate, and to analyse the hydrodynamic damping generated by segmented sections of vibrating floating structures.

The paper is organised as follows. In the next section, the flow and structure of the numerical solvers are described. In Section 3, the coupling between the solvers is introduced. Section 4 describes the numerical experiment and numerical results. The last section presents an explanation of the results and the conclusions.

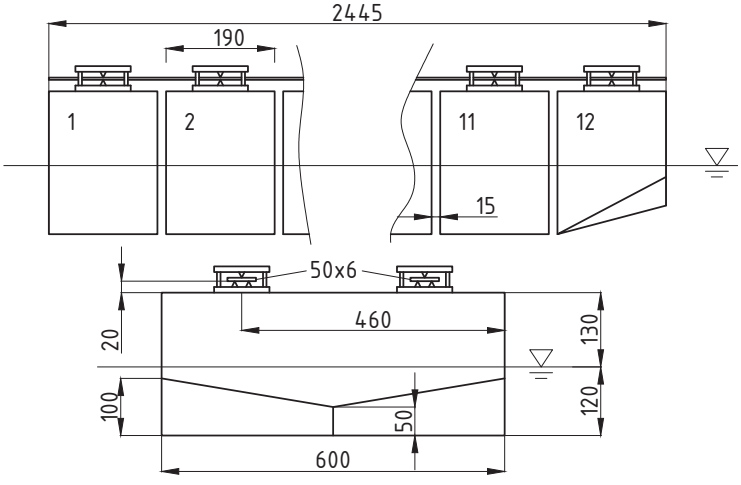

Figure 1. The geometry of the flexible segmented barge (dimensions are in mm).

2. Numerical Methods

2.1. Modal Solver for the Structure

The equation of motion for a multiple-degree-of-freedom (MDOF) system is written as:

$$\mathbf{M}\ddot{\mathbf{x}}(t) + \mathbf{C}\dot{\mathbf{x}}(t) + \mathbf{K}\mathbf{x}(t) = \mathbf{f}(t) \tag{1}$$

where $\mathbf{x}(t)$, $\dot{\mathbf{x}}(t)$ and $\ddot{\mathbf{x}}(t)$ are, respectively, vectors of displacement, velocity and the acceleration responses of the system induced by the time-dependent external force vector $\mathbf{f}(t)$; and $\mathbf{M}$, $\mathbf{C}$ and $\mathbf{K}$ are mass, damping and stiffness matrices, respectively. The addition of damping terms in slightly damped vibration systems may be neglected in the determination of the natural frequencies of the system. Considering the free motion, real mode shapes are the solution to the eigenvalue problem:

$$\left(\mathbf{K} - \omega^2\mathbf{M}\right)\mathbf{\Phi} = 0 \tag{2}$$

where $\mathbf{\Phi}$ is the modal matrix that consists of mode shape vectors for each natural frequency of the system with n degrees of freedom: $\mathbf{\Phi} = [\boldsymbol{\phi}_1, \boldsymbol{\phi}_2, \cdots, \boldsymbol{\phi}_n]$. A mode shape describes the form of the vibration for a particular natural frequency ω_i. The non-trivial solution of eigenvalue problem (2) exists when:

$$\det\left(\mathbf{K} - \omega^2\mathbf{M}\right) = 0. \tag{3}$$

The solution of Equation (3) is the vector of squared values of the system's natural frequencies, $\{\omega_1^2, \omega_2^2, \cdots, \omega_n^2\}$. The obtained eigenvectors of an undampened system are orthogonal to each other, such that $\phi_i^T\mathbf{M}\phi_j = \phi_i^T\mathbf{K}\phi_j = \mathbf{0}$ holds for any i and j modes of vibration, $i \neq j$. From the orthogonality properties, it holds that the modal mass matrix, $\mathbf{\Phi}^T\mathbf{M}\mathbf{\Phi}$, and the modal stiffness matrix, $\mathbf{\Phi}^T\mathbf{K}\mathbf{\Phi}$, are diagonal matrices with the modal quantities on their diagonals. Since the absolute magnitude of a mode shape is not definite, eigenvectors are usually normalised with respect to the system's mass:

$$\widetilde{\mathbf{\Phi}}^T\mathbf{M}\widetilde{\mathbf{\Phi}} = \mathbf{I} \tag{4}$$

where $\widetilde{\mathbf{\Phi}}$ is the mass-normalised modal matrix and $\mathbf{I}$ is the identity matrix. From Equation (2), it follows that

$$\widetilde{\mathbf{\Phi}}^T\mathbf{K}\widetilde{\mathbf{\Phi}} = \mathrm{diag}\left(\omega_1^2, \omega_2^2, \cdots, \omega_n^2\right). \tag{5}$$

The global deformation of the structure can be written as a superposition of the vibration modes:

$$\mathbf{x}(t) = \widetilde{\mathbf{\Phi}}\mathbf{u}(t) \tag{6}$$

where $\mathbf{u}(t)$ is the vector of modal coordinates (or the generalised displacement). Using the modal coordinate transformation (6) and mass-normalised modal matrix, $\widetilde{\mathbf{\Phi}}$, the equation of motion (1) can be expressed as:

$$\widetilde{\mathbf{\Phi}}^T\mathbf{M}\widetilde{\mathbf{\Phi}}\ddot{\mathbf{u}}(t) + \widetilde{\mathbf{\Phi}}^T\mathbf{C}\widetilde{\mathbf{\Phi}}\dot{\mathbf{u}}(t) + \widetilde{\mathbf{\Phi}}^T\mathbf{K}\widetilde{\mathbf{\Phi}}\mathbf{u}(t) = \widetilde{\mathbf{\Phi}}^T\mathbf{f}(t) \tag{7}$$

where $\dot{\mathbf{u}}(t)$ and $\ddot{\mathbf{u}}(t)$ are vectors of modal velocity and the modal acceleration response of the system, respectively. The convenient outcome is that all terms in Equation (7) are diagonal matrices, except the damping term, $\widetilde{\mathbf{\Phi}}^T\mathbf{C}\widetilde{\mathbf{\Phi}}$.

2.2. Rayleigh Damping

In order to uncouple the equation of motion of a MDOF system into n equations of motion of a single degree-of-freedom (SDOF) system, the damping term should also be diagonalised. Lord Rayleigh introduced the damping matrix, which is assumed to be proportional to the mass and stiffness matrices:

$$\mathbf{C} = \alpha\mathbf{M} + \beta\mathbf{K} \tag{8}$$

where α and β are the mass and stiffness coefficients, respectively. There are no physical reasons for the damping matrix to have this kind of relation with the other matrices, but it offers the advantage of diagonalising the equation of motion for the real mode shapes. By inserting the damping matrix (8) into the transformed equation of motion (7), and by using the relations (4) and (5), n uncoupled SDOF equations may be written as:

$$\ddot{\mathbf{u}}_i(t) + \left(\alpha + \beta\omega_i^2\right)\dot{\mathbf{u}}_i(t) + \omega_i^2\mathbf{u}_i(t) = \boldsymbol{\phi}_i^T\mathbf{f}(t). \tag{9}$$

Equation (9) can conveniently be expressed as:

$$\ddot{\mathbf{u}}_i(t) + 2\zeta_i\omega_i\dot{\mathbf{u}}_i(t) + \omega_i^2\mathbf{u}_i(t) = \boldsymbol{\phi}_i^T\mathbf{f}(t) \tag{10}$$

where ζ_i is the modal damping ratio of mode i. This ratio expresses the level of actual damping in a system relative to critical damping, $\zeta_i = c_i/c_c$, where the critical damping coefficient is defined as $c_c = 2m\omega_i$.

The solution to Equation (10) can be obtained for each vibration mode by using direct integration algorithm, e.g., the Newmark integration method or the complementary function and a particular solution method [19].

2.3. Damping Determination

The logarithmic decrement method is used to find the damping ratio of an under-damped system in the time domain. The method relies on the natural logarithm of the ratio of two successive peaks amplitudes:

$$\delta = \ln\frac{|\mathbf{x}(t)|}{|\mathbf{x}(t+T)|} \tag{11}$$

where t is time when the amplitude is reached and T is the period of vibration. The damping ratio is then found from the following expression:

$$\zeta_i = \frac{1}{\sqrt{1 + \left(\frac{2\pi}{\delta}\right)^2}} \tag{12}$$

In addition to the amplitudes, the logarithmic decrement may be calculated using acceleration amplitudes, $\ddot{\mathbf{x}}(t)$ and $\ddot{\mathbf{x}}(t+T)$, if the response is purely single-mode like it is considered to be later in the paper. The above logarithmic decrement method is used to determine the damping ratio based on the numerically obtained structure response.

2.4. Flow Solver

The Navier–Stokes equation that describes conservation of momentum of fluid flow, for the incompressible viscous fluid, reads:

$$\frac{D\boldsymbol{v}}{Dt} = -\frac{1}{\rho}\nabla p + \frac{\mu}{\rho}\nabla^2 \boldsymbol{v} + \frac{1}{\rho}\boldsymbol{a}_{ext} \tag{13}$$

and the equation of continuity that describes the conservation of mass, i.e., the incompressibility constraint, reads:

$$\nabla \cdot \boldsymbol{v} = 0 \tag{14}$$

where $\boldsymbol{v}$ is the velocity vector field, D/Dt denotes material derivative $\partial/\partial t + (\boldsymbol{v} \cdot \nabla)$, p is the pressure field, ρ is the fluid density, μ is the dynamic viscosity of the fluid and $\boldsymbol{a}_{ext}$ denotes external forces acting on fluid (e.g., gravity acceleration). FineMarine CFD software was utilised to model and numerically analyse the flows surrounding the barge. For spatial discretisation of the transport equations, the finite volume method (FVM) was applied. The solver uses incompressible unsteady RANS equations and the VOF approach for free-surface capturing. The pressure equation is solved on the faces of an unstructured three-dimensional mesh whose cells are connected by an arbitrary number of faces. Menter's K–ω turbulent shear stress model was used to capture flow separation. The flow domain extends two barge lengths around the model. The no-slip boundary condition is imposed on the hull by using wall functions. The far-field boundary condition is imposed at the front, back and side boundaries of the domain, where the flow enters or leaves the domain locally. The pressure is specified as a Dirichlet boundary condition at the top and bottom boundaries of the domain. The flow solver has been thoroughly validated [22–24].

3. Modal-Based Coupling

In this paper, we investigate the weakly coupled FSI using a reduced-order model for the structure because this type of model is more computationally efficient than direct models [19]. Reduced-order models are useful when one has to deal with complex structures, such as ships, whose dynamics are governed by well defined modes of vibration. As discussed in Section 2.1, a vibrating structure can be represented by mass-normalised mode shapes and natural frequencies. The right-hand-side of Equation (1) or (10) is the force vector, which is directly responsible for linking the unsteady hydrodynamics and inertial loads with the structural system. The modal, Equation (10), can therefore be solved externally or even directly inside the fluid flow solver at each physical time step, for all known mode shapes. The global deformation of the structure is reconstructed with Equation (6), which is often termed as mode superposition, in order to take the new shape of the structure into account for the flow calculation. Therefore, for the partitioned fluid–structure interaction, the external loads are applied by the fluid flow, but the fluid flow is also influenced by the deformation of the structure.

Prior to the CFD simulation, the structure's dry natural frequencies and mode shapes were calculated outside of the flow solver. Vibrating mode shapes are represented using

generalised displacements, i.e., vectors of modal coordinates relative to the initial structure shape that can be obtained analytically, numerically or experimentally.

Structure and fluid solvers have to exchange forces and displacements, and the structure and fluid interface are differently discretised. A robust way to interpolate values and deform CFD mesh around deforming structures is the radial basis function (RBF) interpolation [25]. A fluid volume mesh has to be deformed at each time step according to the displacements obtained by the modal solver at the interface of the fluid–structure domain. By using RBF, the fluid grid is smoothly deformed by interpolating the displacements of the boundary nodes to all the volume mesh nodes. The system of equations that involves only boundary nodes has to be solved and does not have the need for grid topology information. Therefore, dry mode shapes can be represented with an arbitrary number of generalised displacements at the solid–fluid interface, while taking into account limitations of RBF (e.g., all points should not lie on a single line). Increasing the number of structural nodes (and displacements) increases the size of the transformation matrix and memory requirements, but increases the accuracy of fluid–structure loads and displacements transfer. In order to accelerate inter-grid communication, it advisable to generate connections between fluid boundary grid nodes and structural nodes based on RBF interpolation before running the simulation.

The steps of computational method are shown in Algorithm 1. The equilibrium between the structure and the fluid is not exactly ensured at the end of each solver iteration, i.e., each time step, which is referred to as the weak coupling. The structure solver is second-order time-accurate, and the fluid solver verifying the conservation laws is at least first-order time accurate; thus, the computational method is at least first-order time accurate.

Algorithm 1 Reduced order modal approach to weakly coupled FSI.

1. Calculate dry vibration natural frequencies $\omega_1, \omega_2, \cdots, \omega_n$ and their mass-normalised mode shapes
2. Setup simulation initial conditions (e.g., initial structure displacement and fluid boundary conditions)
3. Build RBF connections fluid face/structural node
4. Simulation loop, for each time-step Δt:
   (a) Transfer fluid loads to structural nodes
   (b) Solve set of Equation (10) for all mode shapes
   (c) Obtain new shape of the structure via Equation (6)
   (d) Perform RBF mesh interpolation from the old to the new structure shape
   (e) Solve flow for time $t + \Delta t$, influenced by the deformation of the structure
   (f) If residuals of fluid solver are too high, go to step 4.(a)

4. Vertical Vibrations of a Flexible Barge

4.1. Barge Characteristics

Numerical experiments were performed on a flexible barge, based on experimental setup from [20]. The experiments which were used in the present work are quite particular, and they are not intended for realistic model ship models. The initial purpose of these experiments was to validate the numerical developments related to global hydroelastic aspects. For that reason, the elasticity of the plates was chosen in such a way that the resonant frequencies got close to the wave frequencies which can be realised in the basin. This was practically possible to achieve only with the segments disconnected from each other, i.e., with gaps included.

The experimental model of a flexible prismatic barge consisted of twelve segments or pontoons (that had the following dimensions: length 190 mm, breadth 600 mm, depth 250 mm). The pontoons were shaped as rectangular boxes, except for the foremost one, which had a slightly modified keel, which is visible in Figures 1 and 2. Two elastic steel plates were positioned above the deck level and were connected to the pontoons, as shown in Figure 1. Each plate had the following dimensions: width 50 mm, height 6 mm. The

draught of the barge was 120 mm, and the pontoons were separated by 15 mm gaps, in order to avoid contact while vibrating.

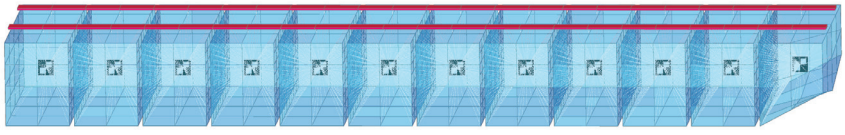

Figure 2. Finite element model of the barge (red— beam elements, blue—plate elements, black—mass elements, white—rigid connections).

In order to extract wet natural frequencies and damping ratios from the experimental model, a modal analysis was performed on the data obtained from series of free decay tests. The tests were initiated by releasing the barge pulled by the first floater out of the water in the vertical direction. The data obtained from the experiment are vertical displacements yielded from six optical sensors placed on the tops of the pontoons. Yielded natural frequencies and average damping ratios for the first two vibration modes are given in Table 1. The modal damping ratios in these cases are unusually high in comparison to regular floating structures. It is rational to assume that this phenomenon is caused by the influence of the barge gaps on the hydrodynamics, so this particular problem qualifies the experiment as a good verification test for a numerical hydroelastic solver. Furthermore, numerical simulations were also performed on the monohull structure without the gaps in order to clarify the impact of the gaps between pontoons on the hydrodynamic response of the floating structure.

Table 1. Wet natural frequencies and damping ratios for the first two vibration modes, obtained using the modal analysis and experimental data.

Mode	Natural Frequency ω_i	Average Damping Ratio ζ_i
1	1.24 Hz	7.3%
2	2.40 Hz	6.2%

4.2. Extraction of Mode Shapes

Natural vibration analysis was performed by using the NASTRAN solver on a finite element (FE) structural model, which was constructed using beam elements that were rigidly connected to the pontoons. Massless and infinitely stiff shells of pontoons were constructed to act as an interface between the structural and fluid model for the hydroelastic analysis. The FE model is shown in Figure 2. The first three mode shapes we obtained of the vertically vibrating barge are rendered in Figure 3. The mode shapes agree with the experimental modal analysis, and they correspond to analytic-mode shapes of a vertically vibrating free-form beam with a constant cross-section.

Since the dry natural frequencies are not known from experimental analysis, the dry natural frequencies obtained using the finite element analysis (FEA) were compared with the analytically obtained results using Timoshenko's theory for beams with uniform cross-sections [1], and the results are presented in Table 2. To validate the beam model by comparing it to Timoshenko's theory for beams, FEA was performed on pontoon masses that were temporary brought upwards to the level of the beam axis. The natural frequencies obtained in this scenario match the analytically obtained values. It can be seen that the natural frequencies obtained numerically through the model with a proper mass distribution, as shown in Figure 2, are somewhat lower than the analytically obtained values. This was expected, due to the emphasised influence of the rotational inertia of heavy pontoons attached to the beams.

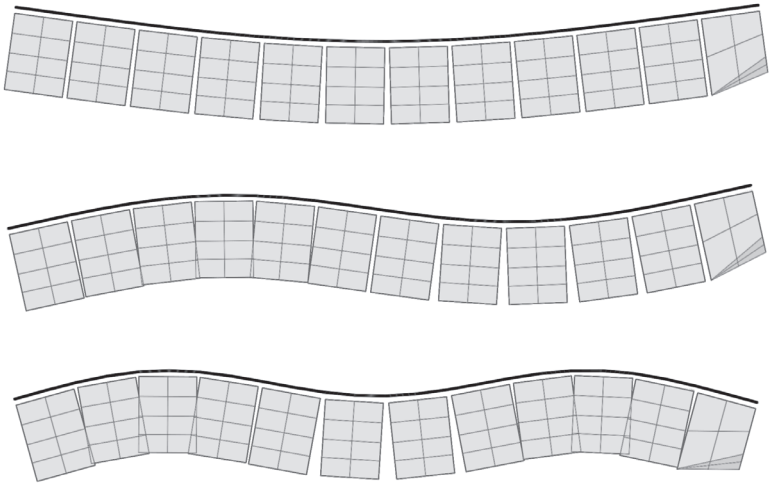

Figure 3. First three shape modes of vertical vibration of a flexible barge.

Table 2. Dry natural frequencies obtained analytically and numerically, in Hz; relative differences compared with the analytical solution.

Mode	Timoshenko	FEM, Mass Above Deck	Relative Difference	FEM, Figure 2	Relative Difference
1	1.367 Hz	1.389 Hz	+1.6%	1.295 Hz	−5.3%
2	3.769 Hz	3.823 Hz	+1.4%	3.346 Hz	−11.2%
3	7.389 Hz	7.487 Hz	+1.3%	5.900 Hz	−20.1%

4.3. Hydroelastic Simulations

Transient hydroelastic simulations were performed with the FineMarine CFD solver, based on the numerical calculations described in Section 2.4. The Navier–Stokes equations were solved with the arbitrary Lagrangian–Eulerian (ALE) formulation, so that the RBF interpolation algorithm can be used to deform the CFD mesh according to the deformation of the structure, as explained in Section 3. Central-difference space discretisation was employed, and a four-stage explicit Runge–Kutta scheme was applied for the temporal discretisation. Time stepping was controlled such that one vibration period was discretised in at least 120 steps, while ensuring CFL criteria and minimal continuity residuals. After testing multiple meshes, a fluid mesh was built using 1.7 million of hexahedral cells around the barge, with the domain big enough to properly damp radiated waves and to capture all flow characteristics around the vibrating barge. Gaps between the pontoons were meshed with 40 layers of cells, and the no-slip boundary condition was imposed along with the Menter's SST turbulence model. The structural modal damping ratio was set to 0.5% to include the damping caused by the hysteresis within the steel beams. The computational domain and the mesh refinement procedure were performed in similar way for the gapless monohull's structural simulation.

Free vibrations in numerical simulations were initialised by releasing the structure deformed in the form of the specific mode shape depicted in Figure 3. The first two modes of vertical vibrations were simulated separately without mixing. Each hydroelastic simulation included exclusively one chosen mode of vibration. When the simulation was started, the barge vibrated with the wet natural frequency, which was lower than the input dry natural frequency due to the effects of water flow. Additional verification of the coupled solver was also done in terms of comparing the wet frequencies and added

mass values obtained with the CFD to the values obtained with the surface panel method that uses distribution of singularities, i.e., sources of constant strength located on panels of the wetted surface [1]. The panel-method solution was obtained through the NASTRAN MFLUID solver on massless and infinitely stiff interface, which is presented in Section 4.2. These results are in agreement with the CFD results. The wet natural frequencies obtained from the experiment, CFD and FEM analysis is given in Table 3.

Table 3. Wet natural frequencies for the first two vibration modes, in Hz, obtained with different methods and models.

Mode	Experiment	CFD, Segmented	Relative Difference	CFD, Monohull	Relative Difference	FEM, Monohull	Relative Difference
1	1.24 Hz	1.26 Hz	+1.6%	1.12 Hz	−9.7%	1.02 Hz	−17.7%
2	2.40 Hz	2.54 Hz	+5.8%	2.33 Hz	−2.9%	2.48 Hz	+3.3%

The experimental values were bounded by the numerical ones. The natural frequencies of the segmented barge are somewhat higher than those of the monohull. For the numerical evaluations, the relative difference of the second natural frequency rose higher from the first natural frequency than the difference from experimental frequencies. Therefore, it may seem the CFD and FEM monohull simulations get close to experimental results. Nevertheless, the CFD segmented simulation yielded a consistent relative difference compared to the experiments. It should be noted that in the case of the segmented barge, the restoring stiffness was lower due to gaps between barge segments. In addition, the added mass of the segmented barge was lower than that of monohull due to the pressure interaction between the segmented walls.

The modal acceleration, velocity and amplitude of a mode under consideration were tracked over time. Small gaps between the pontoons limited maximum initial deflection, to avoid intersection between pontoons. The first vertical vibration mode was initialised using the deflection that the tip of the barge was raised by about 10 cm, similarly to the experimental free-decay tests. Figure 4 shows that the modal acceleration slowly decays. The expected decay is drawn with a dashed line, which is based on extracted the damping ratio from the experimental analysis (given in Table 1). By applying the logarithmic decrement method from Section 2.3 onto the data of the simulated modal accelerations, it can be seen that the damping ratio, ζ, for the first mode of vibration, fluctuated from 5.5% to 8.2% of the critical damping; i.e., the damping ratio varied in time. The values were somewhat larger in the first vibration periods, and the vibrations dampened more slowly later in time, i.e., for lower vibration amplitudes. The expected decay was based on averaged value of the damping ratio; therefore, the numerically obtained values agree on average with the experiment.

The simulation of the second vertical vibration mode was initialised similarly to the first simulation, and the deflection had to be smaller due more complex mode shape and gaps between pontoons. Figure 4 shows decaying modal acceleration for the second vibration mode. By using the logarithmic decrement method, it can be seen that the damping ratio for the second mode of vibration fluctuated from 5.2% to 6.6% of the critical damping, which is in agreement with the experiment.

Contour plots of the free surface elevation during the simulation are shown in Figures 5 and 6, for two modes of vibration, respectively. Wave elevation between the pontoon gaps is also visible from the profile view of the barge; see Figures 7 and 8.

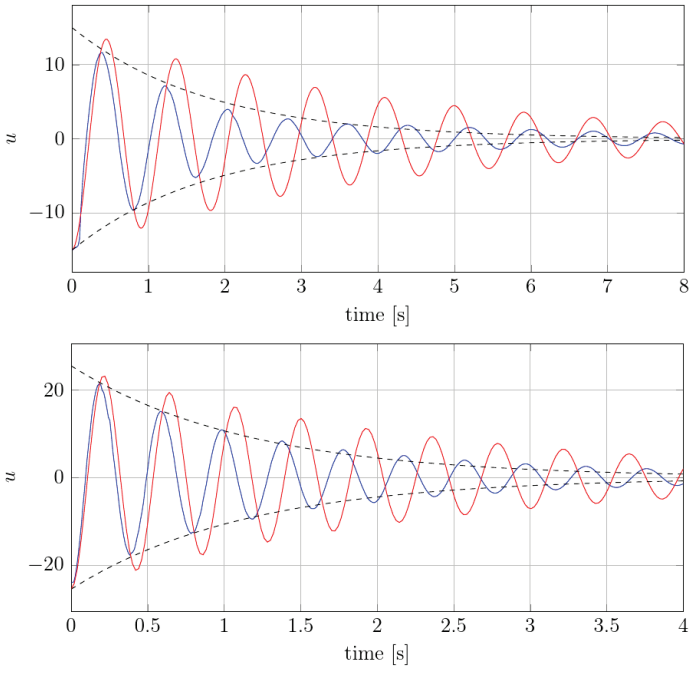

Figure 4. Modal acceleration of first (**top**) and second (**bottom**) vibration modes for the segmented model (blue) and monohull (red), compared to the decay based on experimental modal damping ratio (dashed line).

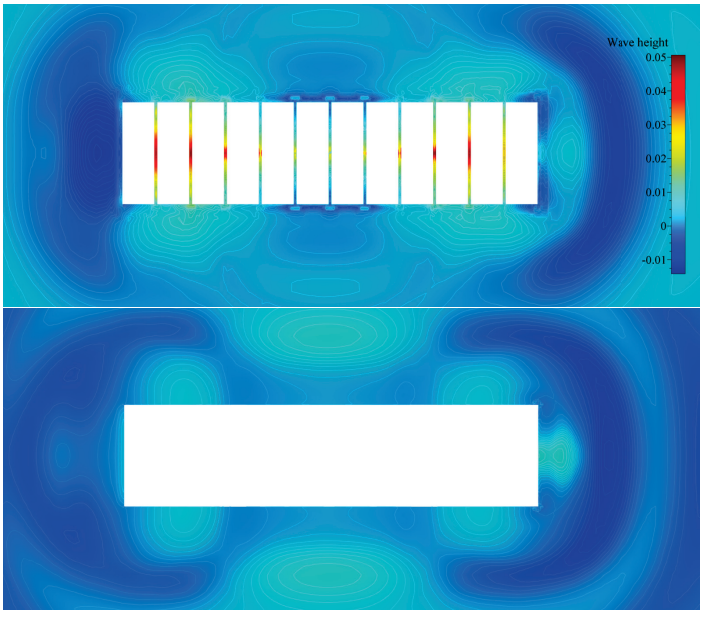

Figure 5. Top view of free surface elevation contours for the first mode of vertical vibration (segmented hull—top image, monohull—bottom image).

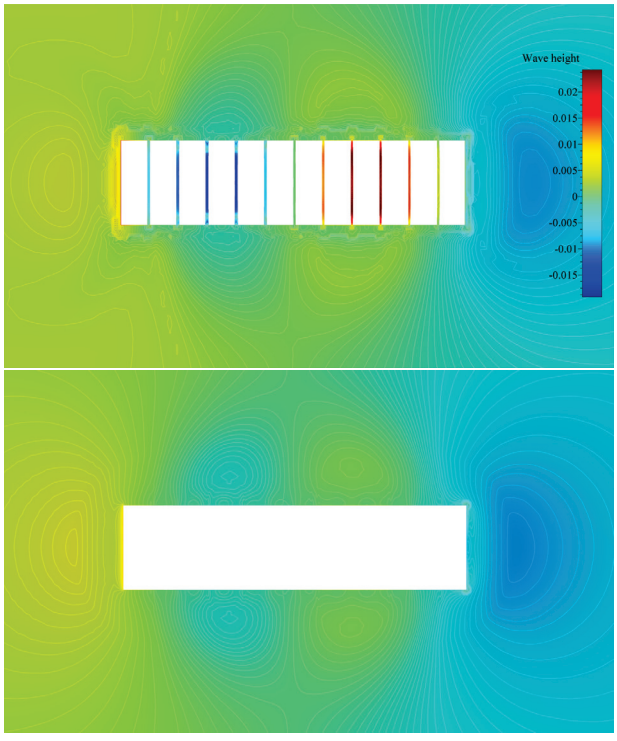

Figure 6. Top view of free surface elevation contours for the second mode of vertical vibration (segmented hull—top image, monohull—bottom image).

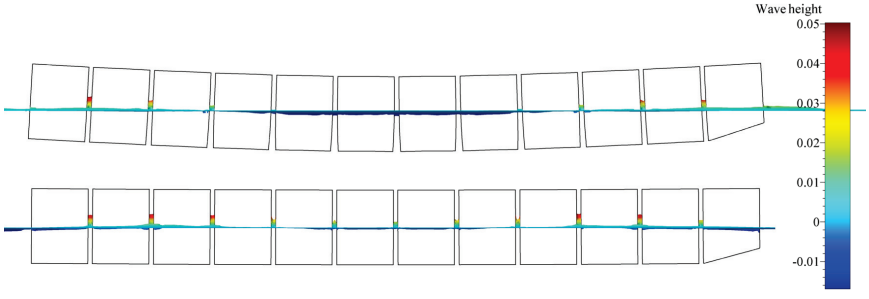

Figure 7. Profile view of free-surface elevation along the barge's length for the first mode of vertical vibration.

4.4. Discussion

By analysing Figures 5 and 6, it may be seen that relatively far from the structure, wave elevation values formed similar contours for both the segmented and monohull simulations. It may be seen that for both vibrating modes, the shape and elevation of generated waves were similar far from the structure. The radiated waves formed bumps and hollows at similar locations relatively far from the structure, with the amplitude of approximately one centimetre for both modes. For the first mode of vibration, Figure 5 shows that a wave formed at the fore and aft shoulders as barge ends rising upwards (see Figure 9), and the generated wave from the midsection of the barge propagated in the transverse direction. For the second mode of vibration, the radiated waves in Figure 6 are even more similar, and wave hollows and bumps follow the motion of the mode shape shown in Figure 8.

On the contrary, local wave generation is very complex in the vicinity of the vibrating segmented barge. The gaps generated trapped waves with amplitudes five times higher than those radiated from the structure. During a period of the vertical vibration, two effects are responsible for producing these localised waves that dissipate away from the structure. This localised 'pumping' effect is also visible in Figures 7 and 8. The first effect responsible for this phenomenon is the that the gaps change size and inclination during vibration. For example, a segment that is going upwards is gradually closing the gap at the keel, which creates gradient of the pressure in order to keep the incompressibility constraint (14) valid, which is pushing the fluid upwards. Similarly, the opposite holds when the structure is vibrating downwards, although the consequent negative elevation of the free surface is lower due to the smaller pressure gradient (at the free surface, the pressure value equals the ambient pressure). Figure 9 shows how the large pressure gradient creates large elevation of the free surface between gaps, and corresponding streamlines that verify the 'pumping' effect. The second effect responsible for the phenomenon is the tangential (wall–velocity) boundary condition imposed on moving walls, which pulls or pushes the water using friction. Other than those two effects, another typical hydrodynamic effect affects the hydrodynamic damping (e.g., vortex creation around corners, as seen in Figure 9). Since the hydrodynamic damping may be defined as the energy loss during a vibration period due to hydrodynamic effects, it can be concluded that the described high-pressure gradients and additional friction are responsible for additional hydrodynamic damping during vibration of a segmented barge, compared to the monohull barge.

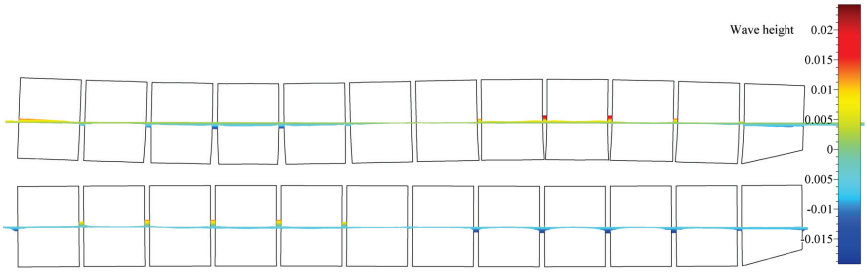

Figure 8. Profile view of free surface elevation along the barge's length for the second mode of vertical vibration.

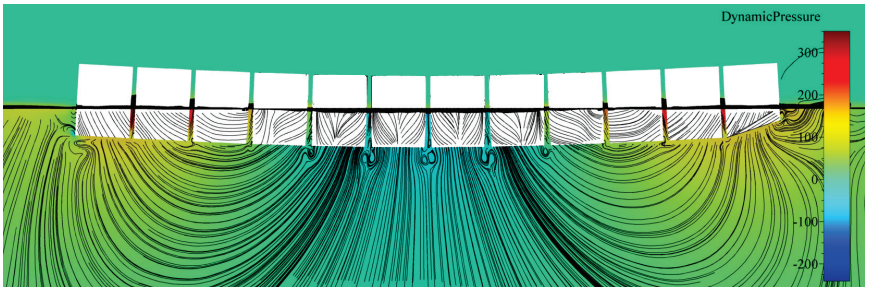

Figure 9. Section cut at the centreline, showing streamlines and the dynamic pressure field for the first mode of vertical vibration of the segmented barge.

5. Conclusions

Model tests of segmented barges with very-low-in-rigidity steel backbones are usually performed for validation of a numerical procedure for hydroelastic behaviour of very large ships. However, in numerical analysis, the segmented barge is usually considered as a monohull. For this reason, numerical analyses for a segmented barge and a monohull barge were performed by coupling fluid and structural solvers using the mode analysis.

An efficient weak coupling method was described, which transfers flow-solver results onto the structure described by its mode shapes, each time step. The proposed coupling method for the unsteady deformation of the structure, by using a time integration of the mode shape, is stable and significantly faster than resolving the whole structure each time step. The results of damping and added mass effects were validated, rendering the method feasible for simulating vibrations of complex ships and floating structures.

Secondly, the results of the hydroelastic behaviour of the segmented barge, compared to its monohull counterpart, have answered the questions on why model tests of segmented floating structures are characterised by large hydrodynamic damping. The 'pumping' effect, and the consequent generation of energy during a vibration period, is caused by the changing of gaps' shapes. The shrinking and expansion of gaps generates large pressure gradients and produces localised elevation of the free surface. In addition, more vortices form and wall-shear grows, which also contributes to large hydrodynamic damping of segmented floating structures compared to the monohulls. In comparison to segmented floating structures (e.g., wave-energy converters), the stiffness of the ship is much higher and ship deformations are much lower so that it is possible to make the connection between the segments watertight using simple means (e.g., sellotape) without affecting the global stiffness.

Author Contributions: Conceptualization, J.B., N.D. and Š.M.; methodology, J.B., N.D. and Š.M.; software, J.B.; validation, N.D. and Š.M.; formal analysis, J.B. and N.D.; investigation, J.B., N.D. and Š.M.; resources, J.B.; data curation, J.B., N.D. and Š.M.; writing—original draft preparation, J.B., N.D. and Š.M.; writing—review and editing, J.B., N.D. and Š.M.; visualization, J.B.; supervision, N.D. All authors have read and agreed to the published version of the manuscript.

Funding: This study has been fully supported by the Croatian Science Foundation under project IP-2020-02-8568.

Institutional Review Board Statement: Not applicable.

Informed Consent Statement: Not applicable.

Data Availability Statement: Not applicable.

Acknowledgments: This study has been fully supported by the Croatian Science Foundation under project IP-2020-02-8568.

Conflicts of Interest: The authors declare no conflict of interest.

References

1. Bašić, J.; Parunov, J. Analytical and Numerical Computation of Added Mass in Ship Vibration Analysis. *Brodogradnja* **2013**, *64*, 1–11.
2. Abd Samad, F.I.; Mohd Yusop, M.Y.; Shaharuddin, N.M.R.; Ismail, N.; Yaakob, O.B. Slamming Impact Accelerations Analysis On Small High Speed Passenger Crafts. *Brodogradnja* **2021**, *72*, 79–94. [CrossRef]
3. Kleivane, S.K.; Leira, B.J.; Steen, S. Development of a reliability model for crack growth occurrence for a secondary hull component. *Brodogradnja* **2023**, *74*, 99–115. [CrossRef]
4. Kim, S.W.; Lee, S.J. Development Of A New Fatigue Damage Model For Quarter-Modal Spectra In Frequency Domain. *Brodogradnja* **2020**, *71*, 39–57. [CrossRef]
5. Wenxi, L.; Huiren, G.; Qidou, Z.; Jingjun, L. Study On Structural-Acoustic Characteristics Of Cylindrical Shell Based On Wavenumber Spectrum Analysis Method. *Brodogradnja* **2021**, *72*, 57–71. brod72204. [CrossRef]
6. Jensen, J.J. *Load and Global Response of Ships*; Elsevier Ocean Engineering Series; Elsevier Science: Amsterdam, The Netherlands, 2001; pp. 268–271.
7. Storhaug, G. Experimental Investigation of Wave Induced Vibrations and Their Effect on the Fatigue Loading of Ships. Ph.D Thesis, Norwegian University of Science and Technology, Trondheim, Norway, 2007.
8. Storhaug, G. The measured contribution of whipping and springing on the fatigue and extreme loading of container vessels. *Int. J. Nav. Archit. Ocean Eng.* **2014**, *6*, 1096–1110. [CrossRef]
9. Norwood, M.N.; Dow, R.S. Dynamic analysis of ship structures. *Ships Offshore Struct.* **2013**, *8*, 270–288. 17445302.2012.755285. [CrossRef]
10. Blake, W.K.; Chen, Y.K.; Walter, D.; Briggs, R. Design and Sea Trial Evaluation of the Containership MV Pfeiffer for Low Vibration. *SNAME Trans.* **1994**, *102*, 107–136.

11. Colomés, O.; Verdugo, F.; Akkerman, I. A monolithic finite element formulation for the hydroelastic analysis of very large floating structures. *Int. J. Numer. Methods Eng.* **2023**, *124*, 714–751. [CrossRef]
12. Chourdakis, G.; Davis, K.; Rodenberg, B.; Schulte, M.; Simonis, F.; Uekermann, B.; Abrams, G.; Bungartz, H.J.; Cheung Yau, L.; Desai, I.; et al. preCICE v2: A sustainable and user-friendly coupling library. *Open Res. Eur.* **2022**, *2*, 51. [CrossRef]
13. Chen, Y.; Zhang, Y.; Tian, X.; Guo, X.; Li, X.; Zhang, X. A numerical framework for hydroelastic analysis of a flexible floating structure under unsteady external excitations: Motion and internal force/moment. *Ocean Eng.* **2022**, *253*, 111288. [CrossRef]
14. Huang, H.; Chen, X.-j.; Liu, J.-y.; Ji, S. A method to predict hydroelastic responses of VLFS under waves and moving loads. *Ocean Eng.* **2022**, *247*, 110399. [CrossRef]
15. Kashiwagi, M.; Kuga, S.; Chimoto, S. Time- and frequency-domain calculation methods for ship hydroelasticity with forward speed. In Proceedings of the 7th International Conference on Hydroelasticity in Marine Technology, Split, Croatia, 16–19 September 2015; pp. 477–492.
16. Seng, S.; Jensen, J.J.; Malenica, S. Global hydroelastic model for springing and whipping based on a free-surface CFD code (OpenFOAM). *Int. J. Nav. Archit. Ocean Eng.* **2014**, *6*, 1024–1040. [CrossRef]
17. Kumar Pal, S.; Iijima, K. Investigation of Springing Responses to High Harmonics of Wave Loads by Direct Coupling Between CFD and FEM. Volume 7: CFD and FSI. In Proceedings of the ASME 2022 41st International Conference on Ocean, Offshore and Arctic Engineering, Hamburg, Germany, 5–10 June 2022;. [CrossRef]
18. Kara, F. Time domain prediction of hydroelasticity of floating bodies. *Appl. Ocean Res.* **2015**, *51*, 1–13. j.apor.2015.02.001. [CrossRef]
19. Debrabandere, F.; Tartinville, B.; Hirsch, C.; Coussement, G. Fluid-Structure Interaction Using a Modal Approach. *J. Turbomach.* **2012**, *134*, 51043. [CrossRef]
20. Malenica, Š.; Molin, B.; Remy, F.; Senjanović, I. Hydroelastic response of a barge to impulsive and non-impulsive wave loads. In Proceedings of the 3rd International Conference on Hydroelasticity in Marine Technology, Oxford, UK, 15–17 September 2003; p. 9.
21. Piro, D.J.; Maki, K.J. Whipping Response of a Box Barge in Oblique Seas. In Proceedings of the 28th International Workshop on Water Waves and Floating Bodies, Marseille, France, 7–10 April 2013; pp. 173–176.
22. Bašić, J.; Degiuli, N.; Dejhalla, R. Total resistance prediction of an intact and damaged tanker with flooded tanks in calm water. *Ocean Eng.* **2017**, *130*, 83–91. [CrossRef]
23. Andrun, M.; Blagojević, B.; Bašić, J. The influence of numerical parameters in the finite-volume method on the Wigley hull resistance. *Proc. Inst. Mech. Eng. Part M J. Eng. Marit. Environ.* **2019**, *233*, 1123–1132. [CrossRef]
24. Andrun, M.; Blagojević, B.; Bašić, J.; Klarin, B. Impact of CFD simulation parameters in prediction of ventilated flow on a surface-piercing hydrofoil. *Ship Technol. Res.* **2021**, *68*, 1–13. [CrossRef]
25. De Boer, A.; van der Schoot, M.; Bijl, H. Mesh deformation based on radial basis function interpolation. *Comput. Struct.* **2007**, *85*, 784–795. [CrossRef]

Journal of *Marine Science and Engineering*

MDPI

Article

Comparative Study of Potential Flow and CFD in the Assessment of Seakeeping and Added Resistance of Ships

Ivan Sulovsky [1,*], Guillaume de Hauteclocque [2], Marilena Greco [3,4] and Jasna Prpić-Oršić [1]

[1] Faculty of Engineering, University of Rijeka, Vukovarska 58, 51000 Rijeka, Croatia
[2] Research Department, Marine & Offshore Division, 92800 Paris, France
[3] Department of Marine Technology, Norwegian University of Science and Technology, 7050 Trondheim, Norway
[4] CNR-INM, Institute of Marine Engineering, 00128 Rome, Italy
* Correspondence: isulovsky@riteh.hr

Abstract: The need for maritime freight transport of various goods has never been greater. Consequently, ships are designed with ever-increasing dimensions, with the emphasis, of course, on length. One of the many challenges in the design of large ships is the prediction of their behavior in waves, i.e., motions, and consequently, added resistance. In this paper, a comparative study of two numerical tools for estimating ship motions and added resistance is presented. The first tool is the well-established DNV's commercial seakeeping code Wasim, a weakly nonlinear potential flow (PF) solver based on a Rankine panel method. The other is the increasingly recognized open-source Computational Fluid Dynamic (CFD) toolkit OpenFOAM®, a viscous flow solver with a turbulence model; it is based on the finite volume method (FVM) combined with a volume-of-fluid (VOF) technique for sea-surface evolution. The study is carried out for two ship seakeeping cases in head-sea regular waves, respectively, without and with ship forward speed. The first case refers to a 6750 TEU containership scale model developed at the LHEEA laboratory in Nantes for a benchmark study, providing experimental data for all test cases. Pitch and heave response is calculated and compared with the experimental values. The second case refers to a KRISO container ship, an extensively researched hull model in ship hydrodynamics. In addition to the pitch and heave, added resistance is also calculated and compared with the experimental values. Hence, it provides a comprehensive basis for a comparative analysis between the selected solvers. The results are systematically analyzed and discussed in detail. For both cases, deterioration of the PF solution with increasing wave steepness is observed, thus suggesting limitations in the modeled nonlinear effects as a possible reason. The accuracy of the CFD solver greatly depends on the spatial discretization characteristics, thus suggesting the need for grid independence studies, as such tools are crucial for accurate results of the examined wave–body interaction scenarios.

Keywords: seakeeping; added resistance; potential flow; CFD

Citation: Sulovsky, I.; Hauteclocque, G.d.; Greco, M.; Prpić-Oršić, J. Comparative Study of Potential Flow and CFD in the Assessment of Seakeeping and Added Resistance of Ships. *J. Mar. Sci. Eng.* **2023**, *11*, 641. https://doi.org/10.3390/jmse11030641

Academic Editors: Nastia Degiuli and Ivana Martić

Received: 21 February 2023
Revised: 14 March 2023
Accepted: 15 March 2023
Published: 17 March 2023

1. Introduction

In ocean engineering, predicting seakeeping responses in high-amplitude waves is of high value for various design aspects. Avoiding unwanted motions and accelerations can result in significant savings in fuel, equipment damage, general comfort, etc. From a structural safety viewpoint, navigating in an extreme sea state can cause large vertical bending moments amidships for slender, long, ocean-going vessels. As for seakeeping performance, relevant wave-induced motions and scattering effects, for instance, lead to added resistance contributions. The adequate prediction of added resistance in waves enables for interventions in terms of reducing fuel consumption in the early stage of ship design. Today, the most common methods for the numerical estimation of ship motions and added resistance involve potential-flow three-dimensional (3D) or strip-theory codes within a perturbation approach. However, these methods cannot properly

capture all nonlinear effects relevant in rather steep waves [1]. The use of Reynolds-averaged Navier–Stokes (RANS) equations coupled with rigid body motion solvers can overcome the limits of the methods above, as it allows nonlinear effects associated with both potential- and real-flow effects to be accounted for. Numerical investigations of the seakeeping characteristics of floating objects in large waves with fully viscous CFD within a finite volume framework are still limited [2–5]; this is reasonably due to the high computational cost on one side and reliability issues on the other. A distinguishing challenge when dealing with high-amplitude body motions within CFD is the generation and application of an appropriate dynamic mesh strategy. This is especially crucial when targeting second- and higher order wave-induced loads, as they are smaller than linear loads and therefore more sensitive to numerical discretization strategies; one must note that they also represent a challenge for experimental studies—in fact, those in this context are somewhat limited. Gao et al. [6] compared and validated several dynamic mesh strategies, including the scenario of ship capsizing in regular beam-sea waves. For large amplitudes of motion, overset (chimera) grids seem to be the most appropriate. The concept behind the overset is to combine any number of independent computational domains with the motion pre-specified or computed for each individual domain. In computational marine hydrodynamics, this concept is a useful tool for evaluating, e.g., rudder–hull–propeller interaction, zig-zag maneuvers, or any other complex hydrodynamic scenarios involving large body motions. For instance, Galbraith and Boulogouris [7] simulated roll motions of a tumblehome hull undergoing a parametric resonance, which can result in very high roll angles depending on the hull geometry, level of damping, ship heave and pitch motions, and incident-wave features. The overset mesh technique has proved its robustness in numerous seakeeping numerical investigations [8] in which large amplitude motions are not restricted, as in more conventional morphing meshes. The price to pay for such a technique is the increased computational cost. Apart from the dynamic mesh strategy, simulating free-surface waves is by no means trivial in computational fluid dynamics. Challenges encountered in creating a numerical wave tank include a loss of wave height in the case of an insufficiently fine mesh (dissipative errors), inaccuracies in the wave-propagation mechanisms (dispersive errors), unwanted wave reflections at the outlet boundary, etc. Jacobsen et al. [9] provide substantial documentation in this field in the context of a publicly available toolbox for free surface wave generation and absorption in OpenFOAM® [10]. Furthermore, appropriate turbulence modeling needs to be addressed for wave generation if turbulence is expected to matter for the examined wave–body interaction problems. The most used turbulence models in marine applications are k-ε and k-ω SST [11]. However, with both models, numerical instability occurs with free-surface waves through the non-physical build-up of turbulent viscosity, thus creating high and unrealistic damping of the waves [12]. The overall influence of turbulence modeling in seakeeping simulations within CFD is speculative, since the pressure and velocity gradients in the flow are very high near the hull, making single-phase turbulence models rogue [13]. Moctar et al. [14] even suggest omitting fine boundary layers along the hull if viscous effects are to be neglected. However, further investigations are needed in this area. In the present paper, a seakeeping response assessment, with added resistance included, is performed for two ships for which model-test results are available. The first case concerns a 6750 TEU containership model with zero speed in head-sea regular waves, in which pitch and heave responses are analyzed. Preliminarily, a thorough investigation was performed regarding the mesh quality within CFD for the propagation of waves with a two-dimensional (2D) numerical wave tank; an assessment was performed for five different wave heights and keeping the wavelength fixed and equal to the ship length. The second case refers to the KRISO containership model advancing in head-sea waves. Both cases are investigated with two numerical tools for marine hydrodynamics: (A) the commercial code Wasim from DNV classification society, based on potential flow theory, i.e., a Rankine panel method, and including second-order nonlinear effects within a perturbation approach, hereafter briefly indicated as PF; and (B) the open source CFD toolkit OpenFOAM® based on the co-located

finite volume method (FVM), hereafter briefly indicated as CFD. This comprehensive study provides additional insights into the performance of these two hydrodynamic tools for estimating ship response and added resistance in waves, their shortcomings, and their advantages. The rest of this paper is structured as follows. In Section 2, the experimental setups and test matrices for the two studied cases are outlined. The two selected numerical tools are described in Section 3. In the same section, the incident-wave parameters for the first experimental case are used to carry out a systematic analysis to identify the grid size and time-step needed to limit the numerical errors of the CFD solver. The results from all seakeeping simulations are documented in Section 4, together with their comparison against the corresponding physical data, and the main conclusions are drawn in Section 5.

2. Benchmark Tests

2.1. 6750 TEU Containership

The experimental data for the first case presented in this paper originate from [15], which addresses the uncertainties of different numerical approaches for the evaluation of extreme vertical bending moments in ship structures. The experiment was conducted in the Hydrodynamic and Ocean Engineering Tank in The Research Laboratory in Hydrodynamics, Energy and Atmospheric Environment (LHEEA) in Nantes, France. The tank is 50 m long, 30 m wide, and with a water depth of 5 m. The ship model, a 6750 TEU containership at 1:65 scale with main dimensions given in Table 1, and the body plan and model are shown in Figure 1a,b, respectively. Figure 1b shows the same hull shape as in [15] but corresponds exactly to [16].

Table 1. Main dimensions of a 6750 TEU containership scale model.

	Units	Model	Full Scale
LPP, length between perpendiculars	m	4.41	286.6
B, breadth	m	0.615	40
T, draught	m	0.1843	11.98
Δ, deadweight	kg	312.61	85,849,972
LCG, longitudinal center of gravity	m	2.13	143.7
VCG, vertical center of gravity	m	0.256	16.66

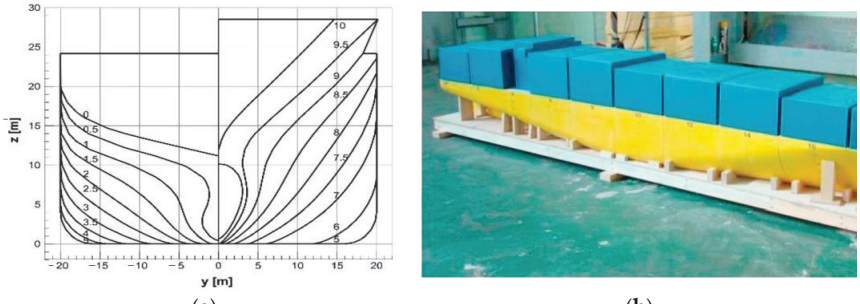

(**a**) (**b**)

Figure 1. Experimental setup of a 6750 TEU containership: (**a**) body plan; (**b**) actual model.

The prescribed regular head-sea waves are given in Table 2. With the intention of limiting excessive surge of the ship, soft mooring is imposed with a resulting surge natural period of 11.8 s. This is achieved using four springs, k_1, k_2, k_3 and, k_4, all of which have the same stiffness of 56 N/m. The angle α between pairs of springs at the bow and stern is equal to 45°. The mooring arrangement is shown in Figure 2.

Table 2. Wave conditions from 6750 TEU containership benchmark study (model scale).

Case Number	Wave Height H (m)	Wavelength λ (m)	Steepness H/λ %
1.	0.09	4.41	2.1
2.	0.17	4.41	3.8
3.	0.23	4.41	5.2
4.	0.38	4.41	8.7
5.	0.45	4.41	10.5

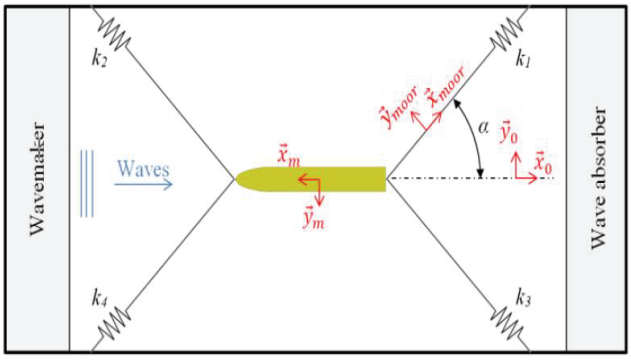

Figure 2. Top-view sketch of the mooring arrangement for a 6750 TEU containership.

2.2. KRISO Container Ship

The KRISO container ship (KCS) model [17] was conceived as a design of a modern container ship with a bulbous bow and tested in a towing tank by the Korea Research Institute for Ships and Ocean Engineering [18,19] to provide benchmark data for validation purposes. The prescribed regular head-sea waves are given in Table 3, while the main ship dimensions are documented in Table 4, with the body plan depicted in Figure 3. The entire set of experimental data is publicly available at [20]. No full-scale ship exists with this exact geometry. Note that the wetted surface S includes the wetted surface area of the rudder as the only appendage included in the experiments.

Table 3. Wave conditions for KRISO containership benchmark study.

Case Number	Wave Height H (m)	Wavelength λ (m)
1.	0.062	3.949
2.	0.078	5.164
3.	0.123	6.979
4.	0.149	8.321
5.	0.196	11.840

Table 4. Main dimensions of a KRISO containership model.

	Units	Model
L_{PP}	m	6.0702
B	m	0.8498
T	m	0.2850
Δ	kg	956
$LCB(\%L_{PP})$, *fwd+*	m	−1.48
VCG	m	0.378
S	m^2	6.697
U	m/s	2.017

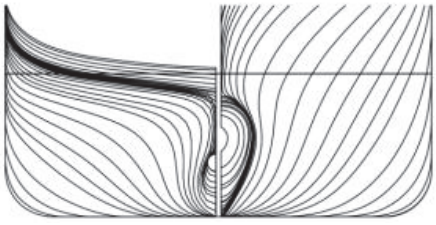

Figure 3. Body plan of a KRISO containership.

3. Numerical Methods

Details of the numerical features specific to PF and CFD are outlined in this section. The numerical schemes that were used are briefly described, followed by computational grid properties for each case. Regarding CFD, OpenFOAM® is an open-source type of software; hence, detailed information about the numerical set-up ensures the reproducibility of this study. Turbulence modeling is summarized for such applications with appropriate boundary conditions used.

3.1. Numerical Schemes—Potential Flow

The potential flow solver used in this study is the DNV's commercial code Wasim. It is a 3D panel method, distributing Rankine sources on the free surface as well as the body, and solves equations of motion in the time domain. It can be applied for ships of arbitrary speeds and shapes with linear or nonlinear motion and wave load analysis [21]. In PF theory, idealization is introduced as fluid being inviscid, irrotational and incompressible. Such idealizations significantly reduce the computational costs in seakeeping problems and are, therefore, one of the main tools for such tasks in marine applications. In the basic Wasim implementation, the restoring and Froude–Krylov pressures are computed at the instantaneous wetted body surface, which is defined by the rigid body motions and the incident waves; the radiation/diffraction effects are estimated within the linear theory, with the corresponding pressures integrated along the mean wetted surface, with the quadratic term in the Bernoulli equation included. The nonlinearities of the incident waves can be modeled using Stokes wave theory or Stream function; other nonlinear terms may be included in the free-surface elevation of the wave–body interaction problem. For the seakeeping of advancing vessels, both Neumann–Kelvin and double-body linearization can be used. In both cases examined in the paper, the Neumann–Kelvin linearization method is applied. The influence of the double-body linearization method was not investigated due to the slenderness of involved ship hulls. Comparative studies of these two methods are extensively documented in [22,23]. Added resistance in waves is calculated as a result of direct pressure integration in time. Temporal discretization within Wasim offers first- and second-order schemes, the choice of which depends on the so-called grid Froude number F_h, Equation (1).

$$F_h = \frac{U}{\sqrt{g h_x}} \tag{1}$$

where U stands for ship speed, g is the gravitational acceleration and h_x represents the smallest panel length in the longitudinal ship direction. For more detailed information on this, the reader is referred to [24]. Computational meshes are shown in Figure 4 for the 6750 TEU containership and KRISO containership, respectively. HydroMesh utility within Wasim offers fast, automatic meshing of both the hull and free surface.

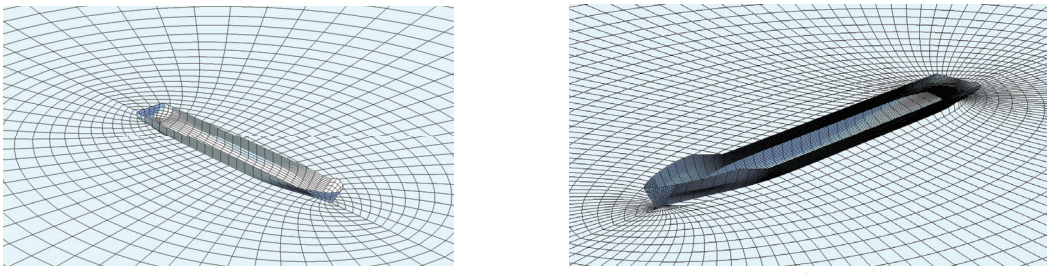

(**a**) (**b**)

Figure 4. Panel meshes for PF solution for both cases: (**a**) 6750 TEU containership mesh; (**b**) KRISO containership mesh.

3.2. Numerical Schemes—CFD

The CFD simulations in this paper are established using OpenFOAM®, in which the co-located finite volume method is applied to solve fluid mechanics equations. Fluid flow is governed by Navier–Stokes (NS) equations for incompressible flows, the continuity Equation (2) and momentum Equation (3):

$$\nabla \cdot \mathbf{u} = 0 \tag{2}$$

$$\frac{\partial \mathbf{u}}{\partial t} + (\mathbf{u} \cdot \nabla)\mathbf{u} - \nu \nabla^2 \mathbf{u} = -\frac{1}{\rho}\nabla p + \mathbf{g} \tag{3}$$

where **u** is the local fluid velocity. The LHS of the NS equation contains the total derivative, i.e., the change of velocity in time, convective term and viscous term, respectively. ∇p is the pressure gradient, **g** is the gravitational acceleration and ν stands for effective kinematic viscosity. For solving these equations, the *interFoam* solver is engaged for two incompressible, isothermal immiscible fluids (water and air). The air–water interface is modeled using the *Volume of Fluid* method (VOF), in which indicator function α is introduced into the partial differential equations. The α function represents a scalar field that enters the NS equations through density ρ and effective kinematic viscosity ν, as depicted in Equations (4) and (5), respectively.

$$\rho = (1 - \alpha)\rho_{air} + \alpha\rho_{water} \tag{4}$$

$$\nu = (1 - \alpha)\nu_{air} + \alpha\nu_{water} \tag{5}$$

The MULES algorithm [25] is used for the bounding of α with the conservation equation. For temporal discretization, the Crank–Nicolson scheme is applied with a coefficient of 0.9, which is a second-order time scheme suitable for such transient problems. The first-order scheme is skipped since it is prone to excessive numerical diffusion. Convective terms are solved with the linear scheme that limits towards upwind, i.e., the direction of the flow in regions of strong gradients. Other gradient terms, i.e., diffusive terms, are discretized with Gaussian linear interpolation. The pressure–velocity coupling is resolved using the PIMPLE algorithm with four iterations per time-step in total, two for pressure residual and two for a momentum matrix. For the hydro-mechanical coupling of the rigid body motions of the ship and fluid flow, the six degrees of freedom solver is employed with imposed restrictions for sway, yaw, and roll.

3.2.1. Two-Dimensional Numerical Wave Tank

To ensure that the selected CFD solver can adequately generate and simulate the incident regular waves required for the seakeeping analysis, a 2D numerical wave tank with no body is preliminarily examined. The length of the tank is obtained from [26] and the height from [27]. The computational grid is created using *blockMesh* and *topoSet* tools within OpenFOAM®, setting the breadth (i.e., the domain size normal to the flow motion)

equal to one-cell size and using proper boundary conditions to ensure two-dimensional wave conditions. Due to the reduced number of cells, this procedure provides results within minutes. Relaxation zones [9] are employed to tackle the problem of wave reflections at the outlet and artificial velocities at the inlet during wave build-up. The length of the relaxation zones is determined as a function of the wavelength λ of the targeted generated waves, as proposed in [26]. The second-order Stokes wave model is used as input for the wave kinematics. Five different wave heights are tested at a given λ, corresponding to the experimental waves listed in Table 1. To measure the simulated wave height, a virtual wave gauge is placed at a longitudinal distance from the wave-generation side that corresponds to the forward perpendicular of the ship model (when the seakeeping simulations are performed); this position is hereafter indicated as L_{PP}. The main individual zones of the numerical wave tank are depicted in Figure 5.

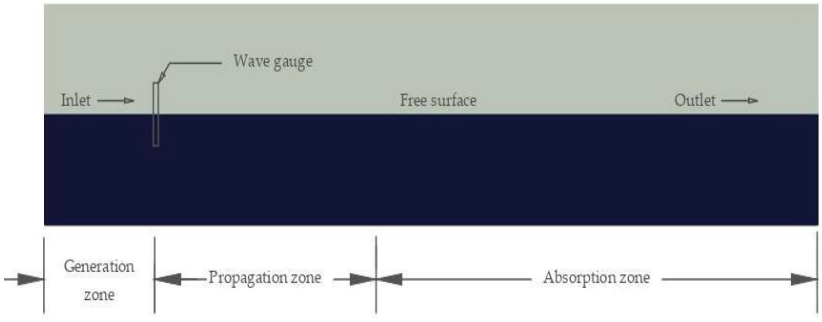

Figure 5. Schematic representation of zones in CFD numerical wave tank.

The main objective of this wave study is to determine the spatial and temporal discretization suitable for accurate and efficient simulations of wave propagation, given the selected wave parameters. Variables to which wave propagation is sensitive include: the number of cells per wave height, number of cells per wave length, and the time-step of the simulation. Since all wave conditions have the same wave length, only the variation of the cells per wave height is investigated. In terms of numerical stability, the time-step Δt should be chosen so that the Courant number Co, Equation (6):

$$Co = \frac{v_i \Delta t}{\Delta x_i} < 1 \tag{6}$$

where v_i is the local fluid velocity and Δx_i is the local cell size in the x direction. Here, to reduce the numerical dissipation at the free surface, the Courant number is kept below 0.2. As for the number of cells per wave height N, three grid densities are examined while keeping the Courant number at the free surface equal to 0.2, so the time-step is modified consistently. Figure 2 confirms the significant influence of N for the development of the free surface wave prescribed for case 3 (see parameters in Table 1) in terms of the wave elevation at the selected virtual gauge. Time histories appear very coarse due to the plotting time interval set to 0.2 s. Asymmetry between wave trough and crest also appears, which happens due to nonlinearities in free surface flows for the examined wave parameters. Turbulence modeling was not employed, since turbulence effects are expected to play a negligible role for these scenarios of wave propagation, as we have in mind sufficiently long gravity-driven waves. Nevertheless, it was also investigated, as seen in Figure 6. After 17 s of simulation time, the damping of the wave height becomes more exaggerated for the targeted wave height of 0.23 m.

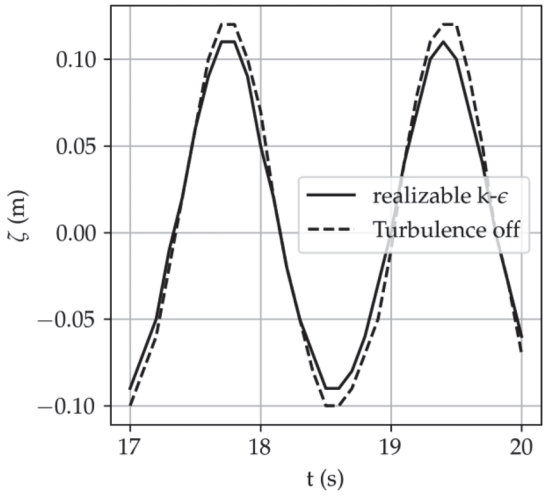

Figure 6. Influence of realizable k-ε turbulence model on wave height dissipation at wave gauge at *LPP*, after 10 oscillation periods and for $N = 8$.

The issue of the artificial damping of the wave height relates to the instability of the turbulence model and is expected to be much more relevant for simulations of longer duration and irregular waves. Therefore, one needs to take proper care of the turbulence modeling in such conditions. One of the possible solutions within OpenFOAM is to implement one of the stabilized turbulence models from Larsen and Fuhrman [12]. In this study, stabilized turbulence models were not implemented.

Following this parametrical study, eight cells per wave height were confirmed to be sufficient for wave propagation and are adopted as a minimum value of cell number per wave height further in the paper. In the horizontal wave-propagation direction, the guideline from Moctar et al. [14] for the coarsest discretization of at least 30 cells per wavelength is far exceeded. For the quantification of wave-height propagation error in a wave tank, the procedure from [28] is adopted. The maximum, η_{max}, and minimum, η_{min}, values of the wave elevation are estimated at the position of $x = LPP$ in a time interval nT, equal to $n = 7$ wave periods T, when nearly steady-state conditions are established. This is used to estimate the wave height in each oscillation period kT, with $1 \leq k \leq n$, as shown in Equation (7). The mean value of the wave height is calculated according to Equation (8), and the percentage error is estimated using Equation (9), where H is the targeted wave height given in Table 1 for each wave case. Corresponding results for $N = 8$ are given in Table 5. while the influence of N on the wave amplitude error is documented in Figure 7 for case 3.

$$H_{LPP,k} = [|\eta_{min}| + \eta_{max}]_{LPP,k} \tag{7}$$

$$\overline{H_{LPP,n}} = \frac{\sum_{k=1}^{k=n} H_{LPP,k}}{n} \tag{8}$$

$$e = \frac{\overline{H_{LPP,n}}}{H} \cdot 100 \tag{9}$$

Regarding the possible errors associated with the temporal discretization, i.e., time-step, three values are examined with respect to the wave period: $T/200$, $T/400$, and $T/600$. Since the benchmark cases involve almost the same wave period, the temporal discretization analysis is only examined for case 3. The procedure is the same as for spatial discretization, i.e., it uses the error in the wave height at x = *LPP*. The results are documented in Table 6.

Table 5. Wave propagation errors due to spatial discretization with eight cells per wave height.

Case Number	$\overline{H_{LPP,n}}$ (m)	e (%)
1.	0.086	4.28
2.	0.162	4.37
3.	0.22	3.12
4.	0.37	2.81
5.	0.45	2.52

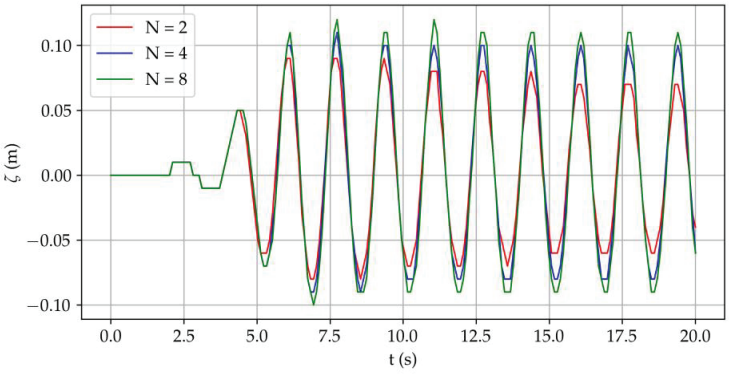

Figure 7. Influence of a number of cells per wave height, N, on wave dissipation for case 3, as defined in Table 1.

Table 6. Wave propagation errors due to temporal discretization for case 3.

Case Number	$\overline{H_{LPP,n}}$ (m)	e (%)
$T/200$.	0.222	3.32
$T/400$.	0.222	3.17
$T/600$.	0.222	3.07

Sensitivity due to time-step size in these ranges is negligible, while the number of cells per wave height has much greater influence over wave propagation within the finite volume framework. Considering the presented results of this wave study, values of eight cells per wave height and a time-step of $T/400$ are obtained as numerical guidelines for the modeling seakeeping response in OpenFOAM®. A computational grid with refinement zones within free surface for case 5 is shown in Figure 8.

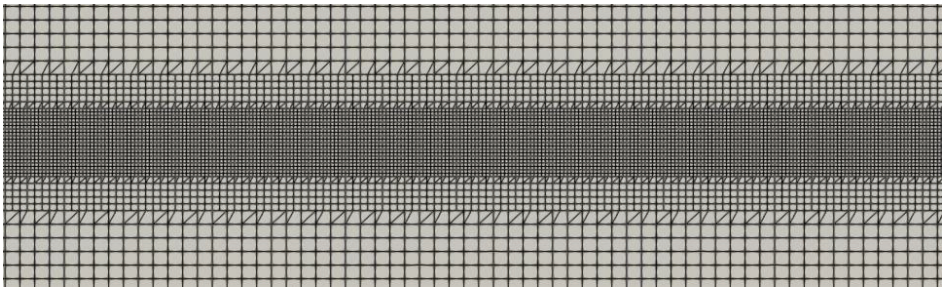

Figure 8. Refinement at the free surface in 2D CFD numerical wave tank.

Case 5 corresponds to the steepest incident-wave scenario examined. In this case, wave breaking is noticed with features similar to spilling breakers, as documented in Figure 9.

The breaking itself is purely numerical, since the wave parameters are far from the wave breaking criteria of $H/\lambda > 0.142$.

Figure 9. Mild wave breaking noticed in the CFD simulations with $H = 0.43$ m.

3.2.2. 6750 TEU Containership: Computational Grid, Linear Solvers and Boundary Conditions

Regarding the PF setup, details are outlined in Section 3.1. Setting up the computational grid for CFD is usually followed by discretizing the hull model into the appropriate format beforehand. The STL (stereolithography) format of the file is chosen, in which the hull surface geometry is split into a series of linked triangles that encloses a watertight volume object. For the case of the 6750 TEU containership, container stackings are also included but with a simplified geometry in order to reduce unwanted sharp edges. Green water protection is also accounted for at the forecastle, which will likely decrease the overflow volume of the water fraction on the deck. The STL geometry of the hull model is shown in Figure 10. No appendages are included in both experimental and numerical models. Hull models for both cases are available online as a Supplementary Material for reproduction of the results.

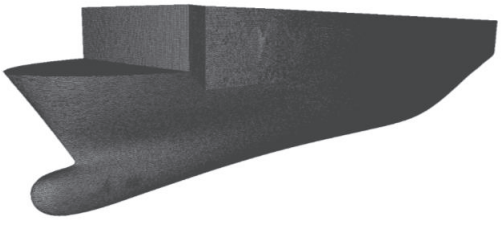

Figure 10. STL hull model of 6750 TEU containership for CFD simulations.

Volume mesh is constructed with the *blockMesh* tool and consists of regular polyhedron cells with an aspect ratio of approximately 1, since it is an intrinsic requirement for overset interpolation. The length of the domain is set to be 5.5λ, while breadth and height are 2λ in total, with λ being the incident wavelength. The relaxation zones are the same as described in Section 3.2.1. Imposing relaxation zones on the sidewalls is skipped because the simulation duration is predicted not to be long enough to capture reflections from the diffracted waves of the ship motions. Since the overset mesh technique is adopted for this case, two separate meshes must be constructed and then coupled through interpolations and information exchange. The *SnappyHexMesh* and *topoSet* tools are used for refinements in the relevant regions. The global arrangement of the computational domain is depicted in Figure 11 with the nomenclature of boundary faces. The background mesh is colored in blue, while the overset mesh is in yellow.

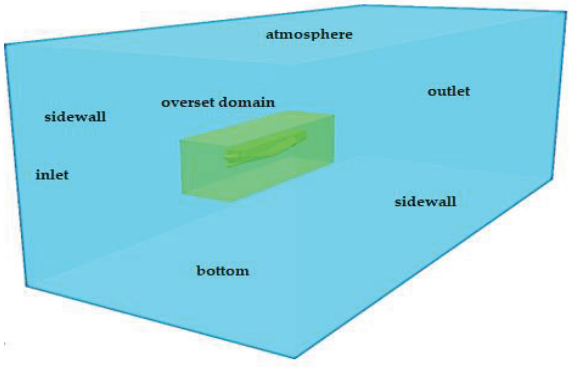

Figure 11. CFD computational domain with relevant boundary faces.

The origin of the coordinate system is located at the intersection between the aft perpendicular of the ship and the free surface for calm water conditions. Particular attention is dedicated to the overlapping region of the overset and background meshes. The connection between these regions is obtained through numerical interpolation, in which the user can choose several numerical schemes for interpolation. In this work, the inverse-distance weighted interpolation method is selected. Detailed numerics and performances of overset interpolation strategies within OpenFOAM® are covered in [29]. The refined mesh in the vicinity of the hull can be seen in Figure 12.

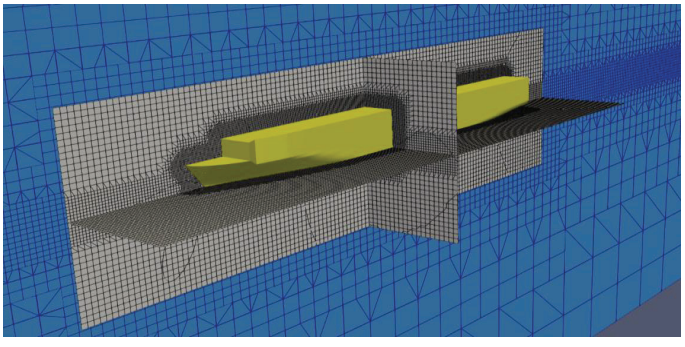

Figure 12. CFD mesh in the vicinity of the 6750 TEU containership.

For the closure of NS equations, a realizable k-ε turbulence model is applied. Boundary conditions specific for wave applications are set for velocity and phase fraction field at the inlet and outlet. The boundary condition for the pressure is the same at the inlet and outlet to correct the pressure gradient accordingly, so that the flux on the boundary is specified by the velocity boundary condition. The slip boundary condition is imposed at both sidewalls, while wall functions are applied to the hull surface. Regarding the mesh size, approximately 4 to 5 million cells are generated for computation for every benchmark case. The leading concept for mesh generation is the minimum of eight cells per wave height, as shown in Section 3.2.1. The entire computational domain is shown in Figure 13, where intense refinements can be seen in the free-surface region, and in the vicinity of the hull, where high gradients of velocities and pressure are expected.

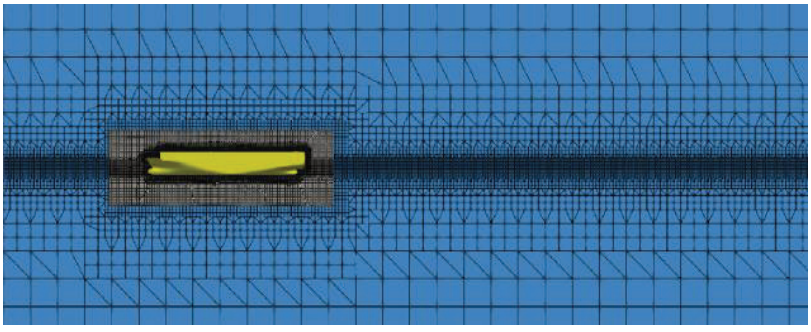

Figure 13. CFD computational domain with refinements.

The time-step for every case is set to 0.005 s, ensuring that the local Courant number is less than 0.2 in the free surface area. All calculations are made on an HPC cluster, most often on eight nodes with 24 cores each, making 192 physical cores available for computation. For the decomposition method, the scotch method is used, where the same number of computational cells are assigned to each physical core. Regarding linear solvers, for solving large sparse matrices that are yielded from a FV mesh, a conjugate gradient (CG) method is chosen with a Cholesky preconditioner. Residual tolerance is set to 1^{-8}. Velocity components and turbulence terms are solved using a smooth solver, i.e., Gauss–Seidel smoother with a residual tolerance of 1^{-8}.

3.2.3. KRISO Containership: Computational Grid, Linear Solvers and Boundary Conditions

Numerical details for the PF solution are listed in Section 3.1. For CFD, the overset approach is skipped, presuming that, due to the lower wave heights, the deforming grids would be sufficient. Moreover, wave damping along the tank differs from the first case. The damping itself is modeled as an explicit damping force applied to the momentum equation proportional to the momentum of the flow in the direction of gravity. For detailed information on this, the reader is referred to [30]. As the first condition of the experimental study of the KRISO case includes calm water resistance with free sinkage and trim, computational grids are adequately built for the calm water and waves scenarios. The grid for the calm water condition is outlined first. For this case, the computational domain is modeled for only half of the ship, thus imposing a symmetric boundary condition, which coincides with the vertical symmetry plane of the center line of the ship. The domain extents are according to ITTC standards [31]. The boundary faces are of the same topology as in Figure 8, except for the omitted overset region. Numerical schemes are the same as those depicted in Section 3.2, except for the calm water condition, where an implicit Euler scheme is chosen for temporal derivatives. The thickness of the boundary layer in the grid is equal to 18.5 mm with an expansion ratio of 1.5, which ensures the average value of y^+ on the hull of approximately 40. These values are determined based on the author's previous experience with such calculations. The K-ω SST turbulence model is applied for calm water conditions, where turbulent kinetic energy k for the far-field boundary conditions is specified as:

$$k = \frac{3}{2}\left(U_{fs}I\right)^2 \tag{10}$$

U_{fs} stands for free stream velocity and I is the turbulence intensity, which is assumed at 3%. The specific dissipation rate is defined following the guideline from Eça and Hoekstra [32]:

$$\omega = 10\frac{U}{L_{PP}} \tag{11}$$

where L_{PP} is the length between the ship perpendiculars. The realizable k-ε turbulence model is chosen for wave conditions, since the dissipation and dispersion errors in the wave

propagation are sufficiently small for short-duration simulations including regular waves if compared to the k-ω SST model. It is assumed that using different turbulent models will not affect any of the physical quantities being investigated in the paper, i.e., rigid body motions and second-order longitudinal force (added resistance in waves). Computational grids are shown in Figures 14 and 15 for calm water and wave conditions, respectively. For the wave application, the mesh in the free-surface zone is refined in horizontal and vertical directions, thus drastically increasing the number of cells. As for the linear solvers, for asymmetrical matrices (turbulence terms, velocity components and α), the setup is the same as depicted in Section 3.2, while for symmetrical matrices, i.e., pressure equation, a Generalized Geometric–Algebraic multigrid solver (GAMG) is chosen with a Gauss–Seidel smoother with a residual tolerance of 1^{-7}. Computational grids for the KRISO containership are outlined in Figures 14 and 15.

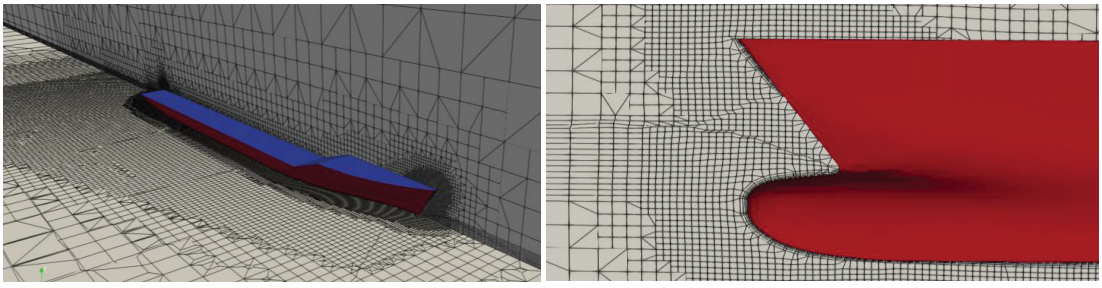

(**a**) (**b**)

Figure 14. CFD computational domain of the KRISO containership in calm water conditions: (**a**) Kelvin wake refinements; (**b**) boundary layer.

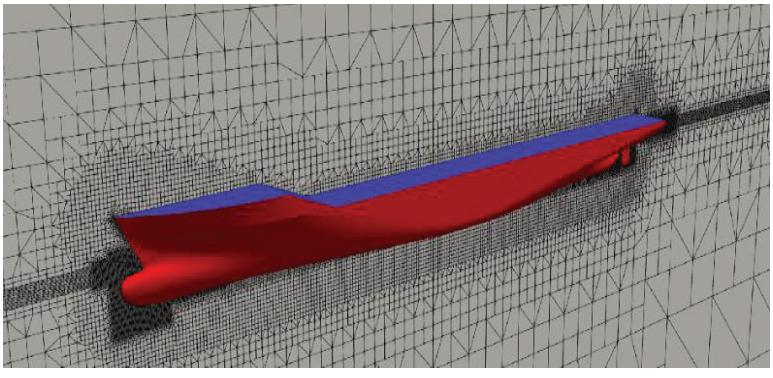

Figure 15. CFD global computational grid for the KRISO containership in wave conditions.

4. Results and Discussion

The results of the simulations for the examined ship seakeeping cases are outlined in this section. Post-processing of the CFD results is also carried out using open-source tools, namely paraView® for visualization and python Spyder for Fourier transformations and plots.

4.1. Heave and Pitch Response of the 6750 TEU Containership

The heave and pitch response for the 6750 TEU containership are examined in this section. Heave amplitude z is made nondimensional by the wave amplitude ς, while the pitch amplitude θ is normalized with wave number k multiplied by wave amplitude. The heave results from PF and CFD are plotted in Figure 16, showing a drastically different trend

of the heave from the two codes. The CFD results indicate a minimum with the unusually low response of the heave for H = 0.17 m, while the PF results predict a monotonous decrease with the wave height. For the two largest wave heights, the heave response from Wasim is significantly lower than from the CFD. Experimental data for heave motion are not shown since they are omitted even in the benchmark study due to insignificantly low amplitudes. However, the results are shown in Figure 16. Figure 17 documents the nondimensional amplitude of pitch for all results. Regarding CFD, overprediction of the pitch motion appears for H = 0.17 m, while the experimental response is underestimated for the lowest wave condition. The solution from the potential-flow solver shows a significant reduction in accuracy for almost all wave conditions, except for the lowest wave case.

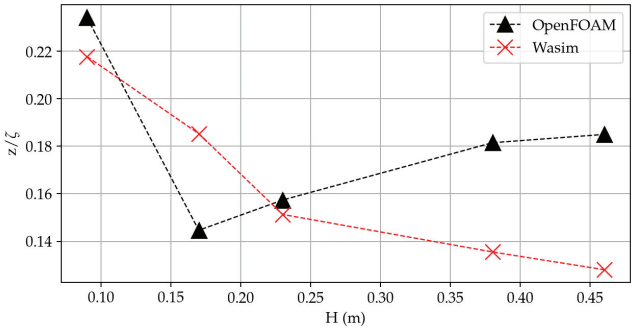

Figure 16. The nondimensional amplitude of heave response for the 6750 TEU containership.

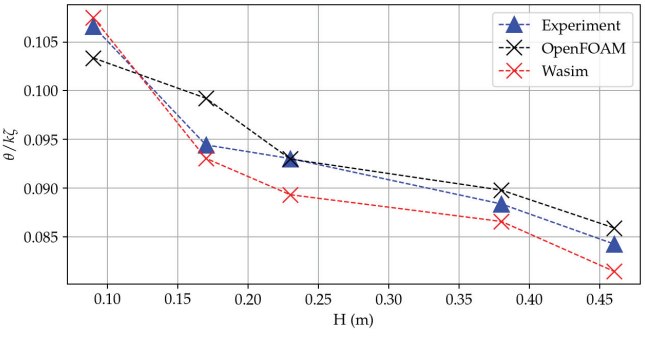

Figure 17. The nondimensional amplitude of pitch response for the 6750 TEU containership.

The quantitative difference of the nondimensional pitch amplitudes from the experiment is listed in Table 7, while it is graphically shown on a bar diagram in Figure 18.

Photos from the experiment compared with snapshots from OpenFOAM are shown in Figure 19 for case 5. As can be seen, both results indicate the occurrence of substantial water on deck. Therefore, pitch motion is influenced by this effect, which can be seen in Figure 20 with magnification over the area of the bow emerging from the water. Clearly, CFD can capture some of these effects; however, for a more accurate solution, the grid density above the freeboard, along with the appropriate multiphase solver that reduces smearing of the free surface, should be considered. One of these solvers is implemented in OpenFOAM, which is based on the more accurate reconstruction of the face fluxes for the cells containing the interface [33].

Table 7. Difference of nondimensional numerical and experimental pitch amplitudes for the 6750 TEU containership.

***H*, m**	**0.09**	**0.17**	**0.23**	**0.38**	**0.46**
OpenFOAM, %	3.06	5.08	0.05	1.60	1.96
Wasim, %	0.82	1.46	3.9	2.03	3.33

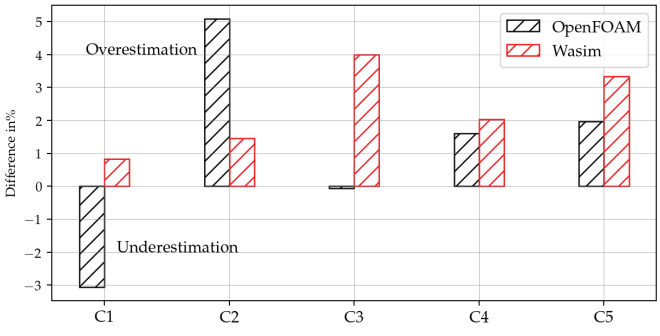

Figure 18. Difference of numerical and experimental nondimensional pitch amplitudes the 6750 TEU containership.

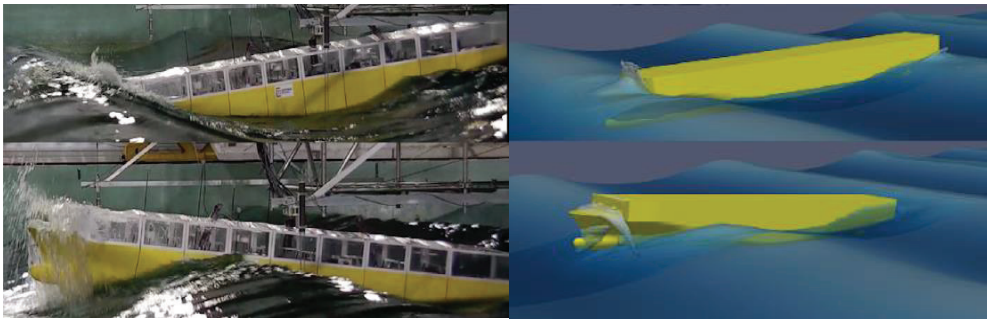

(**a**) (**b**)

Figure 19. 6750 TEU containership in wave case 5. (**a**) Experiment photography; (**b**) OpenFOAM snapshot.

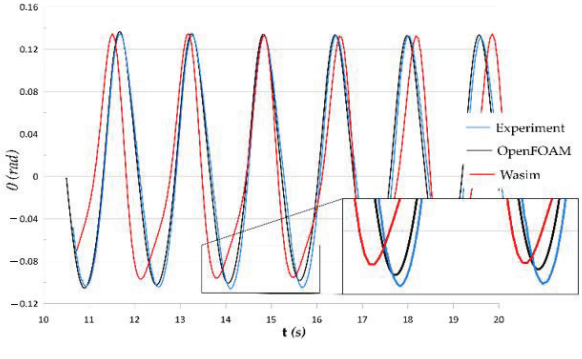

Figure 20. Time signals of pitch motion from experiment and numerics for H = 0.46 m for the 6750 TEU containership.

4.2. Calm Water Resistance with Free Sinkage and Trim of KRISO Containership

The results of calm water resistance with the free sinkage and trim of the KRISO containership are outlined in this section. In Figure 21, the sum of pressure and viscous components is shown as a blue line, i.e., total force and experimental data (EFD) in red. Furthermore, the isolated viscous component is compared with the ITTC 1957 correlation line in Equation (13). The values of the forces are presented in a nondimensional manner with resistance coefficient C_T, Equation (12), in which R_T stands for total resistance, **r** being the fluid density, U the speed of the ship and S_0 the wetted surface area at rest:

$$C_T = \frac{R_T}{0.5\rho U^2 S_0} \tag{12}$$

$$C_F = \frac{0.075}{(log_{10}R_e - 2)^2} \tag{13}$$

Re stands for Reynolds number and is equal to 1047×10^7 for model scale.

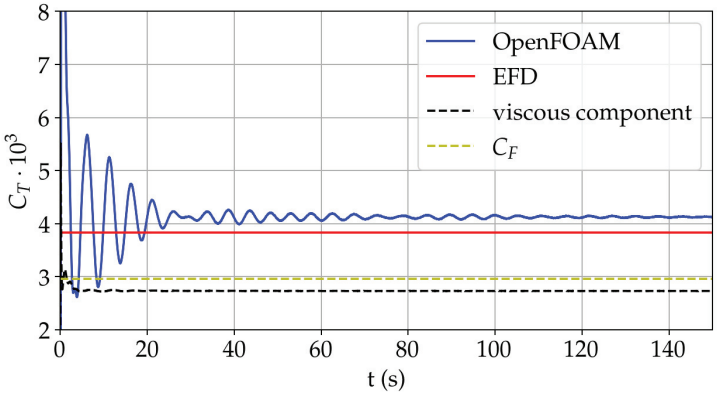

Figure 21. Time histories of horizontal forces on the KRISO containership in calm water and $Re = 1047 \times 10^7$.

It is important to point out that the ITTC empirical formula is for an equivalent smooth plate in turbulent flow conditions. It is reasonable for the ship hull to have a larger frictional coefficient due to its 3D features. Their comparison would indicate a small form factor of about 0.075, which is consistent with a slender ship hull. The numerical results from Figure 21 are summarized in Table 8, where C_T is the resistance coefficient, θ_t is the trim angle in degrees, and z_s is the sinkage in meters, normalized with L_{PP}.

Table 8. Results of the calm water resistance for the KRISO containership.

$R_e = 1047 \times 10^7$	C_T	θ_T	z_s/L_{PP}
CFD	3.835	−0.152	−0.001
EFD	4.096	−0.165	−0.002
(EFD/CFD)·100%	6.372	7.87	50.771

Aside from sinkage, the results agree well with the experiment following the assumption that the coarse mesh adopted for this study yields a high discrepancy of the sinkage.

4.3. Heave, Pitch and Added Resistance of KRISO Containership

The results of the heave, pitch and added resistance of the KRISO containership are outlined in this section. They are presented following the convention of the experiment; raw

signals are processed via Fourier transforms to evaluate the n-th harmonic amplitude for one encounter period T_e, see Figures 22–26. Furthermore, transfer functions are graphically shown to satisfy the more conventional presentation. Regarding the fact that the PF tool, being a seakeeping solver, does not provide calm water resistance, the calm water component of the total resistance coefficient in Equation (12) for Wasim is taken from CFD results. Guidelines for the Fourier transform of the signals are given in [24].

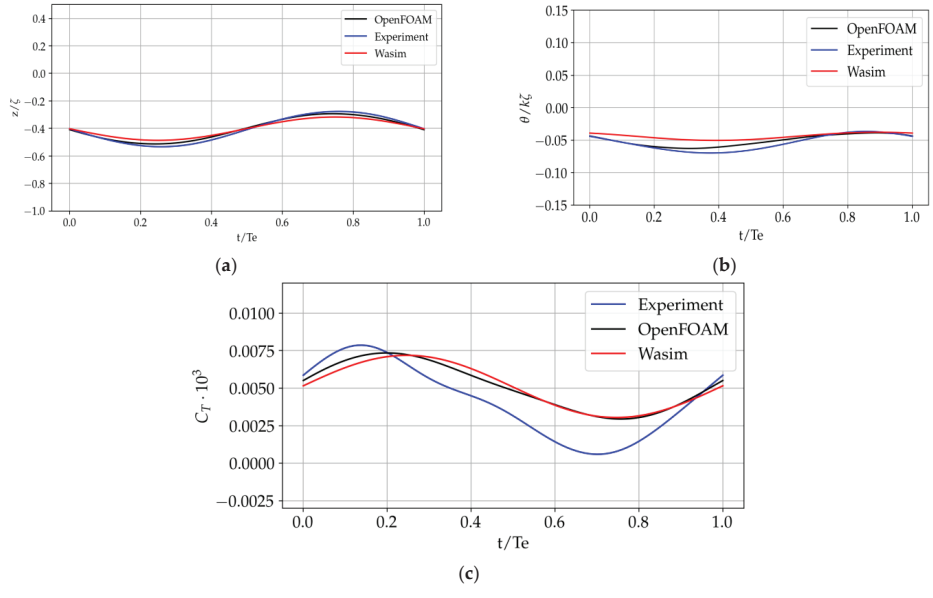

Figure 22. Time histories for case 1 of the KRISO containership: nondimensional (**a**) heave, (**b**) pitch, (**c**) total resistance.

The transfer functions of heave and pitch along with the total resistance coefficient are plotted in Figures 27–29, in which the transfer function is estimated as a sum of the motion amplitude in a stable range of the simulations. Discrepancies with the experimental data are summarized in Tables 9–11 with associated bar diagrams in Figures 30–32.

Table 9. Difference of numerical and experimental heave transfer functions for the KRISO containership.

***H* (m)**	**0.062**	**0.078**	**0.123**	**0.149**	**0.196**
OpenFOAM, %	−14.33	−26.83	−3.76	−0.42	+0.62
Wasim, %	−33.81	+25.12	−31.59	−9.75	−0.348

Table 10. Difference of numerical and experimental pitch transfer functions for the KRISO containership.

***H* (m)**	**0.062**	**0.078**	**0.123**	**0.149**	**0.196**
OpenFOAM, %	−30.41	+26.46	−10.21	+2.40	+2.09
Wasim, %	−36.20	+56.85	−38.62	−36.42	−31.76

Table 11. Difference of numerical and experimental total resistance coefficients for the KRISO containership.

***H* (m)**	**0.062**	**0.078**	**0.123**	**0.149**	**0.196**
OpenFOAM, %	−40.51	−38.82	+19.61	−16.20	−0.79
Wasim, %	−44.36	−40.69	n.a.*	+22.64	+12.76

* Wasim results non applicable due to resonance in measurements.

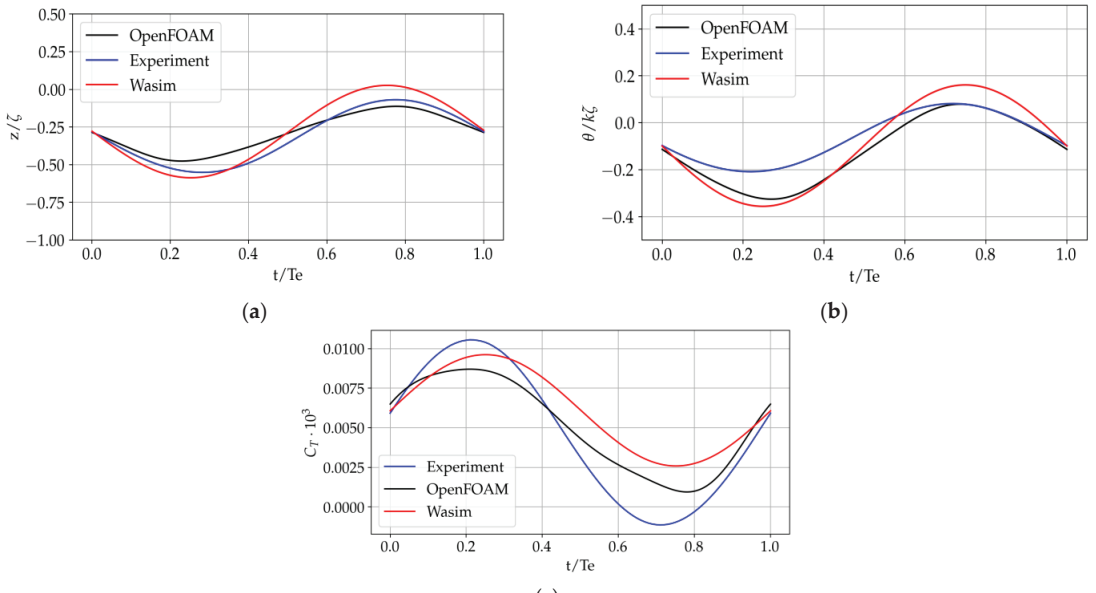

Figure 23. Time histories for case 2 of the KRISO containership: nondimensional (**a**) heave, (**b**) pitch, (**c**) total resistance.

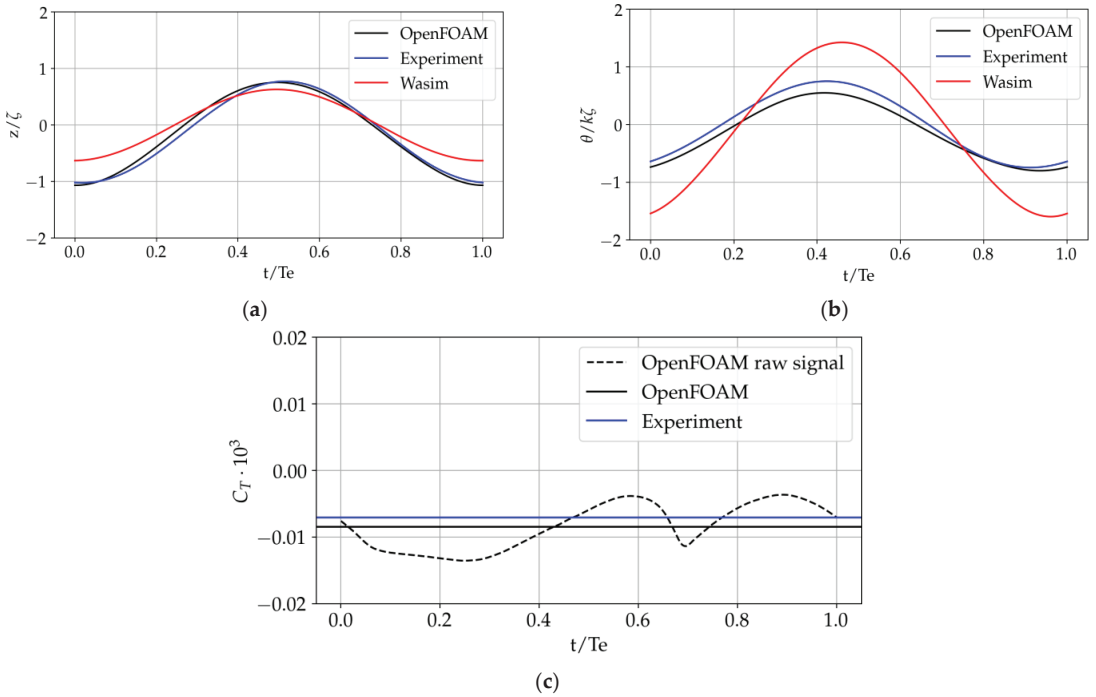

Figure 24. Time histories for case 3 of the KRISO containership: nondimensional (**a**) heave, (**b**) pitch, (**c**) total resistance.

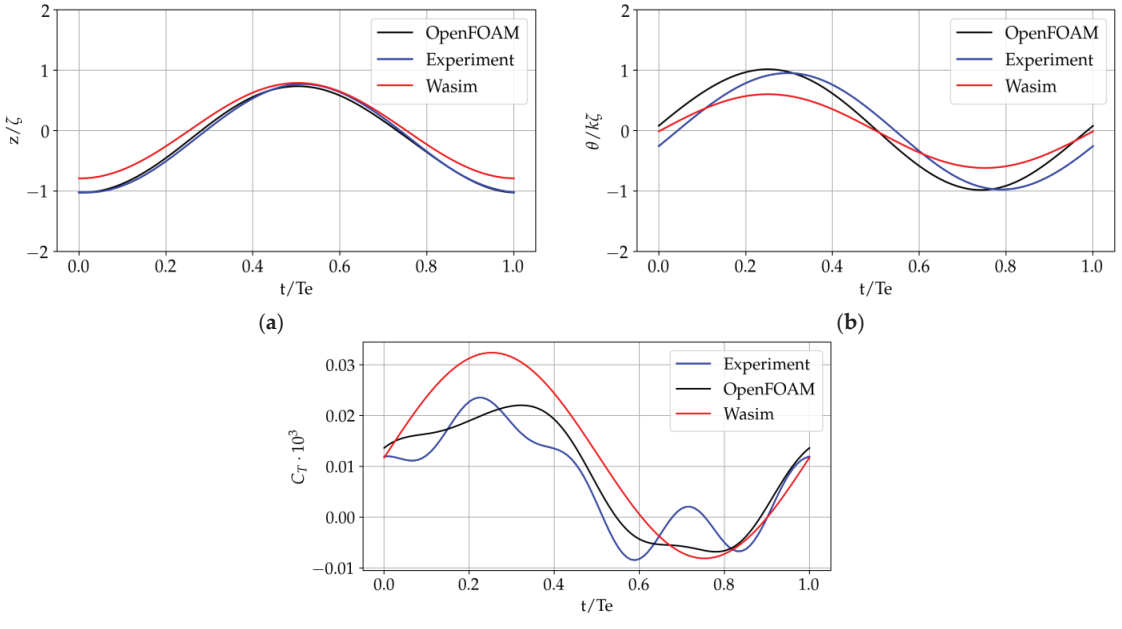

Figure 25. Time histories for case C4: nondimensional (**a**) heave, (**b**) pitch, (**c**) total resistance for the KRISO containership.

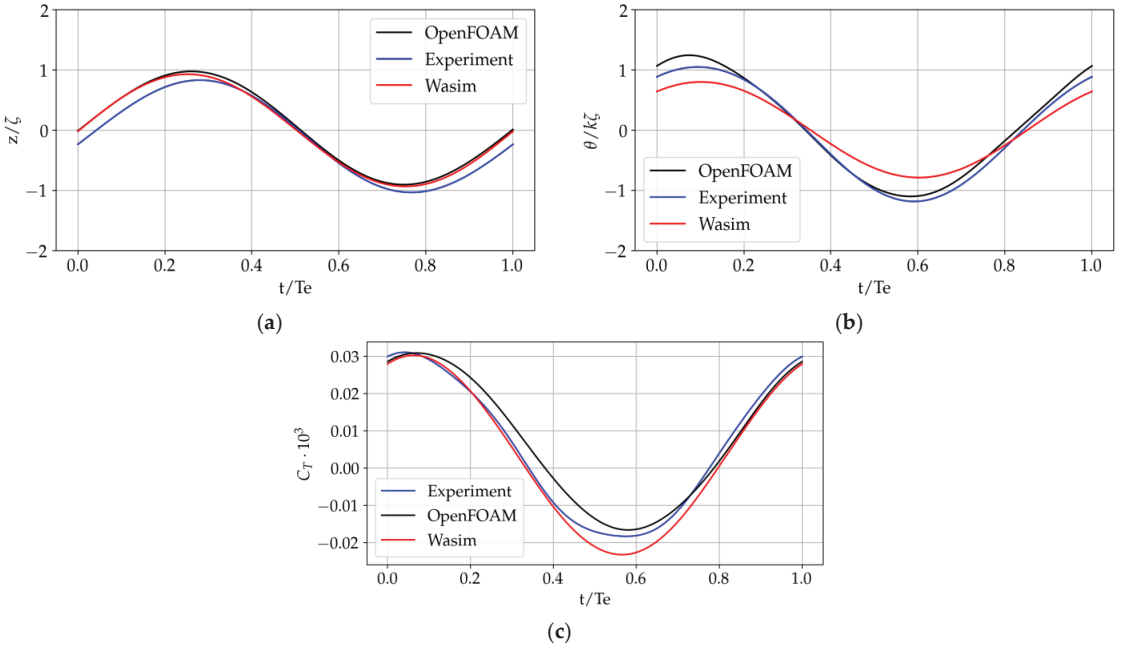

Figure 26. Time histories for case 5 of the KRISO containership: nondimensional (**a**) heave, (**b**) pitch, (**c**) total resistance.

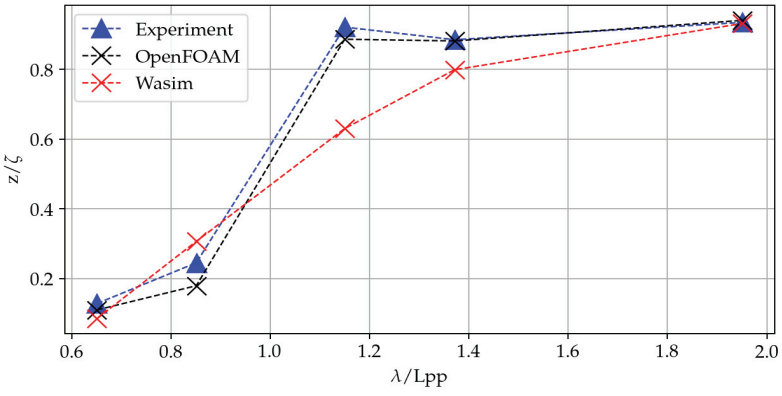

Figure 27. Transfer functions of heave motion for the KRISO containership.

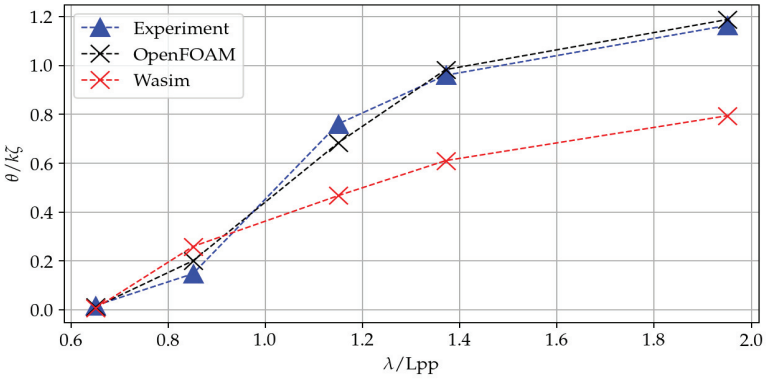

Figure 28. Transfer functions of pitch motion for the KRISO containership.

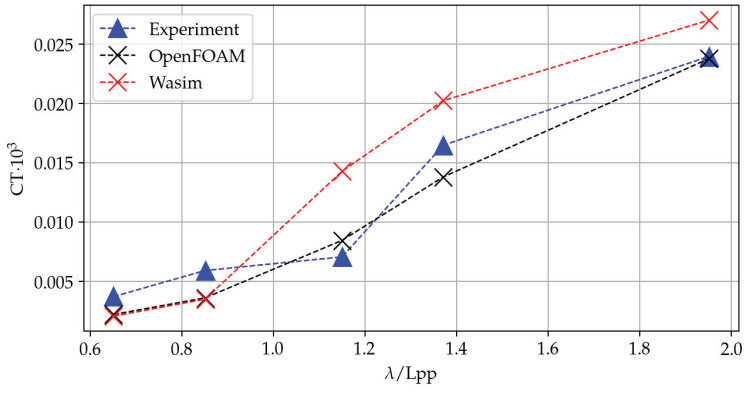

Figure 29. Total resistance coefficients for the KRISO containership.

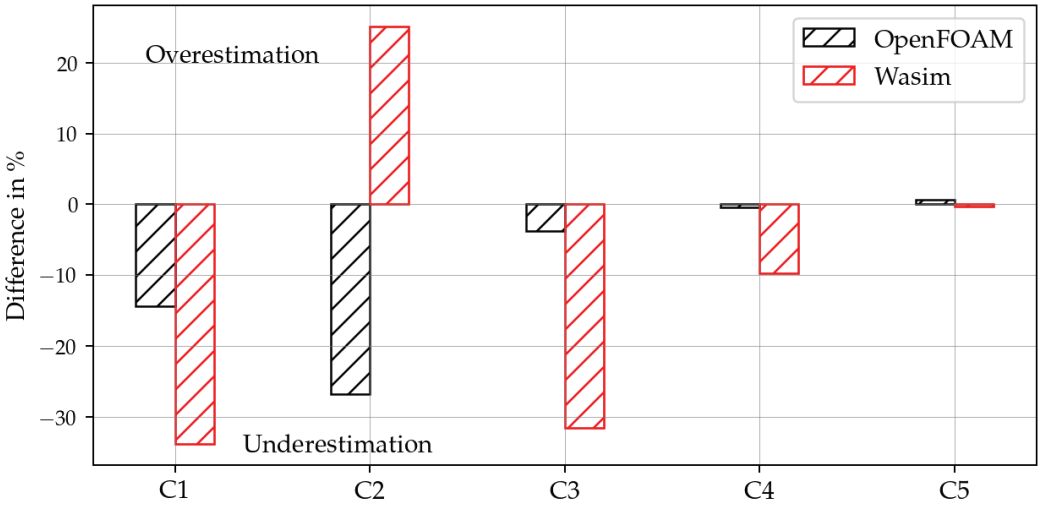

Figure 30. Difference of numerical and experimental heave transfer functions for the KRISO containership.

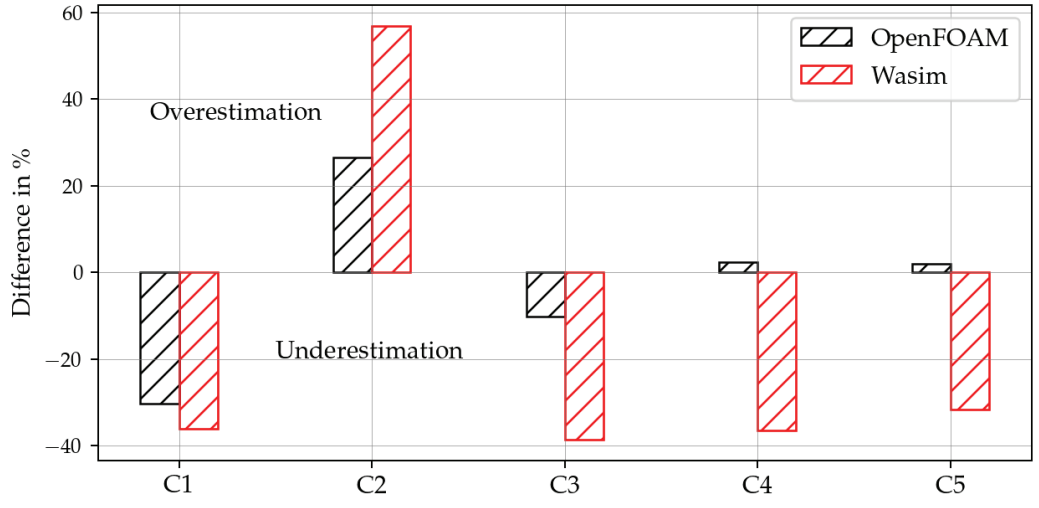

Figure 31. Difference of numerical and experimental pitch transfer functions for the KRISO containership.

Snapshots from the simulations with representative contours of incident waves are shown in Figure 33.

4.4. Discussion

A discussion of the results is outlined in this section for the 6750 TEU containership and KRISO containership, respectively. Regarding the first case, an experiment is chosen in which only the wave height varies, while the wavelength remains constant. It provides an opportunity to investigate wave response with regards to wave steepness for a zero-speed case. Such operating conditions are relevant, for example, FPSO vessels. First, the heave response is analyzed from both codes. The results indicate significant differences between the two tools, with a trend of lower values from the PF code compared to CFD. That is, however, not only the case for the second wave condition (H = 0.17 m). Looking at the pitch

response for which the experimental data are known, CFD performs better as the wave height increases. For smaller wave heights ($H < 0.20$ m), PF gives more accurate results. It can be assumed that for smaller rigid body responses in CFD, more computational cells than eight are needed in the free surface area. Moreover, it is possible that overset interpolation errors are magnified for smaller amplitudes; hence, an appropriate interpolation strategy should be chosen, most preferably the least squares method. Deforming grids should also be considered if the amplitudes are such that the numerical penalties would not appear due to morphing. Furthermore, analyzing the wave conditions for the 6750 TEU containership, at full scale, the biggest incident wave height would be equal to 29.2 m, which represents very extreme but also improbable conditions at sea. These extreme conditions provide a valuable experimental dataset for testing and comparing different seakeeping codes in harsh environments. The second case studied in this paper, the KRISO containership, is unlike the previous one, which is subjected to milder wave conditions. In this case, a model scale containership is subjected to head waves only while towed at a constant forward speed. The results of this case from CFD indicate that all hydrodynamic parameters of interest are prone to under or overprediction for small wave heights independently of the accurate incident wave, as stated in the 2D numerical wave tank study. As seen in Figures 24–26, the difference from the experimental value becomes smaller as the wave height increases. The reason for this could be that for relatively smaller incident wave heights, the number of cells per wave height should be greater than eight, enabling the solver to capture small rigid body amplitudes and pressure changes from cell to cell. The analysis of the transfer functions of Wasim shows that there is a lack of accuracy, and the motion is mostly underestimated. Pitch response has the biggest differences from the experiment, which can be attributed to the lack of viscous damping term; however, further investigation is needed. Finally, added resistance shows a similar trend for both Wasim and OpenFOAM®. In Figure 22c, no report is made for the added resistance from Wasim, since the resonant behavior in the measurements was reported. Interestingly, resonance is also captured in CFD with two force peaks over one encounter period. Observing the total resistance coefficient, i.e., added resistance from Wasim, higher harmonics are not captured.

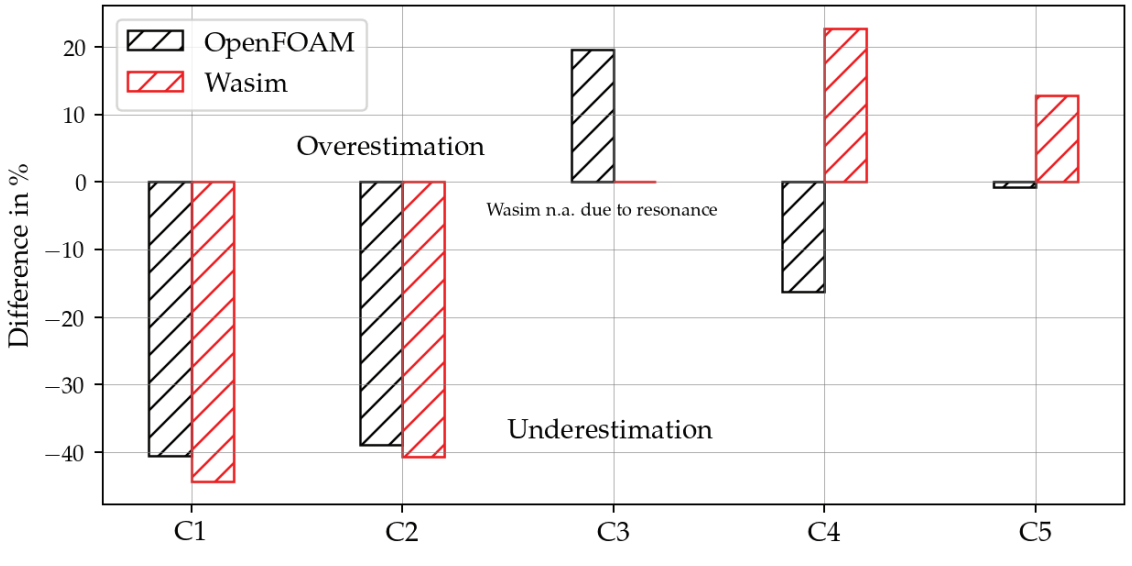

Figure 32. Difference of numerical and experimental total resistance coefficients for the KRISO containership.

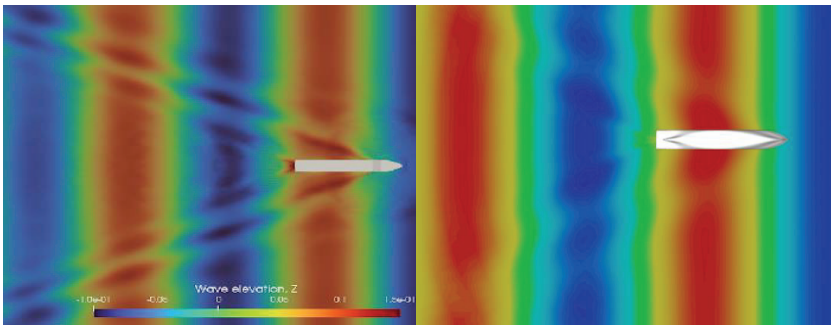

(**a**) (**b**)

Figure 33. Top view snapshots from the simulations for case 3 of the KRISO containership: (**a**) OpenFOAM; (**b**) Wasim.

5. Conclusions

The main objective of this paper is to present a comparison of two hydrodynamic tools for the assessment of seakeeping characteristics and added resistance of seagoing vessels. The first is based on potential flow theory and originates from the classification society DNV—Wasim. The second is an open-source toolbox for computational fluid dynamics—OpenFOAM®. In the study, two different cases are investigated, the first being a 6750 TEU containership scale model without forward speed, subjected to steep head waves. Heave and pitch response are analyzed, while only the latter is compared to the experiment. Regarding heave motion, a different trend of amplitudes is revealed from Wasim and OpenFOAM®. For Wasim, the amplitude is significantly smaller for the bigger wave heights compared to the CFD solver. For the pitch motion, the underestimation of the motion by the potential flow is clear. CFD shows better agreement with the experimental values, leading to the conclusion that for increasingly steep waves, heave can be underestimated with the potential flow tools with Wasim features. The use of CFD can also ensure better accuracy, but grid independence studies should be carried out. It is particularly evident in the second case of this work: a KRISO containership subjected to head waves with forward towing speed. Rigid body motions, i.e., heave and pitch, agree quite well for CFD, while the solution from PF differs for all cases. For the viscous flow method, differences in the experiment for lower wave heights are attributed to an insufficient number of computational cells per wave height, regardless of the accurate incident wave. Regarding second-order effects such as added resistance, CFD also shows better agreement. From a practical point of view, the constant towing speed and the restricted surge motion strongly affect the forces acting on the hull. Hence, the solution is not entirely suitable for estimating the sea margin for a real ocean-going ship. Clearly, the CFD solver will yield a more accurate solution, in which careful modeling of the surge response should be taken care of. Comparing the solutions for the potential flow in both cases, it is clear that the percentage difference is of a very different order of magnitude. This indicates that the forward speed effect in the PF tool should be studied in detail using the double-body linearization method, free-surface nonlinearities, etc. This is the subject of further planned work in future studies. Investigations of seakeeping performance with stabilized turbulence models within CFD are scarce, making it a fruitful area for further research. As a general guideline for the choice of a potential flow tool, or a fully viscous CFD for seakeeping or added resistance derived from this work: If a very sharp accuracy of the solution is required, i.e., a difference of less than 3 or 5%, then a fully viscous CFD is an option, considering the expected high computational cost. If such high accuracy is not of utmost importance, then a potential flow tool with features such as those analyzed here is the right choice, taking care that the vessel is in a linear region of motion, i.e., the height of the incoming waves is relatively low with respect to their characteristic length.

Supplementary Materials: The STL hull models for reproduction can be downloaded at: https://www.mdpi.com/article/10.3390/jmse11030641/s1, STL mesh of KRISO containership: KCS.stl., STL mesh of 6750 TEU containership: 6750 TEU containership.stl.

Author Contributions: Conceptualization, I.S., M.G. and J.P.-O.; Investigation, I.S.; Methodology, I.S., M.G. and J.P.-O.; Project administration, J.P.-O.; Resources, G.d.H.; Software, I.S. and J.P.-O.; Supervision, M.G. and J.P.-O.; Writing—review and editing, I.S. All authors have read and agreed to the published version of the manuscript.

Funding: This work was supported by the Croatian Science Foundation under the project IP-2018-01-3739.

Institutional Review Board Statement: Not applicable.

Data Availability Statement: All data (hull surface geometry, wave conditions, etc.) are available online.

Acknowledgments: The first author is grateful to NTNU (Norwegian University of Science and Technology) for hosting him, as a result of which this paper was produced. The first author also wishes to thank Andro Bakica for his initial help and guidance with OpenFOAM.

Conflicts of Interest: The authors declare no conflict of interest.

References

1. Joakim Tveiten Vigsnes Seakeeping Analysis Comparison between Viscous and Inviscid CFD. Master Thesis. Available online: https://ntnuopen.ntnu.no/ntnu-xmlui/handle/11250/2566949 (accessed on 10 January 2023).
2. Katsidoniotaki, E.; Göteman, M. Numerical modeling of extreme wave interaction with point-absorber using OpenFOAM. *Ocean Eng.* **2022**, *245*, 110268. [CrossRef]
3. Kim, S.-G.P. CFD as a seakeeping tool for ship design. *Int. J. Nav. Archit. Ocean Eng.* **2011**, *3*, 65–71. [CrossRef]
4. Dorozhko, V.M.; Bugaev, V.G.; Kitaev, M.V. CFD Simulation of an Extreme Wave Impact on a Ship. In Proceedings of the Twenty-fifth International Ocean and Polar Engineering Conference, Kona, HI, USA, 21–26 June 2015. [CrossRef]
5. Bi, X.; Zhuang, J.; Su, Y. Seakeeping Analysis of Planing Craft under Large Wave Height. *Water* **2020**, *12*, 1020. [CrossRef]
6. Gao, Z.; Wang, Y.; Su, Y.; Chen, L. Validation of a combined dynamic mesh strategy for the simulation of body's large amplitude motion in wave. *Ocean Eng.* **2019**, *187*, 106169. [CrossRef]
7. Galbraith, A.; Boulougouris, E. Parametric Rolling of the Tumblehome hull using CFD. In Proceedings of the 12th International Conference on the Stability of Ships and Ocean Vehicles, Scotland, UK, 14–19 June 2015.
8. Shen, Z.; Wan, D.; Carrica, P.M. Dynamic overset grids in OpenFOAM with application to KCS self-propulsion and maneuvering. *Ocean Eng.* **2015**, *108*, 287–306. [CrossRef]
9. Jacobsen, N.G.; Fuhrman, D.R.; Fredsøe, J. A wave generation toolbox for the open-source CFD library: OpenFoam®: Wave Generation Toolbox. *Int. J. Numer. Methods Fluids* **2012**, *70*, 1073–1088. [CrossRef]
10. Weller, H.G.; Tabor, G.; Jasak, H.; Fureby, C. A tensorial approach to computational continuum mechanics using object-oriented techniques. *Comput. Phys.* **1998**, *12*, 620. [CrossRef]
11. Pena, B.; Huang, L. A review on the turbulence modelling strategy for ship hydrodynamic simulations. *Ocean Eng.* **2021**, *241*, 110082. [CrossRef]
12. Larsen, B.E.; Fuhrman, D.R. On the over-production of turbulence beneath surface waves in Reynolds-averaged Navier–Stokes models. *J. Fluid Mech.* **2018**, *853*, 419–460. [CrossRef]
13. Gatin, I.; Vukčević, V.; Jasak, H.; Seo, J.; Rhee, S.H. CFD verification and validation of green sea loads. *Ocean Eng.* **2018**, *148*, 500–515. [CrossRef]
14. el Moctar, B.O.; Schellin, T.E.; Söding, H. *Numerical Methods for Seakeeping Problems*; Springer: Cham, Switzerland, 2021; ISBN 978-3-030-62561-0.
15. Bouscasse, B.; Merrien, A.; Horel, B.; Hauteclocque, G.D. Experimental analysis of wave-induced vertical bending moment in steep regular waves. *J. Fluids Struct.* **2022**, *1111*, 103547. [CrossRef]
16. Kim, Y.; Kim, J.-H. Benchmark study on motions and loads of a 6750-TEU containership. *Ocean Eng.* **2016**, *119*, 262–273. [CrossRef]
17. Kim, W.J.; Van, S.H.; Kim, D.H. Measurement of flows around modern commercial ship models. *Exp. Fluids* **2001**, *31*, 567–578. [CrossRef]
18. Larsson, L.; Stern, F.; Visonneau, M. *Numerical Ship Hydrodynamics: An Assessment of the Gothenburg 2010 Workshop*; Springer: Dordrecht, The Netherlands, 2014; ISBN 978-94-007-7189-5.
19. Simonsen, C.D.; Otzen, J.F.; Joncquez, S.; Stern, F. EFD and CFD for KCS heaving and pitching in regular head waves. *J. Mar. Sci. Technol.* **2013**, *18*, 435–459. [CrossRef]
20. Tokyo 2015: A Workshop on CFD in Ship Hydrodynamics. Available online: https://www.t2015.nmri.go.jp/Instructions_KCS/Case_2.10/Case_2-10.html (accessed on 10 January 2023).

21. Heo, J.; Park, D.; Berg-Jensen, J.H.; Pan, Z.; Vada, T.K. Hull Form Optimization to Fulfil Minimum Propulsion Power by Using Frequency and Time Domain Potential Flow Solvers. In *Practical Design of Ships and Other Floating Structures*; Okada, T., Suzuki, K., Kawamura, Y., Eds.; Lecture Notes in Civil Engineering; Springer: Singapore, 2021; Volume 65, pp. 220–236. ISBN 9789811546792.
22. Raven, H.C. *A Solution Method for the Nonlinear Ship Wave Resistance Problem*; TU Delft: Delft, The Netherlands, 1996; ISBN 978-90-75757-03-3.
23. Kim, K.-H.; Kim, Y.-H. Numerical Analysis of Added Resistance on Ships by a Time-domain Rankine Panel Method. *J. Soc. Nav. Archit. Korea* **2010**, *47*, 398–409. [CrossRef]
24. SESAM USER MANUAL—Wasim: Wave Loads on Vessels with Forward Speed. DNV, Norway. 2004. Available online: https://manualzz.com/doc/7270848/wasim-user-manual (accessed on 10 January 2023).
25. Weller, H.G. *Bounded Explicit and Implicit Second-Order Schemes for Scalar Transport*; OpenCFD Ltd.: Bracknell, UK, 2006.
26. Constance, C. Investigation of Floating Offshore Wind Turbine Hydrodynamics with Computational Fluid Dynamics. Ph.D. Thesis, University of Rouen Normandy, Rouen, France, 2021.
27. Shen, Z.; Hsieh, Y.-F.; Ge, Z.; Korpus, R.; Huan, J. Slamming Load Prediction Using Overset CFD Methods. In Proceedings of the Offshore Technology Conference, Houston, TX, USA, 2–5 May 2016; p. D011S014R004.
28. Windt, C.; Davidson, J.; Schmitt, P.; Ringwood, J. On the Assessment of Numerical Wave Makers in CFD Simulations. *J. Mar. Sci. Eng.* **2019**, *7*, 47. [CrossRef]
29. Lemaire, S.; Vaz, G.; Deij-van Rijswijk, M.; Turnock, S.R. On the accuracy, robustness, and performance of high order interpolation schemes for the overset method on unstructured grids. *Int. J. Numer. Methods Fluids* **2022**, *94*, 152–187. [CrossRef]
30. OpenFOAM 10 C++ Source Code Guide. Available online: https://cpp.openfoam.org/v10/ (accessed on 10 January 2023).
31. ITTC—Recommended Procedures and Guidelines (Practical Guidelines for Ship CFD Applications). Available online: https://ittc.info/media/1357/75-03-02-03.pdf (accessed on 15 January 2023).
32. Eça, L.; Hoekstra, M. The numerical friction line. *J. Mar. Sci. Technol.* **2008**, *13*, 328–345. [CrossRef]
33. Roenby, J.; Bredmose, H.; Jasak, H. A computational method for sharp interface advection. *R. Soc. Open Sci.* **2016**, *3*, 160405. [CrossRef] [PubMed]

Journal of
Marine Science and Engineering

MDPI

Article

Prediction of Added Resistance of Container Ships in Regular Head Waves Using an Artificial Neural Network

Ivana Martić , Nastia Degiuli * and Carlo Giorgio Grlj

Faculty of Mechanical Engineering and Naval Architecture, University of Zagreb, Ivana Lučića 5, 10000 Zagreb, Croatia; ivana.martic@fsb.hr (I.M.); carlo.g.grlj@fsb.hr (C.G.G.)
* Correspondence: nastia.degiuli@fsb.hr

Abstract: In this paper, an artificial neural network was used to predict the added resistance coefficient for container ships in regular head waves for various speeds. The data used for training the neural network were gathered based on performed numerical calculations using the Boundary Integral Element Method for various hull forms of container ships. The numerically obtained results were validated against the available experimental data for three benchmark container ships. The data were divided into three classes based on the ship length, and the expressions for the prediction of the added resistance coefficient for each container ship class were provided. The performance and generalization properties of the neural network were evaluated based on the normalized value of the root mean square error. The model enables reliable prediction of the added resistance coefficient within the preliminary design stage of a ship based on the ship characteristics and speed.

Keywords: added resistance in waves; artificial neural network; container ship; potential flow theory; regular head waves

Citation: Martić, I.; Degiuli, N.; Grlj, C.G. Prediction of Added Resistance of Container Ships in Regular Head Waves Using an Artificial Neural Network. *J. Mar. Sci. Eng.* **2023**, *11*, 1293. https://doi.org/10.3390/jmse11071293

Academic Editor: Kostas Belibassakis

Received: 2 June 2023
Revised: 23 June 2023
Accepted: 24 June 2023
Published: 25 June 2023

1. Introduction

Ships incurring added resistance in waves causes a significant increase in the required power to sail in actual sea states while keeping the speed constant. Consequently, it leads to an increase in fuel consumption, which puts the evaluation and reduction of added resistance into the focus of the International Maritime Organization (IMO). The IMO has highlighted the need for developing the so-called "level 1 methods" [1] for the prediction of added resistance in waves simply and efficiently. With an increasingly important goal to reduce the CO_2 emissions caused by maritime transport, the determination of added resistance in waves has become crucial in the design stage of a ship. Added resistance is commonly taken into account through the sea margin, even though it has been proven that added resistance in waves can lead to an increase in the total resistance, and thus in the required power, thereby making it larger than the one usually taken through the sea margin [2]. Kim et al. [3] showed that the sea margin measured as a result of wind and waves was in a range of 17–35% depending on the speed of the S175 container ship for a sea state characterized by Bf 6. Youngjun et al. [4] demonstrated that the sea margin was larger for lower ship operating speeds and that the sea margin of an LNG carrier due to fouling, wind, and waves amounted from 13 to 32% depending on the re-docking period. It should be noted that, in mild sea states or when a ship is sailing at slow steaming speeds, the power reserve taken by the sea margin is sufficient [5].

Considering the added resistance as a time-averaged second-order wave force, which depends on the ship motions and wave diffraction in short waves [6], hydrodynamic calculations should be carried out to determine its contribution to the total resistance with sufficient accuracy. This often implies the use of computational fluid dynamics, which requires the experience and knowledge of a user as well as the 3D model of a ship. The added resistance in waves depends on the hull form and ship speed, along with the wave characteristics and ship motions. In addition, the ship mass characteristics have an impact

on the added resistance in waves, i.e., by changing the value of pitch gyration radius by 1%, the added resistance in regular head waves increases by approximately 15% in the range of moderate and low wave frequencies [7]. The sloshing effect on added resistance in waves was studied by Zheng et al. [8]. The authors concluded that, under specific wave conditions, sloshing caused a decrease in surge and pitch motions and, thus, a decrease in the added resistance. A similar outcome was observed by Martić et al. [9] based on calculations performed using potential flow theory on the example of a S175 container ship. Since added resistance in waves can be considered a non-viscous phenomenon, the use of potential flow theory in its assessment is justified. It should be noted that the viscous part of added resistance accounts for up to 20% of the added resistance at the model scale for higher wave frequencies. The viscous effects are even less significant at full scale [10]. By performing the experimental and numerical assessment of the added resistance in regular head waves for a DTC container ship, an acceptable agreement between the numerical results obtained by the non-linear time domain Rankine panel method and experimental data was achieved, except in the case of the double resonance phenomenon [11]. Based on the experimental and numerical study carried out for the case of an LNG carrier in oblique seas, it was demonstrated that the added resistance estimated by computational fluid dynamics followed the trend of the experimental data [12].

The already-mentioned need for the development of simple methods to evaluate the added resistance in waves resulted in a relatively simple empirical method developed by Liu and Papanikolaou [13–16]. It requires the main particulars of a ship, as well as wave characteristics, as the input. The proposed empirical method has undergone several improvements and has been adopted by the International Towing Tank Conference, as well as incorporated in the IMO guidelines, to obtain the added resistance in waves coming from the head to beam direction [17]. An empirical asymptotic approach for the estimation of added resistance in arbitrary headings and speeds was successfully developed, even for the high wave frequencies and oblique waves [18]. The development of such models could benefit from the ability of artificial neural networks to learn and generalize once they are trained, as well as their superiority in describing nonlinear multiple regression problems. The success of employing neural networks for solving complex problems whose physical backgrounds are not easy to describe with a mathematical model has been proven by numerous studies in the literature. A model based on the neural network, which contributes to the control of harmful gas emissions by optimizing the operability of a ship, was established by Gkerekos et al. [19]. A neural network was successfully applied as part of the decision support system onboard the ship [20,21]. The main particulars, gross and net tonnage, deadweight, and engine power of container ships were estimated utilizing different artificial intelligence techniques based on the number of twenty-foot equivalent units and the ship speed [22]. A neural network model was also utilized to estimate the hawser tensions and displacements of a spread mooring system [23]. To develop a model for the estimation of added resistance in regular waves incoming from different directions, the results of potential flow methods were utilized by Mittendorf et al. [24]. The available experimental data were also used to predict the added resistance coefficient using a neural network [2]. The model requires the main particulars of a ship, the block coefficient, and the Froude number as an input, and the limitation is the range of the wavelength and the ship length ratio, with consideration for the fact that experiments are often carried out in a limited range of incoming wave frequencies. A model was further developed into a set of five neural networks that were trained on different segregated data, which resulted in a slightly improved accuracy of the obtained results in comparison to a single neural network [25]. Experimental data were also used to train an artificial neural network for the prediction of the residual resistance coefficient of a trimaran model. The required inputs of the model are the transverse and longitudinal positions of the side hulls, the longitudinal center of buoyancy, and the Froude number [26]. A neural network for the assessment of added resistance in head waves for container ships at different sea states was proposed by

Martić et al. [27], where various learning algorithms, as well as network topologies, were analyzed.

Within this paper, a multilayer perceptron (MLP) with an input, one hidden and output layer, and a backpropagation learning algorithm was developed for the prediction of the added resistance coefficient in regular head waves for container ships. A neural network was trained based on the results gathered by performing hydrodynamic calculations using the potential flow theory. The expressions for three neural networks were provided for the prediction of the added resistance coefficient for a container ship based on the class to which it belongs. It was shown that a model based on the neural network trained by the numerical results could be developed for the simple and efficient estimation of added resistance in waves, thus overcoming the limited availability of experimental data. The proposed model could be used in the preliminary design stage of a ship for the estimation of the ship power required to sail in actual sailing conditions.

2. Added Resistance in Waves

2.1. Numerical Model

The added resistance in waves for different hull forms of container ships is calculated by the Boundary Integral Equation Method (BIEM) in regular head waves. The hull is discretized by quadrilateral panels with a constant distribution of sources, and the integral equations are solved in an iterative manner to obtain the unknown strengths of the sources, the velocity potential, and the pressure along the panels [28]. Each hull was discretized by about 4000 panels, and the interior free surface was discretized by 6000 panels. The calculations were performed based on the Kelvin-type Green function, with the ship speed taken into account using wave encounter frequency. The irregular frequencies were treated by the Extended BIEM, which imposes Neumann's "rigid lid" condition on the interior free surface [29]. The first-order pressure over the mean wetted surface was integrated to obtain the added resistance in the waves by taking into account the change in the first-order quantities due to ship motions in the incoming waves. The added resistance was determined as a function of the ship response, the first-order velocity potential, the gradient of the velocity potential, and the wave elevation on the mean wetted surface, as well as along the waterline [27].

The numerical results were corrected for the non-linear effects that appear at higher wave frequencies, which are not properly accounted for by the potential flow theory. The correction was based on the experimental results [30] and was taken into account only in the range of higher wave frequencies depending on the hull form and ship speed. The non-dimensional coefficient of added resistance in waves is calculated as:

$$C_{AW} = \frac{R_{AWm} + R_{AWr}}{\rho g \zeta_a^2 B^2 / L} \tag{1}$$

where R_{AWm} is the added resistance obtained using the panel method, R_{AWr} is the correction for diffraction in short waves, ζ_a is the wave amplitude, B is the ship breadth, and L is the ship length.

2.2. Validation Study

The obtained numerical results were validated against the available experimental data for the KCS, S175, and DTC container ships, whose main particulars are given in Table 1. The comparison of the numerical results obtained by the BIEM and experimental data will be presented and discussed in the Results section, along with the comparison of the results obtained using the artificial neural network.

Table 1. Main particulars of the S175, KCS, and DTC container ships.

Main Particular	S175	KCS	DTC
Length, L_{PP}, m	175.0	230.0	355
Breadth, B, m	25.4	32.2	51
Draft, T, m	9.50	10.8	14.5
Displacement, ∇, m^3	24,053	52,030	173,467
Block coefficient, C_B	0.572	0.651	0.661
Prismatic coefficient, C_P	0.589	0.661	0.669
Position of LCG, m	86.5	111.596	174.531
Radius of gyration, k_{yy}, m	43.75	57.5	87.3
Froude number, Fr	0.20	0.26	0.14
	0.25		
	0.30		

3. Case Study

The data gathered to train the neural network are the results of the performed numerical calculations for 75 hull forms of container ships in regular head waves at different speeds. The input variables for the neural network were chosen based on the performed analysis of the impact of ship characteristics on added resistance in waves [7].

The 15 original container ship hull forms were modified with respect to either their block and prismatic coefficient or the position of the longitudinal center of buoyancy (LCB) while keeping the prismatic coefficient constant. The hull forms were modified by changing the positions of hull cross-sections while keeping the area and shape of the cross-sections constant. The ship speed was selected based on the results of regression analysis, which was also used to define the range of variation of the prismatic coefficient [31]. The pitch radius of gyration was varied as 24%, 25%, and 26% of the length between the perpendiculars for each hull form. The ranges of the main particulars and Froude number of the container ships are given in Table 2. The length-to-breadth and breadth-to-draft ratios of the original container ship hull forms are given in Figure 1. The length-to-breadth ratio was in the range from 5.22 to 8.11, while the breadth-to-draft ratio was generally in the range from 2.28 to 3.37, with one ship having a B/T equal to 4.77.

Table 2. Ranges of the container ships' characteristics.

Main Particular	Range
L_{PP}, m	104.8 ÷ 360
B, m	18 ÷ 49
T, m	4.25 ÷ 15
∇, m^3	5648.7 ÷ 174,090
C_B	0.510 ÷ 0.780
C_P	0.530 ÷ 0.811
LCB, m	49 ÷ 180.72
k_{yy}, m	25.15 ÷ 93.6
Fr	0.174 ÷ 0.258

Once the neural network has been established based on all the gathered data, the samples were divided into three classes based on the ship length [31] to simplify the model and to achieve better accuracy in predicting the added resistance in the waves for a particular ship class. The non-dimensional coefficient of the added resistance in waves is a function of the before-mentioned main particulars of the container ship, speed, and wave frequency [7,32]:

$$C_{AW} = f(L_{PP}, B, T, \nabla, C_B, C_P, \text{LCB}, k_{yy}, V, \omega) \quad (2)$$

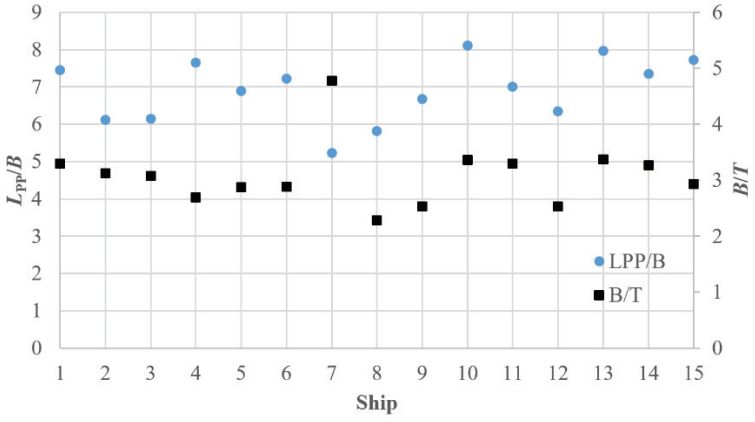

Figure 1. Length-to-breadth and breadth-to-draft ratios of the original container ship hull forms.

4. Artificial Neural Network

To predict the added resistance of regular head waves of a container ship, a feedforward MLP was utilized with an input, one hidden layer, an output layer, and an error backpropagation (EBP) algorithm. As already mentioned, the network has 10 inputs and one output, i.e., the coefficient of added resistance in waves. As can be seen in Figure 2, the input values multiplied by the weights were summed and passed through an activation function within each neuron of the hidden layer. The bias neuron was also included to shift the activation function, thus enabling an additional degree of freedom. The outputs of neurons y within the hidden and output layer are determined as follows:

$$y = \phi\left(\sum_{i=0}^{n} w_i x_i\right) \tag{3}$$

where ϕ is the activation function, w_i are weights, and x_i are input values. The activation function utilized to transform the neuron output is linear in the output layer, and the hyperbolic tangent sigmoid transfer function in the hidden layer is defined as follows:

$$\gamma = \frac{2}{1 + e^{-2x}} - 1 \tag{4}$$

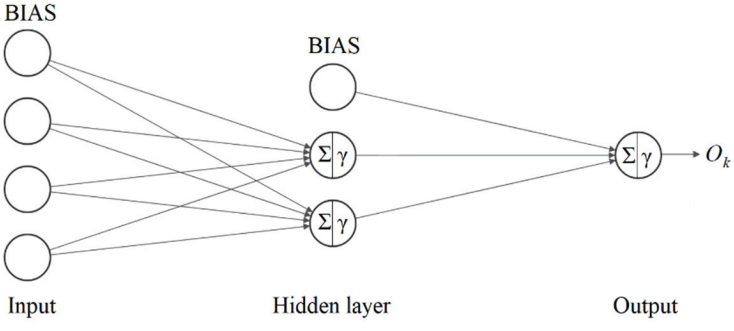

Figure 2. Scheme of the MLP neural network.

Within the training process of the neural network, the optimal weights are determined iteratively by minimizing the error function. The errors are calculated in the forward direction by the backpropagation algorithm based on the inputs and the corresponding

outputs. The weights are changed in a backpropagation manner based on the minimization of the error function.

The performance of the neural network is assessed by the normalized value of the root mean square error (NRMSE), which is calculated as follows:

$$\mathrm{NRMSE} = \frac{\mathrm{RMSE}}{\sigma_{d_n}} = \frac{\sqrt{\frac{\sum_{n=1}^{N}(d_n - O_n)^2}{N}}}{\sigma_{d_n}} \tag{5}$$

where σ_{d_n} is the standard deviation, O_n is the neural network output, d_n is the desired output, and N is the number of samples used either for training or testing the network.

The number of neurons in the hidden layer is varied to achieve the adequate topology of the network to predict the added resistance in waves with sufficient accuracy. The hydrodynamic calculations were performed in the range of incoming wave frequencies from 0.1 to 1.5 rad/s. This resulted in 11,230 samples in total. Firstly, the network was trained based on 95% of the data in total, and 5% of the data was used for testing. Afterward, the container ships were divided into three classes based on their size. The first class contained data for ships from 104 to 155 m, the second class from 178 to 247 m, and the third class from 300 to 360 m in length. The first class contained 5086 samples, the second one contained 3456 samples, and the third one contained 2688 samples in total. Again, 95% of the data was used for training, and 5% was used for testing purposes. The network was trained based on the Levenberg–Marquardt learning algorithm with Bayesian regularization (BR). The validation data set was not established, since BR does not need the validation data. BR is superior in generalization compared to the standard EBP neural network. A nonlinear regression problem is converted into a statistical one using the probabilistic approach. It is difficult to overfit the neural network with BR, since training is conducted with a limited number of weights. The weights that are not relevant to the learning process are discarded by maximizing the posterior probability. The calculation of the Hessian matrix within BR is approximated using the Gauss–Newton method within the LM learning algorithm. The error function consists of the sum of squared errors of desired and predicted outputs E_D and the sum of squared weights E_W [33]:

$$F = \beta E_D + \alpha E_W \tag{6}$$

where α and β are the regularization parameters.

The sum of squared errors is calculated as:

$$E = \frac{1}{2}\sum_{n=1}^{N}(d_n - O_n)^2 \tag{7}$$

At the beginning of the training, the weights and the regularization parameters are initialized as 0 for α and 1 for β. After each iteration step of the training using the LM algorithm, a minimum of the error function F is sought. The number of weights involved in the training process is determined as follows:

$$\gamma = N - 2\alpha \mathrm{tr}\left[\nabla^2 F(\mathbf{w})\right]^{-1} \tag{8}$$

where N is the total number of weights, and $\nabla^2 F(\mathbf{w})$ denotes the Hessian matrix, which is determined based on the Gauss–Newton approximation:

$$\nabla^2 F(\mathbf{w}) \approx 2\beta \mathbf{J}^T \mathbf{J} + 2\alpha \mathbf{I}_N \tag{9}$$

New estimates of the regularization parameters are determined as:

$$\alpha = \frac{\gamma}{2E_W(\vartheta)} \tag{10}$$

$$\beta = \frac{n-\gamma}{2E_D(\vartheta)} \tag{11}$$

A neural network based on the LM learning algorithm and BR was selected for the prediction of added resistance based on its best performance amongst other investigated first- and second-order learning algorithms [27]. One of the main advantages of such a network is that most of the gathered data can be used for training purposes. The accuracy of the neural network output depends on the quality of the data used for the training. For that reason, the data has to be pre-processed and prepared for the training. This includes the removal of the possible outliers and ensuring an equivalent impact of input on output variables. Since the input variables have different ranges and dimensions, the input data were standardized, which resulted in a unit standard deviation and a zero-mean value. One of the data cleaning and pre-processing techniques that was applied is principal component analysis (PCA), which is a dimensionality reduction method that is commonly applied to eliminate the collinearity of dependent variables in a multivariate data set. By creating linearly independent principal components obtained by an eigenvalue decomposition of the data covariance matrix, PCA enables the reduction in the number of inputs while keeping as much data variance as possible. Within this study, all input variables were kept; however, they were replaced by the principal components, which improved the performance of the neural network.

5. Results

The obtained numerical results for three benchmark container ships were validated by comparison with the available experimental data [34,35]. The obtained results of the validation study for the KCS container ship are presented in Figure 3. The numerical results obtained by the BIEM and corrected at short waves were in satisfactory agreement with the experimental data. A slight shift of the numerically obtained curve of the added resistance coefficient towards lower wave frequencies could be noticed in comparison to the experimentally obtained data. However, a noticeable scatter of the experimental results could be observed as well.

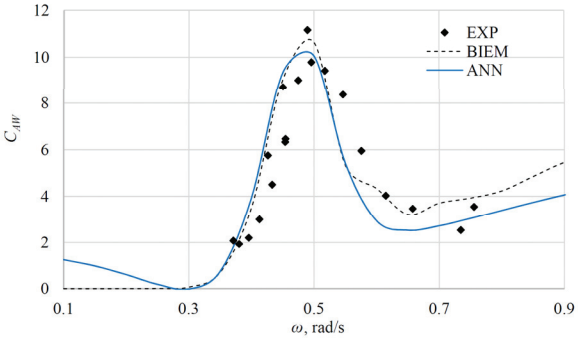

Figure 3. Added resistance coefficient for the KCS at $Fr = 0.26$.

The numerically and experimentally [36] obtained results for the S175 container ship at three Froude numbers are compared and shown in Figures 4–6. The numerical results at $Fr = 0.20$ were in satisfactory agreement with the experimental ones, especially in the range of moderate wave frequencies around the location of the peak position. In the range of higher wave frequencies, the numerical results seemed to underestimate the experimental data despite the applied correction, as shown in Figure 4. For $Fr = 0.25$,

the added resistance coefficient obtained numerically was underestimated for all wave frequencies, with the position of the peak value being slightly shifted towards higher wave frequencies, as shown in Figure 5. The numerical results for $Fr = 0.30$ were in good agreement with the experimental data at short waves, where the experimental data were more consistent, as shown in Figure 6. The experimental data showed a significant scatter in the range of moderate wave frequencies, which makes proper comparison between the results troublesome. For the DTC, which represents a modern post-Panamax container ship [10], it can be seen that BIEM notably underestimated the added resistance coefficients for the wave frequencies around the peak position, as shown in Figure 7.

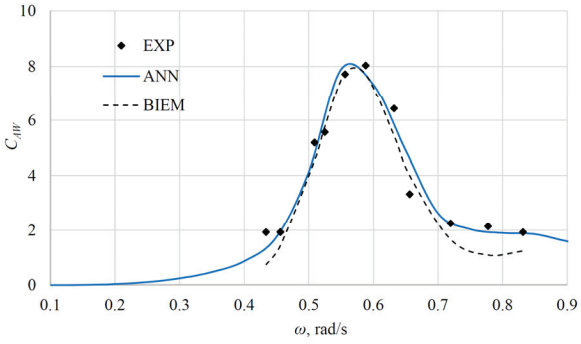

Figure 4. Added resistance coefficient for the S175 container ship at $Fr = 0.20$.

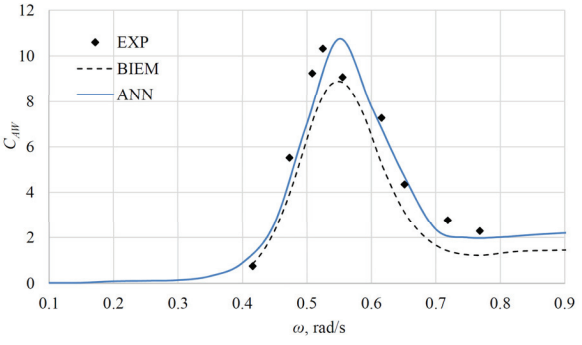

Figure 5. Added resistance coefficient for the S175 container ship at $Fr = 0.25$.

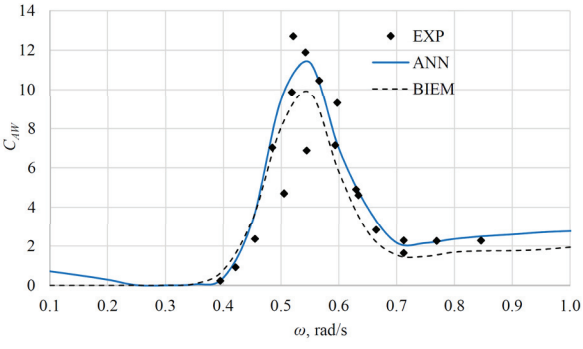

Figure 6. Added resistance coefficient for the S175 container ship at $Fr = 0.30$.

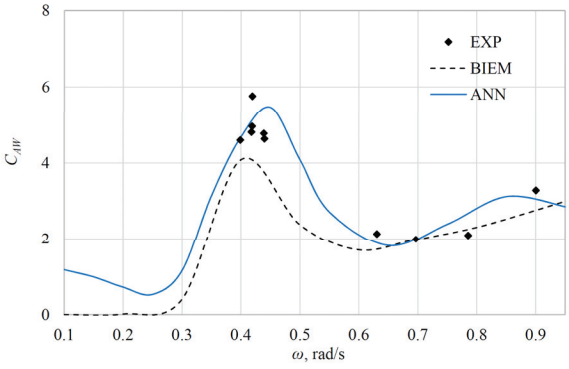

Figure 7. Added resistance coefficient for the DTC container ship at $Fr = 0.14$.

Once all numerical calculations were performed and the outliers were removed, the numerically obtained data were standardized, and PCA was carried out. Based on a detailed inspection of the gathered data, some of the results were discarded as the potential cause of the noise. Namely, for some ships, the appearance of irregular frequencies was noticed at lower frequencies than expected, which means that those results had to be removed from the training and testing data set.

To represent the linear correlation between the input variables, the Pearson correlation coefficient was used [37]. The correlation between the input variables and the added resistance coefficient as the output is given as a heat map in Figure 8. A moderate correlation between all input variables, except for the block and prismatic coefficients, as well as the added resistance in waves, can be observed. The hull form coefficients correlated poorly with the added resistance in waves. On the other hand, a strong correlation between the block and prismatic coefficient can be observed, as well as a moderate correlation between those coefficients and other hull characteristics and speed.

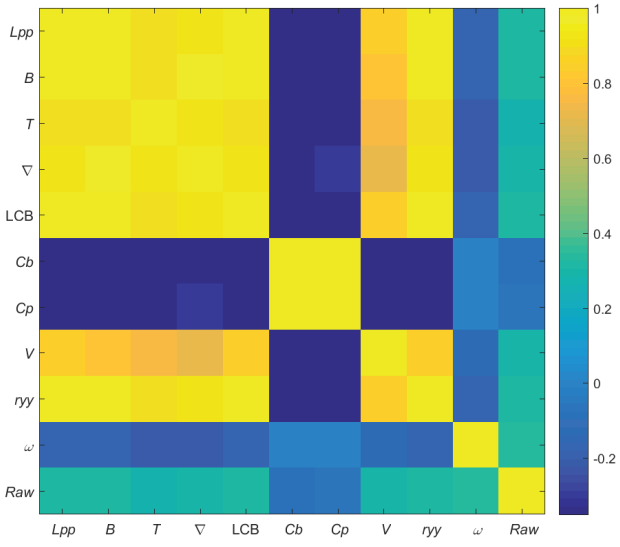

Figure 8. Correlation coefficients between the input variables.

The principal components and the percentage of variance in each of them can be seen in Figure 9. It should be noted that the total variance contained in the first five principal

components was equal to 99.3%, which would potentially enable the reduction in the number of input variables. It is worth mentioning that the learning process based on the linearly independent variables was significantly accelerated. In Figure 10, the variance that can be explained by principal components for the three container ship classes is shown. The obtained results for the first and third class were very similar, while the second principal component for the second class contained somewhat more information in comparison to the other two classes. The output data was normalized before training, thus resulting in a range of added resistance coefficients from 0 to 1.

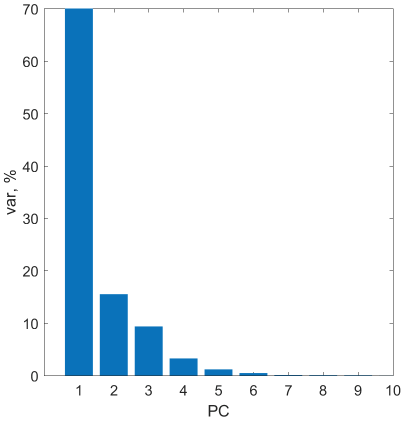

Figure 9. Percentage of the total variance that can be explained by each principal component.

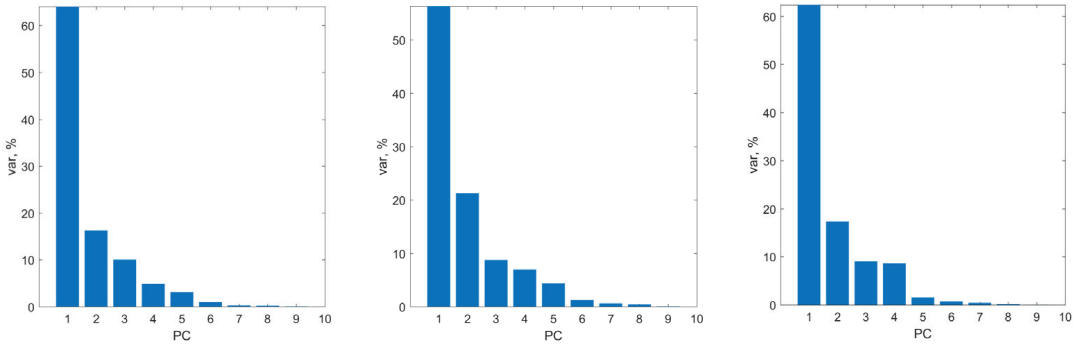

Figure 10. Percentage of the total variance that can be explained by each principal component for first (**left**), second (**middle**), and third (**right**) class.

During the supervised training, the weights were iteratively updated based on the LM algorithm by minimizing an error function, and the NRMSE of the training and testing data set was monitored. The data used for testing purposes consisted of 5% of the numerically obtained data and the experimental data for the benchmark container ships. Based on the performance of neural networks with different topologies, i.e., the number of neurons in the hidden layer, the neural network with 50 neurons in the hidden layer was the most successful one. The NRMSE of the training and testing data, as well as the number of iterations, are given in Table 3. It can be seen that, as the number of neurons within the hidden layer increased, the error decreased. In other words, the neural network adapted better to the data used within the training while avoiding overfitting. Generally speaking, the NRMSE of the testing data was lower for topologies with up to 50 neurons in the hidden layer, unlike for the neural networks with 55 and 60 neurons. It should be noted that, for these neural networks, the NRMSE of the data used for testing was lower in comparison

to the NRMSE of the training data, which means that the neural network has a good generalization ability. The selected neural network topology was the one with 50 neurons in the hidden layer, which adapted well to the testing data while keeping its parsimony characteristics. That does not mean that neural networks with 55 and 60 neurons in the hidden layer have poor generalization ability. It can be noticed that the NRMSE of the testing data for a neural network with 60 neurons in the hidden layer was the lowest among all analyzed topologies.

Table 3. The main particulars of KCS.

Number of Neurons	Number of Iterations	NRMSE (Training)	NRMSE (Testing)
20	511	0.1331	0.1290
30	1187	0.0956	0.0923
40	1367	0.0745	0.0743
45	1487	0.0724	0.0707
50	2050	0.0662	0.0628
55	2537	0.0624	0.0633
60	2987	0.0575	0.0605

The number of weights effectively involved in the training was 588 of 601 parameters in total. For comparison purposes, the NRMSE of the neural network with 50 neurons in the hidden layer with the LM learning algorithm without BR was 0.0895 for the training and 0.0948 for the testing data. The NRMSE for the training and testing data was 0.2419 and 0.2421, respectively when the Scaled Conjugate Gradient algorithm was used, while the learning algorithm based on Steepest Gradient Descend showed a significantly larger error and was discarded from the analysis.

The regression plots for the training and testing data for a neural network with 50 neurons in the hidden layer are shown in Figure 11. In the case of the data used for training, some outliers can be noticed for lower values of added resistance coefficient, despite the careful pre-processing of the data. A high coefficient of determination was obtained for both the training and testing data. Based on the testing data, it can be seen that the added resistance coefficients were well-predicted without significant deviations.

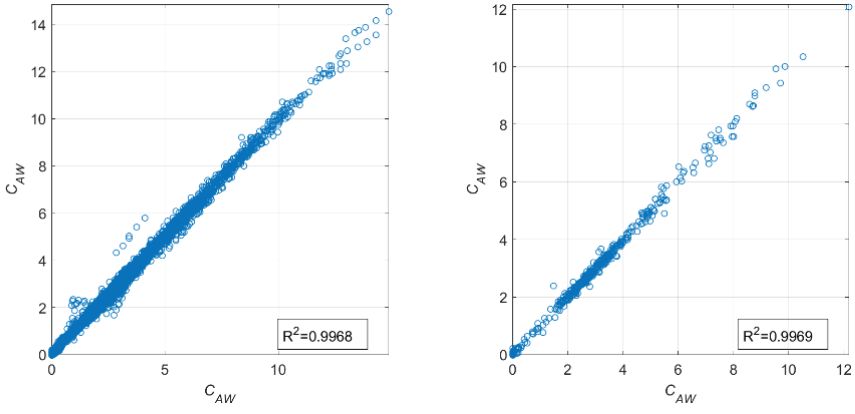

Figure 11. The regression plot for the data used for training (**left**) and testing (**right**).

The residuals calculated as the difference between the desired output and the one obtained by the neural network for the training and testing data are presented in Figure 12. They should be inspected to validate the performance of a regression model and assess whether the error is stochastic and without any visible pattern. As can be seen from Figure 12, the residuals were uniformly distributed. However, similar to the regression plot

for the training data, the outliers within the lower values of the added resistance coefficient can be noticed. Some of the possible reasons for that lie in the incorrect results of the hydrodynamic calculations or an unintentional mistake made in the data pre-processing. The residuals of the testing data were uniformly distributed as well, and the mean relative deviation between the obtained results was equal to -1.42%. Despite the outliers, the established neural network had good generalization ability. The performance of the neural network with a LM learning algorithm and BR with 50 neurons in the hidden layer for the prediction of the added resistance coefficient of the benchmark container ships is given in Figures 3–7.

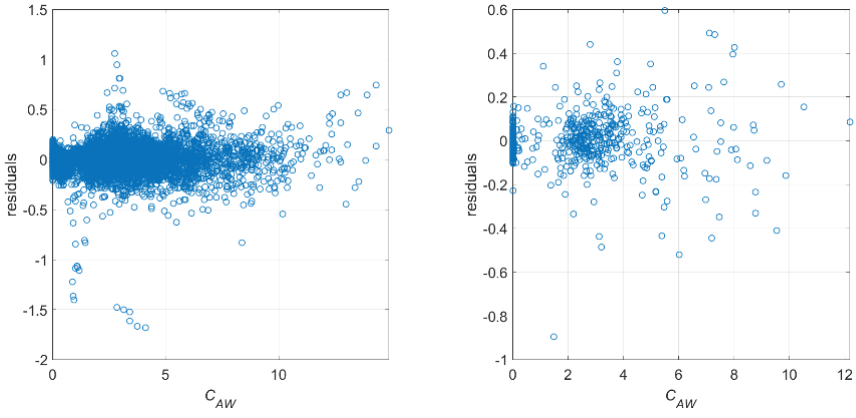

Figure 12. Residuals of the data used for training (**left**) and testing (**right**).

The neural network predicts added resistance coefficient for the KCS with sufficient accuracy, especially in the range of moderate wave frequencies. The peak value was somewhat lower in comparison to the numerically obtained results, while the values at short waves were underestimated, as shown in Figure 3. It can be observed that, instead of approaching zero, the curve of the added resistance coefficient obtained by the neural network tended to rise. For the S175, significantly better agreement between the experimental results and the ones obtained using the neural network was obtained for an $Fr = 0.20$, as shown in Figure 4. The added resistance coefficient was much better predicted, even though the peak position was again slightly shifted towards the lower frequencies. Similar results can be observed for an $Fr = 0.25$, as shown in Figure 5, where the peak position was shifted towards the higher wave frequencies, even though the peak value predicted by the neural network was closer to the experimentally obtained one in comparison to the numerical result. Generally speaking, the added resistance coefficient predicted by the neural network was somewhat larger in the entire frequency range compared to the numerically obtained one and in that way shows a closer agreement to the experimental results. For an $Fr = 0.30$, the peak value of the added resistance coefficient was larger when predicted with a neural network in comparison to the numerically obtained result, and its position was shifted towards the lower frequencies, as shown in Figure 6. Similar to the KCS, the coefficient of added resistance in the waves slightly increased at low wave frequencies. The possible reason for this anomaly could lie in the noise of the data gathered for training, which led the neural network to predict an increase in the added resistance at such low frequencies. The added resistance coefficient for the DTC predicted by the neural network is shown in Figure 7. Again, the peak value and its position were wrongly predicted, and the trend of the curve at higher wave frequencies did not correspond to the one obtained numerically and experimentally. Again, instead of the decreasing trend of the added resistance coefficient at low frequencies, the trend was the opposite. It can be seen that the network failed to predict the added resistance for the DTC, which was a large post Panamax ship with a relatively low sailing speed of 16 knots. Within the data gathered for

the training, the number of samples representing large ships with higher sailing speeds was the lowest.

To improve the obtained results and establish a model that could be readily used, the data were divided into three classes. Training the neural network based on the lower number of samples that contained similar information within the classes enabled a reduction in the number of neurons within the hidden layer. In that way, a model that could be easily implemented and used was proposed. The model contains three neural networks, each for a particular class of container ships based on their length. For each class, four network topologies were analyzed, i.e., five, six, seven, and eight neurons in the hidden layer. In that way, the expressions used to estimate the added resistance coefficient were not too complex, while there was still a sufficient number of neurons in the hidden layer to describe the given phenomenon. All three neural networks were trained based on the LM learning algorithm with BR. The obtained NRMSE, along with the number of iterations for different network topologies, are given in Table 4. For class 1, the neural network with six neurons in the hidden layer was selected. It had the lowest NRMSE for the testing data. It can be seen that, despite the decrease in the NRMSE for the training data, the network adapted better to the data used for training, while the error of the testing data increased. The neural network with seven neurons in the hidden layer was chosen to predict the added resistance coefficient for class 2, with the NRMSE for the testing data equal to 0.1075. The network with the same topology was established for class 3 as well, which yielded the lowest NRMSE for both the training and testing data set. From Table 3, it can be seen that, by increasing the number of neurons within the hidden layer by one, the NRMSE for the training and testing data notably increased as well. In comparison to the results obtained using the neural network trained by the unclassified data, it can be noticed that the errors obtained for both the training and testing data were significantly larger. In other words, the network did not adapt to the data that well; however, it kept its generalization ability while being much less complex and easier to implement.

Table 4. The results obtained for different neural network topologies for three data classes.

Class	Number of Neurons	Number of Iterations	NRMSE (Training)	NRMSE (Testing)
1	5	555	0.1273	0.1534
	6	461	0.1151	0.1185
	7	535	0.1138	0.136
	8	459	0.1124	0.1333
2	5	176	0.123	0.1379
	6	83	0.1114	0.115
	7	166	0.1097	0.1075
	8	140	0.1082	0.111
3	5	40	0.105	0.0987
	6	83	0.0838	0.0783
	7	174	0.0761	0.0701
	8	49	0.0912	0.0903

The regression plots and residuals for the testing data for all three neural networks are given in Figures 13–15. In the case of class 1, the coefficient of determination was equal to 0.9856, and the residuals were randomly distributed, as shown in Figure 13. In comparison to the residuals obtained by the neural network trained by unclassified data, it can be seen that the range of residuals for class 1 was larger. Some outliers can be seen in both the regression and residual plots. A slightly larger coefficient of determination was obtained for class 2, as shown in Figure 14. The residuals were in the same range as the ones for class 1. It should be noted that the values of added resistance coefficient for class 2 were the largest in comparison to the other two classes. As already shown in the comparison between the numerically and experimentally obtained added resistance coefficients for

the DTC container ship, which by length belongs to class 3, the BIEM underestimated the added resistance. The same can be observed by comparing the regression plots for classes 2 and 3, which are shown in Figures 14 and 15. However, it is worth noting that the residuals obtained for class 3 were lower in comparison to the other two classes, and the coefficient of determination was the largest.

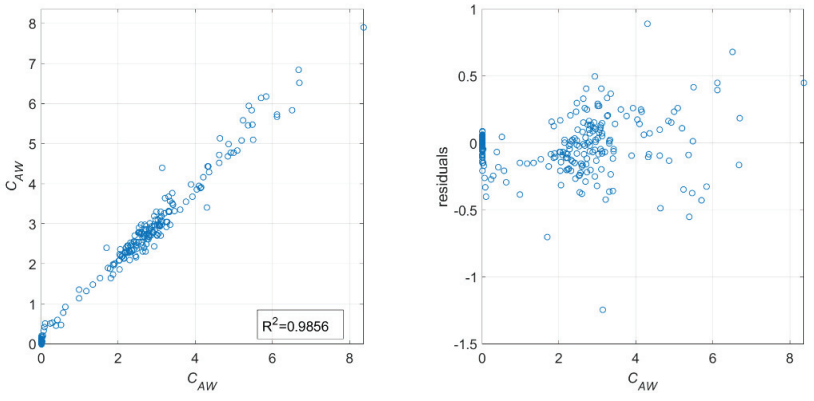

Figure 13. The regression plot (**left**) and residuals (**right**) for the class 1 data used for testing.

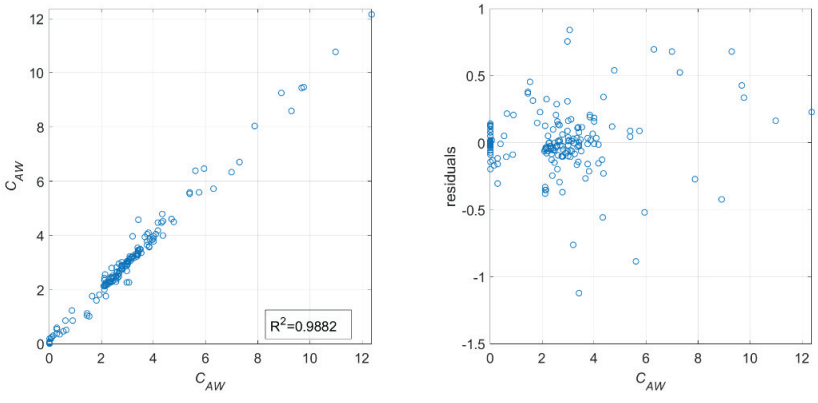

Figure 14. The regression plot (**left**) and residuals (**right**) for the class 2 data used for testing.

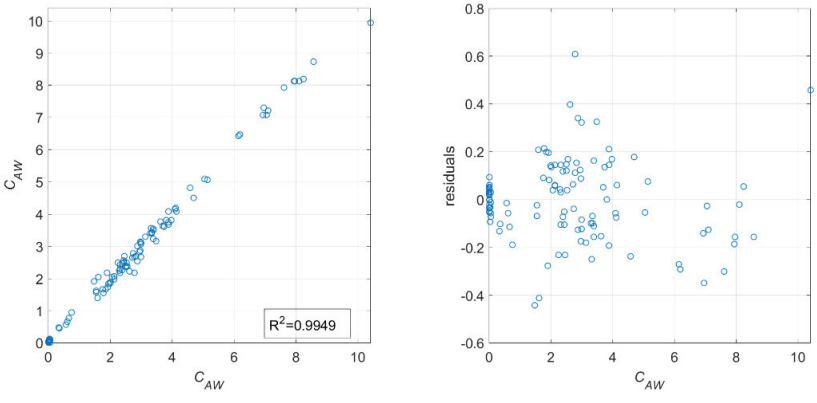

Figure 15. The regression plot (**left**) and residuals (**right**) for the class 3 data used for testing.

Since the KCS and S175 container ships belong to class 2 by their length, the added resistance coefficient was predicted by the second neural network with seven neurons in the hidden layer. The obtained results are presented in Figure 16. In the case of the KCS, a very good agreement between the network output and the experimental data can be seen. However, the network output for very the high wave frequencies was almost constant. In the case of the S175 container ship for an $Fr = 0.20$ it can be noticed that the network significantly overestimated the added resistance, while the peak was slightly shifted to the lower wave frequencies. Since this Froude number was at the bottom boundary for ship speed for class 2, the added resistance coefficient for the S175 was estimated by the first neural network as well, as shown in Figure 17. It is interesting to observe how the peak values obtained by the first and second neural networks were almost the same. On the other hand, the peak position predicted by the first neural network was more accurate.

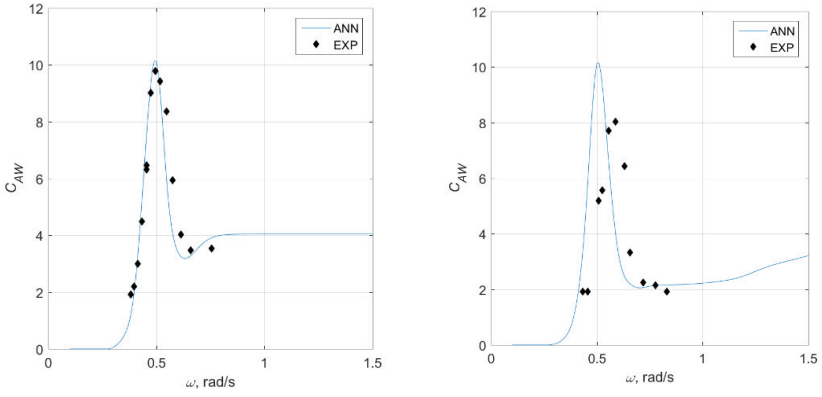

Figure 16. Added resistance coefficient for the KCS for $Fr = 0.26$ (**left**) and S175 container ship for $Fr = 0.20$ (**right**).

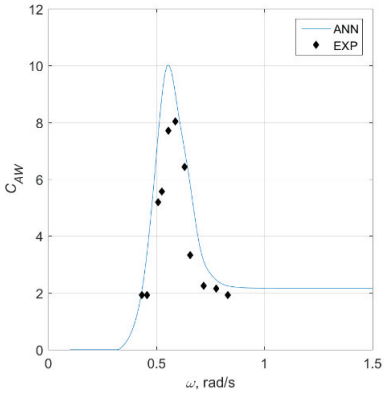

Figure 17. Added resistance coefficient for the S175 container ship for $Fr = 0.20$.

The values for the other two investigated Froude numbers for the S175 container ship were in much better agreement with the experimental data, as shown in Figure 18. Again, the curve of the added resistance coefficient for both Froude numbers, i.e., an $Fr = 0.25$ and an $Fr = 0.30$, was slightly shifted towards the lower wave frequencies. The added resistance coefficients predicted by the third neural network for the DTC container ship were overestimated around the peak area, as shown in Figure 19. In addition, the peak position of the added resistance curve was not predicted accurately by the neural network, as obtained in [2].

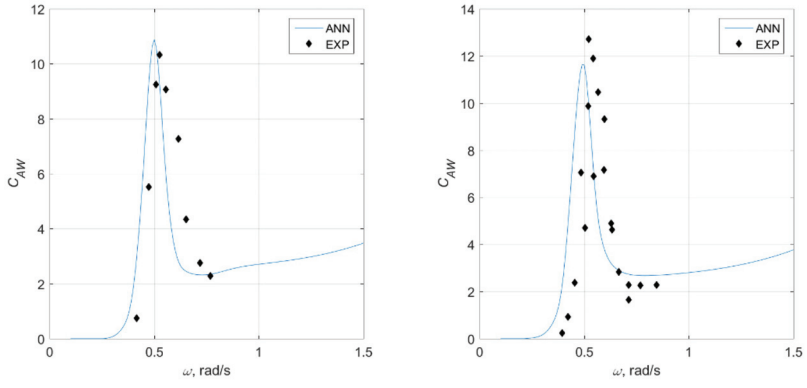

Figure 18. Added resistance coefficient for the S175 container ship for $Fr = 0.25$ (**left**) and $Fr = 0.30$ (**right**).

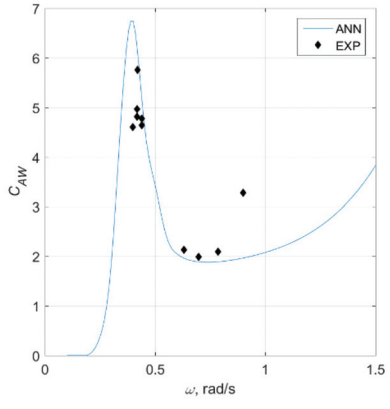

Figure 19. Added resistance coefficient for the DTC container ship for $Fr = 0.14$.

The expressions for the prediction of the added resistance coefficient for all three neural networks are given in the Appendices A–C, and of this paper, and the ranges of the container ships' characteristics for all three container ship classes are given in Table 5.

Table 5. Ranges of the container ships' characteristics for all classes.

Main Particular	Range for Class 1	Range for Class 2	Range for Class 3
L_{PP}, m	104.8 ÷ 155.4	178 ÷ 247	300 ÷ 360
B, m	18 ÷ 25	25.85 ÷ 32.26	37 ÷ 49
T, m	4.25 ÷ 9.2	8 ÷ 12	11 ÷ 15
∇, m^3	5648.7 ÷ 22,672	23,326 ÷ 67,343	67,244 ÷ 174,090
C_B	0.562 ÷ 0.780	0.51 ÷ 0.75	0.53 ÷ 0.65
C_P	0.569 ÷ 0.811	0.53 ÷ 0.768	0.569 ÷ 0.672
LCB, m	49 ÷ 77.7	87.5 ÷ 121	140.9 ÷ 180.7
k_{yy}, m	25.15 ÷ 40.4	42.72 ÷ 64.22	72 ÷ 93.6
V, kn	12.1 ÷ 19	17.3 ÷ 24	19.1 ÷ 26

6. Conclusions

Within this paper, an artificial neural network was used for the prediction of the added resistance in regular head waves. The data used for training and testing the artificial neural network were gathered by performing the calculations based on the Boundary Integral Element Method for various container ships at different speeds. The numerically obtained data

were validated against the experimental data available in the literature. Prior to training the neural network, the data was pre-processed, and the outliers were removed. Because of the appearance of the irregular frequencies, some of the obtained numerical results were discarded from the training and testing data set. The neural network was trained based on the Levenberg–Marquardt learning algorithm with Bayesian regularization. Firstly, 95% of all numerical results were used for training the network, and the topology of 50 neurons in the hidden layer proved to be the most successful one. To simplify the neural network model, the numerical data was divided into three classes based on the container ship length. In that way, for each container ship class, a simple and easy-to-implement model was established. The performance of all three neural networks was demonstrated for three benchmark container ships. The proposed model can be readily used to predict the added resistance coefficient for container ships in regular head waves of frequencies in the range from 0.1 to 1.5 rad/s, and, in that way, the limited availability of the experimental results, when it comes to the range of incoming frequencies, can be overcome. The limitations of the proposed model are the ranges of the container ship particulars and the Froude number, as well as the wave direction, since only the head waves were considered. A simple and efficient model for the rapid determination of added resistance was proposed, which can be used within preliminary ship design. Unlike the hydrodynamic calculations, it does not require a 3D model of the ship hull, and it only requires a model of the main particulars.

Author Contributions: Conceptualization, I.M. and N.D.; methodology, I.M., N.D. and C.G.G.; software, I.M.; validation, I.M., N.D. and C.G.G.; formal analysis, I.M., N.D. and C.G.G.; investigation, I.M., N.D. and C.G.G.; resources, I.M.; writing—original draft preparation, I.M. and N.D.; writing—review and editing, I.M., N.D. and C.G.G.; visualization, I.M.; supervision, N.D. All authors have read and agreed to the published version of the manuscript.

Funding: This study has been fully supported by the Croatian Science Foundation under project IP-2020-02-8568.

Institutional Review Board Statement: Not applicable.

Informed Consent Statement: Not applicable.

Data Availability Statement: Not applicable.

Acknowledgments: This study has been fully supported by the Croatian Science Foundation under the project IP-2020-02-8568.

Conflicts of Interest: The authors declare no conflict of interest.

Appendix A

For the input vector:

$$i_i = \begin{Bmatrix} L_{PP} \\ B \\ T \\ \nabla \\ C_B \\ C_P \\ \text{LCB} \\ k_{yy} \\ V \\ \omega \end{Bmatrix}$$

The C_{AW} for class 1 can be calculated as:

$$C_{\text{AW}} = 10(([w_2] \cdot [Y_i] + b_2)r_0 + m_0)$$

where:

$$X_i = \frac{[C] \cdot \{x_i\} - \{m_i\}}{\{r_i\}}$$

$$y_i = [w_1] \cdot [X_i] + [b_1]$$

$$Y_i = 2/(1 + \exp(-2y_i)) - 1$$

$$\begin{gathered} x_1 = (i_1 - 128.137)/20.664 \\ x_2 = (i_2 - 21.225)/2.367 \\ x_3 = (i_3 - 7.188)/1.635 \\ x_4 = (i_4 - 13396)/5851.7 \\ x_5 = (i_5 - 63.088)/9.686 \\ x_6 = (i_6 - 0.6497)/0.0536 \\ x_7 = (i_7 - 0.6650)/0.0590 \\ x_8 = (i_8 - 15.017)/2.0605 \\ x_9 = (i_9 - 32.035)/5.274 \\ x_{10} = (i_{10} - 0.6936)/0.3715 \end{gathered}$$

$$C = \begin{bmatrix} 0.3824 & 0.3183 & 0.3143 & 0.3664 & 0.3746 & -0.2656 & -0.2857 & 0.2918 & 0.3766 & 0.0047 \\ 0.1656 & 0.4175 & -0.3519 & 0.1172 & 0.2103 & 0.5489 & 0.5195 & 0.0802 & 0.1672 & 0.1040 \\ -0.0261 & -0.0084 & -0.0500 & -0.0537 & -0.0156 & -0.1037 & -0.0841 & 0.0251 & -0.0257 & 0.9872 \\ -0.1121 & -0.1470 & -0.0431 & -0.1552 & -0.1149 & 0.0457 & 0.0572 & 0.9515 & -0.1219 & -0.0343 \\ -0.0280 & -0.3306 & 0.6937 & 0.3884 & -0.1200 & 0.3706 & 0.3029 & -0.0101 & -0.0323 & 0.1150 \\ -0.2631 & 0.2852 & -0.2257 & 0.7195 & -0.2417 & -0.1633 & -0.0538 & 0.0456 & -0.4365 & -0.0149 \\ -0.2128 & -0.3993 & -0.3545 & 0.3168 & -0.2327 & -0.0216 & -0.0385 & 0.0158 & 0.7161 & -0.0008 \\ 0.2364 & -0.5774 & -0.3093 & 0.2331 & 0.5911 & 0.0643 & -0.0775 & -0.0052 & -0.3180 & -0.0003 \\ 0.7647 & -0.0837 & -0.1382 & 0.0416 & -0.5679 & 0.1522 & -0.1804 & 0.0005 & -0.0959 & 0.0039 \\ 0.2392 & -0.1099 & -0.0196 & 0.0098 & -0.0553 & -0.6509 & 0.7096 & -0.0068 & -0.0036 & -0.0038 \end{bmatrix}$$

$$m_i = \begin{bmatrix} 0.0477 \\ -0.0800 \\ 0.2045 \\ 0.0625 \\ -0.1135 \\ -0.6706 \\ -0.1488 \\ -0.0371 \\ 0.0118 \\ 0.0009 \end{bmatrix}, \; r_i = \begin{bmatrix} 4.1408 \\ 2.7599 \\ 2.1591 \\ 1.1327 \\ 1.4761 \\ 1.1258 \\ 0.5133 \\ 0.3707 \\ 0.1735 \\ 0.0493 \end{bmatrix}$$

$$w_1 = \begin{bmatrix} -0.2636 & -0.8257 & 6.0417 & 0.9972 & 0.6782 & -2.4651 & 0.0816 & 0.8970 & -0.8842 & 4.3507 \\ -0.5278 & -0.1650 & -1.4982 & -0.2688 & -0.7439 & -0.1655 & 0.0158 & 0.1891 & -0.2910 & 0.9044 \\ 0.3583 & 0.8629 & -6.0848 & -1.0298 & -0.7040 & 2.6013 & -0.0774 & -0.9215 & 0.8775 & -4.3647 \\ -8.5921 & -10.3648 & -78.2030 & 2.3630 & -8.3240 & -4.0775 & -2.9812 & -3.2612 & -0.4898 & -1.1891 \\ 1.1083 & 1.0634 & 8.8737 & -0.0481 & 0.8803 & -0.3321 & 0.1355 & -0.1054 & -0.0112 & -0.0045 \\ -1.0643 & -1.0958 & -8.9089 & 0.0555 & -0.8760 & 0.3089 & -0.0930 & 0.1118 & 0.0087 & 0.0142 \end{bmatrix}$$

$$w_2 = [-3.5051 \; -0.5950 \; -3.4837 \; -0.2601 \; 8.0120 \; 7.9921]$$

$$b_1 = \begin{bmatrix} -0.8818 \\ 2.1630 \\ 0.8534 \\ 5.4844 \\ 1.4481 \\ -1.2624 \end{bmatrix},\ b_2 = -0.1580$$

$$r_0 = 0.4277,\ m_0 = 0.4277$$

Appendix B

The C_{AW} for class 2 can be calculated as:

$$C_{AW} = 100(([w_2] \cdot [Y_i] + b_2)r_0 + m_0)$$

where:

$$X_i = \frac{[C] \cdot \{x_i\} - \{m_i\}}{\{r_i\}}$$

$$y_i = [w_1] \cdot [X_i] + [b_1]$$

$$Y_i = 2/(1 + \exp(-2y_i)) - 1$$

$$x_1 = (i_1 - 198.466)/81.204$$
$$x_2 = (i_2 - 28.334)/8.905$$
$$x_3 = (i_3 - 9.206)/2.838$$
$$x_4 = (i_4 - 43289.8)/45159.2$$
$$x_5 = (i_5 - 96.519)/38.267$$
$$x_6 = (i_6 - 0.6241)/0.0581$$
$$x_7 = (i_7 - 0.6448)/0.0572$$
$$x_8 = (i_8 - 18.463)/3.932$$
$$x_9 = (i_9 - 49.614)/20.375$$
$$x_{10} = (i_{10} - 0.6667)/0.3683$$

$$C = \begin{bmatrix} 0.4095 & 0.3794 & 0.3156 & 0.3704 & 0.4012 & 0.1441 & 0.1576 & 0.2473 & 0.3992 & -0.1564 \\ 0.0444 & -0.2556 & -0.3399 & -0.1598 & 0.0921 & 0.6319 & 0.6168 & -0.0125 & 0.0442 & -0.0350 \\ 0.0563 & 0.0531 & 0.0139 & 0.0457 & 0.0563 & 0.0405 & 0.0414 & 0.1213 & 0.0609 & 0.9833 \\ -0.1379 & -0.1400 & 0.0137 & -0.0730 & -0.1384 & -0.0092 & -0.0041 & 0.9531 & -0.1470 & -0.0813 \\ -0.2675 & -0.1158 & 0.5920 & 0.4804 & -0.3109 & 0.2052 & 0.2799 & -0.1168 & -0.3201 & 0.0227 \\ -0.0353 & -0.1472 & -0.5938 & 0.7691 & 0.0664 & -0.0649 & -0.1236 & 0.0345 & -0.0887 & -0.0120 \\ -0.2204 & -0.5119 & 0.1223 & 0.0768 & -0.1861 & -0.0620 & -0.0743 & -0.0087 & 0.7902 & 0.0034 \\ -0.2225 & 0.6514 & -0.2530 & 0.0309 & -0.5982 & 0.0773 & 0.1444 & 0.0251 & 0.2752 & -0.0154 \\ 0.7928 & -0.2078 & -0.0004 & 0.0277 & -0.5609 & 0.0415 & -0.0910 & -0.0032 & -0.0536 & 0.0025 \\ -0.0934 & 0.0612 & 0.0500 & -0.0034 & 0.0090 & 0.7213 & -0.6816 & 0.0000 & 0.0007 & -0.0000 \end{bmatrix}$$

$$m_i = \begin{bmatrix} 1.4081 \\ 0.4708 \\ -0.0181 \\ 0.0293 \\ 0.0185 \\ -0.5125 \\ -0.0245 \\ 0.0922 \\ -0.0135 \\ 0.0073 \end{bmatrix}, \; r_i = \begin{bmatrix} 8.7163 \\ 5.5926 \\ 4.0274 \\ 2.5232 \\ 3.0464 \\ 2.0211 \\ 0.9304 \\ 1.0471 \\ 0.3201 \\ 0.0480 \end{bmatrix}$$

$$w_1 = \begin{bmatrix} -2.5069 & 1.5576 & 10.3775 & 0.3256 & -1.2813 & 0.5612 & 0.1743 & -0.9947 & 0.3510 & -0.1537 \\ 3.5022 & 0.7051 & -12.2603 & 0.5221 & -0.0151 & 0.1099 & -0.1198 & -0.0062 & 0.0071 & 0.0217 \\ -3.3778 & -0.6539 & 11.8155 & -0.4788 & 0.0686 & -0.1278 & 0.1592 & -0.0303 & -0.0006 & -0.0210 \\ 2.6560 & 0.9430 & -7.8154 & 0.1166 & 0.8166 & -0.6127 & -0.2128 & 0.3213 & -0.4831 & 1.8699 \\ 3.3855 & 1.3891 & 7.9569 & 4.3728 & -0.9070 & -1.0861 & 0.1418 & -1.1713 & -0.2996 & -4.7839 \\ -0.5610 & -0.7253 & -1.1138 & -0.0946 & 0.4045 & -0.0148 & 0.0134 & 0.1175 & 0.0529 & 1.7503 \\ 0.6575 & 0.8673 & 1.1186 & 0.1320 & -0.5260 & 0.0283 & -0.0015 & -0.1663 & -0.0795 & -2.2167 \end{bmatrix}$$

$$w_2 = [0.0882 \; 7.3785 \; 7.5667 \; 0.1366 \; 0.0288 \; -2.2396 \; -1.5010]$$

$$b_1 = \begin{bmatrix} -1.1306 \\ -1.3297 \\ 1.4276 \\ 2.1746 \\ -3.7125 \\ 2.2076 \\ -2.3494 \end{bmatrix}, \; b_2 = -0.1006$$

$$r_0 = 0.0743, \; m_0 = 0.0743$$

Appendix C

The C_{AW} for class 3 can be calculated as:

$$C_{AW} = 100(([w_2] \cdot [Y_i] + b_2)r_0 + m_0)$$

where:

$$X_i = \frac{[C] \cdot \{x_i\} - \{m_i\}}{\{r_i\}}$$

$$y_i = [w_1] \cdot [X_i] + [b_1]$$

$$Y_i = 2/(1 + \exp(-2y_i)) - 1$$

$$\begin{gathered} x_1 = (i_1 - 325.631)/23.260 \\ x_2 = (i_2 - 42.342)/4.504 \\ x_3 = (i_3 - 13.154)/1.765 \\ x_4 = (i_4 - 113672.6)/38252.5 \\ x_5 = (i_5 - 156.090)/12.964 \\ x_6 = (i_6 - 0.5788)/0.0342 \\ x_7 = (i_7 - 0.6077)/0.0294 \\ x_8 = (i_8 - 23.267)/2.213 \\ x_9 = (i_9 - 81.410)/6.395 \\ x_{10} = (i_{10} - 0.5046)/0.2771 \end{gathered}$$

$$C = \begin{bmatrix} 0.3883 & 0.3865 & 0.3892 & 0.3968 & 0.3591 & 0.2578 & 0.2040 & -0.0254 & 0.3633 & -0.1458 \\ -0.1596 & -0.0765 & -0.0324 & -0.0570 & -0.2885 & 0.5526 & 0.5913 & -0.4364 & -0.1606 & -0.0997 \\ 0.0182 & -0.0344 & 0.0374 & 0.0545 & -0.0036 & 0.1832 & 0.2586 & 0.3678 & 0.0209 & 0.8706 \\ -0.0592 & -0.1677 & 0.0183 & -0.0101 & -0.0873 & 0.1556 & 0.2719 & 0.8048 & -0.0711 & -0.4577 \\ -0.1641 & -0.1747 & -0.1761 & -0.1559 & -0.2216 & -0.0129 & 0.0487 & -0.0125 & 0.9139 & -0.0155 \\ -0.0385 & -0.2141 & 0.8076 & 0.0347 & -0.4959 & -0.0144 & -0.2272 & -0.0207 & 0.0055 & 0.0326 \\ 0.0584 & 0.7246 & -0.2047 & -0.0411 & -0.5497 & 0.1993 & -0.2522 & 0.1492 & -0.0123 & 0.0067 \\ 0.5356 & -0.1684 & -0.2218 & 0.4025 & -0.4262 & -0.4425 & 0.3025 & -0.0560 & -0.0367 & -0.0075 \\ -0.4091 & -0.1680 & -0.1979 & 0.7931 & -0.0353 & 0.2237 & -0.2917 & 0.0009 & 0.0017 & -0.0002 \\ 0.5778 & -0.3968 & -0.1798 & -0.1346 & -0.0002 & 0.5333 & -0.4169 & -0.0001 & -0.0001 & -0.0000 \end{bmatrix}$$

$$m_i = \begin{bmatrix} 0.1552 \\ 0.3436 \\ 0.1382 \\ 0.3508 \\ -0.0099 \\ 0.0657 \\ -0.0457 \\ -0.0277 \\ -0.0055 \\ -0.0009 \end{bmatrix}, \; r_i = \begin{bmatrix} 8.2643 \\ 6.6737 \\ 4.7253 \\ 4.3074 \\ 1.2906 \\ 1.2726 \\ 0.9943 \\ 0.5246 \\ 0.1578 \\ 0.0248 \end{bmatrix}$$

$$w_1 = \begin{bmatrix} 1.4744 & 1.0656 & -5.7174 & 2.6766 & 0.0209 & -0.0026 & -0.0724 & -0.0137 & 0.0041 & -0.0269 \\ 1.4574 & 1.0166 & -5.6633 & 2.6476 & 0.0242 & -0.0062 & -0.1001 & -0.0323 & 0.0017 & -0.0307 \\ 1.8720 & 1.3636 & -7.2758 & 3.4471 & 0.0257 & -0.0065 & -0.0676 & -0.0237 & 0.0107 & -0.0213 \\ 2.5293 & 1.9130 & -10.4909 & 4.8362 & -0.0306 & -0.2229 & -0.0725 & 0.0870 & 0.0234 & 0.0254 \\ 2.4175 & 1.7917 & -9.6471 & 4.5501 & 0.0243 & -0.0836 & -0.0616 & 0.0026 & 0.0193 & 0.0031 \\ -0.8937 & 1.3660 & -1.5650 & -0.3778 & 0.0388 & -0.1974 & 0.7997 & -0.6389 & 0.1650 & -0.0091 \\ 1.3786 & 2.1212 & 1.8082 & 0.7687 & -0.0483 & 0.2299 & -1.3497 & 1.0794 & -0.2447 & 0.0424 \end{bmatrix}$$

$$w_2 = [10.8421 \; -3.6182 \; -15.4236 \; -4.5217 \; 12.5591 \; -3.7253 \; -2.6440]$$

$$b_1 = \begin{bmatrix} -0.1402 \\ 0.3235 \\ -0.6701 \\ -1.7062 \\ -1.1831 \\ 1.6929 \\ -2.0934 \end{bmatrix}, \; b_2 = 0.2445$$

$$r_0 = 0.0520, \; m_0 = 0.0520$$

References

1. International Maritime Organization. Interim guidelines for determining minimum propulsion power to maintain the manoeuvrability of ships in adverse conditions. *IMO Resolut. MEPC* **2013**, *232*, 65.
2. Cepowski, T. The prediction of ship added resistance at the preliminary design stage by the use of an artificial neural network. *Ocean Eng.* **2020**, *195*, 106657. [CrossRef]
3. Kim, M.; Hizir, O.; Turan, O.; Incecik, A. Numerical studies on added resistance and motions of KVLCC2 in head seas for various ship speeds. *Ocean Eng.* **2017**, *140*, 466–476. [CrossRef]
4. Youngjun, Y.; Jin Woo, C.; Dong, Y.L. Development of a framework to estimate the sea margin of an LNGC considering the hydrodynamic characteristics and voyage. *Int. J. Nav. Archit. Ocean Eng.* **2020**, *12*, 184–198.
5. Degiuli, N.; Martić, I.; Farkas, A.; Gospić, I. The impact of slow steaming on reducing CO2 emissions in the Mediterranean Sea. *Energy Rep.* **2021**, *7*, 8131–8141. [CrossRef]

6. Vinayak, P.P.; Prabu CS, K.; Vishwanath, N.; Prakash, S.O. Numerical simulation of ship navigation in rough seas based on ECMWF data. *Brodogradnja* **2021**, *72*, 19–58. [CrossRef]
7. Martić, I.; Degiuli, N.; Farkas, A.; Gospić, I. Evaluation of the Effect of Container Ship Characteristics on Added Resistance in Waves. *J. Mar. Sci. Eng.* **2020**, *8*, 696. [CrossRef]
8. Zheng, M.; Ni, Y.; Wu, C.; Jo, H. Experimental investigation on effect of sloshing on ship added resistance in head waves. *Ocean Eng.* **2021**, *235*, 109362. [CrossRef]
9. Martić, I.; Degiuli, N.; Ćatipović, I. Evaluation of the added resistance and ship motions coupled with sloshing using potential flow theory. *Brodogradnja* **2016**, *67*, 109–122. [CrossRef]
10. Sigmund, S.; Moctar, O. Numerical and experimental investigation of added resistance of different ship types in short and long waves. *Ocean Eng.* **2018**, *147*, 51–67. [CrossRef]
11. Chirosca, A.M.; Medina, A.; Pacuraru, F.; Saettone, S.; Rusu, L.; Pacuraru, S. Experimental and Numerical Investigation of the Added Resistance in Regular Head Waves for the DTC Hull. *J. Mar. Sci. Eng.* **2023**, *11*, 852. [CrossRef]
12. Kim, T.; Yoo, S.; Kim, H.J. Estimation of added resistance of an LNG carrier in oblique waves. *Ocean Eng.* **2021**, *231*, 109068. [CrossRef]
13. Liu, S.; Papanikolaou, A. Fast approach to the estimation of the added resistance of ships in head waves. *Ocean Eng.* **2016**, *112*, 211–225. [CrossRef]
14. Liu, S.; Papanikolaou, A. Approximation of the added resistance of ships with small draft or in ballast condition by empirical formula. *Proc. Inst. Mech. Eng. Pt. M J. Eng. Marit. Environ.* **2019**, *233*, 27–40. [CrossRef]
15. Liu, S.; Papanikolaou, A. Regression analysis of experimental data for added resistance in waves of arbitrary heading and development of a semi-empirical formula. *Ocean Eng.* **2020**, *206*, 107357. [CrossRef]
16. Liu, S.; Papanikolaou, A. Improving the Empirical Prediction of the Added Resistance in Regular Waves of Ships with Extreme Main Dimension Ratios through Dimensional Analysis and Parametric Study. *Ocean Eng.* **2023**, *273*, 113963. [CrossRef]
17. International Maritime Organization. Guidelines for Determining Minimum Propulsion Power to Maintain the Manoeuvrability of Ships in Adverse Conditions. MEPC.1/Circ.850/Rev.3, 2021. Available online: https://www.classnk.or.jp/hp/pdf/activities/statutory/eedi/13_MEPC.1-Circ.850-Rev.3.pdf (accessed on 2 June 2023).
18. Lee, J.; Kim, Y. Development of enhanced empirical-asymptotic approach for added resistance of ships in waves. *Ocean Eng.* **2023**, *280*, 114762. [CrossRef]
19. Gkerekos, C.; Lazakis, I.; Theotokatos, G. Machine learning models for predicting ship main engine Fuel Oil Consumption: A comparative study. *Ocean Eng.* **2019**, *188*, 106282. [CrossRef]
20. Farag, Y.B.A.; Olçer, A.I. The development of a ship performance model in varying operating conditions based on ANN and regression techniques. *Ocean Eng.* **2020**, *198*, 106972. [CrossRef]
21. Tarelko, W.; Rudzki, K. Applying artificial neural networks for modelling ship speed and fuel consumption. *Neural. Comput. Appl.* **2020**, *32*, 17379–17395. [CrossRef]
22. Majnarić, D.; Šegota, S.B.; Lorencin, I.; Car, Z. Prediction of main particulars of container ships using artificial intelligence algorithms. *Ocean Eng.* **2022**, *265*, 112571. [CrossRef]
23. Mentes, A.; Yetkin, M. An application of soft computing techniques to predict dynamic behaviour of mooring systems. *Brodogradnja* **2022**, *73*, 121–137. [CrossRef]
24. Mittendorf, M.; Nielsen, U.D.; Bingham, H.B. Data-driven prediction of added-wave resistance on ships in oblique waves-A comparison between tree-based ensemble methods and artificial neural networks. *Appl. Ocean. Res.* **2022**, *118*, 102964. [CrossRef]
25. Cepowski, T. The use of a set of artificial neural networks to predict added resistance in head waves at the parametric ship design stage. *Ocean Eng.* **2023**, *281*, 114744. [CrossRef]
26. Yildiz, B. Prediction of residual resistance of a trimaran vessel by using an artificial neural network. *Brodogradnja* **2022**, *73*, 127–140. [CrossRef]
27. Martić, I.; Degiuli, N.; Majetić, D.; Farkas, A. Artificial Neural Network Model for the Evaluation of Added Resistance of Container Ships in Head Waves. *J. Mar. Sci. Eng.* **2021**, *9*, 826. [CrossRef]
28. Chen, X. Hydrodynamics in Offshore and Naval Applications—Part I. In Proceedings of the Keynote Lecture at the 6th International Conference on Hydrodynamics, Perth, Australia, 24–26 November 2004; pp. 1–28.
29. Martić, I.; Degiuli, N.; Farkas, A.; Malenica, Š. Discussions on the convergence of the seakeeping simulations. In Proceedings of the 37th International Conference on Ocean, Offshore & Arctic Engineering, OMAE, Madrid, Spain, 17–22 June 2018; pp. 1–10.
30. Tsujimoto, M.; Shibata, K.; Kuroda, M.; Takagi, K.A. Practical Correction Method for Added Resistance in Waves. *J. Jpn. Soc. Nav. Archit. Ocean Eng.* **2008**, *8*, 177–184. [CrossRef]
31. Kristensen, H.O. *Statistical Analysis and Determination of Regression Formulas for Main Dimensions of Container Ships Based on IHS Fairplay Data*; Project no. 2010-56, Report; Technical University of Denmark: Lyngby, Denmark, 2013.
32. Martić, I.; Degiuli, N.; Komazec, P.; Farkas, A. Influence of the approximated mass characteristics of a ship on the added resistance in waves. In Proceedings of the IMAM 2017, 17th International Congress of the International Maritime Association of the Mediterranean, Maritime Transportation and Harvesting of Sea Resources, Lisabon, Portugal, 9–11 October 2017.
33. MacKay, D.J. Bayesian interpolation. *Neural Comput.* **1992**, *4*, 415–447. [CrossRef]
34. Simonsen, C.D.; Otzen, J.F.; Joncquez, S.; Stern, F. EFD and CFD for KCS heaving and pitching in regular head waves. *J. Mar. Sci. Technol.* **2013**, *18*, 435–459. [CrossRef]

35. Simonsen, C.D.; Otzen, J.F.; Nielsen, C.; Stern, F. CFD prediction of added resistance of the KCS in regular head and oblique waves. In Proceedings of the 30th Symposium on Naval Hydrodynamics, Hobart, Australia, 2–7 November 2014.
36. Fujii, H.; Takahashi, T. Experimental Study on the resistance increase of a ship in regular oblique waves. In Proceedings of the 14th ITTC, International Towing and Tank Conference, National Research Council of Canada, Ottawa, ON, Canada, 2–11 September 1975; pp. 351–359.
37. Deng, J.; Deng, Y.; Cheong, K.H. Combining conflicting evidence based on Pearson correlation coefficient and weighted graph. *Int. J. Intell. Syst.* **2021**, *36*, 7443–7460. [CrossRef]

Journal of
Marine Science and Engineering

MDPI

Article

The Impact of Numerical Parameters on the Resistance Characteristics of a Container Ship at the Model and Full Scale

Carlo Giorgio Grlj, Nastia Degiuli * and Ivana Martić

Faculty of Mechanical Engineering and Naval Architecture, University of Zagreb, Ivana Lučića 5, 10000 Zagreb, Croatia; carlo.g.grlj@fsb.hr (C.G.G.); ivana.martic@fsb.hr (I.M.)
* Correspondence: nastia.degiuli@fsb.hr

Abstract: Computational Fluid Dynamics (CFD) is a powerful tool used to predict the resistance characteristics of a ship. However, it is important to determine the numerical and modelling errors to assure accurate results. The aim of this study is the investigation of the impact of different numerical parameters on the total resistance, wave pattern and ship motion in numerical simulations at the model and full scale. These include the turbulence model and discretization schemes for convection, gradient and temporal terms within the governing equations. The numerical model used in numerical simulations is based on Reynolds Averaged Navier-Stokes (RANS) equations which are discretized using the Finite Volume Method (FVM). To locate and track the free surface, the Volume of Fluid (VOF) method is employed. The Grid Convergence Index (GCI) method is used for the verification study. The obtained results show that the selection of the discretization scheme for temporal term does not have impact on the median value of the total resistance and that the first-order scheme assures faster convergence in numerical simulations at the full scale. A higher portion of the frictional resistance in the total resistance is obtained with numerical simulations at the model scale in comparison to the full scale.

Keywords: CFD; discretization scheme; turbulence model; container ship; resistance test

Citation: Grlj, C.G.; Degiuli, N.; Martić, I. The Impact of Numerical Parameters on the Resistance Characteristics of a Container Ship at the Model and Full Scale. *J. Mar. Sci. Eng.* **2023**, *11*, 1672. https://doi.org/10.3390/jmse11091672

Academic Editor: Kostas Belibassakis

Received: 20 July 2023
Revised: 22 August 2023
Accepted: 22 August 2023
Published: 25 August 2023

1. Introduction

Nowadays, Computational Fluid Dynamics (CFD) is a commonly used tool for the prediction of flow around the ship and ship hydrodynamic characteristics, since computational power has been increasing continuously. The main advantage of CFD simulations is that it can reduce the required number of expensive towing tank experiments. Another benefit of the numerical simulations over the towing tank experiments is the possibility of avoiding the extrapolation methods by performing full-scale CFD simulations [1]. Recently, Orych et al. [2] conducted a validation study for the delivered power estimated with numerical simulations based on Reynolds Averaged Navier-Stokes (RANS) equations coupled with a body force propeller method for modelling the effects of a rotating propeller, which is based on the lifting line theory. Numerical uncertainty was determined for numerical simulations at the model and full scale, while the validation was based on sea trial results. The authors obtained an average comparison error between the numerically obtained and sea trial results of about 1%, which is considerably lower than the validation uncertainty equal to 7%. Saydam et al. [3] performed numerical simulations of the resistance, open water and self-propulsion tests for a case of a tanker in order to quantify the numerical simulation uncertainties. The authors found an error of 4% for the prediction of the total resistance, while larger uncertainties were obtained for torque predictions and, consequently, the delivered power.

Degiuli et al. [4] investigated the influence of slow steaming on carbon dioxide (CO_2) emissions by using full-scale CFD simulations based on RANS equations for the determination of resistance and propulsion characteristics. Other aspects, such as the influence

of biofouling on resistance, were studied by Demirel et al. [5]. Song et al. [6] emphasized the importance of including the roughness effects within the CFD simulations for the determination of the frictional and viscous resistance of different hull forms. Feng et al. [7] conducted CFD simulations of a KRISO container ship (KCS) in different water depths for the determination of the total resistance and dynamic sinkage. The numerical results were validated against the benchmark experimental results, and the comparison error was between 1% and 4% with larger errors obtained for the model scale numerical simulations. Full-scale CFD simulations were validated by Niklas and Pruszko [8], and the obtained relative deviation of total resistance in calm water was from −10% to 4% compared to the sea trial data and extrapolated towing tank results. The authors emphasized the importance of determining the form factor, which can vary depending on the method used, and thus, it can have a great influence on the ship resistance predictions. Terziev et al. [1] used CFD simulations to investigate the influence of ship speed and scale on the form factor and concluded that it depends on the Froude number for very low ship speeds, while larger differences in the form factor were obtained for different scales and turbulence models. Dogrul [9] pointed out scale effects on the propulsion characteristics, such as nominal wake, thrust deduction fraction, and open-water propeller and propulsion efficiencies for the case of a Joubert BB2 submarine.

Although full-scale CFD simulations may be a good alternative to towing tank tests, since the extrapolation of the measured values is avoided, there is still a need for a more systematic and comprehensive sea trials in order to validate the numerical simulations at the full scale for the determination of the ship resistance characteristics and the nominal wake [10]. In addition, there is a need to investigate the influence of numerical parameters such as the discretization schemes for solving the convection, gradient and temporal terms within the governing equations. Such a study was conducted by Andrun et al. [11], where the authors assessed the effect of different schemes for solving the gradient terms within the Volume of Fluid (VOF) method by conducting numerical simulations of the flow around the model of the Wigley hull. It was concluded that second-order schemes have to be used on realistic hull forms, for which the non-linear effects are more pronounced, to determine the resistance and wave elevation more accurately. A more recent study was conducted by Huang et al. [12], in order to determine the ideal numerical setup for full-scale numerical simulations. The authors showed that the second-order scheme should be used for spatial discretization, while for temporal discretization, either first or second-order schemes can be applied. The effect of different draughts on the hydrodynamic characteristics was investigated by Farkas et al. [13]. Based on the obtained results, the authors concluded that although RSM turbulence model is the most accurate one, by using the Realizable $k - \varepsilon$ (RKE), satisfactory agreement with the extrapolated towing tank results can be obtained. Degiuli et al. [14] numerically investigated the impact of the bulbous bow on the total resistance of a yacht and validated the results by comparing them with the towing tank results. Within the study, the authors achieved satisfactory agreement with the experimentally obtained values for total resistance using different turbulence models.

In this study, numerical simulations of viscous flow around the hull of a container ship are systematically performed in order to assess the effects of different discretization schemes and turbulence models on the hydrodynamic performance in calm water. The effect of numerical parameters are investigated at the model and full scale. The post-Panamax 6750-TEU container ship is chosen since the geometry and inertial properties are available in the literature [15]. An extensive verification study for grid size and time step is performed using the Grid Convergence Index (GCI) method. For numerical simulations at the model scale, a validation study is conducted by comparing the numerical results against the measured values from towing tank tests. The paper is organized as follows. The description of the container ship used in the numerical simulations is provided in Section 2. The mathematical background, the numerical setup and an overview of the verification and validation studies are given in Section 3. The results are discussed in Section 4, and

finally, the conclusions drawn from the comprehensive numerical study are summarized in Section 5.

2. Case Study

The post-Panamax 6750-TEU container ship is selected as a case study. Table 1 shows the geometrical and inertial properties of the model in scale ($\lambda = 35.18$) and full-scale container ship [15], while Figure 1 shows the 3D model used in the simulations.

Table 1. Post-Panamax 6750-TEU container ship data.

Property	Full Scale	Model Scale
λ, -	1	35.18
L_{OA}, m	300.891	8.553
L_{PP}, m	286.6	8.147
L_{WL}, m	281.3	7.996
T, m	11.98	0.341
B, m	40	1.137
Δ, t	85,562.7	1.965
KM, m	18.662	0.531
GM, m	2.1	0.06
KG, m	16.562	0.471
L_{CG} from AP, m	138.395	3.934
k_{xx}, m	14.6	
k_{yy}, m	70.144	
k_{zz}, m	70.144	

Figure 1. Geometry of the post-Panamax 6750-TEU container ship.

The towing tank experiments were conducted at the Brodarski Institute in Zagreb [16]. The resistance tests were carried out in a large towing tank of a length of 276 m, a width of 12.5 m, and a depth of 6 m. The ship model was made of wood at a scale of $\lambda = 35.18$. The resistance tests were conducted at 14 speeds in the range from 12 to 25 knots corresponding to full-scale ship. For purpose of the validation study, the experimental results of the resistance test at 2.168 m/s are used, corresponding to 25 knots for the full-scale ship.

3. Methods

In this study, numerical simulations based on RANS equations are conducted. The Finite Volume Method (FVM) is used for the discretization of the governing equations. A multiphase flow model based on the Eulerian approach; i.e., the VOF method is used for locating and tracking the free surface. To maintain a sharp interface between two fluids, High-Resolution Interface Capturing (HRIC) scheme is used. The Dynamic Fluid Body Interaction (DFBI) model with two degrees of freedom is used to predict the trim and sinkage.

3.1. Mathematical Model

The commercial software package STAR-CCM+ [17] is used in this study. The mathematical model is based on the RANS equations, which are derived from the conservation of mass and momentum laws. For incompressible, unsteady case the RANS equations read as follows:

$$\frac{\partial \bar{u}_i}{\partial x_i} = 0 \tag{1}$$

$$\rho \frac{\partial \bar{u}_i}{\partial t} + \rho \frac{\partial}{\partial x_j}\left(\bar{u}_i \bar{u}_j + \overline{u_i' u_j'}\right) = -\frac{\partial \bar{p}}{\partial x_i} + \frac{\bar{\tau}_{ij}}{\partial x_j} \tag{2}$$

where ρ is the fluid density, $\bar{u}_i$ is the averaged Cartesian components of the velocity vector, $\rho\overline{u_i' u_j'}$ is the Reynolds Stress Tensor (RST), and $\bar{p}$ is the mean pressure. The mean viscous stress tensor $\bar{\tau}_{ij}$ is defined by:

$$\bar{\tau}_{ij} = \mu\left(\frac{\partial \bar{u}_i}{\partial x_j} + \frac{\partial \bar{u}_j}{\partial x_i}\right) \tag{3}$$

where μ is the dynamic viscosity of the fluid. The turbulence models are then used to close the system of Equations (1) and (2) to be able to solve them.

3.2. Turbulence Models

Three turbulence models are used in this study: RKE, Shear Stress Transport $k-\omega$ (SSTKO) and RSM. The RANS turbulence models are based on the modelling of the RST. The RKE and SSTKO turbulence models belong to the group of eddy viscosity models, which are based on the similarity between the molecular gradient-diffusion process and turbulent motion. These types of turbulence models use the Boussinesq approximation to model the RST as follows:

$$-\rho\overline{u_i' u_j'} = \mu_t\left(\frac{\partial \bar{u}_i}{\partial x_j} + \frac{\partial \bar{u}_j}{\partial x_i}\right) - \frac{2}{3}\rho k \delta_{ij} \tag{4}$$

where μ_t is the turbulent eddy viscosity, and k is the turbulence kinetic energy.

The RSM turbulence model calculates the components of the RST directly. Thus, it has the potential to predict complex turbulent fluid flows more accurately by considering the anisotropy of the RST, but at the cost of more computational power. More details regarding the applied turbulence models can be found in the literature [13].

3.3. Realizable $k-\varepsilon$ (RKE) Two-Layer

The Realizable $k-\varepsilon$ Two-Layer turbulence model solves one equation for the turbulent kinetic energy k and one for the turbulent dissipation rate ε. The eddy viscosity is calculated as follows:

$$\mu_t = \rho C_\mu \frac{k^2}{\varepsilon} \tag{5}$$

where C_μ is the model coefficient defined with the following equation:

$$C_\mu = \frac{1}{A_0 + A_S U^* \dfrac{k}{\varepsilon}} \tag{6}$$

where $A_0 = 4$ and A_S is given by:

$$A_S = \sqrt{6}\cos\phi \tag{7}$$

$$\phi = \frac{1}{3}\arccos\left(\sqrt{6}W\right) \tag{8}$$

$$W = \frac{S_{ij}S_{jk}S_{ki}}{\left(\sqrt{S_{ij}S_{ij}}\right)^3} \tag{9}$$

and U^* is defined as:

$$U^* = \sqrt{S_{ij}\cdot S_{ij} + W_{ij}\cdot W_{ij}} \tag{10}$$

The strain rate tensor is given by the equation:

$$S_{ij} = \frac{1}{2}\left(\frac{\partial u_i}{\partial x_j} + \frac{\partial u_i^T}{\partial x_j}\right) \tag{11}$$

and the rotation rate tensor by:

$$W_{ij} = \frac{1}{2}\left(\frac{\partial u_i}{\partial x_j} - \frac{\partial u_i^T}{\partial x_j}\right) \tag{12}$$

The transport equations for k and ε are defined as:

$$\frac{\partial}{\partial t}(\rho k) + \frac{\partial}{\partial x_i}(\rho k\bar{u}_i) = \frac{\partial^2 k}{\partial x_i^2}\left(\mu + \frac{\mu_t}{\sigma_k}\right) + f_c G_k + G_b - \mathrm{Y}_M - \\ - \rho(\varepsilon - \varepsilon_0) + S_k \tag{13}$$

$$\frac{\partial}{\partial t}(\rho\varepsilon) + \frac{\partial}{\partial x_i}(\rho\varepsilon\bar{u}_i) = \frac{\partial^2 \varepsilon}{\partial x_i^2}\left(\mu + \frac{\mu_t}{\sigma_\varepsilon}\right) + \frac{1}{T_\varepsilon}C_{\varepsilon 1}(f_c Sk + C_{\varepsilon 3}G_b) - \\ - C_{\varepsilon 2}f_2\rho\left(\frac{\varepsilon}{T_\varepsilon} - \frac{\varepsilon_0}{T_0}\right) + S_\varepsilon \tag{14}$$

where $\bar{u}_i$ is the averaged velocity vector, σ_k and σ_ε are the turbulent Schmidt numbers, f_c is the curvature correction factor, G_k is the turbulent production term, G_b is the buoyancy production term, ε_0 is the ambient turbulence value that counteracts turbulence decay, Y_M is the dilatation dissipation, C_{ε_1}, C_{ε_2} and C_{ε_3} are the model depending coefficients, S_k and S_ε are the user-defined source terms, and S is the modulus of the mean strain tensor.

3.4. Shear Stress Transport $k-\omega$ (SSTKO)

The $k-\omega$ turbulence model is a two-equation model that solves transport equations for the turbulent kinetic energy k and another for the specific dissipation ω:

$$\frac{\partial}{\partial t}(\rho k) + \frac{\partial}{\partial x_i}(\rho k\bar{u}_i) = \frac{\partial^2 k}{\partial x_i^2}(\mu + \sigma_k\mu_t) + G_k + G_{nl} + G_b - \\ - \rho\beta^* f_{\beta^*}(\omega k - \omega_0 k_0) + S_k \tag{15}$$

$$\frac{\partial}{\partial t}(\rho\omega) + \frac{\partial}{\partial x_i}(\rho\omega\bar{u}_i) = \frac{\partial^2 \omega}{\partial x_i^2}(\mu + \sigma_\omega\mu_t) + G_\omega + D_\omega - \rho\beta f_\beta(\omega^2 - \omega_0^2) + S_\omega \tag{16}$$

where σ_k, σ_ω, β and β^* are the model depending coefficients, G_{nl} is the non-linear production term, f_β is the free-shear modification factor, f_{β^*} is the vortex-stretching modification factor, and finally, k_0 and ω_0 are the ambient values that counteract turbulence decay. Menter [18] modified the Standard $k-\omega$ model, which blends the $k-\varepsilon$ model in the

far-field with the $k-\omega$ model near the wall. The turbulent eddy viscosity is given with the following equation:

$$\mu_t = \rho k T \tag{17}$$

where T is the turbulent time scale given with the equation:

$$T = \min\left(\frac{\alpha^*}{\omega}, \frac{a_1}{SF_2}\right) \tag{18}$$

where α^* and a_1 are the model coefficients, and F_2 is the blending function coefficient that depends on the distance to the wall.

3.5. Reynolds Stress Model (RSM)

The Reynolds Stress Model consists of solving the transport equation for RST. The transport equation is defined as:

$$\frac{\partial}{\partial t}(\rho R_{ij}) + \frac{\partial}{\partial x_i}(\rho R_{ij}\bar{u}_i) = \frac{\partial}{\partial x_m}\left[\left(\mu + \frac{\mu_t}{\sigma_k}\right)\frac{\partial R_{ij}}{\partial x_m}\right] + P_{ij} + G_{ij} - \\ - \frac{2}{3}\Upsilon_M + \phi_{ij} - \rho\varepsilon_{ij} + S_R \tag{19}$$

where P_{ij} is the turbulent production term, G_{ij} is the buoyancy production term, ϕ_{ij} is the pressure–strain tensor, and ε_{ij} is the turbulent dissipation rate tensor. This model requires seven equations to be solved, six equations for the RST components and one equation for the isotropic turbulent dissipation. The Quadratic Pressure–Strain model was used within the simulations with high y^+ wall treatment to model the pressure–strain term.

3.6. Computational Domain and Boundary Conditions

An unstructured hexahedral mesh is used for the discretization of the computational domain. Only half of the computational domain is created, since the flow is symmetric with respect to the ship symmetry plane. The domain boundaries are placed at a distance to avoid their influence on the flow around the ship hull and consequently on the obtained results. The inlet and bottom boundaries are placed at $2L_{PP}$ from the ship, the top boundary is placed at L_{PP} above the waterline, while the outlet boundary is placed at $4L_{PP}$ behind the ship. The side boundary is placed at $2.5L_{PP}$ to avoid reflection of the waves. Boundary conditions are set as the VOF wave velocity at the inlet, top and bottom boundaries. The pressure outlet is assigned at the outlet boundary, while both sides of the domain are defined as symmetry planes. The no-slip wall boundary condition is set at the hull surface. The computational domain with the respective boundary conditions and its main dimensions is given in Figure 2. In order to prevent wave reflection against the domain boundaries, the wave damping layer approach is used in the numerical simulations. The wave damping is applied at the inlet, outlet and side boundaries.

Different regions around the ship are carefully discretized. The grid is more refined in the area where the free surface is expected to be located as well as the Kelvin wake region behind the ship, following the ITTC recommendations [19]. The region close to the ship hull is refined with more attention given to the bow and stern regions.

The prism layers are carefully generated so that the non-dimensional wall distance y^+ is in the range $30 < y^+ < 100$, i.e., the log-law region [20]. The approximate distance between the wall and the centre of the first prism layer near the wall is calculated as:

$$y = \frac{y^+ L}{0.172 Re^{0.9}} \tag{20}$$

where Re is the Reynolds number. The obtained non-dimensional wall distance y^+ is within the limits, as shown in Figure 3, meaning that the application of wall functions is justified. Figure 4 shows the fine grid with the described refinements, which is used

within the numerical simulations. Figure 5 shows a detailed view of the stern and bow regions. It can be noticed that the prism layers are carefully created to obtain a smooth transition between the prism layers and the rest of the grid. The stretching factor for the prism layers is about 1.5, and the number of prism layers depends on the scale for which the numerical simulations are conducted. A lower number of prism layers are created at the model scale and a higher number at the full scale to achieve a prism layer thickness that assures a smooth transition from prism layers to the rest of the grid. The prism layers are not generated on the deck and transom stern surfaces.

The distributions of the pressure coefficients along the hull surface obtained from numerical simulations at the model and full scale are shown in Figure 6. Lower pressure coefficients are achieved in the bulbous bow region for the model scale in comparison to full scale.

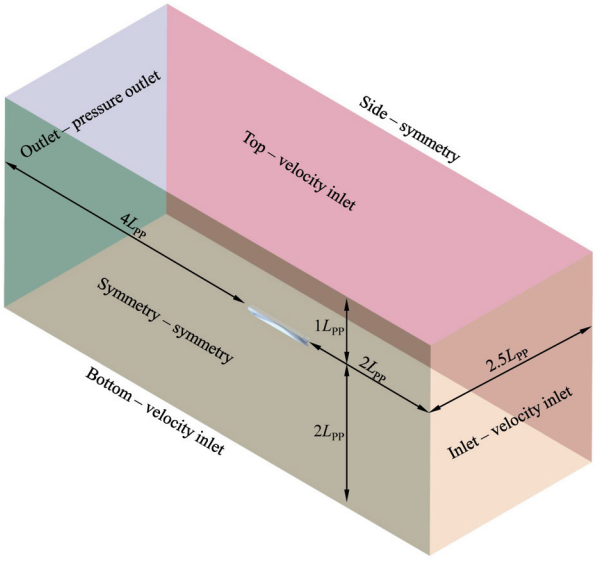

Figure 2. Dimensions and boundaries of the computational domain for the free surface simulations.

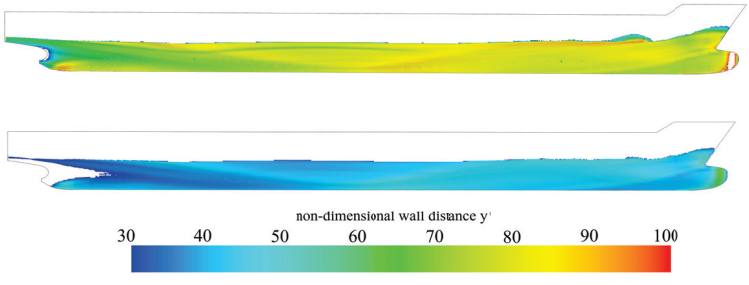

Figure 3. Distribution of the non-dimensional wall distance y^+ on the full scale (**top**) and model scale (**bottom**) hull surface.

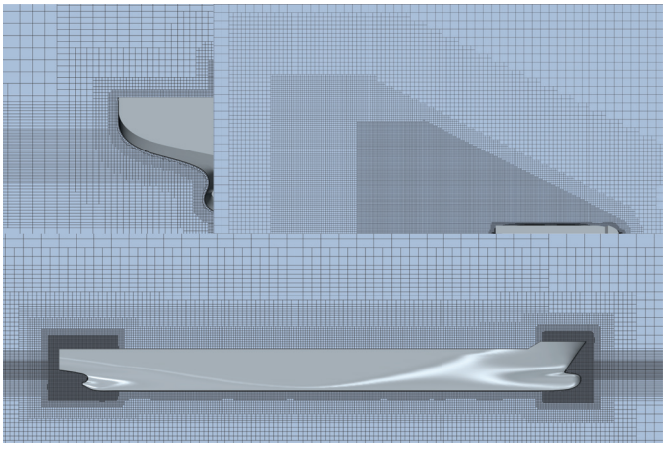

Figure 4. Fine grid with refinements.

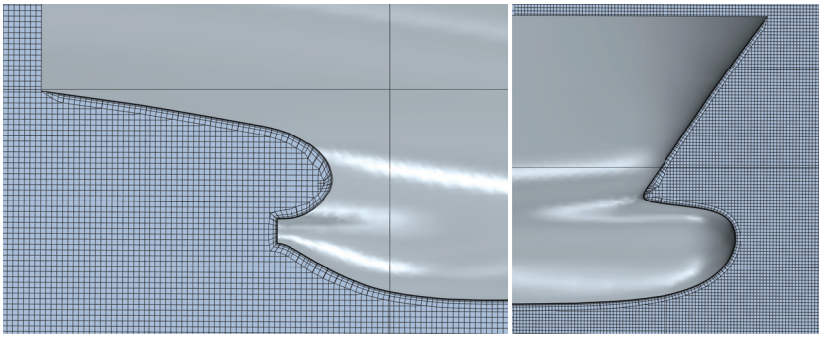

Figure 5. Detailed view of the prism layers at the stern (**left**) and bow (**right**).

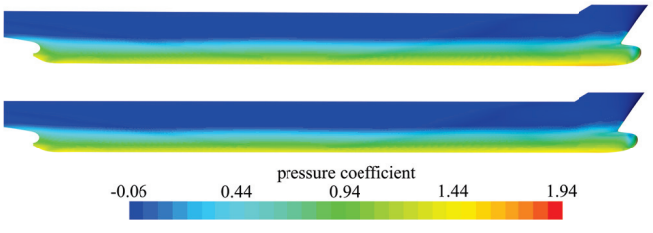

Figure 6. Distribution of the pressure coefficient on the hull surface at full scale (**top**) and model scale (**bottom**).

In the numerical simulations, a speed of 25 knots corresponding to the full-scale ship is used. Froude similarity is used to calculate the speed for the numerical simulations at the model scale.

3.7. The Verification And Validation Study

The GCI method is used for the verification study, which is based on the Richardson extrapolation [21]. This method was successfully used in [20,22,23]. The first step is to calculate the apparent order of the method p using the following equations:

$$p = \frac{1}{\ln r_{21}} \cdot \left| \ln \left| \frac{\varepsilon_{32}}{\varepsilon_{21}} \right| + q(p) \right| \tag{21}$$

$$q(p) = \ln\left(\frac{r_{21}^{p} - s}{r_{32}^{p} - s}\right) \tag{22}$$

$$s = 1 \cdot \mathrm{sgn}\left(\frac{\varepsilon_{32}}{\varepsilon_{21}}\right) \tag{23}$$

where r is the grid refinement ratio, and ε is defined as $\varepsilon_{ij} = \phi_i - \phi_j$, with ϕ being the solutions. The order of the method p is calculated by solving the Equations (21)–(23) iteratively.

Extrapolated values and the approximate and extrapolated relative errors are calculated using the Equations (24)–(26), respectively:

$$\phi_{\mathrm{ext}}^{21} = \frac{r_{21}^{p}\phi_1 - \phi_2}{r_{21}^{p} - 1} \tag{24}$$

$$e_{\mathrm{a}}^{21} = \left|\frac{\phi_1 - \phi_2}{\phi_1}\right| \tag{25}$$

$$e_{\mathrm{ext}}^{21} = \left|\frac{\phi_{\mathrm{ext}}^{21} - \phi_1}{\phi_{\mathrm{ext}}^{21}}\right| \tag{26}$$

Finally, GCI for fine grid can be calculated with following equation:

$$GCI_{\mathrm{fine}}^{21} = \frac{1.25 e_{\mathrm{a}}^{21}}{r_{21}^{p} - 1} \tag{27}$$

The convergence condition R is calculated with the following equation:

$$R = \frac{\varepsilon_{21}}{\varepsilon_{32}} \tag{28}$$

Convergence conditions R are used to evaluate the obtained extrapolated values and are defined as:

- Monotonic convergence: $0 < R < 1$;
- Oscillatory convergence: $R < 0$;
- Divergence: $R > 1$.

The described method can be used for the calculation of the uncertainty due to time step [24]. Fine grid is used, and three time steps are varied in the numerical simulations for the determination of the uncertainty due to time step.

3.8. Discretization Schemes

The RANS equations are discretized in order to be able to numerically solve them. More precisely, the governing Partial Differential Equations (PDE) are transformed into a system of algebraic equations. In this study, different discretization schemes for spatial and temporal discretization are used, and the obtained results are compared. Specifically, the convection terms are solved using three discretization schemes, while the gradient and temporal terms are solved using two discretization schemes.

The convection terms in the segregated flow and turbulence models can be solved using different schemes within the software package STAR-CCM+. The second-order scheme is used for the verification and validation study. Thereafter, first- and third-order schemes are investigated. The results obtained by the first and second-order discretization schemes for gradient terms are then compared. Finally, the investigated parameters, i.e., discretization schemes for gradient, convection terms and temporal discretization are all set as first and second order. An overview of the different combinations used in numerical simulations can be found in Section 4.

4. Results and Discussion

4.1. The Verification and Validation Study

The verification study is performed for time step and grid size at the model and full scale. Time steps are selected according to the ITTC recommendations [19] in the range $0.005L_{WL}/v - 0.01L_{WL}/v$. The largest time step used in this study is $0.02L_{WL}/v$, and hence, the refinement ratio is equal to 2, and consequently, the iterative procedure for obtaining the order of the method p is avoided.

The details of the used grid resolutions are presented in Table 2. The grid spacing value h is defined as:

$$h = \sqrt[3]{\frac{1}{N}\sum_{i=1}^{N}(\Delta V_i)} \tag{29}$$

where N is the total number of cells in the grid, and V_i is the volume of the i-th cell.

Table 2. Details of the used grid resolutions.

Index	N		h, m	
	Model Scale	Full Scale	Model Scale	Full Scale
1	2.3 M	3.7 M	0.189	7.70
2	1.0 M	2.3 M	0.248	8.99
3	0.4 M	1.0 M	0.327	11.99

Tables 3 and 4 show all the calculated variables and the estimation of errors for two verification studies at the model and full scales. The approximated and extrapolated relative errors are presented alongside the GCI. Monotonic convergence is obtained for the full-scale numerical simulations and oscillatory convergence for both verification studies at the model scale. The obtained numerical uncertainty is below 2% for all cases, which shows that the fine grid size and time step are adequate for the remaining numerical simulations. It is worth noting that the obtained GCI for full-scale numerical simulations is slightly higher in comparison to model scale numerical simulations. One of the reasons is the grid setup within the numerical simulations.

Table 3. Verification study for the time step.

Parameter	Model Scale	Full Scale
ε_{32}	−7.906 N	80.524 kN
ε_{21}	1.259 N	31.774 kN
r_{32}	2	2
r_{21}	2	2
R	−0.159	0.395
p	2.650	1.342
e_a^{21}	0.014%	0.01%
e_{ext}^{21}	0.003%	0.01%
GCI_{fine}^{21}	0.34%	1.13%

Table 4. Verification study for the grid size.

Parameter	Model Scale	Full Scale
ε_{32}	1.897 N	80.756 kN
ε_{21}	−0.013 N	9.885 kN

Table 4. *Cont.*

Parameter	Model Scale	Full Scale
r_{32}	1.319	1.335
r_{21}	1.314	1.167
R	−0.006	0.123
p	18.142	6.228
e_{a}^{21}	0.0001%	0.44%
e_{ext}^{21}	0.000001%	0.27%
GCI_{fine}^{21}	0.0001%	0.34%

The obtained numerical results for the model scale are validated against the measured values obtained by the towing tank tests. To compare the numerical and experimental results, the relative deviation is calculated as follows:

$$RD = \frac{\phi_{\mathrm{CFD}} - \phi_{\mathrm{EXP}}}{\phi_{\mathrm{EXP}}} \cdot 100\% \tag{30}$$

where ϕ_{CFD} and ϕ_{EXP} are numerically and the experimentally obtained values, respectively. Table 5 shows the numerically and experimentally obtained total resistance and the calculated relative deviations for the speed of 25 knots and three turbulence models. It can be seen that the relative deviations are quite high, but that is in accordance with a previous study conducted by Farkas et al. [13], where the highest relative deviations are obtained using the SSTKO turbulence model. Similar results were shown in a review paper by Pena and Huang [25], where the authors showed that relative deviations of 10% can be expected with eddy viscosity turbulence models when wall functions are applied. It is important to note that the numerical simulations are performed for a smooth hull surface, so underprediction of the total resistance is expected. Thus, although the RKE turbulence model shows the lowest relative deviation, it overpredicts the total resistance. In conclusion, the SSTKO turbulence model is selected since it is the best compromise between the computational time and the accuracy of the results.

Table 5. Validation study for the total resistance.

Turbulence Model	$R_{\mathrm{TM,CFD}}$, N	$R_{\mathrm{TM,EFD}}$, N	RD, %
RKE	96.617	94.994	1.709
SSTKO	87.780		−7.595
RSM	91.352		−3.834

4.2. Turbulence Models

In Section 4.2, the SSTKO turbulence model is compared to the RKE and RSM models. The numerical simulations with the SSTKO turbulence model were conducted until the total resistance converged. After the stable oscillations of the total resistance were reached, the simulations were performed for an additional 200 s for the full scale and around 100 s for the model scale. The medians of these oscillations are calculated, and the obtained total resistances are shown in Table 6.

Table 6. Total resistance obtained with RKE, SSTKO and RSM turbulence model.

Turbulence Model	R_{TS}, kN	R_{TM}, N
RKE	2321.11	96.62
SSTKO	2302.87	87.73
RSM	2356.26	91.35

Figure 7 shows the values of the total resistance as a function of physical time for three turbulence models. The oscillations are caused partly by the trim and sinkage of

the ship. The total resistance obtained with the SSTKO turbulence model at the full scale is slightly lower than for RSM and RKE models, which predict similar results. From Table 6 and Figure 7 it can be seen that the RSM turbulence model yields the highest total resistance at the full scale. Also, the trend of the total resistance curve is almost the same for all three turbulence models. It should be noted that the median values of total resistance obtained by all turbulence models are similar. At the model scale, the trend of the total resistance curve varies significantly with the turbulence model, where the RKE predicts significantly higher values in comparison to the SSTKO and RSM turbulence models. One of the reasons for this is that the numerical setups are different regarding the discretization of the boundary layer, with less prism layers generated at the model scale when compared to the full scale. The reason for the higher values obtained with the RKE turbulence model is that the eddy viscosity is calculated differently than when using the SSTKO turbulence model. This effect is visible at the model scale since the boundary layer is relatively larger when compared to the full scale.

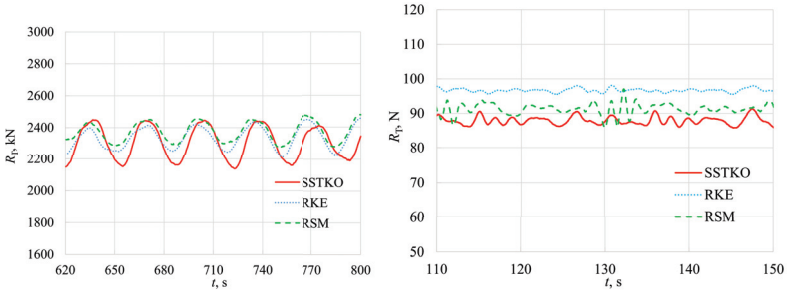

Figure 7. Comparison of total resistance obtained using three turbulence models at full scale (**left**) and model scale (**right**).

Figure 8 shows the sinkage and trim as a function of the physical time at the full scale and model scale. The sinkage obtained with numerical simulations at the model scale is scaled with $\lambda = 35.18$ for the comparison with full-scale results. It can be seen that trim does not depend on the chosen turbulence model at the full scale, while sinkage is slightly lower for the RSM turbulence model. At the model scale, the RSM turbulence model predicts lower sinkage and higher trim values. The sinkage and trim obtained with the RKE and SSTKO turbulence model are nearly the same at the full and model scale. The sinkage and trim obtained using the RSM turbulence model at the model scale are similar to the results at the full scale. However, the trim is lower and sinkage is higher when using the SSTKO and RKE turbulence models at the model scale in comparison to the full scale.

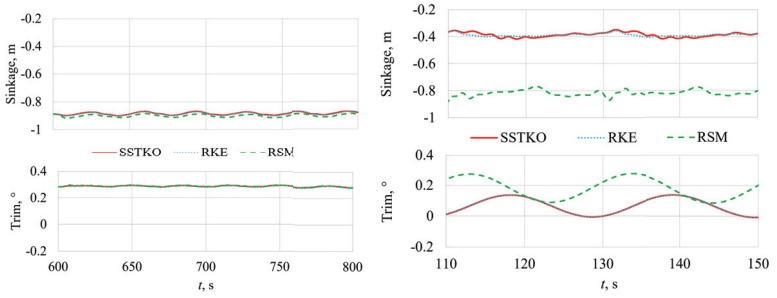

Figure 8. Sinkage and trim values as a function of physical time for three turbulence models at full scale (**left**) and model scale (**right**).

Figure 9 shows the wave elevations along the hull and Figure 10 on the longitudinal cuts located at $B/4$, $B/2$ and B from the centreline of the ship, obtained with different turbulence models at the model and full scale. The wave elevations are presented in the non-dimensional form by dividing the x-axis and wave elevations η with length between perpendiculars L_{PP}. The differences between turbulence models are not significant, although at both scales, there are some discrepancies near the bow. At the full scale, the RSM and SSTKO turbulence model predict similar wave elevations, while the RKE yields slightly different results. Also, at the full scale, the RKE turbulence model predicts a higher wave elevation at longitudinal distance between $0.2L_{PP}$ and $0.3L_{PP}$. Similar results are obtained using the RSM and RKE turbulence model at the model scale but with lower values near the bow in comparison to the full scale.

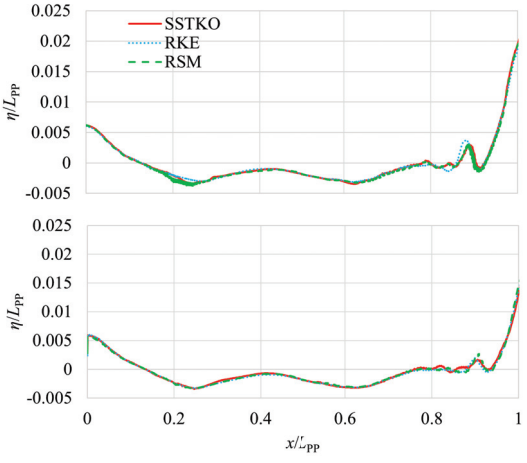

Figure 9. Wave elevations along the hull at full scale (**top**) and model scale (**bottom**) for different turbulence models.

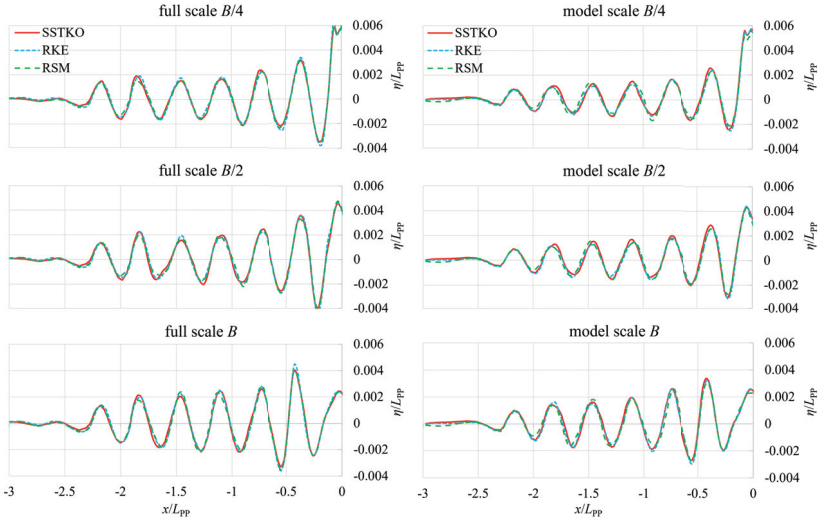

Figure 10. Wave elevations behind the stern at longitudinal cuts $B/4$, $B/2$ and B from the centreline of the ship obtained with numerical simulations at full scale (**left**) and model scale (**right**).

4.3. Discretization Schemes

The impact of the discretization schemes for spatial and temporal discretization is analysed using the fine grid and time step as in the verification study for the full and model scale. The SSTKO turbulence model is used in the remaining numerical simulations. For the cases given in Table 7, the numerical setups are the same at the full and model scales. The STAR-CCM+ default discretization schemes [26] are used in case 1, while remaining cases use different discretization schemes, as shown in Table 7.

Table 7. Different combinations of discretization schemes used in the numerical simulations.

Case	Temporal	Convection	Gradient
1	1st	2nd	2nd
2	1st	1st	2nd
3	1st	3rd	2nd
4	1st	2nd	1st
5	2nd	2nd	2nd
6	1st	1st	1st

4.4. Convection Terms

In this study, the discretization schemes for convection terms are varied within the equations of the turbulence models as well as within the momentum and continuity equations, while maintaining the discretization schemes for gradient and temporal terms as second and first-order, respectively. The considered discretization schemes for convection terms are first-, second- and a hybrid third-order scheme. The third-order scheme is named MUSCL 3rd-order/Central differencing, and it is worth noting that the scheme lowers the order of accuracy in the regions of non-smooth flows.

Figure 11 shows the total resistance values obtained from three numerical simulations at the full scale and three at the model scale. The time range in the graph is displayed from the beginning of the simulations. Using first-order discretization schemes, the total resistance tends to converge considerably faster than in the case with the second-order scheme for the convection terms. Nevertheless, it must be pointed out that the total resistance has higher values for case 2 both at the full and model scale. The amplitudes of the total resistance obtained by second-order discretization scheme are larger and the convergence is much slower than the ones obtained by the first-order scheme. As expected, using the MUSCL 3rd order/Central differencing scheme, the obtained values of total resistance are similar to the ones obtained using second-order scheme. The reason is that this scheme lowers the order of accuracy in the regions of the non-smooth flow.

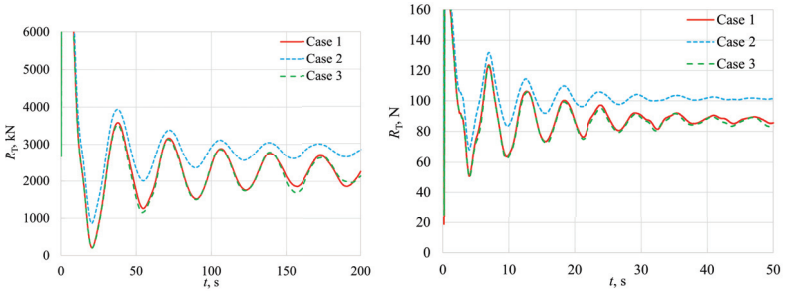

Figure 11. Comparison of three discretization schemes for convection terms at full scale (**left**) and model scale (**right**).

Figure 12 shows the values of sinkage and trim as a function of physical time at the full and model scale. The sinkage obtained with numerical simulations at the model scale is scaled with $\lambda = 35.18$ for the comparison with the full-scale results. There are no significant

differences in the obtained sinkage values other than the slightly lower amplitude of the oscillations in the case when first-order scheme is used. On the other hand, the trim values obtained via the first-order scheme for convection terms show a slightly faster convergence at the full scale, while slightly lower amplitudes are obtained at the model scale. The sinkage and trim depend significantly on the scale, with higher sinkage and lower trim values obtained with numerical simulations at the model scale compared to the full scale.

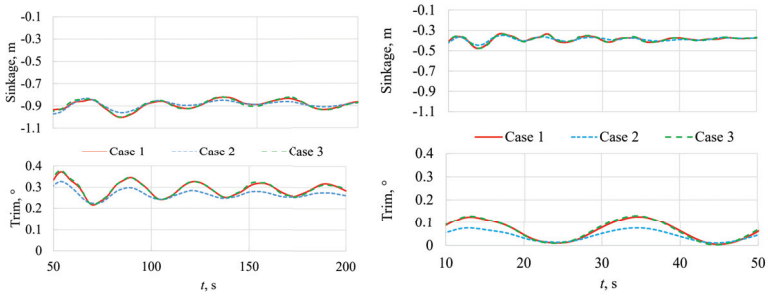

Figure 12. Sinkage and trim values as a function of physical time for different discretization schemes for convection terms at full scale (**left**) and model scale (**right**).

Figures 13 and 14 show the wave patterns obtained using the different discretization schemes for convection terms at the full and model scale. The wave elevations obtained with the first-order schemes are noticeably lower in comparison to the ones obtained using higher order schemes. Also, the Kelvin wake is barely visible both at the full and model scale when using the first-order scheme for convection terms. Non-physical perturbations of the free surface outside the Kelvin region can be seen in case 3, where the hybrid third-order discretization scheme for convection terms is used. This effect is slightly less pronounced for the model scale.

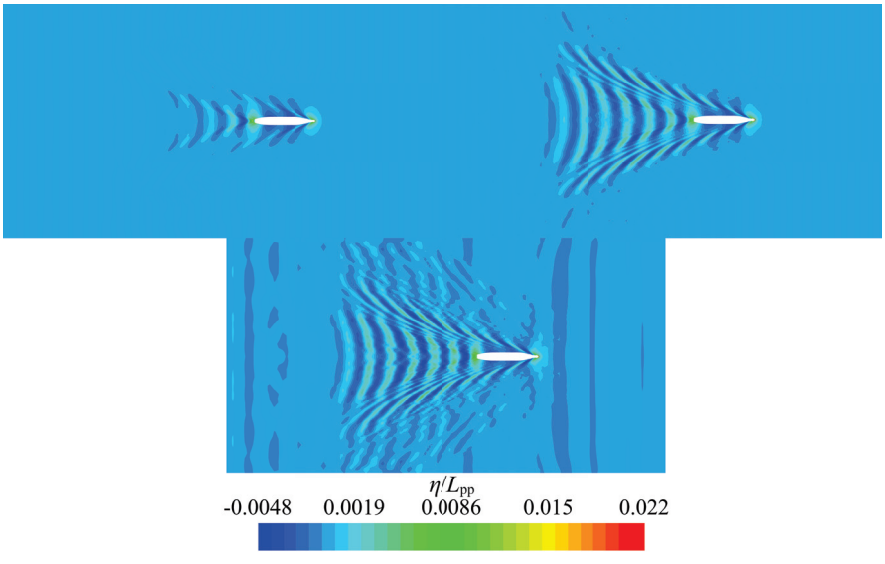

Figure 13. Wave patterns obtained with first-order (**top-left**), second-order (**top-right**) and hybrid third-order (**bottom**) discretization scheme for convection terms at full scale.

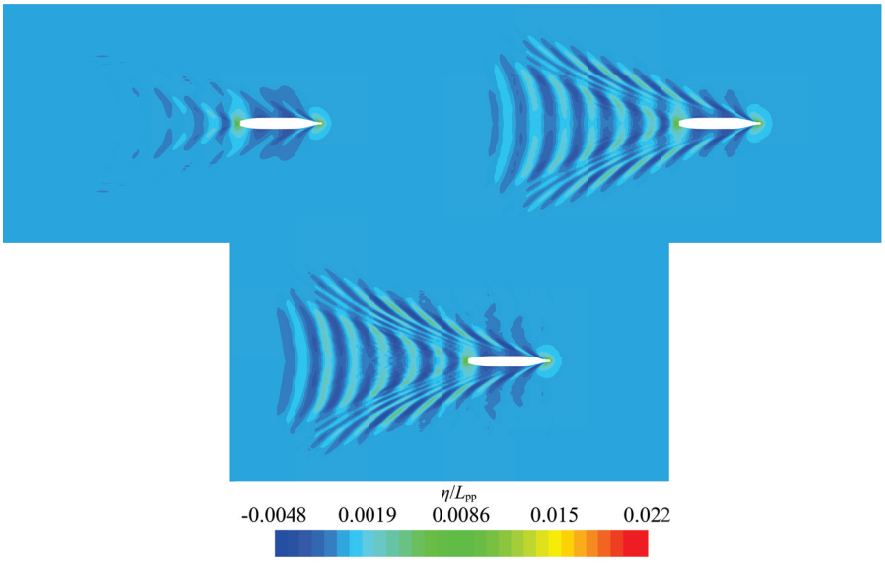

Figure 14. Wave patterns obtained with first-order (**top-left**), second-order (**top-right**) and hybrid third-order (**bottom**) discretization scheme for convection terms at model scale.

Finally, the wave elevations at the centreline of the ship behind the stern and in front of the bow are presented in Figures 15 and 16, respectively, while the wave elevations along the hull are shown in Figure 17. Also, the wave elevations obtained with numerical simulations at the full and model scale behind the stern at longitudinal cuts $B/4$, $B/2$ and B from the centreline of the ship are presented in Figure 18. The results suggest that the choice of the discretization scheme for the convection terms is crucial for the determination of the wave pattern. The wave amplitudes behind the stern decrease significantly faster with first-order scheme in comparison to second and third-order scheme. The same effect can be seen at the full and model scale. The wave elevations along the hull at the model scale are very similar for all three discretization schemes. At the full scale, the first-order scheme yields the lowest elevations, while the hybrid third-order scheme predicts slightly higher elevations.

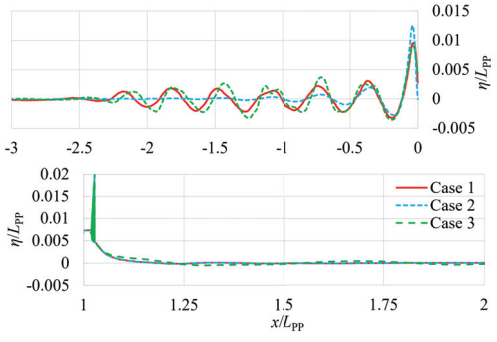

Figure 15. Wave elevations behind the stern (**top**) and in front of the ship (**bottom**), obtained using different discretization schemes for convection terms at full scale.

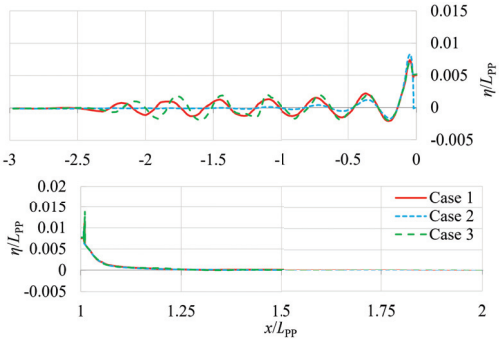

Figure 16. Wave elevations behind the stern (**top**) and in front of the ship (**bottom**), using different discretization schemes for convection terms at model scale.

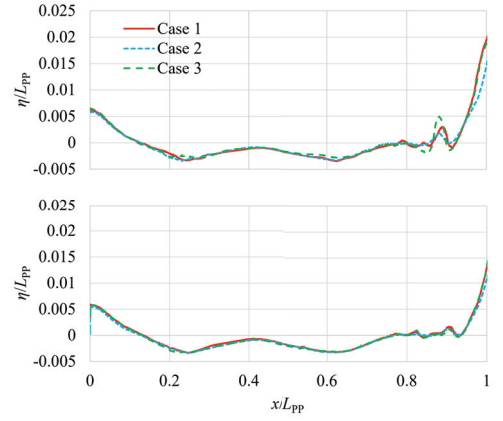

Figure 17. Wave elevations along the hull at full scale (**top**) and model scale (**bottom**) using different discretization schemes for convection terms.

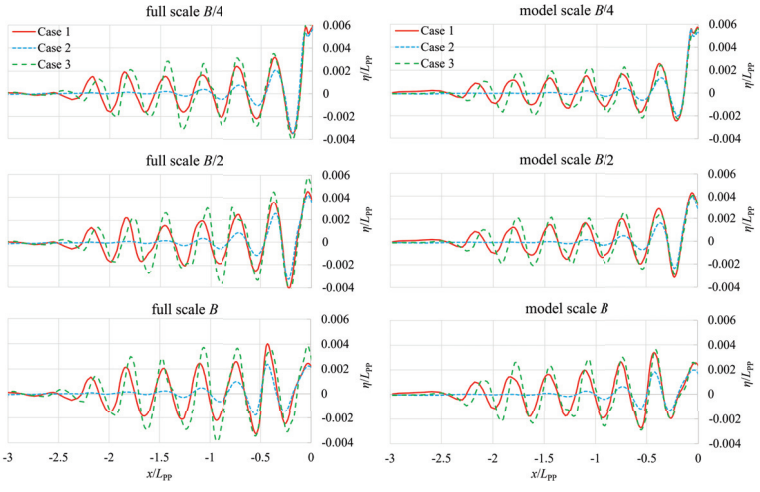

Figure 18. Wave elevations behind the stern at longitudinal cuts $B/4$, $B/2$ and B from the centreline of the ship obtained with numerical simulations at full scale (**left**) and model scale (**right**).

4.5. Gradient Terms

In Section 4.5, the discretization schemes for gradient terms are varied between the first and second order, while the convection terms are kept as second order. The total resistance converges faster with a higher median value using the first-order scheme, as obtained for convection terms in the previous subsection. By comparing Figures 11 and 19, it can be noticed that using the first-order scheme either for gradient or convection terms yields similar results for total resistance. The same is valid for the full and model scale. The main difference between the full and model scale is the faster convergence at the model scale.

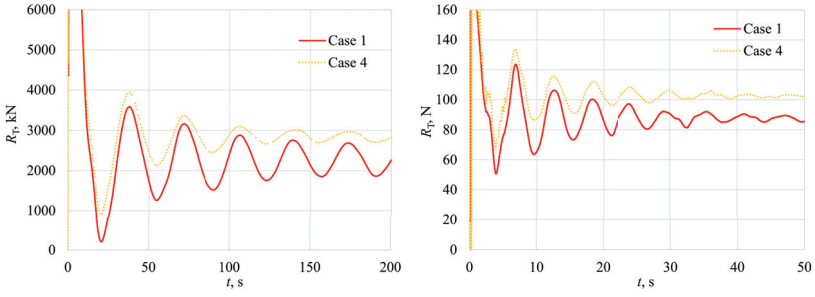

Figure 19. Comparison of two discretization schemes for gradient terms at full scale (**left**) and model scale (**right**).

Figures 20 and 21 show a comparison of the wave elevations at the centreline of the ship, obtained using the first- and second-order scheme for gradient terms at the full and model scales. The wave elevations behind the ship obtained using the first-order scheme are significantly lower than the ones obtained using the second-order scheme. The same is obtained in the previous subsection, where the discretization scheme for convection terms is varied. The wave elevations in front of the ship are almost the same in both cases. Figure 22 shows the wave elevations along the hull for different discretization schemes for gradient terms at the full and model scale. Like in the previous analysis of the discretization schemes for convection terms, the first-order scheme for gradient terms yields lower wave elevations along the hull at the full scale. The differences between two discretization schemes at the model scale are negligible in comparison to the full scale.

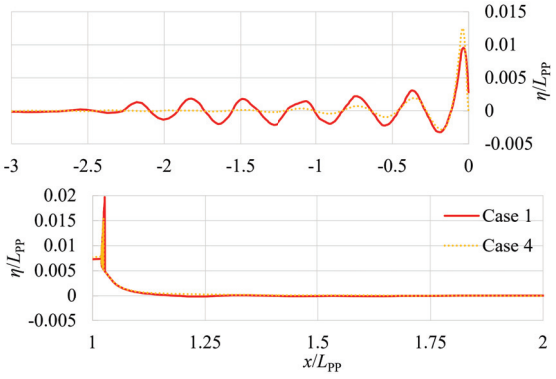

Figure 20. Wave elevations behind the stern (**top**) and in front of the ship (**bottom**), obtained using the first and second-order scheme for gradient terms at full scale.

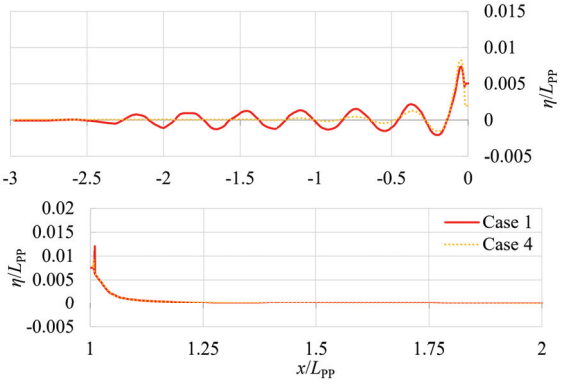

Figure 21. Wave elevations behind the stern (**top**) and in front of the ship (**bottom**), obtained using the first and second-order scheme for gradient terms at model scale.

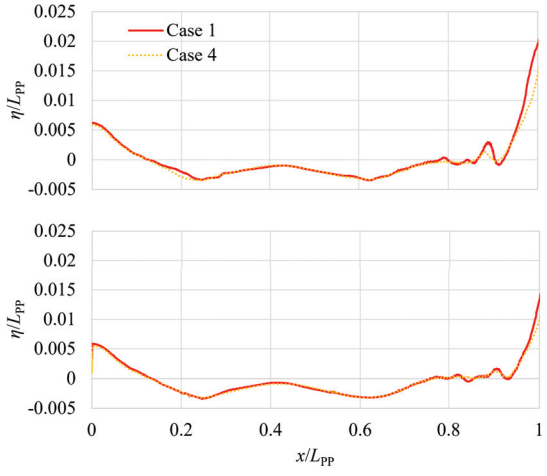

Figure 22. Wave elevations along the hull at full scale (**top**) and model scale (**bottom**) using different discretization scheme for gradient terms.

A comparison between discretization schemes for convection and gradient terms is presented in Figure 23 at the full and model scale in order to assess their impact on numerical results. There are no significant differences between the obtained values of the total resistance at the full and model scale. Thus, it can be concluded that the discretization schemes for solving the convection and gradient terms have a similar impact on the total resistance.

4.6. First-Order vs. Second-Order Schemes

In this Section 4.6, the discretization schemes for all the terms, including temporal discretization, are varied between first and second-order scheme. The details of cases 5 and 6 can be seen in Table 7. The comparison between first- and second-order discretization scheme for gradient, convection and temporal terms is presented in Figure 24 at the full and model scale. A significantly slower convergence of the total resistance is obtained by using the second-order scheme. The oscillations reach higher amplitudes, but with a lower median value. The same is valid for the results obtained using the numerical simulations at the full and model scale, with model scale showing faster convergence using both the first

and second-order discretization scheme, as can be seen from the physical time shown on the abscissa.

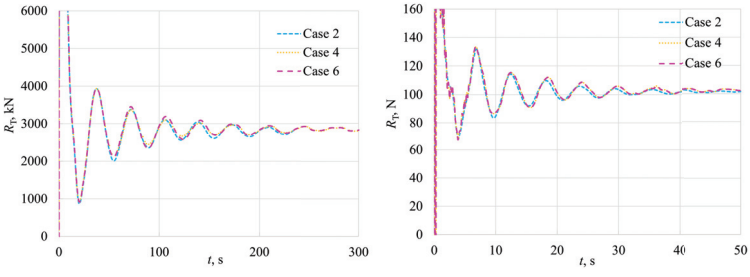

Figure 23. Comparison between first-order scheme for convection and gradient terms at full (**left**) and model scale (**right**).

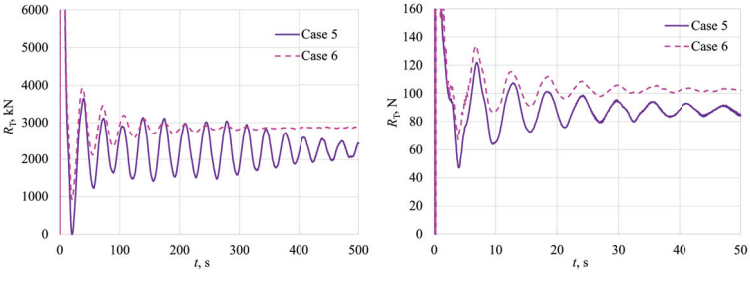

Figure 24. Comparison between first and second-order discretization scheme for gradient, convection terms and temporal discretization at full scale (**left**) and model scale (**right**).

Figures 25 and 26 show the obtained wave elevations at the centreline of the ship at full and model scale, respectively. The numerical dissipation, when first-order scheme is applied, is visible at the full and model scale. Figure 27 shows the wave elevations along the ship hull for the full and model scale, obtained using the first and second-order scheme for convection, gradient and temporal terms. Again, lower elevations can be seen at full scale when the first-order scheme is used, while at model scale, the differences are almost negligible. The impact of the discretization scheme for the temporal term on the total resistance at full and model scale is shown in Figure 28. Faster convergence with no significant effect on the median value is obtained with the first-order discretization scheme for the temporal term. At model scale, this effect is negligible in comparison to full-scale results, nevertheless, it is still visible.

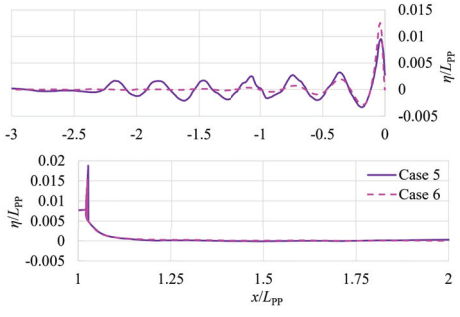

Figure 25. Wave elevations behind the stern (**top**) and in front of the ship (**bottom**), obtained using different discretization schemes for spatial and temporal terms at full scale.

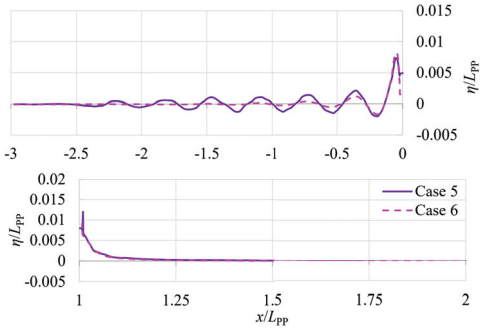

Figure 26. Wave elevations behind the stern (**top**) and in front of the ship (**bottom**), obtained using different discretization schemes for spatial and temporal terms at model scale.

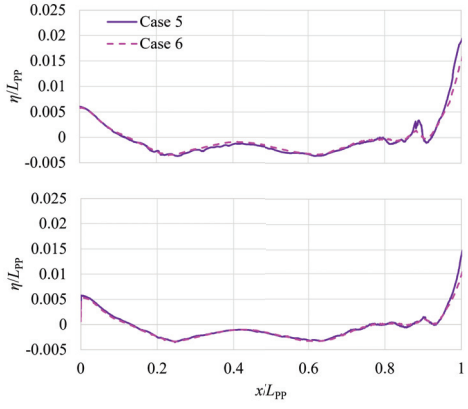

Figure 27. Wave elevations along the hull at full scale (**top**) and model scale (**bottom**) using different discretization schemes for spatial and temporal terms.

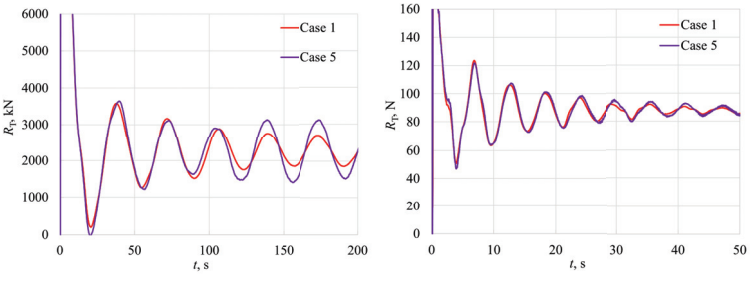

Figure 28. The impact of the temporal discretization on the total resistance at full scale (**left**) and model scale (**right**).

Figure 29 shows the wave elevations behind the stern at longitudinal cuts $B/4$, $B/2$ and B from the centreline of the ship obtained with numerical simulations at the full and model scale. The wave elevations obtained from numerical simulations at the full scale are higher for case 5 in comparison to case 1. On the contrary, at the model scale, the wave elevations behind the ship for case 5 are lower in comparison to case 1. As expected, lower elevations can be seen at sections further away from the centreline of the ship for the full and model scales.

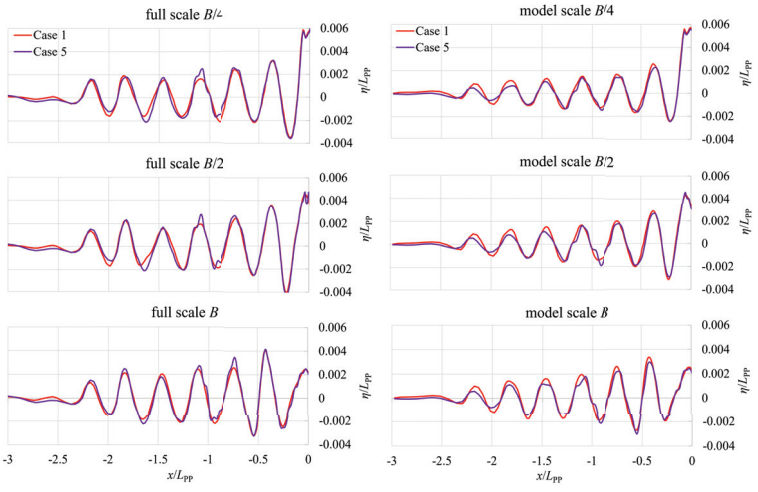

Figure 29. Wave elevations behind the ship at longitudinal cuts $B/4$, $B/2$ and B from the centreline of the ship obtained with numerical simulations at full scale (**left**) and model scale (**right**).

4.7. Resistance Components

In Section 4.7, the total resistance obtained within the free surface simulations is decomposed into the frictional R_F and pressure R_P resistance. These components are obtained by integrating the tangential stress and pressure, obtained with free surface simulations, over the wetted surface, respectively. The results obtained with numerical simulations at the full and model scale are shown in Figures 30 and 31 for the cases listed in Table 7. The frictional resistance is almost the same for all the cases at the full and model scales. The pressure resistance changes with the different discretization schemes more significantly in comparison to the frictional resistance. Also, the portion of the frictional resistance in the total resistance is significantly higher at the model scale, with a median value of 76.2%, than at the full scale, where its portion is 59.5%. It can be concluded that the portion of the frictional resistance decreases, while the portion of the pressure resistance becomes more significant at the full scale in comparison to the model scale.

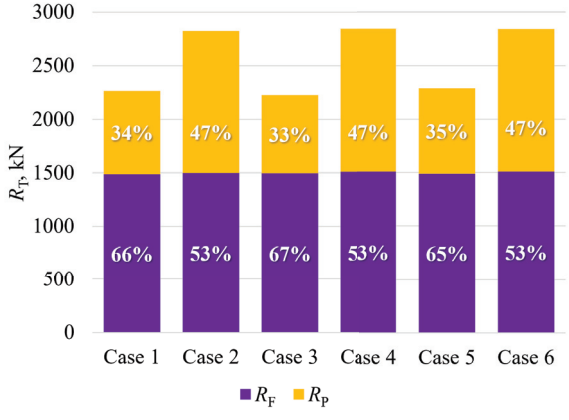

Figure 30. The portions of the total resistance components obtained with numerical simulations at full scale.

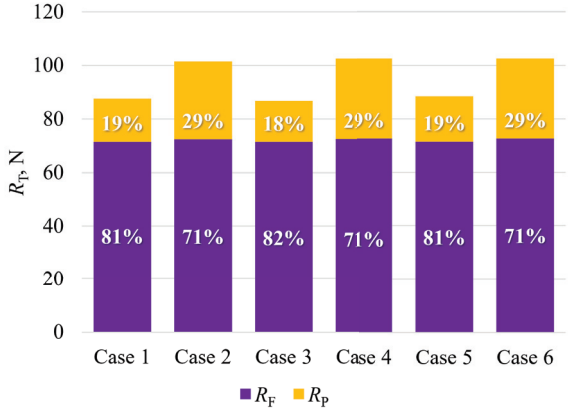

Figure 31. The portions of the total resistance components obtained with numerical simulations at model scale.

Figure 32 shows the portions of the total resistance components obtained with three turbulence models within the numerical simulations at the full and model scale. Similarly to the results of the previous analysis, the median value of the portion of the frictional resistance in the total resistance at the model scale is 82%, which is noticeably higher than that at the full scale, where the median value of the portion of the frictional resistance is 66.7%. The portions of the total resistance components do not change significantly with different turbulence models, even though the total resistance does change.

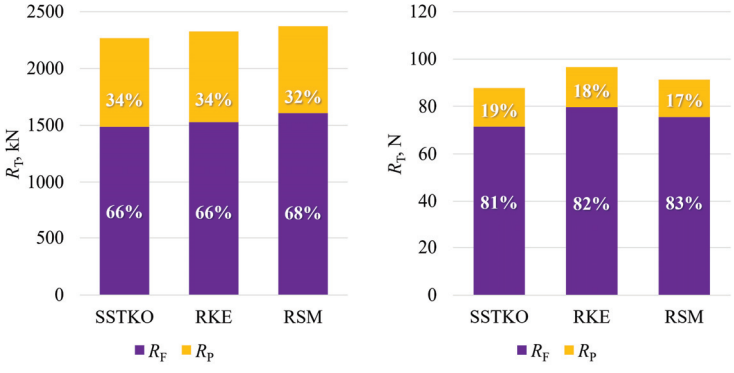

Figure 32. The portions of the total resistance components obtained with different turbulence models within the numerical simulations at full scale (**left**) and model scale (**right**).

5. Conclusions

Numerical simulations of the flow around the model- and full-scale post-Panamax container ship were performed, and the numerical setup was described in detail along with the overview of the meshing process. The grid was refined in the region of the Kelvin wake, the approximate location of the free surface and the boundary layer around the ship hull. In order to apply wall functions, the boundary layer was discretized to maintain the non-dimensional wall distance y^+ in the range $30 < y^+ < 100$. The numerical uncertainty was calculated using the Grid Convergence Index (GCI) method for the grid size and time step. The monotonic convergence of the results was obtained for three grid sizes and three time steps at the full scale, while oscillatory convergence was obtained for numerical simulations at the model scale. A validation study was conducted using the

numerical results obtained with three turbulence models and experimental results from the towing tank. After the verification and validation studies were completed, the impact of different numerical parameters on the total resistance, wave pattern and ship motion was analysed. These included turbulence models and the discretization schemes for the convection, gradient and temporal terms. The considered turbulence models included the Realizable $k - \varepsilon$ (RKE), Shear Stress Transport $k - \omega$ (SSTKO) and Reynolds Stress (RSM). The results have shown that the total resistance obtained using the SSTKO turbulence model at the full scale differs from the ones obtained using RKE and RSM. A similar trend was noticed for numerical simulations at the model scale, where the SSTKO turbulence model yielded lower values of the total resistance in comparison to RKE turbulence model. Also, the total resistance obtained by the RSM turbulence model differs with scale. The total resistance obtained by RSM turbulence model at the full scale is almost the same as the one obtained with RKE, while at the model scale, the values are closer to the ones obtained by SSTKO turbulence model. Slightly lower sinkage values are obtained using the RSM model for the model and full scale, while the trim does not depend on the chosen turbulence model.

For the convection terms, the first-, second- and hybrid third-order discretization schemes were analysed. Faster convergence of the total resistance was obtained when the first-order scheme was applied, but the total resistance was higher than that with the second- and hybrid third-order scheme. Also, the wave pattern obtained with the first-order scheme had lower amplitudes and dissipated faster behind the ship in comparison to the other two schemes. The wave pattern obtained by the hybrid third-order scheme showed some unphysical perturbations in the region outside the Kelvin wake. This effect was slightly less visible at the model scale. Similarly, the impact of the discretization scheme for solving the gradient terms on the numerical results was assessed. The gradient terms in this analysis are solved using the first and second-order discretization scheme. Similar results are obtained as in the analysis of the convection terms. Higher total resistance was obtained with faster convergence when the first-order scheme was applied. The wave elevations at the centreline of the ship had lower amplitudes behind the stern. After the discretization schemes for convection and gradient terms were analysed separately, their impact on the obtained numerical results together with the discretization scheme for temporal terms was assessed. Compared to the second-order scheme, faster convergence with a higher median value of total resistance was obtained with the first-order scheme. Finally, the impact of the discretization scheme for temporal term was assessed. It has been shown that the selection of the discretization scheme for solving the temporal term does not impact the median value of the total resistance and that the first-order scheme assures faster convergence in numerical simulations at the full scale. In numerical simulations at the model scale, the first-order scheme speeds up the convergence of the total resistance as well, but at a slower rate.

Finally, the total resistance was decomposed into frictional and pressure resistance. It has been shown that the frictional resistance does not depend significantly on the discretization scheme for the convection, gradient and temporal terms. On the other hand, the discretization schemes for convection and gradient terms affect the pressure resistance, which is higher when the first-order scheme is used. The total resistance changes with the chosen turbulence model, but the portions of frictional and pressure resistance remain nearly the same. Also, both analyses showed that a higher portion of frictional resistance within the total resistance is obtained with numerical simulations at the model scale in comparison to the full scale.

Author Contributions: Conceptualization, C.G.G., N.D. and I.M.; methodology, C.G.G., N.D. and I.M.; software, C.G.G.; validation, C.G.G., N.D. and I.M.; formal analysis, C.G.G., N.D. and I.M.; investigation, C.G.G., N.D. and I.M.; resources, N.D.; writing—original draft preparation, C.G.G., N.D. and I.M.; writing—review and editing, C.G.G., N.D. and I.M.; visualization, C.G.G.; supervision, N.D.; project administration, C.G.G., N.D. and I.M. All authors have read and agreed to the published version of the manuscript.

Funding: This study was funded by the Croatian Science Foundation under project IP-2020-02-8568.

Institutional Review Board Statement: Not applicable.

Informed Consent Statement: Not applicable.

Data Availability Statement: Not applicable.

Acknowledgments: This study has been fully supported by the Croatian Science Foundation under project IP-2020-02-8568.

Conflicts of Interest: The authors declare no conflicts of interest.

References

1. Terziev, M.; Tezdogan, T.; Demirel, Y.K.; Villa, D.; Mizzi, S.; Incecik, A. Exploring the effects of speed and scale on a ship's form factor using CFD. *Int. J. Nav. Arch. Ocean* **2021**, *13*, 147–162.
2. Orych, M.; Werner, S.; Larsson, L. Validation of full-scale delivered power CFD simulations. *Ocean Eng.* **2021**, *238*, 109654.
3. Saydam, A.Z.; Küçüksu, G.N.; İnsel, M.; Gökçay, S. Uncertainty quantification of self-propulsion analyses with RANS-CFD and comparison with full-scale ship trials. *Brodogradnja* **2022**, *73*, 107–129.
4. Degiuli, N.; Martić, I.; Farkas, A.; Gospić, I. The impact of slow steaming on reducing CO_2 emissions in the Mediterranean Sea. *Energy Rep.* **2021**, *7*, 8131–8141.
5. Demirel, Y.K.; Turan, O.; Incecik, A. Predicting the effect of biofouling on ship resistance using CFD. *Appl. Ocean Res.* **2017**, *62*, 100–118.
6. Song, S.; Demirel, Y.K.; Muscat-Fenech, C.D.M.; Tezdogan, T.; Atlar, M. Fouling effect on the resistance of different ship types. *Ocean Eng.* **2020**, *216*, 107736.
7. Feng, D.; Ye, B.; Zhang, Z.; Wang, X. Numerical Simulation of the Ship Resistance of KCS in Different Water Depths for Model-Scale and Full-Scale. *J. Mar. Sci. Eng.* **2020**, *8*, 745.
8. Niklas, K.; Pruszko, H. Full-scale CFD simulations for the determination of ship resistance as a rational, alternative method to towing tank experiments. *Ocean Eng.* **2019**, *190*, 106435.
9. Dogrul, A. Numerical Prediction of Scale Effects on the Propulsion Performance of Joubert BB2 Submarine. *Brodogradnja* **2022**, *73*, 17–42.
10. Song, K.; Guo, C.; Sun, C.; Wang, C.; Gong, J.; Li, P.; Wang, L. Simulation strategy of the full-scale ship resistance and propulsion performance. *Eng. Appl. Comp. Fluid* **2021**, *15*, 1321–1342.
11. Andrun, M.; Blagojević, B.; Bašić, J. The influence of numerical parameters in the finite-volume method on the Wigley hull resistance. *Proc. Inst. Mech. Eng. M.-J. Eng.* **2019**, *233*, 1123–1132. [CrossRef]
12. Huang, L.; Pena, B.; Thomas, G. Towards a full-scale CFD guideline for simulating a ship advancing in open water. *Ship Technol. Res.* **2023**, 1–17. [CrossRef]
13. Farkas, A.; Degiuli, N.; Martić, I. Assessment of hydrodynamic characteristics of a full-scale ship at different draughts. *Ocean Eng.* **2018**, *156*, 135–152. [CrossRef]
14. Degiuli, N.; Farkas, A.; Martić, I.; Zeman, I.; Ruggiero, V.; Vasiljević, V. Numerical and experimental assessment of the total resistance of a yacht. *Brodogradnja* **2021**, *72*, 61–80. [CrossRef]
15. Kim, Y.; Kim, J.H. Benchmark study on motions and loads of a 6750-TEU containership. *Ocean Eng.* **2016**, *119*, 262–273. [CrossRef]
16. Brodarski Institute. *Report 6655-M. Resistance, Self-Propulsion and 3D Wake Measurement Test Results*; Brodarski Institute: Zagreb, Croatia, 2022.
17. Siemens. STAR-CCM+ User Guide. 2020. Available online: https://www.cfd-online.com/Forums/star-ccm/240557-star-ccm-user-guide-tutorials.html (accessed on 19 July 2023).
18. Menter, F.R. Two-equation eddy-viscosity turbulence models for engineering applications. *AIAA J.* **1994**, *32*, 1598–1605. [CrossRef]
19. ITTC. Practical Guidelines for Ship CFD Applications, 7.5-03-02-03. In *ITTC-Recommended Procedures and Guidelines*; ITTC: Rio de Janeiro, Brazil, 2011.
20. Grlj, C.G.; Degiuli, N.; Farkas, A.; Martić, I. Numerical Study of Scale Effects on Open Water Propeller Performance. *J. Mar. Sci. Eng.* **2022**, *10*, 1132. [CrossRef]
21. Celik, I.B.; Ghia, U.; Roache, P.J.; Freitas, C.J.; Coleman, H.; Raad, P.E. Procedure for estimation and reporting of uncertainty due to discretization in CFD applications. *J. Fluids Eng.* **2008**, *130*, 0780011–0780014.
22. Song, S.; Demirel, Y.K.; Atlar, M.; Dai, S.; Day, S.; Turan, O. Validation of the CFD approach for modelling roughness effect on ship resistance. *Ocean Eng.* **2020**, *200*, 107029. [CrossRef]
23. Mikkelsen, H.; Walther, J.H. Effect of roughness in full-scale validation of a CFD model of self-propelled ships. *Appl. Ocean. Res.* **2020**, *99*, 102162. [CrossRef]
24. Kahramanoglu, E.; Yıldız, B.; Çakıcı, F.; Yilmaz, H. Numerical roll damping prediction of a planing hull. *Ship Offshore Struct.* **2021**, *16*, 363–372. [CrossRef]

25. Pena, B.; Huang, L. A review on the turbulence modelling strategy for ship hydrodynamic simulations. *Ocean Eng.* **2021**, *241*, 110082. [CrossRef]
26. Mikulec, M.; Piehl, H. Verification and validation of CFD simulations with full-scale ship speed/power trial data. *Brodogradnja* **2023**, *74*, 41–62. [CrossRef]

Journal of
Marine Science and Engineering

MDPI

Article

Numerical Assessment of the Resistance of a Solar Catamaran in Shallow Water

Ivana Martić, Nastia Degiuli *, Kornelija Borčić and Carlo Giorgio Grlj

Faculty of Mechanical Engineering and Naval Architecture, University of Zagreb, Ivana Lučića 5, 10000 Zagreb, Croatia; ivana.martic@fsb.hr (I.M.); k.kornelija.borcic@gmail.com (K.B.); carlo.g.grlj@fsb.hr (C.G.G.)
* Correspondence: nastia.degiuli@fsb.hr

Abstract: In this paper, a numerical assessment of the effect of shallow water on the total resistance of the solar catamaran SolarCat is carried out using computational fluid dynamics within the software package STAR–CCM+. The unsteady viscous fluid flow was modelled based on the Reynolds-averaged Navier–Stokes (RANS) equations with the application of the $k-\omega$ SST ($k-\omega$ Shear Stress Transport) turbulence model. The RANS equations were discretized by the finite volume method, and the position of the free surface is determined by the volume of fluid method. In shallow water conditions, a mesh morphing algorithm is applied. Numerical simulations were carried out for the deep water and limited depths corresponding to $h/T = 7.6$, $h/T = 4$, and $h/T = 2$ at two speeds. The verification study was carried out and the total numerical uncertainty was calculated for the total resistance and sinkage of the catamaran. A detailed analysis of the flow around the catamaran was carried out.

Keywords: catamaran; shallow water; resistance; sinkage; trim; computational fluid dynamics; Reynolds averaged Navier–Stokes equations

Citation: Martić, I.; Degiuli, N.; Borčić, K.; Grlj, C.G. Numerical Assessment of the Resistance of a Solar Catamaran in Shallow Water. *J. Mar. Sci. Eng.* **2023**, *11*, 1706. https://doi.org/10.3390/jmse11091706

Academic Editor: María Isabel Lamas Galdo

Received: 18 July 2023
Revised: 25 August 2023
Accepted: 26 August 2023
Published: 29 August 2023

1. Introduction

In the last few years, the development and raising of environmental awareness have led to the expansion of green technologies aimed at preserving and protecting the environment. The idea of an environmentally friendly and energy-efficient sustainable vessel has resulted in the first solar-electric catamaran for passenger transportation named SolarCat [1]. SolarCat has an integrated solar power plant that derives all the necessary energy from its sources, thus representing a significant technological breakthrough. The use of solar power systems on ships is one of the best ways to utilize green energy as an alternative to fossil fuels [2]. Due to the slower energy conversion of solar panels, solar energy is primarily applied as the main energy source in smaller vessels, while on larger ships it serves as an auxiliary energy source [3]. Furthermore, it has been confirmed that solar-assisted power production on larger vessels can potentially decrease carbon dioxide emissions by up to 12% [4]. Additionally, it has been proven that the use of solar energy meets the greenhouse gas emission requirements for ships according to the recommendations of the International Maritime Organization (IMO) [5]. Sornek et al. [6] highlighted that solar-powered small autonomous surface vehicles for performing water quality measurements can successfully become part of water quality monitoring systems. Low-carbon maritime transport has an important role in the reduction of the greenhouse gas emissions, contributing to a sustainable future. The requirement for technological innovations within the design of zero-emission ships will be a challenge for the maritime industry in the near future [7].

Catamarans that operate at moderate speeds meet the requirements of highly efficient transportation with minimal environmental impact [8]. The increase in fuel prices and the promotion of environmental consciousness have resulted in the development of more energy-efficient catamarans that have greater carrying capacity but operate at lower speeds.

The combination of catamaran length and speed transfers the catamaran from the planing regime with dominant tangential stresses to a transitional speed between the displacement and planing regime with tangential and normal stresses of similar magnitude. Improved transverse stability, dependent on the separation of the catamaran demihulls, reduced roll motions in waves compared to monohull vessels, improved seakeeping characteristics in oblique waves, and a smaller draught that enables sailing in shallow water are just some of the advantages of catamarans over monohull vessels [9]. The determination of the multihull configuration is crucial to improve the hydrodynamic performance [10,11], since it has a great influence on the interference resistance [12] Therefore, an investigation of the hydrodynamic characteristics of catamarans is of great interest. When operating in shallow water, the shallow water effect on the total resistance, trim, and sinkage of the catamaran should be taken into account. Ulgen and Dhanak [13] showed that the total resistance coefficient of the catamaran increases by over 40% at transcritical Froude numbers, which are close to the critical value of the Froude number based on water depth.

Scientific interest in the effects of shallow or confined water on ship resistance has existed for a very long time but has become more intense in recent years with growth in ship size and increasing congestion of the shipping routes [14]. The results of the performed numerical calculations for the DTC containership in moderate water depths showed that viscosity affects the ship trim and that the viscous effects become dominant with decreasing under keel clearance [15]. When a ship moves in shallow and restricted water, the flow around the ship hull changes due to the interaction between the hull and the bottom or walls of the waterway [16]. An increase in the flow velocity around the ship hull results in a decrease in the pressure and can lead to maritime accidents such as grounding or stranding. Therefore, to ensure safe navigation, it is crucial to accurately predict the hydrodynamic forces acting on the ship hull, taking into account the influence of shallow water [17]. The increase in the flow velocity around the ship hull is primarily caused by the pressure gradient due to a restricted waterway, leading to an increase in the resistance, draft, and trim of the ship [18]. In shallow water, the pressure on the midship part of a hull decreases, while the pressure on the bow and stern increases. Consequently, the water level rises at the bow and stern and decreases at the midship part of the ship. The occurrence of a squat in shallow water at high speeds can result in grounding if the under-keel clearance is insufficient [19].

Given the importance of water depth and ship speed, the Froude number based on depth $Fr_h = v/\sqrt{gh}$ is defined representing the ratio of the ship speed to the critical speed of the wave propagation in shallow water [20]. The critical ship speed is determined based on the Fr_h. When $Fr_h < 1$, the ship speed is called subcritical, while for $Fr_h > 1$ the speed is supercritical. In the case of subcritical speed, the increase in both bow and stern drafts is greater compared to their difference [21]. The three main parameters affecting the ship squat are the blockage factor, the block coefficient, and the ship speed [22]. The blockage factor is the ratio of the submerged midship cross-sectional area and the underwater area of the canal or channel.

According to Schlichting's research on the effects of shallow water, a decrease in the ship speed in shallow water is determined based on the assumption that the wave resistance in shallow water is the same as the one in deep water [14]. Maintaining the same speed in shallow water as in deep water results in increased resistance, draft, and trim of the ship, which can lead to grounding [23]. Shallow water affects wave resistance through changes in the wave pattern depending on Fr_h. In general, the value of the wave resistance coefficient significantly increases when Fr_h reaches the critical value ($Fr_h = 1$), but it rapidly decreases with a further increase in Fr_h [24]. The importance of predicting the ship behavior in shallow and confined waters is multiple [25]; it contributes to the decision-making when it comes to the channels' dredging, influences the safe levels of the sea state and ship speed prescribed by the port authorities, and enables the creation of adequate mathematical models for ship maneuvering in shallow waters which are then implemented in bridge simulators and navigators. Lataire et al. [26] proposed a new

mathematical model for the determination of the ship sinkage by taking into account the forward speed, propeller action, lateral position in the fairway, total width of the fairway, and water depth. The new model is based on the results of the performed model tests for large crude carrier in canals of different widths.

There are various approaches to predicting ship resistance in shallow water, including empirical or analytical expressions, numerical calculations, and experiments. Analytical methods mostly rely on assumptions of potential flow theory, considering the ship as a slender body. Tuck [27] proposed formulae for the prediction of the wave resistance and vertical forces of a ship sailing at subcritical and supercritical speeds at limited depths based on the slender body theory. Based on the vertical forces sinkage and trim can be obtained. The proposed formulae were further extended to include the effects of limited width on the ship as well [28]. Gourlay [29] proposed a general Fourier transform method for the determination of the ship squat in open water, a rectangular canal, a dredged channel, a stepped canal, or a channel of arbitrary cross-section. As an extension to Schlichtings's method, Lackenby [30] proposed a diagram for the estimation of the shallow water effects, i.e., speed loss under the incipient shallow water conditions.

Empirical expressions have certain limitations and conditions that need to be satisfied when applied. Furthermore, effects that are neglected in potential theory, such as wave breaking, turbulence, and viscosity, are significant in shallow water and should be considered. Reynolds-averaged Navier–Stokes (RANS) equations provide a good alternative to potential flow theory as they consider the viscous effects of fluid flow [31]. Numerical tools based on RANS equations have proven to be highly effective in determining the total resistance and resistance components of catamarans operating at moderate speeds [8]. The combination of experimental and Computational Fluid Dynamics (CFD) currently represents the best practice for the investigation of hydrodynamic characteristics. For example, by performing the experimental and numerical investigations of the influence of the lateral separations on the maneuvering performance of a small waterplane area twin hull, Dai and Li [32] showed that turning performance decreased for the intermediate demihull separation, while the demihull separation showed little impact on zigzag maneuver. CFD allows for accurate prediction of the draft, trim, and ship resistance in shallow water [22], and, as such, it can serve as an alternative to expensive and time-consuming experimental tests in towing tanks that are capable of performing tests in shallow and restricted water.

The rest of the paper is organized as follows: in Section 2 the case study is given. Section 3 describes the mathematical model, and the numerical setup is summarized in Section 4. The obtained numerical results, along with the discussion, are given in Section 5 followed by the conclusions in Section 6.

2. Case Study

The numerical simulations of the resistance test in deep and shallow water were conducted for the solar catamaran with main particulars given in Table 1 [1]. The influence of shallow water on the total resistance, sinkage, and trim was assessed.

Table 1. Main particulars of the solar catamaran.

Main Particular	Symbol	Value
Length between perpendiculars	L_{PP}	15 m
Breadth	B	5 m
Demihull breadth	b	1.59 m
Draught	T	0.68 m
Displacement mass	Δ	15.45 t
Vertical position of the center of gravity	KG	1.78 m
Longitudinal position of the center of gravity	LCG	6.88 m

A 3D model of the catamaran is shown in Figure 1. The coordinate system is located at the symmetry plane of the catamaran at the center of gravity according to Table 1. The

positive direction of the x-axis is oriented towards the bow, the y-axis towards the port side, and the z-axis upwards. Accordingly, the sinkage of the catamaran represents a displacement in the negative direction of the z-axis, the negative trim angle represents bow down, and the positive trim angle bow up.

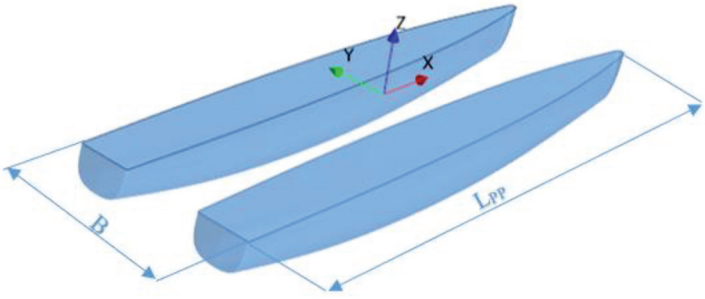

Figure 1. 3D model of a solar catamaran.

3. Mathematical Model

Reynolds-averaged Navier–Stokes equations along with the continuity equation are used to describe the unsteady incompressible turbulent flow:

$$\frac{\partial(\rho\overline{u}_i)}{\partial t} + \frac{\partial}{\partial x_j}\left(\rho\overline{u}_i\overline{u}_j + \rho\overline{u'_i u'_j}\right) = -\frac{\partial\overline{p}}{\partial x_i} + \frac{\partial\overline{\tau}_{ij}}{\partial x_j} \tag{1}$$

$$\frac{\partial(\rho\overline{u}_i)}{\partial x_i} = 0 \tag{2}$$

where $[yellow]\rho$ is the fluid density, $\overline{u}_i$ is the averaged Cartesian components of the velocity vector, $\rho\overline{u'_i u'_j}$ is the Reynolds stress tensor, and $\overline{p}$ is the mean pressure. The mean viscous stress tensor is defined as:

$$\overline{\tau}_{ij} = \mu\left(\frac{\partial\overline{u}_i}{\partial x_j} + \frac{\partial\overline{u}_j}{\partial x_i}\right) \tag{3}$$

where μ is the dynamic viscosity.

Within this study, the $k-\omega$ SST turbulence model was applied for the closure of Equations (1) and (2), which incorporates two additional transport equations, one for the specific kinetic energy and one for the specific dissipation rate [33].

4. Numerical Setup

The governing equations are discretized using the finite volume method and solved in a segregated manner. The convection terms in RANS equations are discretized using second-order upwind scheme, while for temporal discretization, the first-order temporal scheme is used. To track and locate the free surface the Volume of Fluid (VOF) method is utilized combined with the High-Resolution Interface Capturing (HRIC) scheme.

4.1. Computational Domain and Boundary Conditions

Since the catamaran is symmetric, only half of the computational domain is discretized. The boundaries of the computational domain for the numerical simulations in deep water were set as follows. The inlet and top boundaries were placed $1.5L_{PP}$ away from the hull. The outlet boundary was placed $3L_{PP}$ behind the hull, the bottom boundary $2.5L_{PP}$ below the hull, and the side boundary $2L_{PP}$ from the symmetry plane of the catamaran. In numerical simulations for limited water depth, the bottom boundary of the computational domain was placed according to the h/T ratio as $0.3L_{PP}$, $0.14L_{PP}$, and $0.05L_{PP}$ below the keel line for $h/T = 7.6$, $h/T = 4$, and $h/T = 2$, respectively.

It should be noted that the water depth to draught ratio $h/T = 7.6$ corresponds to the water depth without the shallow water effect on a ship, which is calculated as follows [34]:

$$\frac{h}{T} \geq 4 + 3Fr_T^3 \tag{4}$$

where $Fr_T = \frac{v}{\sqrt{gT}}$ is the Froude number calculated based on the draught.

The velocity inlet boundary condition was set at the inlet, top, and bottom boundaries of the computational domain for the numerical simulations in deep water. At the outlet boundary, the pressure outlet boundary condition was set, while the symmetry boundary condition was defined at the symmetry plane of the catamaran. The no-slip wall boundary condition was defined for the catamaran hull. In the case of limited depth, a no-slip wall boundary condition was also applied at the bottom with a relative velocity equal to the catamaran speed in the opposite direction [23]. The overview of boundary conditions for deep and limited water depths is given in Figures 2 and 3, respectively.

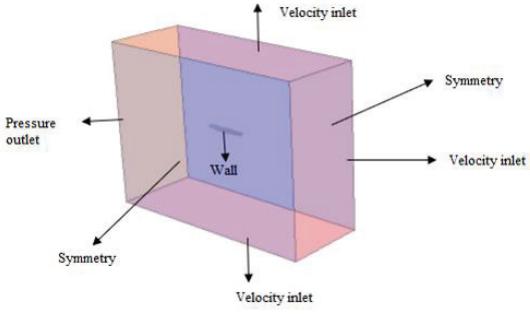

Figure 2. Computational domain and boundary conditions for deep water.

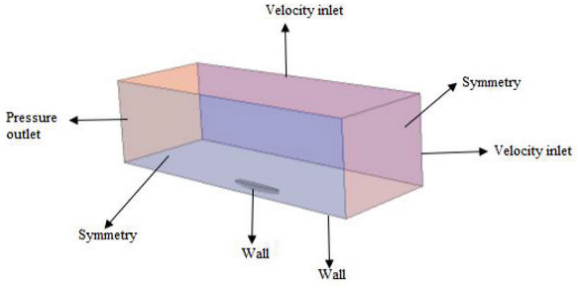

Figure 3. Computational domain and boundary conditions for limited depth.

4.2. Discretization of the Computational Domain

When using CFD tools, the number of cells in the generated mesh has a significant impact on the obtained numerical results, and a compromise needs to be made between the required simulation time and result accuracy [35,36].

To resolve the flow in the areas of interest, the mesh was additionally refined where the free surface was expected, to capture the Kelvin wake around the catamaran demihull, in the area between the catamaran demihulls, as well as between the demihull and bottom within the numerical simulations for limited water depth. In the case of limited water depth, the boundary layer forms at the bottom, and, therefore, the area near the bottom needs to be further refined with prism cells. Since the height of the first cell in the boundary layer depends on the Reynolds number, to ensure the desired value of the non-dimensional distance from the wall (y^+) the discretization parameters for the boundary layer are adjusted for each speed. The discretization of the boundary layer along the catamaran hull

and near the bottom of the computational domain for $h/T = 7.6$ at the speed of 5.5 knots is presented in Figure 4.

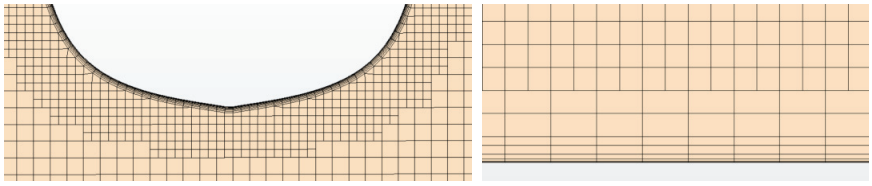

Figure 4. Discretization of the boundary layer along the hull of the catamaran (**left**) and near the bottom (**right**).

Based on the International Towing Tank Conference (ITTC) recommendations, the value of the parameter y^+ should be larger than 30 to describe the flow with a logarithmic velocity profile [37]. To resolve the flow in the boundary layer around the catamaran, wall functions were applied, while on the bottom of the computational domain, the value of the y^+ parameter was kept below 1. Values of the y^+ parameter along the catamaran demihull in deep water at the speed of 5.5 knots are shown in Figure 5, and it can be seen that the y^+ is in the range $30 < y^+ < 300$.

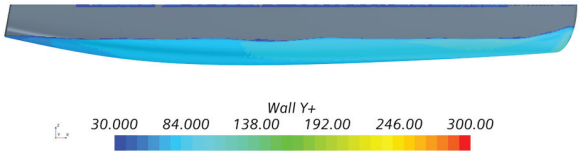

Figure 5. The distribution of the y^+ parameter along the catamaran hull in deep water at the speed of 5.5 knots.

As already mentioned, to obtain the wave pattern around the catamaran, it is necessary to refine the region in which the free surface is expected, Figures 6 and 7. It should be noted that the cross-section of the mesh given in Figure 6 corresponds to $h/T = 2$.

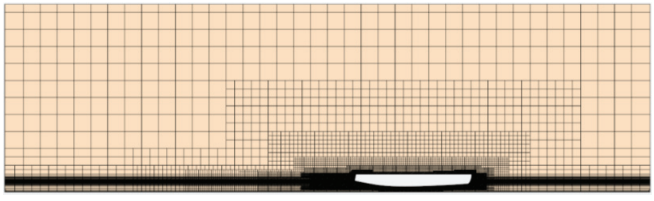

Figure 6. Mesh cross-section for the numerical simulations for $h/T = 2$.

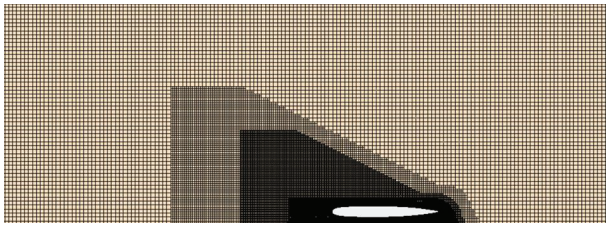

Figure 7. Discretization of the free surface.

The number of cells of the mesh used in the numerical simulations at a speed of 5.5 knots can be seen in Table 2.

Table 2. The number of cells of the mesh used in the numerical simulations at a speed equal to 5.5 knots.

Water Depth	Number of Cells
$h/T \to \infty$	3,488,816
$h/T = 7.6$	4,187,987
$h/T = 4$	4,234,076
$h/T = 2$	4,419,462

4.3. The Verification Study

The verification study enables the estimation of the numerical uncertainty of the obtained numerical results. The total numerical uncertainty U_{SN} is defined based on the number of iterations δ_I, grid size δ_G, time step δ_T, and other parameters δ_P, and is given as follows [38]:

$$U^2{}_{SN} = U_I^2 + U_G^2 + U_T^2 + U_P^2 \tag{5}$$

where U_I is the numerical uncertainty of the number of iterations, U_G is the numerical uncertainty of the grid size, U_T is the numerical uncertainty of the time step, and U_P is the numerical uncertainty of other parameters.

Within this study, the numerical uncertainty of the grid size and time step was assessed for the total resistance and sinkage of the catamaran in both deep and shallow water using the GCI method [39]. The numerical uncertainty arising from the number of iterations and other parameters can be neglected.

To carry out a convergence study, a minimum of three solutions is required to determine the convergence ratio, which is based on the differences between solutions obtained using different grid sizes and time steps:

$$\varepsilon_{ij} = \phi_i - \phi_j \tag{6}$$

$$R = \varepsilon_{21}/\varepsilon_{32} \tag{7}$$

where ϕ is the solution, ε_{ij} is the difference between the obtained results, and R is the convergence ratio.

The convergence types based on the convergence ration are given in Table 3.

Table 3. Convergence types.

Convergence Ratio	Convergence Type
$-1 < R_i < 0$	Oscillatory
$0 < R_i < 1$	Monotonic
$\lvert R_i \rvert > 1$	Divergence

Within the GCI method, the apparent order of the method can be calculated as follows:

$$p = \frac{1}{\ln r_{21}} \cdot \left| \ln \left| \frac{\varepsilon_{32}}{\varepsilon_{21}} \right| + q(p) \right| \tag{8}$$

where $q(p)$ can be determined as:

$$q(p) = \ln\left(\frac{r_{21}^p - s}{r_{32}^p - s} \right) \tag{9}$$

$$s = 1 \cdot \operatorname{sgn}\left(\frac{\varepsilon_{32}}{\varepsilon_{21}} \right) \tag{10}$$

where r is the refinement ratio, which is $\sqrt{2}$ for the grid size, and 2 for the time step [38]. The apparent order of the method p is calculated by solving the Equations (8)–(10) iteratively. Extrapolated values and the approximate and extrapolated relative errors are calculated as follows:

$$\phi_{\text{ext}}^{21} = \frac{r_{21}^{p}\phi_1 - \phi_2}{r_{21}^{p} - 1} \tag{11}$$

$$e_{\text{a}}^{21} = \left| \frac{\phi_1 - \phi_2}{\phi_1} \right| \tag{12}$$

$$e_{\text{ext}}^{21} = \left| \frac{\phi_{\text{ext}}^{21} - \phi_1}{\phi_{\text{ext}}^{21}} \right| \tag{13}$$

The GCI for fine grid can be calculated with following equation:

$$GCI_{\text{fine}}^{21} = \frac{1.25\, e_{\text{a}}^{21}}{r_{21}^{p} - 1} \tag{14}$$

According to [40], GCI for coarser grid can be calculated as:

$$GCI_{\text{medium}}^{32} = r_{21}^{p} GCI_{\text{fine}}^{21} \tag{15}$$

4.4. Physical Model of the Numerical Simulations and Solver Parameters

Two fluid phases are defined based on the Eulerian Multiphase model, and the initial position of the free surface, as well as the fluid velocity, is defined based on the VOF approach. To prevent wave reflections against the boundaries of the computational domain, the damping layer approach was used with a constant value of damping length equal to the length of the catamaran. The damping layer was applied at the inlet, side, and outlet boundaries. The Dynamic Fluid Body Interaction (DFBI) model was enabled to calculate the sinkage and trim, i.e., within the DFBI model, heave and pitch motion of the catamaran are enabled. To accommodate possibly more pronounced sinkage and trim values within the numerical simulations for limited depth, mesh morphing was applied based on the BSpline algorithm [41,42]. The time step is defined based on the following expression:

$$\Delta t = \frac{T}{c} \tag{16}$$

where T is the period defined as:

$$T = \frac{L_{PP}}{v} \tag{17}$$

where v is the ship speed in m/s. The coefficient c for the fine time step was equal to 200, for the medium time step to 100, and for the coarse time step to 50. Therefore, the fine, medium, and coarse time step was equal to 0.01325 s, 0.0265 s, and 0.053 s, respectively. The under-relaxation factors for velocity and pressure were set as 0.7 for the velocity and 0.4 for the pressure. The number of inner iterations was equal to 5.

5. Results and Discussion

Within this section, the obtained results of numerical simulations of the resistance test for the catamaran in deep and shallow water are presented, along with the results of the performed verification study. The results of the validation study for the Series 60 catamaran for a wide range of Froude numbers can be found in [12]. The numerical uncertainty is determined for the total resistance and sinkage of the catamaran at the speed of 5.5 knots in deep water and for $h/T = 2$. The free surface, wave patterns, distribution of hydrodynamic pressure along the catamaran hull, pressure distribution on the bottom of the computational domain, tangential stresses, velocity field in the symmetry plane, and wave elevations are shown. Additionally, a comparison of the obtained results for the total resistance, trim, and sinkage for all investigated depths and speeds is provided.

5.1. The Results of the Verification Study

The verification study was performed for the obtained numerical results in deep and shallow water with $h/T = 2$ at the speed of 5.5 knots. To assess the numerical uncertainty of the grid size, the numerical simulations were conducted using fine, medium, and coarse mesh with the medium time step. The uncertainty of the time step was determined by performing the numerical simulations with medium mesh using three different time steps. The results of the performed verification study for the numerical simulations in deep water are given in Tables 4 and 5. Most verification methods are derived for monotonic convergence when the general Richardson extrapolation (RE) method can be used to estimate the observed order of accuracy [43].

Table 4. The numerical uncertainty of the grid size for the total resistance in deep water.

ε_{21}, N	ε_{32}, N	R	p	e_a^{21},%	e_{ext}^{21},%	GCI_{fine}^{21},%	GCI_{medium}^{32},%
−2.79	−4.67	0.5974	1.4863	0.004	0.0059	0.74	1.24

Table 5. The numerical uncertainty of the time step for the total resistance in deep water.

ε_{21}, N	ε_{32}, N	R	p	e_a^{21},%	e_{ext}^{21},%	GCI_{fine}^{21},%	GCI_{medium}^{32},%
4.4361	10.10	0.4392	1.187	0.0064	0.0051	0.63	1.43

From Tables 4 and 5, it is evident that the monotonic convergence is obtained for the total resistance for different grid sizes and using different time steps. It can be seen that the GCI for the fine mesh and fine time step was below 1%, while for the medium mesh and medium time step, the GCI was lower than 1.5%.

For the case of $h/T = 2$ the numerical uncertainty of the grid size is larger in comparison to the one obtained for the deep water, Table 6. GCI for the time step for $h/T = 2$ was similar to the one obtained for deep water, Table 7. It should be noted that for $h/T = 2$, the monotonic convergence of the total resistance was achieved using different grid sizes and time steps.

Table 6. The numerical uncertainty of the grid size for the total resistance for $h/T = 2$.

ε_{21}, N	ε_{32}, N	R	p	e_a^{21},%	e_{ext}^{21},%	GCI_{fine}^{21},%	GCI_{medium}^{32},%
−8.6373	−11.0897	0.7789	0.7211	0.0086	0.0294	3.79	4.87

Table 7. The numerical uncertainty of the time step for the total resistance for $h/T = 2$.

ε_{21}, N	ε_{32}, N	R	p	e_a^{21},%	e_{ext}^{21},%	GCI_{fine}^{21},%	GCI_{medium}^{32},%
8.61	43.03	0.2001	2.3213	0.0087	0.0022	0.27	1.36

It can be concluded that the grid uncertainty for the total resistance is larger in shallow water in comparison to deep water.

The discretization error can be calculated only if the order of accuracy is larger than 1, i.e., when three grids are in the asymptotic range [44]. If the value of the order of accuracy is within an acceptable range the extrapolated value, the approximate, and extrapolated relative errors can be estimated. If a value of the order of accuracy is too large, i.e., larger than the theoretical one, the error estimate is probably too small. On the other hand, if the order of accuracy becomes too small, it may lead to a too conservative error estimate.

In Tables 8 and 9, the numerical uncertainties of the grid size and time step for the sinkage of the catamaran in deep water are given. It can be seen that the monotonic convergence was obtained for both cases. The numerical uncertainty of the grid size was slightly higher in comparison to the numerical uncertainty of the time step. For the case of

$h/T = 2$, the monotonic convergence was obtained for the grid size, while the oscillatory convergence was obtained for the time step, Tables 10 and 11. Based on the obtained results, it can be concluded that the GCI for the medium mesh and medium time step is acceptably low. Therefore, the remaining simulations were conducted using the medium mesh and medium time step.

Table 8. The numerical uncertainty of the grid size for the sinkage in deep water.

ε_{21}, m	ε_{32}, m	R	p	e_a^{21},%	e_{ext}^{21},%	GCI_{fine}^{21},%	GCI_{medium}^{32},%
−0.000077	−0.000521	0.1478	5.5167	0.0045	0.00078	0.10	0.66

Table 9. The numerical uncertainty of the time step for the sinkage in deep water.

ε_{21}, m	ε_{32}, m	R	p	e_a^{21},%	e_{ext}^{21},%	GCI_{fine}^{21},%	GCI_{medium}^{32},%
0.00035	0.000027	0.2222	2.1699	0.000006	0.0000997	0.01	0.06

Table 10. The numerical uncertainty of the grid size for the sinkage for $h/T = 2$.

ε_{21}, m	ε_{32}, m	R	p	e_a^{21},%	e_{ext}^{21},%	GCI_{fine}^{21},%	GCI_{medium}^{32},%
−0.0004	−0.0005	0.8	0.6439	0.0039	0.0157	1.93	2.41

Table 11. The numerical uncertainty of the time step for the sinkage for $h/T = 2$.

ε_{21}, m	ε_{32}, m	R	p	e_a^{21},%	e_{ext}^{21},%	GCI_{fine}^{21},%	GCI_{medium}^{32},%
0.0004	−0.0009	−0.4444	1.1699	0.0038	0.0031	0.38	0.86

5.2. Comparison of the Results for the Total Resistance, Sinkage, and Trim

The obtained numerical results of the total resistance at both investigated speeds are presented in Table 12. The difference between the total resistance in deep water and for $h/T = 7.6$ was approximately 4% even though the corresponding water depth was the smallest one without the shallow water effect, which was calculated based on the empirical expression. It should be noted that the obtained difference falls within the numerical uncertainty for the total resistance. Additionally, for that particular case, the speed reduction read off Schlichting's diagram was 0–1%, suggesting there was no shallow water effect. Therefore, the numerical simulations in deep water at the speed of 4 knots were not conducted.

Table 12. Comparison of the total resistance in deep and shallow water.

	R_T, N	
Water Depth	***V*=5.5 kn**	***V*=4 kn**
$h/T \to \infty$	683.51	/
$h/T = 7.6$	710.57	348.18
$h/T = 4$	749.54	359.97
$h/T = 2$	989.51	399.06

By decreasing the water depth, an increase in the total resistance is evident. The difference between the total resistance obtained for $h/T = 7.6$ and $h/T = 2$ was almost 40% at the speed of 5.5 knots. On the other hand, by reducing the catamaran speed by 1.5 knots, a significant decrease in the total resistance was achieved. The difference between the total resistance of the catamaran obtained for $h/T = 7.6$ and $h/T = 2$ at the speed of 4 knots was approximately 14.6%.

Table 13 provides a comparison of the pressure and frictional resistance of the catamaran for both analyzed speeds. It can be observed that at the operational speed of 5.5 knots, the depth had a significantly larger effect on the pressure resistance compared to the frictional resistance. The pressure resistance of the catamaran increased by approximately 13% for $h/T = 4$, and almost 100% for $h/T = 2$ in comparison to $h/T = 7.6$. Furthermore, the frictional resistance formed about 70% of the total resistance at $h/T = 4$, while the contribution of the frictional resistance at $h/T = 2$ was about 60% of the total resistance, indicating that reducing the depth increases the portion of pressure resistance in the total resistance of the catamaran.

Table 13. Comparison of the frictional and pressure resistance of the catamaran in shallow water.

	***V*=5.5 kn**		***V*=4 kn**	
Water Depth	R_P, **N**	R_F, **N**	R_P, **N**	R_F, **N**
$h/T = 7.6$	199.84	510.73	64.90	283.28
$h/T = 4$	226.42	523.12	72.36	287.61
$h/T = 2$	394.39	595.12	63.46	335.60

On the other hand, by reducing the catamaran speed to 4 knots, the pressure resistance at $h/T = 2$ was almost the same as the one obtained at $h/T = 7.6$, while the frictional resistance was approximately 20% larger. The frictional resistance formed about 85% of the total resistance of the catamaran at $h/T = 2$. For $h/T = 4$ and speed of 4 knots, an increase of 10% in pressure resistance in comparison to $h/T = 7.6$ was obtained, although the frictional resistance still contributed about 80% to the total resistance.

It can be concluded that for all investigated water depths and both speeds, the portion of the frictional resistance in the total resistance of the catamaran was higher than the pressure resistance. However, it is important to note that the increase in pressure resistance by reducing the water depth at the operational speed significantly contributes to the overall increase in the total resistance of the catamaran.

By analyzing the numerical results for the sinkage, a squat effect can be observed for $h/T = 2$ resulting in a sinkage of approximately 10 cm at the speed of 5.5. knots, Table 14. As the sinkage increased, the wetted surface area of the catamaran increased as well, contributing to an increase in the frictional resistance of the catamaran. By reducing the speed, the sinkage of the catamaran for $h/T = 2$ was significantly lower in comparison with the sinkage obtained for $h/T = 7.6$.

Table 14. Comparison of sinkage of a catamaran in shallow water.

	***z*, m**	
Water Depth	***V*=5.5 kn**	***V*=4 kn**
$h/T \to \infty$	-0.0168	/
$h/T = 7.6$	-0.0206	-0.0093
$h/T = 4$	-0.0321	-0.0141
$h/T = 2$	-0.1041	-0.0307

$h/T \to \infty h/T = 7.6 h/T = 4 h/T = 2$ The trim angle of the catamaran is given in Table 15. It can be observed that by reducing the water depth and speed, the catamaran remained almost at the even keel, suggesting that the influence of the shallow water on the trim angle of the catamaran was almost negligible.

Table 15. Comparison of the trim angle of a catamaran in shallow water.

	t, °	
Water Depth	***V*=5.5 kn**	***V*=4 kn**
$h/T \to \infty$	0.0020	/
h/T= 7.6	0.0076	0.0142
h/T= 4	0.0022	0.0137
h/T= 2	-0.0420	0.0088

$h/T \to \infty h/T$= 7.6h/T= 4h/T= 2

5.3. The Position of the Free Surface along the Hull of the Catamaran

The free surface along the catamaran demihull is shown in Figure 8. It was determined based on the volume fraction of air and water. By comparing the free surfaces along the inner side of the catamaran demihull, it was evident that for h/T= 2 at the speed of 5.5 knots, wave elevations were larger in comparison to the speed of 4 knots, resulting in significantly higher pressure resistance, Table 13.

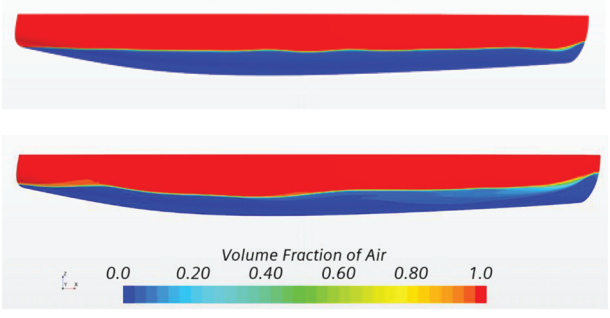

Figure 8. The free surface along the catamaran demihull for h/T= 2 at the speed of 4 knots (**upper**) and 5.5 knots (**lower**).

5.4. Wave Patterns

Figure 9 shows the wave patterns obtained for all the analyzed water depths at the speed of 5.5 knots. The corresponding values of the Froude number based on depth were Fr_h = 0.4 for h/T= 7.6, Fr_h = 0.55 for h/T= 4, and Fr_h= 0.77 for h/T= 2. Fr_h for h/T= 7.6 and h/T= 4 fall within the range of low subcritical values, and as a result, the wave patterns resembled those in deep water. It is important to note that wave amplitudes for h/T= 4 are somewhat higher compared to those in deep water. Additionally, a wave system consisting of transverse and diverging waves, as well as a Kelvin angle of $19°28'$, can be clearly observed. On the other hand, for h/T= 2, a significantly larger wave trough can be observed between the catamaran demihulls in the midship area as well as larger wavelength of the transverse waves. The value of the Froude number based on depth for h/T= 2 was Fr_h= 0.77 at the operational speed of 5.5 knots, which falls within the range of highly supercritical values. Accordingly, the Kelvin angle increased. Consequently, there was an increase in pressure resistance, as shown in Table 13.

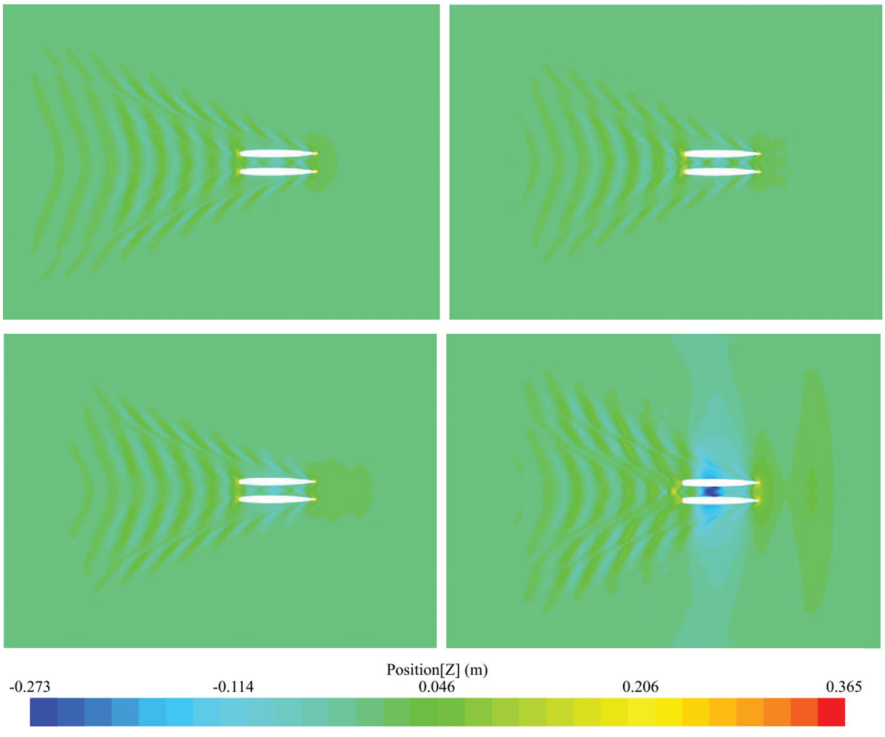

Figure 9. Wave pattern in deep water (**upper left**), for $h/T = 7.6$ (**upper right**), for $h/T = 4$ (**lower left**), and for $h/T = 2$ (**lower right**) at the speed of 5.5 knots.

In Figure 10, the wave patterns obtained for $h/T = 7.6$, $h/T = 4$, and $h/T = 2$ at the speed of 4 knots are shown. By reducing the speed, the value of Fr_h for $h/T = 2$ was $Fr_h = 0.56$ and fell within the range of low subcritical values. The Kelvin angle was smaller compared to the one for the same depth-to-draft ratio at the speed of 5.5 knots. Larger wave elevations can be seen between the catamaran demihulls in the midship area, and the wavelength of the transverse waves is smaller in comparison to the operational speed.

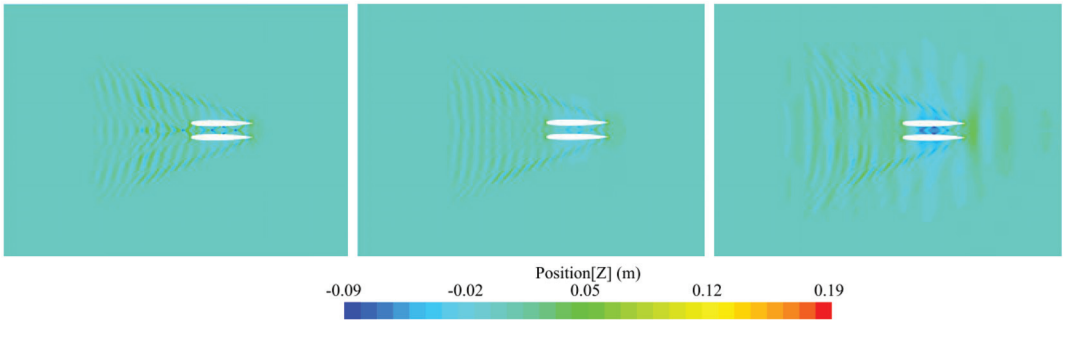

Figure 10. Wave pattern in deep water (upper left), for $h/T = 7.6$ (upper right), for $h/T = 4$ (lower left), and for $h/T = 2$ (lower right) at the speed of 4 knots.

5.5. Distribution of Hydrodynamic Pressure on the Catamaran Demihull and Pressure on the Bottom

The distribution of hydrodynamic pressure along the inner side of the catamaran demihull for all the analyzed water depths at the speed of 5.5 knots is given in Figure 11. The area of high pressure at the bow is clearly visible in all cases. By comparing the obtained results, it can be seen that as the water depth decreases the overpressure in the bow area increases, while the underpressure in the midship area decreases. The decrease in the hydrodynamic pressure is a consequence of a change in the flow velocity around the catamaran hull. An increase in the flow velocity increased the tangential stresses, ultimately affecting the total resistance of the catamaran.

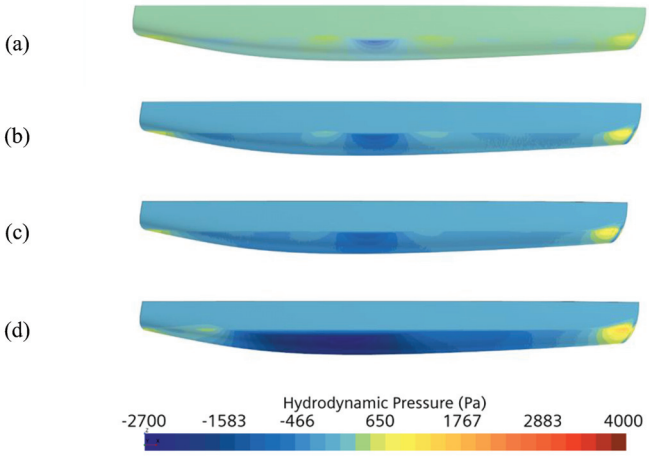

Figure 11. Distribution of hydrodynamic pressure along the inner side of the catamaran demihull in deep water (**a**), for $h/T = 7.6$ (**b**), for $h/T = 4$ (**c**), and for $h/T = 2$ (**d**) at the speed of 5.5 knots.

By reducing the speed by 1.5 knots, the change in the distribution of hydrodynamic pressure along the inner side of the catamaran demihull was less pronounced compared to the speed of 5.5 knots, Figure 12. Furthermore, by comparing Figures 11d and 12c, a significant difference in pressure distribution can be noticed between the two analyzed speeds for $h/T = 2$. Significantly lower values of hydrodynamic pressure at the operational speed can be observed, resulting in higher total resistance. Additionally, at the speed of 4 knots, lower overpressure was obtained in the bow area compared to the operational speed.

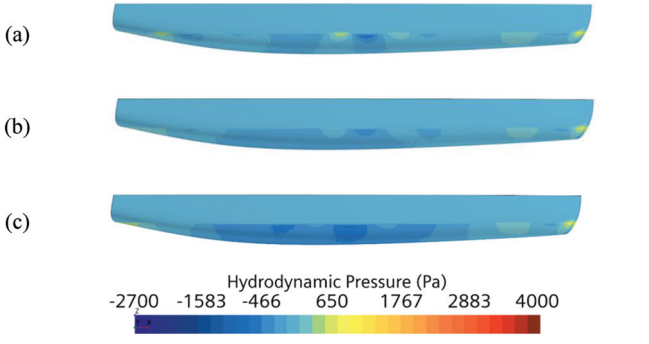

Figure 12. Distribution of hydrodynamic pressure along the inner side of the catamaran demihull for $h/T = 7.6$ (**a**), for $h/T = 4$ (**b**), and for $h/T = 2$ (**c**) at the speed of 4 knots.

The beforementioned changes in the hydrodynamic pressure distribution correspond to changes in the pressure distribution at the bottom of the computational domain. In Figure 13, the pressure distribution on the bottom of the computational domain for $h/T = 4$ and $h/T = 2$ at the speed of 5.5 knots is shown, and it is evident that the pressure is significantly lower for $h/T = 2$ due to the increased flow velocity between the catamaran and the bottom.

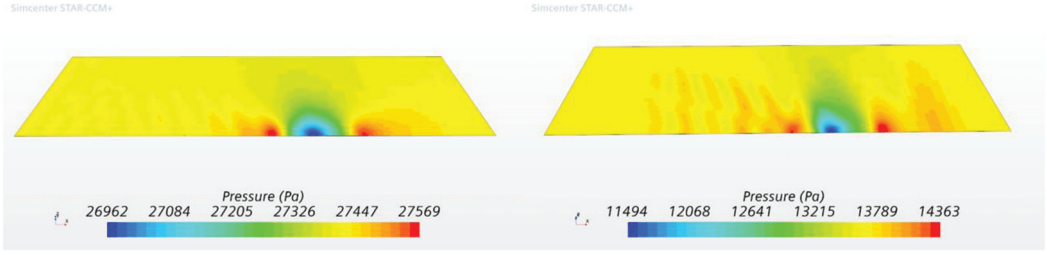

Figure 13. Pressure distribution at the bottom of the computational domain for $h/T = 4$ (**left**) and $h/T = 2$ (**right**) at a speed of 5.5 knots.

Similar results can be found by comparing the pressure distribution at the bottom of the computational domain for $h/T = 4$ and $h/T = 2$ at the speed of 4 knots, Figure 14.

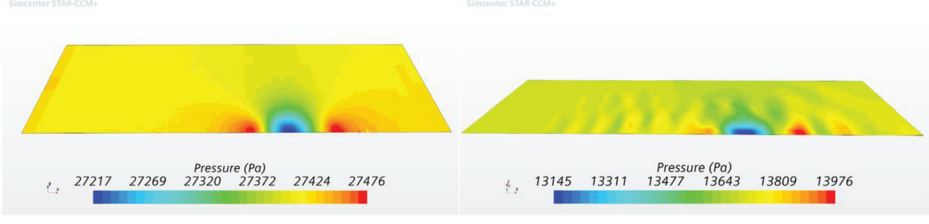

Figure 14. Pressure distribution at the bottom of the computational domain for $h/T = 4$ (**left**) and $h/T = 2$ (**right**) at a speed of 4 knots.

For both $h/T = 4$ and $h/T = 2$, the pressure beneath the midship area was lower at the speed of 5.5 knots compared to 4 knots, while the pressure beneath the bow and stern area was slightly higher at the speed of 5.5 knots. This corresponds to the distribution of hydrodynamic pressure along the inner side of the catamaran demihull.

5.6. Tangential Stresses

As already mentioned, the increase in the flow velocity around the catamaran demihull leads to an increase in tangential stresses, as shown in Figure 15 for $h/T = 2$ at the speed of 5.5 knots. The increase in tangential stresses is caused by the acceleration of the water flow between the catamaran and the bottom, which is particularly noticeable for $h/T = 2$. The increase in tangential stresses results in an increase in frictional resistance, ultimately leading to an increase in the total resistance of the catamaran.

By reducing the speed to 4 knots, a significant decrease in the tangential stresses can be observed for $h/T = 2$, Figure 16.

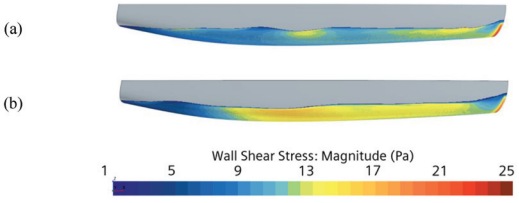

Figure 15. Wall shear stress along the inner side of the catamaran demihull for $h/T = 7.6$ (**a**) and for $h/T = 2$ (**b**) at the speed of 5.5 knots.

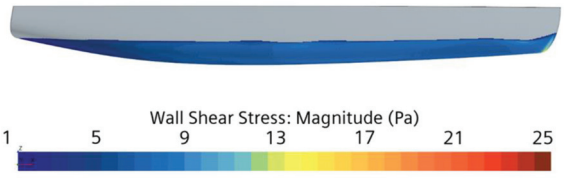

Figure 16. Wall shear stress along the inner side of the catamaran demihull for $h/T = 2$ at the speed of 4 knots.

5.7. Velocity Field

The magnitude of the velocity in the symmetry plane of the catamaran demihull for all analyzed water depths at the speed of 5.5 knots is shown in Figures 17 and 18. By comparing the magnitude of the velocity between the catamaran demihull and the bottom, an increase can be observed for $h/T = 4$, Figure 17b in comparison to $h/T = 7.6$, Figure 17a. A further reduction in depth caused a significant increase in the magnitude of the velocity at the same speed, Figure 18, which corresponded to a substantial reduction in hydrodynamic pressure and an increase in tangential stresses along the catamaran hull.

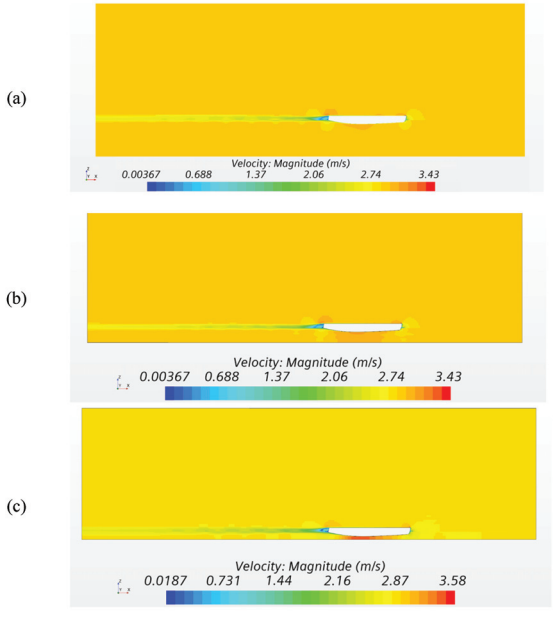

Figure 17. The magnitude of the velocity at the symmetry plane for $h/T = 7.6$ (**a**), for $h/T = 4$ (**b**), and for $h/T = 2$ (**c**) at the speed of 5.5 knots.

The magnitude of the velocity between the catamaran and the bottom for $h/T = 7.6$ was significantly lower at the speed of 4 knots in comparison to the operational speed, Figure 18. Again, a decrease in water depth leads to an increase in the magnitude of the velocity, as can be seen in Figure 17. For $h/T = 2$, it can be noticed that the maximum magnitude of the velocity between the catamaran and the bottom is approximately 30% lower when the catamaran speed is reduced from 5.5 to 4 knots.

5.8. Longitudinal Wave Cuts

A comparison of the longitudinal wave cuts for all investigated water depths at the speed of 5.5. knots is given in Figure 19. The longitudinal wave cuts are given at three planes: symmetry plane, $y = 1.7$ m which corresponds to the symmetry plane of the catamaran demihull, and $y = 3.4$ m which corresponds to the outer side of the catamaran demihull. It can be seen that the wave elevations obtained in the catamaran symmetry plane are the largest for $h/T = 2$. A significant increase in the wave elevations in front of the bow and behind the stern area, and especially in the midship area between the catamaran demihulls can be observed. It is interesting to notice that the wave elevations in the midship area between the catamaran demihulls obtained for $h/T = 7.6$ are larger in comparison to the ones obtained for $h/T = 4$. For $h/T = 2$ the waves start to form in front of the fore perpendicular, which can be observed at all three planes.

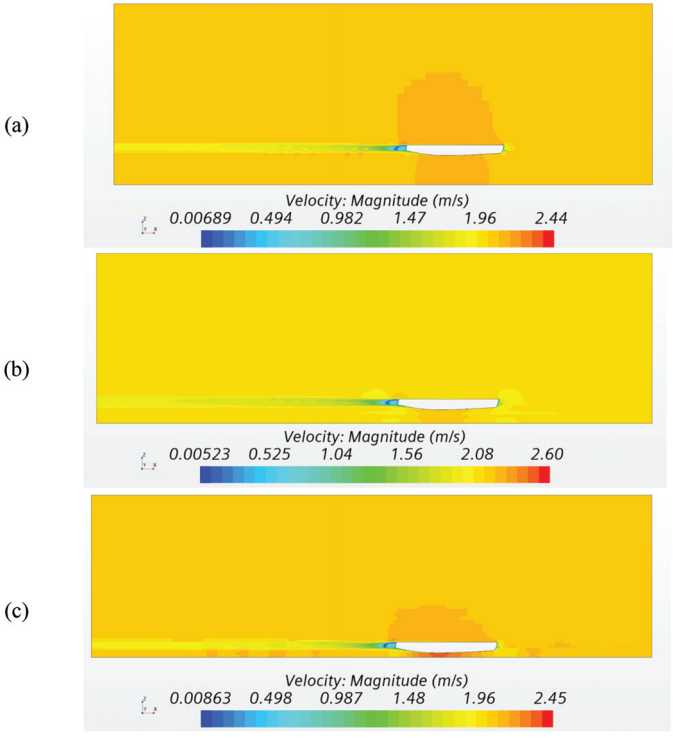

Figure 18. The magnitude of the velocity at the symmetry plane for $h/T = 7.6$ (**a**), for $h/T = 4$ (**b**), and for $h/T = 2$ (**c**) at the speed of 4 knots.

Along the outer side of the catamaran demihull, significantly larger wave troughs are formed for $h/T = 2$. Again, the formation of waves in front of the fore perpendicular can be noticed. In comparison to the other analyzed water depths, the wave heights of the waves behind the stern were significantly smaller for $h/T = 2$. A reduction in the wavelength for all analyzed water depths can be noticed as the speed is reduced to 4 knots, Figure 20.

The largest wave elevations at the catamaran symmetry plane were observed for $h/T = 7.6$. It seems that the waves generated in shallow water for $h/T = 2$ have the largest wave elevations far behind the stern. The same can be observed along the symmetry plane of the catamaran demihull, as well as along the outer side of the catamaran demihull. Similar to the operating speed, the waves are formed in front of the fore perpendicular of the catamaran at the reduced speed as well.

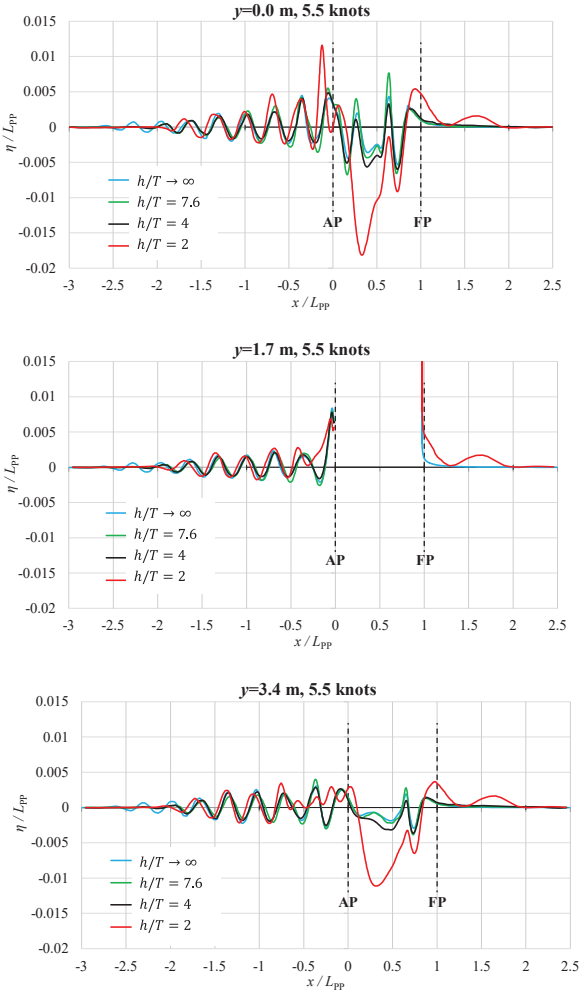

Figure 19. Comparison of the longitudinal wave cuts at the speed of 5.5 knots.

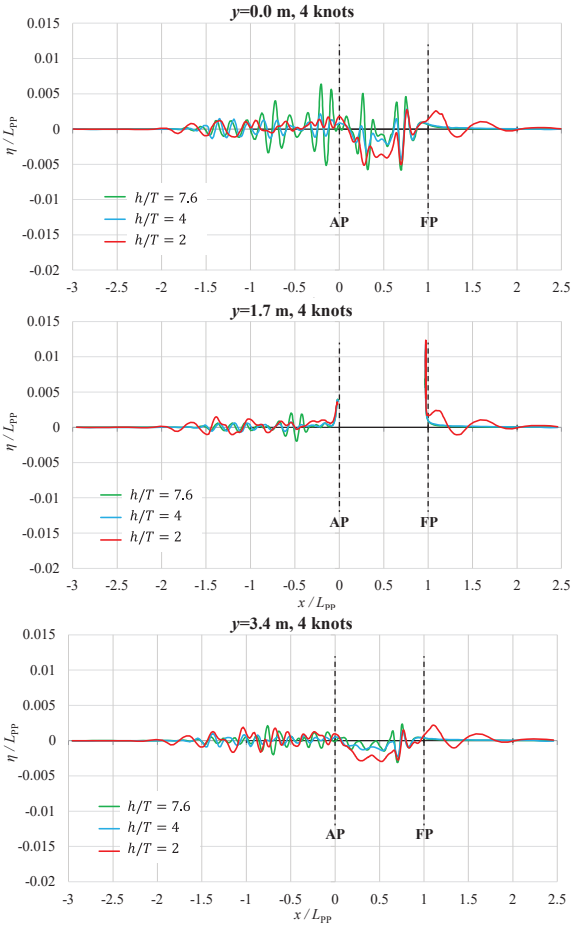

Figure 20. Comparison of the longitudinal wave cuts at the speed of 4 knots.

6. Conclusions

In this study, the effect of shallow water on the total resistance of a solar catamaran was numerically assessed in deep water and for three different depths at two speeds. The numerical simulations were performed using the commercial software package STAR-CCM+. A mathematical model based on the Reynolds-averaged Navier–Stokes (RANS) equations along with the $k-\omega$ SST turbulence model was used. The computational domain and the governing equations were discretized using the finite volume method, and the volume of fluid method was employed to determine the position of the free surface. Within the numerical simulations in shallow water, a mesh morphing algorithm was used to accommodate possibly more pronounced catamaran motions. Based on the performed verification study, the numerical uncertainty of total resistance and sinkage of the catamaran in deep water and for $h/T = 2$ was calculated at the speed of 5.5 knots. The obtained numerical uncertainty of the total resistance of the catamaran in shallow water is somewhat higher in comparison to the deep water, which is in line with expectations considering that the mesh requirements are higher.

The speed reduction for $h/T = 2$ was determined based on Schlichting's diagram which proved to be very practical for estimating the speed reduction in shallow water, intending to avoid negative effects such as potential grounding or stranding. By analyzing the obtained numerical results, it can be concluded that the total resistance of the catamaran

at the operational speed of 5.5 knots increased significantly as the depth decreased, resulting in notable sinkage of the catamaran. On the other hand, it was noticed that the shallow water did not have a significant effect on catamaran trim in this particular case. A reduction in speed by 1.5 knots led to a significant decrease in the total resistance as well as sinkage of the catamaran.

The effect of shallow water on the total resistance of the catamaran was also manifested through the wave pattern. In the case of $h/T = 2$ at the operational speed of 5.5 knots, the Kelvin angle increased along with the wavelength of the transverse waves, increasing the pressure resistance. The decrease in the hydrodynamic pressure along the catamaran demihull is a consequence of a change in the flow velocity. An increase in the flow velocity increased the tangential stresses, ultimately affecting the total resistance of the catamaran. The changes in the distribution of hydrodynamic pressure correspond to changes in the pressure distribution at the bottom of the computational domain. By analyzing the magnitude of the velocity at the symmetry plane of the catamaran demihull, it was noticed that the maximum magnitude of the velocity between the catamaran and the bottom was approximately 30% lower when the catamaran speed was reduced from 5.5 to 4 knots. By analyzing the longitudinal wave cuts, a significant increase in the wave elevations in front of the bow and behind the stern, and especially in the midship area between the catamaran demihulls was observed for the smallest water depth.

It has been demonstrated that the application of computational fluid dynamics enables a detailed analysis of the flow around the catamaran in shallow water conditions, allowing for the determination of the increase in total resistance and changes in sinkage and trim, to avoid potential negative effects associated with sailing in confined waterways.

Author Contributions: Conceptualization, I.M., N.D. and K.B.; methodology, I.M., N.D. and K.B.; software, I.M. and K.B.; validation, I.M., N.D., K.B. and C.G.G.; formal analysis, I.M., N.D., K.B. and C.G.G.; investigation, I.M., N.D., K.B. and C.G.G.; resources, N.D.; writing—original draft preparation, I.M., N.D. and K.B.; writing—review and editing, I.M., N.D. and K.B.; visualization, I.M., K.B. and C.G.G.; supervision, I.M. and N.D. All authors have read and agreed to the published version of the manuscript.

Funding: This study has been fully supported by the Croatian Science Foundation under project IP-2020-02-8568.

Institutional Review Board Statement: Not applicable.

Informed Consent Statement: Not applicable.

Data Availability Statement: Not applicable.

Acknowledgments: This study has been fully supported by the Croatian Science Foundation under the project IP-2020-02-8568.

Conflicts of Interest: The authors declare no conflict of interest.

References

1. iCat. Available online: https://www.icat.hr/hr/ (accessed on 17 July 2023).
2. Wang, H.; Oguz, E.; Jeong, B.; Zhou, P. Life cycle and economic assessment of a solar panel array applied to a short route ferry. *J. Clean. Prod.* **2019**, *219*, 471–484. [CrossRef]
3. Zakiah, D.; Selasdini, V. Solar and wind energy for ship power system, current status and future prospect. *J. Marit. Malahayati* **2023**, *4*, 7–15.
4. Tuswan, T. Current research outlook on solar-assisted new energy ships: Representative applications and fuel & GHG emission benefits. *IOP Conf. Ser. Earth Environ. Sci.* **2022**, *1081*, 12011.
5. Zhu, Y.; Zhou, S.; Feng, Y.; Hu, Z.; Yuan, L. Influences of solar energy on the energy efficiency design index for new building ships. *Int. J. Hydrog.* **2017**, *42*, 19389–19394. [CrossRef]
6. Sornek, K.; Wiercioch, J.; Kurczyna, D.; Figaj, R.; Wojcik, B.; Borowicz, M.; Wielinski, M. Development of a solar-powered small autonomous surface vehicle for environmental measurements. *Energy Convers. Manag.* **2022**, *267*, 115953. [CrossRef]
7. Shi, G.; Priftis, A.; Xing-Kaeding, Y.; Boulougouris, E.; Papanikolaou, A.D.; Wang, H.; Symonds, G. Numerical investigation of the resistance of a zero-emission full-scale fast catamaran in shallow water. *J. Mar. Sci. Eng.* **2021**, *9*, 563. [CrossRef]

8. Haase, M.; Davidson, G.; Thomas, G.; Binns, J.; Bose, N. A practical design approach including resistance predictions for medium-speed catamarans. *Ship Technol. Res.* **2013**, *60*, 4–12. [CrossRef]
9. Yun, L.; Bliault, A.; Rong, H.Z. *High Speed Catamarans and Multihulls: Technology, Performance, and Applications*; Springer, 2018; pp. 1–746.
10. Yildiz, B. Prediction of residual resistance of a trimaran vessel by using an artificial neural network. *Brodogradnja* **2022**, *73*, 127–140. [CrossRef]
11. Degiuli, N.; Werner, A.; Doliner, Z. Comparison of experimental methods for determining wave pattern resistance of a trimaran based on wave measurements in longitudinal cuts. *Int. Shipbuild. Prog.* **2003**, *50*, 57–87.
12. Farkas, A.; Degiuli, N.; Martić, I. Numerical investigation into the interaction of resistance components for a series 60 catamaran. *Ocean Eng.* **2017**, *146*, 151–169. [CrossRef]
13. Ulgen, K.; Dhanak, M.R. Hydrodynamic Performance of a Catamaran in Shallow Waters. *J. Mar. Sci. Eng.* **2022**, *10*, 1169. [CrossRef]
14. Prakash, S.; Chandra, B. Numerical Estimation of Shallow Water Resistance of a RiverSea Ship using CFD. *Int. J. Comput. Appl.* **2013**, *71*, 975–8887.
15. Chillcce, G.; Moctar, O. Viscous effects on squat. *Appl. Ocean Res.* **2022**, *125*, 103252. [CrossRef]
16. Molland, A.F.; Turnock, S.R.; Hudson, D.A. *Ship Resistance and Propulsion: Practical Estimation of Ship Propulsive Power*; Cambridge University Press: Cambridge, UK, 2011.
17. Uliczka, K.; Böttner, C.U.; Kastens, M.; Eloot, K.; Delefortrie, G.; Vantorre, M.; Candries, M.; Lataire, E. International Conference on Ship Manoeuvring in Shallow and Confined Water with Special Focus on Ship Bottom Interaction. In Proceedings of the 4th International Conference on Ship Manoeuvring in Shallow and Confined Water with Special Focus on Ship Bottom Interaction—4th MASHCON, Hamburg, Germany, 23–25 May 2016.
18. Song, S.; Terziev, M.; Tezdogan, T.; Demirel, Y.K.; Muscat-Fenech, C.M.; Incecik, A. Investigating roughness effects on ship resistance in shallow waters. *Ocean Eng.* **2023**, *270*, 113643. [CrossRef]
19. Jachowski, J. Assessment of ship squat in shallow water using CFD. *Arch. Civ. Mech.* **2008**, *8*, 27–36. [CrossRef]
20. Mucha, P.; Moctar, O.; Dettmann, T.; Tenzer, M. An experimental study on the effect of confined water on resistance and propulsion of an inland waterway ship. *Ocean Eng.* **2018**, *167*, 11–22. [CrossRef]
21. Tuck, E.O. Hydrodynamic problems of ships in restricted waters. *Annu. Rev. Fluid Mech.* **1978**, *10*, 33–46. [CrossRef]
22. Terziev, M.; Tezdogan, T.; Oguz, E.; Gourlay, T.; Demirel, Y.K.; Incecik, A. Numerical investigation of the behaviour and performance of ships advancing through restricted shallow waters. *J. Fluids Struct.* **2018**, *76*, 185–215. [CrossRef]
23. Patel, P.K.; Premchand, M. Numerical Investigation of the Influence of Water Depth on Ship Resistance. *Int. J. Comput. Appl.* **2015**, *116*, 975–8887.
24. Zeng, Q.; Hekkenberg, R.; Thill, C.; Hopman, H. Scale effects on the wave-making resistance of ships sailing in shallow water. *Ocean Eng.* **2020**, *212*, 107654. [CrossRef]
25. Sutulo, S.; Rodrigues, J.M.; Guedes Soares, C. Hydrodynamic characteristics of ship sections in shallow water with complex bottom geometry. *Ocean Eng.* **2010**, *37*, 947–958. [CrossRef]
26. Lataire, E.; Vantorre, M.; Delefortrie, G. A prediction method for squat in restricted and unrestricted rectangular fairways. *Ocean Eng.* **2012**, *55*, 71–80. [CrossRef]
27. Tuck, E.O. Shallow-water flows past slender bodies. *J. Fluid Mech.* **1966**, *26*, 81–95. [CrossRef]
28. Tuck, E.O. Sinkage and Trim in Shallow Water of Finite Width, Schiffstechnik Bd. 14. *Heft* **1967**, *73*, 92–94.
29. Gourlay, T. Slender-body methods for predicting ship squat. *Ocean Eng.* **2008**, *35*, 191–200. [CrossRef]
30. Lackenby, H. The effect of shallow water on ship speed. *Shipbuild. Mar. Engine Build.* **1963**, *70*, 21–26.
31. Tezdogan, T.; Incecik, A.; Turan, O. A numerical investigation of the squat and resistance of ships advancing through a canal using CFD. *J. Mar. Sci. Technol.* **2016**, *21*, 86–101. [CrossRef]
32. Dai, K.; Li, Y. Experimental and numerical investigation on maneuvering performance of small waterplane area twin hull. *Brodogradnja* **2021**, *72*, 93–114. [CrossRef]
33. Degiuli, N.; Farkas, A.; Martić, I.; Zeman, I.; Ruggiero, V.; Vasiljević, V. Numerical and experimental assessment of the total resistance of a yacht. *Brodogradnja* **2021**, *72*, 61–80. [CrossRef]
34. Pavlenko, G.E. Water Resistance to the Movement of Ships, Morskoy Transport (Sea Transport), Moscow, 1956 (in Russian). Available online: https://books.google.hr/books/about/Soprotivlenie_vody_dvizhenii%EF%B8%A0u%EF%B8%A1_sudo.html?id=-I14vgAACAAJ&redir_esc=y (accessed on 30 June 2023).
35. Larsson, L.; Stern, F.; Visonneau, M. CFD in ship hydrodynamics-results of the Gothenburg 2010 workshop. In *International Conference on Computational Methods in Marine Engineering, Marine*; Springer Netherlands: Dordrecht, The Netherlands, 2011.
36. Farkas, A.; Degiuli, N.; Martić, I. Numerical simulation of viscous flow around a tanker model. *Brodogradnja* **2017**, *68*, 109–125. [CrossRef]
37. ITTC Specialist Committee. Recommended procedures and Guidelines—Practical Guidelines for Ship CFD Applications. In Proceedings of the 26th International Towing Tank Conference, Rio de Janeiro, Brazil, 28 August–3 September 2011.
38. ITTC-Recommended Procedures and Guidelines, Uncertainty Analysis in CFD Verification and Validation Methodology and Procedures. 2008. Available online: https://ittc.info/media/4184/75-03-01-01.pdf (accessed on 30 June 2023).

39. Celik, I.B.; Ghia, U.; Roache, P.J.; Freitas, C.J.; Coleman, H.; Raad, P.E. Procedure for estimation and reporting of uncertainty due to discretization in CFD applications. *J. Fluids Eng.* **2008**, *130*, 078001.
40. Roache, P.J. Perspective: A method for uniform reporting of grid refinement studies. *J. Fluids Eng.* **1994**, *116*, 405–413. [CrossRef]
41. Siemens, STAR-CCM+, User Guide. 2020. Available online: https://biblio.ugent.be/publication/8624677 (accessed on 30 June 2023).
42. Martić, I.; Chillcce, G.; Tello Ruiz, M.; Ramirez, J.; Degiuli, N.; Ould el Moctar, B. Numerical assessment of added resistance in waves of the DTC container ship in finite water depths. In Proceedings of the 5th International Conference on Ship Manoeuvring in Shallow and Confined Water, Ostend, Belgium, 19–23 May 2019; pp. 273–283.
43. Stern, F.; Yang, J.; Wang, Z.; Sadat-Hosseini, H.; Mousaviraad, M.; Bhushan, S.; Xing, T. Computational ship hydrodynamics: Nowadays and way forward. *Int. Shipbuild. Prog.* **2013**, *60*, 3–105.
44. Eça, L.; Hoekstra, M. A procedure for the estimation of the numerical uncertainty of CFD calculations based on grid refinement studies. *J. Comput. Phys.* **2014**, *262*, 104–130. [CrossRef]

Journal of
Marine Science and Engineering

MDPI

Article

A Numerical Study on the Hydrodynamic Performance of a Tanker in Bow Sea Conditions Depending on Restraint Conditions

Soon-Hyun Lee [1], Seunghyun Hwang [2], Hwi-Su Kim [1], Yeo-Jin Hyun [1], Sun-Kyu Lee [3] and Kwang-Jun Paik [1,*]

[1] Department of Naval Architecture and Ocean Engineering, Inha University, Incheon 22212, Republic of Korea; vori93@naver.com (S.-H.L.); tn5358@naver.com (H.-S.K.); hyj990325@naver.com (Y.-J.H.)
[2] Korea Research Institute of Ships and Ocean Engineering (KRISO), Daejeon 34103, Republic of Korea; shhwang@kriso.re.kr
[3] Hanwha Ocean Co., Ltd., Siheung 15011, Republic of Korea; hunlee@hanwha.com
* Correspondence: kwangjun.paik@inha.ac.kr

Abstract: The importance of accurate ship performance estimation is increasing for efficient ship operation. Ship performance has been evaluated through model tests in the past, but there are limitations in terms of facilities and costs. With the spread of high-performance computers, the method of evaluating the performance of a ship by numerical analysis, especially computational fluid dynamics (CFD), has become common. There have been many numerical studies on added resistance under various wave conditions for many years, showing a high reliability. Meanwhile, most of the studies were conducted under conditions where the degree of freedom (DOF) of the ship was limited due to computational complexity. In this study, we tried to compare the added resistance performance and fluid dynamics of S-VLCC with 6 DOFs in the regular wave conditions. One of the methods for utilizing the 6 DOFs is the soft-mooring system, which allows springs to be attached to the bow and stern to recover the non-restoring force of the hull. The second method considers the free-running condition. The virtual disk is used for the self-propulsion of the ship, and the rudder can be rotated to maintain its course. The propeller rotation speed and rudder angle are controlled through PID control. The bow wave ($\psi = 180°$) and oblique wave ($\psi = 150°, 120°$) conditions were considered, and various regular wave conditions from short to long wavelengths were regarded. The effects of restraint conditions on the added resistance and motion response amplitude operator (RAO), according to each wave condition, were compared. As a result, there was a difference in the roll motion for each restraint condition, and the y-direction force and yaw moment generated on the hull were compared to analyze the cause. In addition, we observed the change in flow characteristics by comparing the streamlines around the hull and the nominal wake on the propeller plane.

Keywords: free-running test; soft-mooring test; degree of freedom; unsteady Reynolds-averaged Navier–Stokes (URANS); regular wave; bow-quartering sea; S-VLCC; fluid dynamics

Citation: Lee, S.-H.; Hwang, S.; Kim, H.-S.; Hyun, Y.-J.; Lee, S.-K.; Paik, K.-J. A Numerical Study on the Hydrodynamic Performance of a Tanker in Bow Sea Conditions Depending on Restraint Conditions. *J. Mar. Sci. Eng.* **2023**, *11*, 1726. https://doi.org/10.3390/jmse11091726

Academic Editors: Nastia Degiuli and Ivana Martić

Received: 6 August 2023
Revised: 21 August 2023
Accepted: 27 August 2023
Published: 1 September 2023

1. Introduction

Efforts to enhance ship performance are intensifying as environmental regulations for ships become more stringent. To estimate ship performance in general, the resistance required for a ship to advance at a constant speed is measured, and the effective horsepower (EHP) is calculated in the calm water condition. On the other hand, Vinayak et al. [1] showed that there are various sea conditions by a real seaway through worldwide oceanic wind and wave data on the ECMWF website. It was pointed out that a large difference occurred by comparing the travel time and fuel consumption according to sea conditions in the same vessel.

Real-world maritime operations contend with unpredictable environmental conditions like waves and wind, with waves having the most pronounced impact, particularly due

to the dense seawater in which ships operate. Studies on estimating the added resistance caused by waves have been conducted for a long time. In particular, added resistance has been estimated through empirical formulae [2–5], model experiments [6–13], and numerical analysis [14–20] so far.

Experimental methods for estimating added resistance can be divided according to the degrees of freedom (DOFs). The DOFs are limited by the experimental facilities and the complexity of the data obtained. Most captive models are rail-type models with a long test tank called a towing tank, and the ship advances without a heading angle. A 2-DOFs experiment is generally performed with the heave and pitch movements as the DOFs.

Sadat-Hosseini et al. [10] compared the resistance performance obtained when the DOF for the surge is given at different experimental institutions. The effect of the surge was insignificant, and the effect of the heave and pitch on the change in resistance was considered large. Hino et al. [21] compared the resistance and motion with a fixed surge and free surge at various experimental institutions. The effect of the surge was insignificant, and the damping effect of the spring installed to consider the surge could affect the resistance results.

Recent studies have considered the conditions of having a heading angle, such as in bow-quartering or beam sea conditions. Islam et al. [17] compared the heave and pitch RAOs according to the DOFs under oblique regular wave conditions using a KVLCC2 hull. Through a computational fluid dynamics (CFD) computation, 2 DOFs (with free heave and pitch), 3 DOFs with added roll, and 5 DOFs with only sway restraints were considered. As the DOFs increased, the effect of the roll increased, and the heave and pitch RAOs were relatively low.

Mousavi et al. [19] estimated the added resistance performance in irregular oblique waves through CFD for a DTMB 5415. Using the STAR-CCM+ DFBI model, the 4-DOFs conditions of free surge, roll, pitch, and heave were considered. As the heading angle became farther from head sea conditions, the roll motion results of strip theory and CFD showed a difference. Mikkelsen et al. [20] applied 4 DOFs to the KCS hull, which was the same as in the study by Mousavi et al. [19]. Using CFD, the added resistance and motion RAOs were systematically compared for waves entering at an angle of 45 degrees from head sea conditions to following sea conditions. In addition, each result was compared, considering various wavelength ratio conditions. They pointed out discrepancies from the experimental results under the same conditions due to experimental uncertainty.

When considering the oblique waves, the difference in the motion RAOs by DOF was confirmed through prior studies. Otherwise, it is relatively easy to constrain the DOFs in numerical analysis, but it is difficult to constrain the DOFs selectively in experiments. Therefore, experimental studies considering 6-DOF conditions have been conducted. One method is applying a soft-mooring system such as a spring to tow the hull. The spring restores the surge, sway, and yaw motion, which are non-restoring motions. Seo et al. [13] applied a spring system to a KVLCC2 in the ocean engineering basin in the Korea Research Institute of Ships and Ocean Engineering (KRISO). Force was measured in the bow and stern with load cells, and tension was also measured as a force in a tension meter. When measuring added resistance, long-period resistance and motion occur from the spring, which means the post-processing of the result is necessary. As a result, a polar diagram of added resistance according to the wave directions is created by comparing potential method results. Similarly, as a numerical study, Cho et al. [22] estimated the added resistance performance in bow-quartering sea conditions using the soft-mooring system. The artificial spring was implemented as an external force on the hull dynamic fluid body interaction (DFBI), which restore the non-restoring forces. The 6-DOF results are compared with those of the 2-DOF and show the difference in the roll RAOs.

In addition to the added resistance, Dai et al. [23] compared the self-propulsion factors in oblique waves using the added resistance results for the KVLCC2 hull. The propeller revolution, thrust, and torque at the self-propulsion point were determined by calculating

the towing force in the oblique wave. Overall, the self-propulsion factor in waves tended to be lower than that in calm water.

Uharek and Hochbaum [16] conducted an experiment in oblique wave conditions with a twin-screw passenger ship for Meyer Werft. The test site was the Technische Universitat Berlin (TUB) and Hamburg Ship Model Basin (HSVA). The surge and sway forces and yaw moment were compared between cases in which all movements were fixed and spring systems in which all movements were free. In addition, the experimental results were compared with computation results from the in-house CFD code (Neptuno).

Another method is a free-running test that maintains a self-propulsion state through propellers and rudder control. The model ship maintains directional stability through the rudder, and the propeller's rotation rate is adjusted to maintain the desired speed. Since the free-running test causes changes in the stern pressure and flow due to the propeller rotation, the added resistance should be calculated while considering the propeller's suction effect [11]. Similarly, Yoo et al. [12] conducted experiments through free running on an LNG carrier with twin skegs, and the resistance and motion were compared with 3-DOF CFD. The wave conditions considered were irregular wave conditions. Overall, the experiment and CFD showed similar tendencies, and it was pointed out that the added resistance estimated using the spectral method was relatively low. In the case of motion, the surge wave slightly drifted due to the difference in the thrust system.

In this study, the three methods described above were implemented by CFD computation. First, with the captive model, the 2- and 3-DOF computations were performed with the heave, pitch, and roll (for the 3-DOF) free. For the soft-mooring system, the 6-DOF calculation was performed by numerically modeling a spring on the bow and stern, similar to Seo et al. [13]. A free-running model was then implemented using a virtual disk for the propeller performance. By implementing proportional integral derivative (PID) control in CFD, the propeller rotation speed and rudder angle were controlled.

Using these three methods, the added resistance coefficient and motion RAOs were compared with the three different heading angles (i.e., 180, 150, and 120 degrees). In the case of 6 DOFs, the y-direction force and yaw moment of the hull were compared. To compare the flow characteristics around the hull according to the wave direction, the streamlines passing around the hull and nominal wake were compared using the condition of $\lambda/L_{PP} = 1.0$. The streamlines were compared in the flow close to the propeller hub and the flow far away. In the case of the nominal wake, the change according to the time-series average and the encounter period was compared.

2. Numerical Conditions

2.1. Governing Equations and Numerical Schemes

For the CFD computation, the governing equations were the unsteady Reynolds-averaged Navier–Stokes (URANS) equations, which model the Reynolds stress term in the Navier–Stokes (N–S) equation with the assumption of incompressible inviscid flow except near walls. Commercial CFD software, STAR-CCM+ 15.06 version, was used to solve the URANS equations.

The URANS equation can be written in tensor form in Cartesian co-ordinates as shown in Equation (1). It includes the Reynolds stress term ($\rho\overline{u_i'u_j'}$), which is a nonlinear term and required to determine. One way to round this out is to use turbulence models, which obtain the unknown values by assuming or implementing the empirical equations. In this study, the realizable k–ϵ (RKE) model has been chosen as the turbulence model; this model can construct a relatively coarse grid near a wall, and the wall Y+ was distributed between 30 and 60. The RKE turbulence tends to be stable in the residual of the calculation and results in a fast convergence. Moreover, wave dissipation can be minimized in the calculation

domain by using 1^{-4} m^2/s^3 and 1^{-5} J/kg for the turbulent dissipation rate (k) value and turbulent kinetic energy (ϵ), respectively.

$$\frac{\partial \overline{u}_i}{\partial t} + \overline{u}_j \frac{\partial \overline{u}_i}{\partial x_j} = -\frac{1}{\rho}\frac{\partial \overline{p}}{\partial x_i} + \frac{1}{\rho}\frac{\partial^2}{\partial x_j}\left(\mu \frac{\partial \overline{u}_i}{\partial x_j} - \rho \overline{u_i' u_j'}\right) \quad (1)$$

where u_i is the three-dimensional velocity vector (i, j = 1,2) in the x and y directions. The flow variables are decomposed into the mean component ($\overline{u}$) and the fluctuating component (u'). p, t, ρ, and μ are the static pressure, time, density, and kinematic viscosity, respectively. To track the movement of the vessel, a dynamic fluid body interaction (DFBI) model was used.

A pressure-based segregated algorithm was used to solve the pressure or pressure correction equation derived by the continuity and motion equations. The pressure-based segregated algorithm converges to a numerical solution through iterative calculations. This algorithm stores the discretized equation over time and applies it to the properties of the fluid. The discretized governing equation is applied to each control volume as Equation (2):

$$\int_V \frac{\partial \rho \phi}{\partial t} dV + \oint \rho \phi \vec{v} \cdot d\vec{A} = \oint \Gamma_\phi \nabla \phi \cdot d\vec{A} + \int_V S_\phi dV \quad (2)$$

$$\frac{\partial \rho \phi}{\partial t} V + \sum_f^{N_{faces}} \rho_f \vec{v}_f \phi_f \cdot \vec{A}_f + \sum_f^{N_{faces}} \Gamma_\phi \nabla \phi \cdot \vec{A}_f + S_\phi V \quad (3)$$

where V is the control volume, ρ is the density, t is the time, ϕ represents the transport of a scalar property, v is velocity, A is the surface area of the control volume, Γ is the diffusion coefficient, and S_ϕ is the source terms, special forms of the partial differential equations for mass, momentum, energy, and species.

The above equation converges as in Equation (3), and it is necessary to determine the convex term ϕ_f. Since the convex term affects the stability and accuracy of the analysis, it is necessary to select an appropriate technique. In this study, the second-order upwind (SOU) technique was used as a convection term. In addition, the hybrid Gauss–least squares method was applied as a gradient method to determine the center and face center values of the grid. And the venkatakrishnan limiter was used to limit the inter-lattice interference. For the diffusion term, the central difference method was used, and the semi-implicit method (SIMPLE), which obtains the pressure field by mass conservation of the coupling between velocity and pressure, was used. In the analysis, the under-relaxation factors of velocity and pressure of 0.6 and 0.4, respectively, were used.

The volume of fluid (VOF) wave model was used to capture the free surface. The VOF method is a method of expressing the fraction value of the fluid phase to be implemented between 0 and 1 in a cell. Moreover, a VOF wave scheme following the fifth-order Stokes theory was used to generate regular and irregular waves. To reduce the dissipation of the generated waves, a second-order temporal discretization scheme was applied. A time step corresponding to 1/400 of the regular wave encounter period was used.

2.2. Geometry

In this study, the main ship was an S-VLCC tanker, which was designed by Samsung Heavy Industries, as shown in Figure 1. The details of the model ship and propeller are listed in Table 1. A 1/68-scale model was chosen, which is the same scale as in the SSPA experiment [11].

Figure 1. Geometry of S-VLCC.

Table 1. Main particulars of objective ship and propeller.

Target ship	S-VLCC		Target propeller	KP458
Ship speed (Fr)	0.137		Full-scale diameter (m)	9.860
	Full-scale	CFD model	Model-scale diameter (m)	0.145
Scale ratio	1	68	Pitch ratio, P/D_P $(0.7R_P)$	0.7212
Length between perpendiculars, L_{PP} (m)	323.0	4.75	Thickness ratio, t/c $(0.7R_P)$	0.0667
Breadth, B_{WL} (m)	60.0	0.882	Chord ratio, c/D_P $(0.7R_P)$	0.2338
Draft, d (m)	21.0	0.309	Number of blades	4
Displacement, ∇ (m^3)	338,154	1.075	Hub ratio	0.155
Vertical center of gravity, KG (m)	17.316	0.255		
Moment of inertia, I_{xx}/B, I_{yy}/L_{PP}, I_{zz}/L_{PP}	0.258, 0.239, 0.241			

As the target propeller, the KP458 KVLCC2 propeller was used. In the co-ordinate system for computation, the x-axis was positive from the stern to the bow, the y-axis goes in the positive direction to the port side, and the z-axis is the opposite direction of gravity. The origin of the co-ordinate system was set as the stern, and the free surface was realized at the point where the z-axis is 0. A wave travels in the negative x-direction.

2.3. Simulation Cases

The CFD cases are shown in Table 2. In the head sea conditions, 2 DOFs (with free heave and pitch) and the free-running method were considered. Under a heading angle of 150 degrees, all cases using 3 DOFs (with free heave, roll, and pitch), soft mooring, and free running were compared. Since the captive model is affected by waves coming from the side, the roll motion was also considered. Finally, in the case of a heading angle of 120 degrees, the captive model was excluded. A total of five conditions ($\lambda/L_{PP} = 0.5,\ 0.9,\ 1.0,\ 1.1,\ 1.4$) were considered for wave conditions from short to long waves, and the wave steepness (H/λ) was set to 0.02 for short waves and 0.01 for long waves.

2.4. Computational Domain and Boundary Conditions

Three grid systems were used to evaluate the added resistance in oblique waves. First, in calm water and head sea ($\psi = 180°$) conditions, calculations were performed using a captive model and soft-mooring system in half-breadth conditions, as shown in Figure 2a. The distance from the hull to the inflow boundary was $0.5L_{PP}$, which is intended to minimize wave dissipation. A length of $3.5L_{PP}$ was applied, including the grid damping area in the downstream area of the hull to prevent wave reflection. The length to the side and bottom boundary was $1.5L_{PP}$, and the length to the top was $1L_{PP}$.

Table 2. Test cases of numerical simulation.

S-VLCC, Design Speed (15 knots, Fr = 0.137)						
Wave Direction (deg)	**Wavelength, λ/L_{PP} (-)**	**Captive Model**		**6 DOFs, Soft-Mooring System**	**6 DOFs, Free Running**	**Wave Steepness H/λ (-)**
		2 DOFs (Heave, Pitch)	**3 DOFs (Heave, Pitch, Roll)**			
180	0.5	O	-	-	O	0.02
	0.9	O	-	-	O	
	1.0	O	-	-	O	0.01
	1.1	O	-	-	O	
	1.4	O	-	-	O	
150	0.5	-	O	O	O	0.02
	0.9	-	O	O	O	
	1.0	-	O	O	O	0.01
	1.1	-	O	O	O	
	1.4	-	O	O	O	
120	0.5	-	-	O	O	0.02
	0.9	-	-	O	O	
	1.0	-	-	O	O	0.01
	1.1	-	-	O	O	
	1.4	-	-	O	O	

To eliminate the effect of reflected waves in the numerical analysis domain, a wave-forcing condition was adopted at the inlet, outlet, and both sides, where the velocity inlet boundary conditions were applied. In the wave-forcing zone, we applied $0.3L_{PP}$ to the inlet and both sides, and $1.5L_{PP}$ to the outlet, to minimize the influence of waves reflected from the domain boundaries. For the boundary conditions, a velocity inlet condition was applied to the inlet, side (far from hull), outlet, and top and bottom. A symmetry condition was adopted on the side plane with the hull. A no-slip wall condition was applied to the hull.

(**a**) ψ = 180°

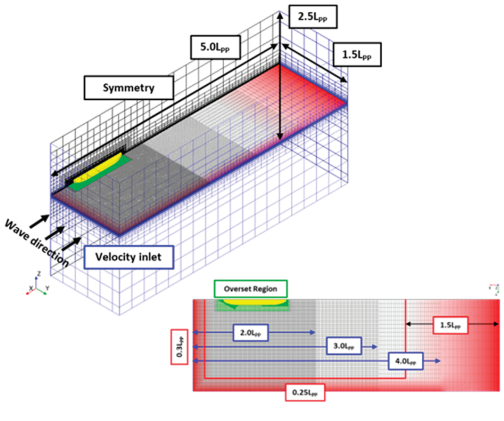

(**d**) ψ = 180°

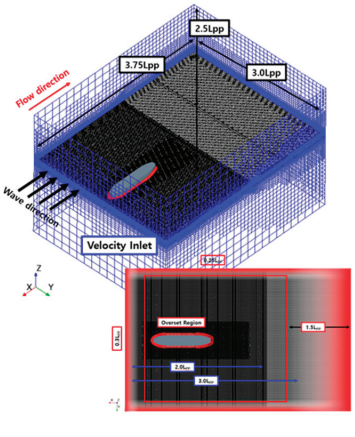

Figure 2. *Cont.*

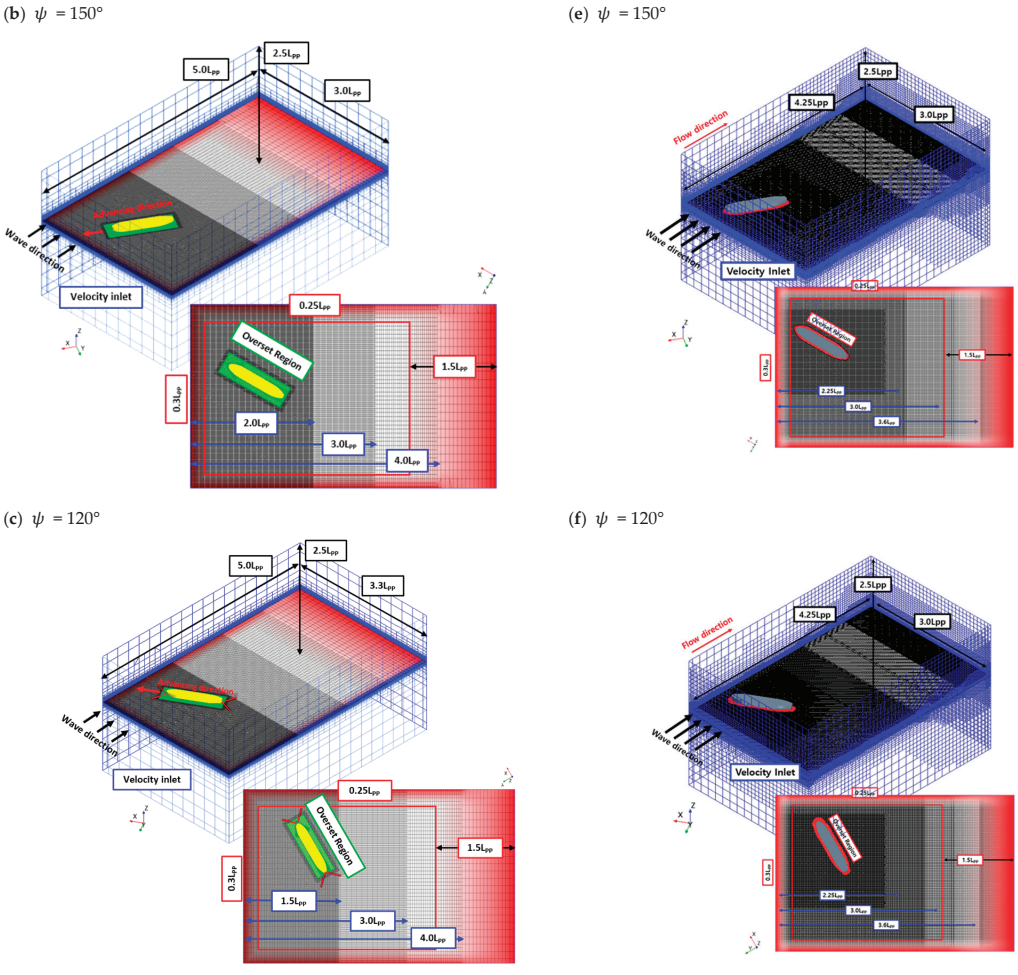

Figure 2. Computational domain and boundary conditions according to heading angles.

In the case of the bow-quartering wave conditions (ψ = 150° and 120°), the full domain was applied with a symmetrical half-width domain, and a velocity inlet condition was applied as shown in Figure 2b,c. A trimmed mesh was used, which had the advantage in realizing the height of a wave. Approximately 2.6 million grid elements were used for the half domain, and approximately 6.2 million grid elements were used for the full domain. The numbers of grid elements in the overset region were 1.5 million and 3.1 million. To consider both the long- and short-wave regions, 120 grid elements per wavelength and 20 grid elements per wave height were applied at λ / L_{PP} = 1.0 and H/λ = 0.01.

The part marked with red is the wave-forcing area and was applied differently according to each boundary surface. The forcing boundary condition applies a theoretical wave to the boundary surface and minimizes the dissipation of the wave in the desired area by applying the transport equation in the input length. A forcing length of $0.3L_{PP}$ was applied to the inlet, $0.25L_{PP}$ applied to the side, and $1.5L_{PP}$ applied to the outlet.

An adaptive mesh refinement (AMR) grid system was used for free-running calculations as shown in Figure 2d–f. The AMR grid can be adjusted so that the cell size becomes fine along the free surface based on the VOF, and the generated waves are accurately implemented without modifying the grid according to the wave conditions. Through a series of

tests, the optimal parameters used for the AMR grid were determined as a transition width of 10 and a free-surface maximum refinement level of 4.

When using the AMR grid system, it is recommended to select an overset area that is a specific length away from the hull surface as shown in Figure 3, and the rudder area is applied as another overset grid system within the overset area to enable rotation. An oblique wave was considered as a method of rotating the ship for each heading angle in the same size domain. The domain was reduced by $0.75L_{PP}$ in the longitudinal direction and $0.3L_{PP}$ in the side direction compared to the fixed grid described above. Similarly, the wave-forcing area was set in the same way as in the fixed grid.

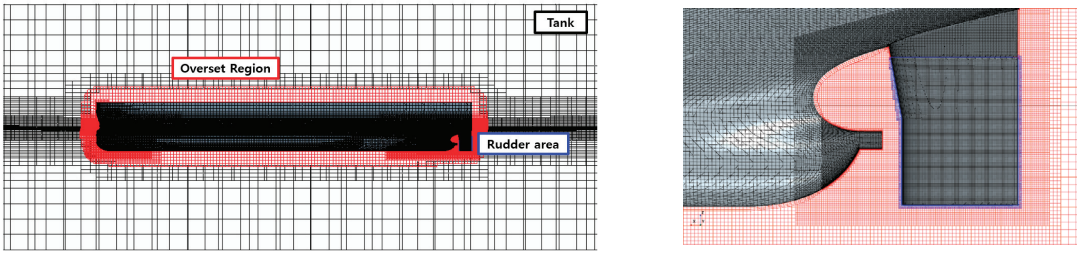

Figure 3. Free-running simulation grid system; left: side view; right: around the rudder.

2.5. Soft Spring System

To apply the 6 DOFs without steering gear, the ship needs a means to regain non-restoring motions such as surge, sway, and yaw. In this study, a soft-mooring system was used, and a method of attaching two springs each to the bow and stern according to the height of the KG was chosen [13]. A spring can be implemented by defining a spring constant and location in STAR-CCM+. The force by the spring acts as an external force on the hull defined in DFBI. According to ITTC [24], when selecting the spring constant, it is recommended that the natural period of the spring be more than six times the wave generation period of the longest wave condition to be considered.

The spring's natural period can be calculated by Equation (4):

$$T_s = 2\pi\sqrt{\frac{m + m_a}{k_s}} \tag{4}$$

where T_s is the natural period of the spring, m is the mass of the ship, m_a is the added mass of the ship, and k_s is the spring constant [25]. In this study, a spring constant of 100 N/m with a sufficiently long natural period was selected. Figure 4 shows the soft spring system attached to the vessel and structure of springs in the numerical simulation.

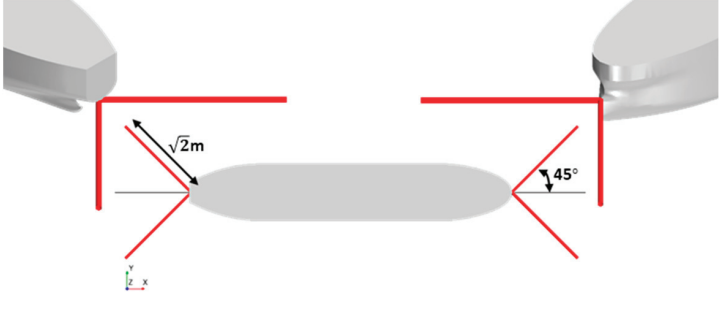

Figure 4. Diagram of soft spring system.

2.6. Free-Running Model Test

A free-running model was adopted to implement 6 DOFs. For free running, the rudder and propeller rotation rate should be controlled to keep the same heading angle and self-propulsion state, respectively. A virtual disk was applied to mimic the propeller performance. The performance of the virtual disk of a KP458 propeller was verified through a POW test and showed similar results to the NMRI experimental results as shown in Figure 5 [26].

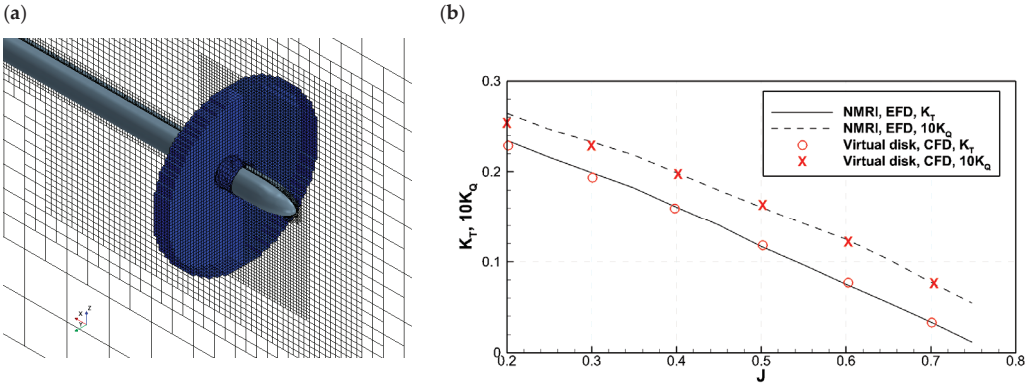

Figure 5. (**a**) POW simulation grid distribution, (**b**) POW performance validation (KP458).

The target vessel of this study was an S-VLCC, but we tested whether free running can be implemented through STAR-CCM+ through a KVLCC2 hull. The type of rudder used was a horn-type rudder, as shown in Figure 6a. It was divided into a moving part (marked in red in Figure 6b) that can move to the port side and starboard side along the rudder axis, and a fixed part connected to the hull. The rotational speed of the rudder was limited to a maximum of 2.32 degrees/s on a full-scale basis, and the rudder can be rotated up to a maximum of 35 degrees.

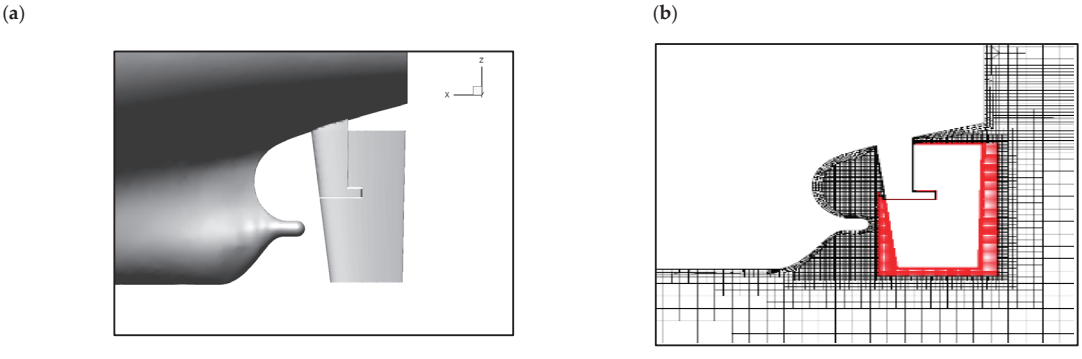

Figure 6. (**a**) Geometry of horn-type rudder of KVLCC2; (**b**) mesh distribution around rudder.

PID control was used to adjust the aforementioned two variables. PID control was utilized in STAR-CCM+ by using the result for every iteration, which can be tracked using a field function, reported, and monitored. The PID gain value needed to be selected to adjust the propeller rotation rate and rudder angle. There are theoretical methods for selecting the PID gain value such as the Ziegler–Nichols method, but, in this study, the gain value was selected through a case study. As shown in Table 3, we tried to select a case with low vibration while converging quickly, which depends on the PID gain values. A total of seven

propeller rotation rates were tested, from Propeller-V1 to V7, and a total of 11 cases were tested to adjust the rudder angle.

Table 3. Numerical analysis of test cases.

Case	K_P	K_I	K_D	State
Propeller-V1	0.001	-	-	Long time to converge
Propeller-V2	0.05	-	-	Divergent
Propeller-V3	0.01	-	-	Long time to converge
Propeller-V4	0.01	0.05	-	Long time to converge
Propeller-V5	0.01	1		Converge high overshoot
Propeller-V6	0.01	1	1×10^{-5}	Converge high overshoot
Propeller-V7	0.01	1	5×10^{-5}	Converge
Rudder-V1	0.1	-	-	Divergent
Rudder-V2	0.01	-	-	Divergent
Rudder-V3	0.001	-	-	Divergent
Rudder-V4	0.001	0.1	-	Long time to converge
Rudder-V5	0.001	0.01	-	Long time to converge
Rudder-V6	0.001	0.1	0.1	Long time to converge
Rudder-V7	0.001	0.1	1.0	Long time to converge
Rudder-V8	0.02	0.1	1.0	Long time to converge
Rudder-V9	0.02	5.0	1.0	Fluctuation
Rudder-V10	0.02	5.0	5.0	Fluctuation
Rudder-V11	0.02	1.0	5.0	Convergence

Figure 7a,b show the yaw angle and the rudder angle according to time, respectively, and the representative cases are plotted. As shown in Figure 7a, there is a difference in the yaw angle's convergence time depending on the gain value. Through the case study, the most stable convergence case was selected and applied to subsequent calculations. The gain values applied to PID control were $K_P = 0.01$, $K_I = 1.0$, and $K_D = 5 \times 10^{-5}$ for the propeller's rotation speed, and $K_P = 0.02$, $K_I = 1.0$, and $K_D = 5.0$ for the rudder angle.

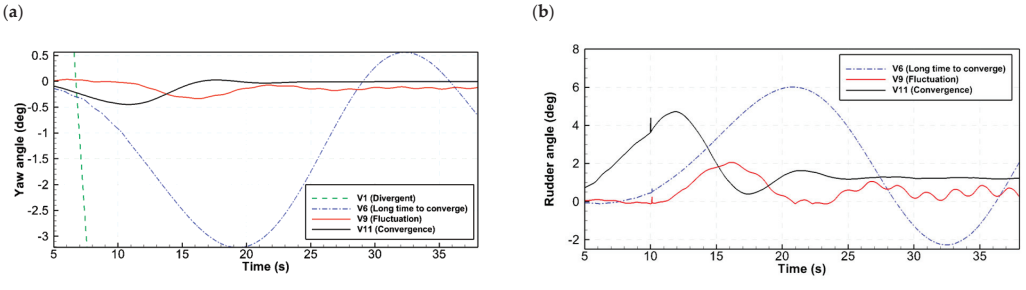

Figure 7. (**a**) Yaw angle and (**b**) rudder angle according to PID gain value.

2.7. Feasibility Test of Free Running Using KVLCC2

The feasibility of the added resistance computation in a wave was tested through the KVLCC2 at the design speed ($Fr = 0.142$) through the free-running state. The method for implementing the free-running technique was described in detail in Section 2.6. However, the propeller rotation speed should be adjusted to maintain the target ship speed during free running.

In this study, the point at which the average resistance and thrust are equal in waves was selected as the self-propulsion point. The resistance of the ship in the wave fluctuates with a large amplitude, as shown with the black solid line in Figure 8a. To maintain the self-propulsion point, the propeller rotation speed should oscillate, which is practically impossible. Therefore, by tracking the average values of resistance and thrust, the point where the two average values are equal was set as the self-propulsion point. The propeller rotation rate converges as shown in Figure 8b.

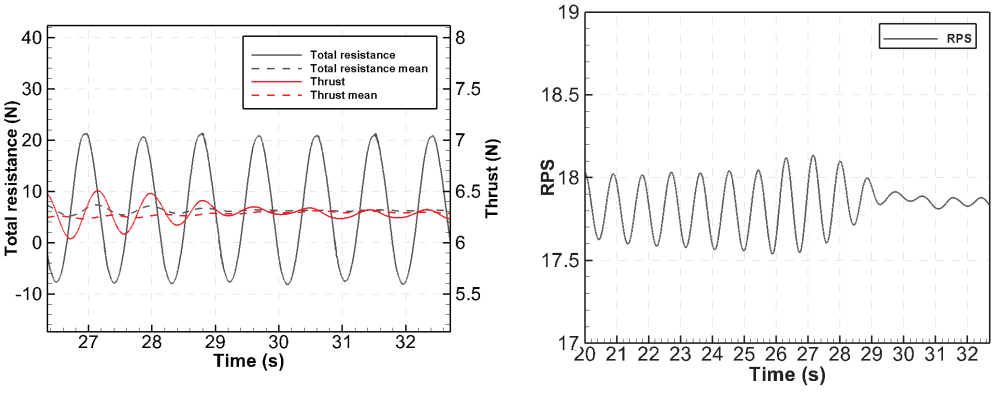

(**a**) In-wave resistance and thrust time series

(**b**) Propeller revolution time series

Figure 8. Convergence of variables over time.

In the free-running state, the added resistance was estimated with Equation (5), which multiplies the difference between the average thrust value and the thrust in calm water by the thrust deduction factor.

$$\left(\overline{T_{Wave}} - T_{Calm}\right) \times (1 - t) = R_{aw} \tag{5}$$

As a reference study, using the KCS hull, [27] Kim et al. (2021) compared the thrust deduction factor in calm water (t_{Calm}) and in wave conditions (t_{Wave}). Through CFD simulations, it was shown that the thrust deduction factor in waves tended to decrease. In particular, the decrease in the thrust deduction coefficient was the largest in the resonance region where the added resistance was the highest. Through this study, we compared the added resistance considering t_{Wave}.

The added resistance coefficient in waves obtained through free running is shown in Figure 9, which was compared with the 2-DOF captive model results (with free heave and pitch). For the captive model, the results from Seoul National University (SNU) [28], Osaka University (OU) [29], and the Inha University Towing Tank (IUTT) [30] showed similar added resistance performance and motion RAOs. Therefore, the computation results are considered to follow the experimental results well. The added resistance coefficient in waves obtained in the free-running test showed similar results to the captive model, but, when t_{Calm} was used, the measured added resistance coefficient was relatively low at the resonance frequency. To examine this, t_{Wave} was compared as shown in Figure 10.

Lee et al. [30] compared the stern pressure in calm water and in a wave as a reason for the lower thrust deduction factor. They pointed out that the effect of the pressure change due to the suction of the propeller in the wave is reduced. They judged that the pressure of the stern part due to the movement of the hull during the wave changes regularly and is larger than the pressure changes due to the propeller.

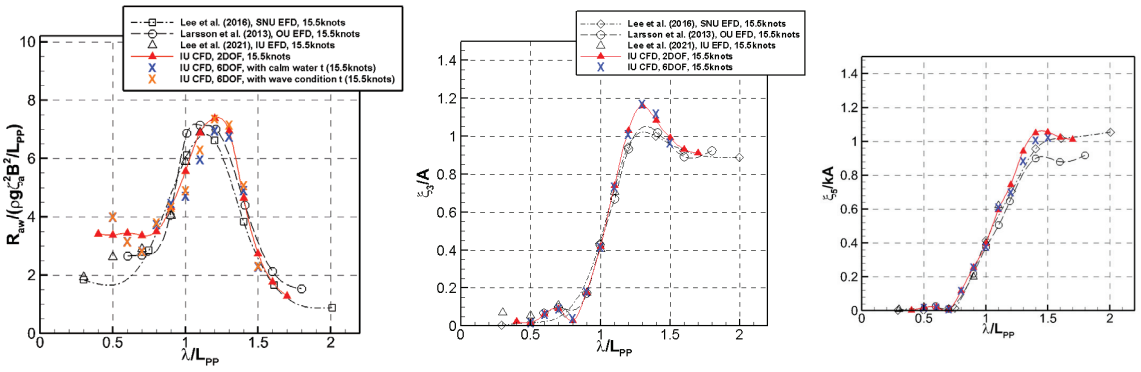

(**a**) Added resistance coefficient (**b**) Heave RAOs (**c**) Pitch RAOs

Figure 9. Comparison of added resistance performance [28–30].

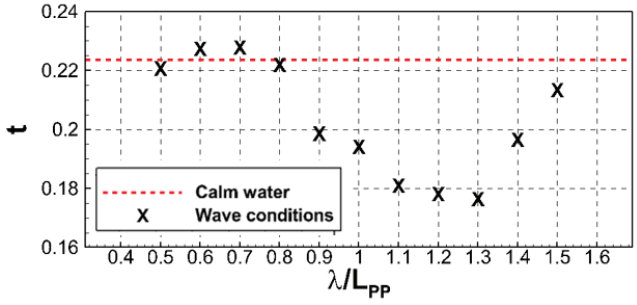

Figure 10. Comparison of thrust deduction factors according to wave conditions.

Similarly, in this study, the change in the thrust deduction factor in free running was greatly reduced in the vicinity of the resonance frequency, where the propeller rotation rate is higher. The difference in the thrust deduction factor is not large compared to that in calm water at a short wavelength. As a result, it is reasonable to multiply the thrust difference by t_{Wave} when calculating the added resistance coefficient in the wave with free-running conditions. In the case of using t_{Calm}, the added resistance near the resonant frequency of the ship was estimated to be relatively low.

2.8. Validation of Generated Regular Wave

A 3D wave test was performed to select CFD analysis conditions and parameters for the added resistance analysis. For the waves used for the 3D wave test, $H/\lambda = 0.01$ and $\lambda/L_{PP} = 1.0$ were applied to the S-VLCC with a scale ratio of 68. In the fixed grid system, 100 cells per wavelength and 20 cells per wave height were generated. The domain used in the computation is shown in Figure 11, and the area where the forcing conditions is applied is shown in Figure 11. The total number of grid elements was about 3 million, and the variables used in the wave test were reviewed by classifying the time discretization method and inner iterations as shown in Table 4.

The generated waves, according to the parameters, were compared at the bow position (FP), the middle of the hull (Mid), and the stern position AP. When second-order time discretization was applied through D1I1 and D2I1, the wave dissipation was smaller than that of first-order discretization. Ten inner iterations showed better results compared with a theoretical wave than when eight iterations were applied. Therefore, in this study, D2I2 conditions were applied for the added resistance computations. In addition, the wave amplitude generated through the AMR method at the same domain size was compared,

and it was confirmed that the reliability of the generated wave was sufficient when using the same conditions as D2I2.

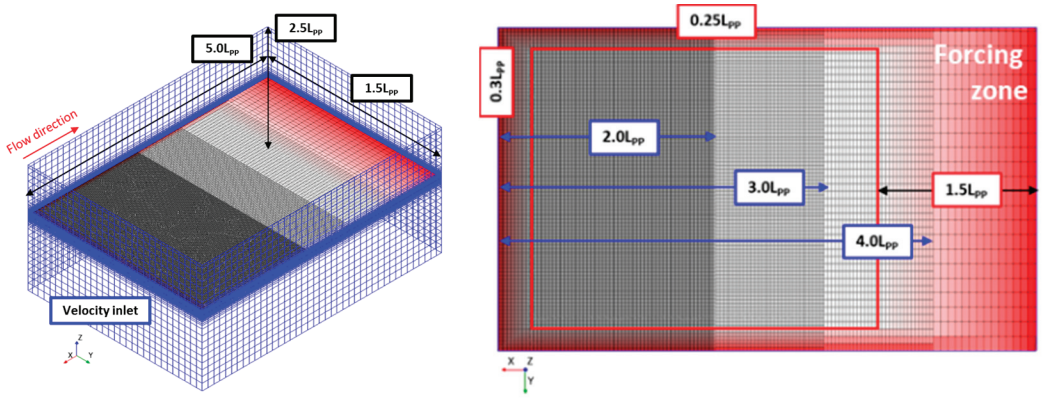

Figure 11. The 3D domain mesh distribution, boundary conditions, and wave-forcing zone.

Table 4. Parametrically generated wave height verification.

Case		Fixed Grid				AMR
		D1I1	D2I1	D2I2	D1I2	
Time step		$\Delta T = T_{e=1.0}/400$				
Time discretization		1st	2nd	2nd	1st	2nd
Inner iterations		8	8	10	10	10
Wave amplitude, error rate from theoretical value	at FP	−2.40%	−1.52%	−0.33%	−2.61%	−0.45%
	at Mid	−7.76%	−3.06%	−0.30%	−4.64%	−0.55%
	at AP	−12.1%	−5.98%	−2.03%	−8.73%	−2.30%

2.9. Convergence Test and Validation of S-VLCC Resistance Performance in Calm Water

A convergence test was conducted in calm water conditions to verify the calculations. Convergence was determined using the grid convergence index (GCI), which is based on the trend of outcomes from the refinement of the grid and time step [31]. The convergence parameters, time step, and grid density were evaluated in three stages. Table 5 shows the GCI of the resistance coefficients, sinkage, and trim.

Table 5. GCI of resistance coefficients and motion RAOs in regular wave (Fr = 0.142).

Variables	Case No.	Number of Grid Elements	Δt (s)	$C_{TM}\times10^3$	GCI (%)	$\zeta_3/T\times10^2$	GCI (%)	ζ_5 (deg)	GCI (%)
Time step	T1G2	2.4 million	0.04	4.615	2.17	3.886	4.07	0.143	0.87
	T2G2	2.4 million	0.02	4.463		3.902		0.145	
	T3G2	2.4 million	0.01	4.387		3.918		0.146	
Grid fineness	T2G1	0.5 million	0.01	4.984	0.000	3.853	0.004	0.143	0.524
	T2G2	1.5 million	0.01	4.773		3.918		0.145	
	T2G3	2.4 million	0.01	4.386		3.918		0.146	
	AMR-G1	1.1 million	0.01	4.705	0.024	3.844	0.000	0.142	0.021
	AMR-G2	1.4 million	0.01	4.768		3.832		0.144	
	AMR-G3	1.6 million	0.01	4.975		3.970		0.151	

First, computations were performed while changing the time step. The test was conducted by reducing the time step by 1/2 at 0.04 s, and the resistance, sinkage, and trim showed

GCIs of 2.17, 4.07, and 0.87%, respectively. The computation results are sensitive to time step changes, and it was judged that the calculation sufficiently converged when the GCI value was less than 5%. The calculation was carried out based on the smallest time step of 0.01 s.

Next, a convergence test was conducted according to the density of the grid. The test was divided into a case using a fixed grid and a case using an AMR grid. Both grid systems showed a complete convergence of the calculations with a GCI index of less than 1%. In the finest condition, although the difference in the total number of grid elements of the two grids was about 0.8 million, the total computation time was similar. The AMR grid had a small number of grid elements, but it took more computation time until the grid converged, according to the free surface.

To validate the computation, the resistance performance in calm water was tested. The resistance coefficient, sinkage divided by the draft (T), and trim value were checked for differences from the experiment. As shown in Table 6, a total resistance coefficient with less than 5% difference from the experiment was obtained. There was a slight difference from the experiment in the sinkage and trim values. Although there was a difference in the exact value due to the scale difference from the experiment, it was judged that the CFD result was sufficient to express resistance and motion.

$$C_P = \frac{P - (\rho g h)}{1/2\, V^2 \rho} \tag{6}$$

Table 6. Difference comparison with experiment.

		SNU EFD	INHA CFD, Fixed Grid	INHA CFD, AMR Grid
Scale ratio		100	68	
Re_M		2,489,775	4,433,761	
Difference	C_{TM} (Error rate)	-	4.96%	2.43%
	$\xi_3/T \times 10^2$	-	−1.06	−2.40
	ξ_5 (deg)	-	0.044	0.032

The dynamic pressure coefficient (C_P) and nominal wake in calm water are shown in Figure 12. The C_P is calculated by Equation (6), where P is a pressure, ρ is a density, h is a water depth from free surface, and V is a velocity. High pressure was observed at the bow part, and, since there was no bulbous bow, the pressure tended to gradually decrease around the center of the hull. Pressure recovery was shown in the stern part and showed the pressure distribution of a general tanker. In the nominal wake distribution in the propeller plane, a distinct hook shape vortex was seen with a blunt stern shape, as shown in Figure 12b.

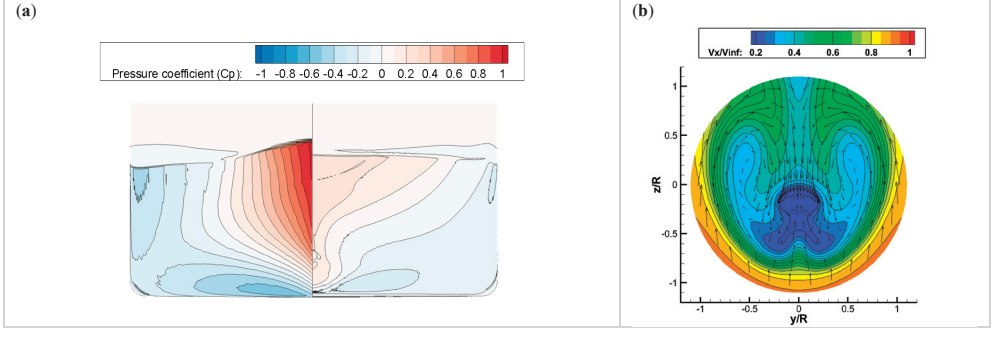

Figure 12. Fluid performance: (**a**) pressure distribution; and (**b**) nominal wake distribution.

3. Results

3.1. Comparison of Added Resistance Performance of S-VLCC

The added resistance coefficient and the motion RAOs of the S-VLCC were studied at a speed of 15 knots in a head wave and bow-quartering wave ($\psi = 150°, 120°$). The numerical analysis results of this study were compared with two experiments (SNU and SSPA) and the Rankine panel method [11]. In the SNU experiment, a captive model test with 3 DOFs was applied, and the heave, pitch, and surge were free. The SSPA experiment was performed under free-running conditions.

The SNU model test was performed only in head wave conditions, and the SSPA model test was performed for all wave directions at 30° intervals from 180° to 0°. In this study, a 2-DOF (with free heave and pitch) computation was performed for head wave conditions. In the 150° bow-quartering wave condition, a computation of the captive model with 3 DOFs (with free heave, roll, and pitch) and 6 DOFs (soft mooring, free running) was conducted to compare the differences according to the DOFs. In the 120° bow-quartering wave condition, only the 6-DOF computations were performed.

Figure 13a–c show the added resistance coefficient under head and bow-quartering wave conditions. In the SNU model test, a general 2-DOF (heave and pitch) captive model test was performed to measure the added resistance and added resistance coefficient derived using the difference in resistance measured in a wave and calm water ($R_{AW} = R_{Wave} - R_{calm}$). The SSPA test was a free-running test that measured the thrust in waves as $(R_{AW} = T_{Wave} - T_{Calm})(1 - t)$ and derived the added resistance coefficient in the wave using the thrust deduction factor (t). In general, the thrust deduction factor in calm water is used with the assumption that the difference in the thrust deduction factor should be small in wave conditions.

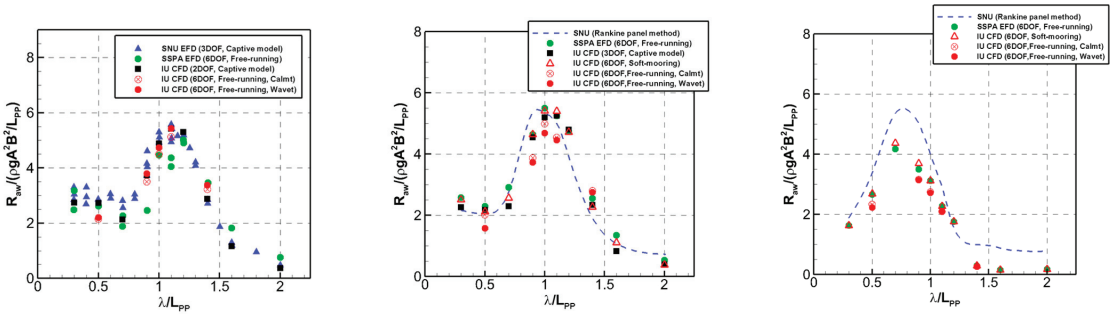

(a) $\psi = 180°$ (b) $\psi = 150°$ (c) $\psi = 120°$

Figure 13. Comparison of added resistance coefficients according to conditions.

In head wave conditions, the added resistance coefficient showed a value similar to the results of the SNU model test and Rankine panel method. The tendency of the added resistance in the bow-quartering wave is similar to that in the SSPA model test results. On the other hand, similar to the KVLCC2 in Section 2.6, when using the thrust deduction factor in waves, the added resistance tended to appear relatively high. This is because the effect of propeller suction became stronger due to the increase in the number of rotations of the propeller due to the added resistance. This results in a difference in accuracy, but it is considered to be a small difference when considering the deviation of the experimental value itself.

Figure 13b shows the added resistance coefficient in the 150° bow-quartering wave conditions. The maximum value of the added resistance was similar to that at 180°; however, the position of the peak was shifted to a shorter wavelength. There was a minor difference in the results of the added resistance between the 3-DOF (with free heave, roll, and pitch) and 6-DOF computations when using the soft-mooring system. Moreover, the SSPA experiment showed a similar trend. However, in the case of free running, the added

resistance was low around the resonant wavelength regardless of the thrust deduction factor used. The tendency appeared to be the same at 120°. Figure 13c shows the added resistance coefficient under the condition of a 120° bow-quartering wave.

In order to analyze the reason for the different added resistance in the case of soft mooring compared to the free-running result, the time-averaged sway and yaw motions of the soft-mooring case are shown in Figure 14 for each wavelength ratio. When using soft mooring, it was observed that the hull moved forward while maintaining a certain sway and yaw under the condition where the difference in the added resistance was large. This periodically recovered the non-restoring motion by the spring, but the ship advanced by a constant amount. The reason for having the largest motions under the condition of a wavelength ratio of 0.9 is that the energy of the wave is the highest because the wave height is the highest. On the other hand, in the case of free running, the average yaw motion does not happen because PID control is performed to maintain the yaw motion at 0. Moreover, a slight drift occurs in the sway direction during PID control, but the value is small and negligible.

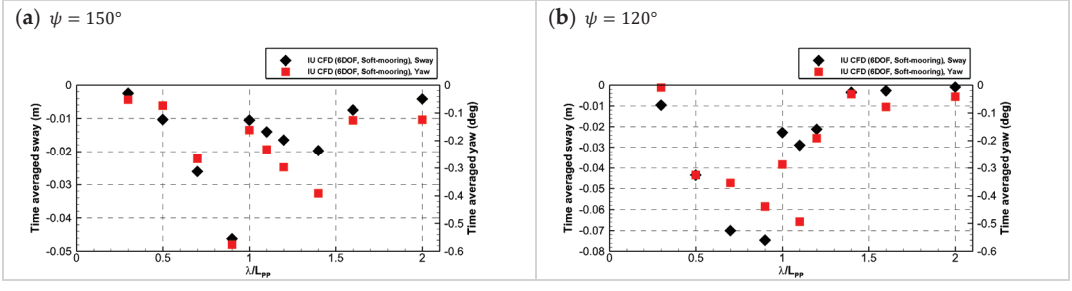

Figure 14. Comparison of sway and yaw motion at different wavelength ratios in bow quartering sea conditions.

With sway and yaw motions, the y-direction force and z-direction moment were compared. As shown in Figure 15, the force fluctuations that occurred in the time series appeared similar. However, when comparing the y-direction force and the z-moment coefficient obtained through the average value of the time series, a difference occurred as shown in Figure 16. This is because a restoring force was applied by the spring, and, in the case of free running, a relatively small y-force and z-moment were measured because propulsion occurs while maintaining a neutral angle using the rudder. The force and moment caused by the spring appeared larger at the heading angle of 120 degrees.

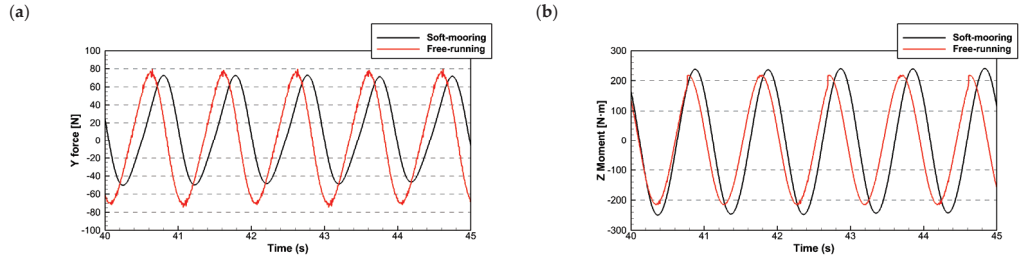

Figure 15. (**a**) Y−force and (**b**) z−moment according to the time series at $\lambda/L_{PP} = 0.5$.

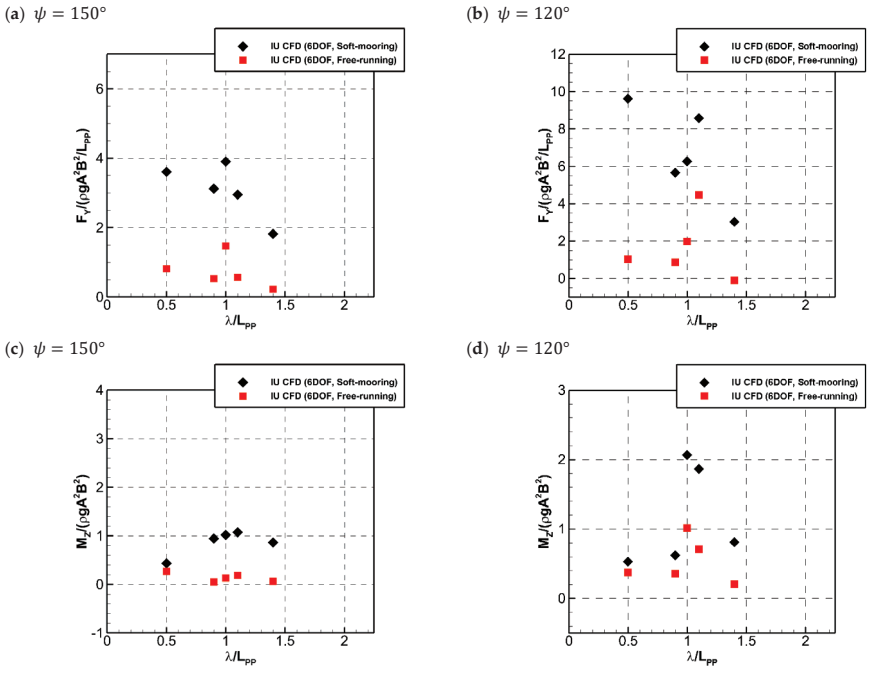

Figure 16. Comparison of (**a**,**b**) y−force coefficients and (**c**,**d**) Yaw moment coefficients in oblique waves.

3.2. Comparison of Motion RAOs of S-VLCC according to Heading Angles

We compared the heave, pitch, and roll RAOs for each wave condition according to the heading angle. In Figure 13, the two model tests (SNU and SSPA) and the results of the Rankine panel method are compared with the captive model and the 6-DOF computation results of this study. First, as shown in Figure 17a–f, in the case of the heave and pitch RAOs, the motion response was similar regardless of the constraint conditions. As the heading angle increased, the encounter wave frequency decreased, and the resonant wavelength with the greatest motion RAO moved to a short wavelength. In the case of the pitch RAO, it tended to decrease as the heading angle increased, and, in the case of $\psi = 120°$, it showed a hollow shape at $\lambda/L_{PP} = 1.0$. As a result, the heave and pitch motions were judged to have little effect from the DOFs.

Figure 17g,h show the roll RAOs in bow-quartering wave conditions. The roll motion is greatly affected by the DOFs, and the difference is particularly large at the wavelength ratio corresponding to the roll natural frequency. At a heading angle of 150 degrees, the roll motion is the largest with 3 DOFs (with free heave, roll, and pitch), followed by soft mooring and free running. The heading angle of 120 degrees also had a large motion when soft mooring was used. With 3 DOFs, it is judged that the roll motion is large because the corresponding difference in the force acting on the hull is greater due to the restraints of the sway and yaw. In particular, the shape of a ship with a long slenderness ratio reacts sensitively to the roll motion and is greatly affected by external forces such as those from restraints in the DOFs or springs. In conclusion, the SSPA experiment and CFD results are most similar under the free-running test conditions.

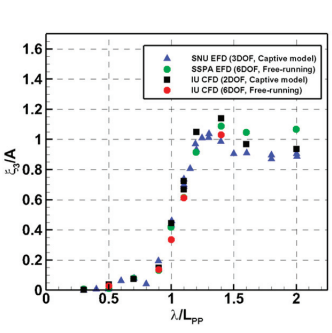

(**a**) ψ = 180°, Heave RAOs

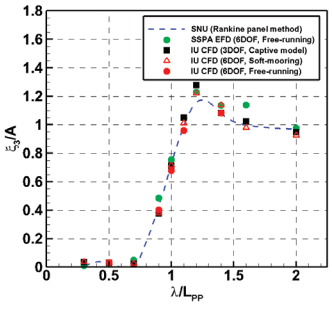

(**b**) ψ = 150°, Heave RAOs

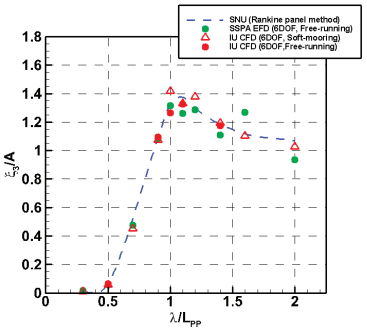

(**c**) ψ = 120°, Heave RAOs

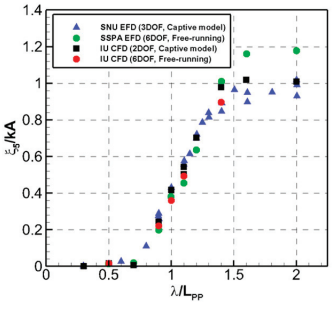

(**d**) ψ = 180°, Pitch RAOs

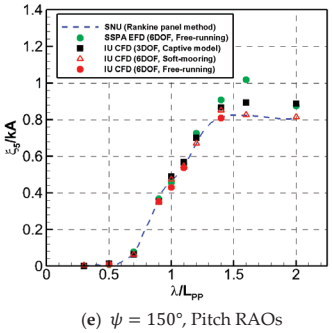

(**e**) ψ = 150°, Pitch RAOs

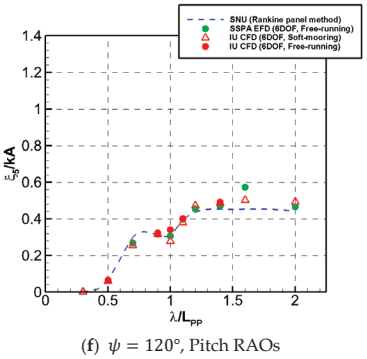

(**f**) ψ = 120°, Pitch RAOs

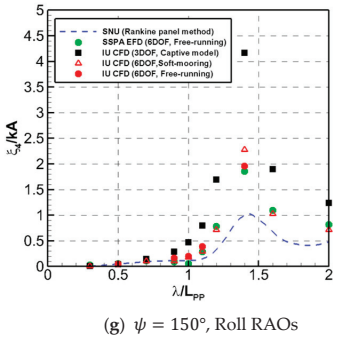

(**g**) ψ = 150°, Roll RAOs

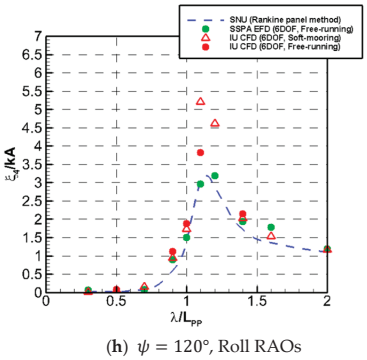

(**h**) ψ = 120°, Roll RAOs

Figure 17. Comparison of motion RAOs by wavelength ratio according to heading angle.

3.3. Comparison of Flow Regime of S-VLCC at Stern according to Heading Angles

In order to compare the flow distribution around the hull according to the wave direction, streamlines passing around the hull were compared under the condition of $\lambda/L_{PP} = 1.0$. The distribution of streamlines passing through $X/L_{PP} = 0.03$ and $X/L_{PP} = 0.1$ in the forward direction of the AP was compared, as shown in Figures 18 and 19. Moreover, wall shear stress contours were shown on the hull surface. The corresponding streamlines and wall shear stress distributions are the results of time-series averaging.

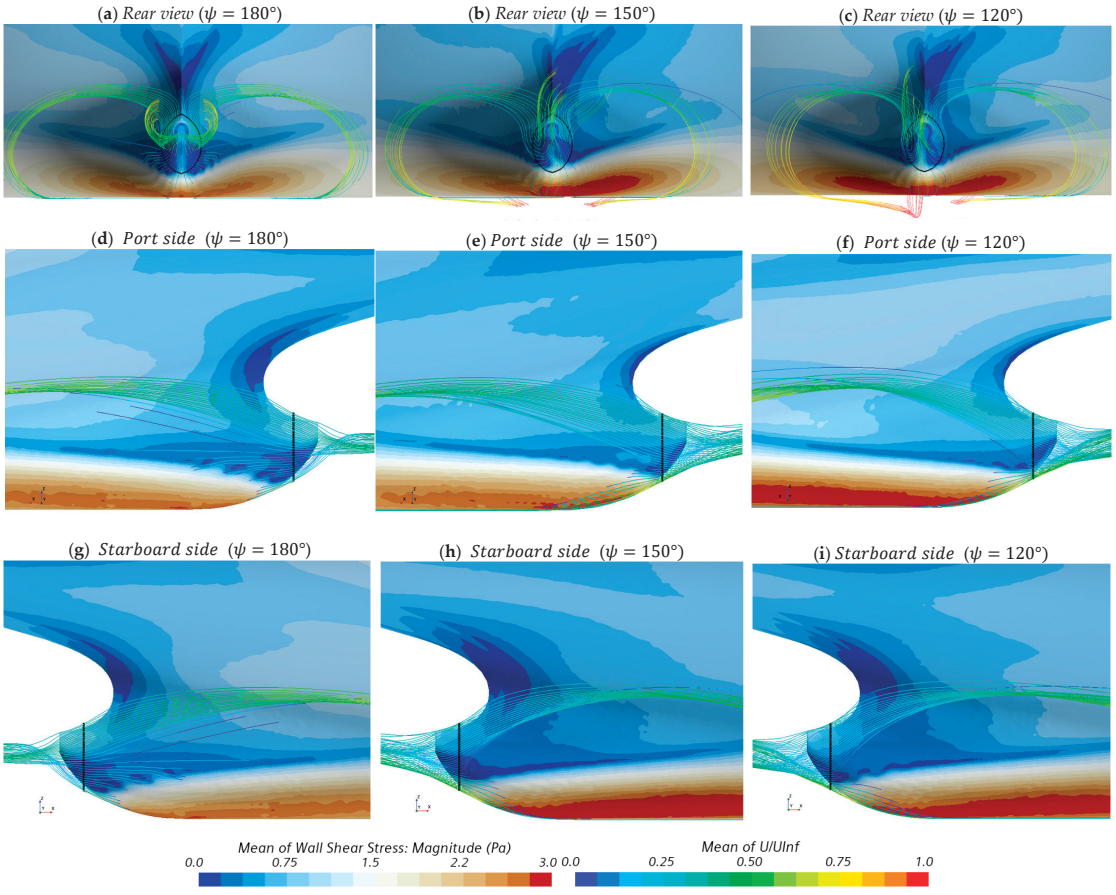

Figure 18. Comparison of time-averaged streamlines and wall shear stress distributions passing $X/L_{PP} = 0.03$.

First, as shown in Figure 18a–c, the flow passing the stern end is mainly affected by the flow rising up the hull. When the flow passes the center of the ship, the flow passing below rises along the skeg shape of the stern and then falls down, forming the flow on the upper part of the propeller surface. Figure 18d–f show the distribution of streamlines on the port side. In the oblique wave condition, the flow velocity is relatively high, and the frictional resistance at the top side is increased. In addition, the streamlines tended to spread widely to the bottom of the ship while flowing along the hull.

Conversely, Figure 18g–i show a distribution of streamlines on the starboard side. Unlike the port side, the flow speed slowed down, and the flow along the hull lasted for a long time, so, compared to the heading angle of 180 degrees, more streamlines were distributed above the hub. This is because the flow into the port side is blocked by the hull, and a low velocity section is formed above the hub.

In the same way, Figure 19 shows the streamline distribution that passes $X/L_{PP} = 0.1$, which is the front part of the hull. The flow passing the bottom of the ship is predominant compared to $X/L_{PP} = 0.03$. As shown in Figure 19a–c, the flow entering along the hull includes the flow rising from the ship bottom and the flow along the top of the skeg. Part of the flow past the bottom of the ship quickly passes the concave part of the stern and creates a swirling streamline. The rotational flow was asymmetrical in the oblique wave condition and appeared stronger on the port side facing the wave. The asymmetry is most

evident in the 150-degree heading condition, and it is judged that the effect of the wave speed is relatively large in that condition.

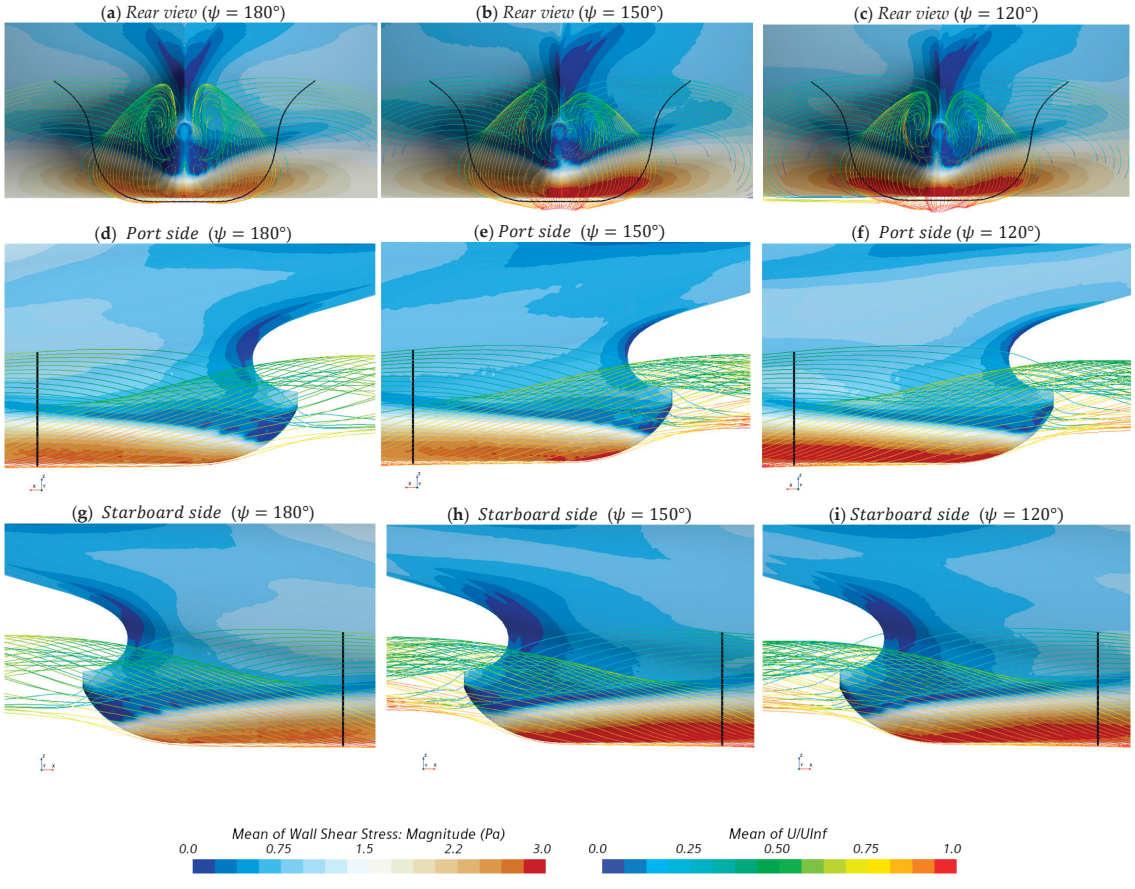

Figure 19. Comparison of time-averaged streamlines and wall shear stress distributions passing $X/L_{PP} = 0.1$.

When the port flow was compared using Figure 19d–f, the difference in streamline distribution was not large, but the shear stress at the bottom part was the largest at a heading angle of 120 degrees. Through this, it can be estimated that the flow velocity at the bottom part is fast under the most oblique wave condition. In Figure 19g–i, the flow velocity at the bottom of the ship in bow-quartering seas is faster on the starboard side compared to the bow wave condition. The streamlines near the hull are similar, and it is judged that the rotational strength was weakened due to the increase in flow speed, as shown in Figure 19a–c. To evaluate the trends of the previously compared flows with quantitative values, nominal wakes for each condition are compared in Table 7. Moreover, Figure 20 shows the distribution of the averaged axial velocity entering the propeller plane in wave conditions compared to calm water conditions.

When comparing the nominal wake coefficient values, the flow rate increases in wave conditions compared to the calm water condition. In terms of the effective wake coefficients, different trends were shown for each condition. It is thought that the added resistance increases the number of rotations of the propeller in the wave, and, as a result, a difference in effective wake occurs due to the influence of the nominal velocity and the interaction velocity. In the wave condition, at the heading angle of 150 degrees, the propeller's rotation

rate was highest, and the effective wake fraction value was lowest (the heading angle of 180 degrees showed the highest value). Therefore, it is difficult to find the trend of the effective wave direction, because the effect of the inflow velocity and the increase in the propeller rotation speed are complex.

Table 7. Comparison of nominal wake fraction, effective wake fraction, and propeller rotation rate.

Wave Condition	$1-w_n$	$1-w_t$	n (RPS)
Calm water	0.541	0.572	12.87
$\lambda/L_{pp} = 1.0,\ \psi = 180°$	0.546	0.625	14.55
$\lambda/L_{pp} = 1.0,\ \psi = 150°$	0.567	0.595	14.95
$\lambda/L_{pp} = 1.0,\ \psi = 120°$	0.560	0.602	14.05

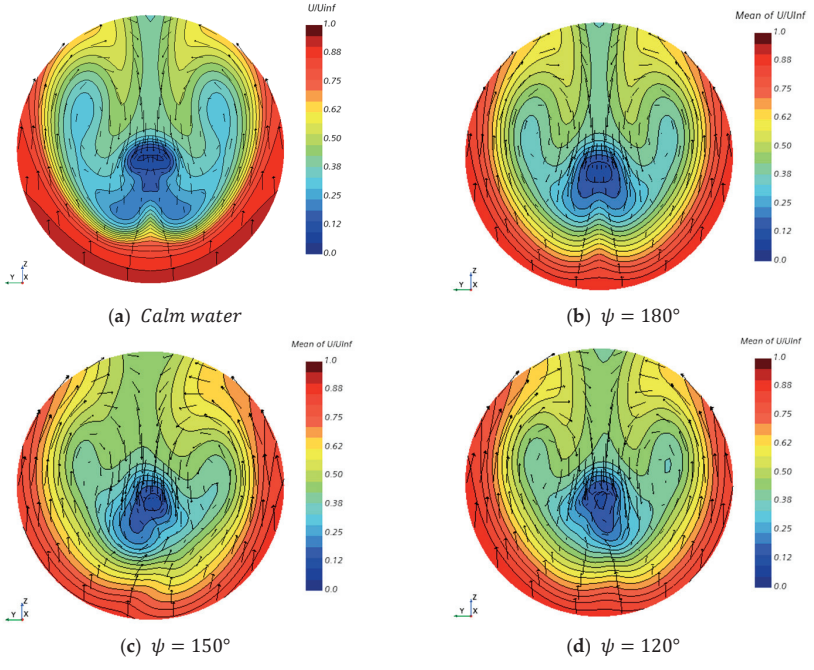

(**a**) *Calm water* (**b**) $\psi = 180°$

(**c**) $\psi = 150°$ (**d**) $\psi = 120°$

Figure 20. Comparison of time-averaged nominal wake distribution.

In the wake distribution in Figure 20, it is shown that the low-speed section of the hook shape is reduced in the wave conditions. The overall flow speed increased, and an asymmetrical nominal wake was observed in the bow-quartering sea condition. The low-speed section at the top of the shaft tended to be biased to the left, and the bias was greater at the heading angle of 150 degrees.

The wake distribution for each encounter period (T_e) among waves is compared in Figure 21. The encounter period was divided into four parts with time (t), and the point where the wave crest crossed the bow was considered as 0. Figure 21a–d show a bow sea condition in which the wake swings up and down. At $t/T_e = 1/4$, where the crest of the wave comes to the middle of the hull, the flow tended to rise upward, which seems to be caused by the rise of the stern. At this time, the high-speed region is widely distributed, and the inflow velocity increases. Conversely, the flow slowed down the most at $t/T_e = 3/4$, where the stern descended.

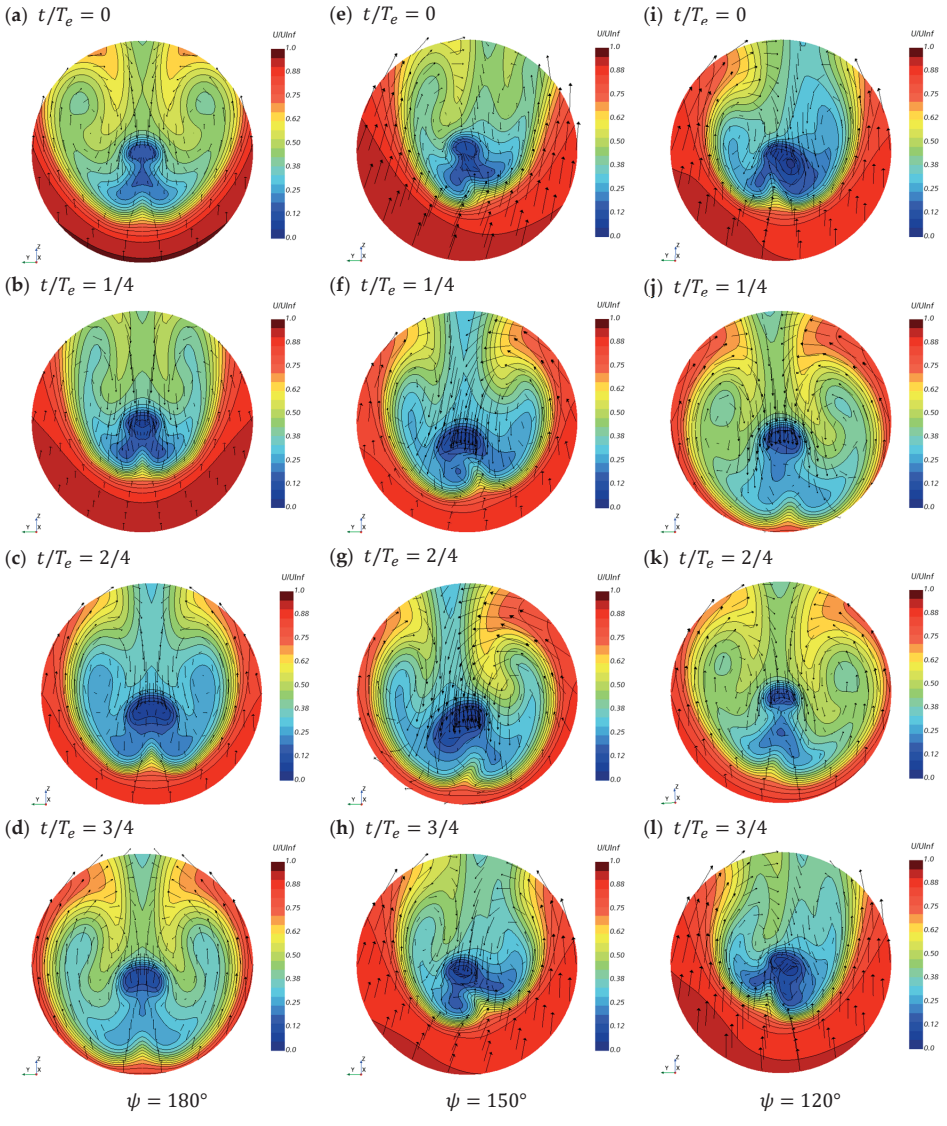

Figure 21. Comparison of nominal wake per wave direction according to wave encounter period.

Under the bow-quartering wave condition, the flow tended to come and go in a tilted line because the hull moved in an oblique direction. In Figure 21e–h, the wake change at $\psi = 150°$ showed a wide high-speed region when the wave crest passed the bow, unlike at $\psi = 180°$. Moreover, through the vector distribution, the overall flow velocity was fast, and a strong vortex occurred at $t/T_e = 3/4$. Even during one cycle, the direction and speed of the flow changed drastically and asymmetrically.

In Figure 21i–l, the trend is the same under the heading angle condition of 120 degrees, and the bias of the flow was less than that at 150 degrees. It is judged that the movement of the hull is reduced when the wave direction is relatively large, so the flow change is also reduced. Due to the following wake changes, it is difficult to estimate the effective wake fraction value in oblique wave conditions. In addition, since the wake in calm water is

taken into consideration when designing the propeller, it causes a change in the propeller efficiency in waves.

4. Conclusions

This study analyzed the added resistance performance of ships in various wave conditions according to constraint conditions through CFD. The target ship's added resistance coefficient and motion RAOs were compared using a 2-DOF captive model (with free heave and pitch) and a 3-DOF model (with free heave, roll, and pitch). Moreover, a soft spring system and free-running model were applied to simulate 6-DOF conditions. A 6-DOF soft-mooring system was simulated through spring coupling in the DFBI body.

1. When calculating the added resistance through the free-running model, it was verified through two hulls that the added resistance showed a similar trend compared to the experiment in head sea conditions. On the other hand, both hulls showed a difference in the value of added resistance according to the thrust deduction factor used. It was assumed that the thrust deduction in waves was similar to that of calm water, but, under the conditions of high wave height and high added resistance, a difference in the thrust deduction compared to calm water can be shown due to the increase in the number of propeller revolutions. The difference was relatively insignificant under the condition of a wave steepness of 0.01, but, when using a higher wave steepness, it is necessary to consider the change of the thrust deduction factor in wave conditions.
2. In terms of the added resistance coefficient, the difference in estimated values was not large according to the DOFs. In a bow-quartering sea, as the heading angle of the ship decreased, the peak wavelength of the added resistance moved to a shorter wavelength, and the magnitude decreased. On the other hand, the added resistance in the free-running condition was lower than with the soft-mooring system. To analyze the cause of the difference, the y-force and z-moment on the hull were compared. The amplitude of fluctuations according to the time series was similar, but the time-averaged y-force and z-moment occurred when soft mooring was used. In addition, the yaw and sway occurred along with force, which is considered to be one of the causes of increased added resistance.
3. The influence of the heave and pitch motions according to the DOFs (3 DOF and 6 DOF) with a 150-degree heading angle was insignificant. However, in the case of the roll motion, the 3-DOF (with free heave, roll, and pitch) model overestimated the roll motion more than the 6-DOF model. A corresponding trend was also found between the soft-mooring system and free running at the heading angle of 120 degrees. The roll motion is sensitive to the DOFs and depend on the case where the sway and yaw are constrained or interfered with by a spring. Therefore, to accurately estimate the motion response in the oblique waves, a computation should consider the 6-DOF motion of the ship.
4. When using the soft-mooring system, it is possible to observe the flow around the hull that occurs along the wave direction. In this study, the streamlines and nominal wake for each heading angle were compared under the condition of a wavelength ratio of 0.1. The streamline passing $X/L_{PP} = 0.03$ from the AP position passes the upper part of the wake plane and flows past the hollow of the stern. In the bow-quartering sea condition, the distribution of streamlines on the left and right changes asymmetrically, and the flow on the port side becomes relatively fast, bringing the streamline distribution closer to the keel line. On the other hand, the streamline passing $X/L_{PP} = 0.1$ was generally distributed in the wake plane, and the flow past the lower part of the hull was predominant. In particular, it was estimated that the flow was the fastest due to the high shear stress at the heading angle of 120 degrees.
5. The mean nominal wake flow velocity increased in oblique wave conditions. The asymmetry of the nominal wake was greatest at a heading angle of 150 degrees. The effective wake was difficult to estimate due to the combined effects of the faster axial velocity and the increase in the propeller's rotational speed. In addition, when

comparing the nominal wake distribution for each wave cycle, the wake change for each encounter wave period was large. The main cause of the wake change was the movement of the ship, and the change was most rapid at the heading angle of 150 degrees, where the movement was the largest.

Through this study, it was confirmed that the 6-DOF implementation method used in the experiment can be reproduced through CFD. Through the simulations, there are differences in the added resistance performance and motion response depending on the constraint conditions and test method. In addition, it was shown that the flow distribution around the hull can change significantly in an oblique wave. For future study, the plan is to observe the added resistance performance using a captive model, a soft-mooring system, and free-running conditions for the same vessel. The flow distribution will be compared under more wave conditions, and we will observe changes in the self-propulsion factors and the number of propeller revolutions during free running. Finally, an irregular wave condition will also be tested.

Author Contributions: S.-H.L.: Conceptualization, computation, data analysis, post processing, and writing—original draft preparation.; S.H.: Conceptualization, data analysis, funding.; K.-J.P.: Conceptualization, data analysis, writing—review, funding, and supervision.; H.-S.K. and Y.-J.H.: Computation, data analysis, post processing.; S.-K.L.: Resources, data curation, funding acquisition. All authors have read and agreed to the published version of the manuscript.

Funding: This research was funded and conducted under the commissioned research project, the "Development of added resistance CFD method in wave using free-running method," of Hanwha Ocean Co., Ltd., Republic of Korea, and the "Development of evaluation technology for ship's performance in extreme environment" of the Korea Research Institute of Ships and Ocean Engineering Endowment Project, which was funded by the Ministry of Oceans and Fisheries (1525012982, PES4290).

Institutional Review Board Statement: Not applicable.

Informed Consent Statement: Not applicable.

Data Availability Statement: Not applicable.

Acknowledgments: All authors included in this section have consented to the acknowledgment.

Conflicts of Interest: The authors declare no conflict of interest.

References

1. Vinayak, P.P.; Prabu, C.S.K.; Vishwanath, N.; Prakash, S.O. Numerical simulation of ship navigation in rough seas based on ECMWF data. *Brodogradnja* **2021**, *72*, 19–58. [CrossRef]
2. Boese, P. Eine einfache methode zur berechnung der widerstandserhöhung eines schiffes im seegang. *J. Schiffstechnik* **1970**, *17*, 1–18.
3. Salvesen, N.; Tuck, E.; Faltinsen, O. Ship motions and sea loads. *Trans. Soc. Nav. Archit. Mar. Eng.* **1970**, *78*, 250–287.
4. Journée, J.M.J.; Adegeest, L.J.M. *Theoretical Manual of Strip Theory Program "SEAWAY for Windows"*; J.M. Adegeest Revision 14–12; TU Delft: Delft, The Netherlands, 2003.
5. Liu, S.; Papanikolaou, A. Approximation of the added resistance of ships with small draft or in ballast condition by empirical formula. *Proc. Inst. Mech. Eng. Part M J. Eng. Marit. Environ.* **2019**, *233*, 27–40. [CrossRef]
6. Denis, M.S.; Pierson, W.J. On the motion of ships in confused seas. *Trans. Soc. Nav. Archit. Mar. Eng.* **1953**, *61*, 280–354.
7. Gerritsma, J.; van den Bosch, J.J.; Beukelman, W. Propulsion in regular and irregular waves. *Int. Shipbuild. Prog.* **1961**, *8*, 235–247. [CrossRef]
8. Fujii, H.; Takahashi, T. Experimental Study on the Resistance Increase of a Large Full Ship in Regular Oblique Waves. *J. Soc. Nav. Archit. Jpn.* **1975**, 132–137. [CrossRef]
9. Kim, W.J.; Van, S.H.; Kim, D.H. Measurement of flows around modern commercial ship models. *Exp. Fluids* **2001**, *31*, 567–578. [CrossRef]
10. Sadat-Hosseini, H.; Wu, P.-C.; Carrica, P.M.; Kim, H.; Toda, Y.; Stern, F. CFD verification and validation of added resistance and motions of KVLCC2 with fixed and free surge in short and long head waves. *Ocean Eng.* **2013**, *59*, 240–273. [CrossRef]
11. Park, D.M.; Lee, J.H.; Jung, Y.W.; Lee, J.; Kim, Y.; Gerhardt, F. Experimental and numerical studies on added resistance of ship in oblique sea conditions. *Ocean Eng.* **2019**, *186*, 106070. [CrossRef]
12. Yoo, S.O.; Kim, T.; Kim, H.J. A Numerical Study to Predict Added Resistance of Ships in Irregular Waves. *Int. J. Offshore Polar Eng.* **2020**, *30*, 161–170. [CrossRef]

13. Seo, M.G.; Ha, Y.J.; Nam, B.W.; Kim, Y. Experimental and Numerical Analysis of Wave Drift Force on KVLCC2 Moving in Oblique Waves. *J. Mar. Sci. Eng.* **2021**, *9*, 136. [CrossRef]
14. Sato, Y.; Miyata, H.; Sato, T. CFD simulation of 3-dimensional motion of a ship in waves: Application to an advancing ship in regular heading waves. *J. Mar. Sci. Technol.* **2000**, *4*, 108–116. [CrossRef]
15. Guo, B.-J.; Steen, S. Evaluation of Added Resistance of KVLCC2 in Short Waves. *J. Hydrodyn.* **2011**, *23*, 709–722. [CrossRef]
16. Uharek, S.; Cura-Hochbaum, A. The influence of inertial effects on the mean forces and moments on a ship sailing in oblique waves Part B: Numerical prediction using a RANS code. *Ocean Eng.* **2018**, *165*, 264–276. [CrossRef]
17. Islam, H.; Rahaman, M.; Akimoto, H. Added Resistance Prediction of KVLCC2 in Oblique Waves. *Am. J. Fluid Dyn.* **2019**, *9*, 13–26. [CrossRef]
18. Lee, C.-M.; Seo, J.-H.; Yu, J.-W.; Choi, J.-E.; Lee, I. Comparative study of prediction methods of power increase and propulsive performances in regular head short waves of KVLCC2 using CFD. *Int. J. Nav. Arch. Ocean Eng.* **2019**, *11*, 883–898. [CrossRef]
19. Mousavi, S.M.; Khoogar, A.R.; Ghassemi, H. Time Domain Simulation of Ship Motion in Irregular Oblique Waves. *J. Appl. Fluid Mech.* **2020**, *13*, 549–559. [CrossRef]
20. Mikkelsen, H.; Shao, Y.; Walther, J.H.H. CFD verification and validation of added resistance and seakeeping response in regular oblique waves with varying wave length. In Proceedings of the 9th Conference on Computational Methods in Marine Engineering (Marine 2021), Online, 2–4 June 2021; Volume 1, pp. 1–23. [CrossRef]
21. Hino, T.; Stern, F.; Larsson, L.; Visonneau, M.; Hirata, N.; Kim, J. *Numerical Ship Hydrodynamics An Assessment of the Tokyo 2015 Workshop*; Springer: Berlin/Heidelberg, Germany, 2021. [CrossRef]
22. Cho, J.-H.; Lee, S.-H.; Oh, D.; Paik, K.-J. A numerical study on the added resistance and motion of a ship in bow quartering waves using a soft spring system. *Ocean Eng.* **2023**, *280*, 114620. [CrossRef]
23. Dai, K.; Li, Y.; Gong, J.; Fu, Z.; Li, A.; Zhang, D. Numerical Study on Propulsive Factors in Regular Head and Oblique Waves. *Brodogradnja* **2022**, *73*, 37–56. [CrossRef]
24. ITTC. Seakeeping Tests–7.5-02-07-02.1. In Proceedings of the 28th International Towing Tank Conference, Wuxi, China, 17–23 September 2017.
25. Costas, R.; Figuero, A.; Peña, E.; Sande, J.; Rosa-Santos, P. Integrated approach to assess resonance between basin eigenmodes and moored ship motions with wavelet transform analysis and proposal of operational thresholds. *Ocean Eng.* **2022**, *247*, 110678. [CrossRef]
26. Jang, Y.-H.; Eom, M.-J.; Paik, K.-J.; Kim, S.-H.; Song, G. A numerical study on the open water performance of a propeller with sinusoidal pitch motion. *Brodogradnja* **2020**, *71*, 71–83. [CrossRef]
27. Kim, D.-H.; Sanada, Y.; Sadat-Hosseini, H.; Stern, F. URANS simulations for a free-running container ship: Part 2. Added power. *J. Hydrodyn.* **2021**, *33*, 448–467. [CrossRef]
28. Lee, J.; Park, D.-M.; Kim, Y. Experimental investigation on the added resistance of modified KVLCC2 hull forms with different bow shapes. *Proc. Inst. Mech. Eng. Part M J. Eng. Marit. Environ.* **2016**, *231*, 395–410. [CrossRef]
29. Larsson, L.; Stern, F.; Visonneau, M. *Numerical Ship Hydrodynamics: An Assessment of the Gothenburg 2010 Workshop*; Springer: Berlin/Heidelberg, Germany, 2013.
30. Lee, S.-H.; Paik, K.-J.; Hwang, H.-S.; Eom, M.-J.; Kim, S.-H. A study on ship performance in waves using a RANS solver, part 1: Comparison of power prediction methods in regular waves. *Ocean Eng.* **2021**, *227*, 108900. [CrossRef]
31. Celik, I.; Ghia, U.; Roache, P.J.; Freitas, C.; Coloman, H.; Raad, P. Procedure of Estimation and Reporting of Uncertainty Due to Discretization in CFD Applications. *J. Fluids Eng.* **2008**, *130*, 078001. [CrossRef]

Journal of
Marine Science and Engineering

MDPI

Article

Effects of Leading-Edge Tubercles on Three-Dimensional Flapping Foils

Ruixuan He [1], Xinjing Wang [1,2,*], Jian Li [3], Xiaodong Liu [1] and Baowei Song [1]

[1] School of Marine Science and Technology, Northwestern Polytechnical University, Xi'an 710072, China; heruixuan@mail.nwpu.edu.cn (R.H.); nwpuliuxiaodong@163.com (X.L.); hanghai@nwpu.edu.cn (B.S.)
[2] State Key Laboratory of Digital Manufacturing Equipment and Technology, School of Mechanical Science and Engineering, Huazhong University of Science and Technology, Wuhan 430074, China
[3] Xi'an Precision Machinery Research Institute, Xi'an 710072, China; jianli@mail.nwpu.edu.cn
* Correspondence: wangxinjing0213@nwpu.edu.cn

Abstract: Recently, inspired by the flippers of humpback whales, researchers have been widely studying leading-edge tubercles for use as passive flow control devices. In this research, we numerically investigated the effects of leading-edge tubercles on a three-dimensional flapping foil coupled with rolling and pitching motions. Appropriate spanwise flexibility is considered to mimic the real flapping motion of humpback whales, and the profile of the angle of attack was analyzed in a representative section under the effects of spanwise flexibility. The motion of flexible foils was decomposed into rigid motion and flexible deflection by using the sliding mesh and dynamic mesh methods, respectively. Then, the hydrodynamic performance of the flexible flapping foils was estimated by solving the unsteady Reynolds Averaged Navier–Stokes equations. The effects of the shape and kinematic parameters on thrust, power consumption, and propulsive efficiency were studied and the mechanism behind these effects was investigated. A maximum efficiency loss of 19.4% was observed for the sharpest tubercle shape. Although the hydrodynamic advantages of leading-edge tubercles were not observed in the present study, the tendency of flow separation over peaking sections was suppressed under low angles of attacks. The results suggest that leading-edge tubercles are more suitable for foils with steady or quasi-steady motions, such as propellers or turbines.

Keywords: flapping foil; leading-edge tubercles; bionic propulsion; computational fluid dynamics (CFD)

Citation: He, R.; Wang, X.; Li, J.; Liu, X.; Song, B. Effects of Leading-Edge Tubercles on Three-Dimensional Flapping Foils. *J. Mar. Sci. Eng.* **2023**, *11*, 1882. https://doi.org/10.3390/jmse11101882

Academic Editors: Nastia Degiuli and Ivana Martić

Received: 10 August 2023
Revised: 25 September 2023
Accepted: 25 September 2023
Published: 27 September 2023

1. Introduction

Owing to millions of years of evolution, aquatic animals demonstrate optimum hydrodynamic performance in terms of morphology and behavior. Therefore, they provide the best bionic inspiration for designing marine vehicles. The humpback whale (Megaptera novaeangliae), one of the largest aquatic animals, has evolved and exhibited outstanding maneuverability despite its huge body. Its maneuverability is attributed to the leading-edge tubercles on its pectoral flippers [1]. Morphological details of the humpback whale flipper have been evaluated and recorded [2]. Since then, numerous researchers have been interested in studying this unique structure to improve the performance of foils and wings.

For static foils, experimental and numerical methods have been employed to evaluate the impact of leading-edge tubercles. Wind tunnel measurements [3] and water tunnel tests [4] have indicated that the addition of leading-edge tubercles to foils delays their stall angle and improves their performance in the post-stall region. A flow visualization experiment [5] indicated that the flow over the peak sections of the tubercles is critical in the post-stall performance. Furthermore, numerical analyses have shown that the flow separation is suppressed over the peak sections owing to the streamwise vortices induced by the leading-edge tubercles [6,7]. This variation in the separation pattern is related to the weakening of the suction peak over the peak sections [8]. Static foils or wings can

take advantage of leading-edge tubercles to improve the performance of rudders, for example [9].

Previous research on the effects of leading-edge tubercles has principally focused on static foils. However, most aquatic animals, especially humpback whales, acquire optimal propulsion and maneuverability by flapping their pectoral and caudal foils. Flapping motions are divided into three configurations: pitching or heaving only, combined pitching and heaving motions, and coupled rolling and pitching motions [10]. The coupled rolling and pitching motions are closest to the real motion of the foils of aquatic animals, such as turtles and humpback whales. In addition, this motion has three-dimensional kinematics, and the other two motions can be considered simplifications of this motion [10–12]. Therefore, this study focuses on coupled rolling and pitching motions, which can reflect the real motion form. A rigid three-dimensional flapping foil with coupled rolling and pitching motions was studied experimentally. The reported thrust and efficiency contours prove the superiority of these flapping foils [13]. The propulsive performance and flow details of the motion have been studied using a numerical method [11]. Flexibility is another key characteristic of bionic flapping foils and has recently received considerable attention. Spanwise flexibility was found to yield a small increase in the thrust coefficient and a small decrease in the power input requirement, resulting in higher efficiency [14]. Flexibility is also beneficial for improving the power extraction efficiency of flapping tidal generators [15].

In most studies, flapping motions have been performed on conventional foils with smooth leading edges. For flapping foils with leading-edge tubercles, a flow visualization experiment indicated that both the positive and the negative spanwise flows were attenuated [16]. Force measurements indicated a deteriorated hydrodynamic performance in the presence of leading-edge tubercles [17]. Numerical analyses also showed that leading-edge tubercles are disadvantageous for flapping performance [1]. These experiments and numerical simulations focused only on the difference between foils with and without leading-edge tubercles and ignored the tubercle shape. The effect of shape on the performance of insect-like flapping wings was studied and similar results were observed [18]. However, the motion was simple and the Reynolds number was low (400), which was not suitable for engineering. In addition, the mechanism of the effect was not focused on. In this research, the performance of three-dimensional flapping foils with leading-edge tubercles that move in coupled rolling and pitching motions was evaluated for different tubercle shape parameters and kinematic parameters at the Reynolds number of 50,000. The effect of leading-edge tubercles on flapping foils and the corresponding mechanism were focused on. Additionally, flexibility was considered to mimic the real flapping motion of humpback whales. The purpose of this study was to gain a deeper understanding of, first, the effect of leading-edge tubercles, and second, the morphology and behavior of humpback whales. These are useful in the design of bionic underwater vehicles.

The remainder of this article is organized as follows. Section 2 provides the problem statement and theoretical analysis. The numerical method used in this study is also described. The results are presented and analyzed in Section 3. In Section 4, the mechanisms of leading-edge tubercles and their effects on flapping foils are discussed. Section 5 summarizes the observations of this study and provides suggestions for further research.

2. Materials and Methods

2.1. Description of Flapping Foils

A typical foil with leading-edge tubercles is shown in Figure 1. All modified foils were designed based on a rectangular foil with a smooth leading edge, chord length c = 100 mm, and span length b = 450 mm. The aspect ratio of a foil is defined as:

$$AR = \frac{b^2}{S} \tag{1}$$

where S is the planform area of the foil. The foils used in this study had an aspect ratio of 4.5, which is approximately equal to that of an idealized representation of a humpback whale flipper specimen [19].

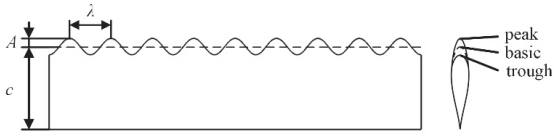

Figure 1. Shape definition of a typical foil with leading-edge tubercles. The sinusoidal leading edge consists of several sections with different local chord lengths. The peak sections have the maximum local chord length, and the trough sections have the minimum local chord length. The basic section is located between these two sections.

The foils are based on the NACA 63_4-021 profile, which is similar to the cross-section of a humpback whale flipper [2]. The shape of the leading-edge tubercles for the modified foils is the same as that of a sinusoidal wave with amplitude A and wavelength λ in the spanwise direction. The cross-section of each modified foil was formed by first separating the head part from the basic profile and scaling its chordwise length and then reattaching it to the rest of the profile to maintain a smooth surface. A cross-section that is consistent with the basic profile exists between the peak and trough sections, where the chord length of the modified foils is defined.

2.2. Kinematics Equations

2.2.1. Rigid Motion

The flapping motion of foils with spanwise flexibility can be decomposed into rigid motion and flexible deflection, as shown in Figure 2. Rigid motion is composed of rolling and pitching motions, which are defined as:

$$\varphi(t) = \varphi_0 \sin(\omega t) \tag{2}$$

$$\theta(t) = \theta_0 \sin(\omega t - \psi_p) \tag{3}$$

where $\varphi(t)$ is the instantaneous rolling angle at which the foil rotates around the x-axis; $\theta(t)$ is the instantaneous pitching angle at which the foil rotates around the pitch axis, which is parallel to the trailing edge and located at distance of $c/3$ from the leading edge of the basic profile; φ_0 and θ_0 are the amplitudes of the rolling and pitching motions, respectively; ω is the circular frequency of the motion; and ψ_p is the phase difference between the rolling and pitching motions, with its value set to $\pi/2$ for optimal performance [20].

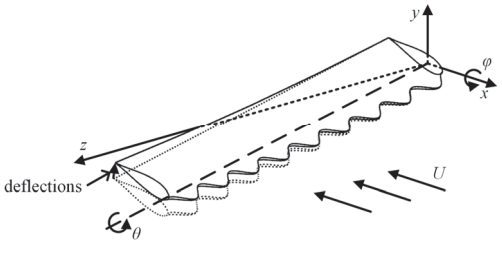

Figure 2. Schematic of flapping motion. The flexible flapping motion can be decomposed into a rigid flapping motion around the x-axis and the pitch axis and a flexible deflection perpendicular to the chord direction.

2.2.2. Spanwise Motion for Flexibility

During rigid motion, the spanwise flexibility is expressed as:

$$h_{def}(t) = B(s/b)^2 \sin(\omega t + \psi_h) \tag{4}$$

where $h_{def}(t)$ is the spanwise deflection function, and B is the amplitude of deflection, with its value set to 0.05 b. Furthermore, s is the spanwise distance from the foil root, and ψ_h is the phase difference between rolling and deflection, with its value set to $\pi/2$. The definition of spanwise flexibility is similar to that of a flapping tidal generator [15]. Moreover, as shown in Figure 2, the positive direction of deflection is defined as being perpendicular to the chord direction and at an acute angle to the y-axis.

The angle of attack varies along the span of the foils and depends on the rigid motion and flexible deflection at different span locations. The motion can be decomposed into 2D heaving and pitching motions at any spanwise location. To describe the kinematic parameters of this motion, a 70% span location was selected, which is a conventional position used in previous studies [13,17].

As shown in Figure 3, in the local velocity coordinates, the heaving motion at the selected location can be described as:

$$h(t) = h_0 \sin(\omega t) - h_{def}(t) \cos(\theta'(t)) \tag{5}$$

where $\theta'(t) = -\theta(t)$ is the pitch angle in the local coordinates, and h_0 is the amplitude of the heaving motion caused by the rolling motion, which is defined as:

$$h_0 = r_{0.7}\varphi_0 \tag{6}$$

where $r_{0.7}$ = 0.7 b is the spanwise distance between the selected location and the roll axis, and h_0/c gives the amplitude of the rolling motion, which was set to 1.5, a value used by previous flapping foil experiments [13].

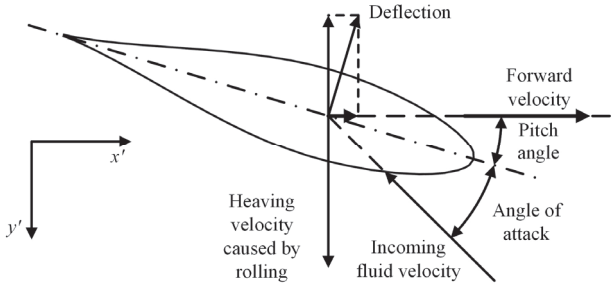

Figure 3. Vector diagram of velocity on 70% span location. The motion in the spanwise sections can be simplified to a typical 2D heave–pitch flapping motion.

The instantaneous angle of attack is expressed as:

$$\alpha(t) = \arctan\left(\frac{d(h(t))/dt}{U + d(h_{def}(t)\sin(\theta'(t)))/dt}\right) - \theta'(t) \tag{7}$$

where U is the forward velocity of the foils.

According to Equation (7), flexible deflection modifies the profile of $\alpha(t)$. Figure 4 shows the variations in $\alpha(t)$ over one cycle for flexible and rigid foils when the maximum angle of attack ($\alpha_{\max}$) is 20°. For rigid foils, by definition, B = 0 in Equation (4). For flexible foils, the moment at which the maximum angle of attack occurs lags behind that of the rigid counterparts. Meanwhile, the profiles on both sides of the extreme value become asymmetric.

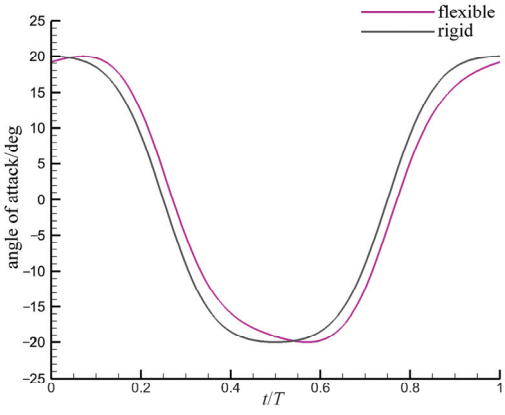

Figure 4. Profile of instantaneous angle of attack over one cycle for flexible and rigid foils. The flexibility changes the profile of the angle of attack.

2.2.3. Dimensionless Parameters

Two dimensionless parameters are defined to describe the kinematics of flapping foils. The Strouhal number (St), based on the heaving amplitude at the selected location, is defined as:

$$St = \frac{2h_0 f}{U} \tag{8}$$

where f is the motion frequency (Hz). At the limit position of the heaving motion, h_{def} is zero, resulting in a heaving amplitude equal to h_0.

The Reynolds number based on the chord length is defined as:

$$\mathrm{Re} = \frac{Uc}{\nu} \tag{9}$$

where $\nu \approx 10^{-6}\mathrm{m}^2/\mathrm{s}$ refers to the kinematic viscosity. A Reynolds number of 50,000 was considered in the present study.

The maximum angle of attack $\alpha_{\max}$ and the Strouhal number St are defined as the free parameters. The amplitude of the pitching motion and the frequency can be calculated based on Equations (7) and (8) for a given $\alpha_{\max}$ and St, respectively, which uniquely determine the motion.

We obtained the force and moment components on the foils along the x-, y-, and z-axes shown in Figure 2. The mean thrust $\overline{F}_x$ and power consumption $\overline{P}$ are defined as:

$$\overline{F}_x = \frac{1}{T}\int_t^{t+T} F_x(t)dt \tag{10}$$

$$\overline{P} = \frac{1}{T}\int_t^{t+T} \left(M_r(t)\varphi'(t) + M_p(t)\theta'(t)\right)dt \tag{11}$$

where T is the period of motion and F_x is the x-component of instantaneous force. Moreover, $M_r(t)$ and $M_p(t)$ are the instantaneous moments in the rolling and pitching axes, respectively, and are expressed as:

$$M_r(t) = -M_x(t) \tag{12}$$

$$M_p(t) = -\left(-M_y(t)\sin(\varphi(t)) + M_z(t)\cos(\varphi(t))\right) \tag{13}$$

where $M_x(t)$, $M_y(t)$, and $M_z(t)$ are the moments on the foil along the x-, y-, and z-axes, respectively. The minus sign denotes the output moment of the actuators.

The nondimensional mean thrust and power coefficients are denoted by $\overline{C}_T$ and $\overline{C}_P$, respectively, and are defined as:

$$\overline{C}_T = \frac{\overline{F}_x}{\frac{1}{2}\rho U^2 S} \tag{14}$$

$$\overline{C}_P = \frac{\overline{P}}{\frac{1}{2}\rho U^3 S} \tag{15}$$

where ρ is the density of water.

The instantaneous thrust and power coefficients, denoted by C_T and C_P, respectively, are defined in the same form as Equations (14) and (15), respectively, by replacing $\overline{F}_x$ and $\overline{P}$ with F_x and P, respectively.

The propulsive efficiency (η) of the foils is given by:

$$\eta = \frac{\overline{F}_x U}{\overline{P}} = \frac{\overline{C}_T}{\overline{C}_P} \tag{16}$$

2.3. Approach

Most flapping foils used for propulsion operated in low-speed and underwater conditions. The ventilation and cavitation can be ignored, unlike the foils that cross free surface [21]. Thus, the flow around flapping foils is single-phase and incompressible. As previously described, both the geometry and motion studied in the present work are in three dimensions. Therefore, the three-dimensional single-phase incompressible unsteady Reynolds Averaged Navier–Stokes (RANS) equations were solved in the three-dimensional computational domain to study the flow over the foils. The governing equations are described as:

$$\frac{\partial \rho u_i}{\partial x_i} = 0 \tag{17}$$

$$\rho \frac{\partial u_i}{\partial t} + \rho \frac{\partial (u_i u_j)}{\partial x_j} = -\frac{\partial p}{\partial x_i} + \frac{\partial}{\partial x_j}\left[\mu\left(\frac{\partial u_i}{\partial x_j} + \frac{\partial u_j}{\partial x_i}\right)\right] + \frac{\partial}{\partial x_j}(-\rho\overline{u'_i u'_j}) \tag{18}$$

where x_i and x_j ($i = 1, 2, 3, j = 1, 2, 3$) are the cartesian coordinate components. u_i and u_j are the velocity components and p is the pressure. $\mu = \rho\nu$ is the dynamic viscosity. $\rho\overline{u'_i u'_j}$ is the Reynolds stress and needs to be solved by additional equations.

As shown in Figure 5a, the domain is divided into two zones: static and moving. The static zone is a cubic zone of 130 $c \times 130\ c \times 130\ c$, with an internal sphere space. A spherical zone of 110 c diameter was considered as the moving zone to achieve flapping motion of the flexible foils. Because the center of the moving zone coincides with the center of rotation of the foils, the rigid motion of the foils, which is described in Equations (2) and (3), can be achieved by rotating the zone around its center. During rotation, the interfaces of the two zones always coincide, making it possible to transmit flow information through the sliding mesh method. In addition, the dynamic mesh method is adopted in the moving zone to achieve spanwise deflection of the foils. The velocity inlet boundary condition was used in the upstream face of the cubic zone. The outflow boundary condition was used in the downstream face. The wall conditions were used in the other faces of the cubic zone and the foil surface. The shear stress of the wall of the cubic zone was set to 0 to ignore viscosity (called slip wall). The details of these boundary conditions can be found in Ref. [22]. The computational domain is discretized in space using a hexahedral grid for the static zone and a tetrahedral mesh for the moving zone, as shown in Figure 5b. A dense zone is defined in the wake region to accurately capture the flow details. A boundary layer mesh was generated by surrounding the surfaces of the foils to accurately obtain flow information near the foils.

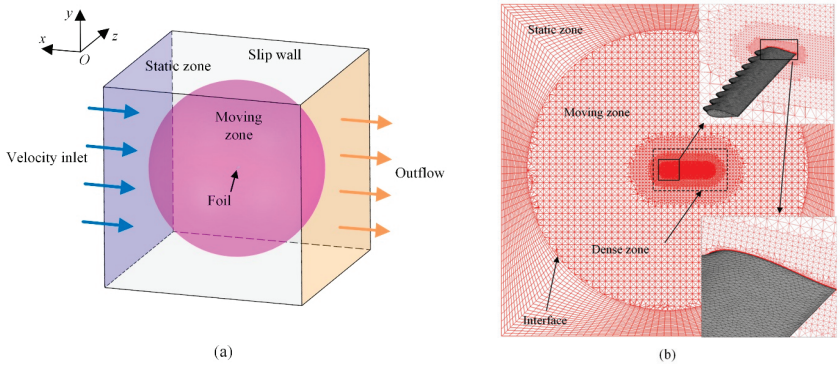

Figure 5. (**a**) The computational domain consists of a static cubic zone used to define the flow boundary and a moving spherical zone used to achieve the motion. (**b**) The domain was discretized in space using a hexahedral grid for the cubic zone and a tetrahedral mesh for the spherical zone. The sliding mesh method was used to transmit flow information through the interface.

The RANS equations were discretized in the computational mesh and solved using the finite-volume commercial code Fluent [23]. The $SST\ k-\omega$ turbulence model [24], developed for predicting flow with strong adverse pressure gradients and separation, was used to derive the Reynolds stress in the RANS equation. As an eddy viscosity-based model, the $SST\ k-\omega$ model has been widely used in industrial applications due to its simplicity and cost-effectiveness. However, the simplification made this model unsatisfactory under specific conditions. For instance, it proved challenging for this model to predict flows with significant effects of mean rotation and cases with non-inertial frames of reference. Concurrently, in turbulent flows where turbulent time scales were significantly smaller than the mean shear time scale, the model was likewise unsuitable [25]. The cases of the present study were outside these constraints. Even though the eddy viscosity assumption and the Reynolds-averaging process resulted in the loss of certain turbulence information, introducing uncertainty into the results [26], the hydrodynamic performance and main flow structures, which were the focus of the present study, could be effectively predicted by the RANS equations and the eddy viscosity-based model. This method has been widely employed in flapping foil simulations [27]. Moreover, the discretization errors associated with spatial and temporal terms, along with solution residuals, were additional sources of uncertainty. The numerical uncertainty was investigated in Section 2.4 using a grid-convergence study, considered the most common, straightforward, and reliable technique for the quantification of uncertainty [28].

In the present study, the pressure was discretized using a second-order scheme, and the momentum was discretized using a second-order upwind scheme. First-order upwind schemes were used for discretizing the turbulent kinetic energy and dissipation rate. The transient formulation is based on a first-order implicit scheme. The SIMPLEC algorithm was used to solve the pressure–velocity coupling equations. The zone motion specified with a user-defined function (UDF) was applied to the moving zone to achieve rigid motion while preserving the mesh quality. The flow information was transmitted between the two zones using a nonconformal sliding mesh interface. Moreover, the deflection of the foils was specified with UDF and was included in the simulations using the dynamic mesh method. The details of those numerical configurations are delineated in Ref [22]. All simulations were conducted for four cycles. In each time step, the convergence criterion of the pressure–velocity iteration was 0.0001 for the continuity. As shown in Figure 6, the residuals of all equations after solution convergence were less than 0.0001 at each time step. Meanwhile, we observed that the variations in forces and moments were periodic.

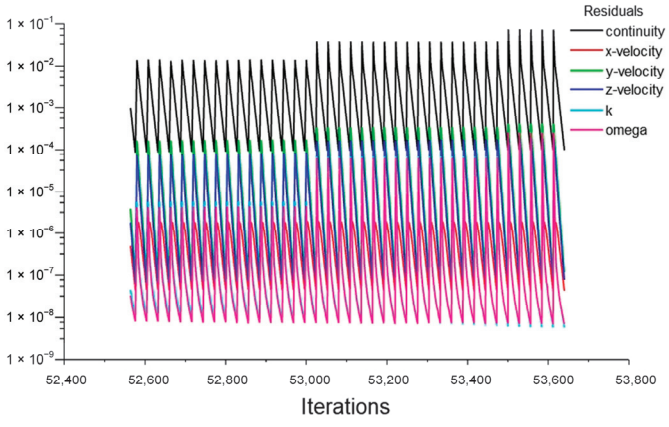

Figure 6. The residuals of simulations after solution convergence. The residuals of all equations are less than 0.0001 at each time step.

2.4. Validation and Verification

A flapping foil with a tubercle amplitude of 0.1 c and a wavelength of 0.25 c was considered for mesh and time validation. The motion parameters were St = 0.3 and α_{max} = 20°. Three different values of mesh densities and time resolutions were considered, as discussed in this section. The details of different mesh densities and time steps and their mean thrust coefficients are listed in Table 1. For all configurations, the observed differences were less than 1%. As shown in Figure 7a, few differences in the instantaneous thrust coefficients were measured for each of the three mesh densities. Figure 7b shows a slice of the spanwise vorticity contours at the 70% span location for different mesh densities. The contours indicate that the flow could be accurately captured by the medium and fine meshes. Additionally, the standard grid-convergence index (GCI) method [29] was used to examine the uncertainty. The GCI_{fine}^{21} result, which describes the uncertainty between medium and fine meshes, was 0.13%. The accuracy of medium mesh is satisfied. Consequently, a medium mesh was used in the present work to balance the resource requirement and accuracy. The corresponding Y+ was less than 1 in most areas of the foil surface. Similarly, as shown in Figure 8, the time step size of $T/500$ was found to be the most economical and was selected for all simulations. The computational time for each case was approximately 86,400 s (24 h) at the selected mesh density and time step size (using two CPU AMD EPYC 7452 @ 2.35 GHZ (Cloud Computing Services Company, Beijing, China), 32 cores).

Table 1. Mean thrust coefficients at different mesh densities and time steps.

Mesh No.	Mesh Densities	Cell Numbers ($\times 10^6$)	Time Steps	Mean Thrust Coefficient	Relative Error/%	e_a^{21}/%	GCI_{fine}^{21}/%
3	Coarse	3.23	T/250	0.2235	−0.75		
			T/250	0.2247	−0.20		
2	Medium	6.58	T/500	0.2252	0.00	1.06	0.13
			T/1000	0.2238	−0.62		
1	Fine	10.04	T/250	0.2271	0.86		

The verification of the method on 2D heaving and pitching flapping foils can be found in our previous work [30]. In the present study, the method was used on 3D NACA0012 foil with coupled rolling and pitching motions to verify the 3D applicability. The foil was a rectangular foil with chord length of c = 100 mm and a span length of b = 400 mm. This foil had a smooth leading edge and displayed a rigid flapping motion in the freestream with a Reynolds number of 50,000. The motion parameters were φ_0 = 60°, St = 0.4, and

$\alpha_{max} = 40°$. The instantaneous thrust was obtained and compared with the experimental results [12]. As shown in Figure 9, the numerical results match well with the experimental data, indicating that the numerical method can effectively predict the hydrodynamic forces of flapping foils.

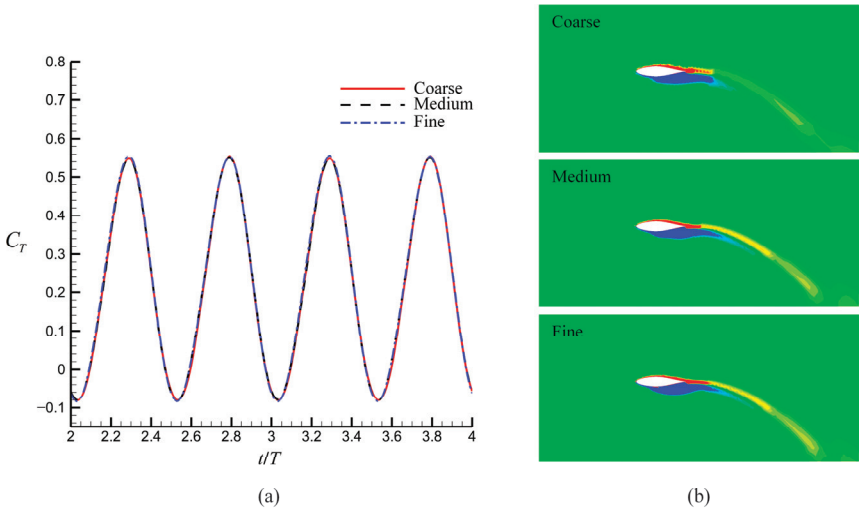

Figure 7. Mesh independence validation using (**a**) instantaneous thrust coefficients and (**b**) slices of spanwise vorticity contours ($A = 0.1\ c$, $\lambda = 0.25\ c$, $St = 0.3$, $\alpha_{max} = 20°$, $Re = 50,000$). The medium mesh was used in the present work because of the satisfactory accuracy in hydrodynamic performance and flow details.

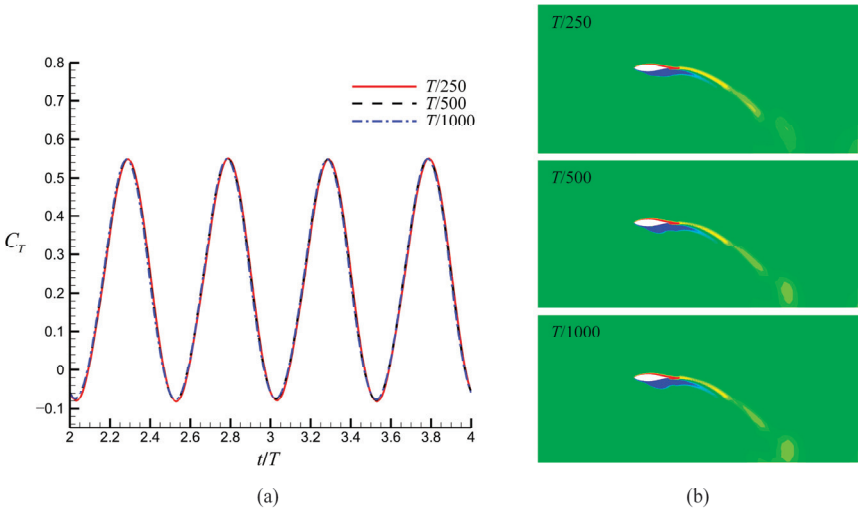

Figure 8. Time independence validation using (**a**) instantaneous thrust coefficients and (**b**) slices of spanwise vorticity contours. ($A = 0.1\ c$, $\lambda = 0.25\ c$, $St = 0.3$, $\alpha_{max} = 20°$, $Re = 50,000$). Similar to the mesh independence validation, the time step size of $T/500$ was used in the present work because of the satisfactory accuracy in hydrodynamic performance and flow details.

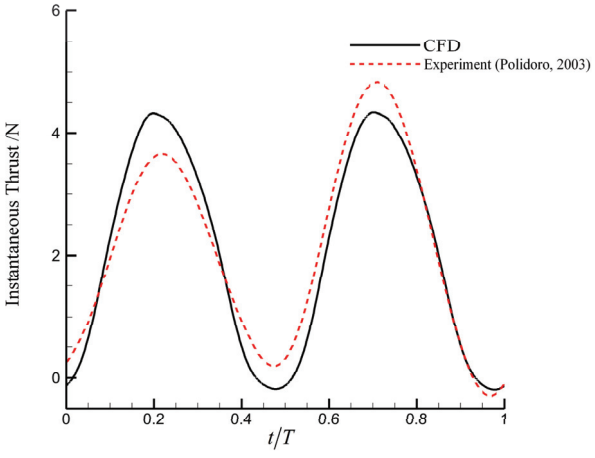

Figure 9. Comparison of instantaneous thrust measurements obtained using CFD and the experiment for a NACA0012 foil with c = 100 mm, b = 400 mm as Re = 50,000, $\varphi_0 = 60°$, St = 0.4, and $\alpha_{max} = 40°$. The CFD results match well with the experimental data [12], indicating that the numerical method can effectively predict the hydrodynamic forces of flapping foils.

3. Results

Based on the representative range of amplitudes and wavelengths of tubercles found on humpback whale flippers [31], a total of four amplitudes and two wavelengths were considered in this study. A foil with a smooth leading edge was used for reference. The effects of St and α_{max} were also investigated. The simulation parameters used in this study are listed in Table 2. The detailed parameters of Equations (2)–(4) under different motions are listed in Table 3. The time step sizes and corresponding Courant–Friedrichs–Lewy (CFL) numbers are also listed in Table 3. The CFL number is defined as $CFL = \Delta t U / \Delta_{min}$, where Δ_{min} is the minimum mesh length.

Table 2. Simulation parameters used in the present study.

No.	Foil Name	A/c	λ/c	St	α_{max} (°)	Re
1	L025A0025	0.025	0.25	[0.2, 0.5], interval 0.1	20	50,000
				0.3	[15, 40], interval 5	50,000
2	L025A005	0.05	0.25	0.3	20	50,000
3	L025A0075	0.075	0.25	0.3	20	50,000
4	L025A01	0.1	0.25	0.3	20	50,000
5	L05A0025	0.025	0.5	0.3	20	50,000
6	L05A005	0.05	0.5	0.3	20	50,000
7	L05A0075	0.075	0.5	0.3	20	50,000
8	L05A01	0.1	0.5	0.3	20	50,000
9	Baseline	0	0	[0.2, 0.5], interval 0.1	20	50,000
				0.3	[15, 40], interval 5	50,000

Table 3. Details of the parameters of motion equations expressed as Equations (2)–(4).

St	α_{max} (°)	ω (Rad/s)	Δt (s)	CFL	θ_0 (°)	φ_0 (°)	B (mm)
0.2	20	2.09	0.0060	1.07	12.33	27.28	22.5
0.3	15	3.14	0.0040	0.71	30.08	27.28	22.5
0.3	20	3.14	0.0040	0.71	24.13	27.28	22.5
0.3	25	3.14	0.0040	0.71	18.74	27.28	22.5
0.3	30	3.14	0.0040	0.71	13.57	27.28	22.5
0.3	35	3.14	0.0040	0.71	8.47	27.28	22.5
0.3	40	3.14	0.0040	0.71	3.40	27.28	22.5
0.4	20	4.19	0.0030	0.54	34.87	27.28	22.5
0.5	20	5.24	0.0024	0.43	46.17	27.28	22.5

3.1. Effect of Tubercle Size

The performances of flapping foils with different tubercle sizes were investigated at $St = 0.3$ and $\alpha_{max} = 20^{\circ}$, under which a high propulsive efficiency has been observed [13]. The mean thrust coefficients ($\overline{C}_T$), power coefficients ($\overline{C}_P$), and propulsive efficiency (η) were obtained and are shown in Figure 10. A decrease in thrust coefficients and an increment in power coefficients was observed under the effects of tubercles, thus reducing the propulsion efficiency. The tubercles exhibited a detrimental effect on the propulsive performance of the flapping foils within the range of wavelengths and amplitudes considered in this study. For both wavelengths, the loss of mean thrust increased approximately linearly with increasing amplitude. For a wavelength of 0.25 c, the maximum thrust loss was 14.4% at $A = 0.1\ c$, whereas the average loss was 3.3% at $A = 0.025\ c$. The power increment increased monotonically from 2% to 6.2% for a wavelength of 0.25 c and from 2.2% to 7% for a wavelength of 0.5 c. Compared with a wavelength of 0.25 c, a wavelength of 0.5 c produced more thrust and required more power. As the amplitude increased, the difference in thrust increased monotonically, reaching a maximum value of 7% at $A = 0.1\ c$. However, the difference in power consumption initially increased till it reached a maximum of 1.3% at 0.075 c, after which it decreased. The results indicate that the effect of the leading-edge tubercles on the flapping foils increases sharply with amplitude, and that its effect on thrust is more significant. Therefore, the variation in the propulsive efficiency is similar to that of the thrust. Under the combined influence of thrust loss and power increment, a maximum efficiency loss of 19.4% was observed in the case of foil L025A01. In addition, because the effect of wavelength varies with the amplitude, it is difficult to consider these two parameters separately.

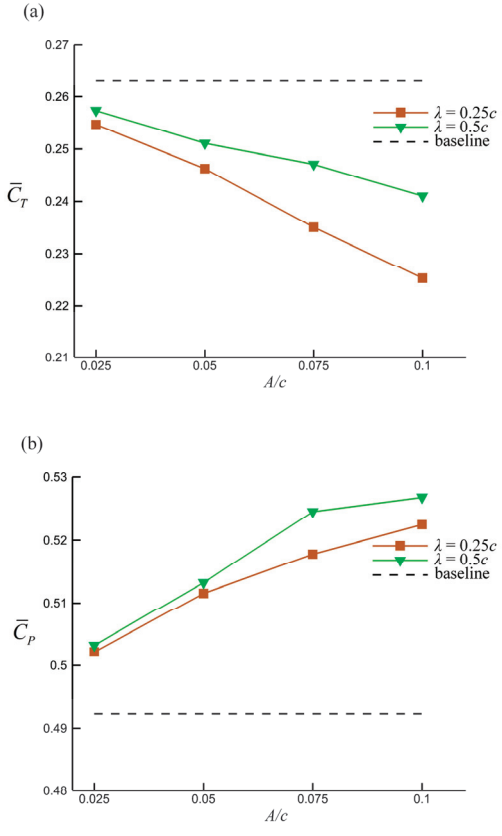

Figure 10. *Cont.*

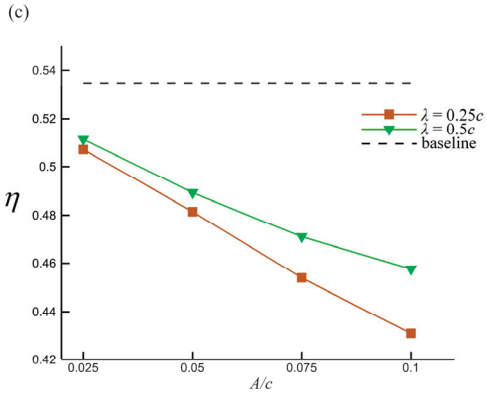

Figure 10. (**a**) Mean thrust coefficient, (**b**) power coefficient, and (**c**) propulsive efficiency of different tubercle shapes ($St = 0.3$, $\alpha_{\max} = 20°$, $Re = 50,000$). The tubercles led to a reduction in thrust and an increase in power consumption, which induced a reduction in propulsion efficiency. The effect was related to the shape parameters.

Figure 11 shows the instantaneous thrust coefficients (C_T) and power coefficients (C_P) for different foils over one cycle, as well as their corresponding positions. The thrust and power coefficients showed distinct periodicity with twice the frequency of the flapping motion. The moment at which the peaks of thrust and power consumption occurred lagged slightly behind the instant at which the foil was at the center of its trajectory; this is related to the angle-of-attack profile. A slight drag and power production were observed near where the roll motion was in the limit position. Under the effects of the leading-edge tubercles, the peak values of the thrust and power coefficients changed significantly. These values are listed in Table 4. The variation in the peak was similar to that of the mean coefficients, indicating that the peak variation is crucial in the hydrodynamic performance loss.

Table 4. Peak values of thrust and power coefficients.

Foil Name	$C_{T\max}$	Relative Error/%	$C_{P\max}$	Relative Error/%
L025A0025	0.6088	−1.66	1.0385	0.80
L025A005	0.5946	−3.95	1.0535	2.26
L025A0075	0.5715	−7.68	1.0755	4.39
L025A01	0.5505	−11.08	1.0841	5.23
L05A0025	0.6149	−0.68	1.0438	1.31
L05A005	0.6085	−1.71	1.0702	3.88
L05A0075	0.6004	−3.03	1.0947	6.26
L05A01	0.5873	−5.13	1.1066	7.41
baseline	0.6191	0.00	1.0302	0.00

To further analyze the effects of the tubercles on the flow, foil L025A01, which had the most distinct effect, was selected. The slices of the spanwise vorticity contour of this foil when the thrust peak occurred are shown in Figure 12a. For reference, the corresponding baseline foil is shown in Figure 12b. The strength of the spanwise vorticity gradually increased along the foil span toward the tip direction. No significant flow separation was observed for either foil; however, a clear distinction was observed between the spanwise vorticities of the modified foil and the baseline. The spanwise vorticities of the modified foil were suppressed near the leading edge in the peak sections and strengthened in the trough sections. Specifically, the separation tendency was suppressed in the peak sections and strengthened in the trough sections, which was observed in static airfoils [4]. However, the suppression of separation led to different effects on the performance of static and flapping foils. A difference in flow behind the tubercle peaks and troughs has also been observed in a static wing with spanwise waviness [32].

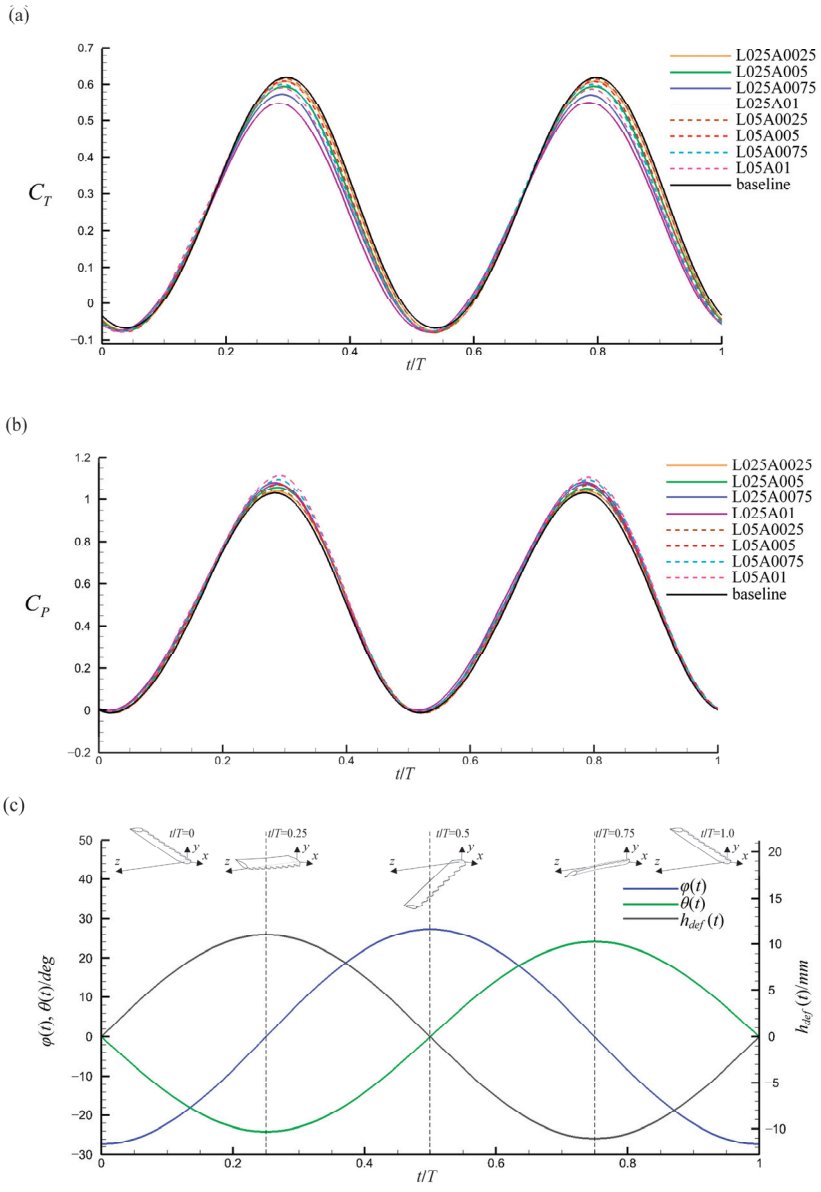

Figure 11. (**a**) Instantaneous thrust and (**b**) power coefficients for different foils, and (**c**) the corresponding positions over one cycle ($St = 0.3$, $\alpha_{\max} = 20°$, $Re = 50,000$). The variation in peak values plays a major role in the hydrodynamic performance loss.

The pressure distribution along the chordwise direction and in the direction perpendicular to it in the peak and trough sections, which are marked in Figure 12a near the 70% span location, are presented in Figure 13a,b. No significant difference was observed in the pressure distribution between these two locations for the baseline. Thus, only the pressure distribution at the location corresponding to the peak section is provided for reference. The pressure distribution of the modified foil differed significantly from that of the baseline in the peak and trough sections. The suction peak decreased in the peak section and increased

in the trough section, which was related to the variation in the hydrodynamic force and flow around the foil.

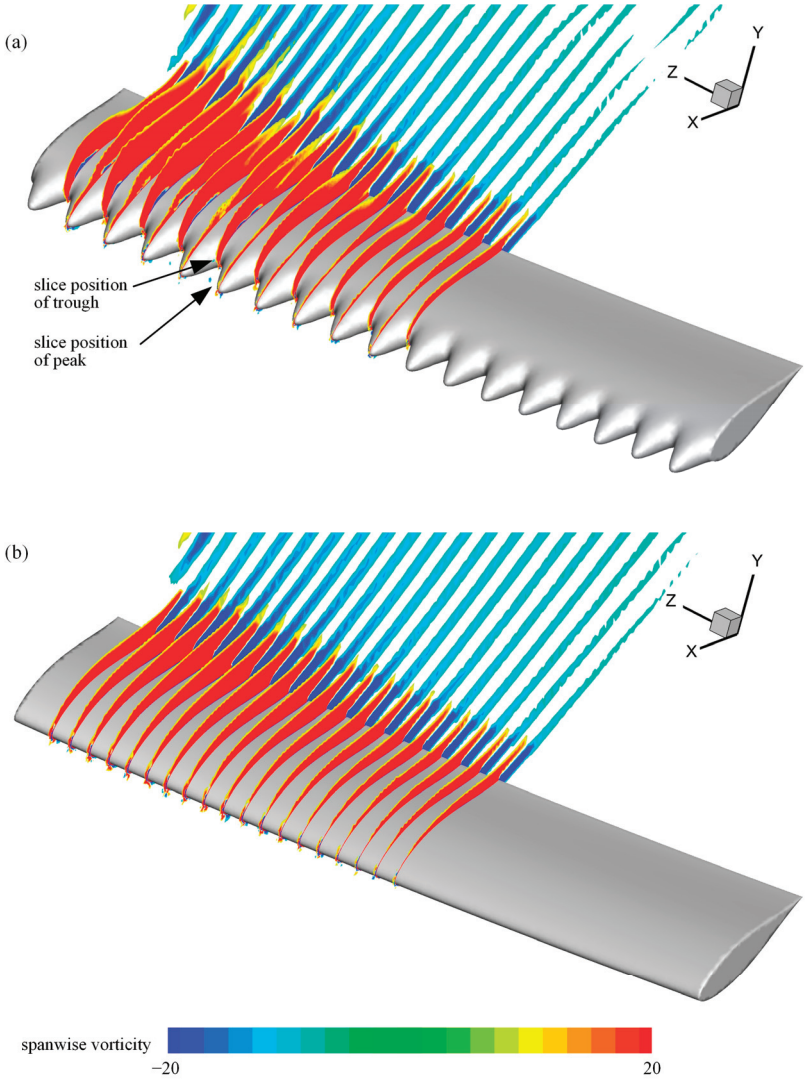

Figure 12. Slices of spanwise vorticity contour for foil (**a**) L025A01 and (**b**) baseline ($St = 0.3$, $\alpha_{\max} = 20°$, $Re = 50,000$). The separation tendency was suppressed in the peak sections and strengthened in the trough sections.

Figure 14 shows the force diagram for a section and the distribution of the pressure vector on the sections corresponding to Figure 13. Under the action of pressure, a force F_c along the chord direction and a force F_{pc} along the direction perpendicular to it are generated on the section. The thrust and power of the foil can be described as:

$$T = \int_0^b F_{pc} \sin(\theta) + F_c \cos(\theta) ds \tag{19}$$

$$P = \int_0^b (F_{pc}\cos(\theta) - F_c\sin(\theta))h'(s,t) + M_s\theta' ds \tag{20}$$

where $h'(s,t)$ is the heaving velocity of the section, and M_s is the moment of the section around the pitch axis. Because the pitch angle approaches its maximum value when the thrust and power peaks occur, the $M_s\theta'$ is small and can be ignored. The variation in pressure distribution primarily occurs in the suction area near the leading edge of the upper portion, which is related to the chordwise force F_c. In the peak section, as shown in Figure 13a, the hydrodynamic force F_{pc} has no significant variation under the combined effect of the weakening of the suction peak and increased local chord length. However, the loss of the area enclosed by the pressure coefficient curve of the peak section shown in Figure 13b indicates that the reduction in the suction peak led to the loss of chordwise force F_c. According to Equations (19) and (20), thrust is reduced and power consumption is increased. In the trough section, the pressure distribution had no significant influence on the hydrodynamic performance, which is caused by variations in the suction peak and the local chord length.

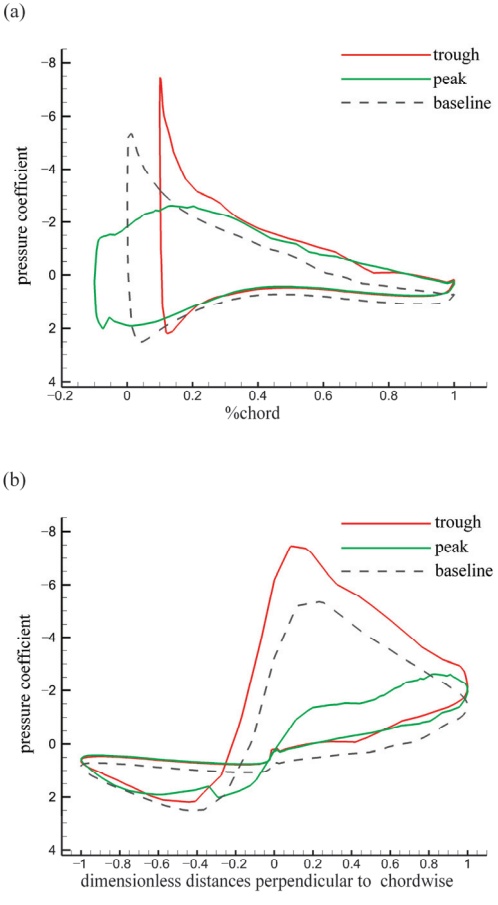

Figure 13. Distribution of pressure coefficients (**a**) along the chordwise direction and (**b**) in the direction perpendicular to it in the peak and trough sections for the modified foil and baseline ($St = 0.3$, $\alpha_{max} = 20°$, $Re = 50,000$). The pressure distribution of the modified foil differed significantly from that of the baseline in the peak and trough sections, which was related to the variation in performance.

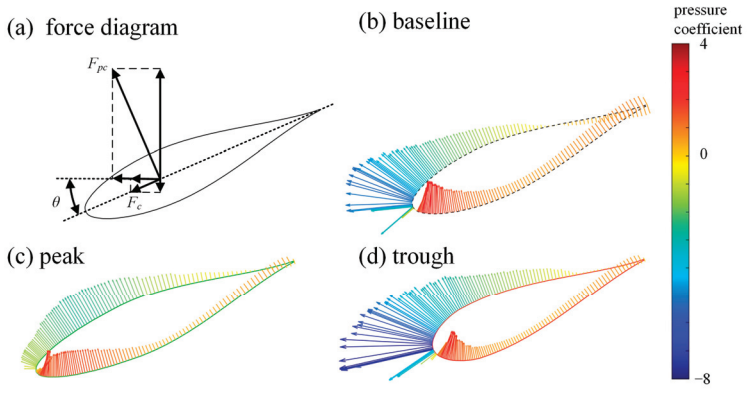

Figure 14. (**a**) Force diagram on sections. Pressure vector distribution on the (**b**) baseline, (**c**) peak, and (**d**) trough ($St = 0.3$, $\alpha_{max} = 20°$, $Re = 50,000$). The loss of chordwise force caused by the weakening of the suction peak on the peak sections played a major role in the variation in performance.

In the peak section, high- and low-pressure regions were created in the lower and upper portions of the foil, respectively; these regions were induced by the angle of attack. The pressure difference drives the flow from the lower to the upper portion through the valleys of the tubercles, which is blocked in the baseline. Figure 15 shows the spanwise velocity contours in the middle section between the peak and trough sections, which are marked in Figure 12a. A positive velocity represents the flow moving from the peak to the trough. The results indicate that the flow moved towards the trough in the lower portion and towards the peak in the upper portion near the leading edge. This flow was similar to that near the tip of the wing and weakened the suction in the peak section, which led to a reduction in adverse pressure gradients. Positive pressure gradients were generated near the leading edge in the upper portion, which contributed to the suppression of the flow separation. Conversely, in the trough section, the suction peak increased under the effects of the flow induced by tubercles. The increase in the suction peak and the reduction in the local chord length resulted in higher adverse pressure gradients, which can strengthen the flow separation. Variations in the suction peak and flow were also observed by Serson et al. [8].

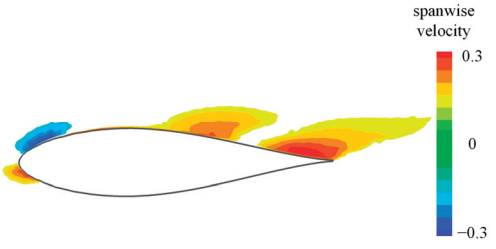

Figure 15. Spanwise velocity contour in the baseline section in the middle section between the peak and trough sections ($St = 0.3$, $\alpha_{max} = 20°$, $Re = 50,000$). The tubercles allowed the flow near the leading edge to move from the lower portion to the upper portion, which was the cause of the variation in pressure distribution.

3.2. Effect of Strouhal Number

For a flapping foil, the Strouhal number is a kinematic parameter that significantly affects propulsive performance. As discussed in Section 3.1, foil L025A01, which had the most distinct effect, was considered in the *St* range of 0.2–0.5 at α_{max} = 20°. The mean hydrodynamic performance is presented in Figure 16. The results indicate that the thrust increased approximately linearly in the *St* range of 0.2–0.4, after which it decreased.

A monotonic increment was observed for power consumption over the entire *St* range considered in the present study; however, the rate of increase declined for *St* values above 0.4. As *St* increased, the propulsive efficiency, which depends on the thrust and power consumption, first increased and then decreased. For the modified foil, the maximum efficiency was observed for *St* = 0.4, whereas that of the baseline was at *St* = 0.3. Although a loss of propulsive performance was observed, the difference between the modified foil and baseline gradually decreased, indicating that the effect of tubercles changed from weakening to enhancement. However, an enhancement of the propulsive performance was not observed in the *St* range considered in this study.

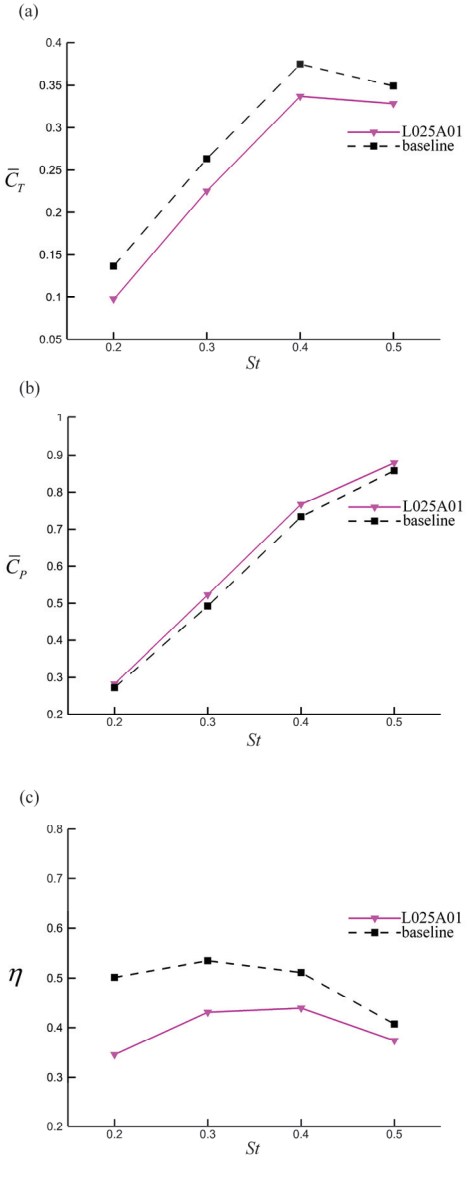

Figure 16. (**a**) Mean thrust coefficients, (**b**) power coefficients, and (**c**) propulsive efficiency measured at different Strouhal numbers ($\alpha_{\max} = 20^{\circ}$, $Re = 50,000$). The loss of performance decreased with the increase in *St*.

We further investigated the effects of tubercles at different Strouhal numbers. Figure 17 shows the pressure distribution of the modified foil in the same sections as that in Section 3.1 at $St = 0.5$, when the foil had the maximum instantaneous thrust. The results of $St = 0.3$ are also presented as a reference. The pressure distribution pattern does not depict a significant difference between different Strouhal numbers, indicating that the flow was not drastically changed by the variation in Strouhal numbers. However, the pressure difference between the upper and lower portions of the foil increased at a high Strouhal number, indicating an increase in thrust and power consumption. In addition, we observed less weakening of the suction peak in the peak section and an increase in the suction peak in the trough section, which benefitted the propulsive performance. Compared with the suction at a low Strouhal number, that near the leading edge in the upper portion of the foil decreased in the peak section and increases in the trough section, indicating that the effects of the tubercles were enhanced at high Strouhal numbers. This variation in the pressure distribution indicates that the transition of effects decreases the difference between the modified foil and the baseline as the Strouhal number increases instead of suppressing these effects.

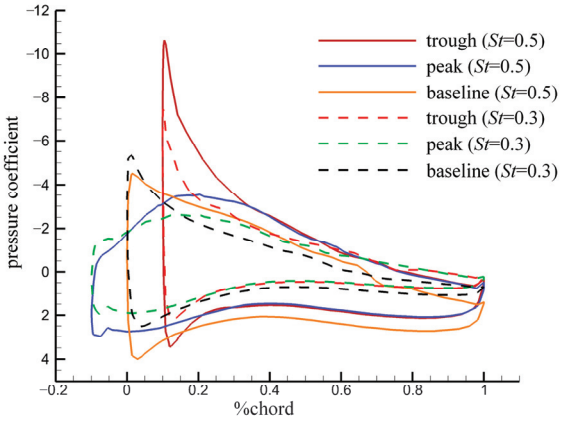

Figure 17. Distribution of pressure coefficients along the chordwise direction in peak and trough sections for modified foil and baseline at $St = 0.5$ (solid lines) and $St = 0.3$ (dashed lines) ($\alpha_{max} = 20°$, $Re = 50,000$). The suction near the leading edge was reduced in the peak section and increased in the trough section at high Strouhal numbers, indicating that the effect of the tubercles was enhanced.

3.3. Effect of Maximum Angle of Attack

In addition to the Strouhal number, the maximum angle of attack (α_{max}) plays a significant role in the flapping foil performance. The performance of foil L025A01 was considered in the α_{max} range of 15–40° at $St = 0.3$. The mean propulsive performance is plotted in Figure 18. With the increment in α_{max}, the mean thrust first increased and reached a peak at $\alpha_{max} = 25°$ for the modified foil and at $\alpha_{max} = 30°$ for the baseline. Then, as α_{max} was increased further, the thrust decreased. The power consumption increased over the entire range of α_{max}, as shown in Figure 18b. The propulsive efficiency first increased till it reached a maximum at $\alpha_{max} = 20°$, after which it decreased. Variation in the effects of the tubercles was observed at different values. A loss of thrust existed in the entire considered range of α_{max} and increased with the increment in α_{max}. The power consumption of the modified foil was greater than that of the baseline in the range of $\alpha_{max} \leq 25°$ and lesser than that for $\alpha_{max} > 25°$. Although the reduction in power consumption was greater at high values, the propulsive efficiency of the modified foil was less than that of the baseline owing to the greater loss of thrust. These results indicate that tubercles cannot benefit the propulsive performance of the flapping foils, even at high values.

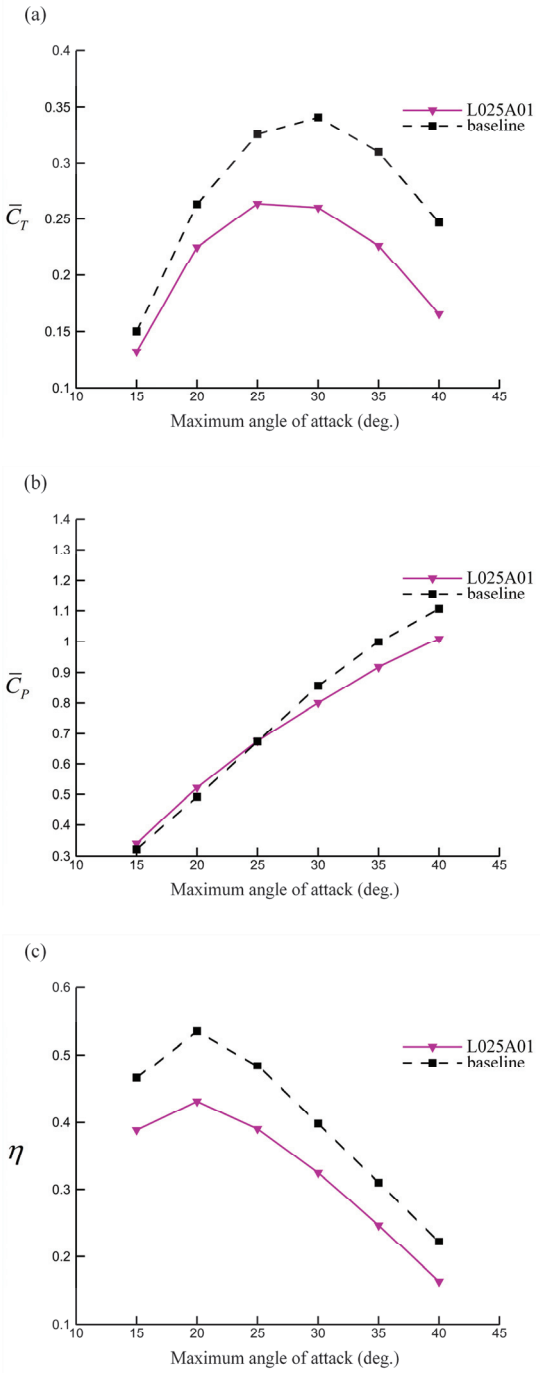

Figure 18. (**a**) Mean thrust coefficients, (**b**) power coefficients, and (**c**) propulsive efficiency at different maximum angles of attack ($St = 0.3$, $Re = 50,000$). Tubercles cannot benefit the flapping foils even at a high maximum angle of attack, which is different from the static foils.

Figure 19 shows the pressure distribution in the same peak and trough sections at $\alpha_{max} = 40°$, which is when the foil had the maximum instantaneous thrust. The pressure distribution on the upper portion of the modified foil varied greatly at a high α_{max}. Multiple suction peaks appeared in the peak and trough sections, indicating that the flow became more complex in these two sections under the effects of a high α_{max}. The maximum suction peaks in these sections were reduced compared with that of the baseline, inducing a loss of thrust and reduction in power consumption. The hydrodynamic performance in the peak and trough sections was weakened, which is different from the low α_{max}. Slices of the spanwise vorticity contour for the modified foil and baseline at $\alpha_{max} = 40°$ are presented in Figure 20. The flow of the baseline foil separated from the leading edge in the outer region with approximately a quarter of the span length and reattached to the upper portion of the foil at the half-chord position. However, the presence of tubercles expanded the separation region and strengthened the flow separation in the peak and trough sections. Only the flow separation near the leading edge on the upper portion of the tubercles in the peak sections was suppressed. The strengthening of the separation led to a reduction in the maximum suction on the upper portion, thus weakening the hydrodynamic performance.

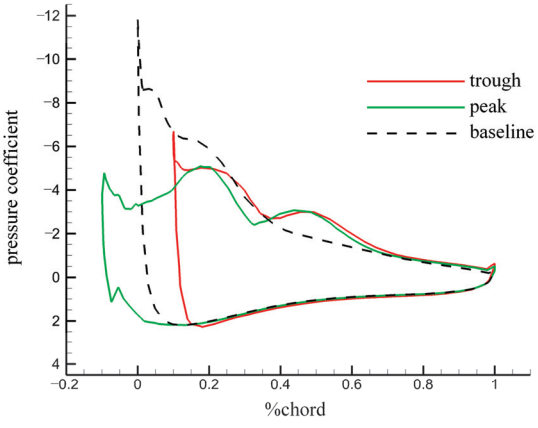

Figure 19. Distribution of pressure coefficients along chordwise direction in peak and trough sections for the modified foil and baseline at $\alpha_{max} = 40°$ ($St = 0.3$, $Re = 50,000$). The suction peaks in both the peak and the trough sections were reduced, inducing a reduction in thrust and power consumption.

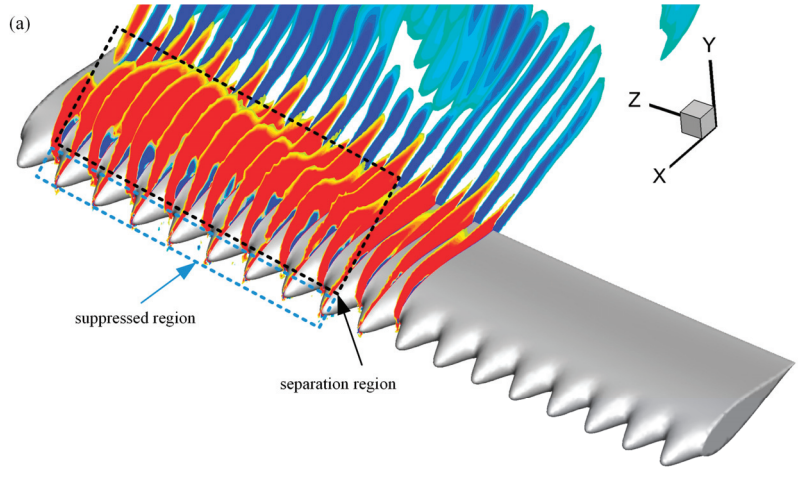

Figure 20. *Cont.*

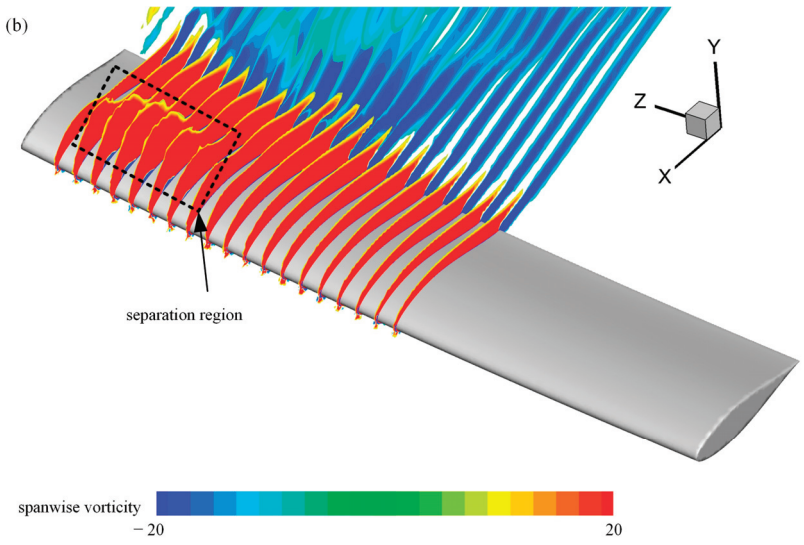

Figure 20. Slices of spanwise vorticity contours for foils (**a**) L025A01 and (**b**) baseline at $\alpha_{max} = 40°$ ($St = 0.3$, $Re = 50,000$). The presence of tubercles may expand the separation region and strengthen the flow separation in the peak and trough sections.

4. Discussion

In contrast to static foil behavior, flapping foils do not take advantage of tubercles. A reduction in the propulsive performance was observed for all modified foils in the considered range of kinematic parameters. For the leading-edge tubercles, suppression of flow separation was observed in the peak sections. However, no significant flow separation occurred on the foil surface. Hence, it was difficult for the tubercles to work. Furthermore, the presence of tubercles strengthened the separation tendency and expanded the separation regions. The variation in the flow changed the pressure distribution on the foil surface, thus diminishing the propulsive performance of the modified foils.

For static foils, the streamwise vortices generated by the tubercles play a pivotal role in delaying stall [33]. The vortices can inject high-momentum fluid into the boundary layer behind the peak sections, thus delaying flow separation [7]. Similar streamwise vortices were also generated for the flapping foils, as shown in Figure 21. However, a similar flow yielded different results. Earlier force measurements showed that the foils with tubercles produced less thrust while consuming the same amount of power. This phenomenon was hypothesized to stem from the breakdown of the thrust wake due to the interaction between the streamwise vortices and those generated by flapping [17]. In the present study, foils with tubercles generated less thrust and consumed more power, except in high angles of attack. Such variances might be attributed to foil tapering. Furthermore, this study interpreted the performance deterioration from a distinct perspective. The vortices generated by the tubercles diminished the suction peak in the peak sections, resulting in a decrease in the chordwise forces and ultimately inducing performance deterioration. However, the interrelationship between the variation in pressure distribution and the thrust wake requires further investigation. On the other hand, the vortices suppressed the flow separation on the tubercle surface in the peak sections, whereas they strengthened the separation in the remaining regions after interacting with the flow of the flapping foil. Moreover, for flapping foils, it is difficult to maintain the instantaneous angles of attack at relatively high values for a long time. Consequently, the flow cannot be fully developed, and the flow separation is suppressed by the motion. However, the presence of streamwise vortices strengthens the flow separation in the trough regions. Therefore, the presence of leading-edge tubercles was found to be disadvantageous.

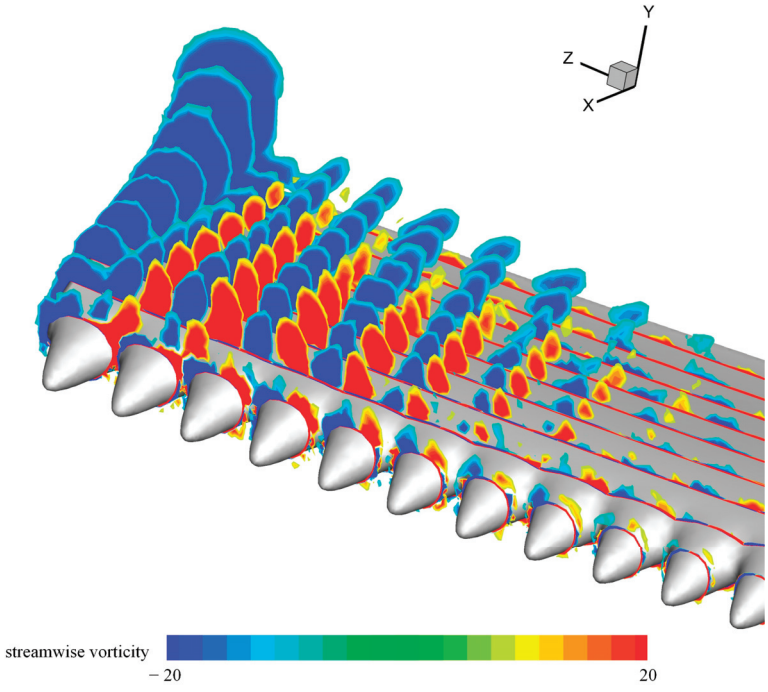

Figure 21. Slices of streamwise vorticity contours for modified foil ($A = 0.1c$, $\lambda = 0.25c$, $St = 0.3$, $St = 0.3$, $Re = 50,000$). Streamwise vortices similar to those of static foils were also observed on flapping foils, but similar flows did not lead to similar results.

Considering these effects of tubercles on the flapping foils, leading-edge tubercles can be considered unsuitable for use in general flapping foils. It makes sense that the tubercles have not evolved in animals that drive themselves by flapping their foils or wings, such as turtles and birds. They are more suitable for foils that move with steady or quasi-steady motions, such as the flippers of humpback whales in nature, and in propellers or turbines used in ocean engineering, where performance improvement has been observed [34,35].

5. Conclusions

In this research, we investigated the effects of leading-edge tubercles on a three-dimensional flexible flapping foil at different Strouhal numbers and maximum angles of attack. The performance of flapping foil was estimated using verified numerical methods. The effects of leading-edge tubercles with different amplitudes and wavelengths were estimated under conditions of high propulsive efficiency. Leading-edge tubercles caused a loss of thrust and an increase in power consumption, thus reducing the propulsive efficiency. The loss of the thrust peak played a major role in this effect. The shape parameters of tubercles, including amplitude and wavelength, were coupled to determine the effects of leading-edge tubercles. Moreover, the effects of the Strouhal numbers and maximum angles of attack were investigated. A high Strouhal number transformed the effects of leading-edge tubercles from disadvantageous to advantageous, which increased the propulsive performance. However, the propulsive performance decreased as the maximum angle of attack was further increased.

In addition, flow visualization was performed to understand the degradation in propulsive performance. The leading-edge tubercles suppressed flow separation in the peak sections, but this was useless for the flapping foils because the separation was suppressed by motion. However, the presence of leading-edge tubercles strengthened the separation in the remaining regions, particularly at high maximum angles of attack. The suction peak on

the upper portion of the peak sections was reduced by allowing the flow to move through the valleys in the middle of the adjacent tubercles. Moreover, the suction peak in the trough sections increased at low maximum angles of attack and decreased at high maximum angles of attack, which is related to flow separation. This variation in the pressure distribution resulted in a degraded propulsive performance.

The effects of leading-edge tubercles on flexible flapping foils were investigated in the present study, and the mechanism was clarified. Although spanwise flexibility was considered, it has not been discussed in detail because it is a complex motion-related factor. Furthermore, foil tapering was not considered as one of the ways to improve the performance of flapping foils. Both should be investigated in future research to help understand the behavior of humpback whales.

Author Contributions: Conceptualization, R.H. and X.W.; methodology, R.H., J.L. and X.W.; software, R.H.; validation, J.L.; resources, X.W. and B.S.; writing—original draft preparation, R.H. and X.L.; writing—review and editing, R.H., X.W. and X.L.; visualization, X.L.; supervision, X.W. and B.S. All authors have read and agreed to the published version of the manuscript.

Funding: This research was funded by the National Natural Science Foundation of China (grant numbers 52205268 and 52175251) and the National Basic Scientific Research Program (grant number JCKY2021206B005).

Institutional Review Board Statement: Not applicable.

Informed Consent Statement: Not applicable.

Data Availability Statement: All data generated or analyzed during this study are included in this published article.

Conflicts of Interest: The authors declare no conflict of interest.

References

1. Wang, Y.; Hu, W.; Zhang, S. Performance of the Bio-Inspired Leading Edge Protuberances on a Static Wing and a Pitching Wing. *J. Hydrodyn. Ser. B* **2015**, *26*, 912–920. [CrossRef]
2. Fish, F.E.; Battle, J.M. Hydrodynamic Design of the Humpback Whale Flipper. *J. Morphol.* **1995**, *225*, 51–60. [CrossRef] [PubMed]
3. Miklosovic, D.S.; Murray, M.M.; Howle, L.E.; Fish, F.E. Leading-Edge Tubercles Delay Stall on Humpback Whale (*Megaptera novaeangliae*) Flippers. *Phys. Fluids* **2004**, *16*, L39. [CrossRef]
4. Johari, H.; Henoch, C.; Custodio, D.; Levshin, A. Effects of Leading-Edge Protuberances on Airfoil Performance. *AIAA J.* **2007**, *45*, 2634–2642. [CrossRef]
5. Zhang, M.M.; Wang, G.F.; Xu, J.Z. Aerodynamic Control of Low-Reynolds-Number Airfoil with Leading-Edge Protuberances. *AIAA J.* **2013**, *51*, 1960–1971. [CrossRef]
6. Pedro, H.C.; Kobayashi, M. Numerical Study of Stall Delay on Humpback Whale Flippers. In Proceedings of the 46th AIAA Aerospace Sciences Meeting and Exhibit, Reno, Nevada, 7–10 January 2008.
7. Skillen, A.; Revell, A.; Pinelli, A.; Piomelli, U.; Favier, J. Flow over a Wing with Leading-Edge Undulations. *AIAA J.* **2015**, *53*, 464–472. [CrossRef]
8. Serson, D.; Meneghini, J.R.; Sherwin, S.J. Direct Numerical Simulations of the Flow around Wings with Spanwise Waviness. *J. Fluid Mech.* **2017**, *826*, 714–731. [CrossRef]
9. Troll, M.; Shi, W.; Stark, C. *Leading-Edge Tubercles Applied onto a Flapped Rudder*; American Society of Mechanical Engineers Digital Collection: Hamburg, Germany, 2022.
10. Perkins, M.; Elles, D.; Badlissi, G.; Mivehchi, A.; Dahl, J.; Licht, S. Rolling and Pitching Oscillating Foil Propulsion in Ground Effect. *Bioinspir. Biomim.* **2017**, *13*, 016003. [CrossRef]
11. Li, C.; Dong, H. Three-Dimensional Wake Topology and Propulsive Performance of Low-Aspect-Ratio Pitching-Rolling Plates. *Phys. Fluids* **2016**, *28*, 071901. [CrossRef]
12. Polidoro, V. *Flapping Foil Propulsion for Cruising and Hovering Autonomous Underwater Vehicles*; Massachusetts Institute of Technology: Cambridge, MA, USA, 2003.
13. Techet, A.H. Propulsive Performance of Biologically Inspired Flapping Foils at High Reynolds Numbers. *J. Exp. Biol.* **2008**, *211*, 274–279. [CrossRef]
14. Heathcote, S.; Wang, Z.; Gursul, I. Effect of Spanwise Flexibility on Flapping Wing Propulsion. *J. Fluids Struct.* **2008**, *24*, 183–199. [CrossRef]
15. Le, T.Q.; Ko, J.H. Effect of Hydrofoil Flexibility on the Power Extraction of a Flapping Tidal Generator via Two- and Three-Dimensional Flow Simulations. *Renew. Energy* **2015**, *80*, 275–285. [CrossRef]

16. Ozen, C.A.; Rockwell, D. Control of Vortical Structures on a Flapping Wing via a Sinusoidal Leading-Edge. *Phys. Fluids* **2010**, *22*, 021701. [CrossRef]
17. Stanway, M.J. Hydrodynamic Effects of Leading-Edge Tubercles on Control Surfaces and in Flapping Foil Propulsion. Master's Thesis, Massachusetts Institute of Technology, Cambridge, MA, USA, 2008.
18. Anwar, M.B.; Shahzad, A.; Mumtaz Qadri, M.N. Investigating the Effects of Leading-Edge Tubercles on the Aerodynamic Performance of Insect-like Flapping Wing. *Proc. Inst. Mech. Eng. Part C J. Mech. Eng. Sci.* **2021**, *235*, 330–341. [CrossRef]
19. Miklosovic, D.S.; Murray, M.M.; Howle, L.E. Experimental Evaluation of Sinusoidal Leading Edges. *J. Aircr.* **2007**, *44*, 1404–1408. [CrossRef]
20. Read, D.A.; Hover, F.S.; Triantafyllou, M.S. Forces on Oscillating Foils for Propulsion and Maneuvering. *J. Fluids Struct.* **2003**, *17*, 163–183. [CrossRef]
21. Andrun, M.; Blagojević, B.; Bašić, J.; Klarin, B. Impact of CFD Simulation Parameters in Prediction of Ventilated Flow on a Surface-Piercing Hydrofoil. *Ship Technol. Res.* **2021**, *68*, 1–13. [CrossRef]
22. ANSYS FLUENT 12.0 User's Guide. Available online: https://www.afs.enea.it/project/neptunius/docs/fluent/html/ug/node236.htm (accessed on 4 September 2023).
23. *Ansys® Academic Research Fluent, Release 19.0, Help System*; ANSYS Fluent User's Guide; ANSYS, Inc.: Canonsburg, PA, USA, 2018.
24. Menter, F.R.; Kuntz, M.; Langtry, R. Ten Years of Industrial Experience with the SST Turbulence Model. *Heat Mass Transf.* **2003**, *4*, 625–632.
25. Mishra, A.A.; Mukhopadhaya, J.; Iaccarino, G.; Alonso, J. Uncertainty Estimation Module for Turbulence Model Predictions in SU2. *AIAA J.* **2019**, *57*, 1066–1077. [CrossRef]
26. Duraisamy, K.; Iaccarino, G.; Xiao, H. Turbulence Modeling in the Age of Data. *Annu. Rev. Fluid Mech.* **2019**, *51*, 357–377. [CrossRef]
27. Wu, X.; Zhang, X.; Tian, X.; Li, X.; Lu, W. A Review on Fluid Dynamics of Flapping Foils. *Ocean Eng.* **2020**, *195*, 106712. [CrossRef]
28. Roache, P.J. Quantification of Uncertainty in Computational Fluid Dynamics. *Annu. Rev. Fluid Mech.* **1997**, *29*, 123–160. [CrossRef]
29. Celik, I.B.; Ghia, U.; Roache, P.J.; Freitas, C.J. Procedure for Estimation and Reporting of Uncertainty Due to Discretization in CFD Applications. *J. Fluids Eng.* **2008**, *130*, 078001.
30. Li, J.; Wang, P.; An, X.; Lyu, D.; He, R.; Zhang, B. Investigation on Hydrodynamic Performance of Flapping Foil Interacting with Oncoming Von Kármán Wake of a D-Section Cylinder. *J. Mar. Sci. Eng.* **2021**, *9*, 658. [CrossRef]
31. Custodio, D.; Henoch, C.W.; Johari, H. Aerodynamic Characteristics of Finite Span Wings with Leading-Edge Protuberances. *AIAA J.* **2015**, *53*, 1878–1893. [CrossRef]
32. Serson, D.; Meneghini, J.R.; Sherwin, S.J. Direct Numerical Simulations of the Flow around Wings with Spanwise Waviness at a Very Low Reynolds Number. *Comput. Fluids* **2017**, *146*, 117–124. [CrossRef]
33. Stanway, M.J.; Techet, A.H. Spanwise Visualization of the Flow around a Three-Dimensional Foil with Leading Edge Protuberances. *APS Div. Fluid Dyn. Meet. Abstr.* **2006**, *59*, EO.003.
34. Shi, W.; Rosli, R.; Atlar, M.; Norman, R.; Wang, D.; Yang, W. Hydrodynamic Performance Evaluation of a Tidal Turbine with Leading-Edge Tubercles. *Ocean Eng.* **2016**, *117*, 246–253. [CrossRef]
35. Stark, C.; Shi, W.; Troll, M. Cavitation Funnel Effect: Bio-Inspired Leading-Edge Tubercle Application on Ducted Marine Propeller Blades. *Appl. Ocean Res.* **2021**, *116*, 102864. [CrossRef]

Journal of
Marine Science and Engineering

MDPI

Article

Assessment of Numerical Captive Model Tests for Underwater Vehicles: The DARPA SUB-OFF Test Case

Vito Vasilis Zheku *, Diego Villa, Benedetto Piaggio, Stefano Gaggero and Michele Viviani *

Department of Electrical, Electronic, Telecommunication Engineering and Naval Architecture, University of Genova, Via All'Opera Pia, 11A, 16145 Genova, Italy; diego.villa@unige.it (D.V.); benedetto.piaggio@unige.it (B.P.); stefano.gaggero@unige.it (S.G.)
* Correspondence: vitovasil.zheku@edu.unige.it (V.V.Z.); michele.viviani@unige.it (M.V.)

Abstract: During the early design stage of an underwater vehicle, the correct assessment of its manoeuvrability is a crucial task. Conducting experimental tests still has high costs, especially when dealing with small vehicles characterized by low available budget. In the current investigation, virtual towing tank tests are simulated using the open-source OpenFOAM library in order to assess the reliability of CFD methods for the prediction of hydrodynamic forces and moments. A well-known case study, the Defence Advanced Research Projects Agency (DARPA) SUB-OFF model, is used, and the outcomes are compared to the experimental results available in the literature. Five different configurations are investigated for pure drift tests, rudder tests and pure rotation in both vertical and horizontal plane. The results show an overall good agreement with the experimental data with a quite low demanding mesh arrangement of 3M cells, a favourable balance between accuracy and computational time. In more detail, the expected error in the most significant forces during manoeuvres is less than 2% for the fully appended configuration (the submarine real operative condition), whereas the accuracy is moderately reduced for the barehull configuration (a case not representative of a real hull) with an expected error of 15%. A possible reason for the differences observed could be attributed to the description of the two streamwise vortices generated when manoeuvring. Apart from the lateral force and yaw moment, the results of the longitudinal force are also presented, having a greater disparity when compared to the experimental data. Nevertheless, the longitudinal force has no important role for the purpose of making stability and control predictions. The study contributes to the validation and consolidation of CFD methods, offering insights into their accuracy and limitations for practical applications in underwater vehicles.

Keywords: naval hydrodynamics; CFD; submarines; RANS; underwater vehicles; DARPA; manoeuvrability

Citation: Zheku, V.V.; Villa, D.; Piaggio, B.; Gaggero, S.; Viviani, M. Assessment of Numerical Captive Model Tests for Underwater Vehicles: The DARPA SUB-OFF Test Case. *J. Mar. Sci. Eng.* **2023**, *11*, 2325. https://doi.org/10.3390/jmse11122325

Academic Editors: Nastia Degiuli and Ivana Martić

Received: 6 November 2023
Revised: 29 November 2023
Accepted: 2 December 2023
Published: 8 December 2023

1. Introduction

Nowadays, more and more underwater vehicles (UVs) are being used, not only for military, but also for exploration or scientific purposes [1]. Underwater vehicles (like submarines or small crafts) are characterized by complex shapes, yet during the design stage, the correct assessment of the manoeuvrability and stability of a submarine is a crucial task. Thus, additional dedicated studies are needed. Unfortunately, the reference literature is limited, and industrial or military restrictions often limit the access to experimental data.

The main notions for studying the manoeuvrability of submarines are very similar to that of surface ships, with the main difference the increase to 6-DoF [2] and the influence of the restoring forces on the vertical plane, with crucial consequences for the vertical stability and change depth ability [3]. Often, during the design phase, to simplify the problem, the motions in 6-DoF are decoupled into the horizontal and vertical components, making the analysis simpler and enabling the separation of the main effects and aspects. As a consequence of that, it is clear that the reliable evaluation of the hydrodynamic

coefficients is a crucial aspect in predicting the motion of the vehicles for manoeuvring prediction purposes.

Studies have been carried out traditionally to predict the hydrodynamic derivatives of a submarine using either empirical formulae, or captive model experiments, considering all available types of tests such as translational, rotating arm and PMM (planar motion mechanism) ones (see among others [4,5]). Fureby et al. [6] conducted an experimental and numerical study of the Defence Science and Technology Organisation (DSTO) generic submarine model in both straight-ahead conditions and a 10° side-slip in the low-speed wind tunnel at Fishermans Bend in Melbourne. Similar measurements were carried out by Anderson et al. [4] and Quick et al. [5], presenting an experimental campaign focused on generic conventional submarine hulls, testing different drift and pitch angles. These kinds of results are useful in order to compare and consolidate the use of computational fluid dynamics for the prediction of the hydrodynamic forces, and consequently the extrapolation of the hydrodynamic coefficients. Moreover, in the last decades, thanks to the growth of computational resources, CFD simulations have also been considered as a possible source of data. In the study conducted by Fureby, complementary numerical calculations were carried out, using both RANS (Reynolds-averaged Navier–Stokes equations) with the kOmegaSST formulation (kOmega shear stress transport) and LES (large eddy simulation) with two different models, the LDKM (localized dynamic kinetic energy model) and the MM (mixed model), having unstructured grids with up to 340M cells. Dubbioso et al. [7] investigated the effect of the stern appendages' configuration on the turning qualities of a fully appended notional submarine (CNR-INSEAN 2475), by means of numerical simulations, using an in-house CFD solver. Both cross-shaped and X-rudder configuration were examined, in two different operation conditions, open water and snorkeling depth. Broglia et al. [8] carried out an analysis of the vortices shed in steady drift and pitch advancement of the BB2 submarine at four operative conditions, namely straight ahead, drift, and both positive and negative pitch. Their results were compared with experiments available in the literature [9], showing the accuracy that CFD predictions can provide.

Wackers et al. [10] presented a comprehensive analysis of the KRISO (Korean Institute of Ships and Ocean Engineering) Very Large Crude Carrier no. 2 (KVLCC2) flow field, with a particular emphasis on the effects of vortices. Their paper discusses the challenges of turbulence modelling in accurately simulating these flow patterns and compares computational results with experimental measurements, shedding light on the vital role of turbulence modelling in marine flow simulations. In a study by Zhang et al. [11], the unsteady Reynolds-averaged Navier–Stokes (URANS) method was employed to simulate the surfacing motion of a submarine model (DARPA-SUBOFF) in regular waves. The outcomes showed that in the proximity of the free surface, underwater roll and pitch instability occur. Posa and Balaras [12] reported the findings of computational research on the flow around a submarine model, focusing on how the appendages affected the propeller wake fields, using the high-fidelity LES approach. Morse and Mahesh [13] provided a novel analysis of turbulent boundary layers on streamlined bodies by examining the boundary layer generation at several points using LES. Rocca et al. [14] performed a numerical characterization of the hydrodynamic and hydroacoustic field of a fictitious underwater vehicle shape using large eddy simulation and a wall-layer model. Nevertheless, the LES method requires significantly more computational resources than the RANS method, a fact that limits its application to large-scale simulations. Thus, DES (detached eddy simulation) methods have recently emerged. Lungu [15,16] reported on a thorough investigation of the flow around a submarine model under straight-ahead and static drift conditions, using a range of turbulence models to assess the unique issues of large-scale flow separation involved. Wang et al. [17,18] discovered that the presence of the hull and the interaction with the free surface substantially impacted the propeller performance in a series of computational studies for underwater geometries operating close to the free surface. In order to compare the outcomes of URANS and DDES, Guo et al. [19] carried out numerical research for the flow around the submarine under the conditions of rudder deflection. The DDES (delayed

detached eddy simulation) technique gave a greater capability for recording the flow field parameters around the submarine in constrained manoeuvring situations with noticeable flow separation. Regarding the approximation techniques, a study and comparison of different empirical methods conducted by Jones et al. [20], showed that, despite the fact that they can be used at an early design stage, in order to provide good results, careful calibration is needed.

Even though experimental methods are the most common way to predict the hydrodynamic coefficients, their costs still remain too high to be adopted given the huge captive matrix in 6-DoF, in particular for small vehicles (characterized by a low available budget), making them impossible to be carried out at an early stage of the design. Furthermore, during experimental tests, the influence of the support struts should be taken into consideration carefully. Although measurements of the hydrodynamic forces are conducted considering only the models, so not including the forces on the struts, their presence can significantly influence the flow around the submarine model. The challenges of such measurements extend beyond the supporting struts, encompassing various complexities. Boundary effects arising from interactions with tank walls and the bottom can impact the accuracy of measurements. Wave interference, generated within the towing tank, poses challenges in isolating the desired hydrodynamic responses. Additionally, viscous effects near the submarine surface and the accurate representation of the submarine model full-scale characteristics (new geometries, details like sonar domes and appendages) pose substantial challenges for researchers. Careful consideration and mitigation strategies for these difficulties are essential to ensure the reliability and relevance of the experimental results. Despite the above considerations, some experiments can be found in the literature. The most common models used in the literature are the DARPA SUBOFF and the Joubert/BB1/BB2 model. The SUBOFF model [21] is a typical of a nuclear-powered general-purpose attack submarine (SSN) configuration. Roddy [22] and Huang et al. [23] conducted experimental tests using the DARPA SUBOFF hull in order to investigate the stability and the control characteristics of several configurations with and without appendages. The Joubert submarine [24,25], designed for the Australian Department of Defense, is a conceptual model of a large diesel-electric submarine, specialized for anti-submarine duties (SSK), generally referred to in the literature as BB1. Further modifications to the aft control surfaces and sails [26] led to the BB2 configurations.

On the other hand, computational fluid dynamics methods make it possible to carry out the predictions without the presence of support struts. Furthermore, computations using CFD approaches can provide the contribution of the total force of each individual component of the submarine, for instance rudders, planes and sail, without additional complications of experimental measuring gauges. Some of the disadvantages of these techniques are the high computational costs when dealing with complex configurations, and the constant and rapid development of new numerical methods and simulation paradigms. Numerous investigations in the open literature have employed CFD simulations to rigorously examine surface ships, focusing on the extrapolation of hydrodynamic coefficients, contributing to a comprehensive understanding of the intricate fluid dynamics governing the behaviour of such vessels (see among others [27]), while as mentioned before, there is a difficulty in finding detailed investigations regarding the manoeuvrability of submarines. The aim of the current study is to explore the reliability of CFD predictions, through a systematic comparison with the available measurements, to feed the semi-empirical models of manoeuvrability of submarines usually adopted at the earlier stage of the design cycle as it is hard to find in the literature a full experimental campaign that has been simulated for different geometry configurations and different pitch and drift angles. Of great importance are also the simulations of the hydrodynamic forces acting on the control surfaces, when a rudder angle is present and when it is combined with different drift angles both in the horizontal and the vertical plane. Starting from the experience developed at the University of Genoa in the last few years (see, for instance, [28–30]), towing tank experiments of the

DARPA SUBOFF model are simulated using an open-source RANS solver to calculate the hydrodynamic forces and moments and the resultant coefficients.

In the following sections, after a short theoretical background presentation and the computational setup, the test case is presented, including the geometry of the model under investigation, and the tests performed (Section 2). In Section 3, the mesh sensitivity analysis is reported to assess the overall numerical uncertainty of the present procedure. The results are then presented in Sections 4 and 5, discussing the pure drift test and the rudder test outcomes, respectively. Finally, a summary of the conclusions of the current study is reported.

2. Computational Setup and Test Case

In the current study, numerical simulations are performed with the open-source CFD library OpenFOAM [31]. OpenFOAM provides users with full access to the source code, allowing them to customize and modify the software to suit their specific needs. This flexibility is not typically available in commercial software, which may limit the user's ability to customise it. The governing equations are discretised using the finite volume method with the second-order upwind scheme. For the pressure–velocity coupling, a guess-and-correct procedure, the SIMPLEC (semi-implicit method for the pressure-linked equations) algorithm is employed. The selection of the SIMPLEC algorithm is based on its good convergence rate, especially for steady state analyses, so fewer iterations and a reduced computational time [32] is needed. The incompressible steady RANS system of equations (see Equation (1)) is used to model the flow around the UV geometry.

$$\begin{cases} \dfrac{\partial u_i}{\partial x_i} = 0 \\ \rho u_j \dfrac{\partial u_i}{\partial x_j} = -\dfrac{\partial p}{\partial x_i} + \dfrac{\partial}{\partial x_j}\left(\mu \dfrac{\partial u_i}{\partial x_j} - \rho \overline{u_i' u_j'}\right) \end{cases} \tag{1}$$

where F_i is the body forces, p is the time averaged pressure, μ and ρ are the molecular viscosity and density of the fluid, respectively; u_i and u_i' are the time averaged velocity components and the fluctuating velocity components, respectively, both in Cartesian coordinates x_i $(i = 1, 2, 3)$ and $-\rho\overline{u_i' u_j'}$ is the Reynolds stress tensor.

For the purpose of estimating the Reynolds stress tensor $-\rho\overline{u_i' u_j'}$, hence, to mathematically close the problem, several turbulence models can be adopted. In the present case,four different models are used, $k-\omega$ [33], shear stress transport $k-\omega$ [34], $k-\epsilon$ [35,36] and realizable $k-\epsilon$ [37]. Regarding the schemes, Table 1 shows the selected methods.

Table 1. Schemes used in the current simulations.

Terms	Scheme
Convective term	Bounded Gauss LinearUpWindV (U) Bounded Gauss upwind (k, ω, R, ϵ)
Diffusive term	Bounded Gauss upwind (k, ω, R, ϵ)
Time integration	SteadyState
Laplacian term	Gauss linear limited 0.3

In the present simulations, two linear solvers are used to solve the equations. For the pressure equation, the GAMG (generalized geometric-algebraic multigrid) solver with Gauss–Seidel smoothing was used to ensure robustness and efficiency. For the other equations (such as the momentum or the turbulent ones) the smoothSolver with Gauss–Seidel smoothing is utilized. This solver is a common choice in OpenFOAM simulations and was chosen for its efficiency and robustness.

In the simulations of pure drift and rudder tests, a prismatic box was selected as the computational domain around the UV model, with the upstream boundary located at 2L ahead of the fore part of the UV (where L is the length of the submarine), the downstream boundary at 3L from the aft tip, and lateral sides as well as the top/bottom boundaries at 1.5L from the cylindrical body (Figure 1). Figure 1 also shows the computational domain with the assigned boundary conditions. On the right side of the computational domain, a velocity inlet is assigned (in blue in figure), while on the left side the pressure outlet (in red) is forced. The other surfaces are considered as symmetry planes while on the submarine surfaces, a no-slip wall condition is assigned. The sizes of the domain were such that the far field flow can be considered undisturbed, so avoiding the situation that the boundary conditions affect the flowfield in proximity of the submarine.

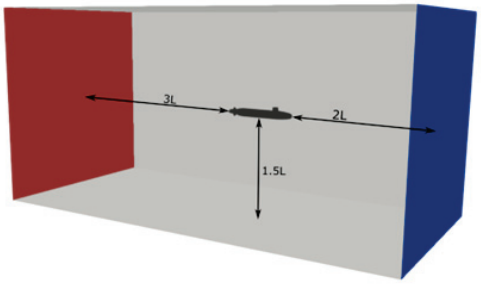

Figure 1. Main dimensions of the computational domain.

The mesh was generated by the open-source tool CfMesh v1.14 [38], which generates a hex-dominant Cartesian mesh around the geometry of interest. Proper mesh-refinement regions, inversely proportional to the distance from the submarine, were introduced to better capture the flow field in the UV near field, with approximately 3M cells for the barehull and 3.7M cells for the fully appended configuration. A sketch of the obtained mesh for zero drift angle is depicted in Figures 2 and 3, showing the boundary layer and the mesh refinement close to the body more closely.

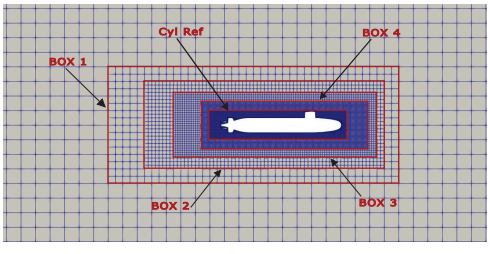

Figure 2. Box and cylindrical refinements of the domain.

Additional local refinements were used to better describe the rudders or sternplanes, in particular when a deflection angle is present, in order to adequately simulate the gap between the appendages and the axisymmetrical hull surface (Figure 4).

As for the simulations having angular velocities q and r, a new, circularly shaped domain was adopted. Figure 5 shows the boundary conditions assigned to the circular domain, with the the velocity inlet in blue and the pressure outlet in red. As in the case of pure drift tests, the other far field surfaces are handled as symmetry planes. The boundary condition on the surfaces of the submarine is a no-slip wall boundary condition. A section of the computational domain used for the pure rotation tests with its refinements is also illustrated. Both these setups follow the mesh layout already successfully adopted for surface vehicles in [29], having the overall domain modelled by the blockMesh OpenFOAM command, while the smallest block is modelled separately by the usage of the

CfMesh library. This is because CfMesh affords the capability to generate a high-quality mesh, ensuring the attainment of precision and accuracy, even in the presence of complex geometric configurations.

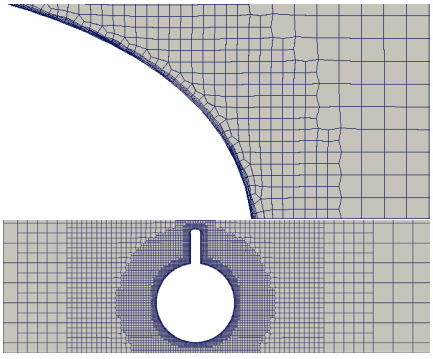

Figure 3. Detail of the mesh refinement close to the body.

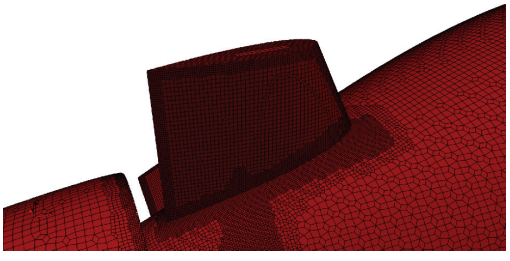

Figure 4. Local refinement for the stern appendages.

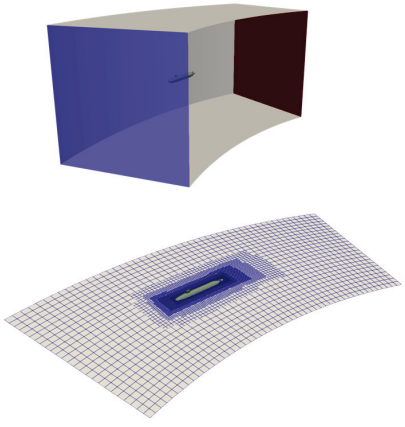

Figure 5. Local refinement (cylindrical) for the stern appendages.

In order to better analyse the turbulent viscous flow around the walls and thus deal with the near wall region in affordable computational times, the wall functions, also implemented in OpenFOAM, were used. These functions are based on empirical equations used to bridge the inner region between the wall and the fully developed turbulence region. In order to ensure the validity of these functions, the first cell centre needs to be within the log-law region from the walls. In the author's previous work [39], simulations with both y^+ between 30 and 50, as well as, $y^+ < 1$ were run, showing that the results are not significantly

affected by the y^+ selection. This is also confirmed by other authors, such as in [40] where a sensitivity analysis of y^+ for different turbulence models is presented. The findings of this study suggest that, for turbulence models such as kOmega and kEpsilon, the values of longitudinal and lateral force exhibit a high degree of insensitivity to y^+, whereas this is not true for more sophisticated turbulence models, such as the baseline Reynolds stress model (BSLRSM), which show a higher sensitivity to the values of y^+. Thus, considering the above findings and also considering the computational effort connected to a smaller y^+, a higher y^+ was preferred. In the simulations, a mean value of y^+ between 30 and 150, the limits of the wall functions, was guaranteed (similar to [41]). Therefore, a value of $y^+ = 50$ was fixed, as a starting point. Table 2 shows the obtained average values of y^+ for the different components of the fully appended configuration.

Table 2. The requested and the obtained average values of y^+.

Component	Requested y^+	Obtained y^+
Hull	50	38.42
Ring Wing	50	48.37
Sail	50	48.37
Upper Rudder	50	44.74
Lower Rudder	50	44.74
STB Sternplane	50	44.74
PS Sternplane	50	44.74

In Figure 6, the obtained values of the y^+ are shown over the surface of DARPA SUBOFF. It is evident that the values fall within the range of the applicability of the wall function as requested by the models. The y^+ pattern highlighted in the figure is a consequence of the adopted grid generator, but in analysing the resulting smooth wall shear stress distribution over the submarine surfaces (Figure 7), it is clear that the proposed mesh layout can be considered adequate for the present analyses.

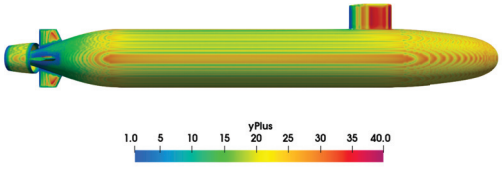

Figure 6. The y^+ values for ther fully appended configuration.

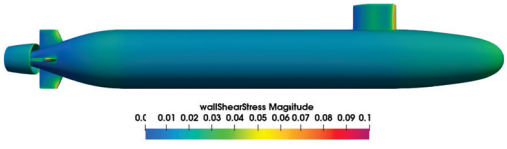

Figure 7. The wall shear stress [m^2/s^2] values obtained for the fully appended configuration.

The UV under investigation is the SUBOFF model, designed and tested in the David Taylor Research Centre (DTRC) for the Defense Advanced Research Projects Agency (DARPA). This model was selected as it is the only submarine for which a significant amount of data were available in the open literature. This because the DARPA SUBOFF model was developed as part of a research programme, which involved a significant amount of experimental testing and validation of the model. Data from the DARPA SUBOFF program, i.e., an extensive campaign of captive model tests, are publicly available

and are widely used to validate and improve CFD models for submerged bodies. The model provided by DTRC is an axisymmetric body, having a sail, four symmetric stern appendages in a cross configuration, and therefore, two horizontal stern planes and two vertical rudders (in the DTRC report, three different configurations related to the trailing edge position of the appendages are shown), and two configurations of ring wing (number 1 and number 2) supported by small struts in an "X" configuration. All the simulations present in this study consider the scale model, as in the experiments, at a model speed of 3.34 m/s, which corresponds to a Reynolds number (based on the length between perpendiculars) of about 14 million. According to DTRC experiments, the hydrodynamic force and moment coefficients show slight variations, becoming almost constant for values of Reynolds number above 14 million, meaning that the scale effects between model and full scale would be negligible for the purpose of making stability and control predictions. The main dimensions of the model and its reference system are given in Figure 8, whereas the equations used to design the geometry of the model can be found in the reference literature [21]. The adopted reference frame is centred about amidship along the symmetry axis of the hull (located at $x = 2.013$ m with respect to the aft perpendicular, see Figure 8, which corresponds to the mid distance between the two perpendiculars). The x-axis is positive, pointing towards the fore part of the submarine, the y-axis is pointing towards the starboard side, and the z-axis is pointing downwards. Angles β and α indicate the drift angle in the horizontal and the angle of attack in the vertical plane, respectively, whereas r and q are the angular velocities in the two planes. The submarine rotation, in the horizontal plane is positive for β towards the starboard side and α going upwards in the vertical plane. The measurements, as well as the outcomes of the numerical simulations, of the rudders and the sternplanes of the submarine are evaluated with respect to local reference systems. Angles δ_S and δ_R represent the sternplane (for vertical motions) and the rudder (for horizontal motions) angles, respectively.

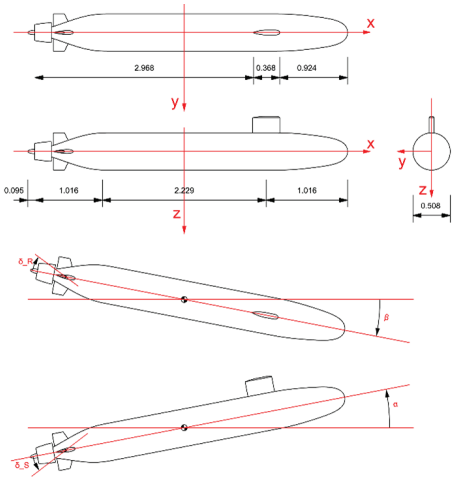

Figure 8. Main dimensions in meters of the DARPA SUB-OFF and reference system.

The forces collected and analysed in this study are the longitudinal force X, the lateral force Y and the vertical one Z, while the moments are K about the x-axis, M about the y-axis and N about the z-axis. The forces and moments are made non-dimensional as follows:

$$\begin{array}{lll} X' = \frac{X}{\frac{1}{2}\rho L^2 V^2} & Y' = \frac{Y}{\frac{1}{2}\rho L^2 V^2} & Z' = \frac{Z}{\frac{1}{2}\rho L^2 V^2} \\ K' = \frac{K}{\frac{1}{2}\rho L^3 V^2} & M' = \frac{M}{\frac{1}{2}\rho L^3 V^2} & N' = \frac{N}{\frac{1}{2}\rho L^3 V^2} \end{array} \quad (2)$$

where L is the distance between the perpendiculars (used also by DTRC) and V is the model scale velocity of experiments, equal to 3.34 m/s.

The tip of the submarine stern was truncated, considering a total hull length of 4.26 m, equal to the length between perpendiculars. The truncated part is 2.2% of the overall length of the UV. This simplification is also made to reduce the computational cost of the model; the tip is much smaller compared to the rest of the body, and a finer mesh would have been required in that region to represent the exact geometry. The truncation of the SUBOFF has been already used also in other studies [42–44] for the mounting of the sting support. For these reasons, the proposed simplification should affect in a negligible way the expected forces. Figure 9 shows the 3D model of the submarine with the truncated tip in the stern region used for the present CFD calculations.

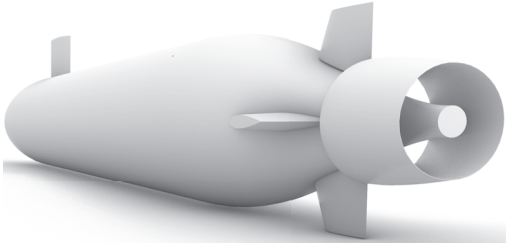

Figure 9. The truncated stern tip of the submarine.

Regarding the stern appendages (stern rudders, planes, and ring wing), as mentioned before, in the captive model experiments carried out by the DTRC institute, three different configurations were considered. Each one differs from the others by the axial position of both the rudders and "ring wing", as the nozzle surrounding the stern of the hull is called in the report of DTRC. In the current paper, the "baseline stern appendage location", using the ring wing number 1 with the trailing edge of the rudder at $x = 4.007$ m, is modelled. To further simplify the adopted geometry, the supportive struts of the wing have been neglected, as shown in Figure 10.

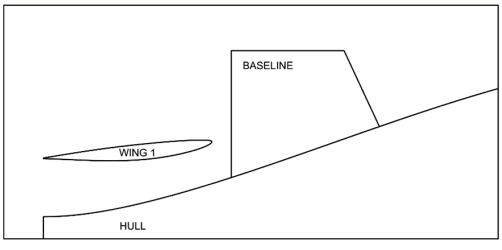

Figure 10. Section of the submarine and the used configuration of the ring wing (number 1).

To provide a sufficient gap for stern appendage movement, a slight offset of the appendages from the axisymmetric hull surface is introduced. It is quite interesting to take into consideration the possible effect that this gap might have on the stern appendages' performance. Since the correct layout of these appendages is not clear from the paper of Groves et al. [21], two different approaches (Figure 11) can be used for this offset: one by cutting with a straight line the root of the appendage, the other by shifting the appendage (then maintaining its initial span).

In Figure 12, the comparison between calculations of the two different configurations and the values measured from DTRC on the upper rudder are reported for the non-dimensional longitudinal and lateral force, respectively X' and Y'. As expected, the shifted version provides a higher force because it has a slightly bigger area (about 5%). Comparing

the measurements with the obtained CFD results for the two configurations, the truncated one gave more reliable results, and so it is used in the current study.

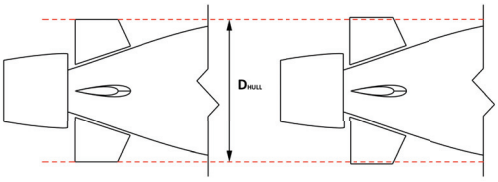

Figure 11. The two different possible solutions for the stern appendages' motion; on the right, the truncated, and on the left, the shifted solution; red dashed line shows the hull diameter.

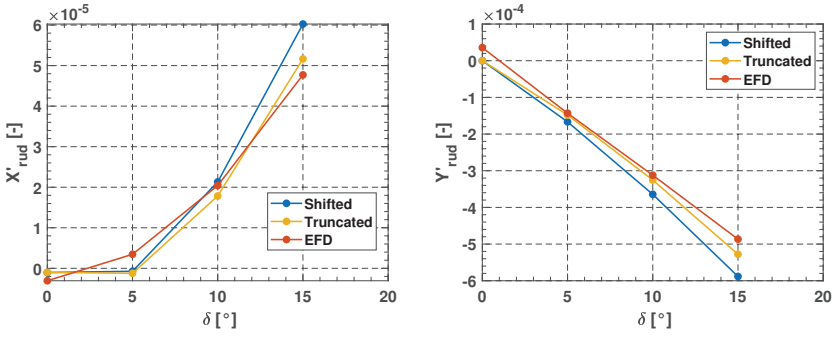

(**a**) (**b**)

Figure 12. Comparison between the two configurations of the stern appendages (shifted and truncated); fully appended, 0° drift; (**a**) longitudinal force; (**b**) lateral force.

A campaign of captive model experiments performed in the David Taylor Model Basin was conducted for both vertical and horizontal planes of motion at deep submergence. Captive model experiments were performed for different configurations of the submarine, never including the presence of the propeller. The investigated drift angles in the horizontal and vertical plane, as well as the rudder and sternplane angles are summarized in Table 3. Given the symmetry of the submarine, only the positive angles are used for the horizontal motions. In the vertical plane, both positive and negative angles are accounted for due to the asymmetry induced by the presence of the sail.

Table 3. Campaign of the captive model tests performed by DTRC, where *BH* is the barehull configuration; *BHS*, barehull with the sail; *BHSTAP*, barehull with stern appendages; *BHRIW*, barehull with ring wing 1 and *FA* the fully appended configuration.

Condition	Configuration	β [°]	α [°]	δ_R or δ_S [°]
Pure drift (Horizontal)	*BH*/*BHS*/*BHSTAP* /*BHRIW*/*FA*	0/+18	0	0
Pure drift (Vertical)	*FA*	0	−18/+18	0
Rudder Tests	*FA*	0	0	+5/+15
Combined Tests (Horizontal plane)	*FA*	0/+18	0	+5/+15
Combined Tests (Vertical plane)	*FA*	0	−18/+18	+5/+15

3. Numerical Model

To assess the reliability of a computational fluid dynamics analysis, two activities are essential: verification and validation. The former concerns the order of convergence with respect to the grid density and the associated numerical uncertainty, the latter the suitability of the mathematical model as a description of the physical problem. This section is divided into two parts: the first part presents the verification process realised using the kOmega SST turbulence model, and the the second half provides an analysis of the results obtained with different turbulence models.

3.1. Mesh Sensitivity Analysis

Regarding the verification, following Richardson's extrapolation and starting from the reference grid size (*gridII*), two additional grid sizes are defined, one coarser (*gridI*) and one finer (*gridIII*), having about 2*M* cells (*I*), 3*M* (*II*) cells and 7*M* cells (*III*). In Figure 13, the three different mesh grids are shown, and in Figure 14, detail of the refinement region closer to the hull is illustrated. All the meshes share the same arrangement of the refinements.

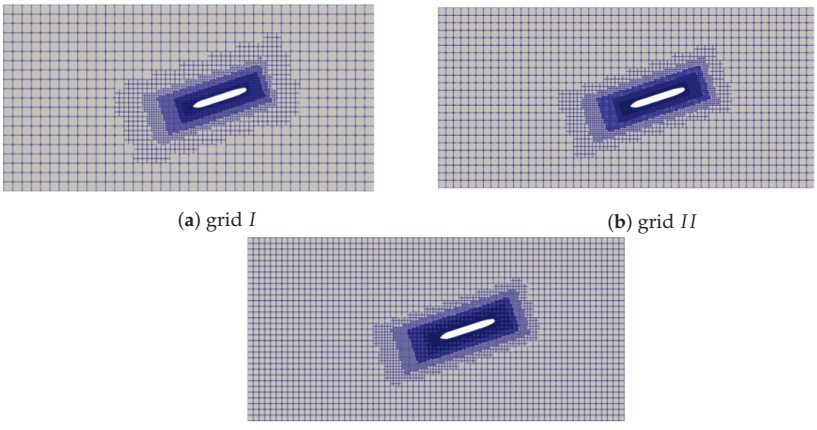

(**a**) grid *I* (**b**) grid *II*

(**c**) grid *III*

Figure 13. The three different mesh grids; (**a**) coarse; (**b**) base; (**c**) fine for 18° drift angle.

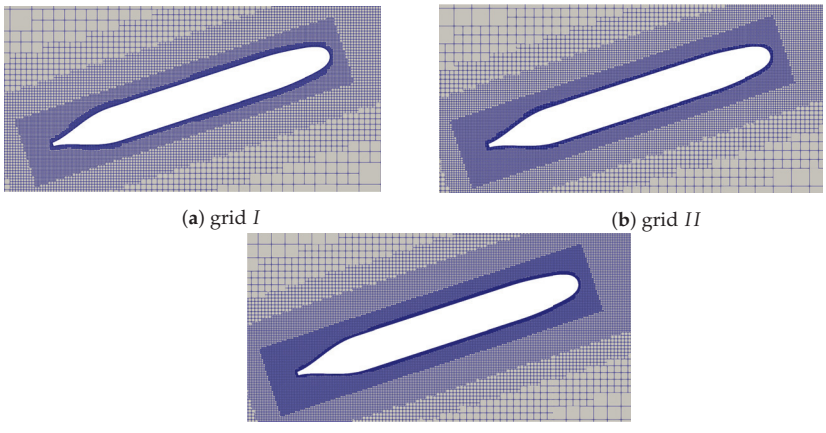

(**a**) grid *I* (**b**) grid *II*

(**c**) grid *III*

Figure 14. Detail of the refinement around the hull for the three different mesh grids; (**a**) coarse; (**b**) base; (**c**) fine for 18° drift angle.

The mesh refinement is achieved varying all the dimensions of the cells in order to obtain equally distributed smaller cells. The input sizes of the cells are such that the grid refinement factor $r = \frac{h_{coarse}}{h_{fine}}$ is greater than 1.3, as prescribed by the extrapolation procedure [45,46]. For this mesh analysis, three global quantities are considered (in non-dimensional form): axial force (X'), lateral force (Y') and moment about the z-axis (N'). To enlarge the analysis, all the different geometry configurations were explored for all the different angles present in the DTRC report. In Figures 15–17, comparisons between the three different grids, for the nondimensional quantities X', Y' and N' in the three different configurations BH, $BHSTAP$ and FA are collected.

Data showing the lateral forces and the yaw moments are almost insensitive to the mesh when using the coarser one where, in principle, higher discrepancies could be expected. The longitudinal component of force, differently, shows a slightly higher sensitivity to the mesh size. The numerical uncertainty originating from the spatial discretization is analysed and estimated according to the Richardson extrapolation, using the grid convergence index (GCI) as a parameters. This index is suggested by Roache to provide a consistent way to describe the findings of grid convergence studies. For the verification analysis, as the grid changes, the solution should not change much and should approach an asymptotic value. CGI is a measure of the percentage the computed value is away from the value of the asymptotic numerical value. Small values of CGI indicate that the computation is within the asymptotic range. The convergence index is calculated as follows:

$$GCI^2 1 = \frac{1.25 e_a^{21}}{r_{21}^p - 1}, \tag{3}$$

where the e_a^{21}, indicates the approximate relative error between the obtained values of a variable ϕ, important for the purpose of the simulation study:

$$p = \frac{1}{\ln r_{21}} \left| \ln \left| \frac{\epsilon_{32}}{\epsilon_{21}} \right| + q(p) \right| \tag{4}$$

$$q(p) = \ln \left(\frac{r_{21}^p - s}{r_{32}^p - s} \right) \tag{5}$$

$$s = 1 \cdot sgn \left(\frac{\epsilon_{32}}{\epsilon_{21}} \right) \tag{6}$$

where $\epsilon_{32} = \phi_3 - \phi_2$ and $\epsilon_{21} = \phi_2 - \phi_1$. Subscripts 1, 2 and 3 are associated to the three different grid densities used for this study, respectively $gridI$ (1), $gridII$ (2) and $gridIII$ (3). Equation (5) can be solved using fixed-point iteration, with the initial guess equal to the first term $(q(p) = 0)$. Tables 4 and 5 show the different values of GCI for the Y force and the N moment for the BH, $BHSTAP$ and FA configurations. These values of the grid convergence index, considered as an average of the values calculated for each angle included in the analyses, confirm the very good rate of convergence observed in the figures and permit the use of the base mesh ($gridII$) for all the subsequent analyses since results can be considered reasonably independent from the adopted mesh.

Table 4. Mean values of GCI of Y force, for 3 different configurations.

Configurations	GCI
BH	0.40%
BHSTAP	1.64%
FA	3.21%

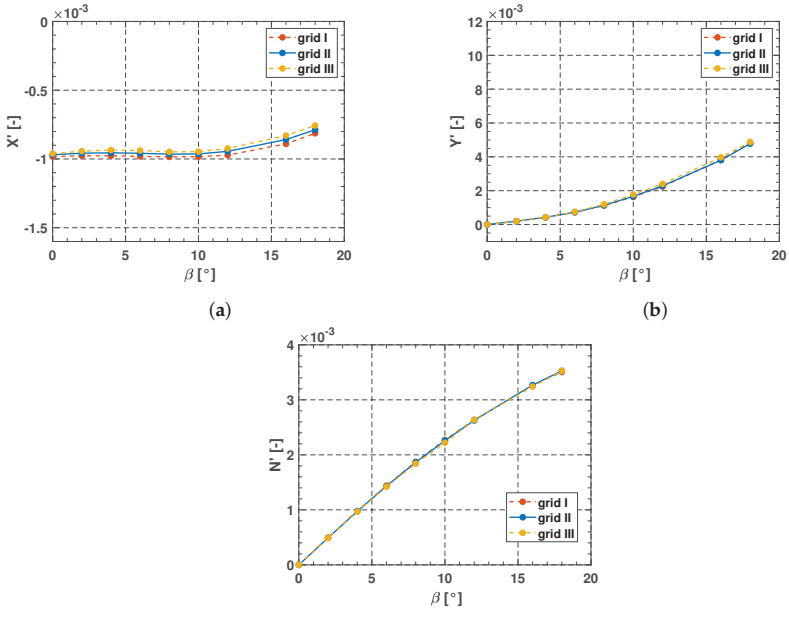

Figure 15. Values of X' (**a**), Y' (**b**) and N' (**c**) for the three different mesh grids, barehull configuration.

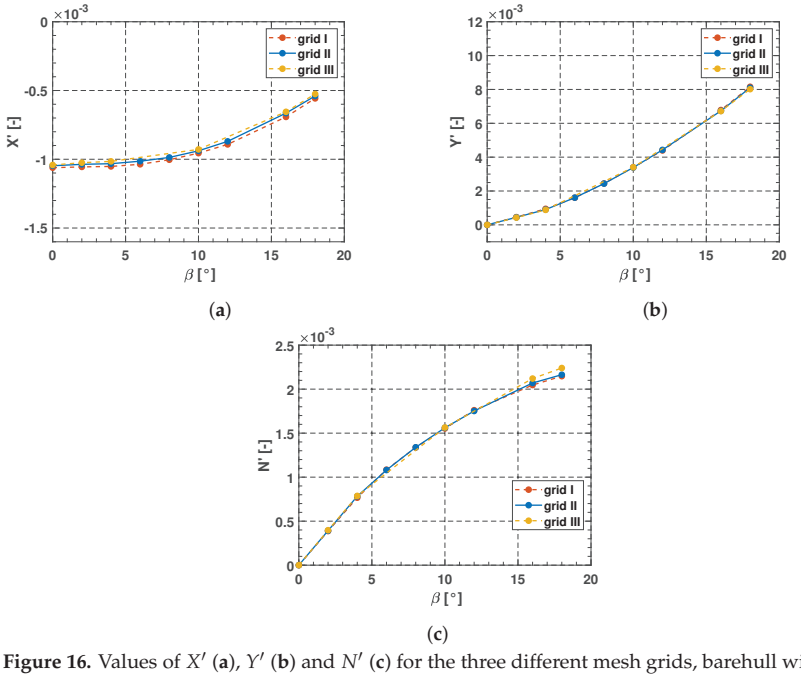

Figure 16. Values of X' (**a**), Y' (**b**) and N' (**c**) for the three different mesh grids, barehull with stern appendages configuration.

Table 5. Mean values of GCI of N moment, for 3 different configurations.

Configurations	GCI
BH	0.45%
BHSTAP	1.82%
FA	2.78%

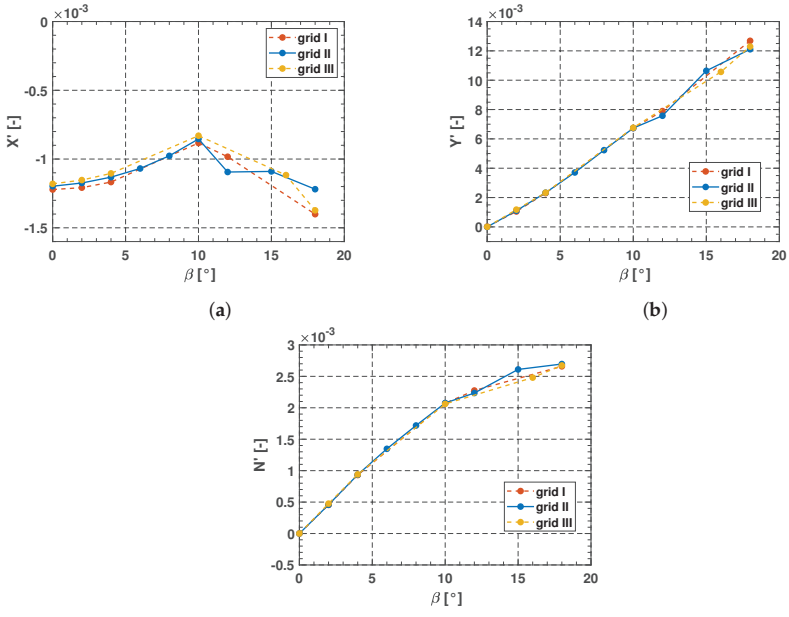

Figure 17. Values of X' (**a**), Y' (**b**) and N' (**c**) for the three different mesh grids, fully appended configuration.

3.2. Turbulence Model Analysis

In the preceding subsection, the effect of grid refinement on simulation accuracy was analysed. In this stage of the study, four different turbulence models present in OpenFOAM are examined, kOmega, kOmega SST, kEpsilon and realizable kEpsilon for the barehull configuration. Several turbulence models are known to forecast certain types of flows, such as boundary layers, shear layers, wake flows or rotating flows, better than others. It is apparent that, currently, there is no universally applicable turbulence model that can consistently and accurately predict all turbulent flow scenarios. As a result, it becomes imperative to validate the suitability of the chosen turbulence model for the particular flow being analysed. Table 6 shows the comparison between the different turbulence models and the data from the DTRC. The two kOmega models give similar results, as well as the two kEpsilon between them, with the kOmega models showing an estimated mean error of 19% and 7% for the lateral force and the yaw moment, whereas the kEpsilon show 10% and 2%, respectively. Thus, in the next sections, all results are obtained with kEpsilon-based models.

A possible explanation for the differences between the turbulence models and the experimental data may be found in the cross-flow separation. In Figure 18, it is evident how the surface pressure distribution and the cross-flow in the boundary layer varies by increasing the drift angle. In fact, in Figure 19, it can be noted how this phenomenon generates two symmetrical streamwise vortices, originating from the downstream side of the body. As the drift angle increases, these vortices become more prominent and extensive.

In general, previous numerical investigations of the flow around a prolate spheroid, similar to the geometry of the current submarine's hull, have observed similar effects [47–50].

Table 6. Comparison between the DTRC data and the predicted values of the lateral force Y' and the yaw moment N' for the different turbulence models; barehull configuration; three different drift angles $\beta = 4°, 6°, 18°$.

	$Y' \cdot 10^{-4}$			$N' \cdot 10^{-4}$		
	4°	**6°**	**18°**	**4°**	**6°**	**18°**
DTRC	4.49	8.86	73.55	9.96	13.85	29.86
kOmega	4.55	7.94	53.64	9.57	14.03	34.77
kOmegaSST	4.27	7.29	47.79	9.73	14.34	35.27
kEpsilon	4.63	8.00	59.66	9.52	13.97	33.46
realizable kEpsilon	3.97	8.77	61.39	9.66	13.70	32.64

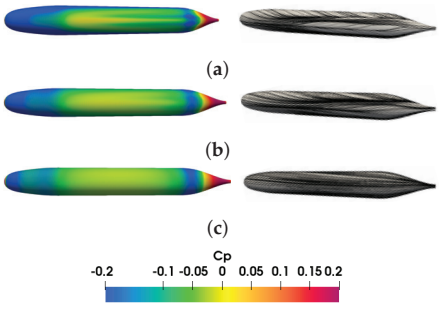

Figure 18. Surface pressure contours and limiting-wall streamlines on the bare hull for three different drift angles $\beta = 18°$ (**a**), 10° (**b**) and 4° (**c**).

The vortices are illustrated in Figure 19 using an iso-surface of the second invariant of velocity, found in the literature as "Q-criterion" [51]. From the physical point of view, the flow around the barehull configuration after a transient phase starts separating in two counter rotating vortices on the downstream side of the hull. This phenomenon is well captured by the CFD predictions. Nonetheless, small errors in the estimation of the starting point of the flow separation might lead to important errors in the description of the pressure, in the velocity fields around the body, especially in large drift angle configuration, where these phenomena become more prominent.

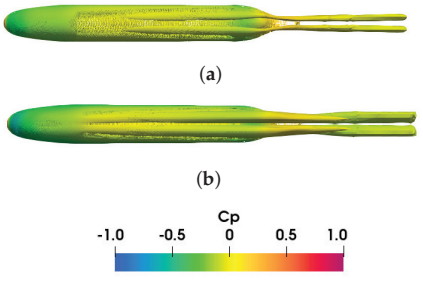

Figure 19. Iso-surface of Q coloured by pressure coefficient magnitude for the barehull configuration, for two different drift angles 10° (**a**) and 18° (**b**).

A closer look at the vortices region shows the same results as Kotapati et al. [48] and Subrahmanya et al. [49] (Figure 20). For small drift angles, Figure 20a shows the vortices are

close to the hull, having a flat elliptic shape. As the drift angle increases and moves closer to the stern, the vortex starts detaching from the body, increasing in size and becoming more circular (Figure 20c).

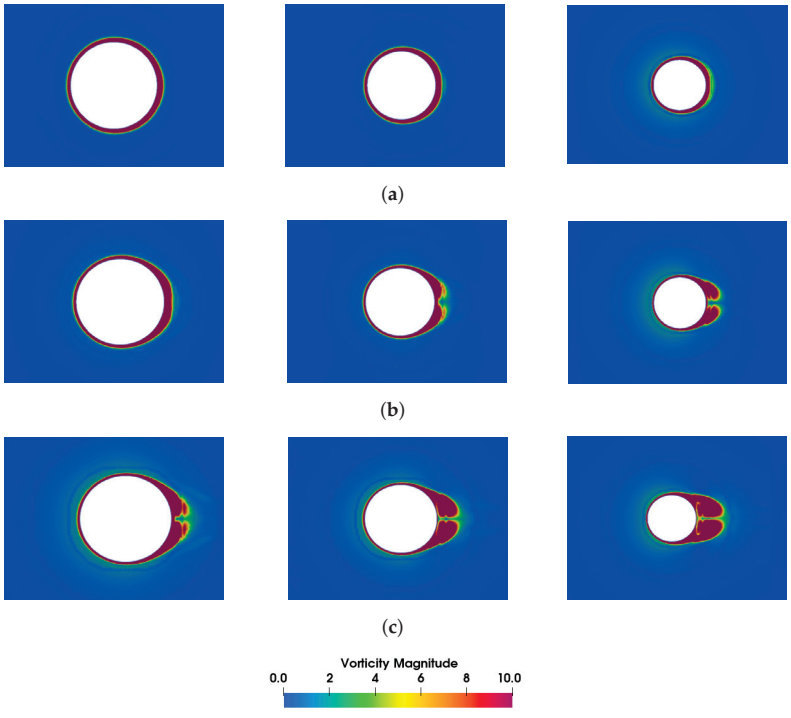

Figure 20. Vorticity around the axisymmetic hull for drift angle values of 4° (**a**), 10° (**b**) and 18° (**c**), sections at 0.55L, 0.35L and 0.15L.

Figure 21 shows the vorticity around the axisymmetric hull modelled with four different turbulence models, kOmegaSST, kOmega, kEpsilon and realizablekEpsilon. It is clear how similarly the two initial turbulence models represent the shaded vortices. However, there are some minor variations, such as the vorticity magnitude in the core of the vortex, which causes the yellow and red scale zones to enlarge slightly. The vortices grow bigger and farther out from the body and from one another. In contrast, the kEpsilon models seem more complex and detailed, with more irregularities and small-scale features, whilst the kOmega models seem smoother and simpler.

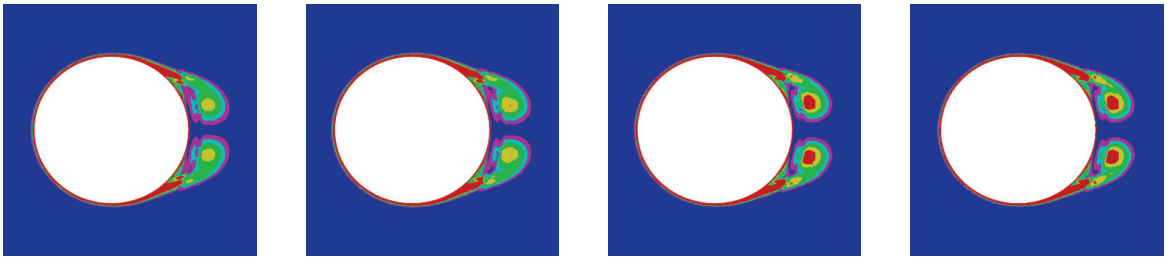

Figure 21. Vorticity around the axisymmetric hull modelled with kOmegaSST and kOmega (**a**,**b**); kEpsilon and realizablekEpsilon (**c**,**d**) for 18° drift angle.

The prominent part of this investigation lays in the impact that these models have on the sectional forces. The submarine was divided into 100 transversal sections, and the forces acting in each section were measured. Figure 22 shows the sectional lateral force coefficient C_y for the different turbulence models.

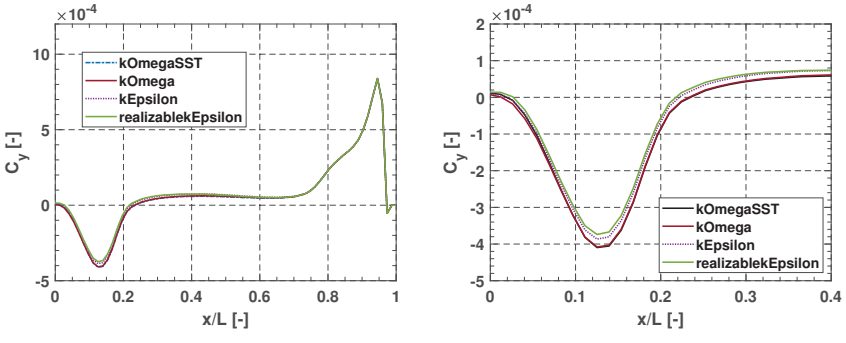

Figure 22. Comparison between the sectional forces of the simulations with the different turbulece models for 18° drift angle (**a**); (**b**) A closer look at the region where the main differences are present.

Observing the values in Table 6 and the trends in Figure 22, it is evident how the closer the outcomes are to the experimental data, the less the negative force in the stern region. This observation validates the initial hypothesis of the authors, that the magnitude of the force at the stern is overestimated by the initial simulations. These findings may also provide insight into how slight alterations in the pressure field may have a substantial impact on the intensity and location of the subsequent forces. This is primarily, because, during the manoeuvre, the difference between the positive bow force and the negative stern component causes the later force. As a result, a tiny disparity that is localised on the pressure field has a significant impact on the forces as a whole. In a previous study [39], the pressure and wall shear stress distribution around the underwater vehicle were also illustrated, giving a hint about the small influence that the wall shear stress might have on the lateral forces.

4. Results: Pure Drift Tests

In the present section, the results of the CFD simulations are collected and compared with the available experimental measurements. In the current study, the measurements conducted by DTRC are exploited for benchmarking purposes. For the validation of the CFD predictions, all the pure drift and rotation conditions are taken into consideration in both the horizontal and vertical planes, inclusively of the pure rudder and sternplane angles tests, as well as the combined tests. The analyses have been carried out for all the configurations tested in the towing tank to deliver an assessment as wide as possible of the accuracy of CFD calculations in the prediction of hull, appendages and ring wing contributions to UV forces and moments.

4.1. Barehull Configuration

Figure 23 shows the comparison between the numerical simulations of the current study and measurements from the experiments of the DTRC. The outcomes of the experimental tests are in orange; a blue line identifies the numerical calculations while a dashed red line represents the linear part of the experimental data as specified in the DTRC report. Numerical results show that the trends between the experimental and the computed data are in good agreement, especially the linear part of the lateral forces and yaw moment.

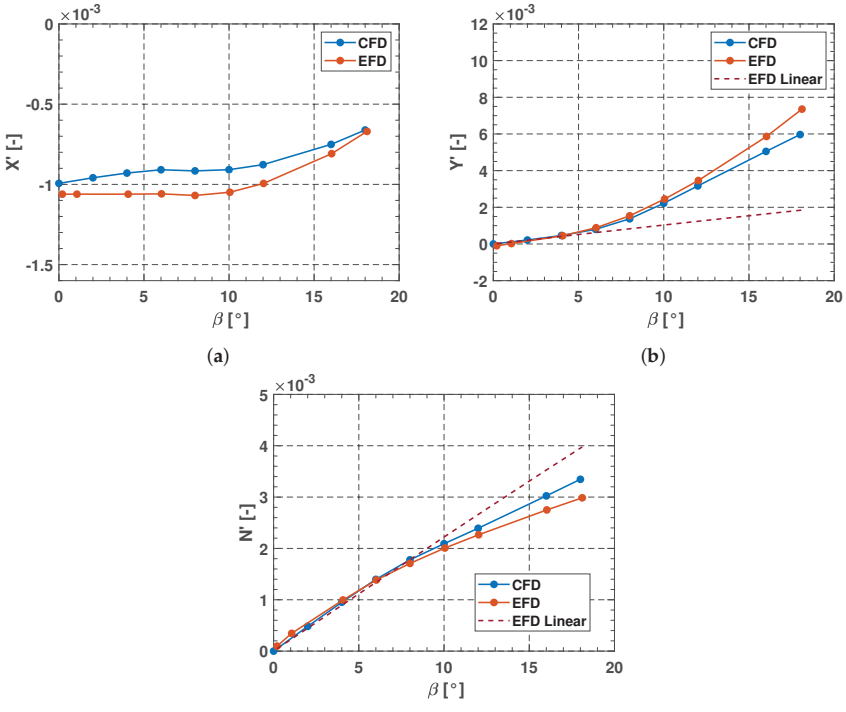

Figure 23. Comparison between the numerical results (blue) and experimental data (orange) of X' (**a**), Y' (**b**) and N' (**c**) for the barehull configuration. The linear component is shown in dashed red line.

For drift angles higher than 6°, nonlinear phenomena become more notable, leading to a gap between the measured and the predicted curves. Similar to the results obtained by Subrahmanya et al. [49], the force Y' is underestimated compared to the experimental data (Figure 23b), whereas the moment is slightly overpredicted (Figure 23c), even though the trend in both cases is well predicted. To sum up, the quality of simulation results is very good in terms of linear derivatives, but with not negligible differences in the nonlinear range. Nevertheless, as it will be stated in the next sections, this mismatch becomes minor when considering the hull with appendage configurations that are close to real shapes, so in line with the design perspective.

4.2. Barehull with Ring Wing

Figure 24 compares measurements and calculations in the case of the barehull with the ring wing. Qualitatively, the CFD calculations follow the physics of the phenomenon. The presence of the ring wing leads to an increment of the lateral forces compared to that of the barehull alone (see Figure 25). For both experimental data and CFD predictions, there is an increment of about 10% of the maximum value of the lateral force between the BH configuration and the BHRIW [52,53]. The CFD results slightly overpredict the effect of the ring. This can be mainly ascribed to the fact that its presence has an impact on the region that was affected by the previously noted differences in the lateral forces. As in the previous case, the linear part is well captured by the simulations, while some differences in the nonlinear part still remain observable.

4.3. Barehull with Stern Appendages

In Figure 26, the forces and moments predicted for the configuration with stern appendages are illustrated. It is clear how the CFD calculations, as far as the lateral forces

are concerned, show a better agreement with measurements for drift angles up to 10°. Also, the results of the yaw moment for this configuration are better if compared to those obtained for barehull or barehull plus ring wing configurations, with the estimated values able to capture in an excellent way the experimental data almost in the whole range of variation of the drift angle. Overall, for this configuration, the non-linear part is also predicted with an acceptable accuracy.

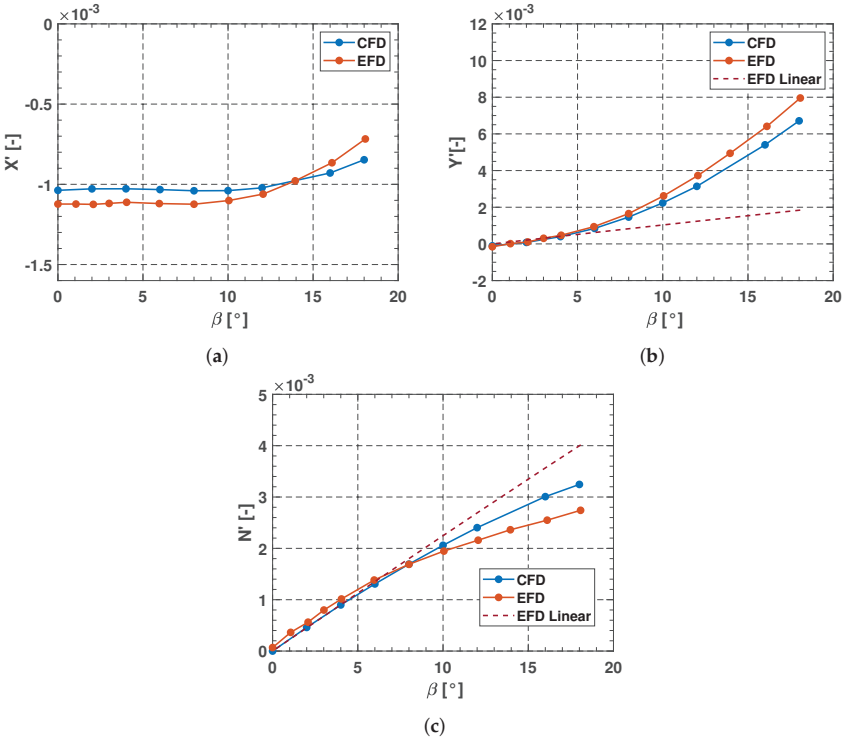

Figure 24. Comparison between numerical results (blue) and experimental data (orange) of X' (**a**), Y' (**b**) and N' (**c**) for the barehull with ring wing configuration. The linear component is shown with dashed red line.

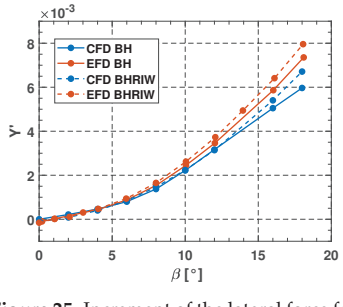

Figure 25. Increment of the lateral force for both the numerical simulation (blue) and the experimental data (orange) due to the presence of the ring wing.

From this standpoint, the significant improvement in the results could be related to the presence of the rudders and sternplane surfaces. The stern appendages have an impact on the pressure fields in that region, reducing the influence and the intensity of the streamwise

vortices generated in the barehull configuration. In Figure 27, the vortices generated on the two configurations are compared.

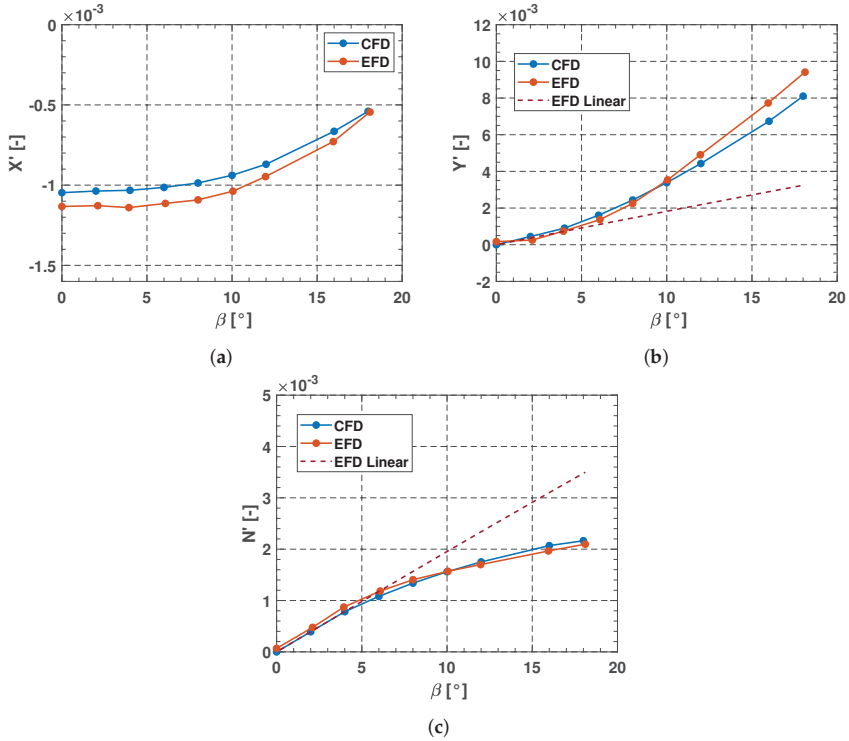

Figure 26. Comparison between numerical results (blue) and experimental data (orange) of X' (**a**), Y' (**b**) and N' (**c**) for the barehull with stern appendages configuration. The linear component is shown with dashed red line.

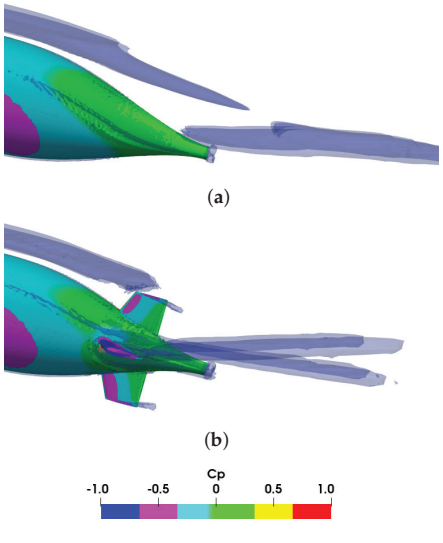

Figure 27. Iso-surface of Q, hull coloured by pressure coefficient magnitude for two different configurations *BH* (**a**) and *BHSTAP* (**b**).

A further investigation is illustrated in Figure 28, considering the sectional forces already defined in Section 5.1. The non-dimensional coefficient of the lateral force for both configurations, *BH* in blue and *BHSTAP* in orange, are compared along the submarine. The reduction in the negative lateral force can be noticed in the stern region where the appendages are present. In this way, the previously mentioned error becomes less important in the definition of the overall hull lateral force and yaw moment, improving, consequently, the agreement with experiments.

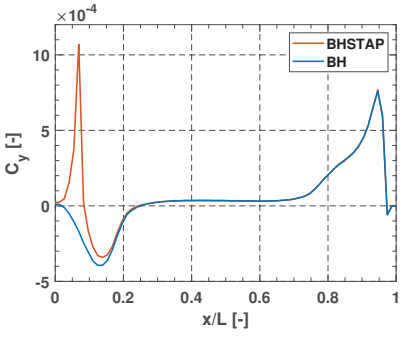

Figure 28. Comparison between the lateral forces for the two different configurations: *BH* (blue) and *BHSTAP* (orange) for 16° drift angle. C_y is the lateral force coefficient.

4.4. Barehull with Sail

As in the previous cases, a good agreement with the experimental data can be noticed from Figure 29 when the sail is included in the analyses. However, a limitation of RANS CFD simulations becomes manifest in the early-stalling phenomenon of the sail (and airfoils in general, as shown in similar cases in [29,52]). For this reason, Figure 29b shows with a purple line (with triangular marks) the impact of the linearization of the sail contribution on the total lateral force, neglecting the possibly erroneous non-linear stall prediction. Linearization is obtained following the procedure devised in Franceschi et al. [29]. With this assumption, the total value of the lateral force acting on the submarine is predicted with a higher accuracy.

As the reference system is that of the hull, in Figure 30, the total axial force is projected in the direction of the drag and the lateral force acting on the sail in that of lift. It is clear how after the 10° of drift angle, the lateral force acting on the sail drops, losing its linear trend, clearly indicating the sail stall. At the same angle, in Figure 29a, where the X' force is shown, the trend of the predicted force changes, compared to the experimental one, and starts decreasing earlier, whereas this occurs at 16° for the experimental data. Without the experimental values for the forces acting on the sail, the previous facts can lead to the hypothesis that at drift angle 16°, the sail stalls experimentally, showing also the influence of the sail stall on the longitudinal force. The axial force when projected in the drag direction continues increasing after the stall point, as expected for an airfoil; this is a phenomenon that cannot be appreciated in Figure 29.

The virtual stalling of the sail can be visualized also in Figure 31, where, as in the previous section, the Q-factor was used to visualize the location of the vortices and the stalling of the sail. For the two considered angles (16° and 18°), the sail tip vortex is reduced and a vast region on the back of the profile is covered by a strong recirculation phenomenon. This behaviour shows the presence of a stalled profile. It is interesting to note that in the previous section, when the rudders and the sternplanes are considered, no stall phenomena were mentioned. This different behaviour can be ascribed to the straightening flow effect induced by the hull in its stern region, which reduces the effective rudder angle to the lifting surfaces.

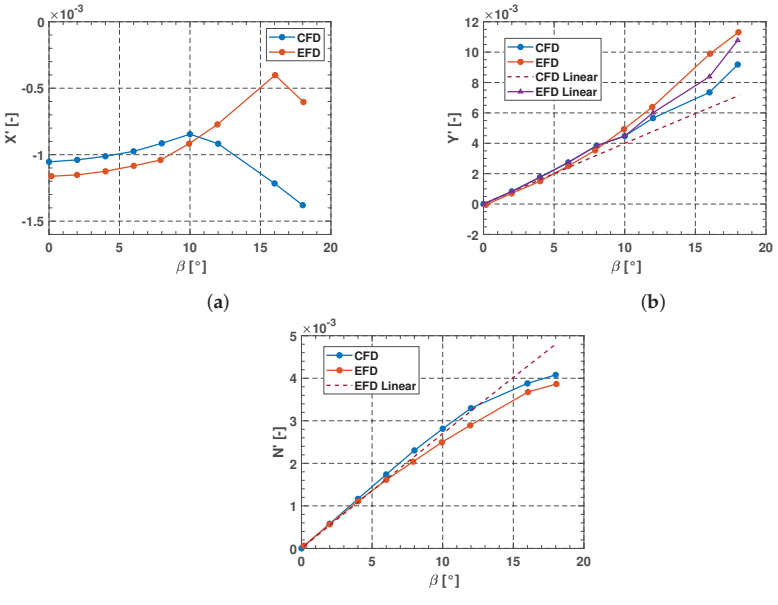

Figure 29. Comparison between numerical results (blue) and experimental data (orange) of X' (**a**), Y' (**b**) and N' (**c**) for the barehull with sail configuration. The linear component is shown with dashed red line.

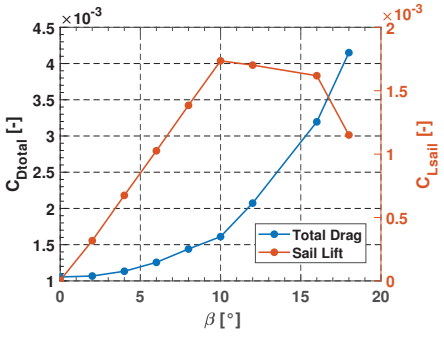

Figure 30. Projected total drag and projected sail lift.

With all the above in mind, the quality of the simulations can be anyway considered satisfactory as a practical compromise between computational effort and accuracy. This is in line with the aim of CFD-based captive model tests, which are used to extract data (as the hydrodynamic coefficients) to be adopted in a lumped parameter simulator [54].

4.5. Fully Appended Configuration

The fully appended results are summarized in Figure 32. As in the configuration with the sail, in this case the trend of the CFD simulation data also shows that the sail still stalls at smaller drift angles with respect to the experimental evidence. Nonetheless, in this configuration, which is also the operating configuration of a real underwater vehicle, there is a very good agreement between calculations and experiments. This may be naturally explained according to the huge relevance and lift effectiveness of the stern rudders and planes in terms of manoeuvring forces with respect to the slender hull and sail shapes. A satisfactory matching of the lateral force and yaw moment can be observed, especially

for smaller drift angles. As mentioned before, the sail stalling occurs earlier for the CFD predictions compared to the experimental data.This gives us a hint that the discrepancy between the experimental and the predicted values of the longitudinal force X, for angles greater than 10° (which is the same angle of the numerical stalling of the sail), may be caused by this exact phenomenon. Of interest for further investigation is the case in which the numerically obtained lift of the sail continues its linear trend, and thus a projected contribution of the force on the x-axis is present. Nonetheless compared to the barehull with sail configuration the differences in the Y and N components in this case are relatively less relevant due to the high influence of the stern appendages. The CFD modelling deficiency remains evident in terms of longitudinal force according to the sudden drop of the lift induced quadratic drag.

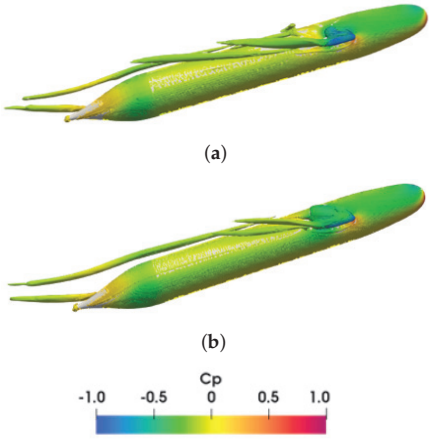

Figure 31. Iso-surface of Q by the pressure coefficient magnitude for two different drift angles $\beta = 16°(a), 18°$ (b), for the BHS configuration.

In addition to the in-plane manoeuvring forces and moments, the out-of-plane components were also investigated, with an eye to the so-called stern dipping phenomenon [55,56]. Figure 33 shows the comparison between the predicted and the measured out-of-plane force Z', roll moment K', and pitch moment M' acting on the fully appended submarine owing to the horizontal drift attitude. The out-of-plane loads are due to the lifting properties of the sail, which, owing to the tip vortex shedding, induce a crossflow braking element of the circulation around the hull aft the sail. This reduces the average crossflow velocity above the hull, thus increasing the pressure, and generates a stern down force. It is evident from the figure that the CFD simulations are successful in describing both the trend and the values of the experimental data, especially for small drift angles. The stall of the sail can be still observed in terms of roll moment drop.

For the fully appended configuration, apart from horizontal drift angle, tests with vertical drift angle (angle of attack) were also conducted. In Figure 34, the predicted forces X', Z' and moment M' about the y-axis are compared to the experimental data. It should be recalled that, in this case, the sail is a symmetry-braking element, but it is not acting as a lifting surface, and thus early stall issues are expected to be eliminated; the test matrix considers both the positive and negative angle of attack in order to capture the above mentioned asymmetry, even if minor differences are visible. In this case, no particular differences can be observed in terms of longitudinal force X', due to the non-lifting condition of the sail; the initial drag bias is maintained all over the drift range, with discrepancies increasing at higher drift angles. The Z' and M' the predictions satisfactorily match the experiments until 10°. The linear part of the experimental measurements, shown in the graphs with the red dashed line, is well captured by the CFD simulations as it is evident from Figure 34b,c. The non-linear discrepancies at the higher angles could be

ascribed to the previously mentioned problem of the pressure recovery in the stern region; in fact, the numerical/experimental gap is of the same order and behaviour of the one shown for the barehull with only rudder configuration.

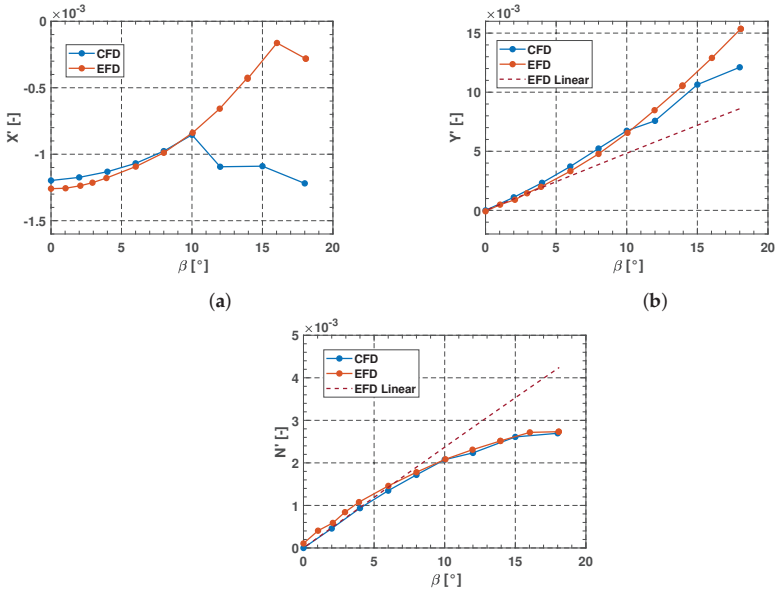

Figure 32. Horizontal plane. Comparison between numerical results (blue) and experimental data (orange) of X' (**a**), Y' (**b**) and N' (**c**) for the fully appended configuration. The linear component is shown with dashed red line.

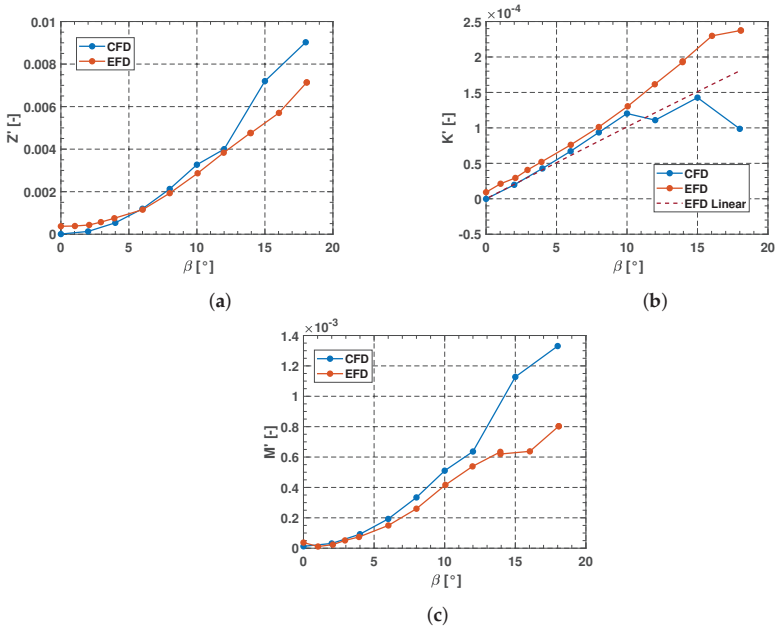

Figure 33. Out-of-plane components for the *FA* configuration with several drift angles; (**a**) vertical force; (**b**) rolling moment; (**c**) pitching moment

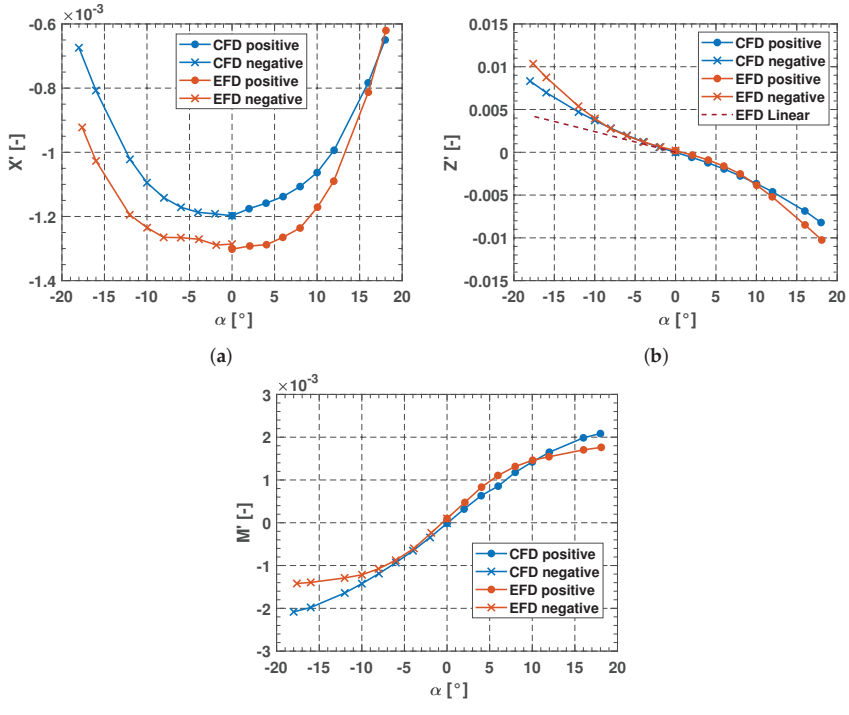

Figure 34. Vertical plane. Comparison between numerical results (blue) and experimental data (orange) of X' (**a**), Z' (**b**) and M' (**c**) for the fully appended configuration. The linear component is shown with dashed red line.

5. Results: Rudder Tests—Fully Appended Configuration

In Figure 35, the results of the rudder tests conducted at DTRC and the CFD simulations are set side by side. The experimental tests include both the total forces acting on the fully appended submarine with rudder δ_r or sternplane angles δ_s (Figure 35), as well as those acting on the single fin (Figure 36). Pressure taps were installed in the upper rudder and the sternplane rudder, thus enabling the verification of the wing–body interactions according to the CFD methodologies.

Both positive and negative angles were investigated by DTRC but given the symmetry of the submarine in the horizontal plane, the outcomes of the two measurements should theoretically match. The remaining differences between the outcomes of the two ranges might be considered an estimation of experimental uncertainty.

From Figure 35, it can be noticed how the simulation results fall within that uncertainty, both in terms of longitudinal X' and steering force Y'. Overall, the trend of the experimental outcomes is well captured by the CFD simulations. By looking at the single upper rudder measurements, reported in Figure 36, a good correspondence is visible, allowing a satisfactory validation of the methodology. It is quite curious that the value of the X' force for 5° of rudder angle is very similar to the case of no rudder angle. For the sake of the direct comparison between the predicted and the measured forces acting on the rudders, the former values were rotated from the body frame of reference to the normal and chordwise directions of the control surface, where the measurements were conducted. The rotation of such values might be the possible justification for the values of the longitudinal force on the upper rudder for $\delta_R = 5°$. Anyway, the most important force component during a manoeuvre is the lateral one, which is accurately predicted. This

rotation has an impact also on the Y' force, but its magnitude is negligible, compared to that on X'.

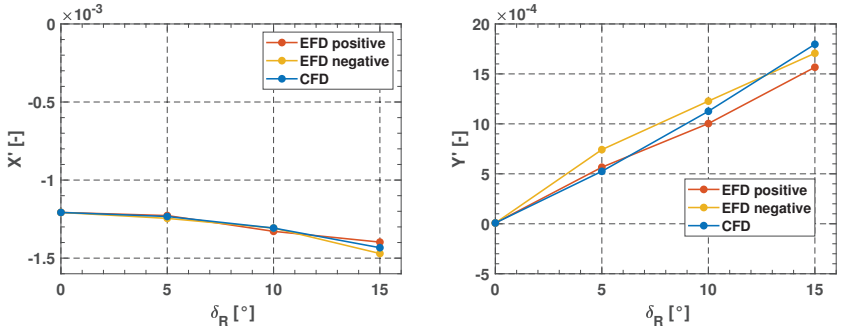

(**a**) (**b**)

Figure 35. Comparison between the numerically estimated values and the experimental data of the acting forces X' (**a**), and Y' (**b**) on the fully appended configuration for different rudder angles (δ). Experimental data for both positive (orange) and negative (yellow) rudder angles.

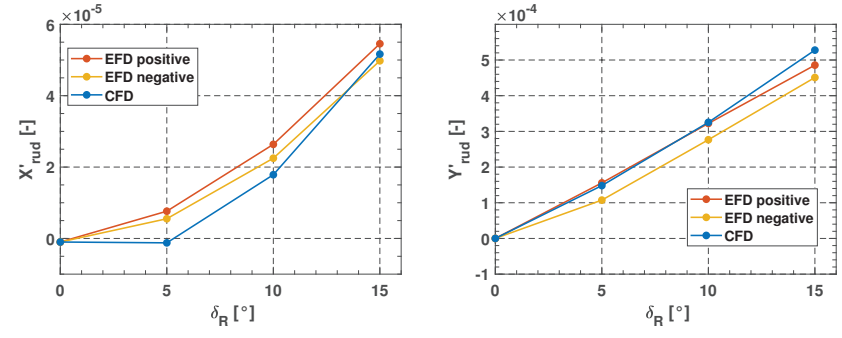

(**a**) (**b**)

Figure 36. Comparison between the numerically estimated values and the experimental data of the forces X'_{rudder} (**a**), and Y'_{rudder} (**b**), acting on the upper rudder of the fully appended configuration for different rudder angles (δ_R).

According to the previous observations, an interesting aspect of the investigation concerns the evaluation of the wing–body interaction at the stern. This can be studied according to the comparison between the total forces acting on the submarine and the isolated sum of those on the upper and lower rudders. Figure 37 shows in orange the sum of the lateral forces on the upper and the lower rudder and in blue the total lateral force on the submarine (both values are from CFD calculations).

This figure clearly shows how the pressure field on the stern appendages has an impact on the hull as well, leading to the generation of lateral forces on it. This amplification phenomenon is well known in the literature, especially in the case of small stern body radii with respect to the wing planform [54,57,58]. In the current analysed case, these hull amplification forces account for about 50% of the rudder forces. Therefore, the phenomenon heavily affects the manoeuvring in terms of global control forces; the correct capturing of this aspect is thus fundamental for the early design stage study of an underwater vehicle.

Switching to the vertical manoeuvring plane, Figure 38 and Figure 39 show, respectively, the total forces X' and Z' relevant to the stern planes execution, as well as the X'_{rudder} and Z'_{rudder} referring to the forces acting on the portside sternplane alone. The prediction of the longitudinal force shows a better accuracy in terms of global force with respect to the

single fin case, whereas the vertical force has a good accuracy for both cases. Again, the overall trend of the experimental data is well described by the simulation outcomes.

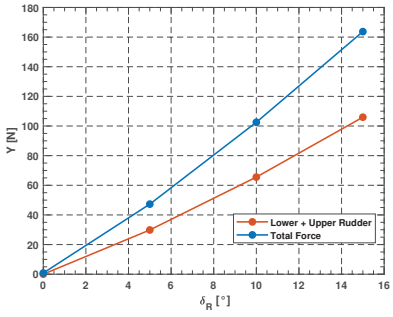

Figure 37. Comparison between the sum of the lateral forces acting on the two rudders (orange) and the total lateral force acting on the submarine (blue) for the *FA* configuration.

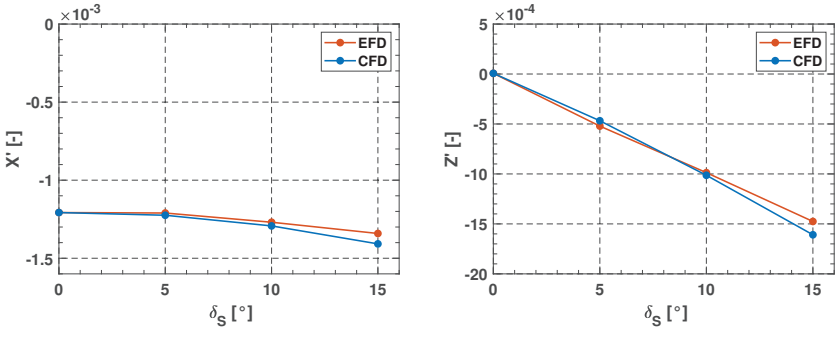

(**a**) (**b**)

Figure 38. Comparison between the numerically estimated values and the experimental data of the acting forces X'_{rudder} (**a**), and Z'_{rudder} (**b**), on the fully appended configuration for different sternplane angles (δ_S).

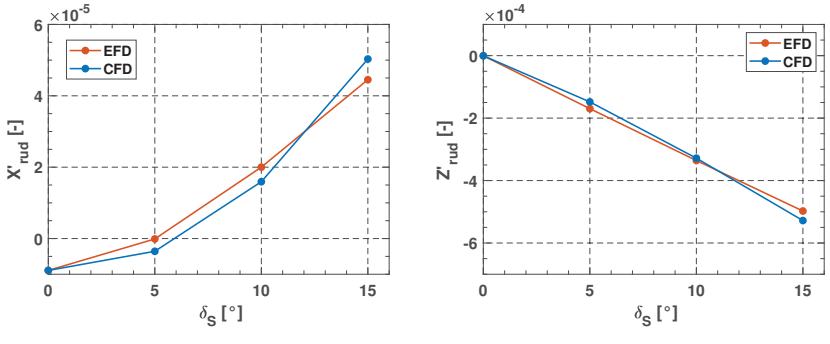

(**a**) (**b**)

Figure 39. Comparison between the numerically estimated values and the experimental data of the forces X'_{rudder} (**a**), and Z'_{rudder} (**b**), acting on the portside sternplane of the fully appended configuration for different sternplane angles (δ_S).

Also, in this case, the total vertical force Z is higher than the sum of the vertical forces acting on the sternplanes, as reported in Figure 40, with a similar amplification factor.

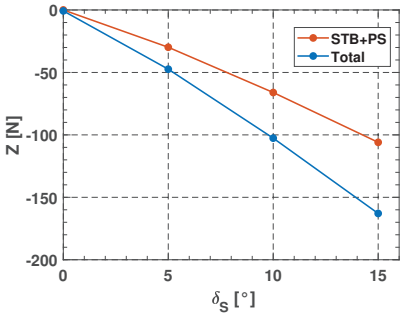

Figure 40. Comparison between the sum of the vertical forces acting on the two rudders (orange) and the total vertical force acting on the submarine (blue) for the *FA* configuration.

Finally, combined rudder and drift tests were considered, as reported in Figure 41. The values of the forces measured by simulations have the same trend observed in experiments, and the linear behaviour of the combined tests is well predicted. The discrepancies between the predicted and the measured data, for 0°, are those already discussed, even though in this illustration they appear more marked. Considering the aim of the captive model tests, the rudder hydrodynamic derivatives are well captured, no matter the reported discrepancies when the rudder angle is zero.

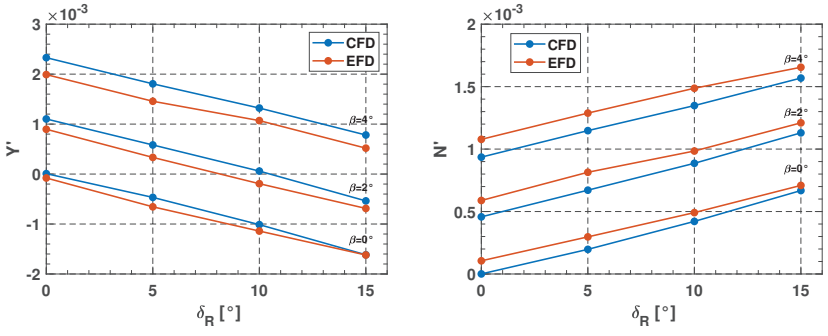

(**a**) (**b**)

Figure 41. Comparison between predicted and experimentally measured values of non-dimensional lateral force Y'_{rudder} (**a**), and moment N'_{rudder} (**b**), for *FA* configuration, for different drift angles (β) and rudder angles (δ_R).

5.1. Results: Pure Rotation

CFD predictions were also carried out for the pure rotation case. Both the vertical and the horizontal plane cases were investigated. The results are compared with the angular velocity derivatives reported in Roddy [22]. Unfortunately, complete experimental measurements were not available for a systematic comparison, and only linear trends were considered. Figure 42 and Figure 43 (for the horizontal and vertical plane, respectively) show the results obtained from the numerical simulations (in blue) compared to the experimental data (in orange). Small differences between the predicted values and the pure linear trend obtained by the derivative can be noted for the moments N' and M' and for the vertical force Z'. The vertical force and the two moments, differently from the lateral force, are characterized by limited nonlinear parts. Globally, the overall agreement is very good also for the rotation cases. This, furthermore, enhances the reliability of the proposed numerical procedure to feed a manoeuvring simulator for UVs.

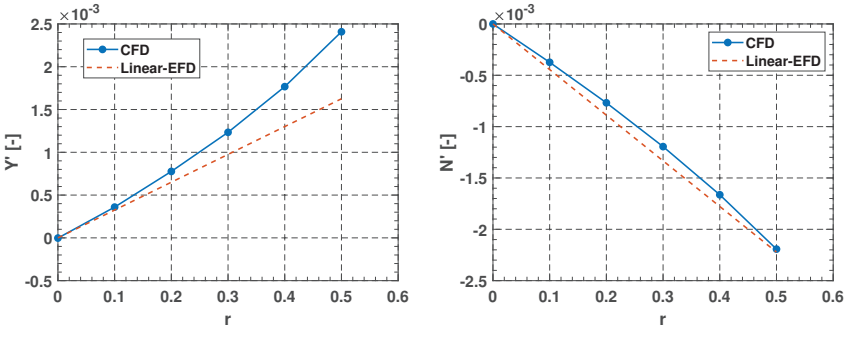

Figure 42. Comparison between CFD predictions and the experimental data for different angular velocity values in the horizontal plane; (**a**) lateral force; (**b**) yaw moment.

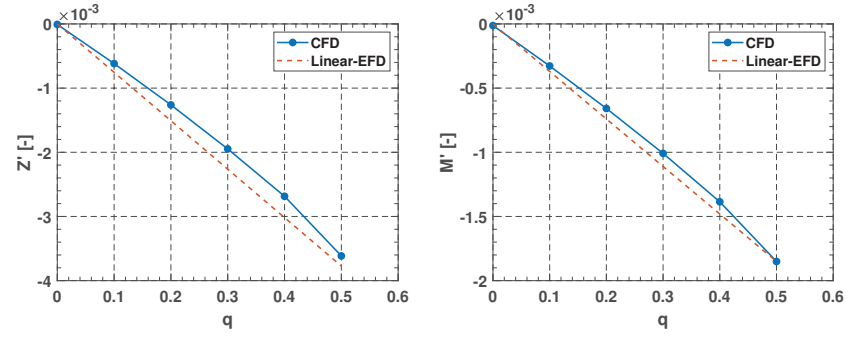

Figure 43. Comparison between CFD predictions and the experimental data for different angular velocity values in the vertical plane; (**a**) vertical force; (**b**) pitching moment.

6. Conclusions

In the current study, an extensive validation of RANS methodologies for the prediction of the hydrodynamic coefficients of the DARPA SUBOFF in five different configurations, corresponding to BH, BHS, BHSTAP, BHRIW, and FA underwater vehicles, is presented. Pure drift and rotation tests (in the horizontal and vertical plane) were investigated, as well as pure rudder or sternplate angles tests and some combined drift and rudder tests, consistently with captive model experiments conducted by DTRC [22]. The aim of this study was to consolidate the reliability of the CFD simulations to predict the hull and the appendages forces during a manoeuvre of underwater vehicles with an eye to a modular approach of each single hydrodynamic component.

The open-source OpenFOAM software was successfully employed. Three different meshes were used to verify the grid sensitivity, showing a good convergent trend of the global forces already with a quite low demanding mesh arrangement of about 3 million cells, representing a good compromise between the computational time and the accuracy of the results. The expected uncertainty for the most important manoeuvring forces is within 2%, with a slightly lower performance for the fully appended configuration about 3%.

The results of the horizontal and vertical drift and rotation cases showed an overall good agreement with the experimental data. The linear part is captured in an excellent way from the results of the simulations in all the horizontal and vertical plane cases, considering both in- and out-of plane components (the latter generated by the sail effect). Regarding the barehull configuration, two streamwise vortices were noticed to have an important impact on the non-linearities present in the bare hull results in the drifting attitudes, when the stern

appendages are not installed. An increment of the lateral force for both experimental and numerical results occurs when the ring wing is present. The stall of the sail when dealing with the barehull with sail configuration occurs numerically earlier than in the experiments (approximately at 10°); this might be the cause of the discrepancies in the longitudinal force. Further investigation is needed in this direction. These differences are present also in the fully appended configuration; however, compared to the barehull with sail case, these are relatively less relevant due to the high influence of the stern appendage. Nevertheless, the X force, when dealing with manoeuvring simulators, is not so relevant as most of the time, it is calculated separately. The numerical results for the rudder tests capture well the trend of the experiments, enabling the assessment of the control forces, including the hull–wing amplification interactions. This aspect is worth studying deeply in further research; in fact, it has a significant impact on the manoeuvring ability of a submerged vehicle.

The expected errors between the measured data and the predictions for the fully appended configuration are within 5% for the linear part and 15% for the higher drift angles. From an engineering point of view, this makes the approach reliable, as the operating configuration of a submarine is the fully appended one. In conclusion, the proposed numerical methodology allows a proper assessment of both the linear stability and controllability features of an underwater vehicle with respect to both the manoeuvring planes. Further investigation is needed in order to build high confidence in such methods for the early-stage design of an underwater vehicle, especially in the wider nonlinear ranges of motion. Different turbulence models should be investigated in order to better capture and describe the generated vortices while manoeuvring, especially for the barehull configuration. This further analysis requires the availability of more experimental data on different geometries.

Author Contributions: Conceptualization, D.V., B.P., S.G. and M.V.; methodology, D.V., B.P., S.G. and M.V.; data curation, V.V.Z.; writing—original draft, V.V.Z.; writing—review and editing, D.V., B.P., S.G. and M.V. All authors have read and agreed to the published version of the manuscript.

Funding: This research received no external funding.

Institutional Review Board Statement: Not applicable.

Informed Consent Statement: Not applicable.

Data Availability Statement: Data are contained within the article.

Conflicts of Interest: The authors declare no conflict of interest.

References

1. Lin, Y.H.; Tseng, S.H.; Chen, Y.H. The experimental study on maneuvering derivatives of a submerged body SUBOFF by implementing the Planar Motion Mechanism tests. *Ocean Eng.* **2018**, *170*, 120–135. [CrossRef]
2. Renilson, M. *Submarine Hydrodynamics*; Springer: Berlin/Heidelberg, Germany, 2015; Volume 31.
3. Hoyt, E.D.; Imlay, F.H.; David Taylor Model Basin Washington DC. *The Influence of Metacentric Stability on the Dynamic Longitudinal Stability of a Submarine SRD 542/46 NS 512-001*; David Taylor Model Basin Washington DC: Washington, DC, USA, 1948.
4. Anderson, B.; Chapuis, M.; Erm, L.; Fureby, C.; Giacobello, M.; Henbest, S.; Jones, D.; Jones, M.; Kumar, C.; Liefvendahl, M.; et al. Experimental and computational investigation of a generic conventional submarine hull form. In Proceedings of the 29th Symposium on Naval Hydrodynamics, Gothenburg, Sweden, 26–31 August 2012.
5. Quick, H.; Widjaja, R.; Anderson, B.; Woodyatt, B.; Snowden, A.D.; Lam, S. *Phase I Experimental Testing of a Generic Submarine Model in the DSTO Low Speed Wind Tunnel*; Client Report, DSTO-TN-1101; Defence Science and Technology Organisation: Victoria, Australia, 2012.
6. Fureby, C.; Anderson, B.; Clarke, D.; Erm, L.; Henbest, S.; Giacobello, M.; Jones, D.; Nguyen, M.; Johansson, M.; Jones, M.; et al. Experimental and numerical study of a generic conventional submarine at 10 yaw. *Ocean Eng.* **2016**, *116*, 1–20. [CrossRef]
7. Dubbioso, G.; Broglia, R.; Zaghi, S. CFD analysis of turning abilities of a submarine model. *Ocean Eng.* **2017**, *129*, 459–479. [CrossRef]
8. Broglia, R.; Posa, A.; Bettle, M.C. Analysis of vortices shed by a notional submarine model in steady drift and pitch advancement. *Ocean Eng.* **2020**, *218*, 108236. [CrossRef]
9. Lee, S.K.; Manovski, P.; Kumar, C. Wake of a cruciform appendage on a generic submarine at 10 yaw. *J. Mar. Sci. Technol.* **2020**, *25*, 787–799. [CrossRef]

10. Wackers, J.; Deng, G.; Guilmineau, E.; Leroyer, A.; Queutey, P.; Visonneau, M. What is happening around the KVLCC2? In Proceedings of the 18th Numerical Towing Tank Symposium (NuTTS 2015), Cortona, Italy, 28–30 September 2015.
11. Zhang, Z.; Guo, L.; Wei, P.; Wang, X.; Feng, D. Numerical simulation of submarine surfacing motion in regular waves. *Iran. J. Sci. Technol. Trans. Mech. Eng.* **2020**, *44*, 359–372. [CrossRef]
12. Posa, A.; Balaras, E. A numerical investigation of the wake of an axisymmetric body with appendages. *J. Fluid Mech.* **2016**, *792*, 470–498. [CrossRef]
13. Morse, N.; Mahesh, K. Large-eddy simulation and streamline coordinate analysis of flow over an axisymmetric hull. *J. Fluid Mech.* **2021**, *926*, A18. [CrossRef]
14. Rocca, A.; Cianferra, M.; Broglia, R.; Armenio, V. Computational hydroacoustic analysis of the BB2 submarine using the advective Ffowcs Williams and Hawkings equation with wall-modeled LES. *Appl. Ocean Res.* **2022**, *129*, 103360. [CrossRef]
15. Lungu, A. DES-based computation of the flow around the DARPA suboff. In Proceedings of the IOP Conference Series: Materials Science and Engineering, Kazimierz Dolny, Poland, 21–23 November 2019; Volume 591, p. 012053.
16. Lungu, A. Large flow separations around a generic submarine in static drift motion resolved by various turbulence closure models. *J. Mar. Sci. Eng.* **2022**, *10*, 198. [CrossRef]
17. Wang, L.; Martin, J.; Carrica, P.; Felli, M.; Falchi, M. Experiments and CFD for DARPA suboff appended with propeller E1658 operating near the surface. In Proceedings of the 6th International Symposium on Marine Propulsors, Rome, Italy, 26–30 May 2019; pp. 1–9.
18. Wang, L.; Martin, J.E.; Felli, M.; Carrica, P.M. Experiments and CFD for the propeller wake of a generic submarine operating near the surface. *Ocean Eng.* **2020**, *206*, 107304. [CrossRef]
19. Guo, H.; Li, G.; Du, L. Investigation on the flow around a submarine under the rudder deflection condition by using URANS and DDES methods. *Appl. Ocean Res.* **2023**, *131*, 103448. [CrossRef]
20. Jones, D.A.; Clarke, D.B.; Brayshaw, I.B.; Barillon, J.L.; Anderson, B. *The Calculation of Hydrodynamic Coefficients for Underwater Vehicles*; Technical Report; Defense Technical Information Center: Fort Belvoir, VA, USA, 2002.
21. Groves, N.C.; Huang, T.T.; Chang, M.S. *Geometric Characteristics of DARPA Suboff Models: (DTRC Model Nos. 5470 and 5471)*; David Taylor Research Center: Bethesda, MD, USA, 1989.
22. Roddy, R.F. *Investigation of the Stability and Control Characteristics of Several Configurations of the DARPA SUBOFF Model (DTRC Model 5470) from Captive-Model Experiments*; DTRC/SHD-1298-08; David Taylor Research Center, Ship Hydromechanics Department: Bethesda, MD, USA, 1990.
23. Huang, T.T.; Liu, H.L.; Groves, N.C. *Experiments of the Darpa (Defense Advanced Research Projects Agency) Suboff Program*; David Taylor Research Center, Ship Hydromechanics Department: Bethesda, MD, USA, 1989.
24. Joubert, P. *Some Aspects of Submarine Design: Part 1: Hydrodynamics*; Australian Department of Defence: Canberra, Australia, 2004.
25. Joubert, P. *Some Aspects of Submarine Design. Part 2. Shape of a Submarine 2026*; Technical Report; Australian Department of Defence: Canberra, Australia, 2006.
26. Overpelt, B.; Nienhuis, B.; Anderson, B. Free running manoeuvring model tests on a modern generic SSK class submarine (BB2). In Proceedings of the Pacific International Maritime Conference, Sydney, Australia, 6–8 October 2015; pp. 1–14.
27. Du, P.; Cheng, L.; Tang, Z.j.; Ouahsine, A.; Hu, H.b.; Hoarau, Y. Ship maneuvering prediction based on virtual captive model test and system dynamics approaches. *J. Hydrodyn.* **2022**, *34*, 259–276. [CrossRef]
28. Franceschi, A.; Piaggio, B.; Villa, D.; Viviani, M. Development and assessment of CFD methods to calculate propeller and hull impact on the rudder inflow for a twin-screw ship. *Appl. Ocean Res.* **2022**, *125*, 103227. [CrossRef]
29. Franceschi, A.; Piaggio, B.; Tonelli, R.; Villa, D.; Viviani, M. Assessment of the Manoeuvrability Characteristics of a Twin Shaft Naval Vessel Using an Open-Source CFD Code. *J. Mar. Sci. Eng.* **2021**, *9*, 665. [CrossRef]
30. Piaggio, B.; Villa, D.; Viviani, M. Numerical analysis of escort tug manoeuvrability characteristics. *Appl. Ocean Res.* **2020**, *97*, 102075. [CrossRef]
31. Weller, H.G.; Tabor, G.; Jasak, H.; Fureby, C. A tensorial approach to computational continuum mechanics using object-oriented techniques. *Comput. Phys.* **1998**, *12*, 620–631. [CrossRef]
32. Versteeg, H.K.; Malalasekera, W. *An Introduction to Computational Fluid Dynamics: The Finite Volume Method*; Pearson Education: Upper Saddle River, NJ, USA, 2007.
33. Wilcox, D.C. *Turbulence Modeling for CFD*; DCW Industries: La Canada, CA, USA, 1998; Volume 2.
34. Menter, F.R. Two-equation eddy-viscosity turbulence models for engineering applications. *AIAA J.* **1994**, *32*, 1598–1605. [CrossRef]
35. Launder, B.E.; Spalding, D.B. *Lectures in Mathematical Models of Turbulence*; Academic Press: London, UK; New York, NY, USA, 1972; 169p.
36. Spalding, D.B. The numerical computation of turbulent flow. *Comp. Methods Appl. Mech. Eng.* **1974**, *3*, 269.
37. Shih, T.H.; Liou, W.W.; Shabbir, A.; Yang, Z.; Zhu, J. A new k-epsilon eddy viscosity model for high reynolds number turbulent flows. *Comput. Fluids* **1995**, *24*, 227–238. [CrossRef]
38. Juretic, F. *cfMesh User Guide*; Creative Fields, Ltd.: London, UK, 2015; Volume 1.
39. Zheku, V.; Villa, D.; Gaggero, S. A Detailed Analysis of Manoeuvring Performance of Solid of Revolutions. In Proceedings of the MARINE Conference, Madrid, Spain, 27–29 June 2023.

40. Kim, H.; Leong, Z.Q.; Ranmuthugala, D.; Forrest, A. CFD modelling and validation of an AUV undergoing variable accelerations. In Proceedings of the ISOPE International Ocean and Polar Engineering Conference, Busan, Republic of Korea, 15–20 June 2014; p. ISOPE-I.
41. Pan, Y.C.; Zhang, H.X.; Zhou, Q.D. Numerical prediction of submarine hydrodynamic coefficients using CFD simulation. *J. Hydrodyn.* **2012**, *24*, 840–847. [CrossRef]
42. Amiri, M.M.; Esperança, P.T.; Vitola, M.A.; Sphaier, S.H. An initial evaluation of the free surface effect on the maneuverability of underwater vehicles. *Ocean Eng.* **2020**, *196*, 106851. [CrossRef]
43. Amiri, M.M.; Esperança, P.T.; Vitola, M.A.; Sphaier, S.H. How does the free surface affect the hydrodynamics of a shallowly submerged submarine? *Appl. Ocean Res.* **2018**, *76*, 34–50. [CrossRef]
44. Dawson, E. An Investigation into the Effects of Submergence Depth, Speed and Hull Length-to-Diameter Ratio on the near Surface Operation of Conventional Submarines. Ph.D. Thesis, University of Tasmania, Hobart, Australia, 2014.
45. Celik, I.B.; Ghia, U.; Roache, P.J.; Freitas, C.J. Procedure for estimation and reporting of uncertainty due to discretization in CFD applications. *J. Fluids Eng.-Trans. ASME* **2008**, *130*. [CrossRef]
46. Roache, P.J. Quantification of uncertainty in computational fluid dynamics. *Annu. Rev. Fluid Mech.* **1997**, *29*, 123–160. [CrossRef]
47. Hoang, N.; Wetzel, T.; Simpson, R. Unsteady measurements over a 6: 1 prolate spheroid undergoing a pitch-up maneuver. In Proceedings of the 32nd Aerospace Sciences Meeting and Exhibit, Reno, NV, USA, 10–13 January 1994; p. 197.
48. Kotapati-Apparao, R.B.; Squires, K.D. Prediction of a prolate spheroid undergoing a pitchup maneuver. In Proceedings of the 41 st AIAA Aerospace Sciences Meeting & Exhibit, Reno, NV, USA, 6–9 January 2003.
49. Subrahmanya, M.; Rajani, B. Numerical Investigation of the Flow Past 6: 1 Prolate Spheroid. 2019.
50. Chesnakas, C.J.; Simpson, R.L. Detailed investigation of the three-dimensional separation about a 6: 1 prolate spheroid. *AIAA J.* **1997**, *35*, 990–999. [CrossRef]
51. Jeong, J.; Hussain, F. On the identification of a vortex. *J. Fluid Mech.* **1995**, *285*, 69–94. [CrossRef]
52. Villa, D.; Gaggero, S.; Tani, G.; Viviani, M. Numerical and experimental comparison of ducted and non-ducted propellers. *J. Mar. Sci. Eng.* **2020**, *8*, 257. [CrossRef]
53. Andersson, J.; Eslamdoost, A.; Vikström, M.; Bensow, R.E. Energy balance analysis of model-scale vessel with open and ducted propeller configuration. *Ocean Eng.* **2018**, *167*, 369–379. [CrossRef]
54. Piaggio, B.; Vernengo, G.; Ferrando, M.; Mazzarello, G.; Viviani, M. Submarine Manoeuvrability Design: Traditional Cross-Plane vs. x-Plane Configurations in Intact and Degraded Conditions. *J. Mar. Sci. Eng.* **2022**, *10*, 2014. [CrossRef]
55. Watt, G.; Gerber, A.; Holloway, A. Submarine hydrodynamics studies using computational fluid dynamics. In Proceedings of the CMHSC, Halifax, NS, Canada, 21–22 September 2007.
56. Bettle, M.C. *Baseline Predictions of BB2 Submarine Hydrodynamics for the NATO AVT-301 Collaborative Exercise*; Defence Research and Development Canada: Toronto, ON, Canada, 2018.
57. Pattison, D. *Stability and Control of Submarines: A Review of Design Criteria and Derivative Prediction Techniques*; Admiralty Experiment Works-Haslar: Gosport, South Hampshire, 1975.
58. Pitts, W.C.; Nielsen, J.N.; Kaattari, G.E. *Lift and Center of Pressure of Wing-Body-Tail Combinations at Subsonic, Transonic, and Supersonic Speeds*; Technical Report; US Government Printing Office: Washington, DC, USA, 1957.

Journal of
Marine Science and Engineering

MDPI

Article

A Data-Driven Method for Ship Motion Forecast

Zhiqiang Jiang, Yongyan Ma and Weijia Li *

School of Naval Architecture and Ocean Engineering, Huazhong University of Science and Technology, 1037 Luoyu Road, Hongshan District, Wuhan 430074, China
* Correspondence: liweijia@hust.edu.cn; Tel.: +86-13507114896

Abstract: Accurate forecasting of ship motion is of great significance for ensuring maritime operational safety and working efficiency. A data-driven ship motion forecast method is proposed in this paper, aiming at the problems of low generalization of a single forecast model and insufficient forecast accuracy under unknown conditions. First, the fluid dynamics simulations of the ship are carried out under multiple node conditions based on overset mesh technology, and the obtained motion data is used for training the Bidirectional Long Short-term Memory network models. One or more pre-trained forecast models would be selected based on the correlation of condition nodes when forecasting ship motion under non-node conditions. The Golden Jackal Optimization Algorithm is used to compute the regression coefficient of each node model in real time, and finally, the dynamic model average is calculated. The results show that the method proposed in this study can accurately forecast the pitch and heave of the KCS ship in 5 s, 10 s, and 15 s of forecast duration. The accuracy of the multi-order forecast model improves more in longer forecast duration tasks compared with the first-order model. When forecasting ship motion under non-node conditions, the method shows stronger model generalization capabilities.

Keywords: ship motion forecast; CFD; BiLSTM; Golden Jackal Optimization

Citation: Jiang, Z.; Ma, Y.; Li, W. A Data-Driven Method for Ship Motion Forecast. *J. Mar. Sci. Eng.* **2024**, *12*, 291. https://doi.org/10.3390/jmse12020291

Academic Editors: Nastia Degiuli and Ivana Martić

Received: 11 January 2024
Revised: 2 February 2024
Accepted: 3 February 2024
Published: 5 February 2024

1. Introduction

In the course of offshore operations in real maritime environments, ships are affected by environmental factors such as wind, waves, and currents, resulting in motion with six degrees of freedom. Abrupt changes in ship motion have the potential to inflict damage upon equipment, interrupt work processes, or cause harm to personnel [1]. By forecasting ship motion, measures can be taken in advance to ensure the stability of equipment, thereby enhancing the safety of offshore operations. Simultaneously, high-precision compensation for ship motion reduces the impact of waves and currents on the ship, enabling engineering equipment to operate more stably. In engineering operations necessitating precision, such as offshore lifting and ship replenishment, the stability of equipment proves crucial for the execution of operations [2]. Accurate forecasting of ship pitch and heave holds significant importance for the maritime operations of engineering ships, contributing to enhanced safety in offshore operations and the reduction of maritime incidents [3]. As a result, research on ship motion forecasting has consistently garnered significant attention.

Currently, time series forecasts are predominantly categorized into two groups: those based on mathematical model methods and those utilizing machine learning techniques [4]. Mathematical model methods for forecasts encompass approaches such as the Kalman Filter, Autoregressive Integrated Moving Average model, and others. Nie, ZH et al. introduced a detrended autoregressive (AR) model based on detrended fluctuation analysis (DFA) for forecasting the motion of large ships [5]. Peng, XY et al. proposed an improved unscented Kalman filter (MUKF) algorithm proficient in mitigating the impact of abnormal data on dynamic positioning ship motion state estimation [6]. Jiang, H, et al. investigated hull scale effects in real-time motion using an autoregressive (AR) model, revealing a negative correlation between prediction accuracy, and spectrum bandwidth, and peak

frequency [7]. Takami, T et al. utilized the autocorrelation function (ACF) of short-term measurements for real-time deterministic forecasting of ship motion induced by waves [8]. Mathematical model-based forecasting methods typically exhibit high complexity and low computational efficiency. Furthermore, the capacity of such mathematical models to forecast non-stationary nonlinear time series is somewhat restricted, such as ship motion in irregular waves.

Neural network models demonstrate the ability to learn and capture intricate, nonlinear relationships. In the case of time series data involving multiple variables and interaction effects, neural networks can perform learning without the need for explicit data preprocessing, showing flexibility in forecasting tasks for nonlinear time series [9]. D'Agostino, D et al. conducted performance tests on Recurrent Neural Networks (RNN), Long Short-term Memory Neural Networks (LSTM), and Gate Recurrent Unit models (GRU) using computational fluid dynamics data from self-propelled destroyer-type ships [10]. Silva, K.M et al. utilized motion data from the DTMB5415 ship model in long-peak irregular waves to establish a ship motion prediction system based on LSTM, aiming to predict the ship motion response induced by waves [11]. Diez, M et al. proposed an equation-free ship motion response prediction method based on dynamic mode decomposition (DMD) and analyzed the navigation data of the free-sailing DTMB5415 ship and the KRISO ship [12].

Even though neural network models excel at handling complex nonlinear relationships and offer numerous advantages in time series forecasting, deep neural networks are often considered black-box models, with the internal representations being challenging to interpret [13]. The lack of interpretability can be a limitation in certain applications where a clear understanding of the model is essential. Consequently, some studies have emerged that seek to combine the strengths of mathematical models and neural networks to achieve comprehensive ship motion forecasts. Suhermi, N et al. combined an autoregressive integral moving average model with an artificial neural network (ANN) to predict the rolling motion of a floating production unit (FPU). The findings indicated that the ARIMA model was more adept at capturing the linear characteristics of motion, while the ANN model exhibited superior fitting characteristics for the nonlinear aspects of the model [14]. Xu, WZ et al. utilized second-order wave theory data to employ the LSTM model in predicting the intricate nonlinear input-output relationships within ocean systems [15]. Additionally, some researchers have explored using pre-trained neural network models for predicting new data through transfer learning. Ye R et al. proposed a hybrid algorithm (TrEnOS-ELMK) based on transfer learning an online sequential extreme learning machine with a kernel (OS-ELMK), and ensemble learning. This approach effectively leverages latent knowledge from past data to make predictions about future data [16]. YT Du et al. proposed AdaRNN for transfer learning on time series regression and prediction tasks, addressing the Temporal Covariance Shift (TCS) problem [17]. Transfer learning has demonstrated excellent performance in human activity identification, air quality prediction, and financial analysis. However, the continuous data distribution in time series poses challenges, leading to the instability of data distribution. Additionally, the intricate structure and gradient propagation issues of RNN complicate the direct application of existing transfer learning methods. These challenges may hinder the effective transfer of pre-trained forecast models to the task of ship motion forecasting in unknown conditions.

In time series forecasting, the predictive performance of a single model is often constrained by its structure and parameter selection, leading to limitations such as the absence of estimates for uncertainty in model outputs. While a model may perform well on training data, it may underperform in generalizing effectively to new series. Model averaging is a technique that addresses these challenges by combining predictions from multiple models [18]. When faced with changing data distributions or uncertainties, model averaging proves valuable in mitigating the risk of overfitting that a single model may encounter under specific conditions, thereby enhancing the robustness of the forecasting model. Darbandsari, P et al. proposed an entropy-based Bayesian model averaging (BMA) algorithm, utilizing it in daily flow prediction across various watersheds [19]. Naser, H used dy-

namic model averaging (DMA) to forecast West Texas Intermediate crude oil (WTI) prices. The results demonstrated that the dynamic model averaging method outperformed other alternative models used in the forecasting exercise [20].

Most existing forecast methods for ship motion rely on given ship motion data, utilizing either mathematical models or machine learning techniques to create a priori ship motion response forecasting models. However, these models often lack generalization ability under new conditions, leading to a decrease in prediction performance when confronted with changing ship operation conditions. In ship motion forecasting, the characteristics and distributions of ship motion time series vary under different conditions. The actual conditions often differ from those encountered during pre-training, leading to the inability of the pre-trained model to accurately forecast new conditions. Due to disparities in the spatiotemporal characteristics between datasets, the model may overly adapt to the spatiotemporal features of specific conditions, resulting in a diminished ability to generalize to other conditions. A data-driven ship motion forecasting method is proposed in this paper to address this challenge, building on the research conducted by previous researchers [10,20–23]. The approach employs one or more pre-trained neural network models to forecast ship motion under unknown conditions. Initially, numerous numerical simulations are conducted on the target ship in various sea states or wave approach angles, utilizing overset grid technology. The motion and wave elevation data are then used to train Bidirectional Long Short-term Memory network models (BiLSTM). When forecasting pitch and heave under unknown conditions, multiple pre-trained node models are selected. The Golden Jackal Optimization Algorithm (GJO) is employed to compute the regression coefficients for each pre-trained node model, and the Dynamic Model Averaging (DMA) is calculated. The diversity of sea conditions and ship motion states are taken into account in the method, resulting in more comprehensive and reliable forecasts. The model becomes better adapted to the complexities of ship motion in diverse sea states by leveraging data from each node's conditions. This approach (see Figure 1) holds significant importance for enhancing offshore operation safety and improving operational efficiency.

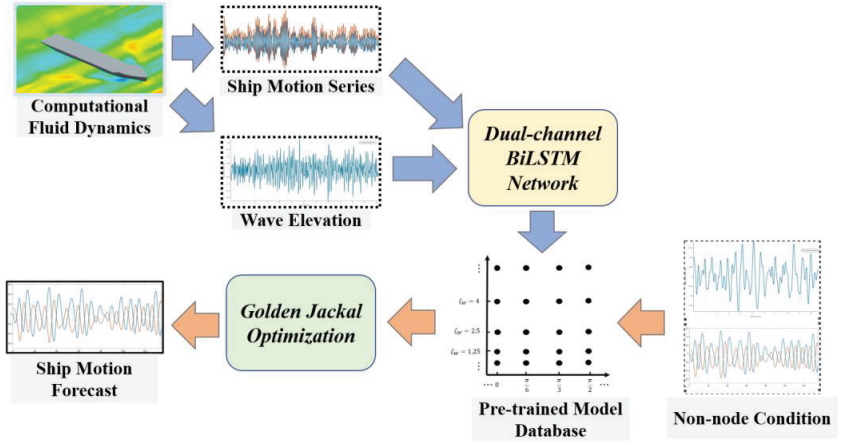

Figure 1. Model Framework.

2. Methods

2.1. Ship Motion Response Model

The irregular motion of a ship is induced by the influence of irregular waves. When ships perform offshore operations in relatively stable sea conditions, it can be assumed to function as a time-invariant linear system [24]. In this research, the disturbance is

represented by the wave passing through the hull. The ship's 6-dof motion serve as the system's responses. The system input and output can be described as:

$$Y(t) = L[\zeta(t)] \tag{1}$$

where, $\zeta(t)$ represents the time series of wave elevation and $Y(t)$ is the ship's motion response. When the wave elevation input consists of regular sinusoidal waves, the dynamic characteristics of the ship can be described using a frequency response function within the frequency domain. The relationship between the dynamic input $\zeta(t)$ and output $Y(t)$ of a linear system can be expressed using constant-coefficient differential equations:

$$\sum_{i=0}^{n} b_{n-i} \frac{d_Y^{n-i}}{d_t^{n-i}} = \sum_{j=0}^{m} a_{m-j} \frac{d_\zeta^{m-j}}{d_t^{m-j}} \tag{2}$$

The equation above is Laplace transformed and let $S = j\omega$, the transfer function of the linear system can be derived as:

$$Y_{y\zeta}(j\omega) = \frac{Y(j\omega)}{\zeta(j\omega)} = \frac{Y_0}{\zeta_0} e^{j\delta} \tag{3}$$

where, Y_0/ζ_0 represents the amplitude-frequency characteristics of the system and $e^{j\delta}$ denotes the phase-frequency characteristics of the system. $Y_{y\zeta}$ is the 6-dof motion response function of the ship. In real maritime conditions, wind and waves are highly irregular, with the amplitude, wavelength, and period of each wave being subject to random variations. According to the principle of linear superposition of irregular waves, the energy of irregular waves is equal to the sum of the energies of individual regular waves [25]. The distribution of energy across different frequency components of irregular waves can be described using the wave spectrum density function:

$$S_\zeta(\omega) = \frac{\zeta_a^2}{2\Delta\omega} \tag{4}$$

where, $S_\zeta(\omega)$ represents the wave spectrum density function and ζ_a is the wave amplitude. Therefore, when the wave elevation input is an irregular wave, the ship's motion at any given moment can be considered the superposition of the motion generated under the input of individual regular waves, expressed as:

$$Y(t) = \sum_{n=1}^{\infty} Y_{y\zeta}(\omega_n)\zeta_{an} cos(K_n\xi - \omega_n t + \varepsilon_n) \tag{5}$$

where, ζ_{an} is the amplitude of individual regular waves, K_n is the wave number of individual regular waves, ω_n is the circular frequency of individual regular waves, and ε_n is the phase of individual regular waves. According to the energy superposition theorem and referencing the wave spectrum density function, the motion spectrum density function of the ship under irregular waves is defined as:

$$S_{y\zeta}(\omega) = \frac{[Y_{y\zeta}(\omega)\,\zeta_a]^2}{2\Delta\omega} = Y_{y\zeta}^2(\omega) \cdot S_\zeta(\omega) \tag{6}$$

where, $Y_{y\zeta}^2$ represents the system response amplitude operator. It can be seen from the equation that the motion response of the ship is simultaneously influenced by both the ship's intrinsic factors and environmental factors. In this study, the Pierson-Moskowitz wave spectrum is used for the numerical simulation of irregular waves. The P-M spectrum

is a semi-empirical wave spectrum, primarily derived from well-developed waves in the Atlantic [26].

$$S_\zeta(\omega) = \frac{0.78}{\omega^5} exp\left(-\frac{0.74g^4}{U^4\omega^4}\right) \tag{7}$$

where, U is the average wind speed at a height of 19.5 m, and the approximate relationship with the significant wave height is given by $U = 6.85\sqrt{\overline{\zeta}_W}$. Consequently, the relationship between the Pierson-Moskowitz spectrum and the significant wave height can be obtained as:

$$S_\zeta(\omega) = \frac{0.78}{\omega^5} exp\left(-\frac{1}{\overline{\zeta}_W{}^2} \cdot \frac{0.74g^4}{6.85^4\omega^4}\right) \tag{8}$$

While a ship is moored at sea for offshore operation, the navigational speed $V = 0$, and the encounter frequency ω_e of the waves are the same as the original wave frequency ω. When there is a wave approach angle μ between the wave propagation direction and the ship's heading, the wavelength λ_1 through the ship's longitudinal section is given by:

$$\lambda_1 = \frac{\lambda}{cos\mu} \tag{9}$$

The simultaneous equations of the ship's pitch and heave motion response can be expressed as:

$$\begin{pmatrix} S_{\psi\zeta} \\ S_{Z\zeta} \end{pmatrix} = \begin{cases} F_{\psi,Z}\left(\mu, \overline{\zeta}_W{}^2\right) \\ M_{\psi,Z}\left(\mu, \overline{\zeta}_W{}^2\right) \end{cases} \tag{10}$$

From the equations above, it is evident that the ship's motion response equation can be treated as an implicit function of the wave approach angles μ and the significant wave height $\overline{\zeta}_W$. The time series of ship motions under each condition node are used for training neural network models, thereby obtaining the respective motion forecasting models. Due to the fact that ships cannot be treated as a linear system under rough sea conditions, this research predominantly focuses on the prediction of pitch and heave of ships under the upper limit of level-6 sea state.

2.2. BiLSTM Network

Bidirectional Long Short-Term Memory (BiLSTM) is a variation of Recurrent Neural Network (RNN) designed for series processing. BiLSTM incorporates hidden layers in two directions: one for processing the sequence in chronological order (from past to future) and the other for processing the sequence in reverse order (from future to past) [27]. This framework is capable of considering both past and future contextual information, enhancing its ability to capture long-term dependencies within the sequence. The bidirectional information flow structure of BiLSTM enables the model to comprehensively capture the temporal dependencies in series, a crucial aspect for longer time series prediction tasks. Simultaneously, the bidirectional architecture helps alleviate issues related to gradients vanishing or exploding, contributing to a more stable training process. This is attributed to the fact that gradients can propagate from both directions, facilitating a smoother update of model parameters. For each time step, BiLSTM receives an input and produces an output. In sequence tasks, the output can be obtained at the last time step or at every time step, depending on the inherent nature of the task. The structure of a single-layer BiLSTM is illustrated in Figure 2:

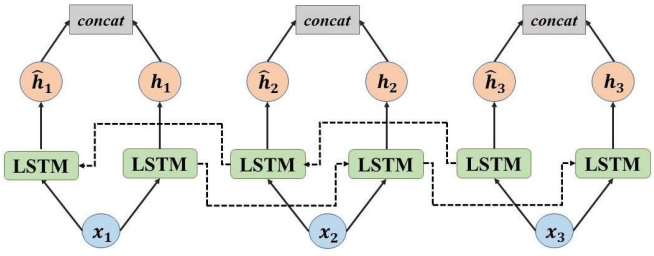

Figure 2. BiLSTM Network.

In contrast to the Gated Recurrent Unit (GRU) model, the BiLSTM model effectively addresses long-term dependencies through the incorporation of explicit memory units. Despite the relatively intricate structure and parameter abundance inherent, BiLSTM consistently demonstrates superior performance in the context of intricate sequential tasks, particularly those demanding the retention of long-term memory. Long Short-Term Memory (LSTM) is a type of recurrent neural network designed for processing sequential data [28]. LSTM manages the information flow through gating units, including input gates, forget gates, and output gates, enabling effective handling of long-term dependencies. Bidirectional LSTM (BiLSTM) enhances the network's capability to model long-term dependencies by employing LSTM units in both forward and reverse directions. In this study, the Dual-channel BiLSTM network (see Figure 3) is employed to train ship motion forecasting models under various node conditions, with forecast durations of 5 s, 10 s, and 15 s. Subsequently, the method generates pre-trained forecast models corresponding to each node condition and makes forecasts for ship motion under non-node conditions.

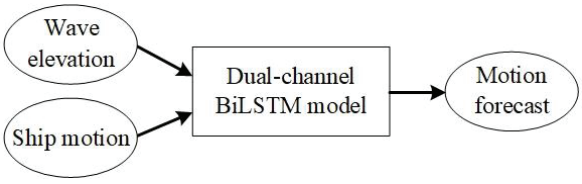

Figure 3. Dual-channel Forecasting Model.

2.3. Dynamic Model Averaging Based on GJO

The ship's motion response varies significantly under different conditions, especially with varying wave approach angles and sea states. A single pre-trained model struggles to provide accurate predictions for ship motion. Therefore, an effective method is essential for accurately forecasting the ship's motion in various conditions. This study employs a dynamic model averaging based on the Golden Jackal algorithm to forecast ship motion responses. The main method is to leverage pre-trained ship motion forecast models under multiple node conditions to forecast the ship's motion under non-node conditions. By systematically modeling the ship's motion response under different node conditions, the motion characteristics in diverse environments can be captured. These condition nodes correspond to different sea states and navigational speeds, forming a multidimensional parameter space for the model database. The Golden Jackal algorithm is utilized to calculate the dynamic regression coefficients for multiple node condition models under unknown conditions, facilitating the forecast of ship motion responses.

Dynamic Model Averaging (DMA) is a model ensemble method employed to amalgamate predictions from multiple models, thereby enhancing overall performance. In contrast to conventional model averaging approaches, dynamic model averaging enables the adaptive adjustment of model weights over time to accommodate alterations in data

distribution or shifts in model performance [29]. The state space model of dynamic model averaging encompasses the following components:

$$y_t = x_t^T \alpha_t + \varepsilon_t \tag{11}$$

$$\alpha_t = \alpha_{t-1} + \delta_t \tag{12}$$

where, y_t is the deviation of the output thickness of samples, x_t^T is the cor-responding vector of independent variables of the regression model, α_t is a vector of regression parameters, and the innovations ε_t, δ_t are distributed in a Normal distribution with a mean of 0. In real sea conditions, the significant wave height and wave approach angle of the ship often deviate from those of the condition nodes. When forecasting ship motion under such non-node conditions, a thorough assessment must be conducted, taking into account nearby node conditions. This method employs one or more comparable ship motion forecast models for predictions, followed by the result of the dynamic model average. The pseudocode of the condition node selection Algorithm 1 is as follows:

Algorithm 1: Condition Node Select

Input: $[m, n]$, where m and n are parameters of ship motion response functions; Condition nodes coordinate sets X, Y
Output: Condition Nodes
$X(m+)$, $Y(n+)$**: Node greater than** ***m*** **or** ***n*** **in that dimension**;
$X(m-)$, $Y(n-)$**: Node less than** ***m*** **or** ***n*** **in that dimension**;
if $m \in X$ ***and*** $n \in Y$ **then**
    Condition Nodes $\leftarrow \{[m, n]\}$;
else if $m \in X$ ***and*** $n \notin Y$ **then**
    Condition Nodes $\leftarrow \{[m, Y(n+)], [m, Y(n-)]\}$;
else if $n \in Y$ ***and*** $m \notin X$ **then**
    Condition Nodes $\leftarrow \{[X(m+), n], [X(m-), n]\}$;
else
    Condition Nodes $\leftarrow \{[X(m+), Y(n+)], [X(m+), Y(n-)], [X(m-), Y(n+)], [X(m-), Y(n-)]\}$;
return *Condition Nodes*

Algorithm 1 outputs one or more node operating conditions that are closest to the current condition. The pre-trained model is selected according to the node conditions output by Algorithm 1 in subsequent ship motion predictions. When forecasting ship motion under non-node conditions, the output of a single pre-trained node model can be expressed as:

$$Y(t) = \widetilde{Y}(t) + \widetilde{\varepsilon}(t) \tag{13}$$

where, $Y(t)$ represents the actual ship motion response time series under the specific condition, while $\widetilde{Y}(t)$ denotes the motion time series predicted by the pre-training model. The term $\widetilde{\varepsilon}(t)$ corresponds to the forecast error. The relationship between the outcomes of multiple pre-training models and the actual motion series can be expressed as:

$$Y(t) = \sum_{i=1}^{n} \left[\alpha_i \widetilde{Y}_i(t) + \widetilde{\varepsilon}_i(t) \right] = \sum_{i=1}^{n} \alpha_i \widetilde{Y}_i(t) + \varepsilon(t) \tag{14}$$

where, α_i represents the regression coefficients for each node forecast model, and n signifies the model order, indicating the count of participating pre-trained models in the forecast. The selection of the node model is determined by the correlation between the forecasting

condition and the node conditions. To evaluate the correlation under a consistent standard between the node conditions and the forecasting conditions, the significant wave heights and wave approach angles of the node conditions are subjected to Min–Max normalization. The normalization process ensures that the values remain characteristic features on the same scale. The formula for the model normalization calculation is:

$$x' = \frac{x - \min(x)}{\max(x) - \min(x)} \tag{15}$$

As the ship motion forecasts in this research are all conducted in relatively stable sea states, the significant wave height range aligns with the upper limit of sea states from level 0 to level 6. Additionally, the wave approach angles fall within the range $[0, \pi/2]$. For pitch and heave motions, the correlation coefficient $R_{Z\psi}$ for the condition node is defined as:

$$R_{Z\psi} = \sqrt{(\mu - \mu_n)^2 + (\zeta - \overline{\zeta}_n)^2} \tag{16}$$

where, μ_n and $\overline{\zeta}_n$ represent the wave approach angle and significant wave height, respectively, under normalized node conditions. The selection of the node forecast model is based on the model correlation coefficient. When the model order n = 1, ship motion is forecasted solely by the pre-trained model of the node condition with the highest correlation. During this scenario, each ship motion forecast opts for the pre-trained model with the highest posterior probability, known as the Dynamic Model Selection (DMS) forecast. The selection of 1st to 4th-order forecast models is illustrated in Figure 4. For ship motion forecasts involving second-order models and beyond, this research employs the Golden Jackal optimization algorithm. The optimization process utilizes the absolute mean error as the objective function to determine and optimize the regression coefficients of each pre-trained model.

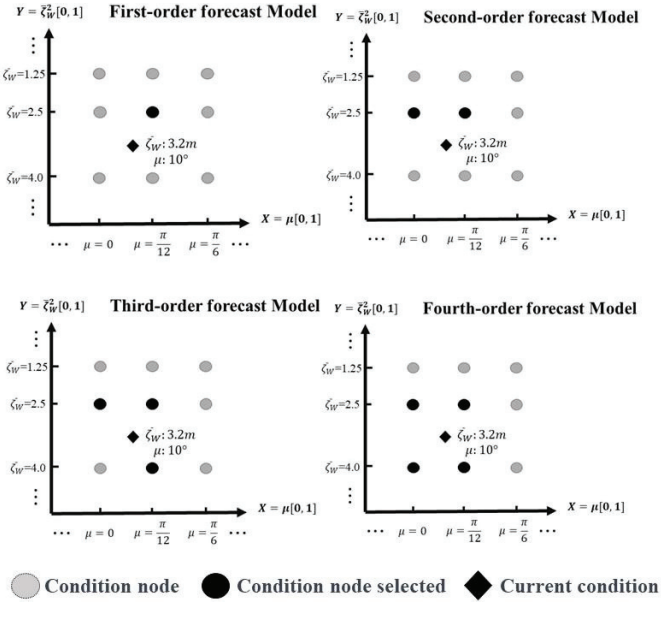

Figure 4. 1st–4th order Forecasting Model.

The Golden Jackal Optimization (GJO) is a global optimization algorithm inspired by the cooperative hunting behavior of golden jackals [30]. The GJO algorithm computes the fitness matrix using the prey population position matrix and a designated fitness function.

In the prey search stage, the mathematical model for the relative position of each individual in the prey population, inspired by the golden jackal, is expressed as follows:

$$\begin{cases} Y_{1i}(t) = Y_M(t) - E \cdot |Y_M(t) - rl \cdot X_i(t)| \\ Y_{2i}(t) = Y_{FM}(t) - E \cdot |Y_{FM}(t) - rl \cdot X_i(t)| \end{cases} \tag{17}$$

where, t denotes the current iteration count, X_i represents the position of the i-th prey, Y_M and Y_{FM} respectively indicates the positions of male and female golden jackals, rl signifies a random number based on the Levy distribution, and E denotes the prey's escape energy, calculated as follows:

$$rl = 0.05 \cdot LF() \tag{18}$$

$$E = 3(random[0,1] - 1) \cdot \left(1 - \frac{t}{T}\right) \tag{19}$$

where, $LF()$ is the Levy flight function and T is the total number of iterations. During hunting, the relative position of the golden jackal is as follows:

$$\begin{cases} Y_{1i}(t) = Y_M(t) - E \cdot |rl \cdot Y_M(t) - X_i(t)| \\ Y_{2i}(t) = Y_{FM}(t) - E \cdot |rl \cdot Y_{FM}(t) - X_i(t)| \end{cases} \tag{20}$$

The regression coefficients of each pre-trained model are determined by the GJO algorithm according to the errors between real motion and predicted motion from the previous period. These regression coefficients are then utilized for forecasting the ship's motion in the subsequent time period. To maintain the model's timeliness, the regression coefficients for each pre-trained model are regularly recalculated at certain intervals.

3. Experiment

3.1. Numerical Simulation of the KCS Ship

To validate the research methodology, a KCS ship model is employed as the subject for ship motion forecasting. As a standard ship model, the KCS model finds extensive application in towing tank experiments and numerical simulations. Figure 5 and Table 1 illustrate the KCS ship model along with its main parameters:

Figure 5. The KCS Hull Form.

Table 1. Main Geometric Parameters.

	Full Scale	Model
Scale	1	80.87
Length between perpendiculars (m)	230	2.844
Design waterline breadth (m)	32.2	0.398
Draught (m)	10.8	0.134
Displacement space(m^3)	52,030	0.09836

The entire KCS ship model is used for numerical simulation under specific node conditions, leading to the establishment of the motion forecast model database. Node coordinates within the model database are defined based on a wave approach angle of 15° and a significant wave height from the sea state level (see Table 2) specified by the National

Marine Environmental Forecasting Center of China [31]. The total number of condition nodes is not fixed. The range and density of condition nodes are determined based on specific usage requirements. A broader range and higher density of nodes imply a more extensive and accurate forecast capability. However, it also results in a larger computational workload for simulations. In subsequent calculations, it is assumed that a full-scale ship is engaged in seaborne operations at a standstill while the waves move in relation to the ship at a speed of 7.71 m/s (15 kn). Adhering to the Froude similarity criterion and applying a scale ratio of 80.87, the length of the ship model is set to L = 2.844 m, and the wave propagation speed is set to V = 0.858 m/s. The motion series obtained from the simulation were enlarged in equal proportions according to the scale ratio of 80.87 and the Froude similarity criterion and used as the motion data of the full-scale ship for subsequent research.

Table 2. Sea State Level.

Level	Sea State	Wave Height
0	Calm-Glassy	0 m
1	Calm-Rippled	0–0.1 m
2	Smooth-Wavelet	0.1–0.5 m
3	Slight	0.5–1.25 m
4	Moderate	1.25–2.5 m
5	Rough	2.5–4.0 m
6	Very Rough	4.0–6.0 m

The mesh of the ship model is shown in Figure 6. According to the ITTC specifications, the numerical tank velocity inlet is positioned a ship length from the bow, the pressure outlet is located three ship lengths from the stern, and the side boundaries are set at one ship length. The total length of the domain is five ship lengths, while the total width is two ship lengths. Overset mesh is applied to the body and the background, with localized refinement at the free surface and hull [32]. The total number of mesh cells is 6 million. For this numerical simulation of irregular waves, the Pierson-Moskowitz wave spectrum is employed, and a probe is set a half-ship length from the bow to monitor wave elevation. When ships are navigating or operating at sea, a wave approach angle larger than 75° is uncommon. Beams in the sea or waves close to a 90° approach angle can significantly impact the safety of the ship. In more severe sea conditions, ships would not be qualified for maritime operations. Therefore, numerical simulations of ship motion based on sea state levels and a 15° angle difference are conducted in subsequent experiments. Figures 7 and 8 display the free surface and wave elevation.

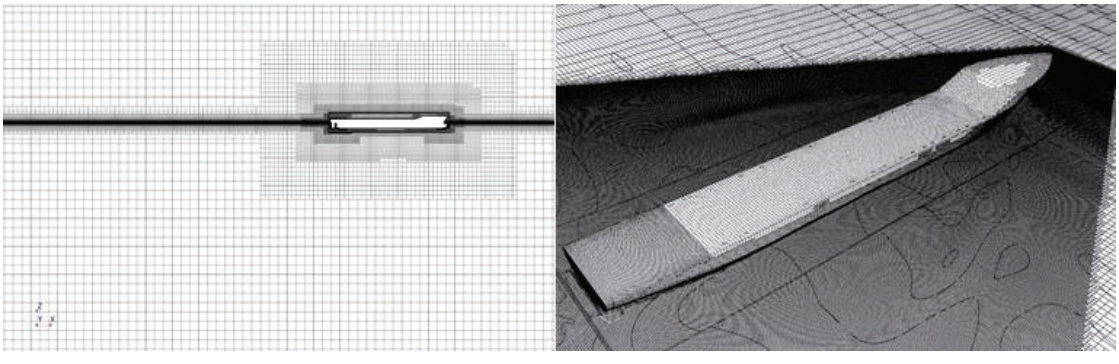

Figure 6. Computational Domain and Hull Mesh.

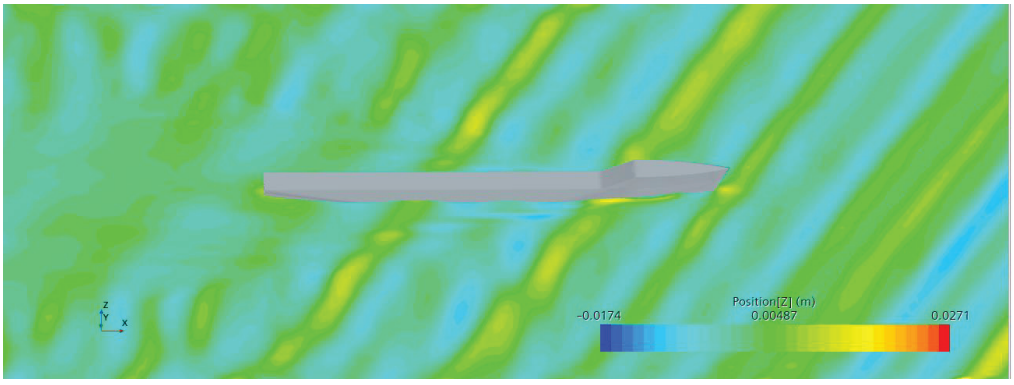

Figure 7. KCS Model on a Free Surface.

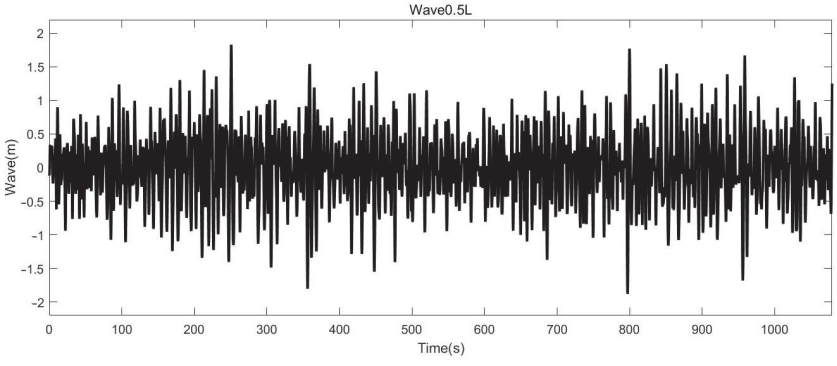

Figure 8. Wave Elevation at 0.5 L ($\overline{\zeta}_W = 2.5$ m).

In each numerical simulation, the time-domain response of the ship model's pitch and heave motion under node conditions is sampled at a frequency of 100 Hz, serving as training data for the neural network model. The duration of the full-scale ship motion data for each condition is 1200 s. Part of the ship motion series is presented in Figures 9 and 10.

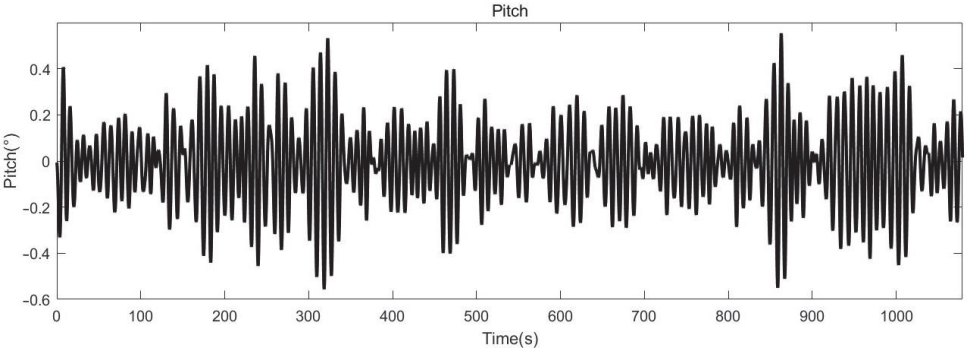

Figure 9. Pitch Time Series ($\overline{\zeta}_W = 2.5$ m, $\mu = 15°$).

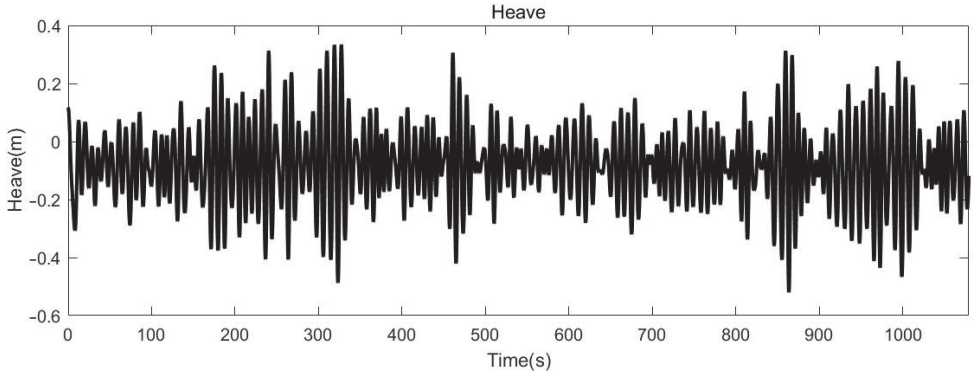

Figure 10. Heave Time Series ($\overline{\zeta}_W = 2.5$ m, $\mu = 15°$).

3.2. Pre-Trained Models under Node Conditions

The wave elevation and ship motion series under each node condition are used to train the dual-channel BiLSTM network models. The forecast duration is set to 5 s, 10 s, and 15 s, respectively. Each ship's motion time series obtained by numerical simulation is divided into a training set and a test set. The samples of the BiLSTM network model training set for each condition node are 5000, the test set is 1000. The training set is used for model training and parameter adjustment, while the test set is utilized to assess the model's effectiveness. Since the wave elevation probe is located half a ship length ahead of the bow, the forecast time window is set to 15 s, aligning with the time for the wave to propagate to the bow. The dual-channel BiLSTM network structure, depicted in Figure 11, consists of two layers of BiLSTM with 128 and 64 hidden units, respectively. The output layer is a Fully Connected Layer with a dimension of 1, producing the forecast motion response. The loss function adopted is the root mean square error, and the optimizer utilized is Adam. Additionally, to prevent overfitting, DROPOUT is applied to each layer with a parameter set to 0.2.

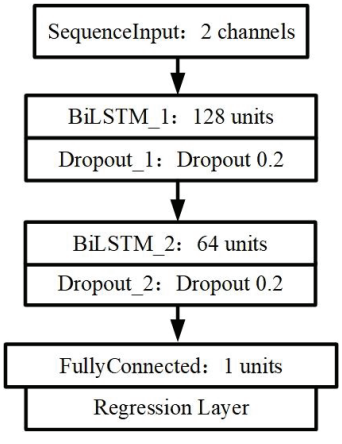

Figure 11. Dual-channel BiLSTM Model Structure.

To evaluate the performance of the neural network model, ship motion forecasts were conducted on the test set of each condition node with forecast durations of 5 s, 10 s, and 15 s. The results were then compared with the actual motion series. To enhance the training efficiency and stability of the model, the Min–Max normalization method was applied to

standardize the data features to the same scale before training. Figures 12 and 13 depict the forecast results after denormalization for some condition node models.

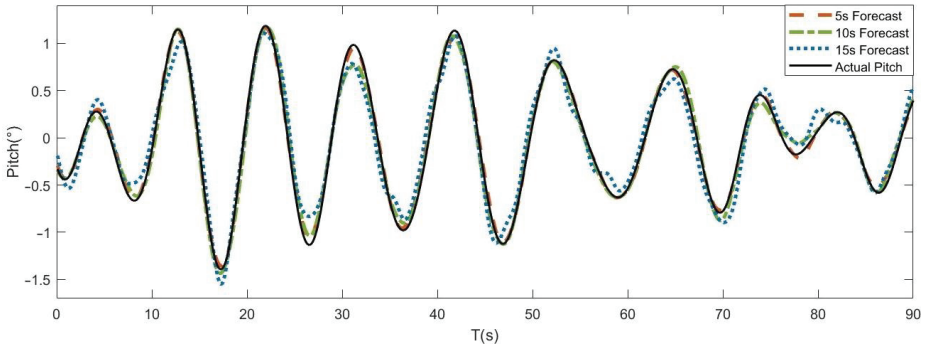

Figure 12. Pitch Forecast Series ($\overline{\zeta}_W = 4$ m, $\mu = 15°$).

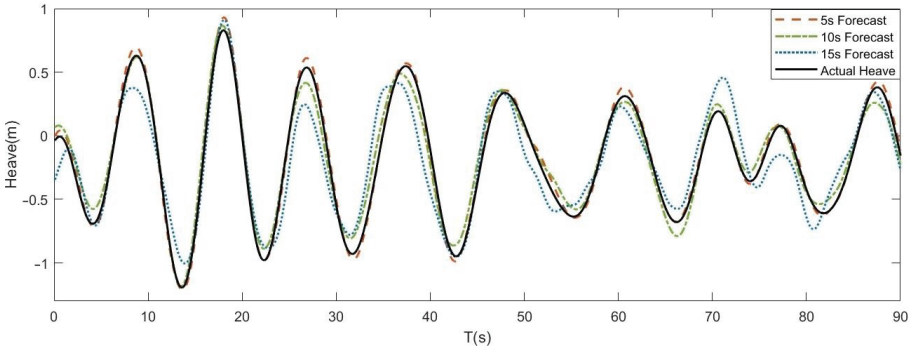

Figure 13. Heave Forecast Series ($\overline{\zeta}_W = 4$ m, $\mu = 15°$).

The Mean Absolute Error (*MAE*), Root Mean Square Error (*RMSE*), and Spearman Correlation Coefficient (R_s) were selected to evaluate the forecasting capability of the models. The denormalized test set was used for evaluations. The formulas for the three indicators are as follows:

$$MAE = \frac{1}{n}\sum_{i=1}^{n}|y_i - \hat{y}_i| \tag{21}$$

$$RMSE = \sqrt{\frac{1}{n}\sum_{i=1}^{n}(y_i - \hat{y}_i)^2} \tag{22}$$

$$R_s = 1 - \frac{6\sum_{i=1}^{n} d_i^2}{n(n^2-1)} \tag{23}$$

where, y_i represents the actual value, $\hat{y}_i$ is the forecast value, and d_i is the grade difference between the forecast value and the actual value. *MAE* is the mean absolute value of the observation error, without considering the square of the error. *RMSE* is the square root of the mean square of the forecast errors, assigning greater weight to larger errors. Compared to *MAE*, *RMSE* is more sensitive to large errors. R_s is a rank-based correlation calculation method for assessing the nonlinear relationship between two series. In the context of nonlinear and non-stationary time series, such as ship motion, the Spearman correlation coefficient is robust against outliers and data distribution. Part of the forecast accuracy evaluation results for some pre-trained models are as follows:

As illustrated in Tables 3–5, the increase in sea state level corresponds to larger amplitudes of the ship's pitch and heave, resulting in more substantial changes in both *MAE* and *RMSE*. Simultaneously, the nonlinearity of ship motion intensifies, leading to increased forecast difficulty and a decrease in R_s. With an escalation in forecast duration, the *MAE* and *RMSE* of the forecast results rise, R_s declines, indicating a reduction in accuracy. The change in forecast accuracy is slightly less pronounced when the forecast duration increases from 5 s to 10 s. However, when the forecast duration extends to 15 s, the forecast accuracy experiences a more noticeable decrease, yet it still remains above 90%. The test set results affirm that the pre-trained neural network forecast model exhibits robust adaptability to unknown series, demonstrating its efficacy for motion prediction under non-node conditions.

Table 3. Forecast Results of 5 s Duration.

Wave Approach Angle / Sea State			0°		15°		30°		
			Pitch	Heave	Pitch	Heave	Pitch	Heave	
…			…	…	…	…	…	…	
Level-3 ($\overline{\zeta}_W = 1.25$ m)	*MAE*		0.0077	0.0092	0.0081	0.0110	0.0108	0.0139	
	RMSE		0.0098	0.0101	0.0105	0.0137	0.0126	0.0187	
	R_s		0.9927	0.9901	0.9945	0.9914	0.9901	0.9952	
Level-4 ($\overline{\zeta}_W = 2.5$ m)	*MAE*		0.0191	0.0173	0.0178	0.0267	0.0133	0.0272	
	RMSE	…	0.0234	0.0218	0.0230	0.0318	0.0168	0.0323	…
	R_s		0.9923	0.9870	0.9964	0.9933	0.9979	0.9963	
Level-5 ($\overline{\zeta}_W = 4.0$ m)	*MAE*		0.0314	0.0352	0.0443	0.0609	0.0343	0.0527	
	RMSE		0.0411	0.0435	0.0550	0.0755	0.0428	0.0647	
	R_s		0.9975	0.9937	0.9985	0.9957	0.9981	0.9916	
…	…		…	…	…	…	…	…	

Table 4. Forecast Results of 10 s Duration.

Wave Approach Angle / Sea State			0°		15°		30°		
			Pitch	Heave	Pitch	Heave	Pitch	Heave	
…			…	…	…	…	…	…	
Level-3 ($\overline{\zeta}_W = 1.25$ m)	*MAE*		0.0093	0.0101	0.0075	0.0139	0.0191	0.0176	
	RMSE		0.0178	0.0186	0.0165	0.0208	0.0232	0.0254	
	R_s		0.9891	0.9922	0.9907	0.9854	0.9927	0.9863	
Level-4 ($\overline{\zeta}_W = 2.5$ m)	*MAE*		0.0179	0.0231	0.0213	0.0196	0.0198	0.0240	
	RMSE	…	0.0214	0.0282	0.0262	0.0260	0.0238	0.0305	…
	R_s		0.9945	0.9783	0.9960	0.9930	0.9978	0.9924	
Level-5 ($\overline{\zeta}_W = 4.0$ m)	*MAE*		0.0390	0.0372	0.0529	0.0592	0.0618	0.0871	
	RMSE		0.0218	0.0476	0.0649	0.0718	0.0777	0.1102	
	R_s		0.9960	0.9927	0.9984	0.9959	0.9917	0.9762	
…	…		…	…	…	…	…	…	

Table 5. Forecast Results of 15 s Duration.

Wave Approach Angle / Sea State			0°		15°		30°		
			Pitch	Heave	Pitch	Heave	Pitch	Heave	
…			…	…	…	…	…	…	
Level-3 ($\overline{\zeta}_W = 1.25$ m)	*MAE*		0.0243	0.0324	0.0237	0.0303	0.0294	0.0408	
	RMSE		0.0377	0.0433	0.0482	0.0502	0.0412	0.0597	
	R_s		0.9698	0.9742	0.9707	0.9654	0.9662	0.9595	
Level-4 ($\overline{\zeta}_W = 2.5$ m)	*MAE*		0.0359	0.0353	0.0549	0.0469	0.0577	0.0515	
	RMSE	…	0.0460	0.0431	0.0676	0.0573	0.0698	0.0622	…
	R_s		0.9743	0.9513	0.9732	0.9671	0.9706	0.9615	
Level-5 ($\overline{\zeta}_W = 4.0$ m)	*MAE*		0.1455	0.1509	0.1571	0.2017	0.1614	0.1765	
	RMSE		0.1805	0.2062	0.2075	0.2908	0.1988	0.2185	
	R_s		0.9785	0.9655	0.9814	0.9423	0.9469	0.9398	
…	…		…	…	…	…	…	…	

3.3. Motion Forecast under Non-Node Conditions

By utilizing the pre-trained motion forecast model under node conditions, ship motion under non-node conditions is forecasted. In this section, three different cases are used to evaluate the performance of the model, as illustrated in Table 6.

Table 6. Cases Used to Verify the Algorithm.

	Case 1	Case 2	Case 3
$\overline{\zeta}_W$ (Full Scale, m)	1.617	3.235	3.235
$\overline{\zeta}_W$ (Model, m)	0.020	0.040	0.040
μ (°)	5°	10°	20°

All other things being equal, numerical simulations of the KCS ship model are conducted in Case 1, 2, and 3. The wave elevation at half a ship's length ahead of the bow and the time series of the ship's pitch and heave are monitored. The numerical simulation of the full-scale ship motion series length is 135 s. Figures 14–16 illustrate the wave elevation, KCS ship pitch, and heave series in three cases:

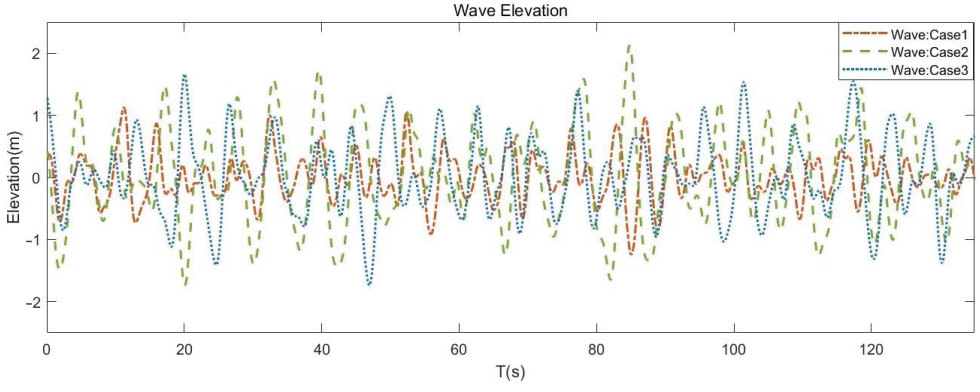

Figure 14. Wave Elevation in Three Cases.

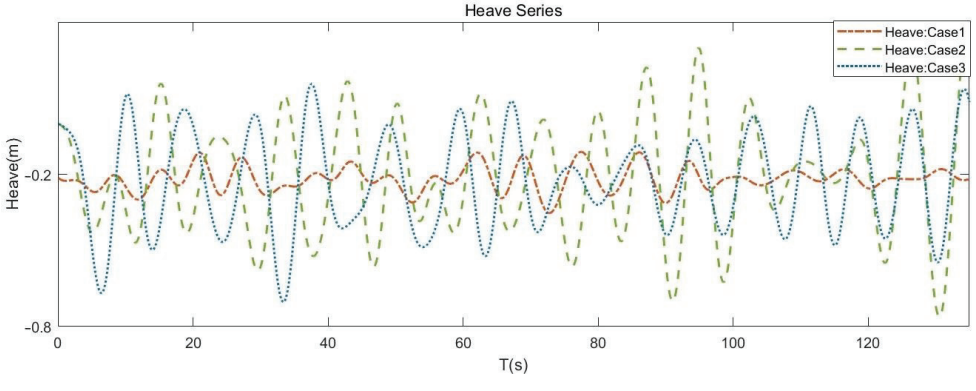

Figure 15. Heave Series in Three Cases.

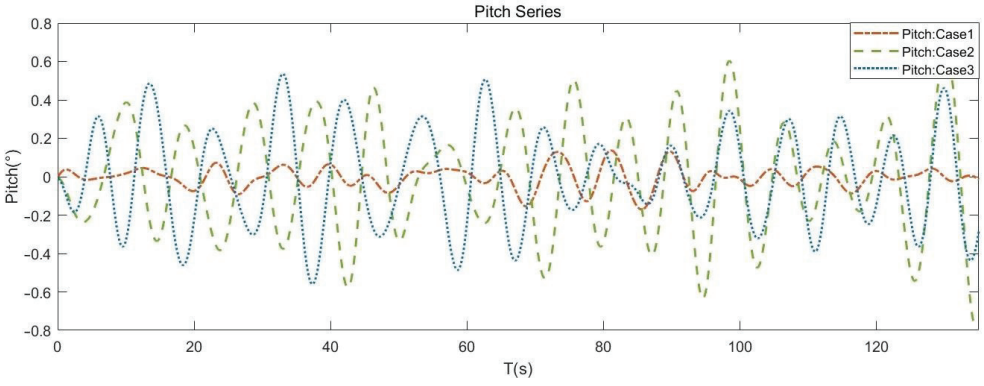

Figure 16. Pitch Series in Three Cases.

Ship motion series in three cases are forecasted by the method. Pre-trained node models are selected based on the correlation between node conditions and current conditions. The pre-trained model size is shown in Table 7 and selection for the three cases is depicted in Figures 17–19:

Table 7. Model Size.

	First-Order	First-Order	First-Order	First-Order
Params (K)	298.6	597.2	895.8	1194.5

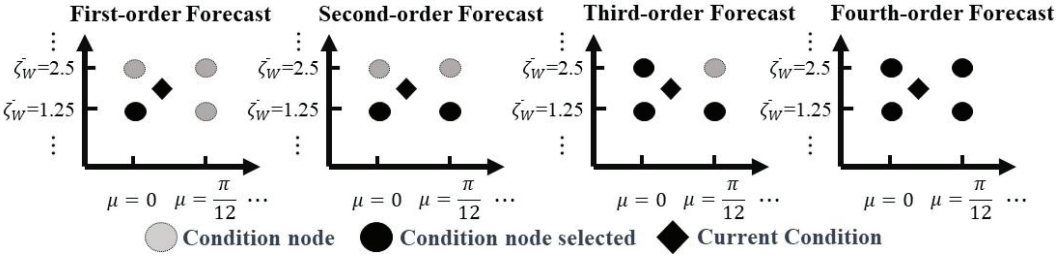

Figure 17. Pre-trained Model Selection in Case 1.

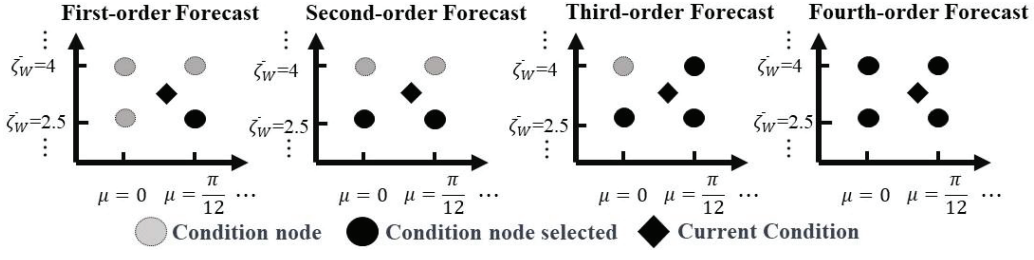

Figure 18. Pre-trained Model Selection in Case 2.

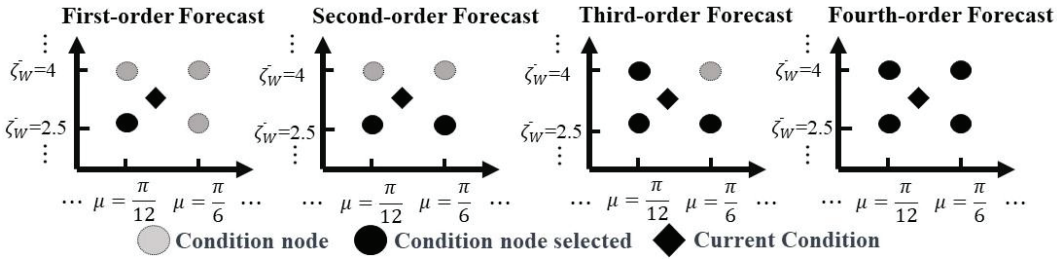

Figure 19. Pre-trained Model Selection in Case 3.

Pitch and heave motion forecasts with a duration of 5 s, 10 s, and 15 s are conducted for three cases, respectively. Leveraging the pre-training model selection results, 1-4 order models are used for each motion forecast. Throughout this experiment, the regression coefficients of the multi-order forecast model were set to be calculated and updated every 20 s. The forecast pitch series for case 3 is shown in Figures 20–22.

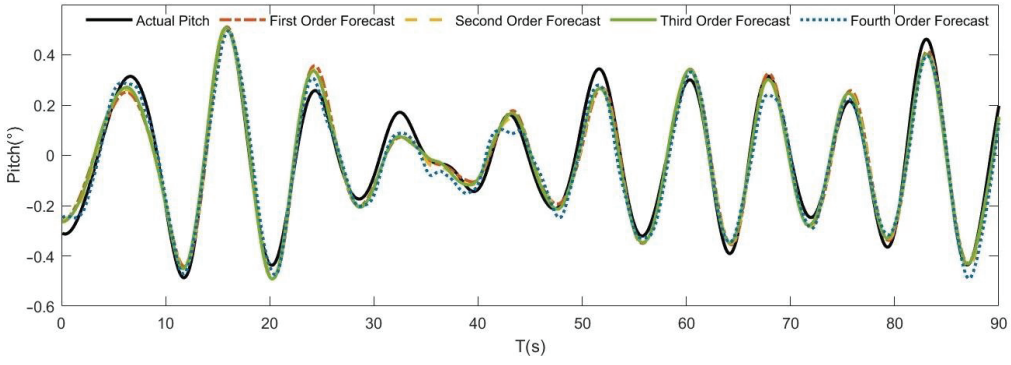

Figure 20. 1st–4th Pitch Forecast of 5s Duration in Case 3.

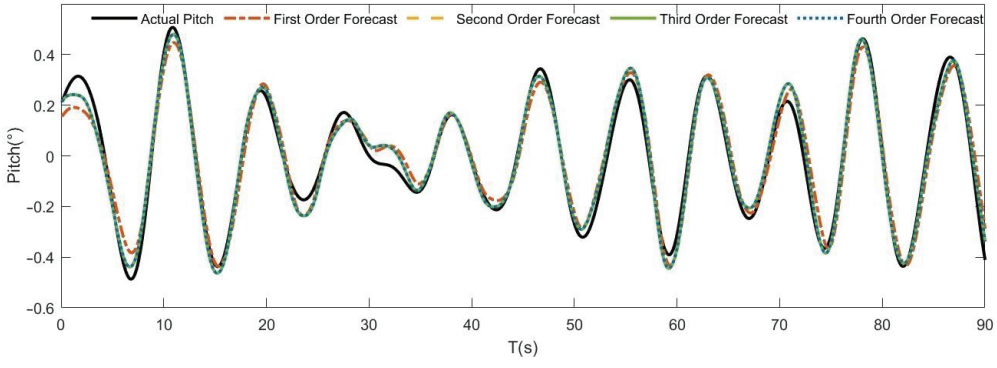

Figure 21. 1st–4th Pitch Forecast in 10s Duration in Case 3.

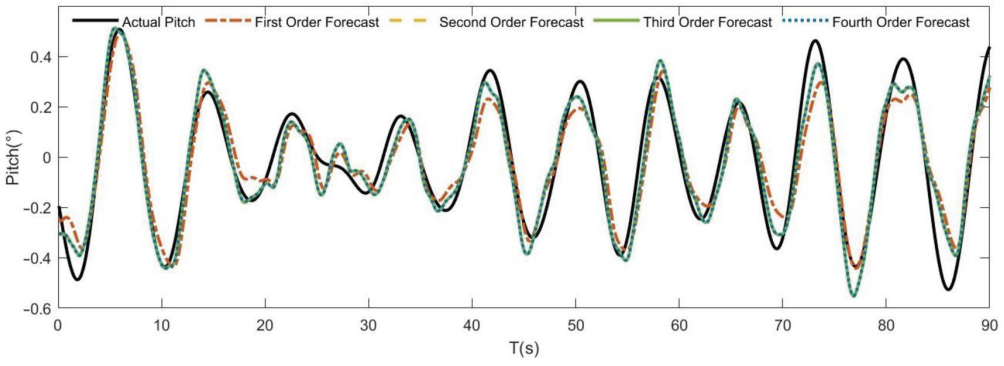

Figure 22. 1st–4th Pitch Forecast in 15s Duration in Case 3.

MAE, *RMSE*, and R_s are used to evaluate the forecast accuracy. The forecast results of three cases are presented in Tables 8–11. The results reveal that the forecast accuracy of the multi-order model is higher than that of the first-order model. The first-order forecast model exhibits the largest forecast error and the least accuracy under identical conditions and forecast durations. However, since the first-order forecasted model is essentially is a dynamic model selection in the absence of optimal computation, it has the smallest number of parameters and the fastest forecast speed.

Table 8. First-order Model Forecast.

		Case 1		Case 2		Case 3	
		Pitch	**Heave**	**Pitch**	**Heave**	**Pitch**	**Heave**
5 s Forecast	*MAE*	0.0118	0.0109	0.0462	0.0495	0.0360	0.0267
	RMSE	0.0291	0.0188	0.0583	0.0627	0.0437	0.0523
	R_s	0.9594	0.9531	0.9801	0.9736	0.9821	0.9750
10 s Forecast	*MAE*	0.0207	0.0282	0.0542	0.0493	0.0402	0.0415
	RMSE	0.0314	0.0340	0.0643	0.0644	0.0478	0.0548
	R_s	0.9415	0.9495	0.9764	0.9698	0.9807	0.9522
15 s Forecast	*MAE*	0.0387	0.0305	0.0935	0.0753	0.0701	0.0618
	RMSE	0.0442	0.0479	0.1163	0.0959	0.0892	0.0784
	R_s	0.9139	0.9277	0.9410	0.9105	0.9384	0.9132

Table 9. Second-order Model Forecast.

		Case 1		Case 2		Case 3	
		Pitch	**Heave**	**Pitch**	**Heave**	**Pitch**	**Heave**
5 s Forecast	*MAE*	0.0102	0.0103	0.0443	0.0455	0.0349	0.0226
	RMSE	0.0265	0.0164	0.0563	0.0572	0.0410	0.0338
	R_s	0.9643	0.9562	0.9814	0.9749	0.9847	0.9826
10 s Forecast	*MAE*	0.0193	0.0257	0.0465	0.0468	0.0302	0.0397
	RMSE	0.0302	0.0339	0.0590	0.0600	0.0368	0.0540
	R_s	0.9430	0.9546	0.9790	0.9698	0.9879	0.9545
15 s Forecast	*MAE*	0.0346	0.0287	0.0628	0.0654	0.0677	0.0592
	RMSE	0.0412	0.0455	0.0788	0.0838	0.0833	0.0745
	R_s	0.9315	0.9410	0.9607	0.9233	0.9534	0.9237

Table 10. Third-order Model Forecast.

		Case 1		Case 2		Case 3	
		Pitch	**Heave**	**Pitch**	**Heave**	**Pitch**	**Heave**
5 s Forecast	*MAE*	0.0101	0.0103	0.0442	0.0455	0.0319	0.0220
	RMSE	0.0265	0.0164	0.0564	0.0572	0.0391	0.0328
	R_s	0.9644	0.9562	0.9814	0.9741	0.9859	0.9833
10 s Forecast	*MAE*	0.0193	0.0258	0.0465	0.0467	0.0302	0.0390
	RMSE	0.0301	0.0339	0.0590	0.0598	0.0368	0.0540
	R_s	0.9430	0.9546	0.9790	0.9698	0.9879	0.9546
15 s Forecast	*MAE*	0.0344	0.0295	0.0627	0.0643	0.0677	0.0592
	RMSE	0.0412	0.0451	0.0787	0.0832	0.0833	0.0745
	R_s	0.9317	0.9413	0.9607	0.9254	0.9534	0.9237

Table 11. Fourth-order Model Forecast.

		Case 1		Case 2		Case 3	
		Pitch	**Heave**	**Pitch**	**Heave**	**Pitch**	**Heave**
5 s Forecast	*MAE*	0.0102	0.0103	0.0442	0.0455	0.0319	0.0220
	RMSE	0.0265	0.0166	0.0563	0.0572	0.0391	0.0328
	R_s	0.9643	0.9562	0.9814	0.9741	0.9858	0.9833
10 s Forecast	*MAE*	0.0193	0.0257	0.0465	0.0467	0.0301	0.0397
	RMSE	0.0302	0.0339	0.0590	0.0598	0.0368	0.0539
	R_s	0.9430	0.9545	0.9790	0.9698	0.9879	0.9545
15 s Forecast	*MAE*	0.0344	0.0295	0.0628	0.0643	0.0679	0.0592
	RMSE	0.0412	0.0455	0.0788	0.0832	0.0836	0.0745
	R_s	0.9315	0.9410	0.9607	0.9254	0.9531	0. 9237

When the multi-order model is used for forecasting, both *MAE* and *RMSE* exhibit a 4% to 15% decrease compared with the first-order model forecast in all forecast durations. In the 5s duration forecast, R_s of the second-order forecast model experiences an approximately 0.5% increase. This is because the forecast duration is relatively short, so the distinctiveness of series characteristics is not obvious. In the 10s duration forecast, R_s of the second-order model forecast increases by 0.5% to 1%. In the 15 s duration forecast, the R_s increases by about 2%. This is because as the forecast duration increases, the distinctiveness of the series distribution characteristics becomes more significant. Therefore, the improvement of R_s in forecasting is also greater in second-order model. In the multi-order model prediction, the *MAE* and *RMSE* of the third-order forecast model are reduced by less than 5% compared with the second-order model, with a slight or no improvement in R_s. Compared with the third-order prediction model, the fourth-order forecast model exhibits nearly no improvement across the three evaluation indicators while having the largest number of parameters.

In conclusion, for ship motion forecasting with a 5-s forecasting duration, the first-order forecast model demonstrates a quicker response and a smaller model size, making it more suitable for very short-term forecast tasks with high real-time requirements and limited resources [33]. The second-order forecast model showcases higher accuracy and smaller errors. As the forecast duration increases to 10 s and 15 s, the accuracy of the second-order model improves even more significantly. Although the accuracy of the third-order model is slightly higher than that of the second-order model, the size of the model and computation time are also higher. In comparison, the fourth-order model demonstrates almost no improvement in accuracy, and it has the largest model size. The selection of different forecast models necessitates trade-offs between forecast performance, computational efficiency, and model size.

4. Conclusions

While conducting operations at the actual sea surface, ships frequently encounter diverse sea conditions, such as waves, tidal currents, and wind forces. A data-driven ship motion forecast method is proposed in this paper, aiming at the problem of single application scenarios and the diminished generalization ability of existing methods in ship motion forecasting. This model integrates machine learning techniques with potential flow theory methods to enhance forecasting accuracy and broaden its applicability. The main components are as follows:

(1) Substantial numerical simulations using the KCS ship model are conducted. The obtained motion response series were then used to train BiLSTM network models, creating a pre-trained forecast model database with varying forecast durations.

(2) A calculation method of condition correlation is proposed, facilitating the 1–4 order forecast models, which are determined through the method. The Golden Jackal optimization algorithm is employed to compute the regression coefficients for each pre-trained model. The dynamic model averaging is calculated to forecast the motion of the ship under non-node conditions.

The results indicate that when forecasting ship motion under non-node conditions, the first-order forecast model exhibits the lowest accuracy compared with the multi-order model. As the forecast duration extends, the accuracy of the multi-order forecast model shows more obvious improvement. While the third-order forecast model demonstrates slightly superior performance to the second-order model, it comes at the cost of a larger number of model parameters. The fourth-order prediction model has the largest number of parameters and almost no improvement in accuracy.

The approach in this study makes forecasting more comprehensive and reliable, considering the diversity of sea conditions and ship motion states. The pre-training model can be better adapted to the ship motion forecast under non-node conditions by making full use of the data under node conditions. The method is of significance for improving safety and operational efficiency in offshore operations. However, challenges persist in ship motion and wave elevation detection. The accuracy of a ship motion forecast can be affected by the presence of missing data and noise. Further enhancements are needed in the robustness of the forecast model to address these concerns. In subsequent research, the accurate identification of wave elevations on the sea surface and the model's adaptability to ship motion under high sea conditions will also be studied. Additional research methods, such as Variational Mode Decomposition, may be explored to augment the algorithm's capacity for forecasting ship motion in challenging sea conditions.

Author Contributions: Conceptualization, W.L.; Data curation, Y.M.; Formal analysis, Y.M.; Methodology, Z.J.; Project administration, W.L.; Resources, Z.J.; Supervision, W.L.; Validation, Y.M.; Writing—original draft, Z.J.; Writing—review and editing, Z.J. and W.L. All authors have read and agreed to the published version of the manuscript.

Funding: This research received no external funding.

Institutional Review Board Statement: Not applicable.

Informed Consent Statement: Not applicable.

Data Availability Statement: Data will be made available on request.

Conflicts of Interest: The research was conducted in the absence of any commercial or financial relationships that could be construed as a potential conflict of interest.

References

1. Kubo, M.; Mizui, S.; Inoue, K. Safety evaluation of ship entering a harbor under severe wave conditions. In Proceedings of the 10th International Offshore and Polar Engineering Conference (ISOPE-2000), Seattle, WA, USA, 28 May–2 June 2000; Grundy, P., Koo, J., Langen, I., Knapp, R., Eds.; ISOPE: Mountain View, CA, USA, 2000; Volume IV, pp. 330–336.
2. Chu, Y.G.; Li, G.Y.; Hatledal, L.I.; Holmeset, F.T.; Zhang, H.X. Coupling of dynamic reaction forces of a heavy load crane and ship motion responses in waves. *Ships Offshore Struct.* **2021**, *16*, 58–67. [CrossRef]

3. Neupert, J.; Mahl, T.; Haessig, B.; Sawodny, O.; Schneider, K. A heave compensation approach for offshore cranes. In Proceedings of the 2008 American Control Conference, Seattle, WA, USA, 11–13 June 2008; IEEE: Piscataway, NJ, USA, 2008; Volume 1–12, p. 538.
4. Yang, H.; Pan, Z.; Bai, W. Review of Time Series Prediction Methods. *Comput. Sci.* **2019**, *46*, 21–28.
5. Nie, Z.H.; Lu, Z.F.; Lai, P.; Zhou, J.P.; Yao, F.J. Short-term Prediction of Large Ship Motion Based on Empirical Mode Decomposition and Autoregressive Model. In Proceedings of the 2022 IEEE 6th Advanced Information Technology, Electronic and Automation Control Conference (IAEAC), Beijing, China, 3–5 October 2022; IEEE: Piscataway, NJ, USA, 2022; pp. 933–937.
6. Peng, X.Y.; Zhang, B.; Rong, L.H. A robust unscented Kalman filter and its application in estimating dynamic positioning ship motion states. *J. Mar. Sci. Technol.* **2019**, *24*, 1265–1279. [CrossRef]
7. Jiang, H.; Duan, S.L.; Huang, L.M.; Han, Y.; Yang, H.; Ma, Q.W. Scale effects in AR model real-time ship motion prediction. *Ocean Eng.* **2020**, *203*, 107202. [CrossRef]
8. Takami, T.; Nielsen, U.D.; Jensen, J.J. Real-time deterministic prediction of wave-induced ship responses based on short-time measurements. *Ocean Eng.* **2021**, *221*, 108503. [CrossRef]
9. Ramadevi, B.; Bingi, K. Chaotic Time Series Forecasting Approaches Using Machine Learning Techniques: A Review. *Symmetry* **2022**, *14*, 955. [CrossRef]
10. D'Agostino, D.; Serani, A.; Stern, F.; Diez, M. Time-series forecasting for ships maneuvering in waves via recurrent-type neural networks. *J. Ocean Eng. Mar. Energy* **2022**, *8*, 479–487. [CrossRef]
11. Silva, K.M.; Maki, K.J. Data-Driven system identification of 6-DoF ship motion in waves with neural networks. *Appl. Ocean Res.* **2022**, *125*, 103222. [CrossRef]
12. Diez, M.; Serani, A.; Campana, E.F.; Stern, F. Time-series forecasting of ships maneuvering in waves via dynamic mode decomposition. *J. Ocean Eng. Mar. Energy* **2022**, *8*, 471–478. [CrossRef]
13. Burkart, N.; Huber, M.F. A Survey on the Explainability of Supervised Machine Learning. *J. Artif. Intell. Res.* **2021**, *70*, 245–317. [CrossRef]
14. Suhermi, N.; Suhartono; Prastyo, D.D.; Ali, B. Roll motion prediction using a hybrid deep learning and ARIMA model. In *Proceedings of the 3rd INNS Conference on Big Data and Deep Learning (INNS BDDL), Kota Denpasar, Indonesia, 17–19 April 2018*; Ozawa, S., Tan, A.H., Angelov, P.P., Roy, A., Pratama, M., Eds.; Elsevier: Amsterdam, The Netherlands, 2018; Volume 144, pp. 251–258.
15. Xu, W.Z.; Maki, K.J.; Silva, K.M. A data-driven model for nonlinear marine dynamics. *Ocean Eng.* **2021**, *236*, 109469. [CrossRef]
16. Ye, R.; Dai, Q. A novel transfer learning framework for time series forecasting. *Knowl.-Based Syst.* **2018**, *156*, 74–99. [CrossRef]
17. Du, Y.T.; Wang, J.D.; Feng, W.J.; Pan, S.N.; Qin, T.; Xu, R.J.; Wang, C.J. AdaRNN: Adaptive Learning and Forecasting for Time Series. In Proceedings of the 30th ACM International Conference on Information & Knowledge Management (CIKM), Gold Coast, Australia, 1–5 November 2021; ACM: New York, NY, USA, 2021; pp. 402–411.
18. Dormann, C.F.; Calabrese, J.M.; Guillera-Arroita, G.; Matechou, E.; Bahn, V.; Barton, K.; Beale, C.M.; Ciuti, S.; Elith, J.; Gerstner, K.; et al. Model averaging in ecology: A review of Bayesian, information-theoretic, and tactical approaches for predictive inference. *Ecol. Monogr.* **2018**, *88*, 485–504. [CrossRef]
19. Darbandsari, P.; Coulibaly, P. Introducing entropy-based Bayesian model averaging for streamflow forecast. *J. Hydrol.* **2020**, *591*, 125577. [CrossRef]
20. Naser, H. Estimating and forecasting the real prices of crude oil: A data rich model using a dynamic model averaging (DMA) approach. *Energy Econ.* **2016**, *56*, 75–87. [CrossRef]
21. Jiang, Y.S.; Jia, M.Q.; Zhang, B.; Deng, L.W. Ship Attitude Prediction Model Based on Cross-Parallel Algorithm Optimized Neural Network. *IEEE Access* **2022**, *10*, 77857–77871. [CrossRef]
22. Wei, Y.Y.; Chen, Z.Z.; Zhao, C.; Tu, Y.H.; Chen, X.; Yang, R. A BiLSTM hybrid model for ship roll multi-step forecasting based on decomposition and hyperparameter optimization. *Ocean Eng.* **2021**, *242*, 110138. [CrossRef]
23. Zhang, G.Y.; Tan, F.; Wu, Y.X. Ship Motion Attitude Prediction Based on an Adaptive Dynamic Particle Swarm Optimization Algorithm and Bidirectional LSTM Neural Network. *IEEE Access* **2020**, *8*, 90087–90098. [CrossRef]
24. Do, K.D.; Jiang, Z.P.; Pan, J. Robust global stabilization of underactuated ships on a linear course: State and output feedback. *Int. J. Control* **2003**, *76*, 1–17. [CrossRef]
25. Seo, M.G.; Kim, Y. Numerical analysis on ship maneuvering coupled with ship motion in waves. *Ocean Eng.* **2011**, *38*, 1934–1945. [CrossRef]
26. Yang, W.; Liang, Y.K.; Leng, J.X.; Li, M. The Autocorrelation Function Obtained from the Pierson-Moskowitz Spectrum. In Proceedings of the Global Oceans 2020: Singapore—U.S. Gulf Coast, Biloxi, MS, USA, 5–30 October 2020; IEEE: Piscataway, NJ, USA, 2020.
27. Peng, T.; Zhang, C.; Zhou, J.Z.; Nazir, M.S. An integrated framework of Bi-directional long-short term memory (BiLSTM) based on sine cosine algorithm for hourly solar radiation forecasting. *Energy* **2021**, *221*, 119887. [CrossRef]
28. Yu, Y.; Si, X.S.; Hu, C.H.; Zhang, J.X. A Review of Recurrent Neural Networks: LSTM Cells and Network Architectures. *Neural Comput.* **2019**, *31*, 1235–1270. [CrossRef]
29. Raftery, A.E.; Kárny, M.; Ettler, P. Online Prediction Under Model Uncertainty via Dynamic Model Averaging: Application to a Cold Rolling Mill. *Technometrics* **2010**, *52*, 52–66. [CrossRef]

30. Chopra, N.; Ansari, M.M. Golden jackal optimization: A novel nature-inspired optimizer for engineering applications. *Expert Syst. Appl.* **2022**, *198*, 116924. [CrossRef]
31. *GB/T 42176-2022*; The Grade of Wave Height. General Administration of Quality Supervision. Inspection and Quarantine of the People's Republic of China: Beijing, China, 2022.
32. Shen, Z.; Wan, D.; Carrica, P.M. Dynamic overset grids in OpenFOAM with application to KCS self-propulsion and maneuvering. *Ocean Eng.* **2015**, *108*, 287–306. [CrossRef]
33. Li, Y.; Xiao, L.; Wei, H.; Kou, Y.; Li, X. Comparative Study of Two Neural Network Models for Online Prediction of Wave Run-up on Semi-Submersible. *Shipbuild. China* **2023**, *64*, 28–40.

Journal of
Marine Science and Engineering

MDPI

Article

Fluid Structure Interaction Using Modal Superposition and Lagrangian CFD

Manigandan Paneer [1,2,*], Josip Bašić [1], Damir Sedlar [1], Željan Lozina [1], Nastia Degiuli [3] and Chong Peng [2]

[1] Faculty of Electrical Engineering, Mechanical Engineering and Naval Architecture, University of Split, Ruđera Boškovića 32, 21000 Split, Croatia; jobasic@fesb.hr (J.B.); dsedlar@fesb.hr (D.S.); lozina@fesb.hr (Ž.L.)
[2] Engineering Software Steyr, Berggasse 35, 4400 Steyr, Austria; chong.peng@essteyr.com
[3] Faculty of Mechanical Engineering and Naval Architecture, University of Zagreb, Ivana Lučića 5, 10000 Zagreb, Croatia; nastia.degiuli@fsb.hr
* Correspondence: manigandan.paneer.00@fesb.hr

Abstract: This study investigates the impact of fluid loads on the elastic deformation and dynamic response of linear structures. A weakly coupled modal solver is presented, which involves the solution of a dynamic equation of motion with external loads. The mode superposition method is used to find the dynamic response, utilizing predetermined mode shapes and natural frequencies associated with the structure. These essential parameters are pre-calculated and provided as input for the simulation. Integration of the weakly coupled modal solver is accomplished with the Lagrangian Differencing Dynamics (LDD) method. This method can directly use surface mesh as boundary conditions, so it is much more convenient than other meshless CFD methods. It employs Lagrangian finite differences, utilizing a strong formulation of the Navier–Stokes equations to model an incompressible free-surface flow. The elastic deformation of the structure, induced by fluid forces obtained from the flow solver, is computed within the modal coupling algorithm through direct numerical integration. Subsequently, this deformation is introduced into the flow solver to account for changes in geometry, resulting in updated flow pressure and velocity fields. The flow particles and vertices of the structure are advected in Lagrangian coordinates, resulting in Lagrangian–Lagrangian coupling in spaces with weak or explicit coupling in time. The two-way coupling between fluid and structure is successfully validated through various FSI benchmark cases. The efficiency of the LDD method is highlighted as it operates directly on surface meshes, streamlining the simulation setup. Direct coupling of structural deformation eliminates the conventional step of mapping fluid results onto the structural mesh and vice versa.

Keywords: FSI; LDD; natural frequencies; mode shapes

Citation: Paneer, M.; Bašić, J.; Sedlar, D.; Lozina, Ž.; Degiuli, N.; Peng, C. Fluid Structure Interaction Using Modal Superposition and Lagrangian CFD. *J. Mar. Sci. Eng.* **2024**, *12*, 318. https://doi.org/10.3390/jmse12020318

Academic Editor: Csaba Pákozdi

Received: 6 January 2024
Revised: 6 February 2024
Accepted: 8 February 2024
Published: 12 February 2024

1. Introduction

The Fluid–Structure Interaction (FSI) is the most prevalent physical phenomenon in various engineering applications. Some of the applications, such as the interaction between waves and vegetation in coastal wetlands and wave–ice interactions in the Arctic environment [1], are crucial in mitigating coastal flooding [2]. FSI plays a pivotal role in the refinement of structural designs for optimal performance under fluid loads, ensuring both efficiency and reliability [3], e.g., the construction of offshore installations and the design of windmills and ships. Identifying FSI-related issues early allows cost-effective design changes, reducing the need for any modifications during manufacturing or operation [4]. Similarly, FSI affects the hydrodynamic performance of propellers, e.g., [5,6]. The damping represents energy dissipation within vibration cycles and emerges as a key factor in resonance phenomena, impacting harmonic vibration amplitudes and the count of noteworthy vibrations in time-dependent scenarios. In most cases, the role of damping can be negligible in slightly damped vibrations. However, in the natural frequencies, their

influence becomes pronounced, especially in near-resonant conditions, where excitation is balanced solely through damping. Damping in the structure is generally low, except when near resonance and the vibration cycle maintains a substantial level of independence [7].

However, simulating FSI effectively is complex, requiring certain assumptions in both structural and fluid simulations. In most of the Computational Fluid Dynamics (CFD) simulations, the consideration of elastic deformation at the boundaries is ignored [8]. Similarly, in most of the structural simulations, a constant pressure is considered at the interior and exterior boundaries. Paik et al. [9] presented methods for coupling the CFD solver with rigid and elastic models of a ship hull to compute structural loads. One-way and two-way coupling approaches were used when considering the ship as elastic. In one-way coupling, forces from CFD were used for structural loads analysis, but deformations were not feedback to CFD. In two-way coupling, hull deformations influenced the CFD solution. A URANS/DES overset solver with the modal superposition method is used for the analysis. The gluing method was applied to transfer forces and deformations between non-matching CFD and structural grids [9].

Different varieties of approaches have been formulated to tackle the intricacies of one-way and two-way coupling of the FSI. A prominent approach involves fully coupled (monolithic) methods that integrate structural and flow calculations in a single solver [10,11]. Conventional CFD solvers predominantly use an Eulerian-based approach. However, such coupling of structural formulations, which mostly use Lagrangian-based approaches, leads to a stiffer computation for the structural component compared to the fluid component. Moreover, employing a unified scheme for extensive scenarios becomes computationally intensive [12].

Grid-based partitioned methods offer a more feasible alternative to monolithic methods by tackling both the flow and structural formulation on two different meshes using distinct solvers [13]. These methods necessitate the establishment of a communication protocol at the interface between grids to appropriately transfer fluid loads to the structural mesh and, conversely, to map the deformation onto the fluid mesh. In mesh-based solvers, effective adjustment of the fluid mesh boundaries requires precise manipulation of adjacent mesh nodes to prevent mesh entanglement or deformation [14,15]. Recent advances have demonstrated the successful application of partitioned methods, such as coupling thin-walled girder theory with potential flow theory [16,17] and linking modal structure solvers with RANS-VOF solvers, Boundary-Integral Equation Methods [18]. Solid4Foam with the finite volume library is provided by OpenFOAM [19,20].

The meshless-based partitioned method offers several advantages, especially in scenarios that involve free surfaces, violent flow, complex models, and large deformations [21]. In this approach, the need for re-meshing of the model after deformation is effectively avoided. FSI is achieved by coupling the Smooth Particle Hydrodynamics (SPH) with different structural solvers such as the Finite Element Method (FEM) [22–24] and Discrete Element Method (DEM) [25–27] to compute the structural deformation. However, transferring the information is not easy, as it is necessary to resolve the interfacial energy balance [28]. Solving the structural deformation is computationally expensive but less so than the monolithic method.

In recent days, the Mode Superposition method has been used to solve structural deformation, and it is the most robust, fast, and computationally inexpensive method. Debrabandere et al. (2012) presented a new reduced-order modeling approach for FSI simulations. The method uses modal analysis to represent structural dynamics, solving the modal equations within the computational fluid dynamics solver using a complementary function and a particular integral method. Results for simple test cases compare well with full-order models and experiments. FSI predictions for realistic turbomachinery configurations demonstrate the potential of the method for efficient aeroelastic analysis of flexible structures [29]. Sun et al. (2019) presented the Moving Particle Semi-implicit (MPS) with the mode superposition method to simulate violent hydroelastic issues [30]. Corrado et al. (2020) validated the two-way coupling between CFD and FEM solvers and a

more efficient modal superposition approach with the help of the HIRENASD test case [31]. Modal superposition is a useful technique for evaluating structures that are subjected to dynamic loads due to its computational efficiency and simplicity. However, when dealing with large structural deformations, the accuracy of this method tends to decrease. This is because modal superposition assumes linear behavior and uncoupled modes, which may not hold true in scenarios involving significant nonlinearity or mode coupling. Despite these limitations, modal superposition remains a widely used and valuable tool, especially when applied within its valid range [29–31]. Weak coupling in FSI offers simplicity and ease of implementation, making it suitable for scenarios with transient events. However, its limitations include stability issues necessitating small time steps, which can lead to computational inefficiency, and potential accuracy trade-offs compared to implicit methods, especially in large-scale simulations where the fluid and structural solvers use time steps of different magnitudes [32]. The convenience of using modes superposition is that the structural solver adds insignificant computational cost [17,29] and therefore, can adjust to the flow solver requirements.

The aim of this study is to develop a model for Fluid–Structure Interaction (FSI) by combining the Mode Superposition method and the Lagrangian Differencing Dynamics (LDD) method in two-way partitioned weak coupling or explicit coupling. In terms of computational efficiency, the LDD method is advantageous compared to most popular meshless approaches, such as Smoothed Particle Hydrodynamics (SPH), Moving Particle Semi-implicit (MPS), finite point set method, and finite point method [33–35]. The LDD method achieves large time steps with lower computational costs while maintaining second-order accuracy. It is well-suited for complex transient problems since it has the advantage of directly working on the meshes [8,16,17,36]. Using the mode superposition method with LDD, structural deformation is calculated for the fluid load using precalculated mode shapes and natural frequencies from the modal analysis. This approach leads to stable, robust, and computationally efficient FSI simulations. The method enables fluid-induced structural deformation to be weakly coupled into the flow solver. The deformation is obtained by using direct integration. The flow particles and vertices of the structure are advected in Lagrangian coordinates. This results in Lagrangian–Lagrangian coupling in space, while there is weak or explicit coupling in time. This ensures a more accurate representation of the interaction between fluid and structure in ship and offshore hydrodynamics. The efficiency of the LDD and Mode Superposition methods, operating directly on surface meshes, may lead to practical and effective ship and offshore hydrodynamic simulations.

This paper discusses fluid–structure interaction (FSI) modeling using the two-way weak coupling approach. Specifically, this paper details the governing equation of the LDD method and the mode superposition technique in Section 2. The methodology of implementing two-way coupling of FSI is then explained in Section 3. In Section 4, various benchmark cases are presented that are then validated and verified with modal coupling results. Finally, concluding remarks and a summary of the findings are given in Section 5.

2. Governing Equation

2.1. Incompressible Fluid Flow

An incompressible fluid flow solver known as LDD is employed, which utilizes a generalized finite difference method with a meshless approach. It uses a robust and implicit formulation of the Navier–Stokes equations to simulate incompressible free-surface fluids. This solver is utilized to address initial boundary value problems, achieving second-order accuracy in its solution. It has been successfully validated in various scenarios, including lid-driven cavity, dam break, sloshing, water entry, etc. [8,36,37]. The continuity and momentum equations are provided below:

$$\frac{D\boldsymbol{u}}{Dt} = -\frac{1}{\rho}\nabla p + \nu\nabla^2\boldsymbol{u} + \boldsymbol{g}, \qquad x \in \Omega, \tag{1}$$

$$\nabla.\boldsymbol{u} = 0 \qquad x \in \Omega \cup \Gamma_w \cup \Gamma_{fs}, \tag{2}$$

$$\boldsymbol{u} = \boldsymbol{U} \qquad x \in \Gamma_{w,} \tag{3}$$

$$\boldsymbol{u}(t=0) = \boldsymbol{u_0} \qquad x \in \Omega \tag{4}$$

In this context, $\frac{D}{Dt}$ signifies the time rate of change of a property, $\boldsymbol{u}$ stands for the velocity vector, ρ represents the fluid density, p denotes the dynamic pressure, v symbolizes the kinematic viscosity, g represents gravity, $\boldsymbol{U}$ corresponds to the wall velocity, and $\boldsymbol{u}_0$ denotes the initial velocity vector.

The pressure and velocity equations are solved in a decoupled manner. The pressure Poisson and the pressure gradient equations are presented as follows:

$$\begin{aligned} \nabla^2 p &= -\rho \nabla \cdot D\boldsymbol{u}/Dt \qquad x \in \Omega, \\ \boldsymbol{n} \cdot \nabla p &= \rho \boldsymbol{n} \cdot [-\frac{D\boldsymbol{u}}{Dt} + \boldsymbol{g} + \nu \nabla^2 \boldsymbol{u}] \qquad x \in \Gamma_w \\ p &= p_{atm,} \qquad x \in \Gamma_{fs} \end{aligned} \tag{5}$$

where $\boldsymbol{n}$ represents the normal vector at walls, p_{atm} represents atmospheric pressure, and $\boldsymbol{g}$ is the gravity constant. Additional information can be found in [8,36–38]. The gradient and Laplacian operators from Basic et al. [38] are utilized to discretize the equations mentioned above. To calculate the value of a general function, denoted by f, at a specific node i, the neighbouring nodes represented by j within a compact radius of h are taken into account. The differential operators, which are based on [38], are defined as:

$$\langle \nabla f \rangle_i = \boldsymbol{B}_i \sum_{j \in I} W_{ij} \boldsymbol{r}_{ij} (f_j - f_i) \tag{6}$$

$$\langle \nabla^2 f \rangle_i = \frac{2d \sum_{j \epsilon N} W_{ij} (f_j - f_i)(1 - \boldsymbol{r}_{ij}.\boldsymbol{B_i o_i})}{\sum_{j \epsilon N} W_{ij} (1 - \boldsymbol{r}_{ij}.\boldsymbol{B}_i \boldsymbol{o}_i) \parallel \boldsymbol{r}_{ij} \parallel^2} \tag{7}$$

where, $\boldsymbol{r}_{ij} = \boldsymbol{r}_j - \boldsymbol{r}_i$ denotes the vector between locations of points i and j, while $\boldsymbol{r}_i$ and $\boldsymbol{r}_j$ denote the positions of points i and j in the fluid domain. The distance between these points is a scalar defined as $r_{ij} = \|\boldsymbol{r}_{ij}\|$. The weighting function $W_{ij} = W(\boldsymbol{r}_{ij}, h)$ depends on the distance r_{ij}, defined within some radius of the compact sphere, h. Here, f_i and f_j represent the function values at locations $\boldsymbol{r}_i$ and $\boldsymbol{r}_j$, respectively. The symmetric renormalization tensor $\boldsymbol{B}_i$, and the offset vector $\boldsymbol{o}_i$ are, respectively, defined as:

$$\boldsymbol{B}_i = \left(\sum_{j \in I} W_{ij} \boldsymbol{r}_{ij} \otimes \boldsymbol{r}_{ij} \right)^{-1} \tag{8}$$

$$\boldsymbol{o}_i = \sum_{j \in I} W_{ij} \boldsymbol{r}_{ij} \tag{9}$$

The solution of a time step in the LDD method initiates with the Lagrangian advection of points, i.e., the points are moved in space according to their velocities. The streamlines compressibility issues that arise during Lagrangian advection are resolved using the Particle-Based Dynamics (PBD) technique, which iteratively rearranges the locations of points by enforcing a uniform distances between neighbor points [8]. Following this, the pressure Poisson Equation (PPE) defined above is discretized by using the discrete operators, that are defined above and analyzed in [38]. In this study, the PPE is solved using the preconditioned BiCGSTAB linear solver, as explained in [8]. After solving the PPE, the velocity equation arising from the momentum Equation (1) is explicitly determined for each time step.

2.2. Mode Superposition

The method of modal superposition is employed to analyze the dynamic behavior of structures. It is estimated through the superposition of a limited number of modal frequencies obtained from the modal analysis. Modal analysis comes into play to determine the vibration characteristics, primarily the modes of operation and the natural frequencies of a mechanical system or component. Natural frequency, or eigenfrequency, denotes the frequency at which a system naturally oscillates without any external driving force. On the other hand, mode shapes, also referred to as eigenvectors, depict the inherent behavior of the component at its natural frequency. Both these parameters hold significance in the structural design process, especially for scenarios involving dynamic loads. This approach is particularly effective in minimizing computational efforts when evaluating the dynamic response of linear structures [16,39]. This technique proves advantageous especially when dealing with limited known loading frequencies. However, it is less applicable to the issues that encompass exceedingly high frequencies [29,31].

The dynamic equation for a structure can be represented in matrix form as follows:

$$\boldsymbol{M\ddot{u}} + \boldsymbol{C\dot{u}} + \boldsymbol{Ku} = \boldsymbol{f}(t) \tag{10}$$

In this equation, $\boldsymbol{M}$ denotes the mass-normalized matrix, $\boldsymbol{C}$ represents the damping matrix, and $\boldsymbol{K}$ stands for the stiffness matrix. The column vector $\boldsymbol{u}$ corresponds to the degree of freedom, while $\boldsymbol{f}(t)$ represents the applied forces over time. These matrices are obtained through the discretization of the physical domain, resulting in an NxN matrix where N signifies the degrees of freedom of the structural model. Mass normalization is convenient in the modal superposition, as it ensures that the modal mass is consistent across all modes, simplifying the modal participation factors and making them directly interpretable as a percentage of total mass.

The foundation of modal superposition is rooted in modal analysis, yielding essential outputs such as eigenfrequencies and their corresponding mode shapes. The eigenfrequencies are computed via the undamped dynamic equation, treated as an eigenvalue problem:

$$(-\omega^2\boldsymbol{M} + \boldsymbol{K})\boldsymbol{\Phi} = 0, \qquad \boldsymbol{\Phi} \neq 0 \tag{11}$$

In this context, the symbol $\boldsymbol{\Phi}$ refers to the modal matrix, which contains a vector of the mode shape corresponding to every natural frequency of the structure with n-DOF, $\boldsymbol{\Phi} = \boldsymbol{\Phi}_1, \boldsymbol{\Phi}_2, ..., \boldsymbol{\Phi}_n$. Usually, the Finite Element Method (FEM) is used to model a structure, and discretize and solve Equation (11). Multiple numerical methods exist for determining natural frequencies and mode shapes, as no single method is universally optimal for all problems. The techniques for extracting eigenvalues fall under the category of transformation methods and/or tracking methods. The eigenvalue equation is initially converted into a specific format in the transformation method, facilitating the extraction of eigenvalues. The tracking method involves extracting the eigenvalues individually through an iterative procedure. In this study, the Lanczos method was used, which combines characteristics of the tracking and transformation methods. Mass normalization involves scaling the mode shapes such that the square of the mode shape integrated over the structure equals one. This ensures that each mode shape has a unit mass and simplifies the subsequent modal superposition calculations.

After the vibration modes and frequencies are extracted, their combination may be used to simulate complex vibration of the structure. The superposition involves expressing the displacement response as a linear combination of modal contributions. The overall displacement $(\boldsymbol{u}(t))$ of the structural system for a time step can be represented as a combination of mode shapes:

$$\boldsymbol{u}(t) = \sum_{i=1}^{n} \boldsymbol{\Phi y_i}(t) \tag{12}$$

where $\boldsymbol{y}(t)$ is the vector of modal coordinates (or generalized displacement). While one can extract many vibration modes from a FEM model, in engineering practice, usually only first few modes are relevant for analysis. By applying the generalized displacement and the mass normalized modal vector $\boldsymbol{\Phi}$ (i.e., substituting Equation (12) into Equation (10)), the following is obtained:

$$\boldsymbol{\Phi}^T \boldsymbol{M} \boldsymbol{\Phi} \ddot{\boldsymbol{y}}(t) + \boldsymbol{\Phi}^T \boldsymbol{C} \boldsymbol{\Phi} \dot{\boldsymbol{y}}(t) + \boldsymbol{\Phi}^T \boldsymbol{K} \boldsymbol{\Phi} \boldsymbol{y}(t) = \boldsymbol{\Phi}^T \boldsymbol{f}(t) \tag{13}$$

To decouple the equation of motion for a Multi-Degree-of-Freedom (MDOF) system into n equations of motion for Single Degree of Freedom (SDOF) systems, it is necessary to diagonalize the damping term. This requires the introduction of a damping matrix, as proposed by Lord Rayleigh, that is assumed to exhibit proportionality to both the mass and stiffness matrices.

$$\boldsymbol{C} = \beta \boldsymbol{K} + \alpha \boldsymbol{M} \tag{14}$$

The final equation of motion to be solved to simulate the FSI is given as follows:

$$\ddot{\boldsymbol{y}}_i(t) + 2\omega_i \zeta_i \dot{\boldsymbol{y}}_i(t) + \omega_i^2 \boldsymbol{y}_i(t) = \boldsymbol{\Phi}_i^T \boldsymbol{f}(t) \tag{15}$$

where ζ_i represents the damping ratio associated with mode i. It signifies the extent of real damping present within a system in comparison to critical damping.

While any integration method may be used to solve the above ordinary differential Equation (15) (ODE), in this proposed coupling method, the equation is solved using the Complementary Function and Particular Integral (CFPI) method [29]. The solution is presented in two parts: the complementary solution and the particular solution.

The complementary solution is defined as:

$$\begin{aligned} \boldsymbol{y}_t &= \boldsymbol{y_{t-1}} \cdot e \cdot (C + \frac{\zeta}{s} \cdot S) + \dot{\boldsymbol{y}}_{\boldsymbol{t-1}} \cdot e \cdot \frac{1}{\omega_n \cdot s} \cdot S \\ \dot{\boldsymbol{y}}_t &= \dot{\boldsymbol{y}}_{\boldsymbol{t-1}} \cdot e \cdot (C - \frac{\zeta}{s} \cdot S) - \boldsymbol{y_{t-1}} \cdot e \cdot \frac{\omega_n}{s} \cdot S \end{aligned} \tag{16}$$

where, $\boldsymbol{y}_t$ is displacement of current time step, $\boldsymbol{y}_{t-1}$ is displacement of previous time step, $\dot{\boldsymbol{y}}_t$ is velocity of current time step and $\dot{\boldsymbol{y}}_{t-1}$ is velocity of previous time step

The particular solution is defined as:

$$\begin{aligned} \boldsymbol{y}_t = &-e \cdot \boldsymbol{F_{t-1}} \cdot \left(\frac{\zeta \cdot \omega_n \cdot dt + 2 \cdot \zeta^2 - 1}{{\omega_n}^2 \cdot \mathrm{W}} \cdot S + \frac{\omega_n \cdot dt + 2 \cdot \zeta}{{\omega_n}^3 \cdot dt} \cdot C \right) \\ &+ \boldsymbol{F_{t-1}} \cdot \frac{2 \cdot \zeta}{{\omega_n}^3 \cdot dt} + e \cdot \boldsymbol{F_t} \cdot \left(\frac{2 \cdot \zeta^2 - 1}{{\omega_n}^2 \cdot \mathrm{W}} \cdot S + \frac{2 \cdot \zeta}{{\omega_n}^3 \cdot dt} \cdot C \right) \\ &+ \boldsymbol{F_t} \cdot \frac{\omega_n \cdot dt - 2 \cdot \zeta}{{\omega_n}^3 \cdot dt} \\ \dot{\boldsymbol{y}}_t = &\, e \cdot \boldsymbol{F_{t-1}} \cdot \left(\frac{\zeta_i + \omega_n \cdot \mathrm{dt}}{\omega_n \cdot wts} \cdot S + \frac{1}{{\omega_n}^2 \cdot \mathrm{dt}} \cdot C \right) - \boldsymbol{F_{t-1}} \cdot \frac{1}{{\omega_n}^2 \cdot \mathrm{dt}} \\ &- e \cdot \boldsymbol{F} \cdot \left(\frac{\zeta_i}{\omega_n \cdot wts} \cdot S + \frac{1}{{\omega_n}^2 \cdot \mathrm{dt}} \cdot C \right) + \mathrm{F} \cdot \frac{1}{{\omega_n}^2 \cdot \mathrm{dt}} \end{aligned} \tag{17}$$

The following coefficients are introduced for easier readability of the equations:

$$\begin{aligned} s &= \sqrt{1 - \zeta^2} \\ W &= \omega_n \cdot dt \cdot s \\ e &= \exp(-\zeta \cdot \omega_n \cdot dt) \\ S &= \sin(W) \\ C &= \cos(W) \end{aligned} \tag{18}$$

The final solution is obtained as the sum of both complementary solutions and particular solutions. The CFPI method of integration was chosen in this study, because it was verified that it is less sensitive to numerical errors when solving high-frequency oscillations, as compared to the Newmark-beta method [29]. Since the vibration of the structure is simply obtained using the direct integration of deformation and velocity value for each mode, the time-step used for CFPI integration may be decoupled to fluid solver time-step criterions. In other words, the high frequencies of the structural vibrations may be accurately reproduced while interacting with fluid flow.

3. Methodology

In this paper, vibration modes are expressed using natural frequencies and mass-normalized mode shapes, as detailed in Section 2.2. Equations (10)–(15) encloses the force vector and the structural deformation of the system. The equation of motion for a single mode (Equation (15)) is directly integrated in time within the fluid flow solver using the CFPI method, resulting in the generalized displacement, denoted $\boldsymbol{y}(t)$. The same process is repeated for all modes at each time step of the simulation. Then, the global deformation of the structure is finally obtained using Equation (12), incorporating the calculated generalized displacement. Thereby ensuring that updated structural shape influences the flow calculations resulting in updated flow pressure and velocity fields [29]. Natural frequencies and corresponding modal vectors are determined externally before commencing the CFD, either by analytical methods or by using external modal solvers.

The workflow of the fluid–structure solver is depicted in Figure 1. The below steps are introduced to establish a two-way coupling of the fluid–structure interaction.

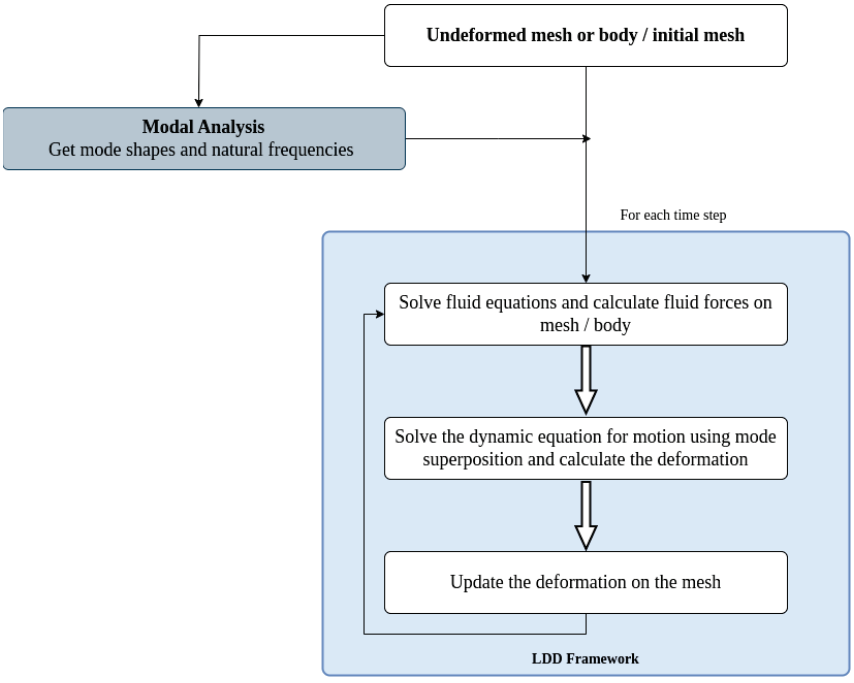

Figure 1. FSI with LDD workflow: This flowchart explains the process of integrating weak coupling of the modal solver.

1. Calculate the mass-normalized mode shapes and corresponding natural frequencies, denoted as $\omega_1, \omega_2, ..., \omega_n$.
2. Define the initial and boundary conditions for the simulation, including the initial displacement of the structural system if any.
3. Create Radial Basis Function (RBF) connections between fluid mesh and structural mesh to transfer the mode shape information if the structural mesh is not the same as the fluid mesh [40].
4. At every time step of the simulation Δt:
   (a) Compute the forces exerted on the structural mesh due to fluid force.
   (b) Solve equation of motion (15) for each mode shapes and natural frequencies
   (c) Determine the overall deformation vector using Equation (12) and apply the resulting deformation to the mesh.
   (d) Solve the fluid equations for time $t + \Delta t$, taking into account of structural deformation.

The coupling scheme based on the mode superposition method is formulated by solving the equation of motion with imposed loads by using mode shapes and natural frequencies which are determined from the modal analysis in the pre-calculation stage (step 1). This modal coupling is integrated into the LDD method, which takes initial and boundary conditions (step 2) from simulation input. This step is needed only in situations where the fluid mesh vertices do not overlap with structural vertices. In such a case, an interpolation is needed to compute the mode shape for the fluid mesh, based on the structural mesh (step 3). The displacement resulting from fluid forces (step 4a) is calculated within the modal coupling algorithm using CFPI method (step 4b). This deformation is applied on the mesh to account for geometric changes for the fluid solver (step 4c), consequently calculating the updated flow pressure and velocity fields using updated mesh (step 4d).

4. Results and Discussion

4.1. Validation of the Flow and Structural Solvers

4.1.1. Sloshing in Cobiodal Tank

The LDD method is validated by comparing the numerically obtained results to the experimental data from one of the Rhee test cases [41]. Rhee's experimental setup uses a simplified cuboidal tank geometry with dimensions of 1200 mm, 600 mm, and 300 mm along the x, y, and z directions, respectively, and shown in Figure 2.

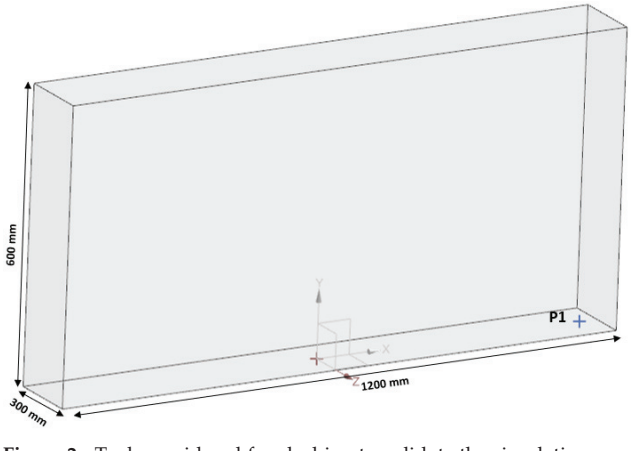

Figure 2. Tank considered for sloshing to validate the simulation pressure with Rhee [41] Experiment pressure.

In this scenario, 20% of the tank volume is filled with water. The tank is subjected to a sinusoidal translation motion along the x-direction(swaying), characterized by an amplitude of 0.06 m and an oscillation period of 1.94 s. This study is based on the experimental work of Rhee [41] and aims to assess and confirm the agreement between the experimental and numerical outcomes for the specified tank geometry, flow properties and motion conditions with the LDD solver. The average pressure signal from the Rhee experiment at sensor location P1 (570 mm in the x-direction from the origin), is compared to the simulation average pressure and comparison plot shown in Figure 3. Also, the corresponding deviation is shown in Table 1.

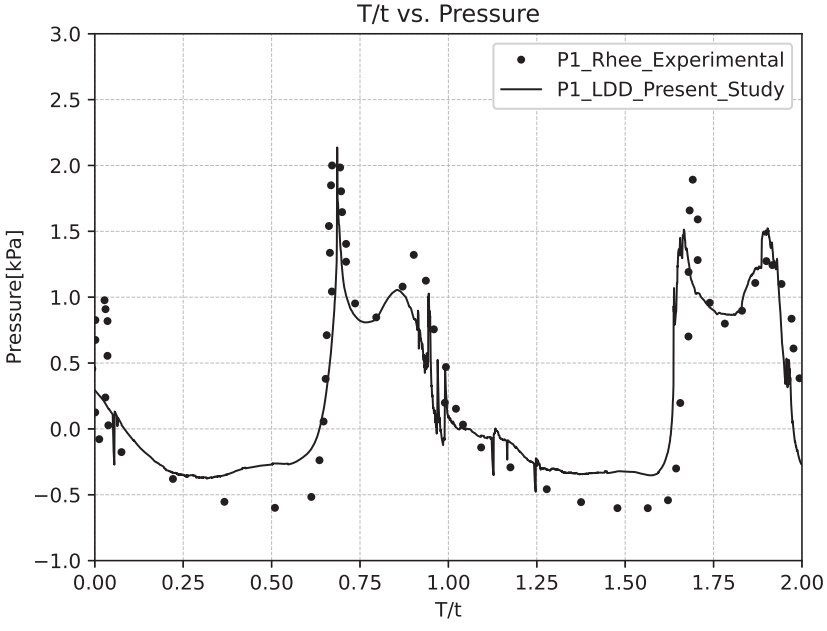

Figure 3. Comparison of pressure from the simulation at P1 location (Refer to Figure 2) with Rhee experiment pressure [41].

Table 1. Deviation of pressure from the simulation with respect to Rhee Experiment at peak location.

Region	1st Peak	2nd Peak
Deviation of pressure [kPa]	0.1	0.35

The numerical results demonstrate a close correspondence with the experimental average impact pressure values at each sloshing peak obtained by the Rhee. This showcases the accuracy and reliability of the flow solver in predicting pressure values. Validating pressure loads is an important step in the modal superposition method. These loads serve as input parameters for calculating the deformation of the structure. Accurate validation ensures that the pressure loads used in the analysis are representative of the actual operating conditions and can provide reliable results. Any errors or inaccuracies in the pressure loads can lead to significant discrepancies in calculating the deformation of the structure. This, in turn, can impact its safety and performance. Therefore, it is crucial to validate the pressure loads through experimental or numerical methods to ensure the accuracy and reliability of the analysis results.

4.1.2. Cantilever Beam Vibration

To verify the implementation of a modal solver, a simple cantilever beam with a constant tip load applied over a time case is considered. An investigation was conducted to compute the dynamic behavior of a cantilever beam with specific geometric characteristics, including a length of 0.079 m and width of 0.005 m, under a 1N tip load and shown in Figure 4. This included the computation of the natural frequencies and their corresponding mode shapes. The initial five modes shapes are used in the simulation and shown in Table 2 and Figure 5.

For theoretical calculation, the damped vibration response of a cantilever beam which is subjected to a tip load (Figure 4) is calculated for various natural frequencies using Equation (19).

$$y(t) = \sum_{i=0}^{n} \frac{F}{\omega_{n_i}^2} \left(1 - e^{-\zeta \omega_{n_i} t} \cos(\omega_{d_i} t)\right) \tag{19}$$

where, $y(t)$ is total displacement of the system at time t, F is magnitude of the load and n is number of natural frequencies. The term $\frac{F}{\omega_n^2}$ scales the magnitude of the load. The exponential term $e^{-\zeta \omega_n t}$ accounts for the damping effect, causing the vibration to decay over time. The cosine term $\cos(\omega_d t)$ represents the oscillatory behavior of the system. ω_n is natural frequency and ζ is damping ratio. Higher damping ratios ζ result in a larger reduction in vibration frequency. ω_d is the damped angular frequency and it is calculated as follows

$$\omega_d = \omega_n \sqrt{1 - \zeta^2} \tag{20}$$

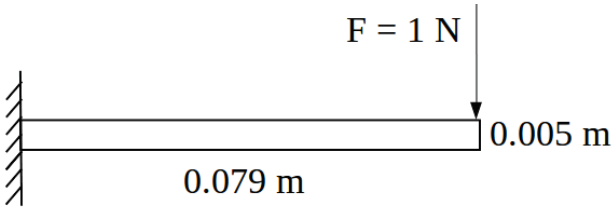

Figure 4. Cantilever beam subjected to the tip load is considered for comparative analysis of Mode Superposition: Theoretical vs. Numerical.

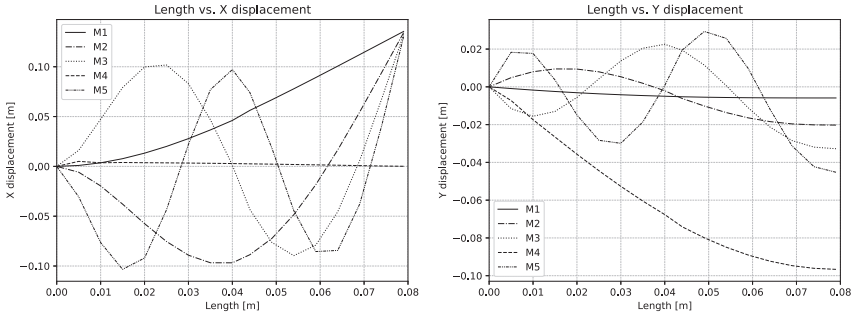

Figure 5. Mode shape of the beam along the length, **Left**: X-Displacement and **Right**: Y-Displacement.

Table 2. Initial 5 Modes and natural frequencies of the cantilever beam.

Mode	1	2	3	4	5
Natural Frequency (Hz)	15.09	93.433	257.66	374.8	495.57

To understand the beam response more deeply, both theoretical and numerical methods were employed. The dynamic response of the system is mainly influenced by a few initial mode shapes. So all simulations were conducted exclusively for the initial five-mode shapes. The natural frequencies of a cantilever were used to calculate its theoretical displacement using Equation (19).

To compare this theoretical value with numerical simulations, the CFPI method was used to solve the dynamic equations of motion. The results were presented graphically in Figure 6. This comparison helped to understand the cantilever beam's dynamic response better. The numerical simulation results closely match the theoretical predictions. The displacement difference is of the order of 1×10^{-4}, providing strong verification of the accuracy and reliability of the implementation. However, this is a simple load case, and more complex loading cases were validated in the upcoming section.

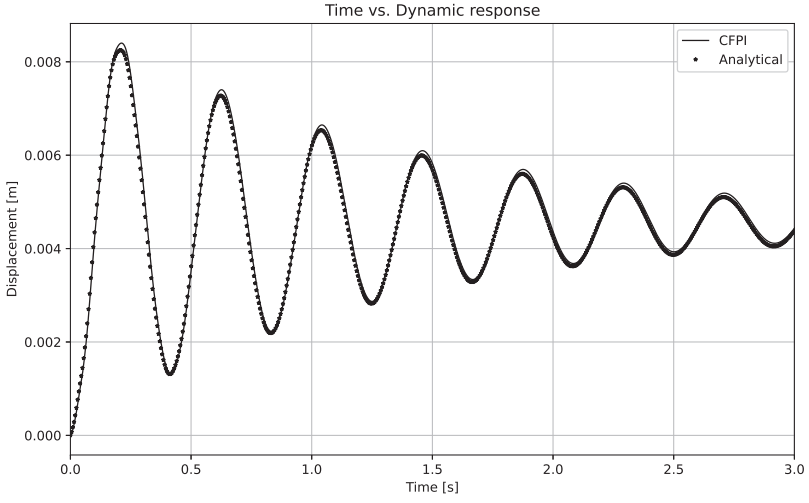

Figure 6. Comparison between the numerical and theoretical dynamic response of beam.

4.2. Deformation of Cantilever Gate

This section describes the initial experiment to verify the coupling implementation, which includes a slowly deforming cantilever beam. The deformation of the beam is induced by the transition from the hydrostatic loads into hydrodynamic loads. The verification of the coupling between flow and modal solver implementations is achieved by replicating an experiment originally conducted by Antoci et al. [42].

The experiment resembles the classic dam-breaking scenario, with gradual fluid loading on a rubber gate that is fixed to a rigid wall along its upper edge, which deforms under fluid forces. The experimental setup features a fluid column within a tank with dimensions: length $(A) = 100$ mm and height $(H) = 140$ mm. The rubber gate, supported by a rigid obstruction, extends downward to touch the floor. The height of the gate is $L = 79$ mm. For modeling, an elastic isotropic material with a density of $\rho_{gate} = 1100$ kg/m^3 and Young's modulus $E = 12$ MPa is employed. The simulation considers only the first mode shape and its associated natural frequency. Validation is undertaken for the tank filled with water, density $\rho = 1000$ kg/m^3 and dynamic viscosity $\mu = 10^{-3}$ Pa.s. Due to the pressure difference, the water flows through the rubber gate exerting the force to deflect it. The elastic deformation of the cantilever due to fluid loading is illustrated in Figure 7.

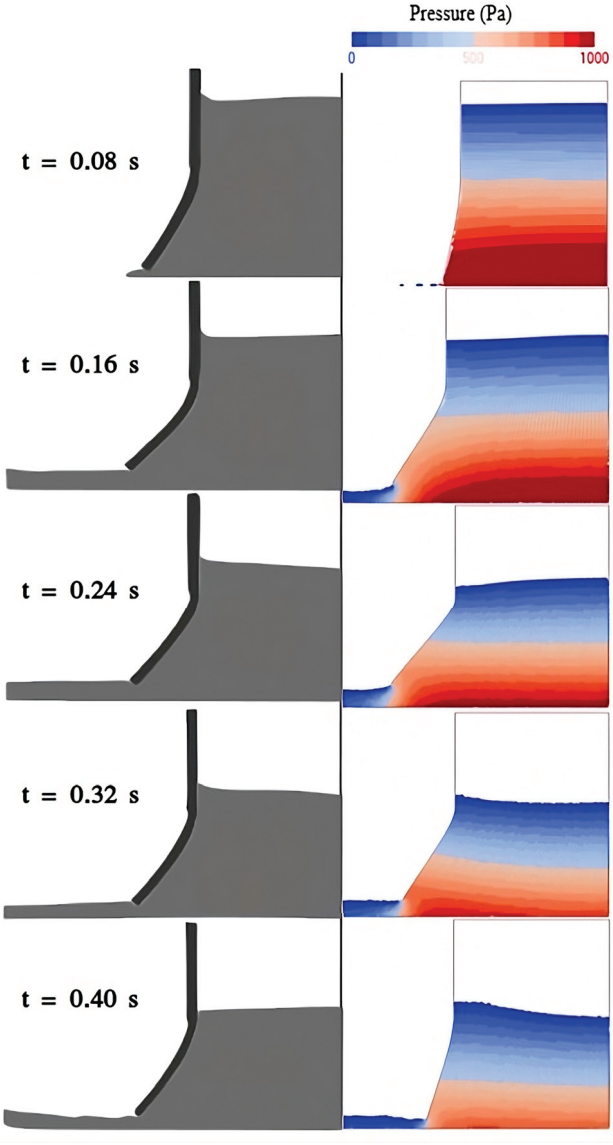

Figure 7. Comparison of cantilever beam deformation from the current study with Antoci et al. [42] at different time steps such as t = 0.08 s, 0.16 s, 0.24 s, 0.32 s and 0.40 s.

An assessment is being conducted to confirm whether the calculated deflection matches the expected magnitude, and to ensure the accuracy of the dynamic solver's equations. The order of magnitude of deformation is the same as that in Antoci et al. [42]. However, this is not ideal for the primary objective of mode superposition. In this particular case, a static solution has been utilized, making the first bending mode sufficient for relevance and a small discrepancy in the predicted solution.

4.3. Elastic Baffle in Sloshing Tank

To investigate the impact of fluid–structure interaction with the complex cyclic load [43–45], an elastic baffle is introduced at the bottom of the tank, it is as same as the tank in Section 4.1.1

Figure 2. The tank is subjected to the same sinusoidal excitation with an amplitude of 0.06 m and a period of 1.94 s. In this study, the walls of the tank are assumed to be rigid, making the baffle the sole flexible component within the tank structure as shown in Figure 8.

The elastic baffle has dimensions of 5 mm, 150 mm, and 120 mm along the x, y, and z directions, respectively. The material property of the baffle includes the density of 4096 kg/m^3, Young's modulus of 38.4 MPa, and Poisson's ratio of 0.3. The first five mode shapes were calculated from modal analysis and used for the simulation. Mode shapes are shown in Figure 9 and corresponding natural frequencies are shown in Table 3. By incorporating the elastic baffle model, the investigation aims to analyze and comprehend the effects of fluid–structure interaction within the tank system. Dimensions, material properties and displacement X at the location D1 (the top left corner of the baffle looking forward as shown in Figure 8) of the baffle are considered from the investigation conducted by Sampann [46]. The reference X-displacement is compared with the X-displacement obtained from the simulation and the results are presented graphically in Figure 10. The comparison shows that both results follow the same trend and also match closely at all the points where the most significant deformation takes place, thus verifying the precision of the modal coupling. At the peak, the deviation of deformation is minimal compared to the transition region where change in deformation takes place, due to the linear effect of mode superposition. The corresponding values are listed in Table 4. This provides an understanding of the baffle dynamic response under the specified sinusoidal excitation, which contributes added value to the present implementation of FSI.

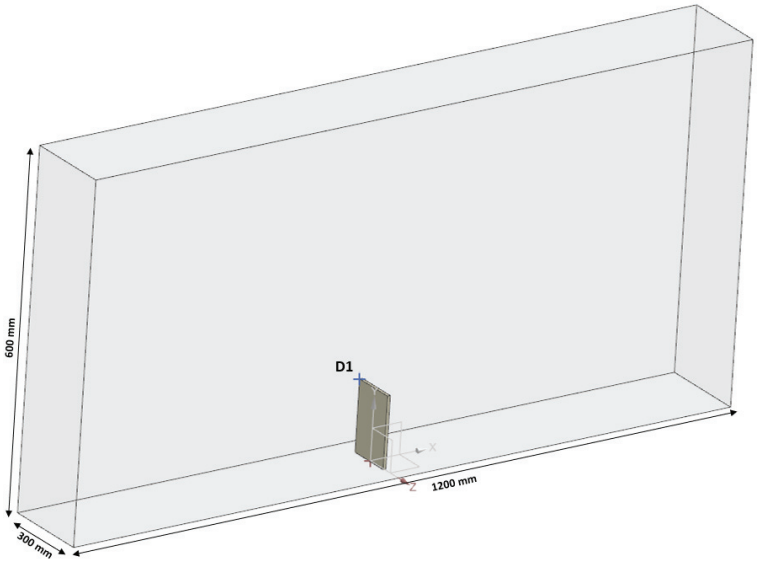

Figure 8. Rhee sloshing tank is considered and an elastic baffle is introduced at the bottom of the tank.

Table 3. Initial 5 Modes and natural frequencies of the elastic baffle.

Mode	1	2	3	4	5
Natural Frequency (Hz)	100.12	270.05	301.33	392.05	505.44

Table 4. Deviation of deformation from the simulation with respect to Sampann.

Region	Peak	Transition
Max Deviation of deformation [m]	0.005	0.01

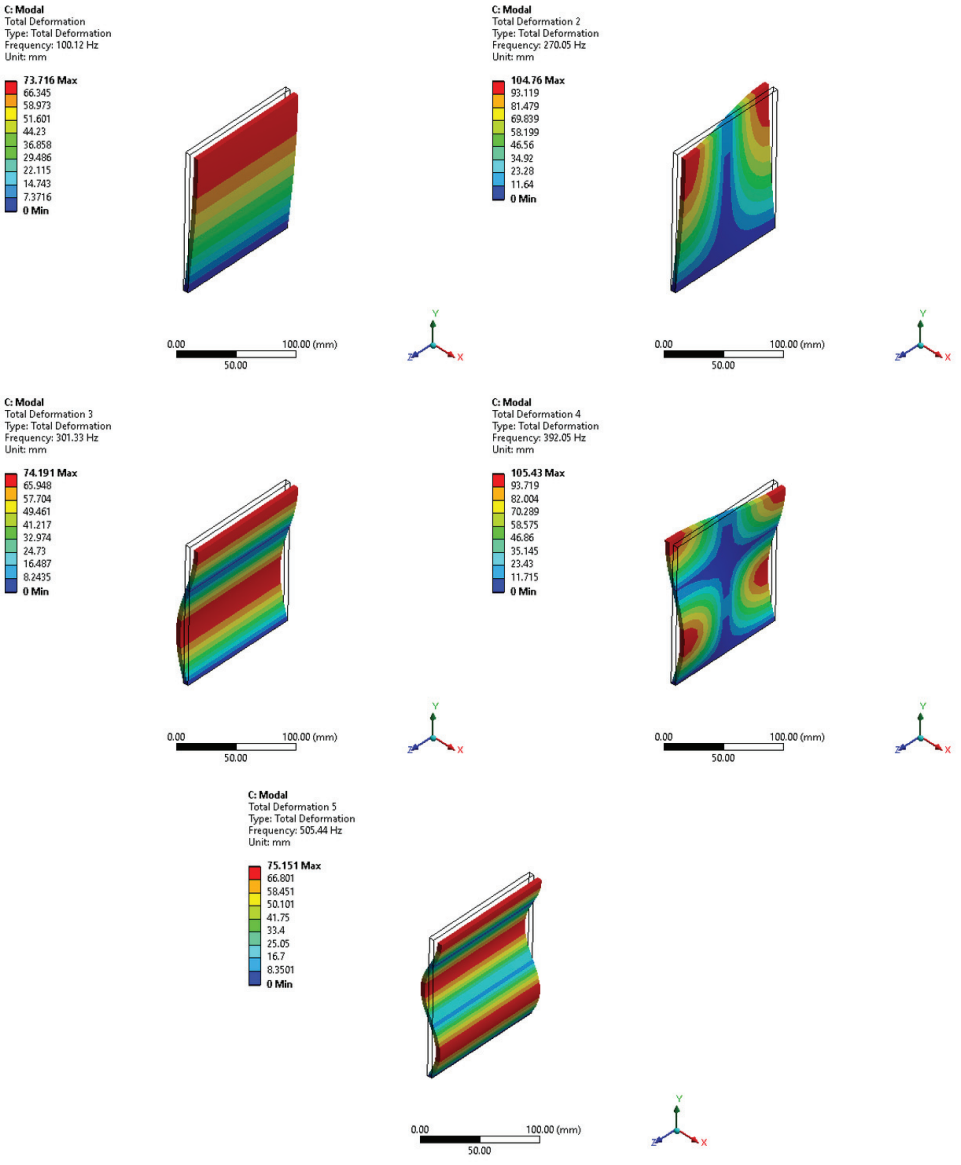

Figure 9. Modal results of an elastic baffle with reference to its undeformed wireframe, i.e., the first five mode-shapes.

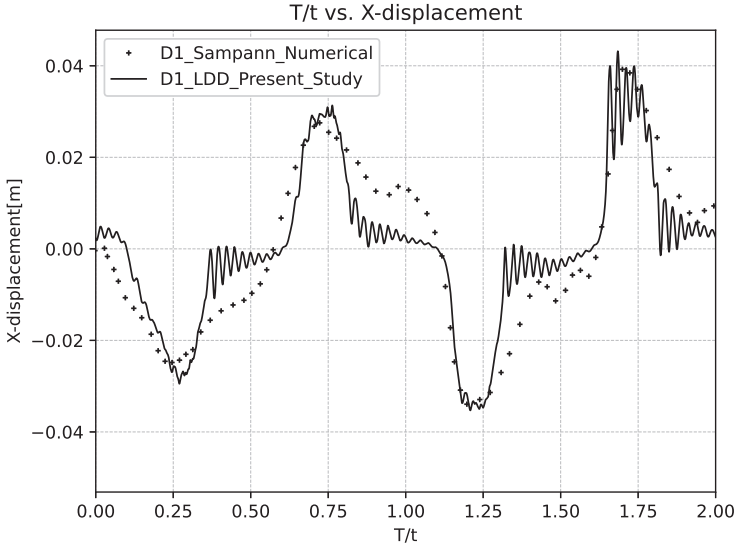

Figure 10. Comparison of X-displacement from the simulation at D1 location (Refer to Figure 8) with numerical results from Sampann [46].

4.4. Elastic Beam in Shallow Oil

The validity of the two-way coupling of fluid and structure has been substantiated through a comparison of both numerical simulations and experimental data obtained from benchmark studies conducted by Idelsohn et al. [47,48]. The experiments centered around the flexible beam exposed to sloshing loads and it is similar to Section 4.3 with different fluid properties and tank. Specifically, a cuboidal tank featuring a clamped elastic beam, made using dielectric polyurethane and filled with sunflower oil was investigated.

For the validation study, a specific test case from Idelsohn et al.'s work was selected. In this test case, the tank was filled with oil up to the height of the beam. The tank dimensions were 609 mm, 344.5 mm, and 39 mm in the x, y, and z directions, respectively. The flexible beam clamped to the tank's bottom, exhibited dimensions of 4 mm, 57.4 mm, and 33.2 mm in the x, y, and z directions as shown in Figure 11. The beam is characterized by a density of 1100 kg/m^3, a Young modulus of 60 MPa, and a Poisson ratio of 0.49. On the other hand, the oil has a density of 917 kg/m^3 and a kinematic viscosity of 5×10^{-5} m^2/s. The first five mode shapes obtained from modal analysis are used for the simulation. Mode shapes are presented in Figure 12 and corresponding natural frequencies are shown in Table 5.

Table 5. Initial 5 Modes and natural frequencies of the elastic beam.

Mode	1	2	3	4	5
Natural Frequency (Hz)	186.4	560.61	673.29	856.07	939.09

The dynamic excitation imposed on the tank involved sinusoidal oscillatory motion about the z-axis, characterized by an amplitude of 4 degrees and a frequency of 0.61 Hz. Figure 13 shows X-displacement data at the tip of the beam, which has been compared with both experimental and numerical data from Idelsohn et al. The comparison indicates a favorable agreement between the results of the current study and the existing data [47]. Although a slight offset has been observed in certain locations, it matches closely with the numerical results from Idelsohn at the maximum deformation locations with a deviation order of 1×10^{-4}. The validation results consistently demonstrate a robust agreement in the accuracy of the implemented two-way coupling for fluid–structure interaction.

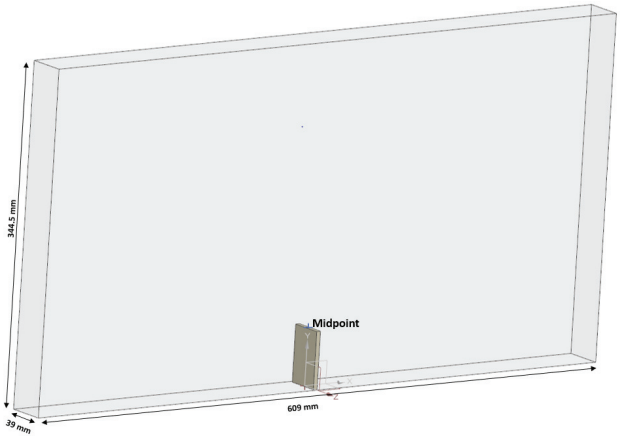

Figure 11. Idelsohn sloshing tank is considered and an elastic beam is introduced at the bottom of the tank.

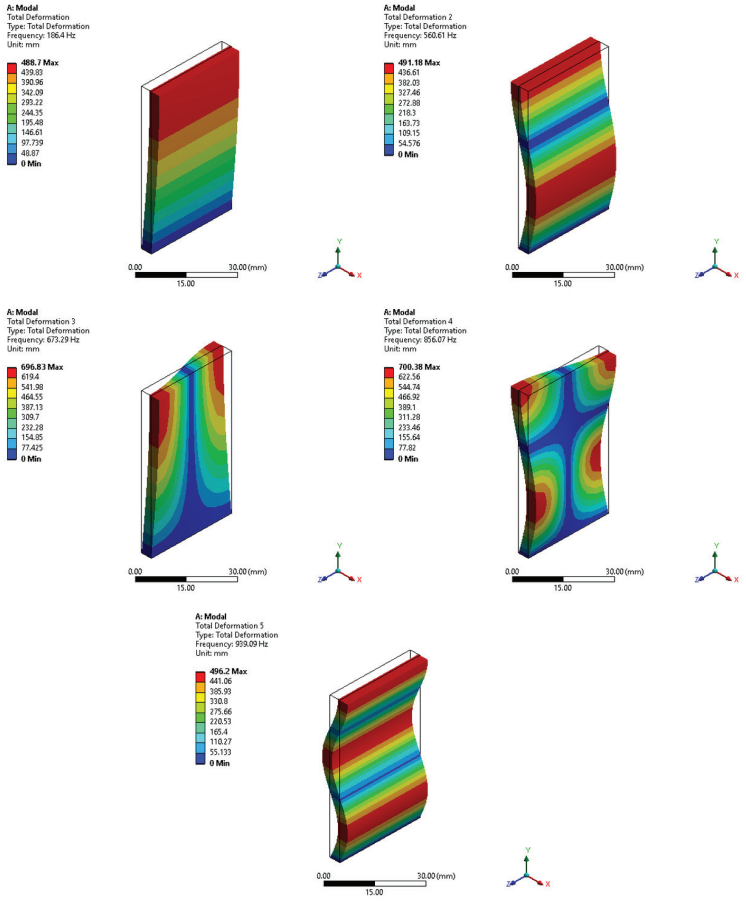

Figure 12. Modal results of an elastic beam with reference to its undeformed wireframe, i.e., the first five mode-shapes.

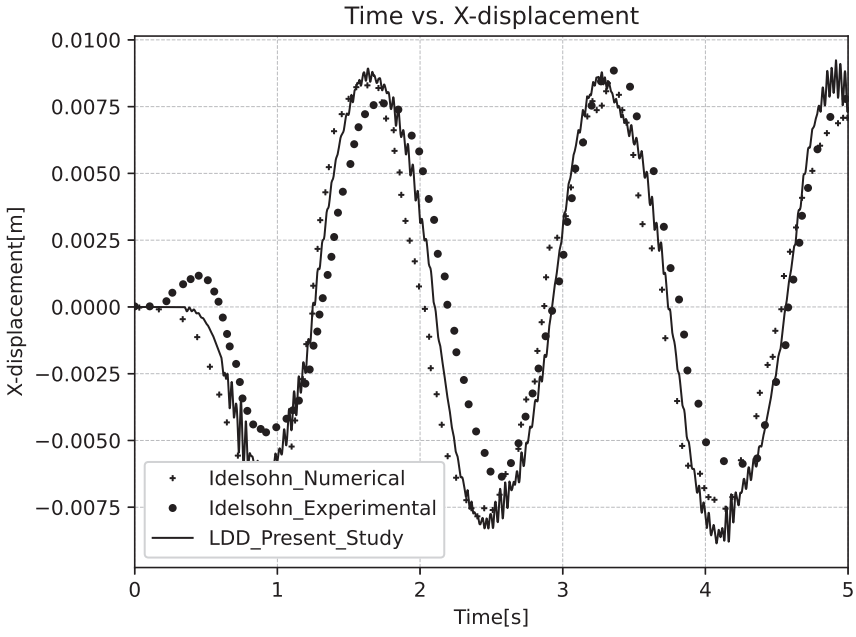

Figure 13. Comparison of X-displacement from the simulation at the end of the beam (Refer to Figure 11) with experimental and numerical results from [47].

4.5. Flow Impact on a Cantilever Beam

After successful verification and validation of the FSI through various benchmark cases in the above Section 4.1, extending the exploration by conducting a study for a cantilever beam is subjected to sudden impact and subsequently oscillatory fluid loads. The geometric dimensions remain consistent with the static case, maintaining a thickness of 5 mm, while the fluid properties remain unchanged. The simulation involves a domain measuring 0.5×0.2 m, where an initial fluid column of dimensions 0.1×0.14 m is positioned at the left end of the domain. A beam is placed at the centerline of the tank, with its fixed end touching the bottom of the tank. The simulation replicates a scenario of a dam-break study, covering a total time of 10 s with intervals of 1×10^{-3} s.

In the simulation, the first five natural frequencies are utilized (as detailed in Table 2) along with their corresponding mode shapes that are illustrated in Figure 5. The dynamic behavior of the cantilever beam is presented in Figure 14.

The response of a beam to a load comes from any one individual mode shape or combination of mode shapes. From Figure 14, the combination of mode shape is clearly visible at 0.2 s and the dynamic response of the beam is dominated by the first mode after 5 s. The displacement of both the tip and mid-section of the beam is captured in the x and y directions, as shown in Figure 15. Figure 16 also shows the same behavior of combination mode shapes at 0.2 s and the dynamic response majorly from the first mode shape after 5 s. This observation highlights the effectiveness of the mode superposition technique in accurately capturing the impact of various modes on the system's response.

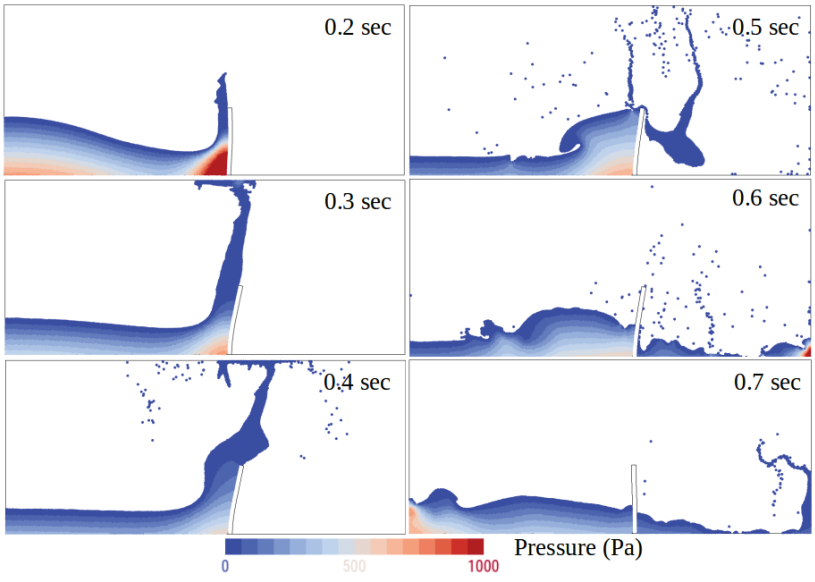

Figure 14. Dynamic response of cantilever beam at different time step.

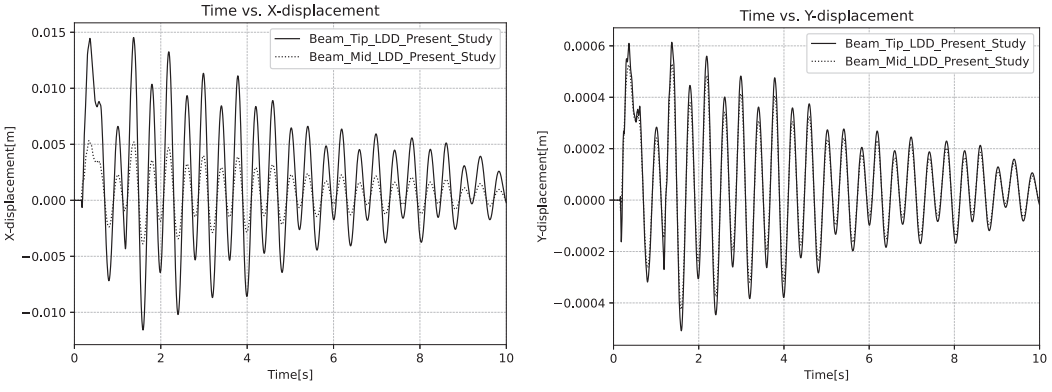

Figure 15. Dynamic response over a time period at the mid and tip section, **Left**: X Displacement and **Right**: Y Displacement.

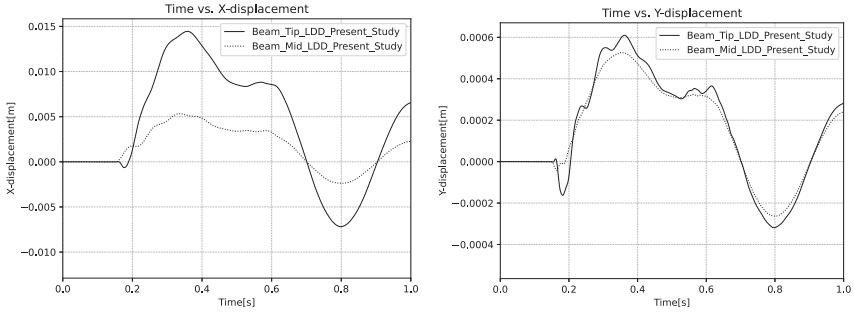

Figure 16. Displacement at the mid and tip section until 1 s, **Left**: X Displacement and **Right**: Y Displacement.

4.6. Water Entry of a Wedge

The investigation on free fall of a wedge in the water case was replicated from the study carried out by Hosseinzadeh [49]. The wedge had a V-shaped variable dead-rise angle at the bottom. The wedge had dimensions of 1500 × 940 × 450 mm in length, breadth and depth. To reinforce the bottom of the wedge, 4 mm thick T−shaped stiffeners (T54 × 3 + 35 × 4 mm) were placed in the middle of the longitudinal and transverse direction on the starboard keel.

The material properties of the wedge were also taken into account, i.e., the wedge was modeled by using a material with density of 2700 kg/m^3, the modulus of elasticity of 68 GPa, and the Poisson's ratio of 0.33. The accuracy of the properties were important to consider, as they can have a significant effect on the behavior of the wedge during the free fall water entry [49]. The tank has dimensions of 5 × 5 × 1.75 m and is filled with water up to a height of 1.5 m in the z direction, as shown in Figure 17. For both structural modal analysis and fluid simulation, the surface mesh of the wedge was represented by 9200 triangles, which is shown in Figure 17. To conduct the numerical analysis of the impact loads, the wedge was dropped vertically from a height of 0.25 m (measured from the free surface up to the keel) into the water, with zero initial velocity. During the free fall, the velocity increased to $U = 2.2$ m/s as the wedge made contact with the water. The numerical time step was taken as constant, $\delta t = 2.5 \times 10^{-3}$. The modal analysis of the structural model resulted in obtaining the first five significant modes, which are shown in Figure 18 and corresponding natural frequencies are shown in Table 6. The same surface mesh and the modes obtained were used as input for the LDD-modal coupling solver.

During the simulation of free fall water entry, the evolution of loads and deformation of the wedge are observed and analyzed. The hydrodynamic pressure measured during the simulation at points PS1 and PP1 was compared with the experimental data given by Hosseinzadeh et al. [49] as shown in Figure 19. It shows that the maximum pressure matches with the experimental data and the deviation between them is 4%. However, it has been observed that the decrease in the pressure signal after the peaks happened faster in the simulation than that reported by the experimental data.

When the wedge impacts the water at a velocity of 2.2 m/s, it deforms in the X, Y, and Z directions. Figure 20 illustrates the deformation in the maximum impact load condition. It has been noted that the maximum amount of deformation observed was 36 µm.

Table 6. Initial 5 Modes and natural frequencies of the wedge.

Mode	1	2	3	4	5
Natural Frequency (Hz)	213.8	376.6	440.95	529.12	535.23

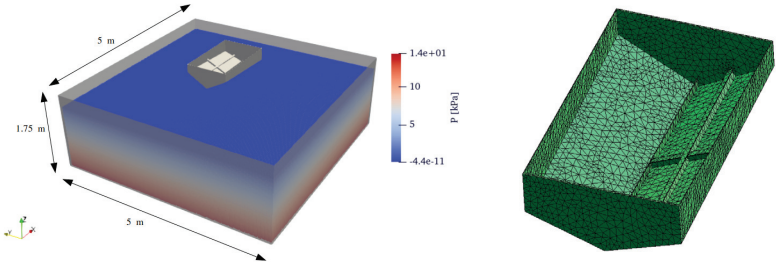

Figure 17. Numerical setup to replicate the experiment of [49]. On the left, a tank filled with water up to 1.5 m and a wedge placed at a distance of 0.25 m above the free surface. On the right, a wedge with a surface mesh was used for the modal coupling solver.

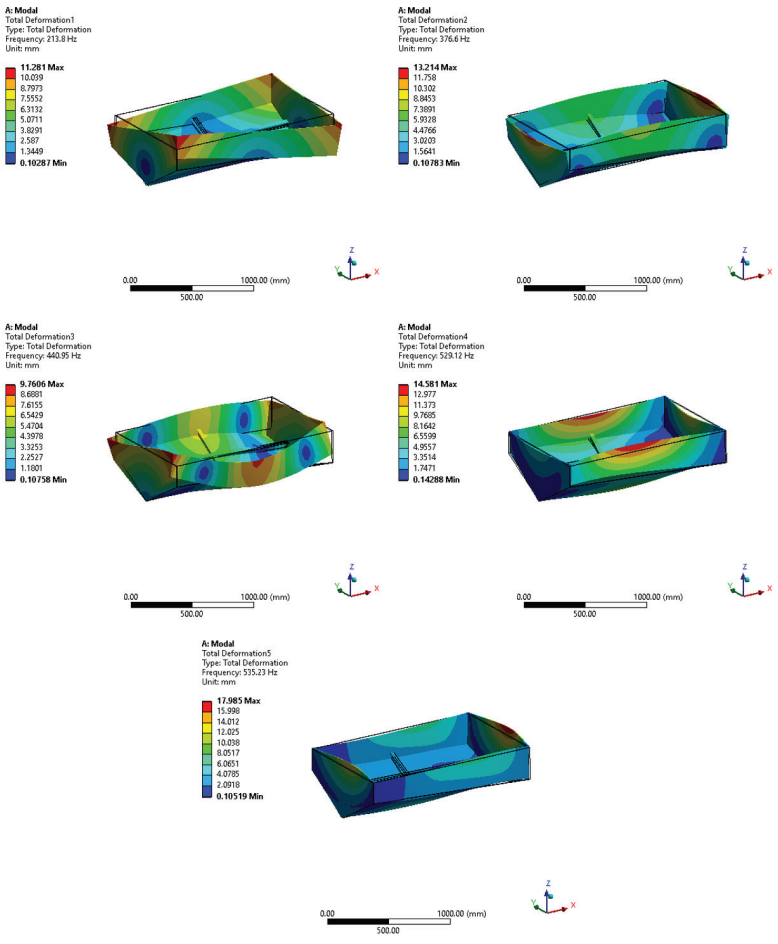

Figure 18. Modal results of a wedge with reference to its undeformed wireframe, i.e., the first five mode shapes.

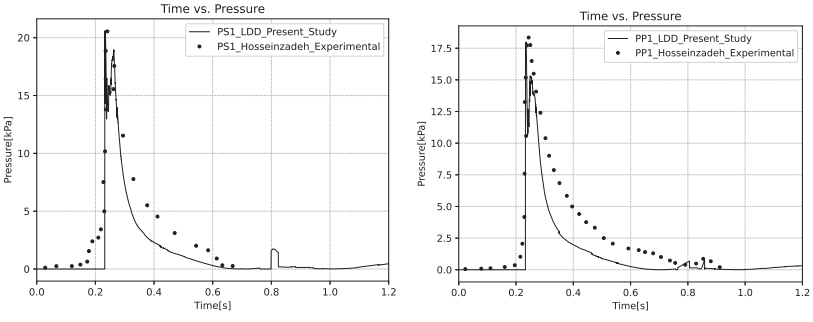

Figure 19. Comparison of dynamic pressure from the simulation with experimental results from [49], **Left**: PS1 point as per [49] and **Right**: PP1 point as per [49].

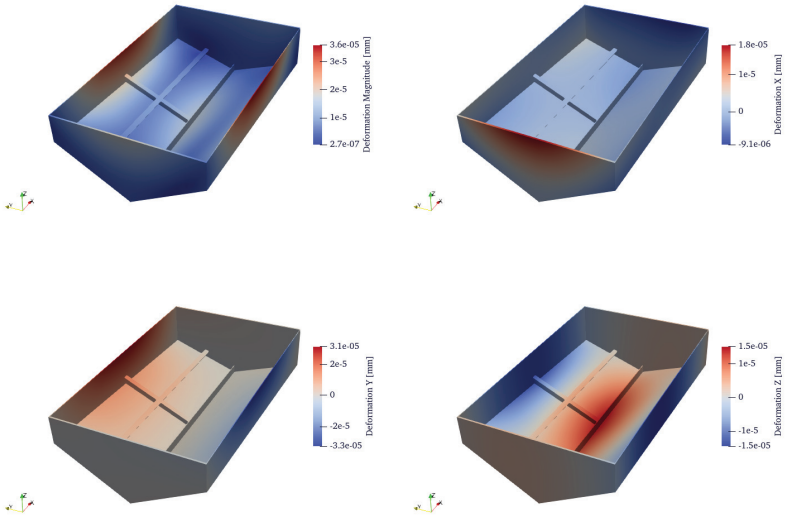

Figure 20. Deformation of Wedge in X, Y, and Z directions and deformation magnitude at maximum impact load condition, where wedge touches the water with 2.2 m/s velocity.

5. Conclusions

The modal-coupling solver has been seamlessly integrated into the Lagrangian Differencing Dynamics (LDD) solver. The numerical experimentation has shown that it enables effective two-way weak coupling of the fluid–structure interaction. The effectiveness of the Modal Coupling approach is attributed to its utilization of the mode superposition method. While the proposed bidirectional coupling is explicit in time, the insignificant cost of computing the structural deformation by using the mode superposition method allows the weak coupling to remain stable for time-steps that are required by the flow solver.

The verification and validation of the bidirectional fluid–structure interaction are successfully demonstrated through seven numerical experiments. The benchmark cases included both slowly and quickly deforming structures, and single or oscillatory fluid loads. The benchmark cases resembled swaying and rotating sloshing experiments (with and without flexible baffles), dam break experiments (with an elastic gate or obstacles) and water-entry experiment (slamming loads applied to a stiffened structure). The comparison between the numerically obtained results and the available experimental data demonstrated the ability of the proposed coupling method to capture complex interactions between fluids and structures.

The efficiency of the modal-coupling solver is accomplished by small computational cost of deforming the structure, by its flexibility to accommodate to the flow solver time-steps, and by using the Lagrangian LDD method to obtain accurate pressure loads. While this allows straightforward and efficient Lagrangian–Lagrangian coupling during the simulation, the engineering advantage is that there is no need for meshing or preparing the coupling interface, since the flow solver operates directly on surface meshes shared by the structural solver.

The above features of the proposed coupling method show practicality and applicability in future ship and offshore hydrodynamic simulations. The implementation process of the coupling scheme substantiates the tool's capability to facilitate the effortless coupling of diverse solvers, all without necessitating changes to solver algorithms or input files. The incorporation of the energy equation into the framework is planned in future work.

This expansion aims to explore the influence of energy on the fluid–structure interaction, thereby broadening the scope and insights of the analysis.

Author Contributions: Conceptualization, M.P. and J.B.; methodology, M.P. and J.B.; software, M.P.; validation, M.P.; investigation, M.P.; writing—original draft preparation, M.P.; writing—review and editing, C.P., J.B. and N.D.; visualization, M.P.; funding acquisition, C.P. and N.D.; supervision, J.B., D.S. and Ž.L. All authors have read and agreed to the published version of the manuscript.

Funding: This study was funded by the Croatian Science Foundation under project IP-2020-02-8568. M.P. and C.P. acknowledge the financial support received from CELTIC-NEXT under project COA-CFD, ID C2021/1-11.

Institutional Review Board Statement: Not applicable.

Informed Consent Statement: Not applicable.

Data Availability Statement: The data presented in this study are available on request from the corresponding author.

Acknowledgments: This study has been fully supported by the Croatian Science Foundation under project IP-2020-02-8568.

Conflicts of Interest: The authors declare no conflicts of interest.

Abbreviations

The following abbreviations are used in this manuscript:

CFD	Computational Fluid Dnamics
LDD	Lagrangian Differencing Dynamics
FSI	Fluid Structure Interaction
RANS	Reynolds-Averaged Navier–Stokes
URANS	Unsteady Reynolds-Averaged Navier–Stokes
VOF	Voluem Of Fluid
RBF	Radial Basis Function
DES	Detached Eddy Simulation
SPH	Smooth Particle Hydrodynamic
FEM	Finite Element Method
DEM	Discrete Element Method
MPS	Moving Particle Semi-implicit
CFPI	Complementary Function and Particular Integral
MDOF	Multi-Degree-Of-Freedom
SDOF	Single-Degree-Of-Freedom
ODE	Ordinary Differential Equation
DOF	Degree-Of-Freedom
PBD	Particle-Based Dynamics

References

1. Huang, L.; Rena, K.; Lib, M.; Tuković, Ž.; Cardiff, P.; Thomas, G. Fluid–structure interaction of a large ice sheet in waves. *Ocean. Eng. Ser.* **2019**, *182*, 102–111. [CrossRef]
2. Danielsen, F.; Sørensen, M.K.; Olwig, M.F.; Selvam, V.; Parish, F.; Burgess, N.D.; Hiraishi, T.; Karunagram, V.M.; Rasmussen, M.S.; Hansen, L.B.; et al. The Asian tsunami: A protective role for coastal vegetation. *Science* **2005**, *310*, 643. [CrossRef] [PubMed]
3. Zhou, W.; Wu, Z.; Mevel, L. Vibration-based damage detection to the composite tank filled with fluid. *Struct. Health Monit.* **2010**, *9*, 433–445. [CrossRef]
4. Chella, M.A.; Tørum, A.; Myrhaug, D. An overview of wave impact forces on offshore wind turbine substructures. *Energy Procedia* **2012**, *20*, 217–226. [CrossRef]
5. Liang, L.; Baoji, Z.; Hao, Z.; Hailin, T.; Weijie, W. Hydrodynamic performance optimization of marine propellers based on fluid–structure coupling. *Brodogradnja* **2023**, *74*, 145–164. [CrossRef]
6. Zhang, Z.; Sun, P.; Pan, L.; Zhao, T. On the propeller wake evolution using large eddy simulations and physics-informed space-time decomposition. *Brodogradnja* **2024**, *75*, 75102. [CrossRef]
7. Jensen, J.J. *Load and Global Response of Ships*; Elsevier: Amsterdam, The Netherlands, 2001; pp. 268–271.

8. Bašić, J.; Degiuli, N.; Blagojević, B.; Ban, D. Lagrangian differencing dynamics for incompressible flows. *J. Comput. Phys.* **2022**, *462*, 111198. [CrossRef]
9. Kwang-JunPaik, A.; Pablo, M.; Carrica, A.; Donghee Lee, B.; Kevin, M. Strongly coupled fluid–structure interaction method for structural loads on surface ships. *Ocean. Eng.* **2009**, *36*, 1346–1357.
10. Hron, J.; Turek, S. A monolithic FEM/multigrid solver for an ALE formulation of fluid–structure interaction with applications in biomechanics. *Fluid–Struct. Interact.* **2006**, *53*, 146–170.
11. Hron, J.; Turek, S. A monolithic FEM solver for an ALE for- mulation of fluid–structure interaction with configuration for numerical benchmarking. In Proceedings of the European Conference on Computational Fluid Dynamics, Egmond aan Zee, The Netherlands, 5–8 September 2006.
12. Rugonyi, S.; Bathe, K.J. On finite element analysis of fluid flows fully coupled with structural interactions. *CMES* **2001**, *2*, 195–212.
13. Degroote, J.; Hojjat, M.; Stavropoulou, E.; Wüchner, R.; Bletzinger, K.U. Partitioned solution of an unsteady adjointnfor strongly coupled fluid–structure interactions and application to parameter identification of a one-dimensional problem. *Struct. Multidiscip. Optim.* **2013**, *47*, 77–94. [CrossRef]
14. Degroote, J.; Haelterman, R.; Annerel, S.; Vierendeels, J. Coupling techniques for partitioned fluid–structure interaction simulations with black-box solvers. In Proceedings of the 10th MpCCI User Forum, Sankt Augustin, Germany, 17–18 February 2009; Fraunhofer Institute SCAI: Sankt Augustin, Germany, 2009; pp. 82–91.
15. Lim, W.Z.; Xiao, R.Y.; Hong, T.; Chin, C.S. Partitioned methods in computational modelling on fluid–structure interactions of concrete gravity-dam. *Comput. Informat. Sci.* **2013**, *6*, 154. [CrossRef]
16. Bašić, M.; Blagojević, B.; Klarin, B.; Bašić, J. Coupling of Non–Newtonian meshless flow with structural solvers. In Proceedings of the VII International Conference on Particle-Based Methods, PARTICLES, Hamburg, Germany, 4–6 October 2021.
17. Bašić, J.; Degiuli, N.; Malenica, Š. Insight into Hydrodynamic Damping of a Segmented Barge Using Numerical Free-Decay Tests. *J. Mar. Sci. Eng.* **2023**, *11*, 581. [CrossRef]
18. Seng, S.; Jensen, J.J.; Malenica, Š. Global hydroelastic model for springing and whipping based on a free-surface CFD code (OpenFOAM). *Int. J. Nav. Archit. Ocean Eng.* **2014**, *6*, 1024–1040. [CrossRef]
19. Cardiff, P.; Karač, A.; De Jaeger, P.; Jasak, H.; Nagy, J.; Ivanković, A.; Tuković, Z. *An Open-Source Finite Volume Toolbox for Solid Mechanics and Fluid-Solid Interaction Simulations*; Elsevier Ltd.: Amsterdam, The Netherlands, 2018.
20. Tuković, Z.; Karač, A.; Cardiff, P.; Jasak, H.; Ivanković, A. OpenFOAM Finite Volume Solver for Fluid-Solid Interaction. *Trans. Famena XLII-3* **2018**, *42*, 1–31. [CrossRef]
21. Schillaci, E.; Favre, F.; Troch, P.; Oliva, A. Numerical simulation of fluid structure interaction in free-surface flows: The WEC case. *J. Phys. Conf. Ser.* **2021**, *2116*, 012122. [CrossRef]
22. Fourey, G.; Oger, G.; Le Touzé, D.; Alessandrini, B. Violent fluid–structure interaction simulations using a coupled SPH/FEM method. *IOP Conf. Ser. Mater. Sci. Eng.* **2010**, *10*, 012041. [CrossRef]
23. Yang, Q.; Jones, V.; McCue, L. Free-surface flow interactions with deformable structures using an SPH–FEM model. *Ocean Eng.* **2012**, *55*, 136–147. [CrossRef]
24. Nunez-Ramirez, J.; Marongiu, J.; Brun, M.; Combescure, A. A partitioned approach for the coupling of SPH and FE methods for transient nonlinear FSI problems with incompatible time-steps. *Int. J. Numer. Methods Eng.* **2017**, *109*, 1391–1417. [CrossRef]
25. Wu, K.; Yang, D.; Wright, N. A coupled SPH-dem model for fluid–structure interaction problems with free-surface flow and structural failure. *J. Comput. Struct.* **2016**, *177*, 141–161. [CrossRef]
26. Nasar, A.M.A.; Rogers, B.D.; Revell, A.; Stansby, P.K. Flexible slender body fluid interaction: Vector-based discrete element method with Eulerian smoothed particle hydrodynamics. *Comput. Fluids* **2019**, *179*, 563–578. [CrossRef]
27. Joseph, O.; Rogers Benedict, D. A fluid–structure interaction model for free-surface flows and flexible structures using smoothed particle hydrodynamics on a GPU. *J. Fluids Struct.* **2021**, *104*, 103312.
28. Degroote, J. Partitioned simulation of fluid–structure interaction. *Arch. Comput. Methods Eng.* **2013**, *20*, 185–238. [CrossRef]
29. Debrabandere, F.; Tartinville, B.; Hirsch, C.; Coussement, C. Fluid-Structure interaction using a Modal Approach. *J. Turbomach.* **2012**, *134*, 051043. [CrossRef]
30. Sun, K.Z.; Zhang, G.Y.; Zong, Z.; Djidjeli, K.; Xing, J.T. SNumerical analysis of violent hydroelastic problems based on a mixed MPS—mode superposition method. *Ocean. Eng.* **2019**, *179*, 285–297. [CrossRef]
31. CoGroth, R.; Biancolini, M.E.; Costa, E.; Cella, U. Validation of High Fidelity Computational Methods for Aeronautical FSI Analyses. In *Engineering Toward Green Aircraft—CAE Tools for Sustainable Mobility*; Springer International Publishing: Berlin/Heidelberg, Germany, 2020; Volume 92, pp. 29–70.
32. Banks, J.W.; Henshaw, W.D.; Schwendeman, D.W.; Tang, Q. A stable partitioned FSI algorithm for rigid bodies and incompressible flow. Part I: Model problem analysis. *J. Comput. Phys.* **2017**, *343*, 432–468. [CrossRef]
33. Tiwari, S.; Kuhnert, J. Finite pointset method based on the projection method for simulations of the incompressible Navier–Stokes equations. In *Meshfree Methods for Partial Differential Equations*; Springer: Berlin/Heidelberg, Germany, 2003; pp. 373–387.
34. Drumm, C.; Tiwari, S.; Kuhnert, J.; Bart, H.J. Finite pointset method for simulation of the liquid–liquid flow field in an extractor. *Comput. Chem. Eng.* **2008**, *32*, 2946–2957. [CrossRef]
35. Onate, E.; Perazzo, F.; Miquel, J. A finite point method for elasticity problems. *Comput. Struct.* **2001**, *79*, 2151–2163. [CrossRef]
36. Peng, C.; Bašić, M.; Blagojević, B.; Bašić, J.; Wu, W. A Lagrangian differencing dynamics method for granular flow modeling. *J. Comput. Geotech.* **2021**, *137*, 104297. [CrossRef]

37. Bašić, J.; Degiuli, N.; Malenica, Š.; Ban, D. Lagrangian finite-difference method for predicting green water loadings. *Ocean Eng.* **2020**, *209*, 107533. [CrossRef]
38. Basic, J.; Degiuli, N.; Ban, D. A class of renormalised meshless Laplacians for boundary value problems. *J. Comput. Phys.* **2018**, *354*, 269–287. [CrossRef]
39. Paneer, M.; Bašić, J.; Lozina, Ž.; Sedlar, D.; Peng, C. Elastic Behaviours of Linear Structure Using Modal Superposition and Lagrangian Differencing Dynamics. In Proceedings of the VIII International Conference on Particle-Based Methods PARTICLES 2023, Milan, Italy, 9–11 October 2023.
40. De Boer, A.; van der Schoot, M.S.; Bijl, H. Mesh deformation based on radial basis function interpolation. *J. Comput. Struct.* **2007**, *85*, 784–795. [CrossRef]
41. Rhee, S.H. Unstructured grid based Reynolds-averaged Navier–Stokes method for liquid tank sloshing. *J. Fluids Eng.* **2008**, *127*, 572–582. [CrossRef]
42. Antoci, C.; Gallati, M.; Sibilla, S. Numerical simulation of fluid–structure interaction by SPH. *J. Comput. Struct.* **2007**, *85*, 879–890. [CrossRef]
43. Eswaran, M.; Saha, U.K.; Maity, D. Effect of baffles on a partially filled cubic tank: Numerical simulation and experimental validation. *Comput. Struct.* **2009**, *87*, 198–205. [CrossRef]
44. Sankar, S.; Ranganathan, R.; Rakheja, S. Impact of dynamic fluid sloshnloads on the directional response of tank vehicles. *Veh. Syst. Dyn.* **1992**, *21*, 385–404. [CrossRef]
45. Nicolici, S.; Bilegan, R.M. Fluid structure interaction modeling of liquid sloshing phenomena in flexible tanks. *Nucl. Eng. Des.* **2013**, *258*, 51–56. [CrossRef]
46. Arora, S.; Vasudevan, S.; Sasic, S.; Etemad, S. A Partitioned FSI methodology for analysis of sloshing-induced loads on a fuel tank structure. In Proceedings of the 6th European Conference on Computational Mechanics (ECCM 6), Glasgow, UK, 11–15 June 2018.
47. Idelsohn, S.R.; Marti, J.; Souto-Iglesias, A.; Onate, E. Interaction between an elastic structure and free-surface flows: Experimental versus numerical comparisons using the PFEM. *Comput. Mech.* **2008**, *43*, 125–132. [CrossRef]
48. Marcela, C.; Laura, B.; Mario, S.; Jorge, D. Numerical Modeling and Experimental Validation of Free Surface Flow Problems. *Arch. Comput. Methods Eng.* **2016**, *23*, 139–169.
49. Hosseinzadeh, S.; Tabri, K. Free-fall water entry of a variable deadrise angle aluminium wedge: An experimental study. In *Developments in the Analysis and Design of Marine Structures*, 1st ed.; CRC Press: Boca Raton, FL, USA, 2021; p. 9.

Journal of
Marine Science and Engineering

MDPI

Article

Ship Flow of the Ryuko-maru Calculated by the Reynolds Stress Model Using the Roughness Function at the Full Scale

Satoshi Matsuda [1,2,*] and Tokihiro Katsui [2]

[1] Akishima Laboratory Inc., Tokyo 190-0031, Japan
[2] Graduate School of Maritime Sciences, Kobe University, Kobe 658-0022, Japan; katsui@maritime.kobe-u.ac.jp
* Correspondence: matsuda@ak.mes.co.jp

Abstract: The k-omega SST turbulence model is extensively employed in Reynolds-averaged Navier–Stokes (RANS)-based Computational Fluid Dynamics (CFD) calculations. However, the accuracy of the estimation of viscous resistance and companion flow distribution for full-sized vessels is not sufficient. This study conducted a computational analysis of the flow around the Ryuko-maru at model-scale and full-scale Reynolds numbers utilizing the Reynolds stress turbulence model (RSM). The obtained Reynolds stress distribution from the model-scale computation was compared against experimental measurements to assess the capability of the RSM. Furthermore, full-scale computations were performed, incorporating the influence of hull surface roughness, with the resulting wake distributions juxtaposed with the actual ship measurements. The full-scale calculation employed the sand-grain roughness function, and an optimal roughness length scale was determined by aligning the computed wake distribution with Ryuko-maru's measured data. The results of this study will allow for the direct performance estimation of full-scale ships and contribute to the design technology of performance.

Keywords: CFD; turbulence model; Reynolds stress model; ship flow; model scale; full scale; wake distribution; wall function; Ryuko-maru

Citation: Matsuda, S.; Katsui, T. Ship Flow of the Ryuko-maru Calculated by the Reynolds Stress Model Using the Roughness Function at the Full Scale. *J. Mar. Sci. Eng.* **2024**, *12*, 783. https://doi.org/10.3390/jmse12050783

Academic Editors: Nastia Degiuli and Ivana Martić

Received: 28 March 2024
Revised: 26 April 2024
Accepted: 29 April 2024
Published: 7 May 2024

1. Introduction

In response to the pressing environmental challenge of global warming, the International Maritime Organization (IMO) has set a target of achieving zero greenhouse gas (GHG) emissions from ships by 2050 [1]. This necessitates adopting alternative fuels and natural energy sources to replace heavy oil as well as developing innovative propulsion systems. Despite alternative energy sources' inherent lower fuel efficiency, there is an urgent need to accelerate the optimization of ship forms and the advancement of energy-saving devices. Consequently, there is a demand for highly accurate prediction technology to evaluate full-scale ship performance.

While numerous studies have focused on Computational Fluid Dynamics (CFD) calculations for ship flow using model ships to achieve accurate estimates of ship performance, there is a growing preference for direct calculations at full-scale Reynolds numbers. This approach avoids the need to extrapolate from model ship Reynolds numbers to full-scale equivalents. Undertaking full-scale CFD calculations at a practical level underscores the importance of validating the CFD methodology by comparing the results with empirical measurement data.

Many CFD analyses have been conducted to predict ship flow, with Pena et al. [2] providing a comprehensive review of turbulence models' efficacy in estimating ship performance. Reynolds-averaged Navier–Stokes (RANS)-based computational methods are widely used, employing two-equation turbulence models like the k–ε or k-omega SST. However, these models exhibit limitations in accurately estimating viscous resistance. Matsuda et al. [3] conducted a comparative study of ship flow calculations using the k-omega

SST (a two-equation model) and the Reynolds stress turbulence model (RSM) (a seven-equation model) at model-scale Reynolds numbers across various hull forms. While the k-omega SST is adequate in estimating form factor K and wake distribution for slender ships, it underestimates form factor K, resulting in a smaller stern longitudinal vortex size at the propeller plane compared to experimental results for full-sized vessels. Matsuda et al. demonstrated that the RSM offers more accurate estimates for form factor and wake distribution, particularly for bulk carriers and oil tankers.

Pena et al. [2] highlighted various applications of CFD at full-scale Reynolds numbers [4–6], citing studies by Song et al. [7] and Pena et al. [8], which examined KCS and KVLCC2 flows at both model- and full-scale Reynolds numbers, accounting for hull surface roughness using wall function boundary conditions. Hull surface roughness significantly increases frictional and viscous drag, wave pattern, and wake distribution. Pena et al. [8] conducted full-scale calculations for a general cargo ship (Regal), analyzing the hull's detailed flow field and discussing velocity, shear pressure, and vorticity distribution. Ohashi [9] calculated the flow around the Ryuko-maru (an older model VLCC) at full-scale Reynolds numbers, accounting for surface roughness through wall-resolved and wall function boundary conditions. These calculations were compared to measured wake distributions obtained from actual ship measurements. The comparison revealed that when roughness effects were considered, the wake distribution obtained from CFD calculations demonstrated improved agreement with the full-scale measured results compared to those assuming a smooth surface. Furthermore, considering uncertainty, the wall function approach was more effective for CFD calculations in full-scale ship scenarios. Sakamoto et al. [10] similarly employed this method for calculations involving bulk carriers and container ships fitted with ducts, mirroring the approach taken by Ohashi [9]. Their findings demonstrated strong agreement in wake flow distribution, even when considering the presence of energy-saving devices. Accurately estimating the additional frictional resistance exerted on painted hull surfaces requires a thorough understanding of the roughness function specific to such surfaces. Many roughness functions employed in CFD calculations are tailored to sand-grain roughness. Consequently, understanding the roughness length scale specific to painted surfaces is crucial for accurate full-scale ship flow calculations. To verify the effectiveness of the RSM in more detail, it is important to evaluate it at the level of Reynolds stress, but there are no previous studies. Few studies have applied the RSM to CFD calculations at the full scale and compared the wake flow distribution with the full-scale test results. Furthermore, there is no standardized method that takes into account the roughness of the hull surface of a full-scale model, and it has not been fully verified how to set the roughness height to perform a reasonable calculation at the full scale.

This study calculated ship flow at the model scale using the RSM for enhanced wake distribution accuracy, validating it against Reynolds stresses from wind tunnel experiments. The influence of hull surface roughness was incorporated using wall function methodology, integrating a sand-grain roughness function, and exploring an appropriate roughness length scale through comparison with empirical wake distribution data. In this study, the effectiveness of the RSM can be confirmed in more detail by comparing the CFD calculation results with the experimental Reynolds stresses. Furthermore, by developing a CFD calculation method that takes into account the surface roughness of the hull, it will be possible to directly estimate the viscous resistance and the wake distribution with high accuracy on a practical number of grids. This will contribute to the improvement in design technology.

2. Comparison of CFD Calculations and Experimental Results of Reynolds Stress at the Model Scale

Prior research has established that the RSM outperforms the k-omega SST, a two-equation model, in predicting form factor K at the model ship scale. This is attributed to its superior accuracy in forecasting wake flow distribution. For a precise estimation of ship flow distribution, it is crucial to assess not only velocity distribution but also Reynolds

stresses. However, validating the RSM's full-scale wake distribution accuracy poses challenges because direct measurements are unavailable. CFD simulations were conducted for the Ryuko-maru at the model ship scale, comparing results from the k-omega SST and the RSM–linear pressure strain correlation model with two layers (LPST) to assess the RSM's Reynolds stress prediction accuracy. The comparison utilized data from wind tunnel tests performed by Suzuki et al. [11] using a 3 m model ship in the Osaka University research wind tunnel (with measurement section dimensions of L × B ×D = 9.5 m × 1.8 m × 1.8 m). The model ship was suspended in the tunnel's center using piano wire, with a wind tunnel blockage rate of approximately 6%. Flow field measurements were obtained using a triple-sensor hot-wire system, with data sampling at 10 kHz, acknowledging inherent errors of approximately 5% for time-averaged flow velocity and approximately 10% for Reynolds stress components. Furthermore, a V&V process was conducted to compare the two-equation k-omega SST model with the RSM–LPST.

2.1. Computational Conditions

The RSM was assessed using the hull form of the Ryuko-maru, a 200,000 DWT tanker built in Japan with a *Cb* value of 0.83. CFD validation data for this vessel, made publicly available by Namimatsu et al. [12], were utilized. The wake distribution of the ship was also measured at the full scale using a five-hole pitot tube. Figure 1 illustrates the 3D model of the Ryuko-maru, while Table 1 provides its principal dimensions.

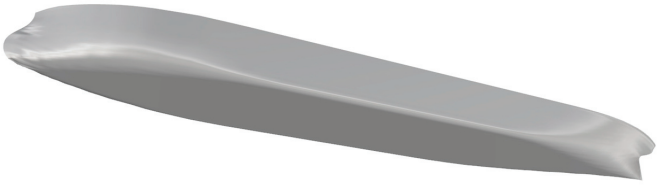

Figure 1. 3D model of Ryuko-maru.

Table 1. Principle dimensions of Ryuko-maru.

Model/Ship	Ship	Model
L_{pp} (m)	300.00	3.000
B (m)	50.00	0.500
D (m)	25.00	0.250
d (m)	18.86	0.189
Dp (m)	9.20	0.092
α	-	100.00
Cb	0.83	

The CFD simulations were conducted using STAR-CCM+ version 16.02. Two turbulence models were employed: k-omega SST and RSM–LPST. The RSM–LPST, based on the LPS (linear pressure strain correlation) model [13] with a wall function developed by Gibson and Launder [14], is specifically designed for low Reynolds numbers, with $y \leq +1$ for grid points near the wall surface. It uses a model coefficient for the pressure–strain correlation term reported by Launder and Shima [15]. Previous research by Matsuda et al. [3] demonstrated the effectiveness of LPST for CFD calculations at model ship scales, thus justifying its selection for this study.

As depicted in Figure 2, the computational domain spans dimensions of 5.0 L_{pp} × 5.0 L_{pp} × 0.625 L_{pp} (both sides), with only the area below the draft considered in the CFD computations. In contrast, wind tunnel tests utilized a double-model setup. A medium grid arrangement, illustrated in Figure 3, shows the surface grid of a 3 m model of the Ryuko-

maru. Figure 4 shows the volume grid of the center plane. Figure 5 shows the volume grid in the propeller plane. Dense grids are arranged to adapt to the complex flow around the stern. The first layer of grids on the hull surface was configured to achieve y+ $\approx$ 1. To ensure accuracy, three grid resolutions (coarse, medium, and fine) were generated for verification purposes, following the methodology employed by Matsuda et al. [3] the simulations were conducted under uniform flow conditions, as detailed in Table 2.

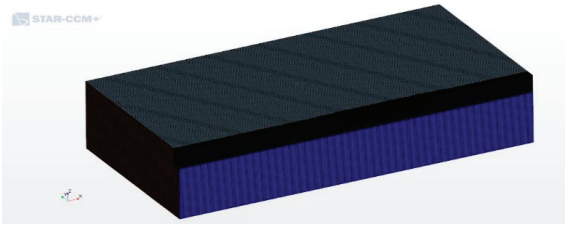

Figure 2. Volume grid of whole area.

Figure 3. Surface grid of 3 m model of Ryuko-maru.

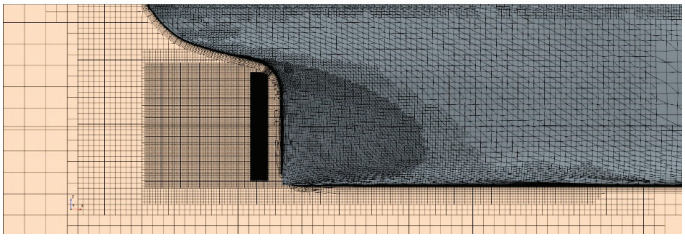

Figure 4. Volume grid around hull of 3 m model.

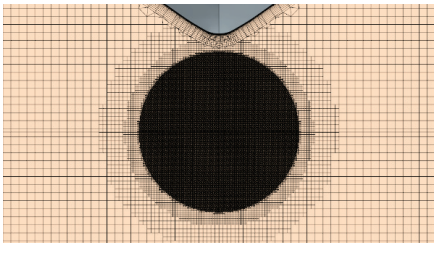

Figure 5. Volume grid of 3 m model in propeller plane.

Table 2. Computational conditions of 3 m model.

V_m (m/s)	20.0
ρ (kg/m^3)	1.146
$\nu \times 10^{-5}$ (m^2/s)	1.6509
$Rn \times 10^6$	3.63

2.2. Verification Method and Results

The verification used the ITTC method [16]. Table 3 depicts the verification grid generation results. The grid counts were determined to maintain an R_i of approximately 1.4, specifically, approximately 22 million for the fine grid, approximately 8 million for the medium grid, and approximately 3 million for the coarse grid.

Table 3. Results of grid refinement ratio r_i of 3 m model.

Fine	NC1	22,101,990
Midium	NC3	8,006,215
Coarse	NC4	2,933,781
	R_i	1.400
	$R_{i,21}$	1.403
	$R_{i,32}$	1.397

The results of the CFD calculations are presented in Table 4. The verification results for ε_{21}, ε_{32}, R, U_i, and U_{SN} are shown in Table 5.

Table 4. Results of CFD calculation of 3 m model.

No.	Turbulance Model	Grid	Fall (N)	Fvis (N)	$CT \times 10^3$	$Cf \times 10^3$
1	k-ω SST	Coarse	2.00	1.60	3.783	3.012
2		Midium	2.07	1.61	3.900	3.048
3		Fine	2.01	1.60	3.796	3.012
4	LPST	Coarse	2.17	1.74	4.091	3.289
5		Midium	2.26	1.81	4.275	3.409
6		Fine	2.18	1.74	4.108	3.285

Table 5. Results of verification of 3 m model.

	ε_{21}	ε_{32}	R	$\varepsilon_{i,32}/\varepsilon_{i,21}$	U_i	U_{SN} (%CT_{fine})
k-ω SST	0.1035	−0.1172	−0.8832	−1.1323	0.059	1.54%
LPS	0.1662	−0.1835	−0.9058	−1.1040	0.092	2.23%

The k-omega SST and the LPST on the three grids performed in this study are not in the direction of convergence as the grids are made finer. This may be due to the fact that even a coarse grid is generally sufficient. In addition, the LPST estimated a larger overall viscous resistance to the k-omega SST. This result follows the same trend as that of Matsuda et al. [3]. The calculated numerical uncertainty U_{SN} (1.54%) of the k-omega SST model is lower than that of the RSM–LPS U_{SN} (2.23%). However, the U_{SN} for both is sufficiently small, and the variation in hydrodynamic forces is also small enough in the three grids. Consequently, a detailed comparison of wake distributions was conducted for the medium grid.

2.3. Results of CFD Calculation of Reynolds Stress

The definition of flow direction is shown in Figure 6. The distribution of the contour plot of Vx/V0 is shown in Figure 7, V_{cf}/V0 in Figure 8, $\overline{u'u'}$ in Figure 9, $\overline{v'v'}$ in Figure 10, $\overline{w'w'}$ in Figure 11, $\overline{u'w'}$ in Figure 12, and turbulence kinetic energy k in Figure 13. Figures 7–13 shows the wind tunnel test results on the left and the CFD calculation results on the right. Vx is the longitudinal velocity (m/s) and V0 is the ship speed (m/s). $\overline{u'u'}$, $\overline{v'v'}$, $\overline{w'w'}$, and $\overline{u'w'}$ are the

Reynolds stresses of u, v, w, and uw. $\overline{u'u'}$, $\overline{v'v'}$, $\overline{w'w'}$, $\overline{u'w'}$, and k are nondimensionalized at $V0^2$. The crossflow velocity magnitude is defined as follows:

$$V_{cf} = \sqrt{V_y^2 + V_z^2} \tag{1}$$

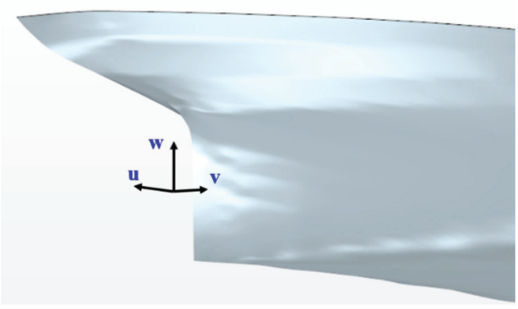

Figure 6. Crossflow distribution of SPIV (**left**) and CFD (**right**) at 110 mm from A.P.

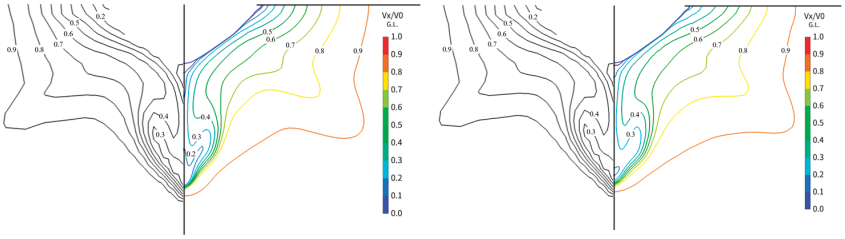

Figure 7. Comparison of contour line of Vx/V0 ((**left**): k-omega SST; (**right**): RSM-LPST).

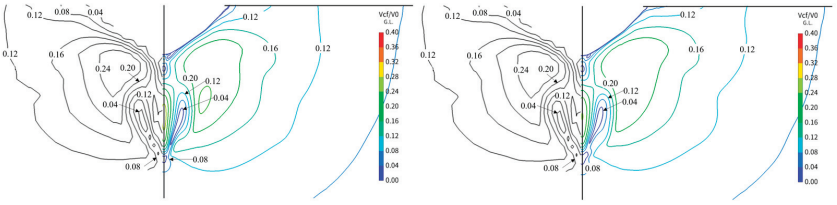

Figure 8. Comparison of contour line of V_{cf}/V0 ((**left**): k-omega SST; (**right**): RSM-LPST).

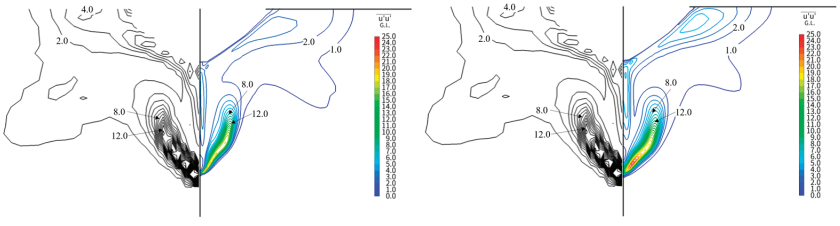

Figure 9. Comparison of contour line of $\overline{u'u'}$ ((**left**): k-omega SST; (**right**): RSM-LPST).

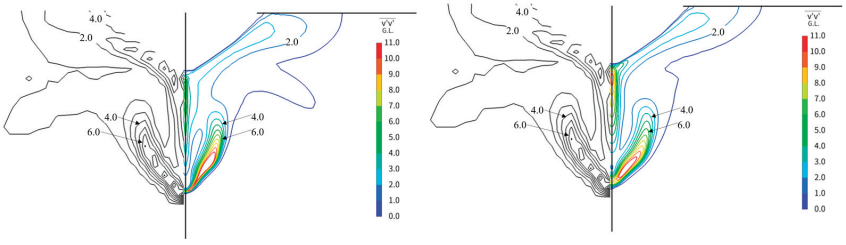

Figure 10. Comparison of contour line of $\overline{v'v'}$ ((**left**): k-omega SST; (**right**): RSM-LPST).

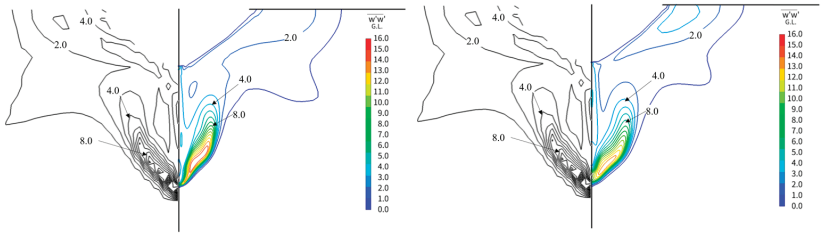

Figure 11. Comparison of contour line of $\overline{w'w'}$ ((**left**): k-omega SST; (**right**): RSM-LPST).

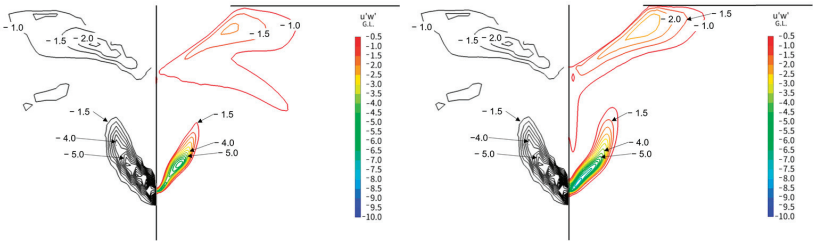

Figure 12. Comparison of contour line of $\overline{u'w'}$ ((**left**): k-omega SST; (**right**): LPST).

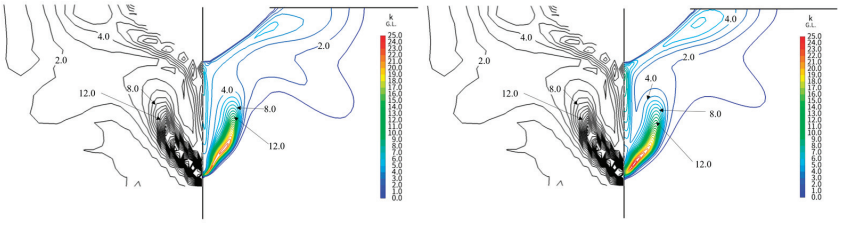

Figure 13. Comparison of contour line of k ((**left**): k-omega SST; (**right**): RSM-LPST).

The distribution of crossflow velocity magnitude is a valuable tool for assessing the intensity of longitudinal vortices and identifying their core locations.

As depicted in Figure 7, the Vx/V0 closely aligns between CFD and EFD when contour levels are from 0.5 to 0.9 for both the k-omega SST and RSM-LPST models. Notably, for the k-omega SST, the stern longitudinal vortex area circled by 0.3 and 0.4 lines is smaller than that of the experimental results. Conversely, the RSM-LPST demonstrates a superior correspondence with the 0.3 and 0.4 lines, an observation also noted by Matsuda et al. [3], with a similar trend observed for V_{cf}, $\overline{u'u'}$, $\overline{v'v'}$, $\overline{w'w'}$, $\overline{u'v'}$, $\overline{v'w'}$, $\overline{u'w'}$, and k.

A comparison is presented for a line $0.5R$ vertically up from the shaft center height for a more detailed comparison between the CFD results of velocity and Reynolds stress distributions and the experimental data. Figure 14 shows the definition and a schematic

view of Y (mm). Figures 15–18 show the cut line distributions of Vx/V0 and the crossflow velocity, $\overline{u'u'}$, $\overline{v'v'}$, $\overline{w'w'}$, $\overline{u'v'}$, $\overline{v'w'}$, $\overline{u'w'}$, and k.

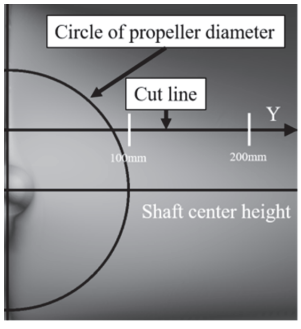

Figure 14. Schematic view of cut line.

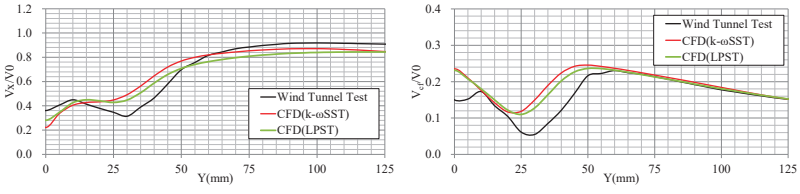

Figure 15. Velocity distribution along horizontal line above propeller shaft ((**left**): Vx/V0; (**right**): V_{cf}).

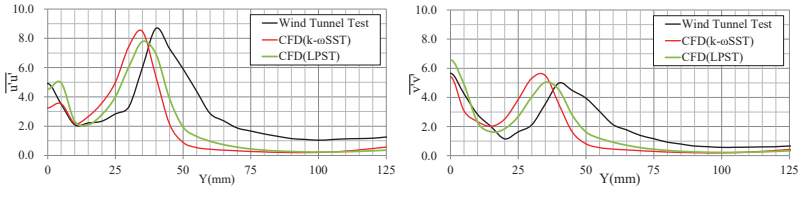

Figure 16. Reynolds stress distribution along horizontal line above propeller shaft ((**left**): $\overline{u'u'}$; (**right**): $\overline{v'v'}$).

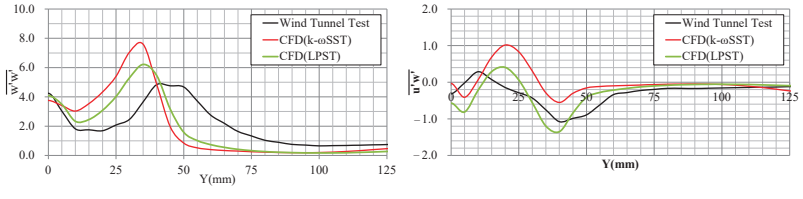

Figure 17. Reynolds stress distribution along horizontal line above propeller shaft ((**left**): $\overline{w'w'}$; (**right**): $\overline{u'w'}$).

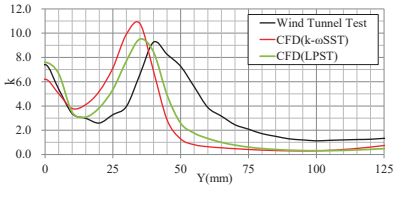

Figure 18. k distribution along horizontal line above propeller shaft.

As shown in Figures 15–18, the RSM-LPST is closer to EFD from Y = 0 to 75 mm. The peak magnitude and location of the RSM-LPST closely resembles the EFD values for the k-omega SST in terms of $\overline{u'u'}$, $\overline{v'v'}$, $\overline{w'w'}$, $\overline{u'w'}$, and k. On the other hand, the range above Y = 75 mm is almost the same for both turbulence models.

The results of CFD computations on the 3 m model indicate that the RSM-LPST tends to exhibit closer agreement with the experimental results compared to the k-omega SST. This confirms the efficacy of the RSM-LPST in achieving more accurate predictions.

3. Full-Scale Calculation of Ship Flow Considering Hull Surface Roughness

To assess the accuracy of predicting wake flow distribution at full-scale Reynolds numbers using the RSM, CFD computations were conducted for the same vessel as in the previous section, the Ryuko-maru. The measured data of the full-scale wake flow distribution for the Ryuko-maru are publicly available in Ogiwara [17], enabling a direct comparison with the calculated results. The calculations were performed using the RSM–LPS, incorporating a wall function to account for hull surface roughness. Extensive research on roughness functions, particularly for sand roughness, supports using this method owing to its high estimation accuracy, as highlighted by Ohashi [9]. Consistent with Ohashi's findings, CFD simulations were performed under towing conditions, given the negligible impact of propeller suction in this scenario. Although only the roughness of the hull is considered here, the propeller in high-roughness conditions will affect the resistance as well as the power required.

3.1. Roughness Function

Surface friction increases in the presence of surface roughness compared to a smooth surface. This effect is evidenced by a reduced mean velocity distribution within the turbulent boundary layer, a phenomenon quantified by the roughness function ΔU^+. The dimensionless velocity distribution within the logarithmic law domain of a rough surface is expressed by Equation (2) proposed by Cebeci and Bradshaw [18]:

$$U^+ = \frac{1}{\kappa}\ln\left(y^+\right) + B - \Delta U^+ \tag{2}$$

where κ is the von Karman constant, y^+ is the nondimensional normal distance from the boundary, B is the smooth wall log–law intercept, and ΔU^+ is the roughness function. The roughness function varies with the roughness characteristics and is determined as a function of the roughness Reynolds number k^+, as in Equation (3), used in Star-CCM+ [19]. The definition of k^+ is shown in Equation (4).

$$\Delta U^+ = \begin{cases} 0,\ k^+ \le k^+_{smooth} \\ \frac{1}{\kappa}\ln\left[C_1\left(\frac{k^+ - k^+_{smooth}}{k^+_{Rough} - k^+_{smooth}}\right) + C_2 k^+\right]^{\alpha}, k^+_{smooth} < k^+ < k^+_{Rough} \\ \frac{1}{\kappa}\ln(C_1 + C_2 k^+),\ k^+ > k^+_{Rough} \end{cases} \tag{3}$$

where:

$$\alpha = sin\left[\frac{\pi}{2}\frac{\log\left(k^+/k^+_{smooth}\right)}{\log\left(k^+_{Rough}/k^+_{smooth}\right)}\right].$$

$$k^+ = \frac{u_\tau k_s}{\nu} \tag{4}$$

where u_τ is the friction velocity, k_s is the characteristic roughness length scale, and ν is the kinematic viscosity. As shown in Table 6, various coefficients have been proposed with k^+_{smooth}, k^+_{Rough}, C_1, and C_2 as parameters. Yigit Karmel Demirel et al. (2014) [20] and Soonseok Song et al. [21] used the same parameters as the default parameter of Star-ccm+. Yigit et al. (2017) [22] calibrated their coefficients to align with the experimental findings of Schultz et al. [23] Andrea Farkas et al. [24] and Henrik Mikkelsen et al. [25] also used

the same parameters. Roberto et al. [26] juxtaposed the parameters of White et al. [27] and Grigson [28], as illustrated in Figure 19. In our investigation, we adopted the values from Yigit et al. (2017) and fine-tuned them to accommodate the lower k^+ range.

Table 6. Table of the coefficients of roughness function.

	C_1	C_2	k^+_{smooth}	k^+_{rough}
STAR-CCM+ [19] Yigit Kemal Demirel (2014) [20] Soonseok Song (2021) [21]	0.000	0.253	2.25	90.00
Yigit Kemal Demirel (2017) [22] Andrea Farkas (2019) [24] Henrik Mikkelsen (2020) [25]	0.000	0.260	3.00	15.00
Roberto Ravenna (2022) [26]	−3.000	0.490	3.00	25.00
White (2006) [27]	1.000	0.300		
Grigson (1992) [28]	1.000	1.000		

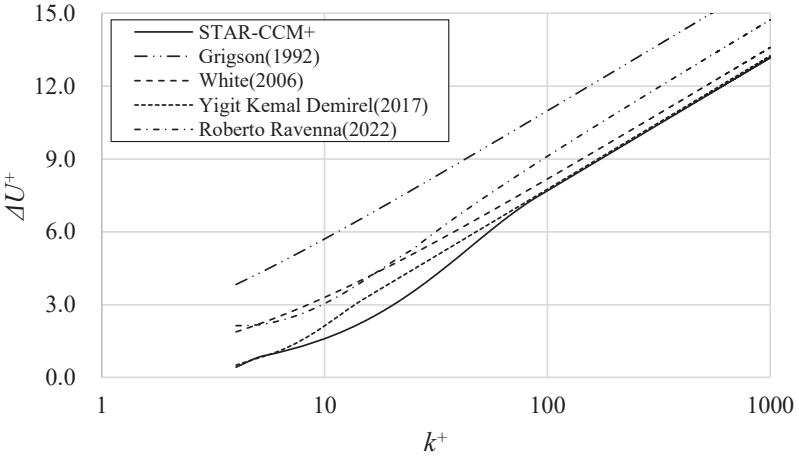

Figure 19. Comparison of roughness function models ([19,22,26–28]).

3.2. Condition of Full-Scale CFD

The conditions for conducting full-scale CFD calculations are shown in Table 7, mirroring those employed in the full-scale experiment conducted by Namimatsu et al. [12]. The calculation methodology remained consistent with that outlined in Section 2.

Table 7. A list of the calculation condition of the objective ships.

L_{pp} (m)	300
B (m)	50
d (m)	18.86
∇ (m^3)	233,554
S (m^2)	23,116
ρ (kg/m^3)	1027.3
V (m/s)	8.334
$\nu \times 10^{-5}$ (m^2/s)	0.098608
$Rn \times 10^9$	2.54

The resulting computations were juxtaposed with the results of the pitot tube measurements of wake flow at the full scale. The turbulence models employed encompassed the k-omega SST and the RSM-LPS.

3.3. Results of CFD Calculation

Initially, smooth conditions and full-scale verifications were conducted. Table 8 presents the grid count and grid refinement ratio r_i. Table 8 shows the calculated resistance results. Verification analyses are detailed in Tables 9 and 10.

Table 8. Results of grid refinement ratio r_i at full scale.

Fine	NC1	38,523,207
Midium	NC2	15,457,974
Coarse	NC3	6,315,456
	R_i	1.352
	$R_{i,21}$	1.356
	$R_{i,32}$	1.348

Table 9. Results of CFD calculation at full scale.

Turbulance Model	Grid	Fall (N)	Fvis (N)	$CT \times 10^3$	$Cf \times 10^3$
k-ω SST	Coarse	1,414,782	1,140,107	1.716	1.383
	Midium	1,413,533	1,140,192	1.714	1.383
	Fine	1,406,526	1,140,616	1.706	1.383
LPS	Coarse	1,501,705	1,194,031	1.821	1.448
	Midium	1,501,398	1,193,697	1.821	1.447
	Fine	1,507,254	1,193,783	1.828	1.448

Table 10. Results of verification of full scale.

	δ_i	δ_{fine} (%(1 + K)$_{\text{fine}}$)	U_i	U_{SN} (%(1 + K)$_{\text{fine}}$)
k-ω SST	0.0103	0.83%	0.0309	1.81%
LPS	-	-	0.0036	0.28%

As indicated in Table 10, the U_{SN} was approximately 1.5% smaller for the RSM-LPS than for the k-omega SST. However, the difference in U_{SN} is negligible for both cases. Consequently, the medium grid was selected for this calculation.

Surface roughness was varied from 29 to 150 μm under smooth surface conditions, and the corresponding current distribution was compared to determine the surface roughness that closely approximated the ΔC_F predicted by the ITTC 1990 equation (Equation (5)). Additionally, Figure 20 displays graphs depicting ΔC_F on the horizontal axis and ks (μm) on the vertical axis.

$$\Delta C_F \times 10^{-3} = 44\left[\left(\frac{ks}{L_{pp}}\right)^{\frac{1}{3}} - 10Rn^{-\frac{1}{3}}\right] + 0.125 \quad (5)$$

where ks is the roughness of the surface (μm), L_{pp} is the perpendicular length (m), and Rn is the Reynolds number.

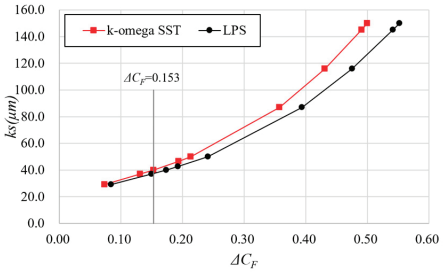

Figure 20. Result of CFD calculation.

As depicted in Figure 20, although both the k-omega SST and the RSM-LPS exhibit a similar trend for ΔC_F, *ks* is larger for the k-omega SST. Specifically, according to the ITTC 1990 equation, $\Delta C_F = 0.153 \times 10^{-3}$ corresponds to *ks* = 40 μm for the k-omega SST and *ks* = 37 μm for the RSM-LPS.

Figures 21–23 compare the experimental results and the CFD-estimated wake distribution. Figure 21 displays the calculation results under smooth conditions, while Figure 22 shows the calculation results for *ks* = 150 (μm). Figure 23 depicts the results for $\Delta C_F = 0.153 \times 10^{-3}$. Here, the Vx/V0 contour is juxtaposed with the results of the full-scale measurements (indicated by the black line).

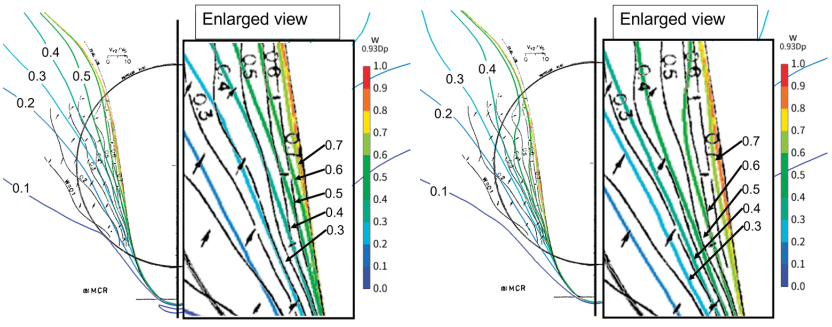

Figure 21. Comparison of results of wake distribution at full scale under smooth conditions ((**left**): k-omega SST; (**right**): RSM-LPS).

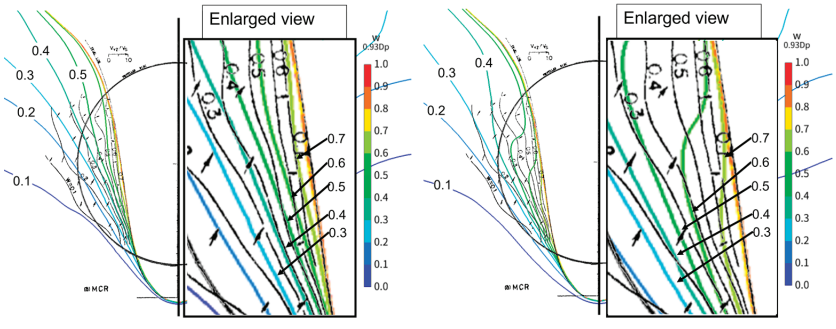

Figure 22. Comparison of results of wake distribution at full scale under rough conditions ((**left**): k-omega SST (*ks* = 150 μm); (**right**): RSM-LPS (*ks* = 150 μm)).

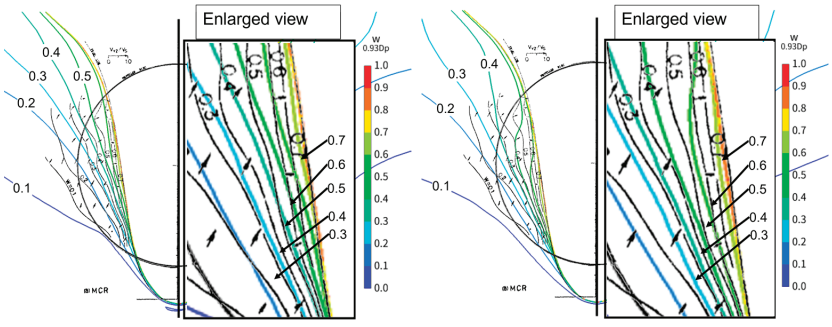

Figure 23. Comparison of results of wake distribution at full scale under rough conditions ((**left**): k-omega SST (*ks* = 40 μm); (**right**): RSM-LPS (*ks* = 37 μm)).

A notable difference emerges after comparing the calculation results on smooth surfaces, as illustrated in Figure 21. Specifically, the k-omega SST has a thin wake flow at lines above 0.3 compared to the experimental results. The RSM-LPS demonstrates closer agreement between the CFD calculation results and the experimental findings, particularly between the 0.2 and 0.4 lines. Also, the LPS shows a bulge of the boundary layer near the center of the shaft. Above the propeller center, the results from the full-scale ship tests exhibit a wave-shaped pattern, which is not replicated by the trend observed in both CFD calculations. In Figure 22, setting *ks* to 150 μm resulted in the ΔC_F of the k-omega SST exceeding twice the ITTC recommendation at the full-scale Reynolds number. However, the wake flow distribution showed good agreement. The LPS estimated the wake flow to be thicker than that of the experimental results. As shown in Figure 23, using ΔC_F of the ITTC recommendation to account for surface roughness, the LPS results show nearly the same wake distribution (0.4–0.6 lines) near the hull surface. The k-omega SST showed a thinner wake distribution (0.4–0.6 lines) near the hull compared to the experimental results. However, above the propeller center, the k-omega SST showed better agreement. These results show that the RSM-LPS has an advantage over the k-omega SST in terms of separation phenomena and is able to estimate the viscous resistance and the wake distribution of the full-sized vessel with high accuracy.

4. Conclusions

In this study, CFD calculations of the Ryuko-maru employing the RSM were conducted to enhance the accuracy of wake distribution estimation. The CFD calculation results at the model scale were juxtaposed with the Reynolds stress distribution measured in wind tunnel tests. Additionally, the CFD calculation results accounting for full-scale roughness effects were compared with those of full-scale wake flow measurements. These findings are summarized as follows.

- The CFD calculations at the model scale revealed that the RSM–LPST exhibited slightly higher accuracy in predicting the wake flow around the stern longitudinal vortex compared to the k-omega SST.
- Full-scale calculations under smooth conditions demonstrated that the k-omega SST exhibited higher velocities than the measured values with almost no hook shape.
- Setting *ks* to 150 μm resulted in the ΔC_F of the k-omega SST exceeding twice the ITTC recommendation at the full-scale Reynolds number. However, the wake flow distribution showed good agreement.
- When *ks* was adjusted to match the ΔC_F of the ITTC recommendation, the wake flow near the hull surface displayed good agreement with the RSM-LPS. However, above the propeller center, the k-omega SST showed better agreement.

- The RSM-LPS has an advantage over the k-omega SST in terms of separation phenomena at the full scale and is able to estimate the viscous resistance and the wake distribution of the full-sized vessel with high accuracy.

Based on the findings outlined above and considering computational costs, it is advisable to utilize the RSM–LPS or the LPST to achieve highly accurate predictions close to the hull in full-scale ships. For a more comprehensive validation of the calculation accuracy of the stern longitudinal vortex, it is imperative to acquire measurement results of the full-scale wake distribution close to the propeller.

Author Contributions: Writing—original draft preparation, S.M.; supervision, T.K. All authors have read and agreed to the published version of the manuscript.

Funding: This research received no external funding.

Institutional Review Board Statement: Not applicable.

Informed Consent Statement: Not applicable.

Data Availability Statement: Data is contained within the article.

Acknowledgments: The wind tunnel test results of the Ryuko-maru were provided by Suzuki of Osaka University. We are deeply grateful to Suzuki.

Conflicts of Interest: Author Satoshi Matsuda was employed by the company Akishima Laboratory Inc. The remaining authors declare that the research was conducted in the absence of any commercial or financial relationships that could be construed as a potential conflict of interest.

References

1. MEPC. 2023 IMO Strategy on Reduction of GHG Emissions from Ships. MEPC 80/WP.12 Annex 1. 2023. Available online: https://wwwcdn.imo.org/localresources/en/MediaCentre/PressBriefings/Documents/Resolution%20MEPC.377(80).pdf (accessed on 27 March 2024).
2. Pena, B.; Huang, L. A review on the turbulence modelling strategy for ship hydrodynamic simulations. *Ocean Eng.* **2021**, *241*, 110082. [CrossRef]
3. Matsuda, S.; Katsui, T. Hydrodynamic Forces and Wake Distribution of Various Ship Shapes Calculated Using a Reynolds Stress Model. *J. Mar. Sci. Eng.* **2022**, *10*, 777. [CrossRef]
4. Korkmaz, K.B.; Werner, S.; Bensow, R. Verification and Validation of CFD Based Form Factors as a Combined CFD/EFD Method. *J. Mar. Sci. Eng.* **2021**, *9*, 75. [CrossRef]
5. Korkmaz, K.B.; Werner, S.; Sakamoto, N.; Queutey, P.; Deng, G.; Gao, Y.; Dong, G.; Maki, K.; Ye, H.; Akinturk, A.; et al. CFD based form factor determination method. *Ocean Eng.* **2021**, *220*, 108451. [CrossRef]
6. Andersson, J.; Shiri, A.A.; Bensow, R.E.; Jin, Y.; Wu, C.; Qiu, G.; Deng, G.; Queutey, P.; Yan, X.-K.; Horn, P.; et al. Ship-scale CFD benchmark study of a pre-swirl duct on KVLCC2. *Appl. Ocean Res.* **2020**, *123*, 103134. [CrossRef]
7. Song, S.; Demirel, Y.K.; Muscat-Fenech, C.D.M.; Tezdogan, T.; Atlar, M. Fouling effect on the resistance of different ship types. *Ocean Eng.* **2020**, *216*, 107736. [CrossRef]
8. Pena, B.; Muk-Pavic, E.; Fitzsimmons, P. Detailed analysis of the flow within the boundary layer and wake of a full-scale ship. *Ocean Eng.* **2020**, *218*, 108022. [CrossRef]
9. Ohashi, K. Numerical study of roughness model effect including low-Reynolds number model and wall function method at actual ship scale. *J. Mar. Sci. Technol.* **2021**, *26*, 24–36. [CrossRef]
10. Sakamoto, N.; Kobayashi, H.; Ohashi, K.; Kawanami, Y.; Windén, B.; Kamiirisa, H. An overset RaNS prediction and validation of full scale stern wake for 1,600TEU container ship and 63,000 DWT bulk carrier with an energy saving device. *Appl. Ocean Res.* **2020**, *105*, 102417. [CrossRef]
11. Suzuki, H.; Miyazaki, S.; Suzuki, T.; Matsumura, K. Turbulence Measurements in Stern Flow of Ship Models–Ryuko-maru (Tanker form), Hamburg Test Case (Container form). *J.-Kansai Soc. Nav. Archit. Jpn.* **1998**, *230*, 109–122. (In Japanese)
12. Namimatsu, M.; Muraoka, K.; Yamashita, S.; Kushimoto, H. Wake Distribution of Ship and Model on Full Ship Form. *J. Soc. Nav. Archit. Jpn.* **1973**, *134*, 65–73. (In Japanese) [CrossRef]
13. Gibson, M.M.; Launder, B.E. Ground effects on pressure fluctuations in the atmospheric boundary layer. *J. Fluid Mech.* **1978**, *86*, 491–511. [CrossRef]
14. Launder, B.E.; Shima, N. Second Moment Closure for the Near-Wall Sublayer. *Dev. Appl. AIAA J* **1989**, *27*, 1319–1325. [CrossRef]
15. Rodi, W. Experience with Two-Layer Models Combining the k-e Model with a One-Equation Model Near the Wall. In Proceedings of the 29th Aerospace Sciences Meeting, Reno, NV, USA, 7–10 January 1991. AIAA 91-0216.
16. ITTC. Recommended procedures and guidelines—Uncertainty analysis in CFD verification and validation methodology and procedures. In Proceedings of the 28th International Towing Tank Conference, Wuxi, China, 17–22 September 2017.

17. Ogiwara, S. Stern Flow Measurements for the Tanker 'Ryuko-Maru' in Model Scale, Intermediate Scale, and Full Scale Ships. *Proc. CFD Workshop Tokyo* **1994**, *1*, 341–349.
18. Cebeci, T.; Bradshaw, P. *Momentum Transfer in Boundary Layers*; Hemisphere Publishing Corp.: Washington, DC„ USA; McGraw-Hill Book Co.: New York, NY, USA, 1977.
19. Siemens Digital Industries Software. User Guide Simcenter STAR-CCM+ 2021.1. Available online: https://docs.sw.siemens.com/ja-JP/doc/226870983/PL20201109101148301.starccmp_installguide_pdf?audience=external&pk_vid=2d7d3ecf2bbd1d6f4858ceeeb21cee311714744815a1775a (accessed on 27 March 2024).
20. Demirel, Y.K.; Khorasanchi, M.; Turan, O.; Incecik, A.; Schultz, M.P. A CFD model for the frictional resistance prediction of antifouling coatings. *Ocean Eng.* **2014**, *89*, 21–31. [CrossRef]
21. Song, S.; Ravenna, R.; Dai, S.; Muscat-Fenech, C.D.; Tani, G.; Demirel, Y.K.; Atlar, M.; Day, S.; Incecik, A. Experimental investigation on the effect of heterogeneous hull roughness on ship resistance. *Ocean Eng.* **2021**, *223*, 108590. [CrossRef]
22. Demirel, Y.K.; Turan, O.; Incecik, A. Predicting the effect of biofouling on ship resistance using CFD. *Appl. Ocean Res.* **2017**, *62*, 100–118. [CrossRef]
23. Schultz, M.P.; Flack, K.A. The Rough-Wall Turbulent Boundary Layer from the Hydraulically Smooth to the Fully Rough Regime. *J. Fluid Mech.* **2007**, *580*, 381–405. [CrossRef]
24. Farkas, A.; Degiuli, N.; Martić, I.; Dejhalla, R. Numerical and experimental assessment of nominal wake for a bulk carrier. *J. Mar. Sci. Technol.* **2019**, *24*, 1092–1104.
25. Mikkelsen, H.; Walther, J.H. Effect of roughness in full-scale validation of a CFD model of self-propelled ships. *Appl. Ocean Res.* **2020**, *99*, 102162. [CrossRef]
26. Ravenna, R.; Song, S.; Shi, W.; Sant, T.; Muscat-Fenech, C.D.M.; Tezdogan, T.; Demirel, Y.K. CFD analysis of the effect of heterogeneous hull roughness on ship resistance. *Ocean Eng.* **2022**, *258*, 111733. [CrossRef]
27. White, F.M.; Majdalani, J. *Viscous Fluid Flow*; McGraw-Hill: New York, NY, USA, 2006; Volume 3.
28. Grigson, C. Drag losses of new ships caused by hull finish. *J. Ship Res.* **1992**, *36*, 182–196. [CrossRef]

Journal of
Marine Science and Engineering

MDPI

Article

Planing Hull Hydrodynamic Performance Prediction Using LincoSim Virtual Towing Tank

Ermina Begovic [1,*], Carlo Bertorello [1], Raffaele Ponzini [2] and Francesco Salvadore [3]

[1] Department of Industrial Engineering, University of Naples Federico II, Via Claudio 21, 80125 Napoli, Italy; bertorel@unina.it
[2] HPC Department, CINECA, Milan Office, Corso Garibaldi, 86 Milano, 20121 Milan, Italy; r.ponzini@cineca.it
[3] HPC Department, CINECA, Rome Office, Cineca, Via dei Tizii 6/B, 00185 Rome, Italy; f.salvadore@cineca.it
* Correspondence: begovic@unina.it

Abstract: This work shows the performance of LincoSim, a web-based virtual towing tank enabling automated and standardized calm water computational fluid dynamics (CFD) data sampling, extending previous published applications to the case of a high-speed hull. The calculations are performed for a 1:10 scale model of a 43 ft powerboat hull form in the Froude number range from 0.3 to 2.0. The counterpart physical model is the experimental fluid dynamics (EFD) campaign performed at the University of Naples Federico II, where the resistance, sinkage and trim data have been measured. The EFD/CFD data comparison is performed and shown with a discussion of the spotted differences. The average percentage differences between the EFD and CFD data for the whole speed range are 1.84, 6.87 and 6.94 for the resistance, dynamic trim, and sinkage, respectively. These results confirm the maturity of the standardized and automated CFD modeling for calm water hydrodynamic analysis included in LincoSim, even at very high Froude numbers. The wetted length of the keel and chine and the wetted surface are calculated from numerical data using the advanced post-processing. Finally, as a work in progress, we test a first comparison for the same hull of the EFD and CFD data, considering two seakeeping conditions for head waves at a given wavelength for two velocity conditions. Also, this kind of analysis confirms the tight correlation between the measured and computed outcomes. This synergic interplay of EFD and CFD can link the advantages of both methods to support hull design but also requires experiment planning and final data analysis to obtain physical parameters not easily measurable in laboratory, such as the wetted surface, wetted lengths, proper viscous contribution, and pressure distribution both in calm water and in waves.

Keywords: CFD; EFD; standardized CFD workflow; planing hull; resistance in calm water; seakeeping

Citation: Begovic, E.; Bertorello, C.; Ponzini, R.; Salvadore, F. Planing Hull Hydrodynamic Performance Prediction Using LincoSim Virtual Towing Tank. *J. Mar. Sci. Eng.* **2024**, *12*, 794. https://doi.org/10.3390/jmse12050794

Academic Editor: Kostas Belibassakis

Received: 16 April 2024
Revised: 1 May 2024
Accepted: 3 May 2024
Published: 9 May 2024

1. Introduction

During the last few years, the computational fluid dynamics (CFD) technique has become a "standard" tool for addressing calm water resistance prediction and studying complex phenomena such as the planing regime of small crafts, characterized by the dynamic trim, flow separation at chine, pressure wetted area and whisker spray area. Remarkable reproduction of the experimental data from the numerical towing tank has been reported by [1–4]. Ref. [5] provided a review of the most recent works on high-speed planing hulls and, for a selected hull in a Froude number *Fr* range from 1.14 to 2.50, performed a calculation of the numerical uncertainty of the resistance, trim and sinkage.

However, CFD modeling of planing hulls requires expert users to decide on different moving mesh techniques (overset/chimera and morphing grid), turbulence models, domain boundaries, and convergence criteria to arrive at a numerical set-up that will provide reliable results.

In [6] an automatic and web-based application of a virtual towing tank named LincoSim specifically designed to perform automatic CFD modeling of hydrodynamic performances in calm water was presented. The tool uses only open-source software and

deploys high-performance computing infrastructures to take advantage of well-established technological bricks. Validation and verification of the LincoSim has been performed in [7] for the planing hull systematic series by [8], showing how the same standardized workflow for all the tested hulls at each velocity condition was effective. The work showed clearly that if the mesh is topologically standardized, then the stopping criteria and the solver setup are coherent, allowing for safe data comparison of different hulls under different flow conditions. In [9] the same approach was tested using a catamaran experimental dataset including the hull dynamics, resistance, and wave pattern measurements. The main outcome was that the standardized and automated CFD workflow proposed in LincoSim was also suitable for the selected multi-hull case.

Today, with the increased computational capabilities and cloud computing, the implementation of the automatic CFD modeling concept can be proposed at a larger scale. Low-fidelity methods, such as the Savitsky method [10] or regression analysis, are extremely fast, based on the assumptions of the prismatic hull form and pure planing condition, and are those widely used in the design stage. In these first steps, completely automatic CFD modeling could be of particular interest for non-expert CFD users who can be assisted by the platform to obtain reliable results and correct trends of hydrodynamic properties when considering hull form modifications and optimization.

Seakeeping of the planing hull in designer practice is often limited to the calculation of the vertical accelerations at the center of gravity and bow, as they are the input for structure scantling and added resistance in waves, according to the regression formula developed by [11,12]. Even though mathematical models developed according to [13–15] have proven validity for the prediction of prismatic hulls, their use is still limited to the research groups, not to the designer communities. The experimental results of the recent systematic series [16–18] are available, but they are often limited to their ranges and provide as the final result the statistical distribution for accelerations.

Today, seakeeping CFD simulations for planing hulls are limited to regular waves and they offer an extremely valid tool for the impact analysis, but the complexity of the numerical setting and required computational time are still limiting factors. Anyway, wave/hull interaction CFD modeling is still an open point in research, especially when considering the usage of open-source libraries. The limited validation dataset availability represents a concrete limitation of the definition of a standardized workflow. Even if under development, a LincoSim seakeeping workflow has been proposed specifically for a research project (e-SHyIPS, see https://www.e-shyips.com (accessed on 15 February 2024), still based on the OpenFOAM toolbox, following a robust methodology proposed by [19] to ensure the minimization of wave reflections using forcing zones. It is worthwhile to underline that the forcing zones were recently made available to the OpenFOAM community in version 11. The forcing zones follow the state-of-the-art principles outlined in [19] but have been implemented by CFD-Direct coherently with the evolution of the OpenFOAM toolbox.

This work shows the performance of the LincoSim web-platform for a high-speed hull, analyzing the suitability of the platform for a wider Froude number range with respect to what was already published in [7] and discussing what could be the future of the open libraries for the non-expert CFD users. The calculations in calm water are performed for the 1:10 scale model of a 43 ft hull form in the Froude number range 0.3–2.0. The hull form is the one studied in [20–23]. New tests have been performed at the University of Naples Federico II and the resistance, sinkage and trim have been measured. Thanks to CFD data's advanced post-processing, the values of the wetted length of the keel and chine are obtained to have a correct prediction of the full scale resistance, as well as the pressure distribution along the hull, showing possible design applications.

Furthermore, experiments and simulations at regular head wave at two different velocities are performed. In detail, the wavelength is selected so that $\lambda/L = 3.56$ and the velocity conditions are specified to match the Froude number Fr values of 0.99 and 1.49, respectively. The numerical outcomes are compared side by side with the experimental

ones by performing the same processing for selected hull signal dynamics, looking at specific nonlinear behaviors related to the selected planing conditions.

2. LincoSim Web Platform

2.1. Simulations Set-Up in Calm Water

The web application named LincoSim, first developed in 2018 for the Horizon 2020 project LINCOLN (http://www.lincolnproject.eu/), (accessed 30 March 2024) has been refactorized and updated today to support early design analyses within the Horizon 2020 e-SHyIPS (https://e-shyips.com/, (accessed 15 February 2024) The e-SHyIPS project aims to define new guidelines for an effective introduction of hydrogen in the maritime passenger transport sector and to boost its adoption within the global and EU strategies for a clean and sustainable environment, toward the accomplishment of a zero-emission navigation scenario. With respect to the functionalities included into the LincoSim web application as available at the end of the LINCOLN project, several new functionalities have emerged as requirements to face the specific activities related to the e-SHyIPS project. The reason behind the necessity of adding new functionalities is strictly related to the signature of the e-SHyIPS project: the presence of H2-based propulsion systems. At the original stage, LincoSim only allowed calm water analysis to be performed, while, thanks to a recent re-design and re-factorization work, new functionalities are under development, also allowing for seakeeping analysis, thus including the presence of regular waves. If, in extreme synthesis, LincoSim was a suitable tool to obtain calm water data form 3D RANS CFD standardized and automated simulation for a given hull shape, the evolution also contains new functionalities such as hydrostatic analysis, stability analysis, and wave hull interaction. These tools open up the possibility of performing numbers of early design evaluations that are fully coherent with other more computationally expensive activities related to calm water and seakeeping simulations, avoiding any possible input-related misleading submission and opening up the possibility for designers to take advantage of complex technologies without any specific competences other than the ones related to the physics of the problem under consideration.

Figure 1 reports the types of simulations developed within the LincoSim platform: hydrostatics/stability, calm water, and seakeeping simulations. Seakeeping simulations, i.e., wave–hull interaction, present automation challenges and their implementations within the LincoSim are still ongoing. For this reason, the simulations were performed using a standardized workflow by means of a command line interface (CLI) instead of using the LincoSim web interface as was possible for the calm water simulations.

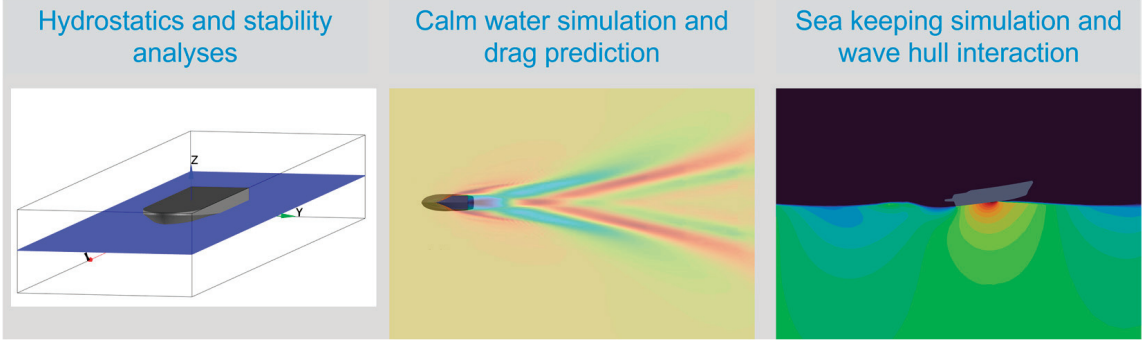

Figure 1. LincoSim modules: hydrostatic and stability analyses (**left**), calm-water simulations (**middle**), and seakeeping simulations (**right**).

The standardization of the calm water CFD modeling is based on the physics of the problem that defines the computational domain and the mesh cell sizes according to a given

standard mesh topology. See [6,7] for more CFD settings and modeling details. In Figure 2, the domain sizes and the mesh topology are shown for the P43 power boat geometry, which is considered in the present work.

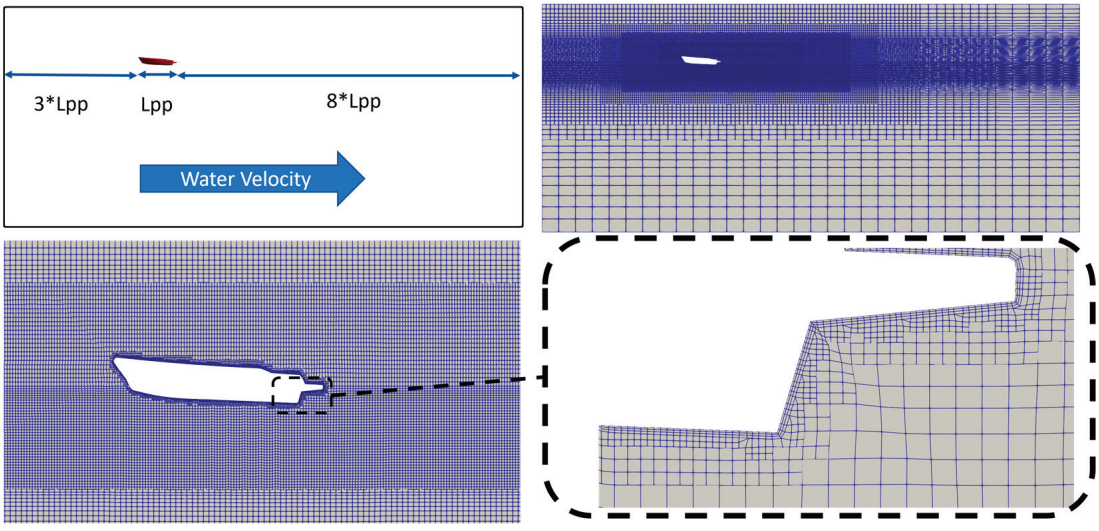

Figure 2. Domain extensions and mesh topology for the P43 hull at Fr = 1.392.

The hull length is used to define the domain extent, as shown in Figure 2 in the top left box and the mesh refinements boxes positioning, while the hull speed is used to define the near wall cell height targeting a dimensionless wall distance (y+) value of about 100; similar settings have been proposed more recently by [24]. The turbulence model selected is the SST k-ω, see [25], which is recognized to be effective in the marine field of application. Standard wall functions are applied. The time step is fixed and is set to ensure, for the given nominal hull velocity, a Courant number value lower than unity. For the lower and higher Froude numbers, the value of the time step is set to 0.00372 s and 0.000165 s, respectively. The CFD model is solved using the interFoam solver as available from the OpenFOAM toolbox. The hull is studied by imposing a symmetry plane at the hull mid-section (half hull). Using this approach, the average mesh cell count is about two million. We underline that this approach has only been tested and validated for the model scale; nevertheless, considering the research applications for full-scale CFD models, like [26], we are looking forward to having a bettser understanding of its applicability for full-scale CFD modeling.

The proposed approach based on a meshing strategy tailored to satisfy the given mesh topology and requirements for each given velocity, thus adjusting the domain size, the mesh cells size and the boundary layer cells, has never been tested on a Froude number greater than 1.7. Therefore, this work, in which the Froude number ranges from 0.3 to 2.0, is a new validation, which is useful to assess the performance of the platform on a wider Froude number range.

2.2. Simulations Set-Up in Regular Waves

As discussed earlier, seakeeping simulation standardization is still ongoing; nevertheless, a Command Line Interface (CLI) tool to manage the workflow is operational and, with reduced manual intervention, can configure and run complete simulations.

For the simulations in regular waves, three degrees of freedom have been considered, namely:

- Heave motion defined by the hull VCG(t) coordinate variation compared to the averaged value;

- Pitch motion, given as the pitch rotation angle;
- Roll motion, given as the roll rotation angle.

All the simulations are performed in the hull reference system with the definition of heading corresponding to $\beta = 0$ degrees for head waves. For the CFD modeling of this kind of problem, a set of good practice strategies according to [27] has been adapted:

The domain specifications are as follows:

- X-direction: five times the maximum between the wavelength and hull length
- Y-direction: same as the x-direction
- Z-direction: two times the maximum between the wavelength and hull length

The background mesh spacing specifications are as follows:

- X-direction: between 30 and 40 mesh cells per wavelength
- Y-direction: same as the x-direction
- Z-direction: between 10 and 15 mesh cells per wave amplitude

Additionally, the target mesh cell size on the hull is set to be equal to 1/250 of the hull length. The meshing strategy to achieve such goals includes vertical one-dimensional refinement, horizontal two-dimensional refinements in nested boxes and surface-based refining and layering. The OpenFOAM snappyHexMesh tool is used, thus realizing a full open-source-based CFD workflow.

Considering the requirements defined above, for a given hull shape, the mesh cell count increases when shifting from long-period to short-period waves. To increase the time to the result by taking advantage of the symmetric domain definition, head waves are treated as half domains with a symmetry plane in correspondence of the *Y*-axis. The resulting mesh size in our test case was about four million cells.

Also, the forcing zones and forcing parameter values have been set according to [27]. In Figure 3, an example of the forcing zone is shown. The general idea is to force the wave equations on an external frame, which is not too close to the hull position and let the solution of the Navier–Stokes equations adapt to the forced condition, transporting the wave into an internal frame directly surrounding the hull. A set of numerical parameters must be defined to simulate waves following such a kind of forcing zone approach: the most important ones are the frame extents, the forcing strength, and the spatial forcing shape function.

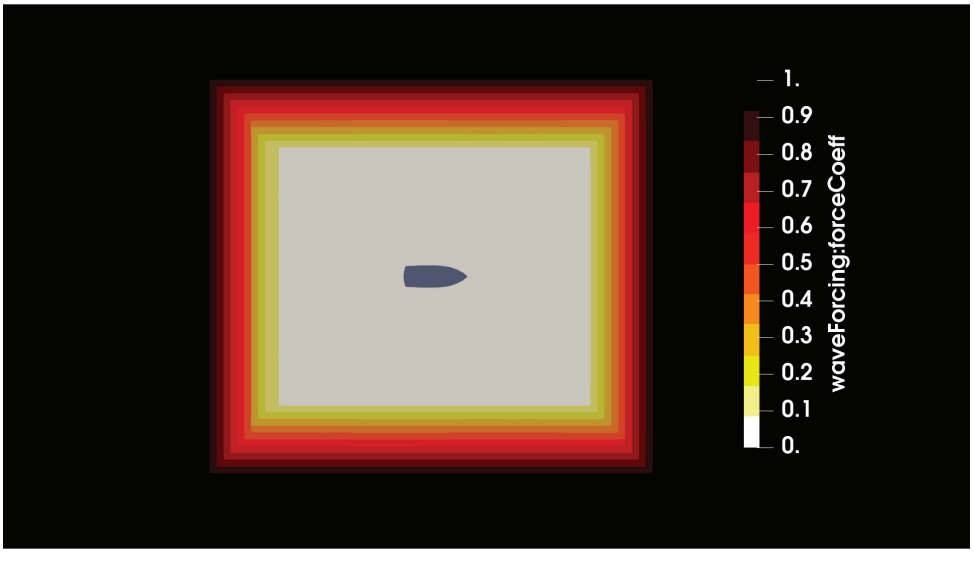

Figure 3. Example of a wave forcing zone.

According to [19] the frame extents are defined according to the imposed wave so that the internal (non-forced) frame extent is equal to 1 wavelength and the external (forced) frame extent is equal to 1.5 wavelengths. The forcing strength is defined by a parameter that is the inverse of a forcing time parameter τ, which basically corresponds to the time needed to force the flow to the given wave form. Therefore, τ can be as a first approximation set equal to the residence time of the flow within the force region, which can be expressed as the ratio between the forcing zone thickness and wave celerity. More accurately, the value has been selected in our simulations, again according to [27] using the code provided by the authors through a GitHub repository (see [28], accessed on 30 April 2024), which minimizes the wave reflections in the computational domain. In a few words, the auxiliary code optimizes the analytical predictions for the reflection coefficient for long-crested free-surface wave propagation when using relaxation zones as described in [27]. A useful manual is distributed along with the code (see [29] (accessed on 30 April 2024) with a general description of the released application and average suitable settings. The code contains recommendations on how to further tune the relaxation zone's parameters depending on the waves, including possible shape functions. In our models, we used the half cosine ramp function.

Moreover, it is worth noting that forcing can be imposed on selected velocity components and/or on the volume fraction. In OpenFOAM implementation, horizontal and vertical velocity components are forced alongside the volume fraction. Finally, according to the availability of regular wave models in OpenFOAM, we selected second-order Stokes wave modeling.

Following the indications of [27], the top and bottom planes are set as the free pressure and no-slip boundary, respectively. For the zero hull velocity simulations, all the vertical boundaries are set as wave equations, while for the non-zero hull velocity simulations, streamwise max e min vertical boundaries are set as the inflow and outflow conditions. To complete the model setup, we use a parametric simulation end-time value equal to 30 wave time periods (T). This value has been considered sufficient to guarantee the onset of a periodic hull dynamics response to the incoming wave. The starting integration time step is set to be equal to 1/150 of the wave period and is automatically adjusted to ensure a value of the Courant number lower than or equal to one. This setting for the time integration step is considered the optimal theoretical value. During the simulation time evolution, we sampled several fluid dynamics and rigid body dynamics quantities. These data are necessary to be able to define relevant output parameters like:

- Incoming wave amplitude.
- Hull rigid body dynamics.
- Accelerations at given hull locations.

The requirement of also monitoring the signal of the incoming wave amplitude is related to the fact that the imposed input values are never reached due to numerical inaccuracies. As such, the effective wave height is measured from the corresponding simulation to evaluate the deviations from the imposed input amplitude and to improve the accuracy of the results where input amplitudes appear. Even if more accurate analysis and validation should be performed to assess the impact of numerical settings on wave signal losses in the non-forced zone, from what is observed so far with the present settings, the choices performed for the meshing and adaptive integration time step limit the wave signal loss, ensuring for more than 90% of the imposed wave signal at the hull reference location.

The qualitative outcomes are presented in Figure 4, where the pressure flow field distribution around the hull is shown over four successive time instants.

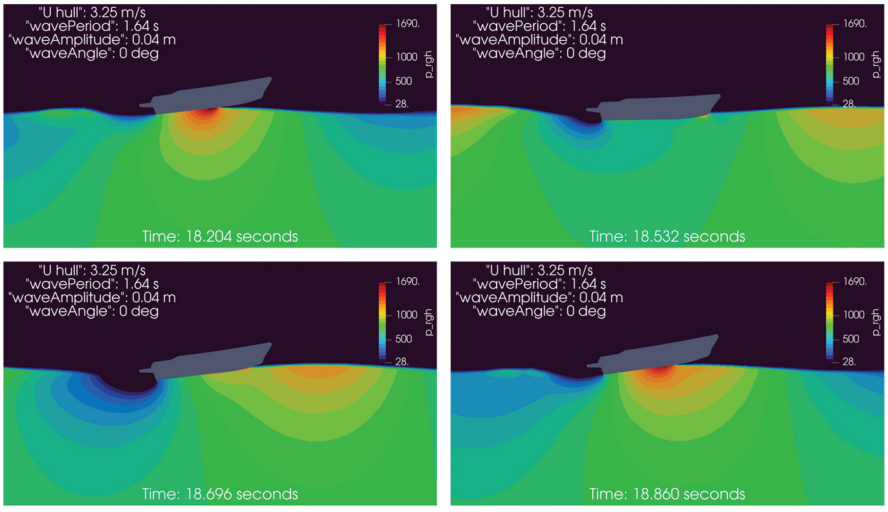

Figure 4. Pressure flow field over time.

3. Experimental Tests of P43 Powerboat

All the experiments have been performed in the towing tank of the University of Naples, Department of Industrial Engineering, whose dimensions are 135 × 9 × 4.2 m. The towing carriage speed ranges from 0.1 to 7 m/s. The P43 planing boat is a deep V hard chine form with a transom deadrise angle of 14 degrees up to 45 degrees at the bow, given in Figure 5. The 1:10 scale GRP built model, complete with the deck without appendages, was fixed to the carriage by the measurement instrument (metallic arm shown in Figure 5) at the position of X_arm = 0.278 m from the transom, at the height of 0.08 m above the waterline. The model was free to pitch and to move along the vertical axis, but it was constrained for surge, sway, roll and yaw. The model's main characteristics are reported in Table 1.

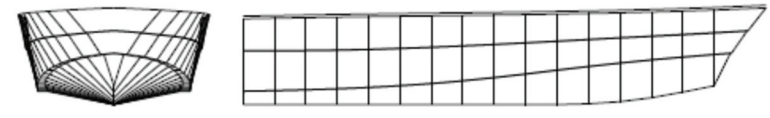

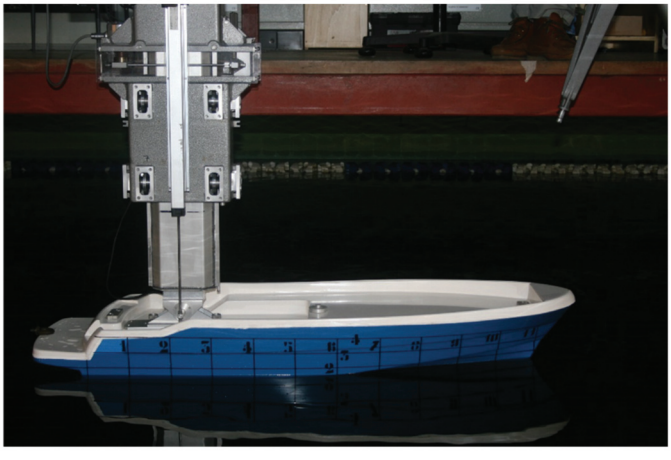

Figure 5. *Cont.*

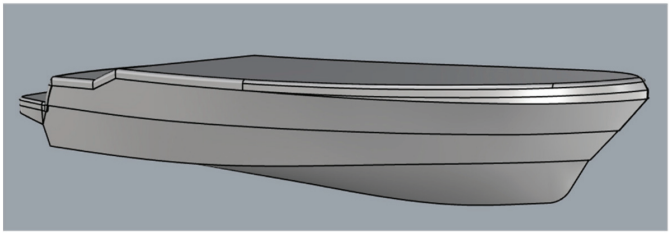

Figure 5. P43 planing hull model body plan from [23], in the towing tank and CAD model.

Table 1. Principal data of the P43 power boat.

$L_{M\text{-}OA}$ (m)	B_C (m)	B_{OA} (m)	T_{AP} (m)	m (kg)	Static Trim (deg)	LCG_T (m)	VCG_{BL} (m)	$r_{44\text{-}air}/B_C$ (-)	r_{55r}/L_{OA} (-)
1.219	0.360	0.425	0.069	11.38	2.32	0.390	0.118	0.284	0.259

3.1. Resistance in Calm Water

The series of runs in calm water starting from the Froude number 0.3 up to 1.96 has been performed, measuring in each run: total resistance, sinkage at the X_arm position and dynamic trim. The sampling frequency was 500 Hz. Uncertainty analysis of the measured values was performed using standard ITTC procedures. All data are reported in Table 2.

Table 2. Experimental results in calm water.

V_M (m/s)	Fr -	R_T (N)	Running Trim τ (deg)	Sinkage (mm)	UA_R %R	UA_T %τ	UA_S %S
0.98	0.30	2.82	0.4	−4.97	1.0088	1.0050	0.1001
1.30	0.40	5.75	1.14	−11.62	1.0026	1.0001	0.1094
1.63	0.50	12.46	3.73	−21.6	1.0009	1.0001	0.1016
1.95	0.60	15.42	4.97	−21.74	1.0006	1.0000	0.1042
2.28	0.70	17.04	5.40	−13.84	1.0012	1.0000	0.1292
2.60	0.80	19.11	6.26	−9.12	1.0009	1.0000	0.1042
2.93	0.90	20.43	6.69	−1.25	1.0011	1.0000	0.4061
3.25	0.99	20.14	6.45	4.91	1.0006	1.0000	0.2141
3.58	1.09	19.59	5.95	13.13	1.0004	1.0000	0.1212
3.90	1.19	19.11	5.38	18.4	1.0009	1.0000	0.1102
4.23	1.29	18.94	4.81	23.6	1.0005	1.0000	0.1108
4.55	1.39	18.94	4.32	24.6	1.0022	1.0000	0.1438
4.88	1.49	19.04	3.91	24.4	1.0011	1.0000	0.1127
5.20	1.59	19.56	3.57	26.4	1.0007	1.0000	0.1200
5.52	1.69	20.38	3.28	28.1	1.0011	1.0000	0.1505
5.83	1.78	21.26	3.00	28.1	1.0014	1.0001	0.1326
6.16	1.89	22.16	2.83	30.2	1.0025	1.0001	0.1455
6.49	1.96	23.44	2.63	31.1	1.0032	1.0003	0.1569

3.2. Seakeeping in Regular Wave

The seakeeping behavior of the P43 hull has been extensively analyzed in [21] for the ship having 30% more displacement and in [23] at 4 velocities in irregular head waves. For the purpose of the first seakeeping calculations by LincoSim, only two tests in regular wave have been performed at two speeds, 3.25 m/s and 4.87 m/s, corresponding to 20 and 30 knots in ship scale, the same as the ones used in previous works. The experiments performed for this research are only for the wavelength where the resonance occur $\lambda/L = 3.557$ and wave amplitude is 44 mm.

The model has been additionally equipped with two accelerometers, one at 0.47 m and one at the bow at the position of 1.09 m from the transom. All the experimental data (both

calm water and seakeeping conditions) are measured with heave at the position of X_arm for physical setup requirements and are then recalculated for the *LCG* reference position in order to be compared to the CFD simulations data that are instead directly monitored at the *LCG* location.

4. Results Comparison

4.1. Measured vs. Calculated Results in Calm Water

The simplest analysis of data is the direct comparison of the measured total resistance, sinkage and trim. The measured and calculated data have been reported in Figures 6–8. The experimental uncertainty is around 1% for resistance and dynamic trim and 0.5% for sinkage. The error bars are drawn inside the markers of experimental data.

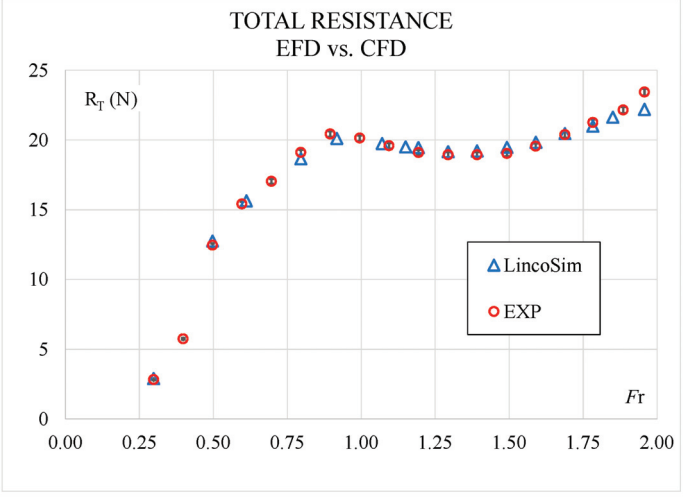

Figure 6. Total resistance comparison.

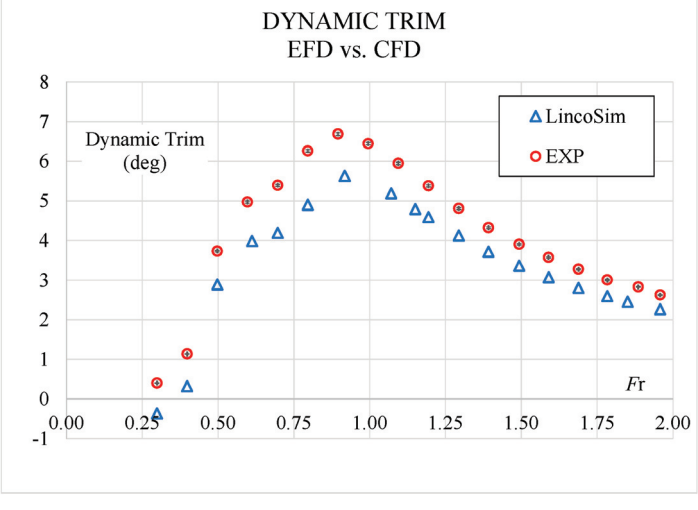

Figure 7. Dynamic trim comparison.

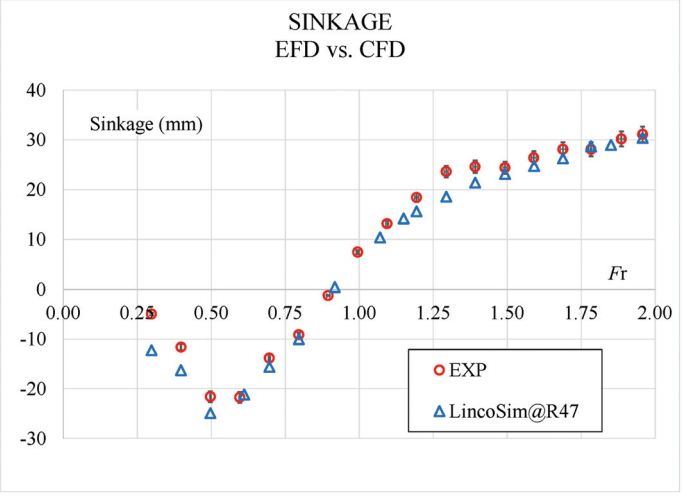

Figure 8. Sinkage comparison.

From Figures 6–8, can be observed that resistance is predicted very well and the average error through all the speed range is 1.84%. For the dynamic trim, the average difference is 6.87%, but the EFD and CFD curves are perfectly aligned with constant offset. In absolute values, the maximum difference is 0.63 deg at Fr = 0.80, where the hull has its maximum trim of 6.26 deg. The average difference for sinkage is 6.94% and it can be seen from Figure 8 that, globally, it has a good agreement, but for some points at low Fr, it shows larger differences.

Even though the experiments are reliable for the total resistance measurement, the transfer to the full scale and correct power prediction of planing boats requires a precise assessment of the dynamic wetted surface. This value is possible to assess from experiments only as a further analysis of the underwater photography or photography of the transparent model bottom. Since Savitsky's work [10], the ship–model correlation was based on the simple approach of a prismatic (monohedral) hull and Savitsky's formula for the projected wetted pressure area. If the wetted lengths on the chine and on the keel are known, then the pressure area can be easily determined. In 2006, [30] proposed the distinction of the pure pressure area and whisker spray area calculated assuming the angle of separation as double as the angle of pressure area. This concept was discussed, and further contribution has been provided in [8] where it has been shown how this angle of separation of the whisker spray area depends on the deadrise angle. Work [30] is always based on the assumption of the full planing where the walls are completely dry, while in [8] the values are obtained for the *Fr* range 0.2–1.5, thus also including non-fully-planing conditions. It is important to highlight that the uncertainty of this "measurement" depends on the photography quality and subsequent postprocessing. It is not often discussed and remains relatively large with respect to other directly measured values, such as resistance, trim and sinkage, and in this case, it was not performed.

It is evident that for these not easily measurable parameters, the use of CFD is intrinsically advantageous because the pressure and viscous contributions are calculated separately, the wetted lengths and dynamic wetted surface are one of the first results of the calculations and the transfer to ship scale is straightforward.

Therefore, the numerical results have been further analyzed to report the wetted lengths and wetted surface in the whole speed range. The visualization in ParaView© is performed using the free surface 3D obtained with an iso value of 0.5 for the *alpha.water* field and the hull pressure distribution. An example of the data elaboration in ParaView©, together with the photo from the towing tank at *Fr* = 1.96, is provided in Figure 9. The

obtained values of the dynamic wetted surface are summarized graphically in Figure 10, while the wetted lengths on the keel, chine and whisker spray on chine are reported in Figure 11 for the whole range of Froude numbers.

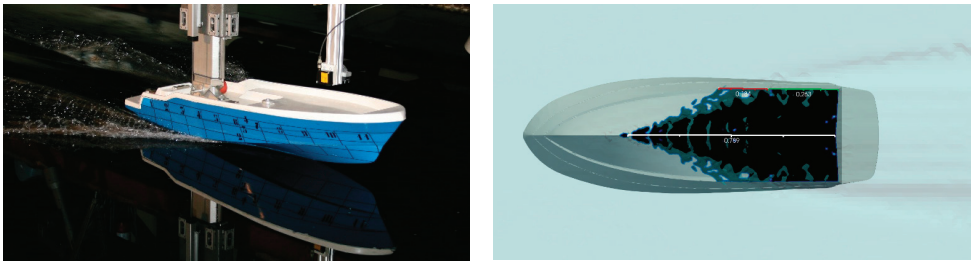

(**a**) (**b**)

Figure 9. Example of dynamic wetted surface and wetted length analysis at $Fr = 1.96$. (**a**) Experimental; (**b**) numerical. For the numerical data only: wetted keel length (white), wetted chine length (green) and whisker spray length (red).

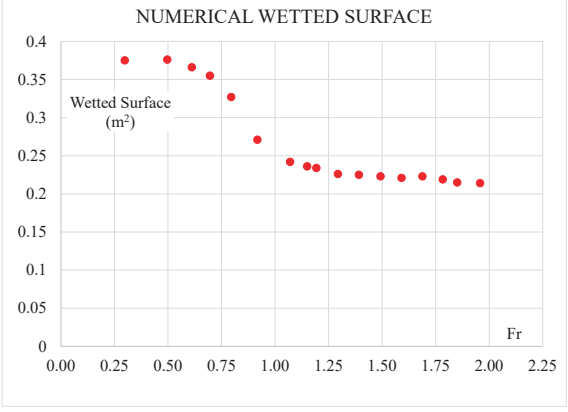

Figure 10. Numerical results for the dynamic wetted surface.

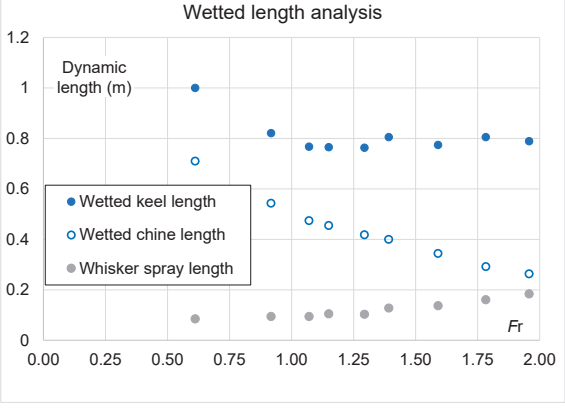

Figure 11. Numerical results for the wetted length at the chine and keel.

4.2. Measured vs. Calculated Results in Regular Waves

For the seakeeping behavior of planing hulls, as characterized by the strong nonlinear phenomena, the simplest approach of comparing the RAO of the first harmonic of response and wave is not optimal. In [14,31,32] authors used the spectral analysis and showed not only the RAO as the first harmonic but also the super-harmonics of pitch and accelerations.

In this work, the comparison, as the first step in the seakeeping calculations by LincoSim, of only the time series has been analyzed in detail. In Figures 12 and 13, a sample of 4 s of the time series of the EFD and CFD is shown, at Fr = 0.99 and 1.49, respectively. In both figures, the comparison of the EFD (red lines) and CFD (blue lines) data is provided for selected quantities: encounter wave, heave, pitch on the left side and acceleration at CG and at bow position on the right side.

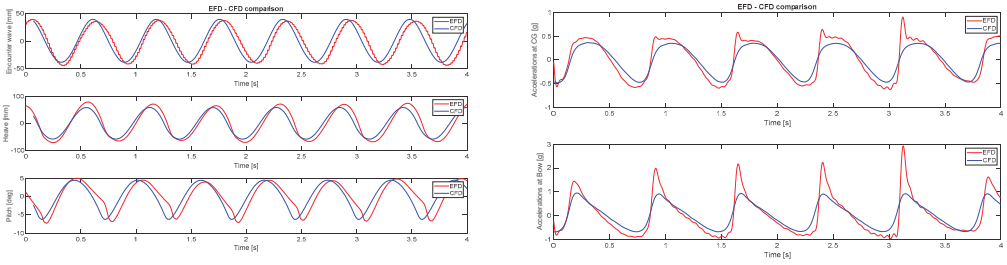

Figure 12. Comparison of measured (red) and simulated (blue) P43 planing hull in wave at Fr = 0.99.

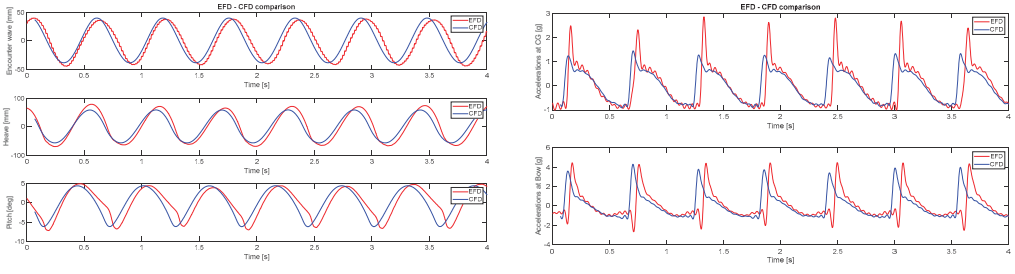

Figure 13. Comparison of measured (red) and simulated (blue) P43 planing hull in wave at Fr = 1.49.

The very good prediction of the heave and pitch can be observed at both speeds. For the acceleration prediction, the trend is perfectly matched, although it can be observed that the numerical values are smoother and little bit lower at both positions. For the acceleration results at higher speed, it can be seen how a small difference in position (experimental results at 0.47 m and CFD results at 0.39 m from stern) influences the motion composition and development of nonlinear responses. For the bow accelerations, extremely good matching is obtained, even a small vibration in the phase after impact is observed in the numerical results. Future work from the experimental side will face a wide range of wave frequencies to validate the LincoSim platform. The overall conclusions for these very first steps are that the results are very promising, as the observed differences between numerical and experimental data for heave and pitch are within a few percents, aligned with the results of [14,32,33]. More importantly, the simulation monitored output for the accelerations can spot the presence of multiple frequencies instead of just the one related to the regular encounter wave signal, thus confirming the ability of CFD simulation to account for relevant nonlinear responses of the ship while planing.

5. Conclusions

A validation of the LincoSim platform performed for the planing powerboat model up to the ship velocity of 40 knots is performed and reported. The simulations in calm water are performed in the length-based Froude number range from 0.3 to 2.0, extending what has been published so far using the LincoSim virtual towing tank.

The average differences in a whole speed range between CFD and EFD for the calm water simulations are 1.84%, 6.87% and 6.94% for resistance, dynamic trim and sinkage, respectively. These values are in line with the results reported in state-of-the-art works, where it was underlined how small differences in the hull geometry, ballasting conditions, and tow point location can have significant effects on the running trim predicted by CFD. From the visual observation of the photos from the experiments and analysis of wetted length on chine and spray length on chine, CFD simulations accurately describe the phenomenon, as confirmed by the excellent agreement of the total resistance.

A preliminary set of results for a seakeeping test in regular waves at two speeds, Fr = 0.99 and 1.49 (20 and 30 knots in ship scale), for a selected wavelength defined by λ/L = 3.56 is provided. The seakeeping analyses performed herein showed that automated CFD simulations can match experimental data, highlighting the complex nonlinear hull/wave interactions of the planing crafts. More precisely, in both the CFD and EFD output datasets, multiple frequencies can be spotted for the acceleration dynamics at given hull points. Even if not fully validated yet, the seakeeping workflow presented for the first time herein is promising in this regard. Deeper investigations of this nonlinear behavior are outside of the scope of the present preliminary test, and they will be analyzed in a future wider work.

The overall results presented here confirm the maturity of standardized and automated CFD modeling for hydrodynamic analysis of planing hulls in the whole speed range investigated. This approach has been tested and validated for only the model scale; nevertheless, considering the research applications for full-scale CFD models, like [26], we are looking forward to having a better understanding of its applicability for full-scale CFD modeling.

This synergic interplay of EFD and CFD can link the advantages of both methods to support hull design but also requires experiment planning and final data analysis to obtain physical parameters not easily measurable in laboratories.

Author Contributions: Experiments design, E.B. and C.B.; software development, R.P. and F.S.; writing—original draft, review and editing, editing and formal analysis, E.B., C.B., R.P. and F.S.; data curation, E.B. and R.P. All authors have read and agreed to the published version of the manuscript.

Funding: This research received no external funding.

Data Availability Statement: Data are contained within the article.

Acknowledgments: The e-SHyIPS project received funding from the Fuel Cells and Hydrogen 2 Joint Undertaking (now Clean Hydrogen Partnership) under grant agreement No. 101007226. This Joint Undertaking received support from the European Union's Horizon 2020 Research and Innovation programme, Hydrogen Europe and Hydrogen Europe Research.

Conflicts of Interest: The authors declare no conflicts of interest.

References

1. Park, S.; Wang, Z.; Stern, F.; Husser, N.; Brizzolara, S.; Morabito, M.; Lee, E. Single- and two-phase CFD V&V for high-speed stepped planing hulls. *Ocean Eng.* **2022**, *261*, 112047.
2. Cui, L.; Chen, Z.; Feng, Y.; Li, G.; Liu, J. An improved VOF method with anti-ventilation techniques for the hydrodynamic assessment of planing hulls-Part 2: Applications. *Ocean Eng.* **2021**, *237*, 109505. [CrossRef]
3. Avci, A.G.; Barlas, B. Investigation of the optimum longitudinal single transverse step location for a high-speed craft. *Brodogradnja* **2023**, *74*, 47–70. [CrossRef]
4. Lee, E.J.; Mousaviraad, M.; Weil, C.R.; Jiang, M.J.; Fullerton, A.M.; Stern, F. Assessment of experiments and CFD for the semi-planing R/V Athena Model in calm water. *Ocean Eng.* **2021**, *236*, 109254. [CrossRef]

5. Judge, C.; Mousaviraad, M.; Stern, F.; Lee, E.; Fullerton, A.; Geiser, J.; Schleicher, C.; Merrill, C.; Weil, C.; Morin, J.; et al. Experiments and CFD of a high-speed deep-V planing hull—-Part I: Calm Water. *Appl. Ocean. Res.* **2020**, *96*, 102060. [CrossRef]
6. Salvadore, F.; Ponzini, R. LincoSim: A Web Based HPC-Cloud Platform for Automatic Virtual Towing Tank Analysis. *J. Grid Comput.* **2019**, *17*, 771–795. [CrossRef]
7. Ponzini, R.; Salvadore, F.; Begovic, E.; Bertorello, C. Automatic CFD analysis of planing hulls by means of a new web-based application: Usage, experimental data comparison and opportunities. *Ocean Eng.* **2020**, *210*, 107387. [CrossRef]
8. Begovic, E.; Bertorello, C. Resistance assessment of warped hullform. *Ocean Eng.* **2012**, *56*, 28–42. [CrossRef]
9. Salvadore, F.; Ponzini, R.; Duque, J.H.; Reinaldos, C.A.; Soler, J.M. CFD analysis of a multiplatform catamaran by means of a web-based application: Experimental data comparison for a fully automated analysis process. *Appl. Ocean. Res.* **2021**, *116*, 102886. [CrossRef]
10. Savitsky, D. Hydrodynamic design of planing hulls. *Mar. Technol.* **1964**, *1*, 71–95. [CrossRef]
11. Hoggard, M.; Jones, M. Examining pitch, heave and accelerations of planing craft operating in a seaway. In Proceedings of the High-Speed Surface Craft Exhibition and Conference, Brighton, UK, 24–27 June 1980.
12. Blount, D.L. (Ed.) *Performance by Design—Hydrodynamics for High-Speed Vessels*; Printed in the USA; Donald L. Blount: Chesapeake, VA, USA, 2014; ISBN 0-978-9890837-1-3.
13. Zarnick, E.E. *A Nonlinear Mathematical Model of Motions of a Planing Boat in Regular Waves*; David Taylor Naval Ship Research and Development Center: Bethesda, MD, USA, 1978.
14. Rosen, A.; Garme, K.; Razola, M.; Begovic, E. Numerical modelling of structure responses for high-speed planing craft in waves. *Ocean. Eng.* **2020**, *217*, 107897. [CrossRef]
15. Tavakoli, S.; Bilandi, R.N.; Mancini, S.; De Luca, F.; Dashtimanesh, A. Dynamic of a planing hull in regular waves: Comparison of experimental, numerical and mathematical methods. *Ocean. Eng.* **2020**, *217*, 107959. [CrossRef]
16. Taunton, D.J.; Hudson, D.A.; Shenoi, R.A. Characteristics of a Series of High Speed Hard Chine Planing Hulls—Part II: Performance in Waves. *Int. J. Small Craft Technol.* **2011**, *153*, B1–B22.
17. Soletic, L. Seakeeping of a systematic series of planning hulls. In Proceedings of the 2nd Chesapeake Power Boat Symposium, Annapolis, MD, USA, 19–20 March 2010.
18. De Luca, F.; Pensa, C. The Naples Systematic Series–Second part: Irregular waves, seakeeping in head sea. *Ocean. Eng.* **2019**, *194*, 106620. [CrossRef]
19. Perić, R.; Abdel-Maksoud, M. Generation of free-surface waves by localized source terms in the continuity equation. *Ocean Eng.* **2015**, *109*, 567–579. [CrossRef]
20. Bertorello, C.; Oliviero, L. Hydrodynamic resistance assessment for not monohedral planing hull form. In Proceedings of the IMAM 2009 13th International Congress of International Maritime Association of Mediterranean, Istanbul, Turkey, 12–15 October 2009; Volume 2, pp. 703–707; ISBN 978-975-561-355-0.
21. Begovic, E.; Bertorello, C. Experimental Assessment of Seakeeping Characteristics for Non-Monohedral Planing Hulls. In Proceedings of the IMAM 2009, 13th International Conference Towards the Sustainable Marine Technology and Transportation, Istanbul, Turkey, 12–15 October 2009; Volume 3, pp. 927–933; ISBN 978-975-561-355-0.
22. Fossati, F.; Muggiasca, S.; Bertorello, C. Aerodynamics Of High Speed Small Craft. In Proceedings of the FAST 2013—12th International Conference on Fast Sea Transportation, Delft, The Netherlands, 2–5 December 2013.
23. Begovic, E.; Bertorello, C.; Pennino, S.; Piscopo, V.; Scamardella, A. Statistical analysis of planing hull motions and accelerations in irregular head sea. *Ocean Eng.* **2016**, *112*, 253–264. [CrossRef]
24. Wang, Z.; Stern, F. Moving Contact Line and No-Slip Boundary Conditions for High-Speed Planing Hulls. In Marine 2023. Available online: https://www.scipedia.com/public/Wang_Stern_2023a (accessed on 25 April 2024).
25. Menter, F.; Carregal Ferreira, J.; Esch, T.; Konno, B.; Germany, A.C. The sst turbulence model with improved wall treatment for heat transfer predictions in gas turbines. In Proceedings of the International Gas Turbine Congress, Tokyo, Japan, 2–7 November 2003; pp. 2–7.
26. Huang, L.; Pena, B.; Thomas, G. Towards a full-scale CFD guideline for simulating a ship advancing in open water. *Ship Technol. Res.* **2023**, *70*, 222–238. [CrossRef]
27. Perić, R.; Vukčević, V.; Abdel-Maksoud, M.; Jasak, H. Optimizing wave generation and wave damping in 3D-flow simulations with implicit relaxation zones. *Coast. Eng.* **2022**, *171*, 104035. [CrossRef]
28. Python Code for Optimal Lambda Computation. Available online: https://github.com/wave-absorbing-layers/relaxation-zones-for-free-surface-waves (accessed on 30 April 2024).
29. Manual Usage of the Python Code for Optimal Lambda Computation. Available online: https://usermanual.wiki/Document/Manual.2128294547.pdf (accessed on 30 April 2024).
30. Savitsky, D.; De Lorme, M.F.; Datla, R. Inclusion of "Whisker Spray" Drag in Performance Prediction Method For High-Speed Planing Hulls. *Mar. Technol. SNAME News* **2007**, *44*, 35–56. [CrossRef]
31. Begovic, E.; Bertorello, C.; Pennino, S. Experimental Seakeeping Assessment of a Warped Planing Hull Model Series. *Ocean. Eng.* **2014**, *83*, 1–15. [CrossRef]

32. Capasso, S.; Tagliafierro, B.; Mancini, S.; Martinez-Estevez, I.; Altomare, C.; Dominguez, J.M.; Viccione, G. Regular Wave Seakeeping Analysis of a Planing Hull by Smoothed Particle Hydrodynamics: A Comprehensive Validation. *Mar. Sci. Eng.* **2023**, *11*, 700. [CrossRef]
33. Samuel, S.; Mursid, O.; Yulianti, S.; Kiryanto, K.; Iqbal, M. Evaluation of interceptor design to reduce drag on planing hull. *Brodogradnja* **2022**, *73*, 93–110. [CrossRef]

Journal of
Marine Science and Engineering

MDPI

Article

Research on Hull Form Design and Numerical Simulation of Sinkage and Trim for a New Shallow-Water Seismic Survey Vessel

Ziyi Ye [1], Shaojuan Su [1,*], Yujie Wu [1,2], Fangxin Guo [3], Haibo Liu [4] and Qixiang Cheng [3]

[1] Naval Architecture and Ocean Engineering College, Dalian Maritime University, Dalian 116026, China; yzy0408@dlmu.edu.cn (Z.Y.); whcj@wmmp.com.cn (Y.W.)
[2] Wuhan Marine Machinery Plant Co., Ltd., Wuhan 430084, China
[3] Dalian Hengxing Marine Engineering Design Co., Ltd., Dalian 116000, China; gfxdmba@163.com (F.G.); 13704112271@163.com (Q.C.)
[4] Bureau of Geophysical Prospecting (BGP), China National Petroleum Corporation (CNPC), Korla 841000, China; liuhaibo@bgp.com.cn
* Correspondence: ssjlpz@dlmu.edu.cn

Abstract: When a ship sails in shallow water, it will show different hydrodynamic performance from that in deep water due to the limitations of water depth. The shallow water effect may lead to hull sinkage and trim, increasing the risk of bottoming or collision. In this study, a new design scheme of a shallow-water seismic survey vessel is proposed to solve the problems of traditional seismic survey vessels in shallow-water marine resources exploration and safety. The RANS (the Reynolds-Averaged Navier–Stokes) method combined with the Overset Mesh and DFBI (Dynamic Fluid Body Interaction) method is used for numerical simulation to analyze the influence of ship type, water depth, and speed on ship sinkage and trim, as well as the influence of the shallow-water ship's attitude on resistance. The results show that with the decrease in water depth and the increase in speed, the pressure distribution around the hull becomes uneven, which leads to the aggravation of the sinkage and trim of the hull. In response to this problem, the shallow-water seismic survey vessel significantly improved the sinkage and trim of the hull in shallow water to ensure its safe navigation. The research also shows that navigation resistance can be effectively reduced by appropriately adjusting the ship's attitude. Therefore, this study provides a reference for the development of shallow-water ships in the future.

Keywords: shallow-water seismic survey vessel; shallow-water effect; sinkage and trim; hull form design

Citation: Ye, Z.; Su, S.; Wu, Y.; Guo, F.; Liu, H.; Cheng, Q. Research on Hull Form Design and Numerical Simulation of Sinkage and Trim for a New Shallow-Water Seismic Survey Vessel. *J. Mar. Sci. Eng.* **2024**, *12*, 1205. https://doi.org/10.3390/jmse12071205

Academic Editors: Michele Viviani, Nastia Degiuli and Ivana Martić

Received: 20 May 2024
Revised: 2 July 2024
Accepted: 16 July 2024
Published: 18 July 2024

1. Introduction

Seismic survey vessels are specialized operation ships designed for the exploration of offshore resources such as oil and natural gas [1,2]. As global exploration of ocean resources deepens, including studies in shallow-water zones, new oil and gas resources continue to be discovered in these regions, leading to an increasing international market demand for shallow-water seismic survey vessels. However, the existing seismic survey vessels in the world are tailored for deep-sea operations, characterized by heavy loads and deep draft, which makes them unsuitable for entering shallow-water areas to meet the demands of marine resource exploration there [3].

When ships operate in shallow-water areas, they encounter significantly different resistance performance compared to deep-water navigation [4], demonstrating a marked 'shallow-water effect' increase in resistance. Furthermore, as ships navigate in shallow waters, the water depth restricts the flow field between the ship and the seabed, leading to an increase in water flow speed. Part of the water flow beneath the ship is also pushed toward both sides of the ship, causing an increase in water flow speed along the sides of the

ship as well. Changes in the surrounding flow field affect the navigation status and force conditions of the ship, resulting in trim and sinkage of the ship, posing risks of grounding or collision [5]. Hydrodynamic phenomena in restricted waters, especially the sinking of ships, pose a serious threat to the operational safety of the waterway, endangering the life and property of the crew [6].

When navigating in shallow waters, the performance of the ship is affected by the shallow-water effect, leading to changes in the attitude of the ship, including sinkage and trim. To prevent grounding and stranding, and ensure the safety of shallow-water seismic survey vessels during navigation and operations, a new type of shallow-water seismic survey vessel is proposed.

Jiang [7] calculated the amount of ship sinkage and trim in shallow waters and the applicable speed range of the ship from subcritical to supercritical speeds through numerical methods. Gourlay [8] investigated the case of a large, flat-bottomed ship, such as a bulk carrier, moving in close proximity to a flat sea floor. The flow beneath the ship could be modeled as a shear flow between two parallel plates, one of which is moving. It discussed the implications of these flow models on squat and viscous resistance. Krishna and Krishnankutty [9] conducted experimental and numerical studies on the trim and sinkage of high-speed catamaran vessels in shallow waterways, investigating the impact of under-keel clearance on safe navigation speed, as well as considering the effect of spacing between hulls on safe navigation speed. Shi et al. [10] analyzed the trim and sinkage of ship hulls under different speeds and water depths in shallow-water conditions using numerical simulations, providing references for the safe navigation of ships in shallow waters. Pavkov and Morabito [11] conducted model tests on the shallow-water effects of two different types of trimaran ships. A significant increase in hull resistance and sinking was observed at speeds close to the critical speed. Deng et al. [12] used the CFD method to calculate the calm water resistance and resistance components of a trimaran test model with and without appendages under different conditions. The calculations took into account the viscous effect and the presence of a free surface in order to investigate the effect of trim and sinkage on the resistance calculation. Ma et al. [13] explored the extent to which sinking and trim affect ship resistance using numerical simulation methods. They discussed how to effectively assess and optimize these effects to reduce resistance. Lungu [14] performed numerical simulations on the motion of a certain KRISO container ship in shallow water based on the CFD method, analyzing the impact of water depth on hull pressure, sinking, trim, and resistance. Bechthold and Kastens [15] analyzed the effects of different sailing speeds on ship trim and squat in shallow waters through numerical simulations, predicting the trim and sinking for Postpanmax container ships in very shallow waters. Feng et al. [16] conducted numerical simulations using full-scale and model-scale KCS as research objects to calculate ship resistance at different water depth/draft ratios, and discussed the hydrodynamic forces, sinkage, trim angle, and wave characteristics at different water depths. According to the research status on the sinking and trim of ships in shallow water, most of them solve the problem of ship attitude in shallow water by numerical simulation, and analyze the details of the flow field in the restricted water area, so as to provide some reference for the safe navigation of ships in shallow water.

In view of the fact that traditional seismic survey vessels cannot meet the needs of marine resources exploration in shallow waters, this study designs a new type of seismic survey vessel based on the original deep-water seismic survey vessel. Based on the RANS (the Reynolds-Averaged Navier–Stokes), combined with the Overset Mesh and DFBI (Dynamic Fluid Body Interaction) method, the numerical simulation of sinking and trim of the shallow-water seismic survey vessel is carried out, and the sinkage and trim during navigation are predicted. Initially, simulations of both the original and the modified new ship types in shallow-water conditions are compared to analyze changes in sinkage and trim. Subsequently, different water-depth scenarios are selected for new ship type, including H/T = INF (infinite water depth), $H/T = 3$ (medium water depth), and $H/T = 1.7$ (shallow water depth), for numerical simulations of sinkage and trim. The comparative

analysis of sinkage and trim values under infinite, medium, and shallow water depths is conducted to evaluate the impact of ship type, water depth, and ship speed on the sinkage and trim of the ship. The numerical simulation of the sinkage and trim of the new ship type in shallow water has a certain reference value for the ship hull design of the shallow-water seismic survey vessel and the safe navigation of the shallow-water ship. At the same time, the ship model resistance of the sinkage and trim value simulation is recorded and compared with the resistance of the unopened sinkage and trim ship model test. Therefore, the research in this study provides a reference for the future development of shallow-water ships and the safety of shallow-water navigation.

2. Research on New Ship Design

2.1. Original Ship Type

Most existing seismic survey vessels are designed for deep-sea operations, with scant information available on the hull design of shallow-water survey vessels for reference. Given the operational characteristics of shallow-water survey vessels, which mainly operate in shallow waters of up to 5 m deep, they are severely restricted by shallow draft conditions. Therefore, based on the operational requirements of shallow-water survey vessels and the hull characteristics of existing deep-sea survey vessels, it was initially determined that the hull form of the shallow-water survey vessel should be a fat shallow draft ship. One of the challenges in designing the hull lines of a fat shallow draft ship lies in the design of the bow and stern sections, as well as ensuring a reasonable transition and alignment with the parallel mid-body.

The presence of a parallel mid-body can lead to excessive fullness in the bow and stern lines of a ship, manifesting primarily as follows: an overly steep bow entrance design may result in a pronounced shoulder bulge at the forward shoulder, generating a bow bilge vortex in that area; if the angle of run at the stern is too great, it can lead to flow separation at the aft of the ship. Conventional deep-sea seismic survey vessels often employ a small bulbous bow design to improve the flow field at the bow and minimize the bow bilge vortex [17]. Unlike deep-sea seismic survey vessels, shallow-water seismic survey vessels are constrained by the depth of water they operate in and have a shallower draft, which precludes them from using the small bulbous bow design of traditional deep-sea seismic survey vessels. Consequently, with consideration for these factors, this study originally proposes a hull form design for a shallow-water seismic survey vessel, as depicted in Figure 1.

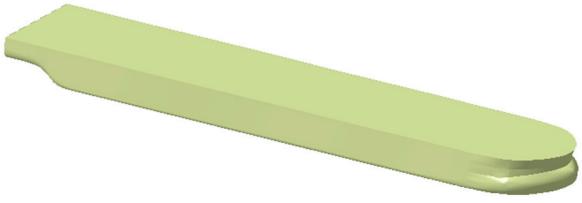

Figure 1. Original hull of shallow-water seismic survey vessel.

To better observe the detailed distribution of the flow field around the hull, CFD numerical simulations are performed on the original ship type. The simulations assess the pressure distribution on the hull in deep water and identify any adverse flow phenomena such as flow separation (boundary layer separation). The computational results are shown in Figures 2 and 3.

From the pressure distribution diagram in Figure 2, it can be seen that a high-pressure area (the red part) forms at the bow of the ship, and a low-pressure area (the blue part) forms at the forward shoulder, along the parallel mid-body, and near the stern. This uneven pressure distribution is caused by the plumper design of the bow and stern lines of the ship: the slower flow velocity at the bow leads to the formation of a high-pressure area;

while in the low-pressure areas, increased flow velocity results in higher local frictional resistance. Such accelerations and decelerations of the water flow along the direction of the hull are normal, but if flow separation or backflow occurs around the hull, modifications and optimizations to the hull form are needed. Flow separation has a significant impact on hull resistance and flow loss, and it is a major consideration in the design of new hull forms. However, as can be seen from Figure 3, there are areas of flow separation or stagnation at the bow, forward shoulder, and stern (the blue part). In these areas, the flow cannot continue to advance along the hull in the direction of the flow, resulting in a large amount of water adhering to the hull due to viscous attachment, thus increasing hull resistance.

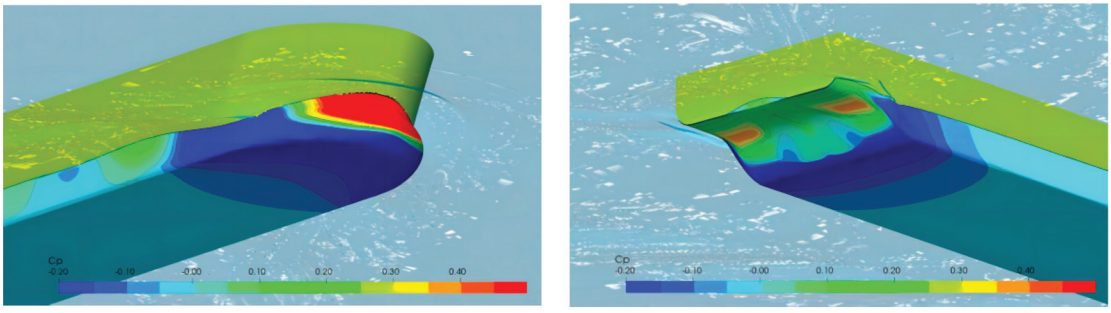

(**a**) (**b**)

Figure 2. Pressure distribution of original hull (10 knots, deep water): (**a**) Flow separation on bow; (**b**) Flow separation on stern.

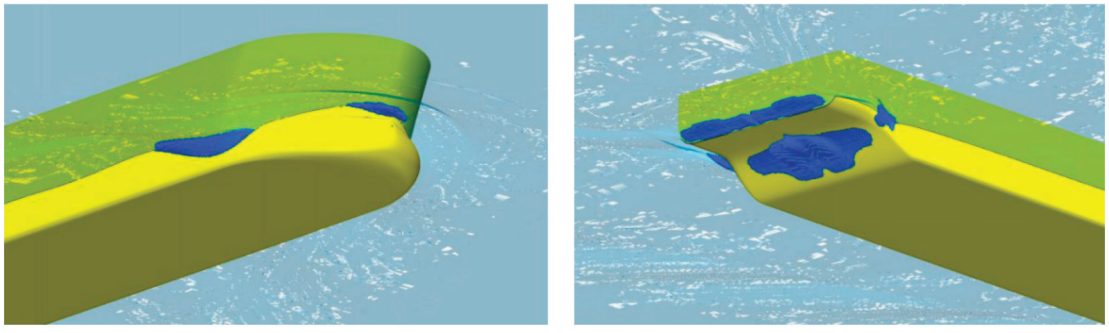

(**a**) (**b**)

Figure 3. Flow separation of original hull (10 knots, deep water): (**a**) Flow separation on bow; (**b**) Flow separation on stern.

When the water flows across the bow, according to the Bernoulli principle, the flow velocity at the bow is the least, causing the water to stagnate at the bow. However, the water will accelerate again along the hull after passing the bow, so the stagnation at the bow does not pose a significant problem. However, due to the excessive curvature at the transition section between the bow and the parallel middle body, flow separation occurs at the forward shoulder. A similar flow separation occurs at the aft shoulder of the hull. In addition, flow separation also occurs at the stern due to excessively full curvature, which may lead to phenomena such as cavitation and vibration near the propeller, negatively affecting propeller performance.

2.2. Design of Hull Form

Based on the computational results obtained in deep water, it can be inferred that the phenomena of flow separation of the hull become more severe in shallow water. In order to minimize flow separation and energy losses, as well as reduce hull resistance, it was decided to make modifications to the original ship type.

1. A proposal is made for a wide and flat bulbous bow, with the breadth exceeding the height, enabling the hull to navigate shallow waters effectively. This design not only mitigates the wave-making resistance encountered while sailing but also increases the proportion of displacement volume at the bow of the ship, which aids in enhancing the stability and sea-keeping of the ship.
2. The curvature at the forward and aft shoulders of the hull is to be smoothed, aiming to minimize the phenomena of flow separation at these locations.
3. Reducing the curvature and the angle of inclination at the stern, with the addition of deadwood to improve flow separation phenomena at the stern, is conducive to improved ship stability [18].

The comparison between the modified new ship type (indicated in red) and the original ship type (indicated in blue) is depicted in Figure 4.

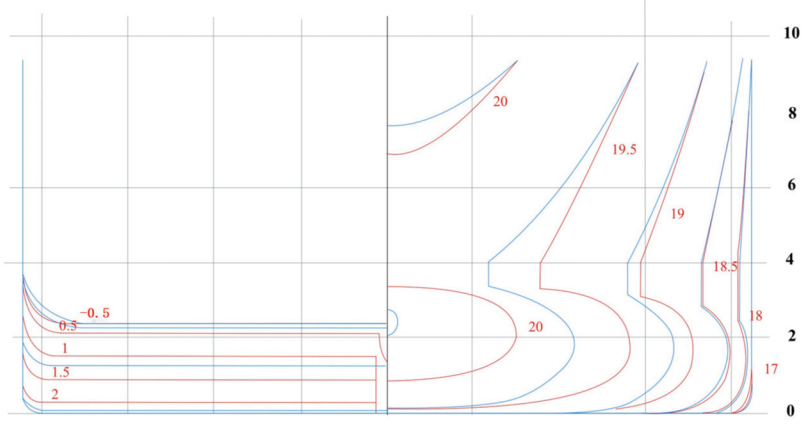

Figure 4. Lines plan of modified hull and original hull.

In order to verify whether the modified new ship type can meet the operational requirements and to assess the improvement of the flow separation phenomenon, CFD calculations were first conducted for the modified ship type at 10 knots in deep water, and the results were compared with those of the original ship type, as shown in Figure 5. A comparison of the flow separation phenomenon between the original ship type and the modified ship type (Figures 3 and 5) reveals significant improvement in flow separation for the modified ship type, particularly at the front and back shoulder of the hull where no flow separation occurred.

Due to the fact that the working water depth of this shallow-water seismic survey vessel is primarily in shallow waters of 5 m, operating at a speed of approximately 5 knots, CFD calculations were performed for the modified new ship type at a water depth of 5 m and a speed of 5 knots to analyze whether flow separation phenomenon would occur under working conditions. The calculation results, as shown in Figure 6, indicate a significant improvement in the flow separation phenomenon around the ship at a water depth of 5 m and a speed of 5 knots, meeting the operational requirements.

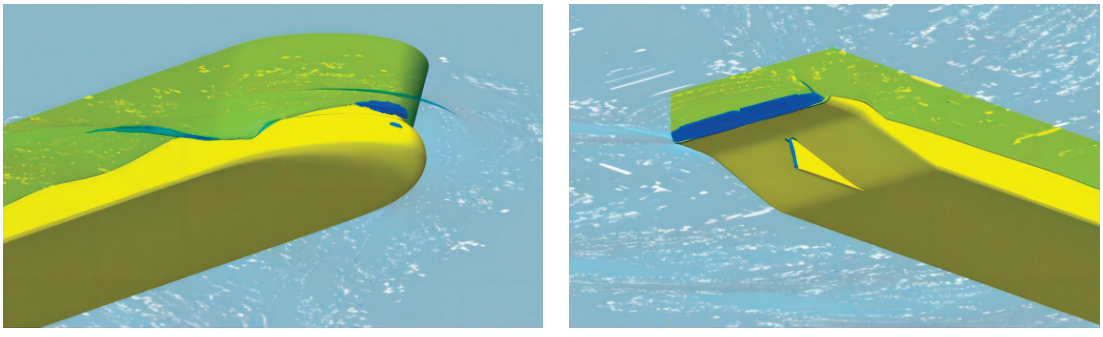

(**a**) (**b**)

Figure 5. Flow separation of modified hull (10 knots, deep water): (**a**) Flow separation on bow; (**b**) Flow separation on stern.

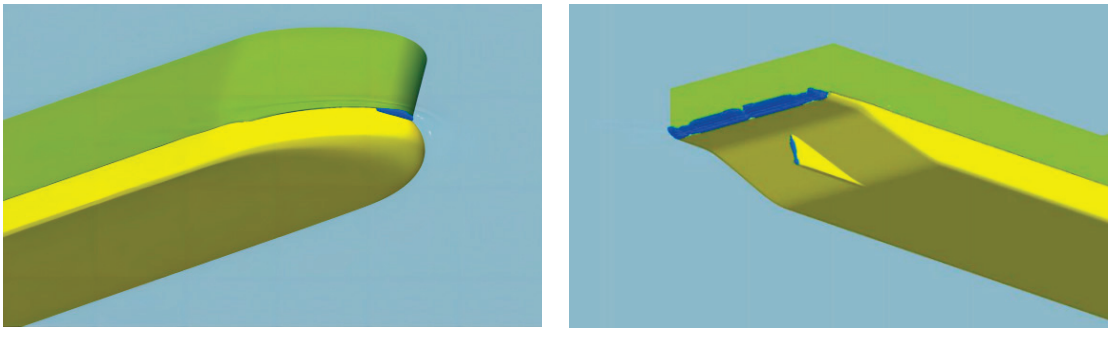

(**a**) (**b**)

Figure 6. Flow separation of modified hull (5 knots, 5m water depth): (**a**) Flow separation on bow; (**b**) Flow separation on stern.

3. Numerical Simulation of Shallow-Water Performance

3.1. The Object of Calculation

The main ship design parameters of the modified shallow-water seismic survey vessel, including both the actual ship and the ship model at a scale of 11.641, are shown in Table 1. The subsequent numerical simulation is carried out by the ship model.

Table 1. Principal particulars of the shallow-water seismic survey vessel.

Particulars	Full Scale	Model
Length overall L_{OA} (m)	88.234	7.58
Length on waterline L_{WL} (m)	88.122	7.57
Length between perpendiculars L_{pp} (m)	84.8	7.28
Breadth B (m)	16.9	1.45
Depth D (m)	5.5	0.472
Draught T (m)	2.82	0.242
Wetted surface S (m^2)	1869	13.79
Displacement volume ∇ (m^3)	3727.8	2.363
Block coefficient C_B	0.922	0.922

3.2. Computational Domains and Mesh

In order to reduce the computational cost and take into account the symmetry of the shallow-water seismic survey vessel during navigation, only half of the computational domain is selected for CFD simulation using STAR-CCM+ 2021.1 (16.02.008-R8) software. Considering the necessity to simulate sinkage and trim motions at various water depths, the dimensions of this computational domain are as follows: the inlet is 1.0 Length Overall (L_{pp}) ahead of the bow, the outlet is $3.0L_{pp}$ aft of the stern, the top boundary is $1.0L_{pp}$ from the free surface, the side boundary distance from the longitudinal section of the hull is $2.0L_{pp}$, and the bottom boundaries are located at 1.7 Draught (T), 3.0 T, and $1.0L_{pp}$ from the free water surface, as illustrated in Figure 7. The computational domain comprises two regions: the background domain, which is static and does not include the ship or move with it, and the motion domain, which includes the ship body and moves in unison with it.

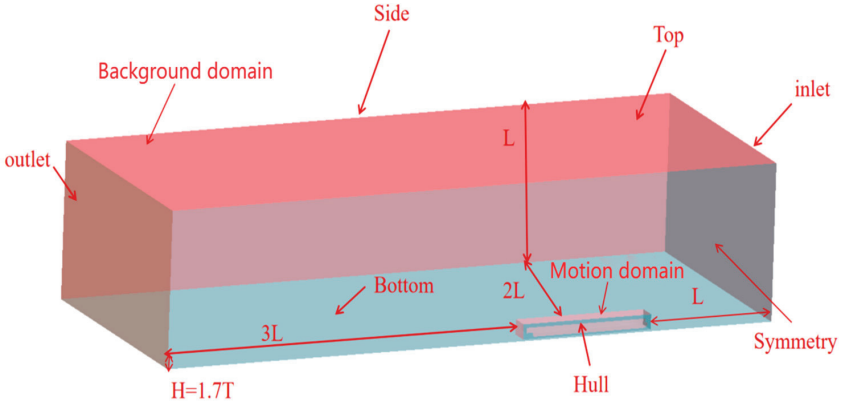

Figure 7. Computational domain of modified hull.

In this study, the mesh of the computational domain was generated using a trimmed grid generator, with local refinement around the bow, stern, and periphery of the hull. The refinement of the volume mesh within the free surface and the wave-making turbulent regions was performed progressively, in accordance with the Kelvin wave system. Near the hull, a prism layer grid generator was employed to produce six boundary layers, with a prism layer growth rate of 1.2. In shallow-water areas, influenced by the bottom boundary, three boundary layers were formed at the bottom edge, with a prism layer growth rate of 1.5. The wall function approach was used to manage flow within the boundary layer, achieving appropriate near-wall thickness to ensure wall y+ values ranged between 30 and 60. In deep-water areas, due to the absence of bottom viscous effects, the treatment of the bottom boundary was consistent with the top boundary, both set as velocity inlets. To mitigate the impact of numerical uncertainties on the results, the original ship type and the new ship type maintained the same mesh size and refinement areas, as shown in Figure 8.

To investigate the sinkage and trim motions of a ship in calm water, the Overset Mesh method was chosen to solve the motion response of the ship. The DFBI model was employed to simulate realistic ship motions. In the DFBI model, the motion of the ship is simulated according to the acting forces induced by the flow [19]. In order to prevent low-quality interpolation or interpolation failure, which could lead to erroneous solutions when using the Overset Mesh method, the mesh in the coupling region between the background domain and the motion domain was refined for both the original and new ship types. This ensured that the mesh sizes in the background domain were comparable to those in the motion domain, and the boundary of the motion domain maintained a minimum of five layers of grids between itself and the hull. The meshes for the motion domains of the original and new ship types are illustrated in Figure 9.

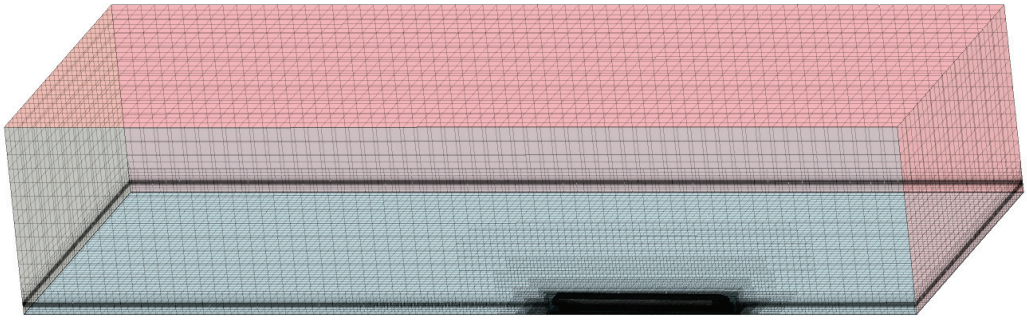

(**a**)

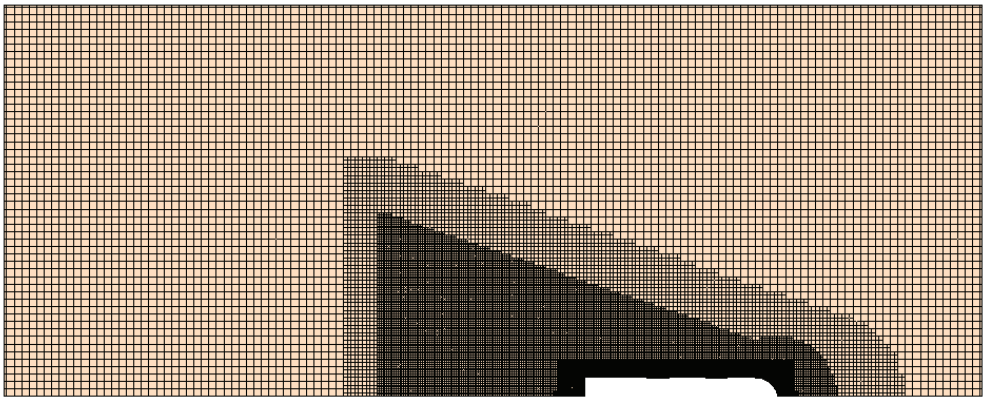

(**b**)

Figure 8. Computational mesh: (**a**) The overall mesh; (**b**) Free surface encryption.

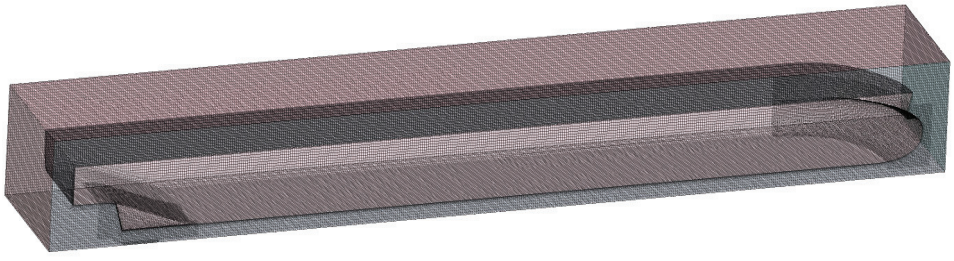

Figure 9. Overset mesh.

3.3. Boundary Conditions and Solvers

The specific settings of the boundary conditions in the numerical simulation of each working condition are shown in Table 2.

To mitigate the effect of numerical uncertainties on the outcomes, both the original ship type and the modified new ship type were subjected to the same boundary conditions and setups. The boundary layer formed at the bottom of the water in shallow water may affect the flow between the ship and the water bottom, the bottom is designated as a no-slip wall surface. The VOF method is utilized in this study to model the free surface [20]. A

three-dimensional unsteady implicit segregated solver was utilized, with the selection of the Eulerian two-phase flow model [21]. The turbulence model is the Realizable *k*-ε model, and the SIMPLE algorithm solver is used to solve the pressure–velocity coupling equation [22]. The convection term is discretized by the upwind scheme with second-order accuracy, the diffusion term is discretized by the central difference scheme, and the time term is discretized by the Euler implicit discrete scheme with first-order accuracy. The time step satisfies that the Courant number is less than one.

Table 2. Boundary condition settings.

Boundaries	Deep Water	H/T = 3
Inlet	Velocity inlet	Velocity inlet
Outlet	Pressure outlet	Pressure outlet
Top	Velocity inlet	Velocity inlet
Side	Velocity inlet	Velocity inlet
Bottom	Velocity inlet	No-slip wall
Hull	No-slip wall	No-slip wall
Symmetry	Symmetry plane	Symmetry plane
Overset boundary	Overset mesh	Overset mesh

3.4. Numerical Verification Method

CFD uncertainty analysis can be categorized into two components: Verification and Validation. The process of verification is to evaluate the uncertainty of the numerical value, and the process of confirmation is to evaluate the uncertainty of the mathematical model. The uncertainty of the numerical method is verified based on the verification method proposed by Stern [23] and Wilson [24].

The convergence analysis of mesh size and time step is carried out under the condition of water depth draft ratio H/T = 1.7 and working speed Vm = 1.110 m/s, and the numerical discrete uncertainty is evaluated to verify the reliability of the numerical simulation method.

In the analysis of mesh convergence, three sets of grids S_1, S_2, and S_3 with mesh foundation size encryption ratio $r = \sqrt{2}$ are set for calculation. When generating the mesh, keep the time step t = 0.02 s and keep the mesh encryption area and other settings the same. In the time step convergence analysis, the medium mesh size S_2 is used and three different time steps T_1, T_2, and T_3 are set up with the growth rate of $r = 2$ for calculation, and other settings remain unchanged. The specific working conditions are set as shown in Table 3.

Table 3. Numerical simulation cases for convergence analysis.

	Base Size (m)	Number of Background Domain Cells (10^6)	Number of Motion Domain Cells (10^6)	Number of Cells (10^6)	Time-Step (s)
S_1	0.1025	6.53	2.89	9.42	0.02
S_2	0.146	2.51	1.14	3.65	0.02
S_3	0.205	0.96	0.46	1.42	0.02
T_1	0.146	2.51	1.14	3.65	0.01
T_2	0.146	2.51	1.14	3.65	0.02
T_3	0.146	2.51	1.14	3.65	0.04

The results of grid convergence analysis and time step convergence analysis are shown in Table 4. The following conclusions can be obtained through the analysis of the results. The grid convergence rates R_G of sinkage and trim value are 0.509 and 0.167, which are monotonically convergent. The grid numerical discretization uncertainty U_G of the two is 0.051% S_2 and 0.218% S_2, and the numerical discretization uncertainty is small. The time step convergence rate R_T of the sinkage and trim value is 0.765 and 0.556, which are also monotonically convergent. The numerical dispersion uncertainty U_T of the time step is 0.972% T_2 and 0.773% T_2, both less than 1%, and the numerical dispersion uncertainty is small.

Table 4. Results of convergence analysis.

	R_G	P_G	U_G (%S_2)	R_T	P_T	U_T (%T_2)
Sinkage	0.509	1.948	0.051	0.765	1.975	0.972
Trim	0.167	2.585	0.218	0.556	2.931	0.773

Based on the validated numerical results mentioned above, considering both numerical precision and computational efficiency, grid 2 and a time step t = 0.02 s were chosen for further numerical simulations. In grid 2, the base grid size was set at 0.146 m, resulting in a total of 3.65 million grid cells for the entire computational domain.

4. Analysis of the Influence of Hydrodynamic Performance

Based on the validated mesh partitioning and numerical simulation methods mentioned earlier, CFD simulations were conducted for the original ship type under shallow-water conditions and the modified new ship type under three different water depth conditions. The simulations aimed to analyze the sinkage and trim of the ships. The numerical simulation results were used to analyze the effects of hull form design, water depth, and sailing speed on the heavy motion of the ships. The objective was to assess whether the new seismic survey vessel design could meet the safety requirements for operating in shallow-water environments.

4.1. The Influence of Ship Type on Ship Sinkage and Trim

The numerical simulation results for the sinkage and trim of both the original and the modified new ship types under shallow-water conditions (H/T = 1.7) are presented in Table 5.

Table 5. Numerical results of sinkage and trim in shallow water of two types of ships.

	Original Ship Type		**New Ship Type**		**E (%)**	
Vm (m/s)	Sinkage (m)	Trim (deg)	Sinkage (m)	Trim (deg)	Sinkage	Trim
0.626	−0.0191	−0.1836	−0.0103	−0.1576	85.4	16.5
1.110	−0.0473	−0.2892	−0.0134	−0.2679	252.9	7.95
1.375	−0.0657	−0.4933	−0.0166	−0.4315	295.8	14.3
1.474	−0.1081	−0.6884	−0.0187	−0.5498	478.1	25.2

In this context, a positive sinkage indicates an upward movement of the hull, denoting a rise or buoyancy, whereas a negative value signifies a downward movement, representing a sinking occurrence. As for trim, a positive value indicates a trim by the head, while a negative value signifies a trim by the stern.

The sinkage and trim values for different ship types, as they vary with ship speed, are plotted in Figures 10 and 11. These graphs reveal that in shallow-water conditions, the sinkage and trim values of both ship types increase with escalating sailing speeds. Both types of ships display a sinking tendency and a stern trim phenomenon.

As the sailing speed changes, the sinkage of the new ship type increases from −0.0103 m to −0.0187 m, an overall increase of 81.6%. In contrast, the original ship type exhibited a sharp increase in sinkage with changes in speed, from −0.0191 m to −0.1081 m, an increase rate of 465.97%. At the same speed, the change in hull form design has a maximum impact rate of 478.1% on the sinkage, which is more than fourfold, indicating that changes in hull form design significantly improve the sinkage phenomenon. However, the change in trim values between the two ship types is not particularly pronounced, with a maximum impact rate of 25.2%, and the trend in hull trim did not change.

Based on the content of the diagrams, it is observed that the wide and flat bulbous bow shape design of the new ship type increases the proportion of the displacement volume at the bow, effectively slows down the trim phenomenon of the ship. Compared to the original ship type, the new ship type is better at resisting the heaving motion, and across the

full speed range of the ship, the maximum sinkage of the new ship type is only −0.0187 m, meeting the requirements for safe navigation without the risk of grounding.

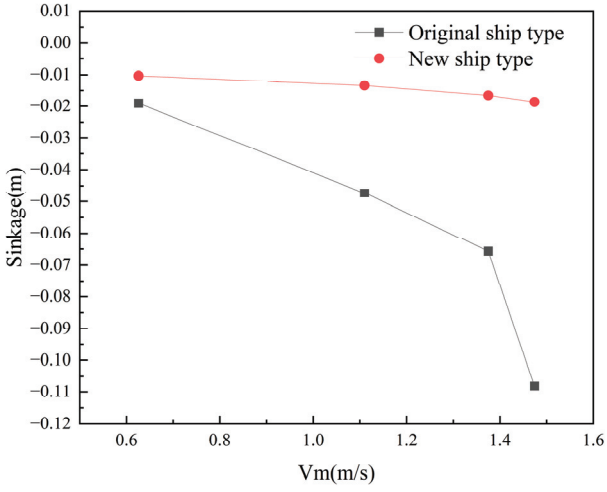

Figure 10. Sinkage under different ship types.

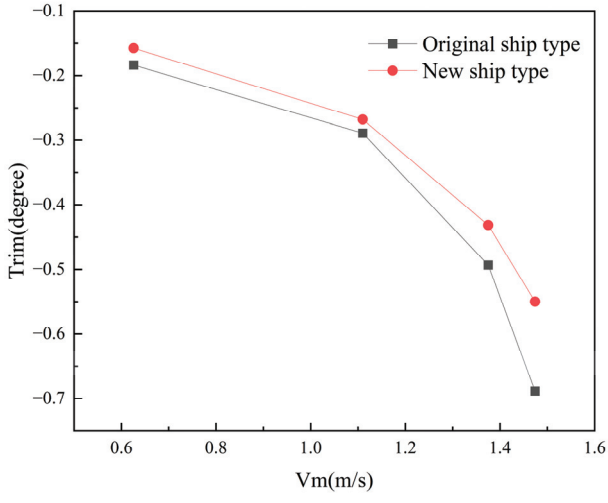

Figure 11. Trim values under different ship types.

4.2. Influence of Water Depth on Ship Sinking and Trim

The numerical simulation results for the sinkage and trim of the modified new ship under different water depths (H/T = INF, H/T = 3, H/T = 1.7) and various speeds are presented in Table 6.

In Table 6, a positive sinkage indicates an upward movement of the hull, denoting a rise or buoyancy, whereas a negative value signifies a downward movement, representing a sinking occurrence. As for trim, a positive value indicates a trim by the head, while a negative value signifies a trim by the stern.

The variation curves of the sinkage and trim of the ship with speed under different water depth conditions are shown in Figures 12 and 13. The data presented in these Figures indicate that, at the same speed, the sinkage in shallow water is greater compared to that in

deep and medium water depths, and this effect becomes more pronounced with an increase in speed. However, the trim in shallow water is also found to be greater than that in deeper waters, and it sharply increases with increased speed. At a speed of 1.474 m/s, the trim value in shallow water is 102.21% higher than that in deep water.

Table 6. Numerical results of sinkage and trim in different water depths.

Water Depth	Vm (m/s)	Sinkage (m)	Trim (deg)
H/T = INF	0.626	−0.0065	−0.1163
	1.110	−0.0076	−0.1509
	1.375	−0.0092	−0.2199
	1.474	−0.0105	−0.2719
H/T = 3	0.626	−0.0075	−0.1513
	1.110	−0.0105	−0.2112
	1.375	−0.0139	−0.2609
	1.474	−0.0151	−0.2877
H/T = 1.7	0.626	−0.0103	−0.1576
	1.110	−0.0134	−0.2679
	1.375	−0.0166	−0.4315
	1.474	−0.0187	−0.5498

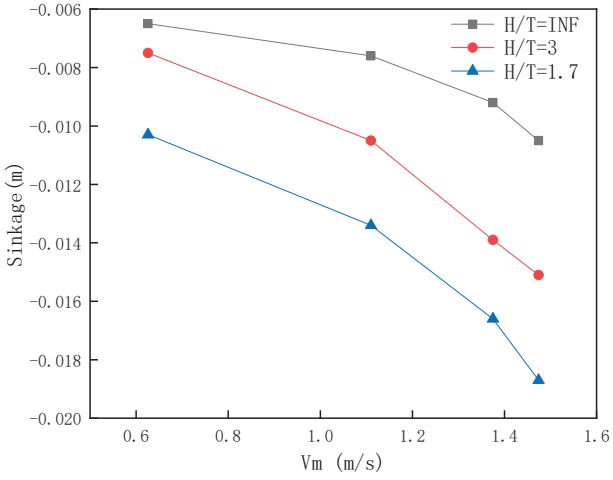

Figure 12. Sinkage under different water depths.

Analyzing the trends in sinkage and trim under different water depths reveals that, for the new ship type, the impact of shallow water on the trim is greater than its effect on the sinkage.

Figure 14 illustrates the axial velocity flow field distribution of a ship under the same speed in both deep and shallow-water conditions. From the diagram, it is evident that in deep water, the distribution of water flow is not restricted by water depth, with the flow primarily moving 'downward' as it passes beneath the hull, and only a small portion of the flow diverting toward the sides at the bow. In shallow water, however, the distance between the bottom of the hull and the seabed decreases, restricting vertical movement of the water flow when passing under the hull. This leads to an accelerated flow toward the sides of the hull, transitioning the water flow from a three-dimensional movement in deep water to a two-dimensional plane flow in shallow water. Due to the limitations imposed by the shallow-water depth, the velocity of the flow increases both beneath the hull and along its sides, causing a reduction in pressure at the bottom of the hull and generating

a 'suction force' that results in the ship experiencing sinkage and trim. This alteration in the hydrodynamic performance of the hull, in turn, induces further sinkage and trim, exacerbating these phenomena. In severe cases, this can lead to grounding incidents.

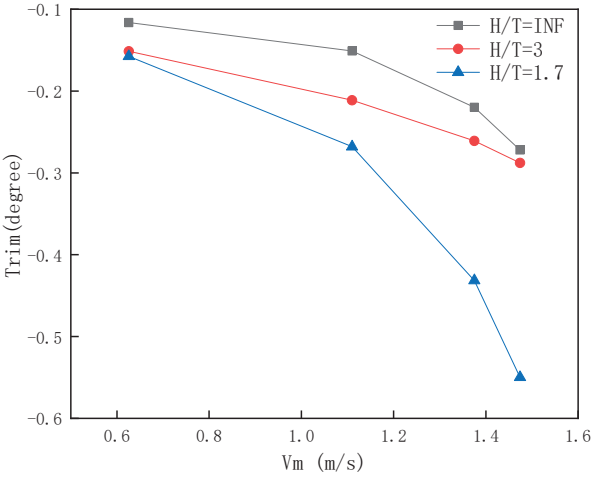

Figure 13. Trim values under different water depths.

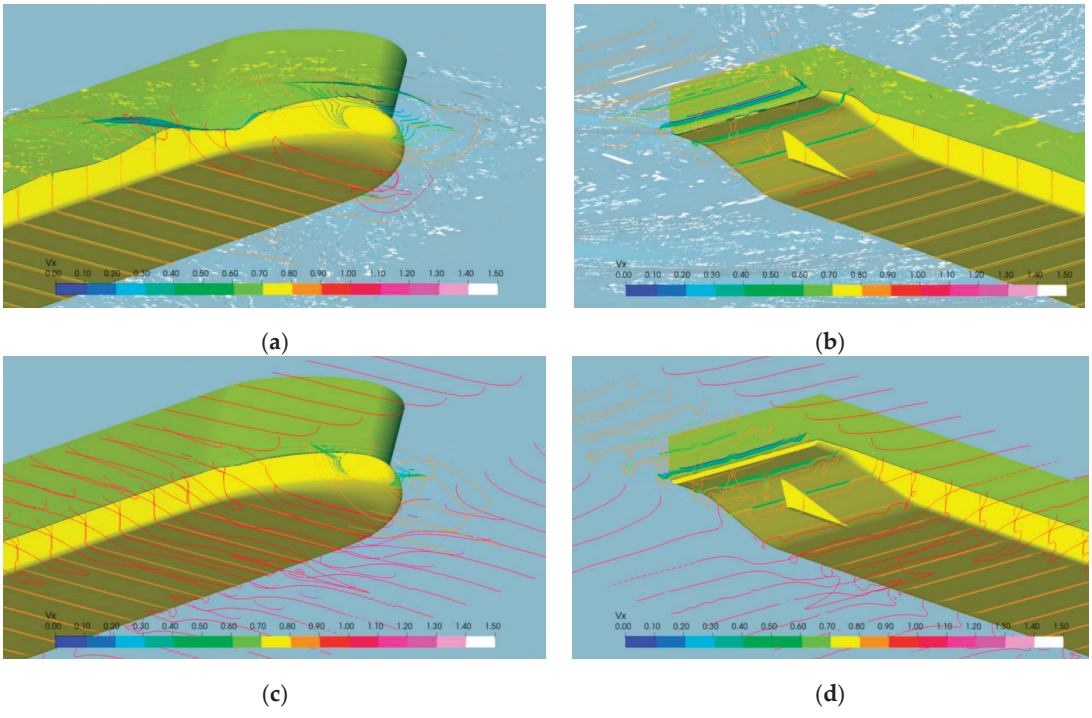

Figure 14. Ship velocity field distribution under different water depths: (**a**) Velocity field distribution on bow in deep-water conditions; (**b**) Velocity field distribution on stern in deep-water conditions; (**c**) Velocity field distribution on bow in shallow-water conditions; (**d**) Velocity field distribution on stern in shallow-water conditions.

4.3. The Influence of Speed on Ship Sinkage and Trim

From the analysis above, it is clear that with an increase in speed, both the sinkage and trim of the ship significantly increase, especially in shallow-water conditions, indicating that speed has a significant impact on the sinkage and trim of a ship in shallow waters. This section focuses on analyzing the impact of speed on the sinkage and trim of the ship through the distribution of pressure on the hull at different speeds.

Figure 15 illustrates the pressure distribution for the modified new ship type under shallow-water conditions, where H/T = 1.7. In shallow-water conditions, high-pressure zones are formed at both the bow and stern, while the forward shoulder and stern area, particularly near the deadwood, each develop into low-pressure zones. This results in a lower pressure at the mid-bottom of the hull compared to the bow and stern, leading to an uneven pressure distribution along the hull. Such a distribution induces sinkage and trim in the ship. At reduced speeds, the hull experiences less pressure. However, as speed increases, so does the velocity of water flow beneath the hull, which in turn amplifies the hull pressure and further aggravates the uneven distribution of pressure. Consequently, this leads to increased sinkage and trim of the ship. As the speed continues to rise, the high-pressure area at the bow expands further while the stern remains under lower pressure compared to the bow, causing greater sinking at the stern than the bow and resulting in a pronounced stern-down trim phenomenon.

4.4. The Influence of Shallow-Water Ship Attitude on Resistance

In this study, a hull sinkage and trim numerical simulation of the original ship type and the modified new ship type under different water depths is carried out. At the same time, the resistance of the new ship type under the open sinkage and trim state of each speed in the shallow-water environment is recorded. The numerical simulation calculation shows that the resistance of the new ship model in the free state is R_{t1}. In this study, the ship model resistance test without opening sinkage and trim is carried out in the shallow-water trailer towing tank of MARIN in the Netherlands. The resistance of the new type ship model test in the constrained state is R_t, and the specific test data are from Su et al. [25]. The results are presented in Table 7.

Table 7. Ship model numerical simulation resistance in free state and ship model test resistance in constrained state.

Water Depth	Vm (m/s)	Trim	Rt_1 (N)	Rt (N)	Resistance Change Rate (%)
H/T = 1.7	0.626	−0.1576	20.71	19.33	5.45%
	0.946	−0.2082	51.01	44.66	6.80%
	1.110	−0.2679	73.34	63.2	8.59%
	1.282	−0.3549	109.51	99.15	8.21%
	1.375	−0.4315	135.67	130.5	1.49%
	1.432	−0.4976	154.04	154.46	−2.06%
	1.474	−0.5498	173.71	181.74	−7.15%

At the same speed, the resistance of the ship model in a free state after open sinking and trimming showed significant changes compared to the constrained state. This is attributed to the motion of the ship causing stern-down trim, alterations in the ship's wetted surface area, wave-making, and other factors, leading to changes in hull resistance. Across the entire speed range, the ships exhibited a stern-down trim condition, with the degree of trim increasing as speed increased. At speeds of 0.626 m/s, 0.946 m/s, 1.110 m/s, 1.282 m/s, and 1.375 m/s, the resistance of the ship model in a free state was greater than in a constrained state. The rate of resistance change increased with speed and the angle of trim before decreasing. At speeds of 1.432 m/s and 1.474 m/s, the resistance of the ship model in a free state was less than in a constrained state. This indicates that at smaller angles of stern trim, compared to the constrained state, the resistance of the ship model increases, however, as the angle of stern trim increases, the resistance tends to decrease.

This suggests that changes in the posture of the ship have a significant impact on resistance, and a certain degree of stern trim can achieve a reduction in navigational resistance.

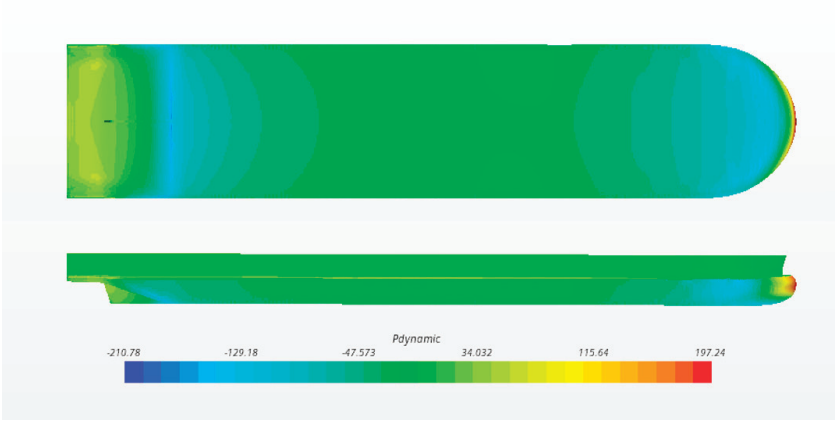

(**a**)

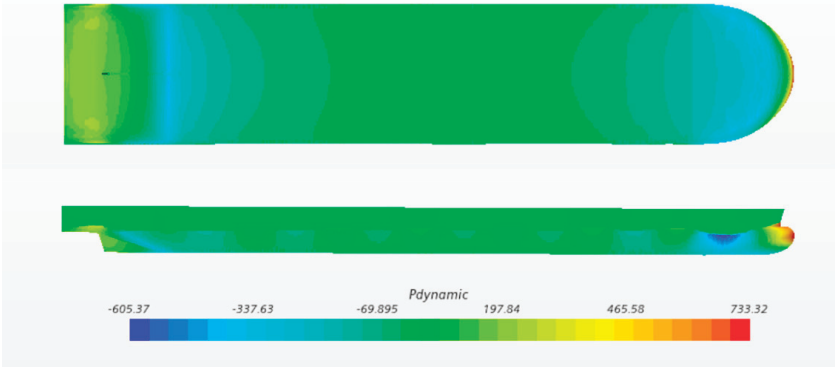

(**b**)

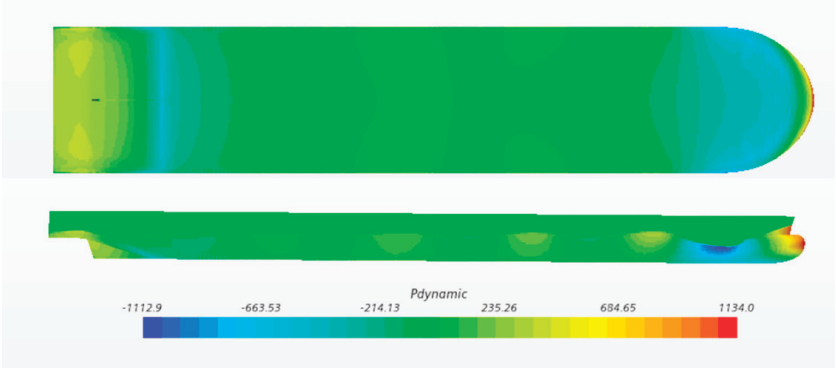

(**c**)

Figure 15. *Cont.*

(**d**)

Figure 15. Ship pressure distribution at different speeds in shallow water: (**a**) Vm = 0.626 m/s; (**b**) Vm = 1.110 m/s; (**c**) Vm = 1.375 m/s; (**d**) Vm = 1.474 m/s.

5. Conclusions

This research conducts numerical simulations of the sinkage and trim of both the original and the new modified hull forms under various water conditions. The resistance of the ship model in the free state is recorded in the numerical simulation process, and it is compared with the resistance of the ship model test in the restricted state. The respective results reveal:

Based on the numerical results of the original and new ship types in shallow water, it can be observed that in shallow-water conditions, compared to the original ship type, the new ship type can effectively improve hull sinkage and trim phenomena. Furthermore, within the full operational speed range, the new ship type does not experience grounding.

Through numerical simulations of sinkage and trim of the new ship type under varying water depths, it is evident that with decreasing water depth and increasing speed, the uneven distribution of hull pressure intensifies. The transition of flow around the hull from three-dimensional to two-dimensional planar flow due to water depth constraints exacerbates hull sinkage and trim.

By analyzing the resistance of the new ship type in shallow water under constrained and free conditions, it can be observed that changes in ship attitude significantly impact the sailing resistance of the ship. A certain stern trim angle during sailing can reduce sailing resistance effectively.

In this study, a new type of shallow-water seismic survey vessel is investigated, focusing on hull sinkage, trim, and resistance under shallow-water conditions. This research is valuable for designing shallow-water ships and ensuring safe navigation in shallow waters. However, the ship model resistance tests did not account for the sinkage and trim. This study lacks support from actual sinkage and trim tests, only conducting numerical simulations for both deep and shallow-water scenarios. Future research should consider opening these degrees of freedom in ship model tests to record and compare sinkage and trim with numerical simulation results.

Author Contributions: Conceptualization, S.S.; methodology, S.S.; software, Z.Y. and Y.W.; validation, Z.Y. and Y.W.; formal analysis, F.G.; investigation, S.S.; resources, Q.C.; data curation, H.L.; writing—original draft preparation, Z.Y. and Y.W.; writing—review and editing, Q.C.; visualization, H.L.; supervision, F.G.; project administration, F.G.; funding acquisition, S.S. All authors have read and agreed to the published version of the manuscript.

Funding: This research received no external funding.

Institutional Review Board Statement: This study did not require ethical approval.

Informed Consent Statement: Informed consent was obtained from all subjects involved in the study.

Data Availability Statement: Data are contained within the article.

Conflicts of Interest: Author Yujie Wu was employed by the company Wuhan Marine Machinery Plant Co., Ltd., Author Fangxin Guo and Qixiang Cheng ware employed by the company Dalian Hengxing Marine Engineering Design Co., Ltd., Author Haibo Liu was employed by the company China National Petroleum Corporation. The remaining authors declare that the research was conducted in the absence of any commercial or financial relationships that could be construed as a potential conflict of interest.

References

1. Yan, Z.; Mao, Y.S.; Liu, C.G. Dynamic Simulation of 12 Streamers Changeable Towed System of Seismic Survey Vessel. In Proceedings of the 3rd International Conference on Transportation Information and Safety, Wuhan, China, 25–28 June 2015.
2. Asuelimen, G.; Blanco-Davis, E.; Wang, J.; Yang, Z.; Matellini, D.B. Formal Safety Assessment of a Marine Seismic Survey Vessel Operation, Incorporating Risk Matrix and Fault Tree Analysis. *J. Mar. Sci. Appl.* **2020**, *19*, 155–172. [CrossRef]
3. Kim, W.; Kim, H.; Shin, J. Development of Small Vessel 3d Seismic Survey System: EOS3D. In Proceedings of the OCEANS-MTS/IEEE Kobe Techno-Oceans Conference (OTO), Kobe, Japan, 28–31 May 2018.
4. Debaillon, P. Numerical Investigation to Predict Ship Squat. *J. Ship Res.* **2010**, *54*, 133–140. [CrossRef]
5. Tezdogan, T.; Incecik, A.; Turan, O. A Numerical Investigation of the Squat and Resistance of Ships Advancing through a Canal Using Cfd. *J. Mar. Sci. Technol.* **2016**, *21*, 86–101. [CrossRef]
6. Kok, Z.; Duffy, J.; Chai, S.H.; Jin, Y.T. Multiple Approaches to Numerical Modeling of Container Ship Squat in Confined Water. *J. Waterw. Port Coast. Ocean. Eng.* **2020**, *146*, 04020017. [CrossRef]
7. Jiang, T. A New Method for Resistance and Propulsion Prediction of Ship Performance in Shallow Water. In *Practical Design of Ships and Other Floating Structures, Proceedings of the Eighth International Symposium on Practical Design of Ships and Other Floating Structures, Shanghai, China, 16–21 September 2001*; Wu, Y.-S., Cui, W.-C., Zhou, G.-J., Eds.; Elsevier Science Ltd.: Oxford, UK, 2001; pp. 509–515.
8. Gourlay, T. Flow beneath a Ship at Small Underkeel Clearance. *J. Ship Res.* **2006**, *50*, 250–258. [CrossRef]
9. Krishna, B.; Krishnankutty, P. Experimental and Numerical Study on Trim and Sinkage of a High Speed Catamaran Vessel in Shallow Waterways. *Int. Shipbuild. Prog.* **2009**, *56*, 159–176.
10. Shi, A.G.; Wu, M.; Yang, B.; Wang, X.; Wang, Z.C. Resistance Calculation and Motions Simulation for Free Surface Ship Based on Cfd. In Proceedings of the International Conference on Advances in Computational Modeling and Simulation (ACMS), Kunming, China, 14–16 December 2011.
11. Pavkov, M.; Morabito, M. Experimental Investigation of Trimaran Models in Shallow Water. *J. Ship Prod. Des.* **2014**, *30*, 66–78. [CrossRef]
12. Deng, R.; Li, C.; Huang, D.B.; Zhou, G.L. The Effect of Trimming and Sinkage on the Trimaran Resistance Calculation. In Proceedings of the 7th International Conference on Fluid Mechanics, Qingdao, China, 24–27 May 2015.
13. Ma, C.; Zhang, C.L.; Huang, F.X.; Yang, C.; Gu, X.C.; Li, W.; Noblesse, F. Practical Evaluation of Sinkage and Trim Effects on the Drag of a Common Generic Freely Floating Monohull Ship. *Appl. Ocean. Res.* **2017**, *65*, 1–11. [CrossRef]
14. Lungu, A. Numerical Simulation of the Squatting of Floating Bodies Moving in Shallow Water. In Proceedings of the 13th International Conference on Interdisciplinarity in Engineering (INTER-ENG), Targu Mures, Romania, 3–4 October 2019.
15. Bechthold, J.; Kastens, M. Robustness and Quality of Squat Predictions in Extreme Shallow Water Conditions Based on Rans-Calculations. *Ocean. Eng.* **2020**, *197*, 106780. [CrossRef]
16. Feng, D.K.; Ye, B.; Zhang, Z.G.; Wang, X.Z. Numerical Simulation of the Ship Resistance of Kcs in Different Water Depths for Model-Scale and Full-Scale. *J. Mar. Sci. Eng.* **2020**, *8*, 745. [CrossRef]
17. Lu, Y.; Gu, Z.H.; Liu, S.W.; Chuang, Z.J.; Li, Z.Y.; Li, C.Z. Scenario-Based Optimization Design of Icebreaking Bow for Polar Navigation. *Ocean. Eng.* **2022**, *244*, 110365. [CrossRef]
18. Im, N.K.; Lee, S.M.; Lee, C.K. The Influence of Skegs on Course Stability of a Barge with a Different Configuration. *Ocean. Eng.* **2015**, *97*, 165–174. [CrossRef]
19. Shivachev, E.; Khorasanchi, M.; Day, S.; Turan, O. Impact of Trim on Added Resistance of Kriso Container Ship (Kcs) in Head Waves: An Experimental and Numerical Study. *Ocean. Eng.* **2020**, *211*, 107594. [CrossRef]
20. Tripathi, S.; Vijayakumar, R. Numerical and Experimental Study of Stern Flaps Impact on Resistance and Propulsion of High-Speed Displacement Ships. *Ocean. Eng.* **2024**, *292*, 116483. [CrossRef]
21. Samuvel, T.J.; Gokulakrishnan, M.; Kumar, A.; Vijayakumar, R. Numerical Estimation of Frictional Drag on Flat Plate in Shallow Water with & without BDR. In Proceedings of the OCEANS Conference, Chennai, India, 21–24 February 2022.
22. Zentari, L.; el Mocta, O.; Lassen, J.; Hallmann, R.; Schellin, T.E. Experimental and Numerical Investigation of Shallow Water Effects on Resistance and Propulsion of Coupled Pusher-Barge Convoys. *Appl. Ocean. Res.* **2022**, *121*, 1034048. [CrossRef]
23. Stern, F.; Wilson, R. Closure to "Discussion of 'Comprehensive Approach to Verification and Validation of Cfd Simulations—Part 1: Methodology and Procedures'" (2002, Asme J. Fluids Eng., 124, P. 809). *J. Fluids Eng.-Trans. ASME* **2002**, *124*, 810–811. [CrossRef]

24. Wilson, R.; Shao, J.; Stern, F. Discussion: Criticisms of the "Correction Factor" Verification Method 1. *J. Fluids Eng.-Trans. ASME* **2004**, *126*, 704–706. [CrossRef]
25. Su, S.J.; Wu, Y.J.; Xiong, Y.P.; Guo, F.X.; Liu, H.B.; Cheng, Q.X. Experiment and Numerical Simulation Study on Resistance Performance of the Shallow-Water Seismic Survey Vessel. *Ocean. Eng.* **2023**, *279*, 113889. [CrossRef]

Journal of
Marine Science and Engineering

MDPI

Article

CFD-Powered Ship Trim Optimization: Integrating ANN for User-Friendly Software Tool Development

Matija Vasilev [1,2,*], Milan Kalajdžić [1,2] and Ines Ivković [1]

[1] Faculty of Mechanical Engineering, University of Belgrade, 11000 Belgrade, Serbia; mdkalajdzic@mas.bg.ac.rs (M.K.); iivkovic@mas.bg.ac.rs (I.I.)
[2] Ocean Pro Marine Engineers Ltd., 11000 Belgrade, Serbia
* Correspondence: matija@oceanpro.eu; Tel.: +381-631-076-996

Abstract: This study presents a comprehensive approach to trim optimization as an energy efficiency improvement measure, focusing on reducing fuel consumption for one RO-RO car carrier. Utilizing Computational Fluid Dynamics (CFD) software, the methodology incorporates artificial neural networks (ANNs) to develop a mathematical model for estimating key parameters such as the brake power, daily fuel oil consumption (DFOC) and propeller speed. The complex ANN model is then integrated into a user-friendly software tool for practical engineering applications. The research outlines a seven-phase trim optimization process and discusses its potential extension to other types of ships, aiming to establish a universal methodology for CFD-based engineering analyses. Based on the trim optimization results, the biggest DFOC goes up to 10.5% at 7.5 m draft and up to 8% for higher drafts. Generally, in every considered case, it is recommended to sail with the trim towards the bow, meaning that the ship's longitudinal center of gravity should be adjusted to tilt slightly forward.

Keywords: EEDI; EEXI; CII; CFD; ANN; trim optimization

Citation: Vasilev, M.; Kalajdžić, M.; Ivković, I. CFD-Powered Ship Trim Optimization: Integrating ANN for User-Friendly Software Tool Development. *J. Mar. Sci. Eng.* **2024**, *12*, 1265. https://doi.org/10.3390/jmse12081265

Academic Editors: Nastia Degiuli and Ivana Martić

Received: 17 June 2024
Revised: 17 July 2024
Accepted: 18 July 2024
Published: 27 July 2024

1. Introduction

With the aim to reduce emissions of greenhouse gasses, in 2013, the International Maritime Organization (IMO) introduced the Energy Efficiency Design Index (EEDI) for new ships and later, in 2023, the Energy Efficiency for Existing Ships Index (EEXI). These new measures initiated changes in the shipbuilding industry. By implementing these regulations, it is anticipated to reduce global CO_2 emissions by 40% by the year 2030 and 70% (or at least 50%) by the year 2050, compared to the levels in 2008. All ships that fall under MARPOL Annex VI and have gross tonnage over 400 must meet the set criteria, which are based on nominal ship data. The IMO determined the parameters and procedure for calculating the required EEDI and EEXI, as well as the formula for calculating the attained EEDI/EEXI that must be lower than the required values. The required value for the EEDI is determined by the formula:

$$\text{Required EEDI} = a(\text{DWT})^{-c}, \tag{1}$$

where parameters a and c are based on the regression curve fit [1] of data from ships that were built between 1999 and 2009, and also depend on the type of ship. The required EEDI decreases over the years according to the formula:

$$\text{Attained EEDI} \leq \text{Required EEDI} = (1 - X/100) \cdot \text{Reference line value}, \tag{2}$$

where X is the specified reduction factor given in [2] through four phases. Values for the EEXI are based on the required EEDI, taken into account with the adequate reduction factor from [3]. The requirements for the EEXI are becoming slightly stricter with time, with the plan for the EEXI and EEDI to become equal in 2025. In addition to the two mentioned

energy efficiency parameters, the IMO introduced operational efficiency indicators. In 2009 [4], the Energy Efficiency Operational Indicator (EEOI) was invented and is defined as the ratio of emitted CO_2 per unit of transport work. The EEOI never became mandatory, but it is a representative value of the ship's operational energy efficiency level for a consistent period of time. Another indicator came into force in 2023, the Carbon Intensity Index (CII), which is calculated as the ratio of the total mass of emitted CO_2 to the total transport work undertaken in a specific calendar year, considering the traveled distance, time spent underway and the amount of consumed fuel over a period of one year. As well as for the EEDI and EEXI, the attained [5] and required [6] values are also calculated for the CII, where the attained CII has to be lower than the required, which decreases over time [7]. Based on the attained CII, the ship belongs to one of five energy efficiency categories (A, B, C, D, E). The boundaries between those categories and the calculation method for each ship type are defined in [8] and they depend on the ship's DWT. Since the CII is a mandatory parameter, all ships of gross tonnage of 5000 or more are from 2019 obliged to record the relevant information (traveled distance, time spent underway and the amount of consumed fuel over a period of one year) under the Data Collection System (DCS) [9]. In the case that a ship achieved class E for at least one year, or class D for three years in a row, it must create a plan for reducing CO_2 emissions and satisfy the requirements for at least class C [10]. In 2013, the IMO introduced the Ship Energy Efficiency Management Plan (SEEMP), which consists of three parts: a ship management plan to improve energy efficiency, a ship fuel oil consumption data collection plan and a ship operational carbon intensity plan. Part I applies to all ships that fall under MARPOL Annex VI and have gross tonnage over 400, while Part II and Part III apply for ships that have gross tonnage over 5000 and fall under MARPOL Annex VI.

Various measures can be considered in order to meet the energy efficiency requirements developed by the International Maritime Organization and attain a reduction in CO_2 emissions. Those measures are divided into two categories: operational methods and technical methods. Operational methods include the following: improvement in voyage execution [11,12], reduction in auxiliary power consumption [11,13], weather routing [10,12], "just in time" voyage [13], optimum ballast [10,12], optimum cargo distribution [12], energy-saving utilities [14], optimum use of rudder and heading control systems [10], optimized hull and propeller maintenance [10], speed optimization [12,15], slow steaming [16,17] and trim optimization [12,18].

These measures can be applied for both existing ships as well as new ships. Technical measures are design-related and therefore more favorable for new ships. These measures refer to wind-assisted propulsion, fuel type change [10,16,19], waste heat recovery [12], upgrading and maintenance of propulsion system, hull retrofit (bulb and/or stern modification, installation of energy-saving devices [10], etc.

Optimum trim means that the angle of the trim for a specific operating condition, regarding the displacement and speed, provides minimum resistance, which directly implies the optimal efficiency level [12]. The resistance of the ship changes depending on the trim, although the displacement and speed stay the same [20]. The beneficial aspect of trim optimization is that neither a hull modification nor engine upgrade is needed. The ship is trimmed if the draught at the bow differs from the draught at the aft section of the ship. While a negative trim indicates that the draught at the bow is greater than the draught at the stern, a positive trim implies the opposite. Every vessel is optimized for a number of conditions (even keel at full load and design speed, ballast condition, etc.), but the actual operating conditions usually differ from the expected ones [21]. It was confirmed in [22] that the trim can affect the total resistance of a ship for various service speeds and the optimum trim for every speed is different. The trim optimization method is intended for minimizing the resistance in calm water and therefore minimizing fuel consumption, which can be accomplished with a specially developed program for the ship. The results of [18] indicate the possibility of reducing the total fuel consumption during a whole voyage by 1.2% by utilizing the calculated optimum trim for the whole voyage. A 4250 TEU container ship sea

trial with the use of a trim optimizing program reported a main engine power reduction of 910 kW and energy-saving rate of 9.2% [23]. The trim of the ship can be influenced by the redistribution of ballast, fuel and/or load between tanks. Parameters that change when the ship is trimmed compared to an even-keel condition are a wetted surface area, the length of the waterline and a submerged hull form at the bow as well as at the stern [24]. Potential disadvantages of this method could be a reduction in visibility, reduced freeboard, emergence of the propeller [25], underkeel clearance, seakeeping, maneuverability [26], seakeeping [27] and shipped water on deck [28], and those should as well be taken into account while finding the optimum trim for an operating condition.

Calculating the ship resistance in calm water by conducting model tests and numerical simulations provides data about the resistance for different drafts and trims. As a result, a set of curves with highlighted lowest resistance for a specific draft are obtained, as in [22,29]. While onboard tools have this information at their disposal, model tests are still common and basins are equipped with traditional procedures and up-to-date insights to provide their proper execution, pursuing the measurement of small power variations within a foreseen range of 0 to 4% of the total installed power [30], or a 2% to 4% fuel consumption reduction [31]. With the advancement of technology and computers, CFD software calculations provide trim tables with an accuracy that can compete with the results gained from traditional model tests, with even less investments. Other methods that can be used to determine the optimum trim are sea trials and machine learning methods. The shortcomings of these methods are that sea trials are fuel- and time-consuming for determining the optimum ballast, while for obtaining information about the optimum trim with the machine learning method, a lot of data from a ship's past voyages are needed [32]. In this study, the aim of this work is focused only on applying the CFD method on one RO-RO car carrier in order to optimize the trim for an energy-efficient voyage and exploitation.

The application of the CFD method for trim optimization for different ship types can be found in various existing studies. For example, in the study by [20], the effect of trim optimization for a container ship like MOERI (KCS) was a total resistance reduction of 2%, similar to the results of trim optimization for a US Navy ship [13]. A CFD investigation of the propulsion performance of a low-speed VLCC tanker at various initial trim angles was conducted by [33] and showed a 1.76–2.12% total resistance reduction. The authors of [34] and [35] report even greater profit, such as fuel savings of up to 5% [34] and a 6% reduction in delivered horsepower [35]. Since the trim conditions can vary significantly, so do the results from trim optimization. The authors of [36] highlight that in Series 60, the total resistance between the worst and best trims varies by up to 11%. The trim optimization of a bulk carrier in [37] results in a total resistance reduction possibility of up to 14%. Savings for RO-RO ships were studied by [12] and indicated a possibility of up to a 10.4% reduction in delivered power, or 1.2 t fuel per day. In addition to the calculation of the optimal trim, specialized software for input parameters that quickly provide information about the optimal trim has been mentioned [35,38].

Up to now, artificial neural networks (ANNs) have found application in predicting fuel consumption, as demonstrated in the studies by [39] and [40], which focused on utilizing NOON reports. Furthermore, an ANN has been employed for forecasting the ship speed, as evidenced by the work of [41]. Moreover, research efforts have extended to utilizing ANNs for the joint prediction of the ship speed and fuel consumption, leveraging data from sails, particularly in the case of a barquentine, as explored by [42]. The study by [43] proposes a real-time hybrid electric ship energy efficiency optimization model considering time-varying environmental factors, aiming to optimize the EEOI under wind and wave conditions while maintaining speed limits, resulting in an average reduction in fuel consumption of 13.4% and real-time EEOI of 15.2%. In [44], a real-time prediction model of ship fuel consumption through BP neural network training-related data is presented and further used for ship speed optimization. The research of [45] developed an ANN model to predict the main engine power and pollutant emissions of 3020 container, cargo and tanker

ships using 14 parameters, demonstrating its potential for use in future studies on fuel consumption and energy efficiency in maritime transport.

In today's complex technological landscape, the integration of various disciplines is becoming increasingly vital for tackling engineering challenges. By bridging the fields of naval engineering, CFD, ANN and practical application development, this study not only underscores the importance of multidisciplinary association but also showcases its benefits in addressing real-world problems within the maritime industry. Through the synergy of these varied fields, novel solutions can be developed to optimize ship operations or design, enhance fluid flow analysis accuracy and streamline decision-making processes. Moreover, the utilization of an ANN enables the creation of sophisticated mathematical models that can effectively capture complex relationships and patterns within maritime systems, paving the way for more precise simulations and predictive analytics. Furthermore, the development of user-friendly applications facilitates the seamless implementation of these advanced methodologies, empowering stakeholders to leverage cutting-edge insights for improved vessel performance and operational efficiency. Essentially, this methodology not only promotes scientific comprehension but also encourages innovation and pragmatic breakthroughs in the field of maritime engineering, thus helping in the long-term growth of maritime technologies.

2. Methods

The conducted work consists of several phases: (1) 3D modeling; (2) first-level verification of the reliability of the digital twin (3D model); (3) open water test (OWT); (4) second-level verification of the reliability of the 3D model; (5) trim optimization; (6) determination of a mathematical model for assessing the optimal trim, ship speed, engine (brake) power, daily fuel consumption and propeller speed; (7) programming an application based on previously conducted analyses. In this study, various software has been used: StarCCM+ version 2021.3 for CFD analysis, aNETka for mathematical model determining and MATLAB (version 2020b) for application development. The goal of this paper, in addition to trim optimization, is to establish an initial procedure for setting up CFD simulations. Therefore, this chapter provides only a brief overview of the governing equations used to solve the problem of ship movement through two fluids. More attention is given to functions that are not predefined in the StarCCM+ software, which the user can define. Consequently, this paper includes formulas that can be found in various publications, ensuring that everything complies with the requirements and guidelines issued by relevant institutions in the maritime industry.

In Table 1, the ship's (RO-RO car carrier) principal particulars are given.

Table 1. Principal particulars.

Parameter *	Dimension	Value
L_{pp}	(m)	158
B	(m)	28
H	(m)	30.65
T_s	(m)	7.8

* L_{pp}—length between perpendiculars, B—breadth, H—depth, T_s—draft.

Propeller geometry characteristics are presented in Table 2.

Table 2. Propeller characteristics.

Parameter *	Dimension	Value
D	(m)	5.5
No. of blades	(-)	5
BAR	(-)	0.83
D_{hub}	(m)	0.98

Table 2. *Cont.*

Parameter *	Dimension	Value
Chord length at $0.7R_p$	(m)	2.0988
P/D at $0.7R_p$	(-)	0.9594

* D—diameter, BAR—blade area ratio, D_{hub}—hub diameter, R_p—propeller radius, P—pitch.

2.1. Three-Dimensional Modeling

Three-dimensional modeling is the first necessary step before conducting CFD simulations. Creating a 3D representation of the RO-RO vessel involved using existing documentation: hull construction drawings, rudder construction drawings and propeller drawings. This digital twin includes detailed modeling of the hull, rudder and propeller, with the goal of faithfully capturing the ship's attributes and performance.

2.2. First-Level Verification

First-level verification involves comparing hydrostatic data such as volume displacement (∇), block coefficient (C_b), longitudinal center of buoyancy (LCB) and wetted surface (WS) of the 3D model with data given in the Trim & Stability booklet for various drafts. No parameter should deviate more than 1% from (as per authors' experience, 1% deviation enables enough accuracy) its corresponding value given in the Stability Booklet.

2.3. Open Water Test

The OWT is a method for determining propeller characteristics such as thrust coefficient, torque coefficient and propeller efficiency. The procedure for determining these coefficients through model tests is defined in [46]. In this case, model testing was not conducted; instead, propeller parameters were determined through CFD simulation, following the procedure described in [47]. According to this document, the CFD results of the OWT are considered valid if they do not differ by more than 3% from the results obtained by model testing within the relevant propeller operating range. It is also emphasized that if the model test results of the propeller are not known, an additional OWT with the appropriate B-series propeller model should be conducted. An appropriate B-series propeller is considered one with the same geometric characteristics (diameter, pitch, ratio of characteristic areas) as the original propeller installed on the considered ship. The 3D model of the B-series propeller was obtained using the B-series Propeller Generator available online [48]. The OWT results of the B-series propeller should not deviate by more than 3% from the results obtained with the mathematical model for the same geometric parameters. If this condition is met, the same CFD calculation methodology is applied to the original propeller, and the results obtained this way are considered valid. A mathematical model can be found in [49].

The simulations are conducted using a steady-state numerical flow model, solved in the rotating frame of reference. The numerical method used is called Multiple Reference Frames (MRFs), where in one part of the domain, the equations are solved in a rotating frame of reference, while in the rest of the domain, a stationary frame of reference is used.

Figure 1 shows the domain of the open water test CFD setup. The outer cylinder shows the far-field boundary of the domain, while the inner, smaller cylinder represents the boundary between the rotational frame of reference and stationary frame of reference. The diameter and length of the small cylinder are 4D, while the diameter and length of the large cylinder are 10D. The propeller is positioned downstream from the shaft. All simulations are conducted in full scale.

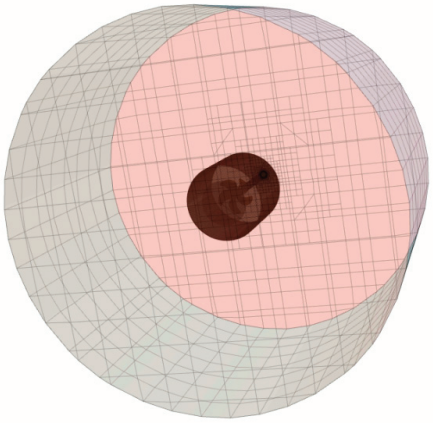

Figure 1. Domain of conducted open water test simulations.

The same grid refinement options were used for both propeller grids (B-series propeller and original propeller) and are presented in Figure 2.

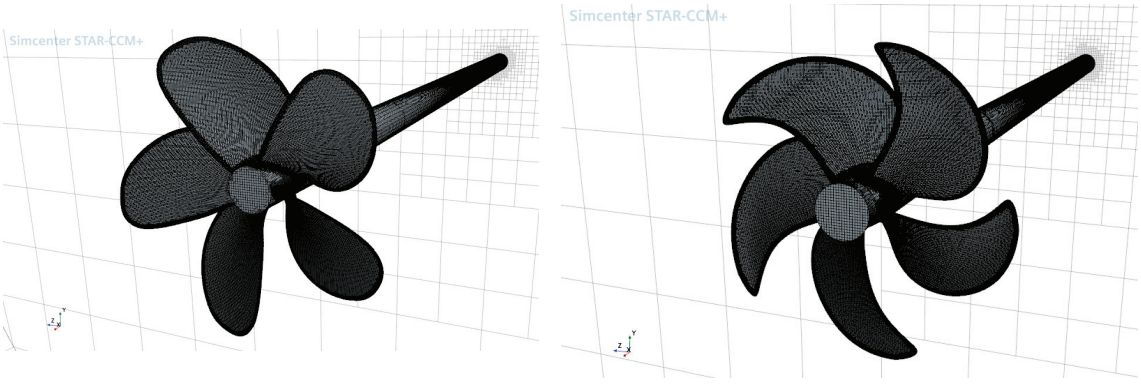

(**a**) (**b**)

Figure 2. Grid of the propellers: (**a**) B-series propeller; (**b**) original propeller.

Turbulence modeling is performed using the k-ω SST model as is required by [47]. The inflow turbulence intensity was set to 1% relative to the inflow speed. The inflow speed conditions and rotation rate of the propeller are selected to closely resemble the conditions expected at self-propulsion conditions.

2.4. Second-Level Verification

Second-level verification involves conducting a CFD simulation for a draft for which there are available results from the model tests or sea trials. The difference between the results obtained by the CFD analysis and model tests/sea trials should not be greater than 5% [47]. This kind of verification is typical in applied CFD analysis in the maritime industry [50,51].

The equations are discretized using the collocated Volume of Fluid (VOF) multiphase method implemented within the software. It is used for large-scale two-phase (in this case, sea water (ρ_w = 1.025 t/m^3) and air (ρ_A = 1.212 kg/m^3) at 18 °C) flows encountered in

naval hydrodynamics. A two-phase, incompressible, turbulent and viscous flow model is employed, governed by the continuity and Navier–Stokes equations:

$$\nabla \cdot (\rho V) = 0, \tag{3}$$

$$\frac{\partial(\rho V)}{\partial t} + \nabla \cdot (\rho V \otimes V) = -\nabla \cdot (p\mathbf{I}) + \nabla \cdot \mathbf{T}_{\mathrm{v}} + f_b, \tag{4}$$

where V stands for the velocity vector field, p is the pressure, $\mathbf{T}_{\mathrm{v}}$ is the viscous stress tensor and f_b is the resultant of the body forces.

The VOF multiphase Eulerian approach model implementation in Simcenter STAR-CCM+ belongs to the family of interface-capturing methods that predict the distribution and the movement of the interface of immiscible phases. This modeling approach assumes that the mesh resolution is sufficient to resolve the position and the shape of the interface between the phases. In this paper, the focus is not on elaborating the theoretical background of the functions in CFD software, but rather on presenting a methodology that can serve as a quick way to set up simulations. Therefore, more about the VOF method can be found in [52], where this concept is detailed.

An important quality of a system of immiscible phases (air and water) is that the fluids always remain separated by a sharp interface. The High-Resolution Interface Capturing (HRIC) scheme is used to mimic the convective transport of immiscible fluid components, resulting in a scheme that is suited for tracking sharp interfaces.

As in the OWT, the k-ω SST turbulence model was used here according to the requirements defined in [47].

2.4.1. Actuator Disk Propeller Model

The body force propeller method is used to model the effects of a propeller such as thrust and thereby creating propulsion without actually resolving the geometry of the propeller. The method employs a uniform volume force distribution over the cylindrical virtual disk. The volume force varies in the radial direction, so the total force can be calculated as the volume integral for the whole modeled cylinder. The radial distribution of the force components follows the Goldstein optimum [53] and is given by

$$f_{bx} = A_x r* \sqrt{1 - r*}, \tag{5}$$

where $r*$ is the normalized disk radius defined as

$$r* = \frac{r' - r'_h}{1 - r'_h}, \tag{6}$$

where $r' = r/R_p$ and $r'_h = R_h/R_p$. Volume force f_{bx} is the body force component in the axial direction, r is the radial coordinate, R_h is the hub radius and R_p is the propeller tip radius. Coefficient A_x is defined as

$$A_x = \frac{105}{8\pi} \frac{T}{t_d(R_p - R_h)(3R_h + 4R_p)}, \tag{7}$$

where T stands for the propeller thrust and t_d is the virtual disk thickness. More about this can be found in [54]. The simulation is performed for a certain operating point specified by the thrust (T). The advance ratio is calculated by solving the following equation numerically (J—advance coefficient, D—propeller diameter):

$$f(J) = K_T - K'_T \tag{8}$$

where K_T is evaluated from the propeller performance curve and K'_T is evaluated as

$$K'_T = \frac{J^2 T_{Operating\ point}}{\rho_w V_A^2 D^2} \tag{9}$$

With K_T available, the thrust is calculated for the propeller:

$$T = \frac{K_T \rho_w V_A^2 D^2}{J^2} \tag{10}$$

With $T(T_{Operating\ point})$ available, the axial body force component can be calculated. Inflow plane is the plane inside the actuator disk where the volume-averaged velocity and density are computed. The input thrust in this part of the simulation is equal to the total resistance that is evaluated as the sum of the pressure resistance and viscous resistance of the hull with the rudder included.

The wake fraction (w) is extracted at the propeller axis plane in a steady resistance simulation.

The thrust deduction factor is calculated as per

$$t = 1 - \frac{R_T}{T}, \tag{11}$$

where R_T is the total resistance of the ship evaluated in the steady resistance simulation.

2.4.2. Steady Resistance Simulations

Total resistance, including viscous and pressure resistance, is obtained by rerunning the self-propulsion simulation with a disabled actuator disk. This procedure implies the same mesh as was used earlier but only without an actuator disk.

2.4.3. Boundary Conditions

Fluid domain dimensions are defined as follows (from origin):

- Inlet: $2.5L_{pp}$—defined as velocity inlet;
- Outlet: $3L_{pp}$—defined as pressure outlet with wave damping boundary option included;
- Bottom: $1.5L_{pp}$—defined as velocity inlet;
- Top: $1L_{pp}$—defined as velocity inlet;
- Port Side: $2L_{pp}$—defined as symmetry plane with wave damping boundary option included;
- Starboard Side: $2L_{pp}$—defined as symmetry plane with wave damping boundary option included.

The wave damping length is defined as two wave lengths, where the wave length is calculated as per

$$2\pi \cdot \mathrm{Fn}_L^2 \cdot L_{pp}, \tag{12}$$

where Fn_L^2 is the Froude number based on the length.

2.4.4. Rigid Body Motion

Two degrees of freedom are allowed for the motion for the vessel, namely pitch and heave, allowing for the dynamic trim and sinkage of the vessel.

2.4.5. Mesh

The triangle surface meshing method has been used to build the mesh. The prism-layer mesher generates prismatic cell layers next to the boundary layer. The number of these layers is calculated as per

$$m = \frac{\ln\left(1 - (1 - sf)\frac{\delta}{y_1}\right)}{\ln(sf)}, \tag{13}$$

where $sf = 1.3$ is the stretch factor, δ is the boundary-layer thickness and y_1 is the first-layer thickness. These cells help to capture the viscous effects in the boundary layer correctly in the region where the thickness is calculated as per [55]

$$\delta = \frac{0.16 L_{wl}}{\sqrt[7]{\mathrm{Re}_{L_{wl}}}}, \tag{14}$$

where L_{wl} is the length at the waterline of the ship and Re is the Reynolds number (L_{wl} in subscription means that the Reynolds number is calculated with the waterline length as a reference value, otherwise L_{pp} is used). The trimmed cell mesher creates a volume mesh by cutting a template mesh with the surface geometry. The first-layer thickness is calculated for y^+ = 150 by following the guidelines in [47] where it is emphasized that y^+ should be in a range from 30 to 300. This value (150) is used as the target factor to ensure that the actual y^+ values will fall within the required range.

$$y_1 = \frac{150\nu}{u_\tau}, \tag{15}$$

where ν is the kinematic viscosity and u_τ is the shear velocity. The shear velocity or frictional velocity is a fictious quantity, it characterizes the shear at the boundary layer, and it is given by

$$u_\tau = \sqrt{\frac{\tau_w}{\rho_w}}, \tag{16}$$

where τ_w is the wall shear stress. This presents a contradiction as follows: determining the thickness of the initial layer requires knowing the stress on the vessel's hull, which in turn needs to be assessed using CFD. Hence, the recommendation from the ITTC [46,56] is utilized in this scenario to compute the wall shear stress for the hull.

$$\tau_w = 0.5((1+k)C_{FS} + C_A)V_s^2 \rho_w, \tag{17}$$

where k is a form factor, C_{FS} is the frictional resistance coefficient and C_A is the correlation allowance.

$$C_{FS} = \frac{0.075}{\left(\log_{10}\mathrm{Re} - 2\right)^2}, \tag{18}$$

$$C_A = \left(5.68 - 0.6\log_{10}\mathrm{Re}\right) \cdot 10^{-3} \tag{19}$$

The form factor is calculated as the mean value of the equations obtained by Grigson, Wright and Conn and Ferguson given in [57]:

$$k = \frac{0.028 + 3.3\left(\frac{WS}{L_{pp}^2}\sqrt{C_B\frac{B}{L_{pp}}}\right) + 18.7\left(C_B\frac{B}{L_{pp}}\right)^2 + 2.48C_B^{0.1526}\left(\frac{B}{T_s}\right)^{0.0533}\left(\frac{B}{L_{pp}}\right)^{0.3856} - 1}{3}. \tag{20}$$

A grid convergence study is performed to assess the convergence of the results by systematically refining a specific input parameter in StarCCM+. In this study, three simulations are conducted, where the chosen input parameter is varied while keeping all other parameters constant. The refinement value used in this study aligns with the guidelines specified in [58] and is set to be uniform ($\sqrt{2}$). By systematically refining the input parameter and comparing the results from the different simulations, the grid convergence study aims to determine the level of convergence and establish the appropriate grid resolution for accurate and reliable results.

The convergence ratio is defined as

$$R = \frac{\varepsilon_{21}}{\varepsilon_{32}}, \tag{21}$$

where ε_{21} is the difference between the solution obtained using medium and fine mesh and ε_{32} is the difference between the solution obtained using coarse and medium mesh. R is used for the estimation of the convergence conditions: monotonic convergence is achieved when $0 < R < 1$, oscillatory convergence is achieved when $-1 < R < 0$ and divergence is achieved when $|R| > 1$. The numerical uncertainty and error for monotonic convergence condition is estimated using generalized Richardson extrapolation (RE). The order of accuracy is calculated as per

$$p = \frac{\ln(\varepsilon_{32}/\varepsilon_{21})}{\ln\sqrt{2}}, \tag{22}$$

$$\delta_{RE} = \frac{\varepsilon_{21}}{\sqrt{2}^p - 1}, \tag{23}$$

The generalized RE solution ($\hat{S}_{RE}$) can be derived by

$$\hat{S}_{RE} = \hat{S}_1 - |\delta_{RE}|. \tag{24}$$

To estimate the grid uncertainty U_G, a safety factor approach is employed, defining U_G as

$$U_G = FS \cdot |\delta_{RE}|, \tag{25}$$

where $FS = 1.25$ is a safety factor. The normalized uncertainties are calculated as follows:

$$\overline{U} = \frac{U_G}{\hat{S}_{RE}} \cdot 100\%. \tag{26}$$

2.4.6. Post-Processing

In the numerical simulations conducted for this study, the direct consideration of the roughness effects and air resistance resulting from the presence of a superstructure is not included. However, these effects are accounted for in the post-processing stage by following the recommended procedures and guidelines outlined in [59]. The ITTC guidelines provide specific methodologies for incorporating the effects of the roughness and air resistance into the analysis, allowing for an assessment of the overall performance and characteristics of the ship. The roughness allowance (ΔC_F) is calculated as per [60]

$$\Delta C_F = 0.044\left[\left(\frac{k_s}{L_{WL}}\right)^{\frac{1}{3}} - 10\mathrm{Re}^{-\frac{1}{3}}\right] + 0.000125 \tag{27}$$

and the air resistance coefficient (C_{AAS}) [54] is

$$C_{AAS} = 0.8\frac{\rho_A \cdot A_{VS}}{\rho_w \cdot WS}, \tag{28}$$

where k_s indicates the roughness of the hull surface equals $150{\cdot}10^{-6}$ m [58], and A_{VS} is the projected area of the ship superstructure to the transverse plane. The new total resistance is calculated as

$$F_T' = \frac{1}{2}V_s^2 \cdot WS \cdot \rho_w \cdot (C_T + \Delta C_F + C_{AAS}), \tag{29}$$

where C_T refers to the total resistance coefficient obtained as a result of the CFD simulation.

The new thrust is calculated as per

$$T' = \frac{R_T'}{1 - t'} \tag{30}$$

Together with the propeller performance data (K_T, K_Q, $\eta_0(J)$), the new operating point is obtained by the numerical solving of equation:

$$\frac{T'}{\rho_w \cdot V_A^2 \cdot D^2} J^2 - K_T(J) = 0 \tag{31}$$

Once the advance ratio coefficient is obtained, the propeller speed (n) and torque (Q_0) can be evaluated:

$$n = \frac{V_A}{JD} = \frac{(1 - w')V}{JD}, \tag{32}$$

$$Q_0 = K_Q \rho_w n^2 D^5, \tag{33}$$

where K_Q is evaluated from the propeller performance curve and Q_0 is the torque in the open water condition. Hence, the actuator disk approach has been used in this case and the relative rotative efficiency is adopted to be 1, which means that the torque is calculated as

$$Q = \frac{Q_0}{\eta_R} \approx Q_0 \tag{34}$$

Finally, the brake power can be evaluated as

$$P_b = \frac{2n\pi Q}{\eta_S}, \tag{35}$$

where η_S is the shaft efficiency, adopted to be 0.99. The hull efficiency is considered to be the same as in the steady resistance simulations, i.e., $w' = w$ and $t' = t$, where w' and t' are the wake fraction coefficient and thrust deduction factor in post-processing.

Calibration factors C_n and C_{Pb} are calculated as the average ration between the model test (MT) results and CFD results for the propeller speed (n) and brake power (P_b).

$$C_n = \frac{n_{MT}}{n_{CFD}} \tag{36}$$

$$C_{Pb} = \frac{P_{b_{MT}}}{P_{b_{CFD}}} \tag{37}$$

2.5. Trim Optimization

Trim optimization was conducted for drafts of 7.5 m, 8 m and 8.7 m at speeds of 12.5 kn, 15 kn and 18 kn at 7 different conditions (trims). The range of trims goes from −1.5 m to 1.5 m with a 0.5 m step. A negative sign means the trim by the bow and a positive sign, the trim by the stern. The outcome of trim optimization in CFD analysis typically involves determining the optimal trim settings for a vessel at considered drafts and speeds. This optimization aims to minimize resistance and ensure optimal performance under different operating conditions. By adjusting the vessel's trim, operators can achieve better hydrodynamic characteristics, leading to improved overall performance and operational efficiency. With the available specific fuel oil consumption (SFOC) curve as a function of P_b, a possible reduction in fuel consumption was also calculated.

2.6. Mathematical Model for Assessing the Outcomes from Trim Optimization

The first outcomes from the CFD simulations are the brake power and propeller speed for one ship speed and draft, i.e., trim, i.e., displacement. The results are presented in the form of relative differences between the brake power of the trimmed ship and the ship on an even keel. A negative sign indicates that there is a saving, i.e., a reduction in the required brake power for that case. A graphical example of the results is shown in Figure 3a, where the relative brake power and fuel oil consumption savings are depicted as an area with the ship speed on the x-axis, trim on the y-axis and relative power/fuel oil consumption

savings on the z-axis. The optimal (favorable) sailing zone is depicted in green on the same diagram, meaning that at the current trim and speed, less power or fuel oil consumption is required compared to when the ship is sailing on an even keel. The yellow zone represents the transitional zone where the change in the required brake power/fuel oil consumption is negligible, while the red zone is the zone to be avoided because more power/fuel oil is needed for the ship to sail at the same speed compared to sailing on an even keel. Each point on the surface in Figure 3a corresponds to a certain displacement, where it depends solely on the trim. For easier calculation, a surface ∇ (trim, V_S) is formed from each line ∇ (trim), and the surfaces for all three considered drafts are shown in Figure 3b. In order to have smooth surfaces, all values estimated from the CFD analysis are linearly interpolated. Therefore, the initial matrix 3 × 7 (3 speeds, 7 trims) is reshaped to 151 × 111 with a speed step of 0.05 kn and trim step of 0.02 m. The main parameters from the initial matrix are depicted with black lines in Figure 3a.

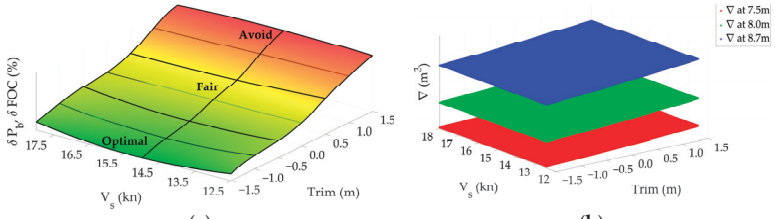

(**a**) (**b**)

Figure 3. Results representation: (**a**) brake power/fuel oil consumption reduction for one draft; (**b**) displacements for three considered drafts and each trim.

Additionally, values between drafts of 7.5 m and 8 m and from 8 m to 8.7 m are linearly interpolated with a step of 0.01 m. Thus, from the initial matrix of 3 × 7 × 3 (3 speeds, 7 trims, 3 drafts), matrices (Σ_m) of size 151 × 111 × 120 are obtained where m is δP_b or ∇.

The daily fuel oil consumption (DFOC) is estimated based on the determined brake power from the CFD simulation and the available specific fuel oil consumption (SFOC) curve for the engine installed on the ship. The SFOC curve is approximated by a sixth-degree polynomial:

$$\mathrm{SFOC} = -5.54 \cdot 10^{-23} {P_b}^6 + 3.75 \cdot 10^{-18} {P_b}^5 - 8.28 \cdot 10^{-14} {P_b}^4 + 8.00 \cdot 10^{-10} {P_b}^3 - 3.11 \cdot 10^{-6} {P_b}^2 - 9.63 \cdot 10^{-4} P_b + 209 \quad (38)$$

The mentioned polynomial provides SFOC values with an average error of 0.02% compared to the exact available values from the reference document.

With the evaluated DFOC for each brake power, the same diagrams as shown in Figure 4 can be created (Figure 5).

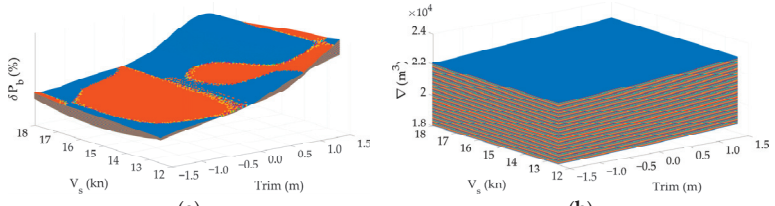

(**a**) (**b**)

Figure 4. Results representation: (**a**) brake power reduction (δP_b) for 120 drafts; (**b**) displacements (∇) for 120 drafts and each trim.

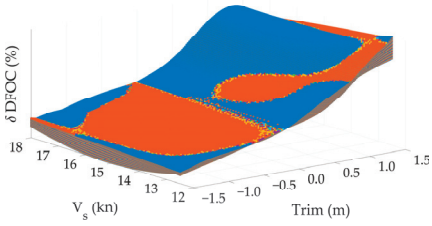

Figure 5. Results representation for DFOC reduction.

In operations, after loading cargo onto the ship, only the displacement is known. The goal of the conducted trim optimization is to find the optimal position, i.e., trim, and recommend the sailing speed based on that single parameter. The optimal trim and recommended speed are those at which the greatest savings in brake power, and consequently fuel consumption, are achieved. The mathematical expression of the above statement is as follows:

$$\delta P_{b_{\min}} = \min_{ijk}\left(\delta P_b{}^{(ijk)} \middle| \left|\nabla^{(ijk)} - \nabla_{LC}\right| \leq \varepsilon \cdot \nabla_{LC}\right), \tag{39}$$

where $\delta P_{b_{\min}}$ is the biggest brake power reduction where the corresponding displacement $\nabla^{(ijk)}$ is within a tolerance (ε= 0.0001) of the target displacement (∇_{LC}). Index i represents the speed, j represents the trim and k represents the brake power reduction, i.e., displacement in matrix Σ_m. When $\delta P_{b_{\min}}$ is found, it is easy to extract indices i, j and k therefore to derive the optimum trim and speed for the corresponding displacement, i.e., mean draft. In practice, there may be a need for speed as an input parameter, which depends on the operational requirements, and this case will be addressed in subsequent work.

Mathematical Model for Assessing Brake Power, DFOC and Propeller Speed

A sophisticated mathematical model utilizing artificial neural networks (ANNs) has been developed based on the CFD results. By specifically addressing the challenges posed by non-simulated loading conditions, this model offers a solution for estimating parameters such as the brake power, propeller speed and DFOC.

At its core, the model employs a feedforward artificial neural network (FFANN), a fundamental architecture in machine learning and deep learning. The FFANN's structure comprises interconnected layers of neurons, including an input layer (white circles in Figure 6), one or more hidden layers (gray circles in Figure 6) and an output layer (black circles in Figure 6). Each neuron is equipped with adjustable parameters called biases, which introduce flexibility by allowing for offsets or shifts in output. During training, these biases are fine-tuned to better fit the data and ensure the accurate estimation of the desired parameters.

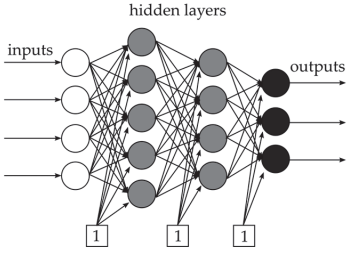

Figure 6. Illustrated ANN structure of interconnected neurons (circles) and biases (squares).

One of the key features of the FFANN is its one-directional flow of information, from the input layer through the hidden layers to the output layer. This design simplifies the learning process and enables the efficient modeling of complex data relationships. Additionally, activation functions embedded within neurons introduce non-linearity, enabling the network to capture patterns present in real-world data.

Overall, this innovative approach represents a significant step forward in the advancement of engineering solutions. It not only addresses the inherent challenges of non-simulated loading conditions but also sets a precedent for the application of artificial intelligence in optimizing the performance of complex systems. As further research and development are conducted in this field, the potential for ANNs to revolutionize engineering practices and transportation systems continues to expand.

In the context of a feedforward artificial neural network (FFANN), the connections between neurons are governed by weights, which dictate the strength of the connections. These weights are adjusted during the training process using an algorithm called backpropagation. The name "backpropagation" stems from its mechanism of iteratively propagating errors backward through the network to adjust the weights and biases of neurons.

The training process involves two phases: the forward pass and the backward pass. During the forward pass, input data are fed into the network, and predictions are made based on the current weights and biases. These predictions are compared to the actual outputs, and the resulting error is calculated.

In the backward pass, this error is propagated backward through the network, layer by layer. The gradient of the error with respect to each weight and bias is computed using techniques like the chain rule of calculus. These gradients indicate the direction and magnitude of adjustment required to minimize the error. The weights and biases are then updated accordingly.

At each neuron, the weighted sum of the inputs is computed by multiplying each input value by its corresponding weight and summing the results. This sum is then combined with the neuron's bias:

$$S_{x,i} = f\left(\sum_i S_{x-1,i} \cdot w_{x,i} + b_{x,i}\right), \tag{40}$$

where f—activation function, $S_{x,i}$—output signal, of ith neuron in xth layer, $S_{x-1,i}$—output of ith neuron in $x-1$th layer, $w_{x,i}$—weights connected to the neuron and $b_{x,i}$—corresponding bias.

The resulting value is passed through an activation function, which introduces non-linearity into the network. Common activation functions include sigmoid, tanh and others, each serving different purposes in facilitating learning and modeling complex data relationships. In this case, the sigmoid function is used as follows:

$$f = \frac{1}{1+e^x} \tag{41}$$

The general form of the function is

$$Y_u = \frac{f_p\left(p + \sum_{w=1}^{r}\left(P_w \cdot f_{p-1}\left(\ldots \cdot f_2\left(b_i + \sum_{j=1}^{m}\left(B_{ij} \cdot f_1\left(a_j + \sum_{k=1}^{n}\left(A_{jk} \cdot (P_k \cdot X_k + R_k)\right)\right)\right)\right)\ldots\right)\right)\right) - G_u}{L_u}, \tag{42}$$

where

- X_k—input parameters (number of neurons in input layer);
- Y_u—output parameters (number of neurons in output layer);
- $f_1, f_2, \ldots, f_{(p-1)}, f_p$—activation function;
- $k, j, i, \ldots, v, w$—number of neurons in each layer;
- $A, B, \ldots, P$—weights between layers;
- $a, b, \ldots, p$—weights between neurons in each layer and bias.

The software that has been used for training the ANN in this study is called aNETka, developed in LabVIEW. The output file from this software is not a direct mathematical model, just weights coefficients and four additional parameters called Down offset Input (DI_k), Down offset Target (DT_u), Up offset Input (UI_k) and Up offset Target (UT_u).

$$DI_k = \min(X_k) \tag{43}$$

$$DT_u = \min(Y_u) \tag{44}$$

$$UI_k = \max(X_k - \min(X_k)) \tag{45}$$

$$UT_u = \max(Y_u - \min(Y_u)) \tag{46}$$

The rest of the parameters are calculated as follows:

$$P_k = \frac{0.9}{UI_k} \tag{47}$$

$$R_k = -\frac{0.9 \cdot DI_k}{UI_k} + 0.05 \tag{48}$$

$$L_u = \frac{0.9}{UT_u} \tag{49}$$

$$G_u = -\frac{0.9 \cdot DT_u}{UT_u} + 0.05 \tag{50}$$

In the trim optimization study, data obtained from CFD analysis, including brake power, DFOC and propeller speed, were utilized as the output layer for training the artificial neural network (ANN), while the draft, speed, trim and displacement are considered as the input layer.

The applicability range of the model is defined within specific boundaries for each parameter: draft (T_s) ranges from 7.5 to 8.7 m, speed (V_s) ranges from 12.5 to 18 kn, trim ranges from −1.5 to +1.5 m and displacement (∇) ranges from 18,079 to 22,884 m^3. The input dataset for training consists of a 63 × 7 matrix, where number 63 represents the total number of CFD simulations conducted and number 7 denotes each parameter. Four parameters are designated as the input layer (draft, displacement, trim, speed), while the remaining three represent the output layer (propeller speed, brake power, DFOC).

Prior to training, all data were normalized within the range of 0.05 to 0.95 to ensure the stability of activation functions, which can be sensitive to extremely small or large input values. This normalization step enhances the convergence and effectiveness of the training process.

For testing purposes, 8% of the total input parameters (5 out of 63) were reserved, while the remaining data were allocated for training. The training process was programmed to iteratively adjust the weights and biases of the network, stopping when the Root Mean Square (RMS) percentage error reached the target threshold of 1%:

$$RMS = \sqrt{\left(\frac{\Sigma \left[\left(\frac{TV - OV}{TV} \right)^2 \right]}{N} \right)}, \tag{51}$$

where TV—target values, OV—ANN output values, N—number of values.

When creating a neural network model, it is vital to carefully consider the number of neurons in each layer and the presence of hidden layers. These decisions must be well informed and tailored to match the complexity of the problem at hand and the specific attributes of the dataset.

In practice, just before leaving the port, the parameters that are categorized into the input layer are usually known, but until now, the fuel consumption could never be predicted in advance. It is very common that fuel consumption and the power engaged by the engine are not monitored during the journey, and the amount of fuel used was always determined retroactively. With such mathematical models and conducted CFD simulations for a larger number of loading conditions, it is possible not only to predict the fuel consumption in advance but also to determine the optimal speed at which the ship should sail to minimize consumption. Knowing the fuel consumption, it is easy to determine the amount of CO_2 emitted and predict the energy rating to which the ship will belong according to [8], which is a direct indicator of energy efficiency.

2.7. Trim Optimization Software Application

Formulas derived for a particular purpose may not always be user-friendly, leading to the creation of an application to facilitate their use. In this case, an application developed using MATLAB's App Designer package offers a user-friendly interface for utilizing these formulas. The application allows users to input only one parameter, i.e., displacement and obtain corresponding output values efficiently: optimum trim, speed, propeller speed, brake power and DFOC. This enables users to quickly obtain results without the need for manual calculations.

3. Results

The results in this section will be presented in subsections in the same order, i.e., following the phases outlined in Section 2 (Methods).

3.1. Three-Dimensional Modeling

In Figure 7, a 3D model and characteristic sections of the waterlines (a), buttocks (b) and frames (c) are depicted in various projections obtained based on the construction drawings.

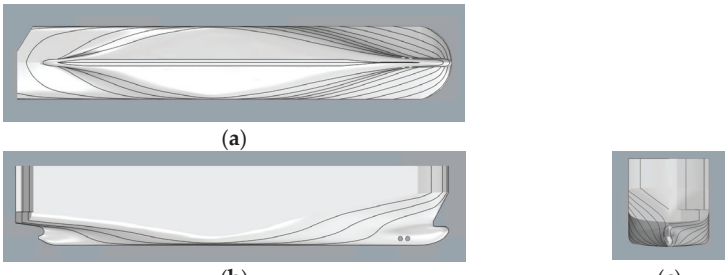

Figure 7. The 3D model of the RO-RO ship: (**a**) bottom view—waterlines; (**b**) starboard side view—buttocks; (**c**) aft view—frames.

The propeller underwent a modeling process, aligning with the specifications outlined in the reference drawing. A comparison was conducted between the 3D model of the propeller and the reference drawing to ensure precise adherence to the intended design. The findings of this comparison are visually presented in Figure 8, offering a clear representation of the propeller's details and shape. The 3D model of the propeller (Figure 9a) enables engineers and designers to perform CFD simulations and evaluate performance characteristics. The rudder was modeled to faithfully represent its original design but without any gaps between the rudder shaft and rudder shell (Figure 9b).

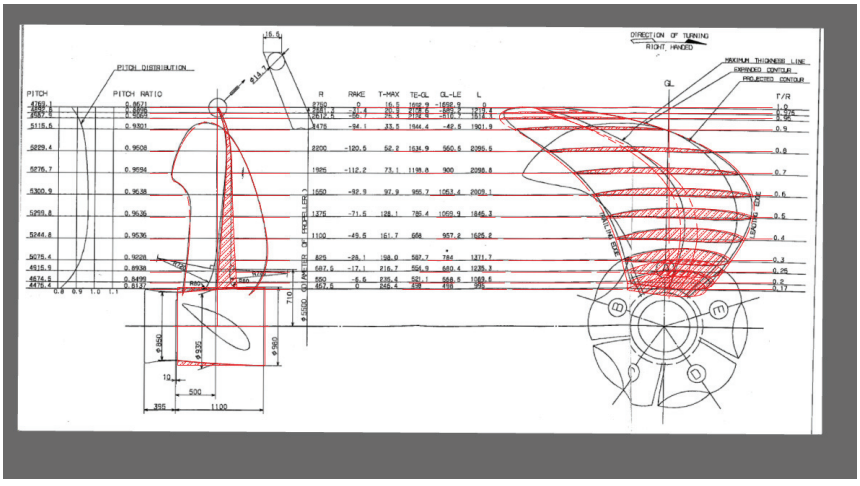

Figure 8. Propeller: comparison between drawing of 3D modeled propeller (red colored) and scanned reference drawing.

(**a**) (**b**)

Figure 9. Propeller and rudder: (**a**) original propeller; (**b**) rudder.

3.2. First-Level Verification

The reliability of the developed 3D model was assessed by comparing its calculated hydrostatic parameters against the corresponding ones given in the Trim & Stability booklet. The corresponding percentage deviations between C_b, ∇, *LCB* and *WS* are listed in Table 3.

Table 3. Comparison between hydrostatics data obtained on the basis of 3D model and Trim & Stability booklet.

T_s (m) (Trim = 0)	C_b	∇	*LCB*	*WS*
4	0.52%	0.88%	−0.03%	0.54%
5	0.43%	0.77%	−0.03%	0.74%
6	0.34%	0.62%	−0.01%	0.63%
7	0.27%	0.51%	0.01%	0.38%
7.5	0.22%	0.43%	0.03%	0.42%
8	0.21%	0.42%	0.03%	0.74%
8.7	0.23%	0.42%	0.03%	0.79%
9	0.31%	0.40%	0.03%	0.82%
10	0.14%	0.31%	0.03%	0.87%

It can be easily observed that deviations between the calculated and reference values of the hydrostatic data are less than 1%, especially for the range of interest (drafts 7.5 m, 8.0 m and 8.7 m).

3.3. Open Water Test

A graphical representation of the CFD results (K_T, K_Q, η_0) from the conducted OWT with the B-series propeller with data obtained with the mathematical model is presented in Figure 10a, while the relative differences between each evaluated parameter are presented in Table 4.

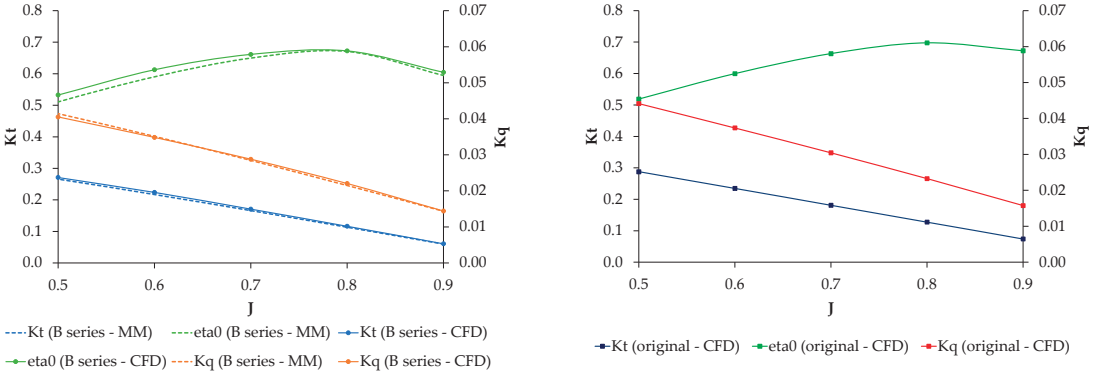

(**a**) (**b**)

Figure 10. Propeller characteristics. MM—results based on mathematical model, CFD—results based on OWT CFD simulations: (**a**) B-series propeller; (**b**) original propeller.

Table 4. Relative differences between data obtained with mathematical model and results from CFD.

J	δK_T	δK_Q	$\delta \eta_0$
0.5	1.9%	−2.3%	2.2%
0.6	2.9%	−0.8%	2.3%
0.7	2.8%	1.1%	1.2%
0.8	2.7%	2.4%	0.2%
0.9	2.2%	0.6%	1.0%

As the results for each of the advance coefficients are within the prescribed 3%, the CFD calculation methodology is considered valid; therefore, with the same setup, the original propeller OWT was conducted, and the results are presented in Figure 10b.

3.4. Second-Level Verification

The obtained results from the CFD OWT simulation with the original propeller are used as the input propeller characteristics data in self-propulsion simulations. The first group of simulations were conducted at a design draft (7.8 m) and speeds of 17 kn, 19 kn and 21 kn because for these draft and speeds model tests, data are available.

In Figure 11, the meshed domain is shown. For a better evaluation of the free surface, additional refinement zones are defined in wave field zones and near the hull (Figure 12a,b).

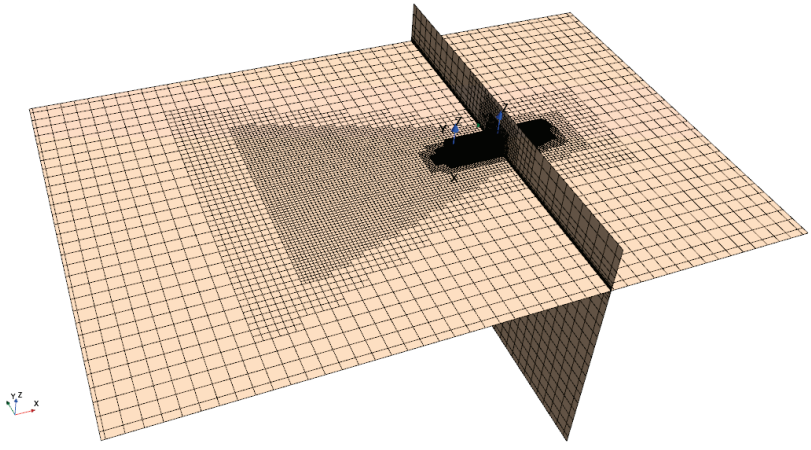

Figure 11. Domain—mesh.

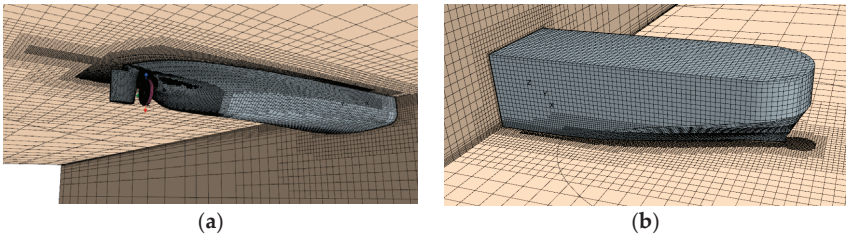

(**a**) (**b**)

Figure 12. Refinement zones: (**a**) stern part; (**b**) bow part.

The results from the completed self-propulsion simulations and steady resistance simulations by following the procedure described in Section 2.4 are presented in Table 5, where R_p is the pressure resistance and R_v is the viscous resistance.

Table 5. Results from CFD analysis for design draft.

V_s (kn)	R_p (kN)	R_v (kN)	R_T (kN)	t (-)	w (-)	T' (kN)	Q (kNm)	η_0 (-)	n (rpm)	P_b (kW)
17	125.454	292.216	475.936	0.1746	0.2487	576.644	466.316	0.6736	103.1	5083
19	178.852	366.869	622.133	0.1579	0.2479	738.831	595.864	0.6721	116.0	7309
21	321.762	438.076	857.035	0.1600	0.2458	1020.295	820.407	0.6656	132.8	11,523

The results from the CFD analysis and model test data are graphically presented in Figure 13. In Figure 13a, the brake power as a function of the ship speed curve is depicted while in Figure 13b, the brake power as a function of the propeller speed is presented.

The calibration factors are C_n = 1.05 and C_{P_b} = 1.04, which means that a 5% deviation requirement in the results compared to the model test is met. Differences in the results obtained from the CFD analysis and model testing can arise from several factors, such as the reliability of the model testing results, the reliability of the method used to extrapolate the results from the model to full scale, as well as the CFD analysis itself. A portion of the difference undoubtedly stems from the differences in the OWT results presented in Table 4. Due to all the aforementioned reasons, an acceptable margin of 5% exists according to [47].

In Figure 14, the y+ values for the underwater part of the hull are presented and the average y+ value is pointed out (average y^+ = 70.61). A particular case is extracted from the steady resistance simulation at a speed of 18 kn at 7.5 m draft. For all other speeds, the y^+ values do not deviate from those aforementioned.

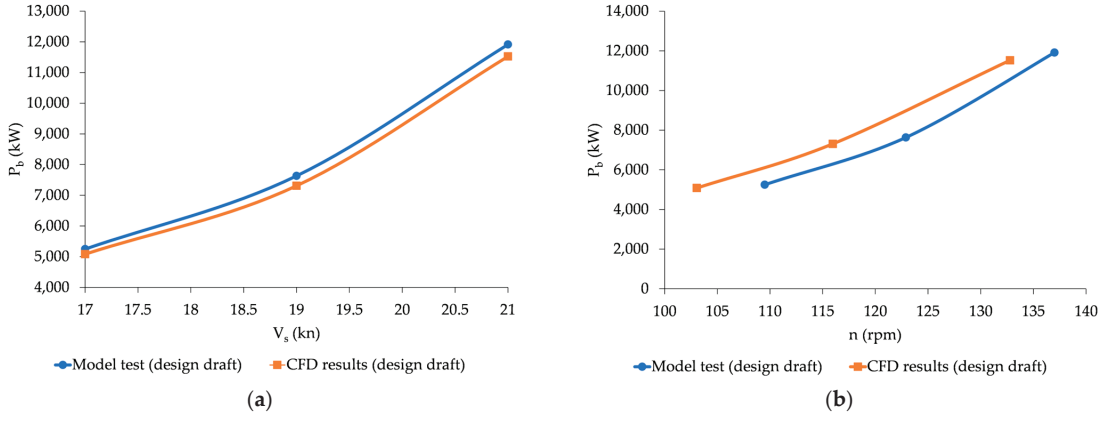

Figure 13. CFD results for design draft: (**a**) P_b as a function of V_s; (**b**) P_b as a function of n.

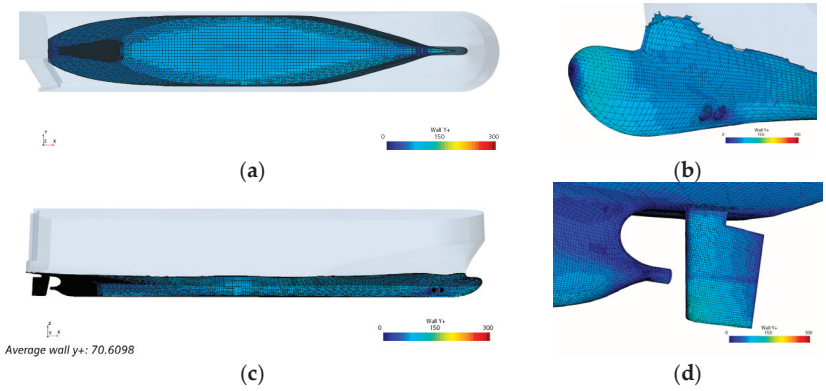

Figure 14. y^+ values: (**a**) bottom view; (**b**) bow part—perspective view; (**c**) starboard side view; (**d**) stern part—perspective view.

Three different meshes were considered for the grid uncertainty study with mesh sizes of 1.852 million cells (coarse), 3.628 million cells (medium) and 7.454 million cells (fine). The study was conducted at a speed of 18 knots at a 7.5 m draft (even keel). The results of the study, including the grid uncertainties for thrust, are presented in Table 6.

Table 6. Grid uncertainty results for thrust.

Mesh Quality	T (kN)
Coarse	544.445
Medium	539.287
Fine	535.586
$\overline{U}$	2.2%

3.5. Trim Optimization

The trim optimization CFD study was performed at a 7.5 m, 8 m and 8.7 m draft for a range of speeds, 12.5 kn, 15 kn and 18 kn, at seven different loading (trim) conditions and coarse mesh. Therefore, the results obtained for the propeller speed, brake power and estimated DFOC are presented in Tables 7–9, respectively.

Table 7. Propeller speed (n [rpm]): CFD analysis results.

		Trim by Bow (m)			Even Keel		Trim by Stern (m)	
	V_s (kn)	−1.5	−1	−0.5	0	0.5	1	1.5
7.5 m	12.5	82.7	83.6	84.2	85.0	86.6	87.9	88.9
	15	97.2	98.3	99.3	100.9	102.2	103.5	105.3
	18	116.8	117.9	119.0	119.7	121.1	122.6	125.1
8.0 m	12.5	82.4	83.1	84.0	84.7	85.7	87.7	89.5
	15	98.3	99.3	100.2	100.7	102.3	103.5	105.8
	18	120.4	120.2	121.2	122.3	123.5	126.1	127.4
8.7 m	12.5	84.4	85.0	85.7	86.4	87.3	89.1	91.2
	15	101.9	102.3	103.1	104.0	105.3	107.1	108.9
	18	125.1	125.6	126.0	127.4	129.1	131.3	132.9

Table 8. Brake power (P_b [kW]): CFD analysis results.

		Trim by Bow (m)			Even Keel	Trim by Stern (m)		
	V_s (kn)	−1.5	−1	−0.5	0	−1.5	−1	−0.5
7.5 m	12.5	2248	2335	2370	2447	2601	2739	2837
	15	3509	3665	3772	3965	4130	4414	4642
	18	5957	6187	6345	6441	6667	7124	7480
8.0 m	12.5	2155	2221	2285	2357	2450	2664	2882
	15	3587	3719	3818	3869	4073	4352	4639
	18	6595	6567	6750	6942	7120	7879	7991
8.7 m	12.5	2293	2353	2403	2478	2564	2771	3048
	15	4018	4072	4181	4303	4504	4890	5113
	18	7531	7663	7707	8003	8405	9143	9361

Table 9. DFOC [t fuel/day]: CFD analysis results.

		Trim by Bow (m)			Even Keel	Trim by Stern (m)		
	V_s (kn)	−1.5	−1	−0.5	0	−1.5	−1	−0.5
7.5 m	12.5	10.70	11.08	11.24	11.57	12.25	12.84	13.26
	15	16.11	16.75	17.20	18.00	18.68	19.85	20.79
	18	26.22	27.18	27.83	28.23	29.18	31.09	32.58
8.0 m	12.5	10.29	10.58	10.86	11.18	11.59	12.52	13.46
	15	16.43	16.98	17.39	17.60	18.45	19.60	20.78
	18	28.88	28.76	29.53	30.33	31.08	34.26	34.73
8.7 m	12.5	10.90	11.16	11.38	11.71	12.08	12.98	14.16
	15	18.22	18.44	18.89	19.39	20.22	21.81	22.73
	18	32.80	33.35	33.53	34.78	36.46	39.56	40.48

3.6. Mathematical Model for Assessing the Outcomes from Trim Optimization

Brake power reduction and DFOC reduction are linearly interpolated for additional trims and speeds (values considered in CFD analysis) and the results are graphically presented for the three considered drafts in Figures 15 and 16. The optimum trim and speed are also depicted with red points in Figure 16. The black line in Figures 15 and 16 represents a neutral line, i.e., the state of the even keel against which the brake power savings and DFOC savings are calculated.

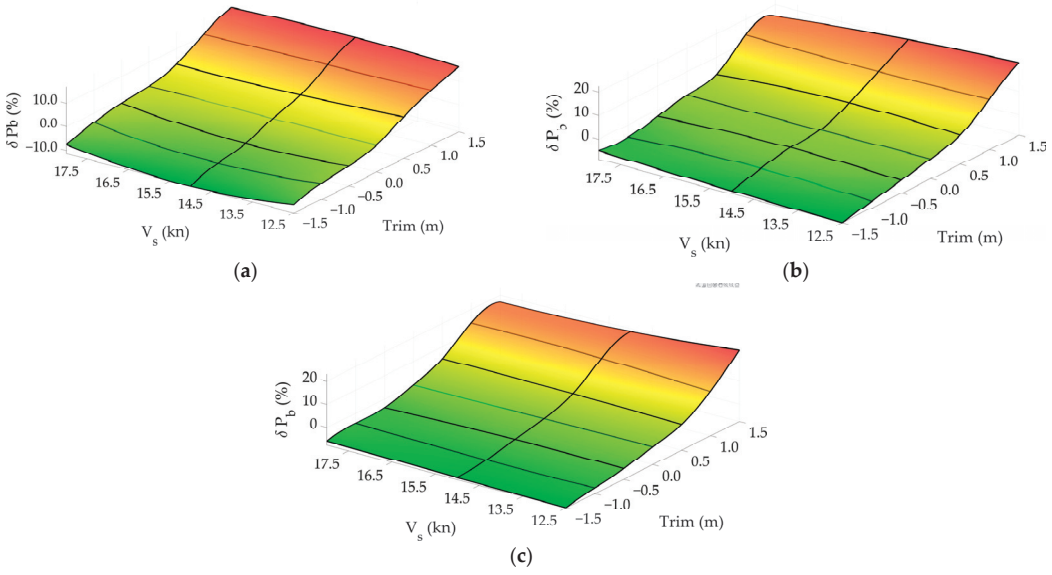

Figure 15. Brake power reduction: (**a**) T_s = 7.5 m; (**b**) T_s = 8.0 m; (**c**) T_s = 8.7 m.

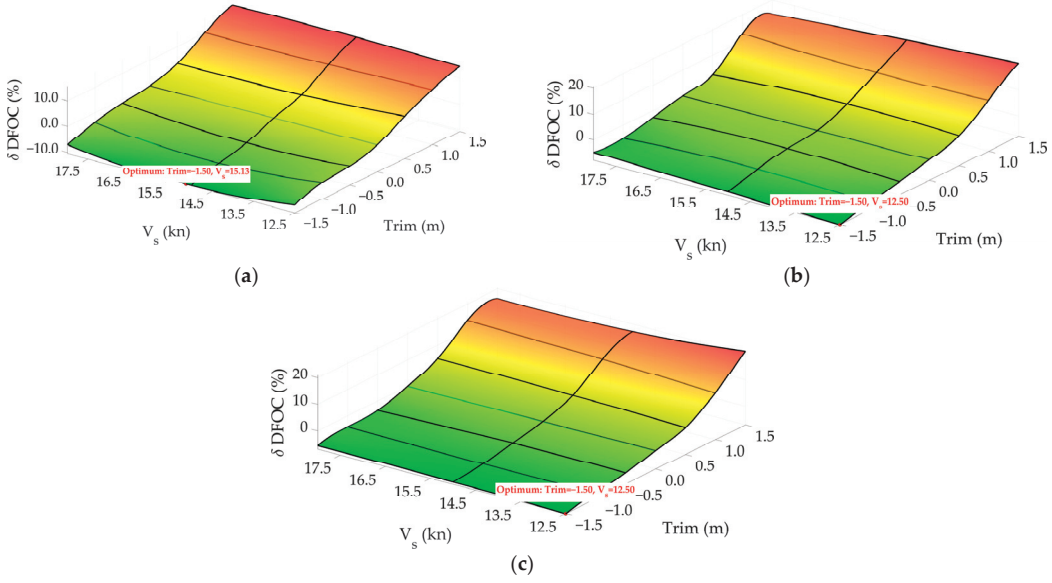

Figure 16. DFOC reduction: (**a**) T_s = 7.5 m; (**b**) T_s = 8.0 m; (**c**) T_s = 8.7 m.

The biggest reduction in the DFOC can be achieved at a 1.5 m trim by the bow, 7.5 m draft and speed of 15.17 kn (10.5%), while for the 8 m and 8.7 m draft, the biggest reduction in brake power is at 12.5 kn (8%, 7%, respectively). Sailing at 12.5 kn instead of 15 kn or 18 kn, and maintaining an even keel, can result in greater fuel savings for higher drafts. Although greater fuel savings might be achievable with a greater trim by the bow, any condition more than −1.5 m trim by the bow cannot be attained on the current ship.

In Figure 17, wave fields are depicted for the case of V_s = 15 kn, T_s = 7.5 m at trim = 0 m (Figure 17a) and at trim = −1.5 m (Figure 17b). It is evident that the total wave amplitude

when trimmed towards the bow by 1.5 m is reduced by 0.25 m, indicating a decrease in the pressure resistance–displacement ratio of 15% (see Table 10). The volume displacement is multiplied by the gravity constant (9.81 m/s^2) and sea water density.

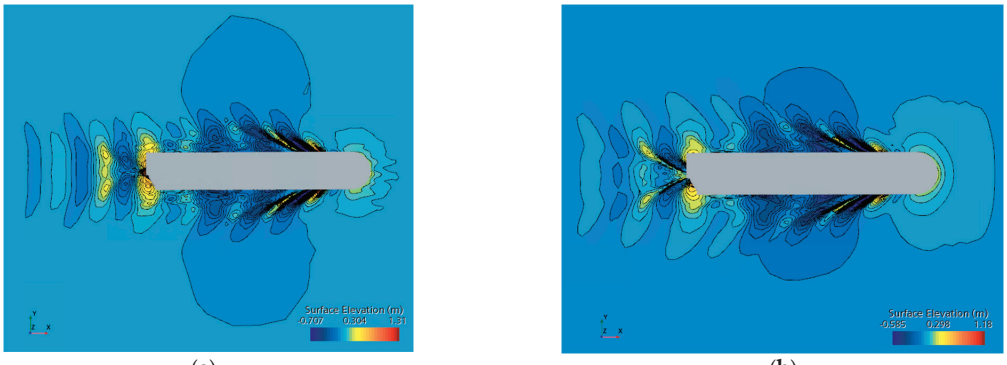

(**a**) (**b**)

Figure 17. Wave patterns: (**a**) V_s = 15 kn, T_s = 7.5 m, trim = 0 m; (**b**) V_s = 15 kn, T_s = 7.5 m, trim = −1.5 m.

Table 10. Pressure resistance decrease.

V_s = 15 kn, T_s = 7.5 m	Trim = 0 m	Trim = −1.5 m
$R_p/\nabla \cdot 10^3$ (-)	0.6039	0.5127

In Figure 18, the free surfaces in the center line and along the hull are presented at two different conditions: trim = 0 m (white hull) and trim = −1.5 m (yellow hull). The black line corresponds to the free-surface level at a zero trim condition while the red line corresponds to the free-surface level at a 1.5 m trim by the bow. In Figure 18a, the bow waves are presented, while in Figure 18b, the stern waves are presented. The peak-to-peak amplitude of the bow wave is reduced by 0.64 m while the stern wave is reduced by nearly 1 m when the ship is trimmed towards the bow by 1.5 m.

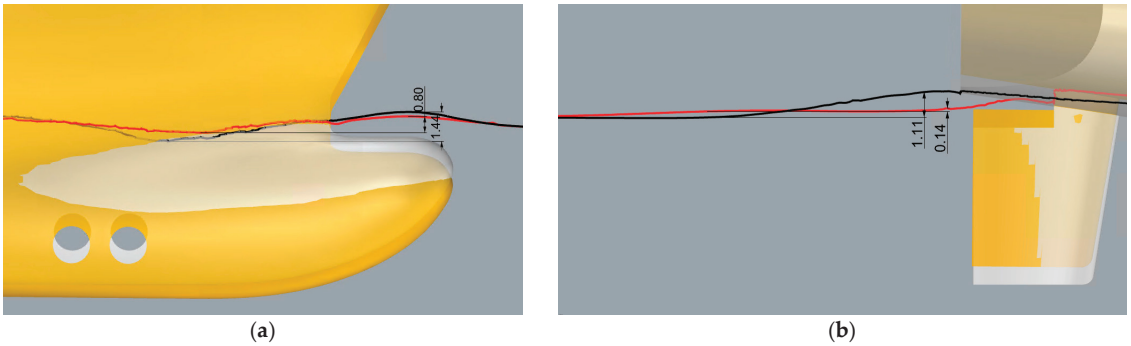

(**a**) (**b**)

Figure 18. Free-surface cuts (V_s = 15 kn, T_s = 7.5 m): (**a**) bow part—white-colored even keel hull; black line represents free-surface elevation for even keel hull, yellow-colored (−1.5 m) trimmed hull; red line represents free-surface elevation for trimmed hull; (**b**) stern part—white-colored even keel hull; black line represents free-surface elevation for even keel hull, yellow-colored (−1.5 m) trimmed hull; red line represents free-surface elevation for trimmed hull.

For other drafts and trims, the impact of the bow trim remains similar; nevertheless, there is a less noticeable reduction in the pressure resistance. It seems that this kind of bulb has a better effect when it is more submerged into the water at lower drafts. This contradicts what is highlighted in numerous literature sources, including [61,62] but it is not the first time that the same conclusion with a fully submerged bulb has been set [63,64].

Mathematical Model for Assessing Brake Power, DFOC and Propeller Speed

Unfortunately, a single mathematical model did not attain the desired RMS within a reasonable training timeframe and iteration count. As a result, two separate mathematical models were devised as follows: one focusing on the brake power and DFOC and the other dedicated to propeller speed prediction. The formula for brake power follows a general form:

$$P_b = \frac{f_3\left(c_{P_b} + \sum_{i=1}^{7}\left(C_{iP_b} \cdot f_2\left(b_i + \sum_{j=1}^{10}\left(B_{ij} \cdot f_1\left(a_j + \sum_{k=1}^{4}\left(A_{jk} \cdot (P_k \cdot X_k + R_k)\right)\right)\right)\right)\right)\right) - G_{P_b}}{L_{P_b}}. \quad (52)$$

The general form of the function for DFOC is

$$DFOC = \frac{f_3\left(c_{DFOC} + \sum_{i=1}^{7}\left(C_{iDFOC} \cdot f_2\left(b_i + \sum_{j=1}^{10}\left(B_{ij} \cdot f_1\left(a_j + \sum_{k=1}^{4}\left(A_{jk} \cdot (P_k \cdot X_k + R_k)\right)\right)\right)\right)\right)\right) - G_{DFOC}}{L_{DFOC}}. \quad (53)$$

The general form of the function for propeller speed is

$$n = \frac{f_3\left(c_n + \sum_{l=1}^{5}\left(C_{ln} \cdot f_2\left(b_l + \sum_{m=1}^{8}\left(B_{lm} \cdot f_1\left(a_m + \sum_{s=1}^{4}(A_{ms} \cdot (P_s \cdot X_s + R_s))\right)\right)\right)\right)\right) - G_n}{L_n}. \quad (54)$$

Configurations of the neurons for both mathematical models are presented in Figure 19a,b.

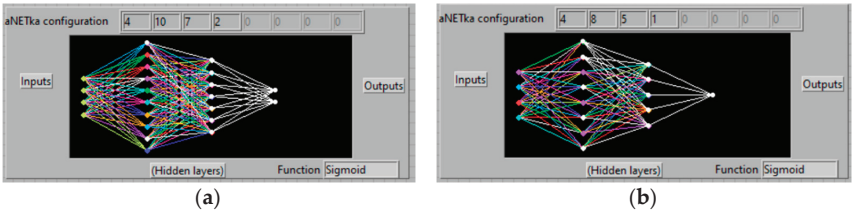

(**a**) (**b**)

Figure 19. Configurations of neurons: (**a**) for brake power and DFOC; (**b**) for propeller speed.

The obtained coefficients for Equations (52) and (53) are given in Tables 11–15, while the coefficients for Equation (54) are given in Tables 16–19.

Table 11. Coefficients A and a for Equations (52) and (53).

A_{j1}	A_{j2}	A_{j3}	A_{j4}	a_j
1.39544	4.80982	−1.76190	−1.30478	−0.75004
0.22339	3.25659	−0.04068	2.23871	−1.54100
−2.10995	3.49346	−0.21458	1.21715	−1.63827
3.03760	4.14154	−2.40221	1.04647	−6.47006
−0.04455	0.71422	1.58515	−0.98086	−0.02750
−1.50944	0.27102	−1.41296	1.52488	1.06833
−0.97408	−0.21472	−0.34123	−0.58728	0.38679
1.83711	2.00358	−9.92587	−1.27416	3.94278
0.08588	0.39723	1.06558	−0.68159	−0.95401
−1.45797	−0.49383	3.67284	−2.41111	0.23743

Table 12. Coefficients B and b for Equations (52) and (53).

B_{i1}	B_{i2}	B_{i3}	B_{i4}	B_{i5}	B_{i6}	B_{i7}	B_{i8}	B_{i9}	B_{i10}	b_i
−3.94741	−1.10676	−1.51183	−3.90542	1.28454	1.37817	1.67905	10.13879	0.82581	2.39590	3.05951
−0.83685	−0.80410	−0.84916	−0.74439	−0.53931	1.20460	0.17759	−0.26222	−0.48840	−0.58512	0.76405
−1.21006	−1.28977	−1.53713	−0.74023	−1.04296	0.87026	0.00654	0.35832	−0.85771	−1.31206	0.45529
0.79825	−0.92382	−0.16195	−3.22868	0.48528	0.41493	0.29515	−2.64142	0.12449	1.60271	0.59712
−0.83157	−1.72121	−1.74315	−1.78391	−0.13521	2.35956	0.85288	1.08050	−0.61823	−0.66071	2.10411
−1.03458	−1.10428	−1.25646	−0.56187	−0.81983	0.76972	−0.00495	0.29741	−0.77011	−1.13999	0.35562
−0.48851	−0.49214	−0.56036	−0.16494	−0.22853	0.26762	−0.48143	1.41729	−0.31051	−1.40889	0.36591

Table 13. Coefficients C_{P_b} and c_{P_b} for Equations (52) and (53).

C_{P_b1}	C_{P_b2}	C_{P_b3}	C_{P_b4}	C_{P_b5}	C_{P_b6}	C_{P_b7}	c_{P_b}
−3.60944	−1.69300	−1.92004	−2.15282	−2.51012	−1.80109	−2.08429	7.38079

Table 14. Coefficients C_{DFOC} and c_{DFOC} for Equations (52) and (53).

C_{DFOC1}	C_{DFOC2}	C_{DFOC3}	C_{DFOC4}	C_{DFOC5}	C_{DFOC6}	C_{DFOC7}	c_{DFOC}
−3.60911	−1.64363	−2.01584	−2.11789	−2.49256	−1.76852	−2.02170	7.32870

Table 15. Coefficients P_k, R_k, G_{P_b}, L_{P_b}, G_{DFOC} and L_{DFOC} for Equations (52) and (53).

P_k	R_k	G_{P_b}	L_{P_b}	G_{DFOC}	L_{DFOC}
0.75000	−5.57500	−0.21915	0.00012	−0.25636	0.02980
0.16364	−1.99545				
0.30000	0.50000				
0.00019	−3.33586				

Table 16. Coefficients A and a for Equation (54).

A_{m1}	A_{m2}	A_{m3}	A_{m4}	a_m
1.60283	1.91017	−1.71984	0.23942	−1.93017
1.62613	2.44722	−0.17892	−1.00908	−3.09041
1.09543	1.09342	2.08237	0.00351	−0.00032
−0.17611	2.37242	0.49469	1.22030	−2.13783
−1.12935	5.25606	−0.88296	−1.08825	−0.79561
−1.10799	−0.07232	−2.85448	0.21127	3.80378
−2.76944	2.04227	4.00000	−0.90497	−1.59122
−0.09699	1.92632	1.05398	−0.48593	−0.22092

Table 17. Coefficients B and b for Equation (54).

B_{l1}	B_{l2}	B_{l3}	B_{l4}	B_{l5}	B_{l6}	B_{l7}	B_{l8}	b_l
−0.85076	−0.86022	−0.92193	−1.21839	−1.28573	0.12384	−0.42344	−0.84941	0.72250
−2.21759	−3.16121	1.26550	−1.20003	−2.78787	4.04679	−1.95753	0.95956	3.10950
−1.04299	−0.99883	−1.19340	−1.29826	−1.50607	0.14846	−0.49616	−1.15469	1.08981
−1.11884	−0.96068	−1.18134	−1.19153	−1.62624	0.20455	−0.46174	−1.00754	1.02576
−0.43893	−1.02698	−1.08333	−1.41701	−0.49332	1.67727	0.33505	−0.39926	1.34012

Table 18. Coefficients C and c for Equation (54).

C_{n1}	C_{n2}	C_{n3}	C_{n4}	C_{n5}	c_n
−2.44334	−5.02627	−2.91111	−2.88484	−2.67661	6.86984

Table 19. Coefficients P_s, R_s, G_n and L_n for Equation (54).

P_s	R_s	G_n	L_n
0.75000	−5.57500	−1.41852	0.01782
0.16364	−1.99545		
0.30000	0.50000		
0.00019	−3.33987		

The standard deviations of the relative differences in the brake power, DFOC and propeller speed calculated the values using Equations (52)–(54), and the results obtained from the CFD analysis for the same three parameters are 0.6%, 0.6% and 0.2%, respectively.

3.7. Trim Optimization Software Application

The development of software focusing on trim optimization is another step forward that demonstrates how engineering and technical practice can be more effectively connected. The equations obtained (52), (53) and (54) are very complex and not suitable for manual calculation. Additionally, the matrix obtained through interpolation of the CFD analysis results contains over 2 million elements (a 151 × 111 × 120 matrix), meaning tabular or graphical representation of the results will be impractical for the average user. Therefore, the most elegant solution is to develop an application with a graphical interface. Today, there are many software tools that operate based on writing in various programming languages, but this task is addressed to other engineering disciplines. This paper demonstrates the development of a software tool within MATLAB App Designer. MATLAB App Designer is highly suitable for the rapid development of simple applications as it has certain functions predefined within the Component Library. In this specific case, only three predefined functions were used: "Button", "Edit Field" and "Label". The interface design is depicted in Figure 20:

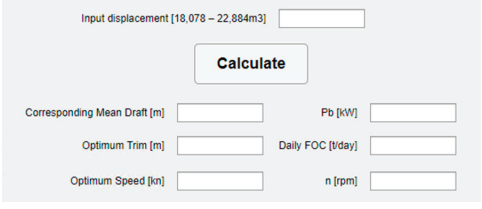

Figure 20. Application interface design.

In the "Input displacement" label, the user should insert the current displacement in cubic meters in the range from 18,078 to 22,884 m^3. The estimation of the optimal trim, corresponding mean draft, estimated speed, brake power, DFOC and propeller speed is performed by simply clicking the "Calculate" button. In case the user inputs a displacement below or above the specified values, despite the stated applicability limits of the mathematical model, and initiates the calculation, a message will appear on the screen: "Displacement is out of range" (see Figure 21).

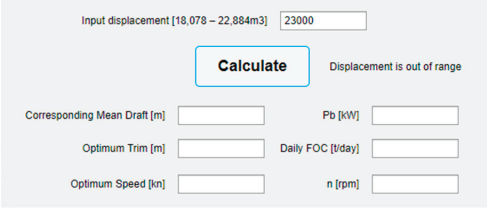

Figure 21. Wrong input.

If a displacement within the specified limits is entered, and the "Calculate" button is clicked, all the data are instantly displayed (see Figure 22).

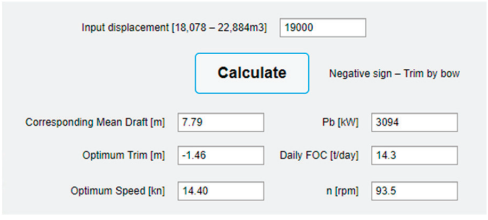

Figure 22. An example input.

The application provides results based on previously obtained mathematical models for estimating the optimal trim, speed, corresponding mean draft, brake power, DFOC and propeller speed. There is also a note that sign "−" in the Optimum Trim label corresponds to the trim by the bow. Due to the specified project task, which required trim optimization at certain speeds, trims and drafts rather than displacements, it is clear that for the same mean draft and different trims, the vessel has different displacements (due to the different position of the ship, the C_b is different and therefore displacement). Considering the upper limit of the performed calculations with a draft of 8.7 m and taking into account various trims, accordingly, the upper limit of displacements for which the calculations were performed at this draft (8.7 m) is variable (refer to Figure 4b). Considering the obtained results, there is a displacement range where the optimal trim is 0 m, meaning that sailing on an even keel is recommended (see Figure 23). This zone starts from the displacement corresponding to a draft of 8.7 m and even-keel position.

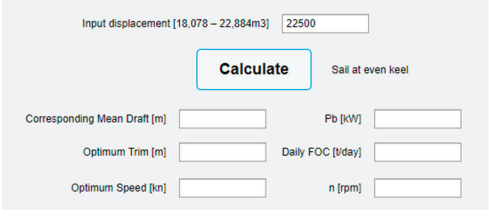

Figure 23. An example input of displacement that is at the upper limit of the mathematical model's application.

The mathematical model does not take draft as an input parameter but determines the mean draft by seeking the optimal trim for a given displacement. It is logical to apply the recommendation of the optimal trim obtained from the mathematical model only through the additional ballasting of the vessel if achieving the optimal trim cannot be attained with the existing ballast water in the tanks (if any). This is manifested by further increasing the displacement. Therefore, it is necessary to rerun the application with the new displacement. Through a few iterations, the optimal trim can be achieved, thus obtaining the estimated ship speed, propeller speed, brake power and DFOC in a reliable manner. It should be noted that the application is not part of the Loading Computer nor does it track stability data for a specific loading condition for a recommended optimal trim. However, it can be integrated into the Loading Computer system to enhance its functionality.

4. Discussion and Conclusions

In this work, not only trim optimization aiming to improve the energy efficiency of the ship, but specifically the CII parameter by reducing the fuel consumption, was presented. The methodology for approaching this issue using CFD software, the application of results

obtained from CFD analysis, i.e., using an ANN to develop a mathematical model that provides estimates of the parameters (brake power, DFOC and propeller speed) for all conditions for which CFD calculations were performed, as well as for all intermediate conditions, was also introduced. Since the use of an ANN resulted in a complex mathematical model that is not straightforward to use in engineering practice, it went a step further, incorporating it into a simple software tool (application).

The entire trim optimization process is described through seven phases that should be applied to other types of ships in future research to develop a universal methodology, not only for trim optimization but also for CFD calculations based on which various engineering analyses such as the optimization of the bow or stern, determination of V_{ref} for EEXI, efficiency of energy-saving devices, etc., can be conducted. For now, the applied methodology, which includes 3D modeling of a digital twin whose hydrostatic parameters differ by up to 1% when comparing the same parameters with data from the Trim & Stability booklet, has proven to be sufficiently good. With additional assumptions about determining the boundary-layer thickness and shear wall stress, i.e., shear velocity, satisfactory accuracy of the y+ parameters, which are very significant for obtaining reliable results, was achieved. The obtained values of y^+(approximately 70–72) differ from the initial target y+ of 150, which is to be expected because the equations used to estimate both the boundary-layer thickness and wall shear stress are not the only ones that can be applied and are very general. For example, the formula for the boundary-layer thickness applies to a flat plate, but in calculating the shear stress, a form factor is included, which is itself obtained based on empirical expressions. Therefore, these formulas cannot provide exact parameter values because these parameters are actually calculated by CFD analysis. However, they can be used to determine enough fine mesh (parameters) so that the results obtained by CFD analysis fall within prescribed limits, according to currently published requirements (up to 5% difference in power brake and shaft speed) for a specific ship case.

The application of an ANN to develop a mathematical model has proven to be very reliable. Generally speaking, artificial intelligence (AI) is increasingly finding applications in various engineering industries, where new design approaches can be developed, and existing ones significantly accelerated based on machine learning. It should be noted that the obtained mathematical model applies to navigation in calm waters, which is practically an almost impossible scenario. This approach, which encompasses multidisciplinarity (CFD analysis, ANN application, software tool programming), can lay the foundation for the further development of the shipbuilding industry from an engineering perspective. In the future, research should further focus on the impact of trim optimization on maneuverability and seakeeping, as these characteristics are crucial for safe navigation. Currently, these aspects are often overlooked in trim optimization projects, as they are not typically included in the project assignments. Addressing this gap will enhance the overall safety and performance of maritime ships.

The further idea is to collect real (measured) data on fuel consumption, engine power, ship speed and navigation conditions during voyages. Monitoring and recording some of these parameters have already become mandatory through [10]. Based on the stored parameters and the formed database, and with the help of machine learning and AI, it will be possible in the future to predict in advance to which energy class the ship belongs and what can be changed during real-time operation to make the ship "green". This can lead to a global reduction in exhaust gas emissions instantly, without ship owners being exposed to penalties imposed by the system because the CII is determined retroactively.

Author Contributions: Conceptualization, M.V. and M.K.; methodology, M.V.; software, M.V.; validation, M.V., M.K. and I.I.; formal analysis, M.V.; investigation, I.I.; resources, M.K.; data curation, M.V. and M.K.; writing—original draft preparation, M.V. and I.I.; writing—review and editing, M.V. and M.K.; visualization, M.V.; supervision, M.K.; project administration, M.V. and I.I.; funding acquisition, M.K. All authors have read and agreed to the published version of the manuscript.

Funding: This research received no external funding.

Informed Consent Statement: Not applicable.

Data Availability Statement: The raw data supporting the conclusions of this article will be made available by the authors on request.

Acknowledgments: Authors would like to thank Ocean Pro Marine Engineers LTD who provided necessary support in CFD simulations and guidelines and Argo Navis Ltd. who provided technical software support. This work was supported by the Ministry of Education, Science and Technological Development of Serbia (Project no. 451–03−65/2024−03/200105 from 5 February 2024).

Conflicts of Interest: Author Matija Vasilev, Milan Kalajdžić was employed by the company Ocean Pro Marine Engineers Ltd. The remaining authors declare that the research was conducted in the absence of any commercial or financial relationships that could be construed as a potential conflict of interest.

References

1. IMO. *2013 Guidelines for Calculation of Reference Lines for Use with the Energy Efficiency Design Index (EEDI)*; Resolution MEPC.231(65), Annex 14; IMO: London, UK, 2013.
2. IMO. *Amendments to the Annex of the Protocol of 1997 to Amend the International Convention for the Prevention of Pollution from Ships. 1973, as Modified by the Protocol of 1978 Relating Thereto*; Resolution MEPC.203(62); IMO: London, UK, 2011.
3. IMO. *Amendments to the Annex of the Protocol of 1997 to Amend the International Convention for the Prevention of Pollution from Ships, 1973, as Modified by the Protocol of 1978 Relating Thereto*; Resolution MEPC.328(76); IMO: London, UK, 2021.
4. IMO. *Guidelines for Voluntary Use of the Ship Energy Efficiency Operational Indicator (EEOI)*; Resolution MEPC.1/Circ.684; IMO: London, UK, 2009.
5. IMO. *2022 Guidelines on Operational Carbon Intensity Indicators and the Calculation Methods (CII Guidelines, G1)*; Resolution MEPC.352(78), Annex 14; IMO: London, UK, 2022.
6. IMO. *2022 Guidelines on the Reference Lines for Use with Operational Carbon Intensity Indicators (CII Reference Lines Guidelines, G2)*; Resolution MEPC.353(78), Annex 15; IMO: London, UK, 2022.
7. IMO. *2021 Guidelines on the Operational Carbon Intensity Reduction Factors Relative to Reference Lines (CII Reduction Factors Guidelines, G3)*; Resolution MEPC.338(76), Annex 12; IMO: London, UK, 2021.
8. IMO. *2022 Guidelines on the Operational Carbon Intensity Rating of Ships (CII Rating Guidelines, G4)*; Resolution MEPC.354(78), Annex 16; IMO: London, UK, 2022.
9. IMO. *Amendments to the Annex of the Protocol of 1997 to Amend the International Convention for the Prevention of Pollution from Ships, 1973, as Modified by the Protocol of 1978 Relating Thereto*; Resolution MEPC.278(70); IMO: London, UK, 2016.
10. IMO. *2022 Guidelines for the Development of a Ship Energy Efficiency Management Plan (SEEMP)*; Resolution MEPC.346(78), Annex 8; IMO: London, UK, 2022.
11. Islam, H.; Carlos, G.-S. Effect of trim on container ship resistance at different ship speeds and drafts. *Ocean. Eng.* **2019**, *183*, 106–115. [CrossRef]
12. Demir, U. Evaluation of Operational Factors for the Energy Efficiency Optimization of High-Speed RORO Vessels by Trim Optimization. Master's. Thesis, Piri Reis University, Istanbul, Turkey, 2019.
13. Le, T.-H.; Vu, M.-T.; Bich, V.-N.; Phuong, N.-K.; Ha, N.-T.-H.; Chuan, T.-Q.; Tu, T.-N. Numerical investigation on the effect of trim on ship resistance by RANSE method. *Appl. Ocean. Res.* **2021**, *111*, 102642. [CrossRef]
14. Hüffmeier, J.; Johanson, M. State-of-the-art methods to improve energy efficiency of ships. *J. Mar. Sci. Eng.* **2021**, *9*, 447. [CrossRef]
15. Sun, C.; Wang, H.; Liu, C.; Zhao, Y. Dynamic prediction and Optimization of Energy Efficiency Operational Index (EEOI) for an Operating Ship in Varying Environments. *J. Mar. Sci. Eng.* **2019**, *7*, 402. [CrossRef]
16. Peričić, M.; Vladimir, N.; Fan, A.; Jovanović, I. Holistic Energy Efficiency and Environmental Friendliness Model for Short-Sea Vessels with Alternative Power Systems Considering Realistic Fuel Pathways and Workloads. *J. Mar. Sci. Eng.* **2022**, *10*, 613. [CrossRef]
17. Zincir, B. Slow steaming application for short-sea shipping to comply with the CII regulation. *Brodogradnja* **2023**, *74*, 2. [CrossRef]
18. Yu, Y.; Zhang, H.; Mu, Z.; Li, Y.; Sun, Y.; Liu, J. Trim and Engine Power Joint Optimization of a Ship Based on Minimum Energy Consumption over a Whole Voyage. *J. Mar. Sci. Eng.* **2024**, *12*, 475. [CrossRef]
19. Prados, J.M.M.; Fernandez, I.A.; Gomez, M.R.; Parga, M.N. The decarbonisation of the maritime sectior: Horizon 2050. *Brodogradnja* **2024**, *75*, 2. [CrossRef]
20. Sherbaz, S.; Duan, W. Ship Trim Optimization: Assessment of Influence of Trim on Resistance of MOERI Container Ship. *Hindawi Publ. Corp.* **2014**, *2014*, 603695. [CrossRef] [PubMed]
21. Korkmaz, K.-B.; Werner, S.; Bensow, R. Investigations on experimental and computational trim optimisation methods. *Ocean Eng.* **2023**, *288*, 116098. [CrossRef]
22. Thiha, S.; Jin, Y. Study on Energy Efficient Operation by ship's Trim Optimization based on Computational Fluid Dynamics. *J. Sci. Res. Sci. Eng. Technol.* **2023**, *10*, 18–28.

23. Jianglong, S.; Haiwen, T.; Yongnian, C.; De, X.; Jiajian, Z. A study on trim optimization for a container ship based on effects due to resistance. *J. Ship Res.* **2016**, *60*, 30–47.
24. Ziylan, K.; Nas, S. A Study on the Relationship Between Ship Resistance and Trim, Supported by Experimental and Software-Based Analysis. *Trans. Mar. Sci.* **2022**, *11*, 5. [CrossRef]
25. Kishev, R.; Georgiev, S.; Kirilova, S.; Milanov, E.; Kyulevcheliev, S. Global View on Ship Trim Optimization. In Proceedings of the 2nd International Symposium on Naval Architecture and Maritime INT-NAM 2014, Istanbul, Turkey, 23–24 October 2014.
26. Park, B.-S.; Donghoon, K.; Kang, I.-K.; Kim, H.-M. The Analysis of the Ship's Maneuverability According to the Ship's Trim and Draft. *J. Fish. Mar. Sci. Educ.* **2015**, *27*, 1865–1871. [CrossRef]
27. Wen, P.; Fadillah, A. The Effect of Trim on Stability and Seakeeping of Tanker, Container and Bulk Carrier. In *IOP Conference Series: Earth and Environmental Science, Volume 972, Proceedings of the 6th International Conference on Marine Technology (SENTA 2021), Surabaya, Indonesia, 27th November 2021*; IOP Publishing Ltd.: Bristol, UK, 2022.
28. Hydrocompinc. Available online: https://www.hydrocompinc.com/blog/article-trim-optimization-using-navcad-for-prediction-confidence/ (accessed on 30 April 2024).
29. Chuan, T.Q.; Phuong, N.K.; Tu, T.N.; Quan, M.V.; Anh, N.D.; Le, T.-H. Numerical Study of Effect of Trim on Performance of 12500DWT Cargo Ship Using RANSE Method. *Pol. Marit. Res.* **2022**, *29*, 3–12. [CrossRef]
30. ABS. *Ship Energy Efficiency Measures. Status and Guidance*; TX 05/13 50000 13015; ABS: Spring, TX, USA, 2013.
31. Ziarati, R.; Bhuizan, Z.; de Melo, G.; Koivisto, H.; Lahiry, H.; OzTurker, E.; Akdemir, B. *MariEMS Train the Trainee (MariTTT) Courses on Energy Efficient Ship Operation. MariEMS*; MTCC-Asia, Guidelines on Ship Trim Optimization—Based on Machine Learning Method; The Global MTCC Network: London, UK, 2017.
32. MTCC-Asia. *Guidelines on Ship Trim Optimization—Based on Machine Learning Method*; The Global MTCC Network: London, UK, 2017.
33. Mahmoodi, H.; Ghamari, I.; Hajivand, A.; Mansoori, M. A CFD investigation of the propulsion performance of a low-speed VLCC tanker at different initial trim angles. *Ocean Eng.* **2023**, *275*, 114148. [CrossRef]
34. Petursson, S. Predicting Optimal Trim Configuration of Marine Vessel with Respects to Fuel Usage. Master's Thesis, Faculty of Industrial Engineering, Mechanical Engineering and Computer Science, School of Engineering and Natural Sciences, University of Iceland, Reykjavík, Iceland, 2009.
35. Lee, J.; Yoo, S.; Choi, S.; Kim, H.; Hong, C.; Seo, J. Development and Application of Trim Optimization and Parametric Study Using an Evaluation System (SoLuTion) Based on the RANS for Improvement EEOI. In Proceedings of the ASME 2014 33rd International Conference on Ocean, Offshore and Arctic Engineering OMAE2014, San Francisco, CA, USA, 8–13 June 2014.
36. Lyu, X.; Tu, H.; Xie, D.; Sun, J. On Resistance Reduction of a Hull by Trim Optimization. *Brodogradnja* **2018**, *69*, 1. [CrossRef]
37. Moustafa, M.M.; Yehia, W.; Hussein, A.W. Energy Efficient Operation of Bulk Carriers by Trim Optimization. In Proceedings of the 18th International Conference on Ships and Shipping Research 2015, NAV 2015, Lecco, Italy, 24–26 June 2015.
38. Reichel, M.; Minchev, A.; Larsen, N.L. Trim Optimization—Theory and Practice. *TransNav Int. J. Mar. Navig. Saf. Sea Transp.* **2014**, *8*, 3.
39. Bal Beşikçi, E.; Arslan, O.; Turan, O.; Ölçer, A.I. An Artificial Neural Network Based Decision Support System for Energy Efficient Ship Operations. *Comput. Oper. Res.* **2016**, *66*, 393–401. [CrossRef]
40. Jeon, M.; Noh, Y.; Shin, Y.; Lim, O.-K.; Lee, I.; Cho, D. Prediction of Ship Fuel Con-sumption by Using an Artificial Neural Network. *J. Mech. Sci. Technol.* **2018**, *32*, 5785–5796. [CrossRef]
41. Bassam, A.M.; Phillips, A.B.; Turnock, S.R.; Wilson, P.A. Artificial Neural Network Based Prediction of Ship Speed Under Operating Conditions for Operational Optimization. *Ocean Eng.* **2023**, *278*, 114613. [CrossRef]
42. Tarelko, W.; Rudzki, K. Applying Artificial Neural Networks for Modelling Ship Speed and Fuel Consumption. *Neural Comput. Appl.* **2020**, *32*, 17379–17395. [CrossRef]
43. Liu, B.; Gao, D.; Yang, P.; Hu, Y. An Energy Efficiency Optimization Strategy of Hybrid Electric Ship Based on Working Condition Prediction. *J. Mar. Sci. Eng.* **2022**, *10*, 1746. [CrossRef]
44. Lin, H.; Chen, S.; Luo, L.; Wang, Z.; Zeng, Y. Research on the Speed Optimization Model Based on BP Neural Network and Genetic Algorithm (GA). In Proceedings of the 29th International Ocean and Polar Engineering Conference, Honolulu, HI, USA, 16–21 June 2019.
45. Ozsari, I. Predicting main engine power and emissions for container, cargo and tanker ships with artificial neural network analysis. *Brodogradnja* **2023**, *74*, 2. [CrossRef]
46. ITTC. 7.5-02-03-02.1—Open Water Test, ITTC Quality System Manual, Recommended Procedures and Guidelines; International Towing Tank Conference, Resistance and Propulsion Committee of the 29th ITTC, 13–18 June 2021. Available online: https://www.ittc.info/media/9621/75-02-03-021.pdf (accessed on 31 March 2024).
47. IMO. *Development of Draft 2022 IACS Guidelines for the Use of Computational Fluid Dynamics (CFD) for the Purposes of Deriving the in the Framework of the EEXI Regulation, Resolution MEPC.78/INF.16*; Internation Maritime Organization: London, UK, 2022.
48. B-Series Propeller Generator. Available online: https://www.wageningen-b-series-propeller.com/ (accessed on 31 March 2024).
49. Bernitsas, M.M.; Ray, D.; Kinley, P. *K_T, K_Q and Efficiency Curves for the Wageningen B-Series Propellers*; College of Engineering, The University of Michigan: Ann Arbor, MI, USA, 1981.
50. Saydam, A.Z.; Küçüksu, G.N.; İnsel, M.; Gökçay, S. Uncertainty quantification of self-propulsion analyses with RANS-CFD and comparison with full-scale ship trials. *Brodogradnja* **2022**, *73*, 107–129. [CrossRef]

51. Mikulec, M.; Piehl, H. Verification and validation of CFD simulations with full-scale ship speed/power trial data. *Brodogradnja* **2023**, *74*, 41–62. [CrossRef]
52. Hirt, C.W.; Nichols, B.D. Volume of Fluid (VOF) Method for the Dynamics of Free Boundaries. *J. Comput. Phys.* **1981**, *39*, 201–225. [CrossRef]
53. Goldstein, S. On the Vortex Theory of Screw Propellers. Proceedings of the Royal Society of London. Series A, Containing Papers of a Mathematical and Physical Character, Volume 123, Issue 792, pp. 440–465. Available online: https://royalsocietypublishing.org/doi/abs/10.1098/rspa.1929.0078 (accessed on 31 March 2024).
54. Šeb, B. Numerička Karakterizacija Brodskog Propelera. Ph.D. Thesis, University of Zagreb, Faculty of Mechanical Engineering and Naval Architecture, Zagreb, Croatia, 2017.
55. White, F.M.; Majdalani, J. *Viscous Fluid Flow*, 4th ed.; McGraw Hill LLC: New York, NY, USA, 2021; pp. 578–583.
56. ITTC. 7.5-02-03-01.4, 1978 ITTC Performance Prediction Method, ITTC Quality System Manual, Recommended Procedures and Guidelines; International Towing Tank Conference, Resistance and Propulsion Committee of the 29th ITTC, 13–18 June 2021. Available online: https://www.ittc.info/media/9872/75-02-03-014.pdf (accessed on 31 March 2024).
57. Molland, A.F.; Turnock, S.R.; Hudson, D.A. *Ship Resistance and Propulsion: Practical Estimation of Propulsive Power*; Cambridge University Press: Cambridge, UK, 2011; p. 108.
58. ITTC. 7.5-03-01-01, Uncertainty Analysis in CFD Verification and Validation, Methodology and Procedures, ITTC Quality System Manual, Recommended Procedures and Guidelines; International Towing Tank Conference, Resistance and Propulsion Committee of the 29th ITTC, 13–18 June 2021. Available online: https://www.ittc.info/media/9765/75-03-01-01.pdf (accessed on 31 March 2024).
59. ITTC. 7.5-03-03-01, Practical Guidelines for Ship Self-Propulsion CFD, ITTC Quality System Manual, Recommended Procedures and Guidelines; International Towing Tank Conference, Qualitu Systems Group of the 28th ITTC, Wuxi, China, 2017. Available online: https://www.ittc.info/media/8169/75-03-03-01.pdf (accessed on 31 March 2024).
60. ITTC. 7.5-03-02-04, Practical Guidelines for Ship Resistance CFD, ITTC Quality System Manual, Recommended Procedures and Guidelines; International Towing Tank Conference, Resistance and Propulsion Committee of the 29th ITTC, 13–18 June 2021. Available online: https://www.ittc.info/media/8167/75-03-02-04.pdf (accessed on 31 March 2024).
61. Kracht, A.M. Design of Bulbous Bows. *SNAME Trans.* **1978**, *86*, 197–217.
62. Molland, A.F.; Turnock, S.R.; Hudson, D.A. *Ship Resistance and Propulsion, Practical Estimation of Ship Propulsive Power*, 2nd ed.; Cambridge Univeristy Press: Cambridge, UK, 2017.
63. Vasilev, M.; Kalajdžić, M.; Suvačarov, A. A Practical Approach to Bulbous Bow Retrofit Analysis for Enhanced Energy Efficiency. In Proceedings of the 25th Numerical Towing Tank Symposium (NuTTS), Ericeira, Portugal, 15–17 October 2023; pp. 191–196.
64. Schneekluth, H.; Bertram, V. *Ship Design for Efficiency and Economy*, 2nd ed.; Butterworth Heinemann: Oxford, UK, 1998.

Journal of
Marine Science and Engineering

MDPI

Article

Hydrodynamic Analysis and Drag-Reduction Design of an Unmanned Underwater Vehicle Based on Computational Fluid Dynamics

Xuecheng Li [1], Desheng Zhang [2,3], Ming Zhao [2,3], Xin Wang [2,3,*] and Yu Shen [2,3]

[1] China Offshore Fugro Geosolutions (Shenzhen) Co., Ltd., Shenzhen 518065, China; lixc@cosl-fugro.com
[2] School of Mechanical Engineering and Automation, Harbin Institute of Technology, Shenzhen 518055, China; 22b353008@stu.hit.edu.cn (D.Z.); 21s153151@stu.hit.edu.cn (M.Z.); 210310306@stu.hit.edu.cn (Y.S.)
[3] Guangdong Provincial Key Laboratory of Intelligent Morphing Mechanisms and Adaptive Robotics, Shenzhen 518055, China
* Correspondence: wangxinsz@hit.edu.cn

Abstract: In order to establish a proper geometry of an Unmanned Underwater Vehicle (UUV) for stable motion control and energy usage reduction, this paper analyzes the hydrodynamic performance of a complex shape underwater vehicle and develops a systematic Computational Fluid Dynamics (CFD) simulation method to solve the hydrodynamic parameters of the system. Based on the simulation method and their results, the streamlines and pressure distributions of the water flow around the underwater vehicle are analyzed, and the geometric model design is improved based on the drag characteristics. Also, a comparison scheme is designed to evaluate the vehicle model before and after the geometry improvement. Simulation result shows that the design schemes brings 18% drag reductions in surge direction and 32% in heave direction. Moreover, by establishing the physical and mathematical models of the UUV on a physical simulation platform, a complete model of the underwater vehicle is constructed, laying the foundation for further simulations and experiments.

Keywords: unmanned underwater vehicle; hydrodynamic analysis; CFD; drag-reduction design; physical simulation platform

Citation: Li, X.; Zhang, D.; Zhao, M.; Wang, X.; Shen, Y. Hydrodynamic Analysis and Drag-Reduction Design of an Unmanned Underwater Vehicle Based on Computational Fluid Dynamics. *J. Mar. Sci. Eng.* **2024**, *12*, 1388. https://doi.org/10.3390/jmse12081388

Academic Editors: Decheng Wan, Nastia Degiuli and Ivana Martić

Received: 1 July 2024
Revised: 3 August 2024
Accepted: 12 August 2024
Published: 13 August 2024

1. Introduction

With the introduction of ocean energy policies and the development of related industries, marine-related industries have begun to focus on deep-sea mining and transportation of energy resources such as natural gas and oil. In addition, the installation and construction of submarine cables and other facilities that support communication between continents have also become a major hotspot [1]. However, due to the complex and variable environments of the ocean, it is difficult for divers to perform complex tasks through saturation diving, hence underwater vehicles has been widely applied to underwater exploration and operations. Among them, unmanned underwater vehicles (UUVs), which do not require divers to dive with them and can be remotely controlled from the surface, have gradually become the mainstream equipment for executing deep-sea operation projects [2]. The design and development of UUVs is a comprehensive and complex engineering task, with a high degree of technological intensity. UUVs can generally be divided into Remotely Operated Underwater Vehicles (ROVs) and Autonomous Underwater Vehicles (AUVs) [3]. ROVs can be further categorized into open-frame structures or enclosed structures. A frame with buoyancy block structure is widely adopted in most ROVs geometry designs, due to its various advantages. This structure enables the carrying and installation of large payloads, and exploration and operation equipment can be conveniently mounted on or removed from the frame-structure for further analysis and maintenance [4]. In the early stages of development, UUV system design placed greater emphasis on drag-reduction

design to enhance navigation speed and energy efficiency. With the diversification of the UUVs' application and functional requirements, loading capacity and motion stability are also be took into account. Thus, the hydrodynamic characteristics of the UUVs, especially drag-reduction performance, become an important research field [5].

For UUVs with complex geometries, such as ROVs, the structural integrity of the vehicles are important to withstand the influence from sea currents and vortices, and it is the cornerstone for ensuring the vehicle's capability to effectively carry out tasks in deep-sea environments [6]. Accomplishing this objective entails a meticulous design of the UUVs' geometry, along with the integration of well-engineered hydrodynamic components both on attachments and the main body, ensuring dynamic stability and drag reduction. Good geometry design not only entails maintaining robust structural stability, but also ensuring consistent hydrodynamic performance. Additionally, considerations must be given to endurance requirements, as well as the specific operational conditions and objectives [7]. Consequently, optimizing the geometry of underwater vehicles serves as the bedrock of the entire vehicle design process and represents a critical step.

To have a further knowledge of the hydrodynamic characteristic of the UUVs, the hydrodynamic model of the system should be established first. And it is fundamental to establish the dynamic mathematical models for UUVs, which play crucial roles in their maneuvering control and motion prediction. Traditional hydrodynamic model construction is based on a fundamental motion, typically uniform straight-line forward movement, to which a small perturbation is added. The multivariate function is then expanded using a Taylor series, with the fundamental motion serving as the reference point for the expansion. The coefficients obtained from the Taylor series expansion are known as hydrodynamic coefficients. Fossen, from the Norwegian University of Science and Technology, has proposed a simplified mathematical model for underwater robots [8]. This model considers the ROV to be symmetrical along three orthogonal planes: vertical, lateral, and fore/aft. In this model, the viscous hydrodynamic forces and moments acting on the underwater robot are also significantly simplified. It is assumed that the viscous hydrodynamic force (torque) in a particular direction is only related to the velocity (angular velocity) in that direction. This reduction in complexity significantly decreases the required hydrodynamic coefficients, thus easing the acquisition process. Chin et al. emphasized a systematic modeling of hydrodynamic damping using the CFD software ANSYS-CFX™ on a complex-shaped ROV [9]. Also from NTNU, Eidsvik established hydrodynamic model and conducted experiments to identify hydrodynamic parameters of several ROVs [10]. Yang et al. [11] proposed a control-oriented modeling approach for a low-speed semi-AUV which has complex-shaped structures. They also used cost-efficient CFD softwares (ANSYS-CFX™, STAR-CCM+™ to predict the two hydrodynamic key parameters.

The common methods for obtaining hydrodynamic coefficients currently in use are experimental methods, semi-empirical formula calculations, and numerical simulation methods based on CFD technology [12]. The experimental method is simple, intuitive, easy to implement, and has high reliability. Many researchers have predicted hydrodynamic coefficients using this method [13,14]. However, the high cost of experiments and the long cycle of the experimental process lead to difficulties using physical experimental method; the semi-empirical formula calculation method is suitable for calculating the hydrodynamic parameters of underwater vehicles with simple shapes and single geometric structures. However, the shapes of AUVs and ROVs are usually more complex, making it difficult for the semi-empirical formula calculation method to accurately obtain all of the added mass and added inertia moments and viscous hydrodynamic forces in the kinematic equations of underwater vehicles. In recent years, numerical simulation methods based on potential flow theory and finite element theory, which have developed from the principles of mass conservation, momentum conservation, and energy conservation, have advanced rapidly. Many researchers used CFD method to estimate hydrodynamic coefficients of AUVs with complex shapes, such as an axisymmetric body, a body with appendages, and a spherical body designed for amphibious tasks [15–19]. Also, the flow status of open-frame vehicles

are studied numerically, which proves the possibility of analyzing the hydrodynamic characteristics of UUVs with complex geography accurately, using CFD method [20]. The co-researchers in Harbin Institute of Technology, Shenzhen, also conduct numerical studies on hydrodynamic characteristics for AUVs and ROVs, they proposed systemic methods and reviewed the CFD method of hydrodynamic analysis [21–23].

The primary strategy for enhancing the efficiency of UUVs involves refining the flow dynamics around the vehicle. Vortices and turbulent flow patterns can significantly diminish the ROV's hydrodynamic capabilities. Altering the vehicle's geometry while preserving its fundamental stability represents the most effective approach. The advancement of computer simulation technology has facilitated comprehensive optimization analyses of underwater vehicles. The iterative design paradigm, integrating ROV analysis with CFD simulation, is extensively utilized in underwater vehicle design processes [24]. For AUVs and other torpedo-shaped underwater robots, researchers focusing on reducing the drag in surge directions to lower the energy consumption [25–29]. And for ROVs and other work-class underwater robots, enhancing the suitability becomes the most important goal [6,30,31]. A comprehensive review on recent trends and applications of simulation-based design optimization (SBDO) of underwater vehicles [32], shows that the studies in SBDO still remains a predominant reliance on simpler, deterministic single-objective formulations. To model and navigate the uncertainties inherent in marine engineering, including factors like wave dynamics and ocean currents more accurately, advanced optimization approaches which are more sophisticated, multi-objective, and stochastic should be applied in to SBDO.

This paper initially establishes a six-degree-of-freedom (6-DOF) dynamics and kinematics equations for a ROV. Concurrently, it employs CFD simulation methods to solve for the most challenging hydrodynamic parameters within the dynamics. A more systematic CFD simulation method for complex-shape vehicles is proposed to calculate these hydrodynamic parameters, thereby establishing the vehicle's dynamic model. By analyzing the motion state of the vehicle in the simulation, optimization schemes for the overall vehicle model based on hydrodynamic parameters are proposed, and the optimized model parameters are determined. Finally, comparative simulation experiments of the model's motion before and after optimization are presented to demonstrate that the optimization scheme can effectively enhance the vehicle's motion capabilities. To facilitate the simulation of underwater operation scenarios, an underwater simulation physical platform for the vehicle has been developed based on the Robot Operating System (ROS). This platform simulates the underwater environment and interference, and integrates various sensors for perception within the simulation environment, providing a channel for algorithm validation for different types of underwater vehicles.

2. Dynamic Model Establishment

To facilitate the determination of the motion state of underwater vehicles, two commonly used system coordinate frames are introduced, namely the Inertial Coordinate System (North East Down) and the Body Fixed Frame. For general types of underwater vehicles, the position and attitude of the vehicle can be described by six different variables, as shown in Figure 1.

For an underwater vehicle, six different motion components are conveniently defined as heave, sway, surge, roll, pitch, and yaw. The symbol definitions for motion parameters are defined by their direction and orientation, where clockwise rotation and movement along the positive direction of the coordinate system are considered positive, otherwise are negative. The descriptions and symbols for the relevant motions under each degree of freedom for underwater vehicles are shown in Table 1.

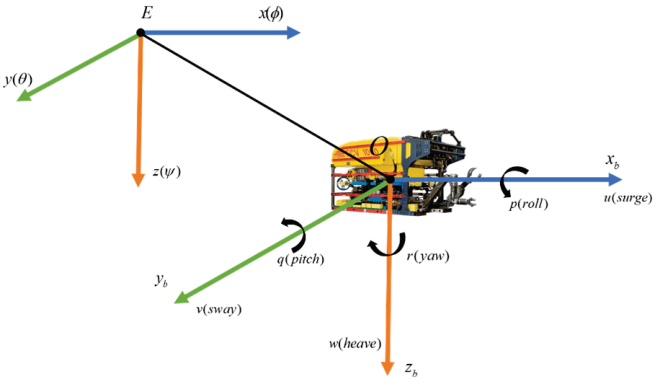

Figure 1. The establishment of coordinate systems for underwater vehicles.

Table 1. The motion definitions for the degrees of freedom of underwater vehicles.

DOF	Motion	Force	Velocity	Coordinate
1	Surge	X	u	x
2	Sway	Y	v	y
3	Heave	Z	w	z
4	Roll	K	p	ϕ
5	Pitch	M	q	θ
6	Yaw	N	r	ψ

For underwater vehicles, the general motion of a six-degree-of-freedom (6-DOF) underwater vehicle with the origin O as the coordinate reference is defined as follows.

The velocity of the underwater vehicle can be decomposed into linear and angular velocities. In terms of linear velocity, the vehicle facilitates coordinate transformations through a rotation matrix, as shown in the following equation:

$$\begin{aligned} \eta &= \left[\eta^N_{B/N}, \Theta^N_{B/N}\right]^T = [x, y, z, \phi, \theta, \psi]^T \\ v &= \left[v^B_{B/N}, \omega^B_{B/N}\right]^T = [u, v, w, p, q, r]^T \\ \tau &= \left[f^B, \tau^B\right]^T = [X, Y, Z, K, M, N]^T \end{aligned} \tag{1}$$

$$\eta^N_{B/N} = R(\hat{z}, \psi)R(\hat{y}, \theta)R(\hat{x}, \phi)v^B_{B/N} = J^V_{B/N}(\Theta^N_{B/N})v^B_{B/N} \tag{2}$$

In the given context, $R(\hat{z}, \psi)$ represents the coordinate transformation matrix for the rotation of the underwater vehicle about the Z-axis, $R(\hat{y}, \theta)$ is the coordinate transformation matrix for rotation about the Y-axis, and $R(\hat{x}, \phi)$ denotes the coordinate transformation matrix for rotation about the X-axis. The aforementioned equation represents the linear velocity rotation matrix between the body-fixed coordinate system and the global (world) coordinate system, with the computation method as illustrated in the equation.

$$J^V_{B/N}(\Theta^N_{B/N}) = \begin{pmatrix} c\psi c\theta & -s\psi c\phi + c\psi s\theta s\phi & s\psi s\phi + c\psi s\theta c\phi \\ s\psi c\theta & c\psi c\phi + s\psi s\theta s\phi & -c\psi s\phi + s\psi s\theta c\phi \\ -s\theta & c\theta s\phi & c\theta c\phi \end{pmatrix} \tag{3}$$

The expressions for angular velocity and linear velocity are consistent, both derived from transformation matrices. Vectors are used to represent the kinematics, and the following equation illustrates the 6-DOF kinematic equations for the underwater vehicle:

$$\dot{\eta} = J_\theta(\eta)v \tag{4}$$

$$\begin{bmatrix} \dot{\eta}_{B/W}^{W} \\ \dot{\Theta}_{B/W}^{W} \end{bmatrix} = \begin{bmatrix} J_{B/W}^{V} & 0_{3\times3} \\ 0_{3\times3} & J_{B/W}^{\omega}(\theta_{B/W}^{W}) \end{bmatrix} \begin{bmatrix} v_{B/W}^{B} \\ \omega_{B/W}^{B} \end{bmatrix} \tag{5}$$

Considering the analysis object of this paper is a general underwater vehicle model, the shape of the underwater vehicle does not change under normal circumstances, and its mass and center of gravity position are fixed. The body coordinate system is established based on the center of gravity of the underwater vehicle, and the three degrees of freedom inertial axes of the underwater vehicle are used as the coordinate axes of the body coordinate system. Additionally, due to the low-speed operational state of the underwater vehicle and the deep-sea working environment, the influence of surface waves does not need to be considered. The dynamic equations of the underwater vehicle can be described using relevant mechanics formulas, as shown in the following equation.

$$F = M_{RB}\dot{V} + C_{RB}(V)V = \begin{bmatrix} mI_{3\times3} & 0_{3\times3} \\ 0_{3\times3} & I_g \end{bmatrix} \dot{V} + \begin{bmatrix} mS(V_2) & 0_{3\times3} \\ 0_{3\times3} & -S(I_gV_2) \end{bmatrix} V \tag{6}$$

In the equation, M_{RB} represents the mass distribution of the UUV, while the Coriolis matrix, denoted as C_{RB}, represents the Coriolis and centrifugal forces acting on the UUV, and it satisfy the relationship $C_{RB}(V) = -C_{RB}^{T}(V)$; F represents the total force and moment acting on the underwater vehicle. In summary, by solving the mass matrix and the Coriolis and centrifugal force matrix, the general kinematic equations for the underwater vehicle can be obtained.

3. Hydrodynamic Coefficients Estimation for the Underwater Vehicle

To establish the dynamic model of the vehicle, this paper employs CFD simulations to solve for its hydrodynamic coefficients. CFD simulation requires meshing of the vehicle's model, necessitating certain simplifications to the shape of the underwater vehicle before computation: (1) for minor structures, which have a negligible impact on drag, simplifications are made by filling in or removing them; (2) the propeller blades and external attachments, which have complex shapes that may cause issues with meshing, are simplified; and (3) for the minor recesses on the aluminum profile structure that have a minimal impact on hydrodynamics, they are optimized using solid square steel. For the load-bearing structures and other appendages that have a minor impact on drag, they are simplified by removal.

The basic numerical simulation process adopted in this paper is depicted in Figure 2. In the pre-processing stage, the underwater vehicle model is first simplified, followed by the meshing of the fluid domain. An unstructured meshing scheme is utilized to avoid meshing failures that may arise due to the irregular shape of the vehicle. In the numerical computation stage, the fluid domain of the vehicle is iteratively solved through CFD simulation. The fluid domain changes are studied frame by frame, and the simulation is iterated to the specified number of iterations to determine if the results have converged. If convergence is achieved, the process proceeds to the post-processing stage. Otherwise, the parameters in the pre-processing stage need to be readjusted. Finally, in the post-processing stage, the simulation software outputs parameters such as streamlines and pressure maps. These data are analyzed and solved using the aforementioned formulas to ultimately determine the hydrodynamic parameters and establish the model of the underwater vehicle.

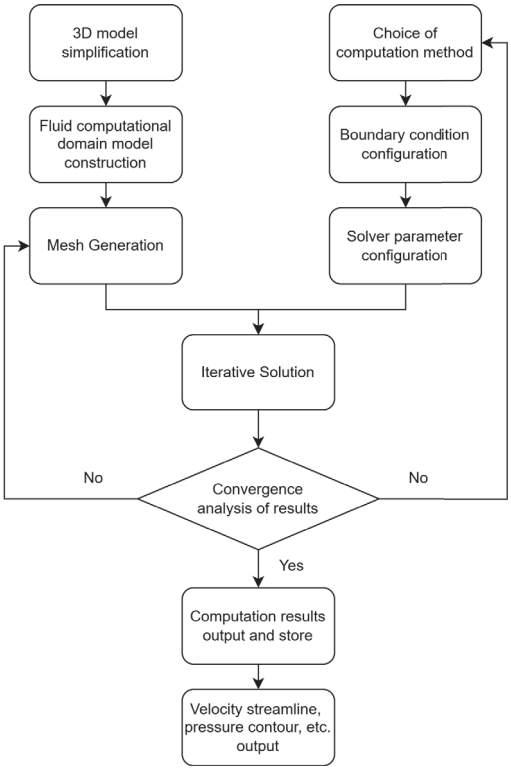

Figure 2. Numerical simulation process.

3.1. Model Simplification and Fluid Domain Design

The basic model of the underwater vehicle obtained after applying the aforementioned simplification rules is shown in Figure 3. After the simplification, the model maintained the main structure of the original model, while it also improve the operability of the meshing process.

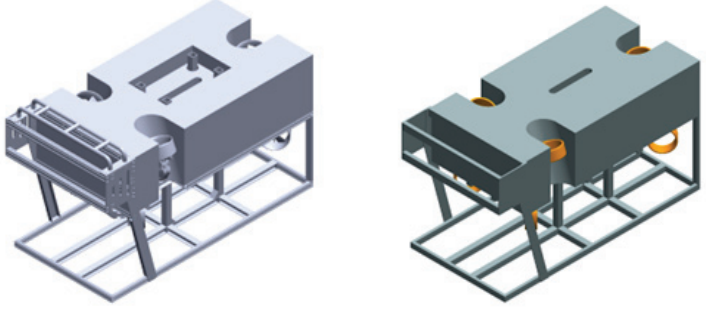

(**a**) (**b**)

Figure 3. Comparison diagram of underwater vehicle model before and after simplification. (**a**) Basic model of underwater vehicles prior to simplification; (**b**) basic model of underwater vehicles post-simplification.

The CFD simulation defines the fluid domain as shown in Figure 4. Following the ITTC guidelines and baseline tests, by defining the length of the underwater vehicle in

the direction of flow as L, the length from the entry surface to the body of the vehicle is designed as $4L$, and the length from the rear of the body to the exit surface is $8L$. The computational domain is characterized by a height and width of $8L$ each, and a length of $12L$.

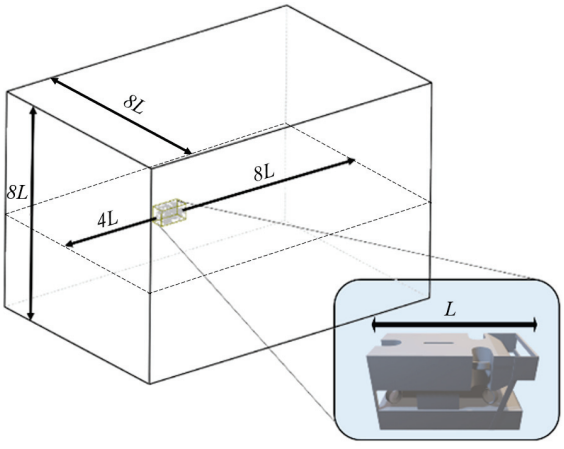

Figure 4. Fluid domain of CFD computation.

The surrounding boundaries of the fluid domain are set as no-slip walls, the inlet face is set as a velocity control face for fluid inflow, the outlet face is set as a pressure control face for fluid outflow, and the surface of the UUV is set as a no-slip wall in order to specify the flow velocity and state of the fluid outside the UUV model. The definitions of each boundary are shown in Figure 5.

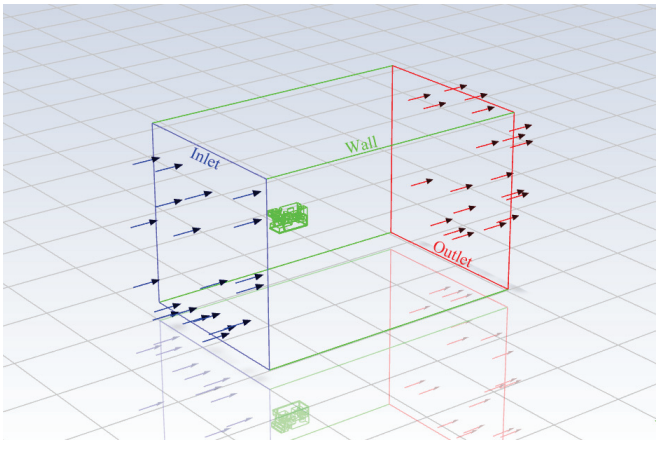

Figure 5. Boundary definition of the computational domain.

3.2. Mesh Generation

By obtaining the model of the underwater vehicle and the fluid domain, the mesh of the model is designed and generated using mesh generation software ANSYS Meshing, the mesh structure and the transition crossing the inflation layer are shown in Figure 6. The SST $k-\omega$ model is chosen as the turbulence model due to its greater accuracy by separately employing $k-\omega$ and $k-\epsilon$ model in the near-wall inflation zone and the developing zone of the mesh grids. According to these features of SST $k-\omega$ model, the value of y^+ can be set to 1 to obtain a first layer of the inflation layer with lower height, which can ensure

a smooth boundary layer transition with finer height changes. Additionally, controlling the surface mesh size of the ROV is essential to minimize boundary layer mesh flatness and enhance its quality. Drawing on the research of Lin et al. [33], and considering the scale of small structural components like the UUV framework, the first layer mesh size for this model is set at 0.025 m. This size ensures that the short-axis surface of the UUV framework is covered by at least five grids, maintaining calculation accuracy. It also allows for approximately 20 boundary layers, balancing computational cost and precision.

After simplifying the 3D model of the UUV, it is necessary to generate separate meshes for steady and unsteady motion simulations. The main parameters and settings for these two types of meshes are detailed in Table 2.

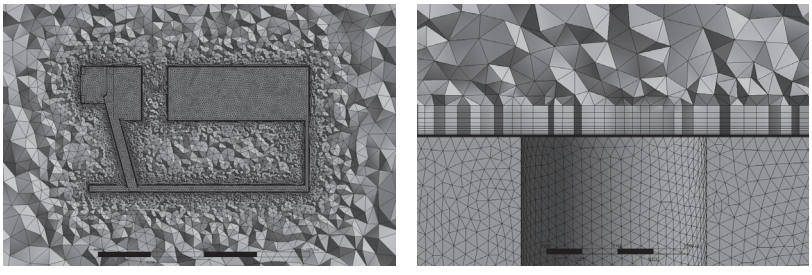

(**a**) (**b**)

Figure 6. Mesh details in cross-section view (**a**) Overall left view; (**b**) Inflation layer.

Table 2. Mesh parameters and settings.

Parameters	Steady Motion	Unsteady Motion
Mesh type	Unstructured	
Size Function	Curvature and Proximity	
Element size	0.99 m	
Max size	1 m	
Inflation layer	With inflation	
Face sizing	0.025 m	
Body sizing	None	0.3 m
Geometry	Flow Zone	Sub Zone
Boundary	ROV Surface	
Inflation option	First, Layer Thickness	
Y plus	1	

3.3. Simulation Settings and Parameters

After proper mesh generation, the hydrodynamic parameters of the vehicle can be calculated through numerical solvers in CFD simulation software ANSYS Fluent 2021. Once the model simplification and the computational fluid domain are established, mesh generation is performed using the built-in methods of the CFD software, and the momentum exchange approach for the simulation process is determined. The CFD simulation parameters and settings for the underwater vehicle are shown in Table 3. For steady-state simulations, the convergence residuals are set to 10^{-6}, but the number of iterations is limited to 2000, which can satisfy our convergence criterion that the drag coefficient output in last 100 iterations stay stable (difference less than 0.5%), and decrease the computation load at the same time.

Table 3. Simulation parameters of CFD.

Items	Steady Motion	Unsteady Motion
Numerical solution method	FVM	
Turbulence model	SST $k-\omega$	
Solver algorithm	SIMPLEC	
Discretization scheme	Second-order upwind scheme	
Boundary conditions	Custom velocity inlet, no-slip wall	
Grid type	Unstructured	
Number of iterations	2000	$100/T$ [1]

[1] T stands for the period of the sine motion in unsteady-state motion simulations.

3.4. Mesh Independence Study

During mesh generation, variations in parameters such as face sizing, body sizing, and grid transition smoothness can affect grid refinement, resulting in differences in the quantity of grids for the same model. It is crucial to evaluate simulation accuracy across various grid scales and ensure that adjustments in grid density within an appropriate range maintain the precision of simulation outcomes.

To verify the grid's independence within a specific range and its impact on hydrodynamic simulation results for ROV model with different mesh scales, experiments are conducted under five different face sizing settings. These experiments are conducted under the condition of Y-direction straight-line motion at 1.0 m/s. Drag in Y direction under different grid scale at Re = 1,482,475.247 are shown in Table 4.

Analysis of the drag data reveals that increasing the face sizing of the ROV surface to 0.1 m results in the inability to generate the boundary layer of the framework properly. This occurs because the size of individual grids exceeds the width of some thin rods of the ROV frame, leading to the failure of the calculation. However, upon calculating the Y-directional drag under other mesh sizes, it is observed that the relative error of damping remains within 2.8 percent within the mesh quantity range of 2.9 to 5.0 million. This indicates that the influence of mesh quantity on the results begins to converge. The trend of Y-directional damping with the change in mesh number is depicted in Figure 7.

Therefore, balancing the accuracy and calculation load, 0.025 m was chosen as the face sizing value.

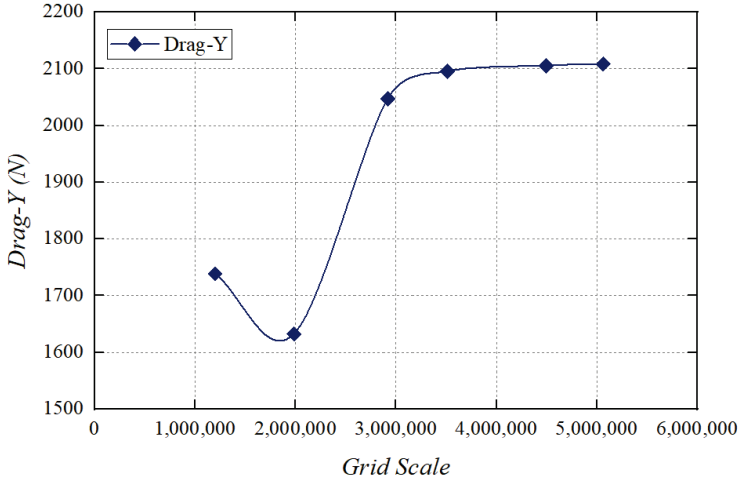

Figure 7. Trend of Y-direction drag with the change in grid number.

Table 4. Drag in Y-directional with variation in mesh scale.

Face Sizing (m)	Mesh Scale	Drag (N)
0.022	5,062,880	2108.3
0.025	4,493,577	2105.168
0.03	3,511,002	2095.363
0.035	2,919,002	2046.842
0.05	1,985,662	1632.463
0.075	1,200,385	1738.659
0.1	abnormal grid	/

3.5. Validation of the Simulation Method

To validate the CFD method employed in the simulations in this work, A standard model called SUBOFF, which designed as a standard underwater vehicle model for testing from a past research conducted by DARPA, is simulated under same process and parameter decision method with this research. The original towing test data for the SUBOFF model can be sourced from a comprehensive series of experiments detailed in the experiment report [34]. By comparing the simulation results with these experimental data under identical operating conditions, we can ascertain the accuracy of the CFD method. Further details regarding the validation procedures can be found in our earlier publication [21]. Figure 8 shows the geometry of the SUBOFF model and also the simulation flow zone. And the errors between the simulations and physical experiments are shown in Table 5.

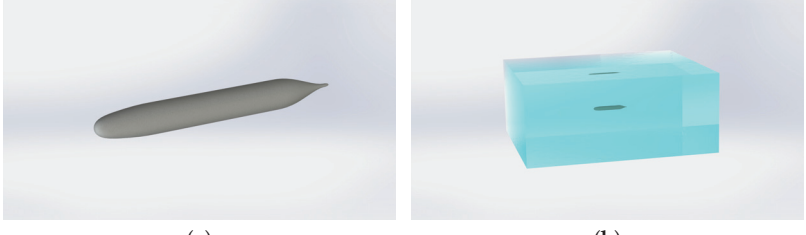

(**a**) (**b**)

Figure 8. SUBOFF model. (**a**) SUBOFF geometry; (**b**) simulation flow zone.

Table 5. Comparison of the numerical results with the experimental data reported in [34].

Velocity (Kn)	Experimental Results of Drag-X (N)	Numerical Results of Drag-X (N)	Errors (%)
5.92	87.4	90.6	3.63
10.00	242.2	238.7	1.45
11.84	332.9	330.5	0.72
13.92	451.5	447.1	0.97
16.00	576.9	582.9	1.04
17.99	697.0	716.4	2.82

To further validate the simulation method with a open-framed model, we simplified the open-source BlueROV2 model as another validation model. The simplified model and the flow zone for the CFD simulation are shown in Figure 9. By conducting towing test simulations in surge direction under the same velocity gradient comparing with a experimental towing test for BlueROV2 from Li et al. [35], the drag force results and the errors between the simulations and the physical experiments are shown in Table 6.

(**a**) (**b**)

Figure 9. BlueROV2 model. (**a**) Simplified BlueROV2 geometry; (**b**) Simulation flow zone.

Table 6. Comparison of the numerical results with the experimental data reported in [35].

Velocity (m/s)	Experimental Results of Drag-X (N)	Numerical Results of Drag-X (N)	Errors (%)
0.2	1.169	1.209	3.45
0.4	6.259	6.621	5.78
0.6	16.167	16.366	1.23
0.8	29.162	31.142	6.79
1.0	44.701	45.248	2.67

3.6. Steady and Unsteady Motion Simulation

By employing the aforementioned CFD method, the hydrodynamic coefficients of the UUV can be obtained. These coefficients can be primarily divided into three parts, corresponding to the coefficients solved for straight-line motion in the X, Y, and Z directions, respectively. Using least squares method for the fitting, hydrodynamic coefficients can be calculated from the simulation results (force and moment). Detailed calculating process are presented in our previous work [21]. As examples, Z-direction straight-line motion and pure heave motion simulations settings are as follows.

3.6.1. Z-Direction Straight-Line Motion Simulation

In this simulation set, a total of 10 velocity conditions were simulated in the positive and negative directions for the Z-directional straight-line navigation. The experimental plan is shown in Table 7.

Table 7. Experiment condition of Z-direction straight-line motion.

Motion Type	Motion Direction	Experiment Condition	Number of Simulation
Z-direction straight motion	Z-positive	relative velocity 0.1–1.0 m/s	10
	Z-negative	variation interval 0.1 m/s	10

3.6.2. Pure Heave Motion Simulation

In this simulation set, a total of five motion frequency conditions were simulated for the pure heave motion. The experimental plan is shown in Table 8.

Table 8. Experiment condition of pure heave motion.

Motion Type	Experiment Condition	Number of Simulation
Pure heave motion	relative velocity: 0.5 m/s amplitude: 0.02 m frequency: 0.2–1.0 Hz variation interval: 0.2 Hz	5

3.6.3. Simulation Results

The final normalized hydrodynamic coefficients of the UUV model are presented in Table 9. Based on these obtained coefficients, the complete dynamic model of the UUV can be described and imported to the physical simulation platform in Section 7.

Table 9. Normalized hydrodynamic coefficients.

Steady	Coefficients	Normalized Value	Unsteady	Coefficients	Normalized Value
X straight	X_{uu}	0.2326	heave	Z_w	−0.4045
	$X_{u\|u\|}$	0.2087		M_w	−0.0142
	Z_{uu}	0.0396		Z_w	−0.1223
	$Z_{u\|u\|}$	−0.00826		M_w	−0.1059
	M_{uu}	0.0260	sway	Y_v	−0.1461
	$M_{u\|u\|}$	0.00397		K_v	0.018
Y straight	Y_{vv}	0.4131		N_v	0.0077
Z straight	Z_{ww}	−0.4740		Y_v	−0.4097
	$Z_{w\|w\|}$	−0.0791		K_v	0.0109
XOY drift	X_{uv}	0.0381		N_v	0.1412
	Y_{uv}	−0.416	yaw	Y_r	−0.0044
	Z_{uv}	−0.0144		K_r	0.0009
	K_{uv}	0.0121		N_r	0.008
	M_{uv}	−0.00928		Y_r	−0.1208
	N_{uv}	0.00625		K_r	0.004
XOZ drift	X_{uw}	−0.00427		N_r	0.0269
	$X_{u\|w\|}$	−0.00041	pitch	X_q	-0.0056
	Z_{uw}	−0.501		Z_q	−0.0032
	$Z_{u\|w\|}$	0.0811		M_q	−0.0084
	M_{uw}	0.00625		X_q	−0.0338
	$M_{u\|w\|}$	−0.00607		Z_q	−0.0013
Surge	X_u	−0.1573		M_q	−0.0117

4. Baseline Parameter Selection of Underwater Vehicle Geometry Design

To identify the geometry of the underwater vehicle body with lower drag, a CFD simulation on the basic body model of the ROV is conducted to analyzed the flow pattern and the pressure distribution around the model, as Figure 10 shows. It can be observed from the velocity streamline and the pressure distribution contour that the highest pressure mainly distributed on the upstream surface of the buoyancy block. Thus, when designing the geometry of the vehicle, emphasis should be placed on optimizing the front part of the vehicle. The design should ensure that after the optimization of the parameters, the flow distribution around the vehicle is even, separations generation is minimized, and the pressure on the upstream surface of the buoyancy block is reduced.

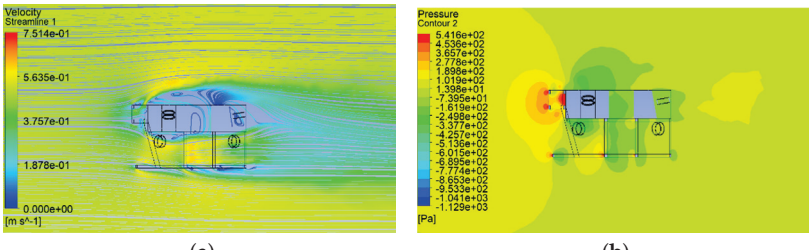

(**a**) (**b**)

Figure 10. Simulation results of 1 knot surge motion of the ROV basic model. (**a**) Velocity streamline; (**b**) pressure distribution.

The principle of the ROV's geometry design is to optimize the front part of the buoyancy block while ensuring the mid and rear body of the buoyancy block remains in same volume to provide adequate buoyancy, as shown in Figure 11. By studying existing design schemes from some of the work-class ROV buoyancy block design in the industry, the shape of the front part of the buoyancy block is altered to streamlined forms in to reduce the drag in surge direction. Two geometry models, concave and convex model were selected, as shown in Figure 12.

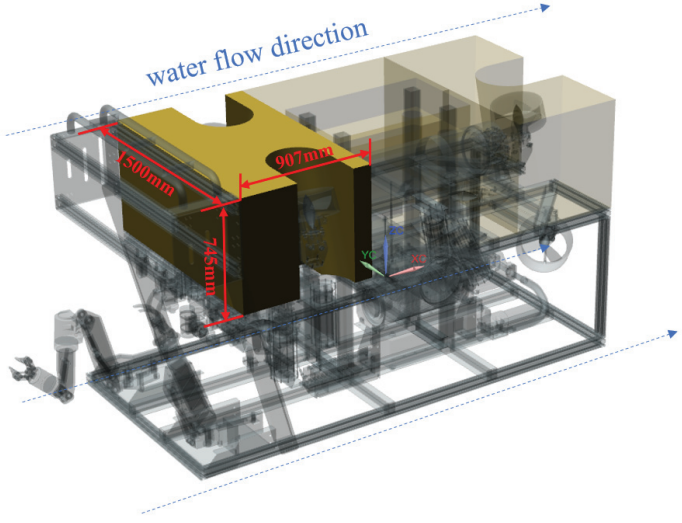

Figure 11. Position of the buoyancy blocks.

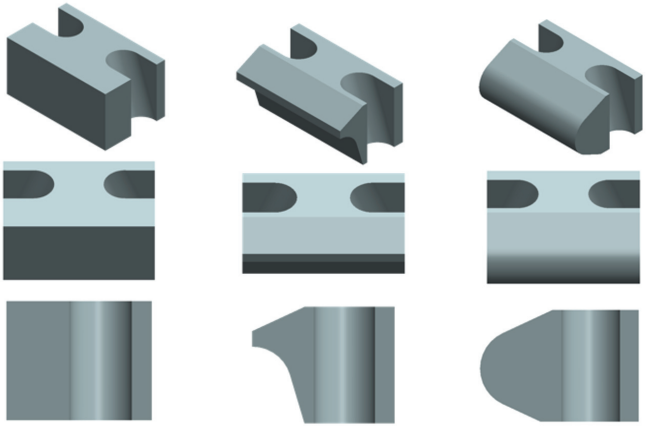

Figure 12. Comparison of buoyancy block geometry of drag-reduction design. (**a**) Basic geometry; (**b**) concave design; (**c**) convex design.

By conducting simulations on the baseline and optimized models of the buoyancy block, as shown in Figure 13, it can be observed that the streamlines above and below the buoyancy block are relatively more sensitive to the cross-section shape at their same side. In light of this, main geometry parameters were designed to decide the cross-section shape of the upstream side in surge direction of the buoyancy block, as Figure 14 shows.

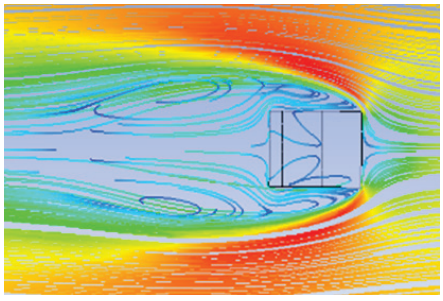

Figure 13. Velocity streamline of the basic shape.

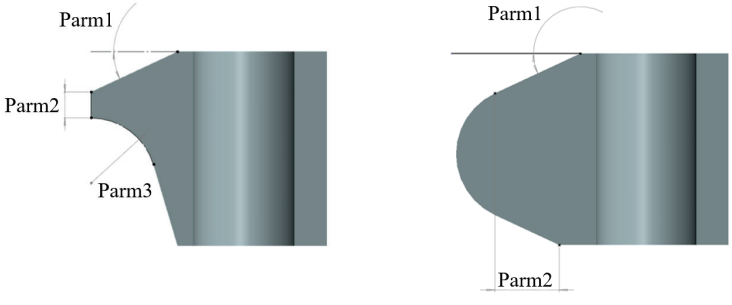

Figure 14. Geometry parameters of the buoyancy block. (**a**) Concave shape; (**b**) convex shape.

In both cross-section shape conditions, parameter 1 is used to optimize the flow state on the upper side independently. For the concave shape design, two exclusive parameters are used for cross-section shape constraint, while for convex shape design, one exclusive parameter is used. Each parameter is assigned with a range to obtain optimized drag-reduction results, as Table 10 shows.

Table 10. Ranges of the geometry parameters.

Parameters	Concave Shape	Convex Shape
Parameter 1	0°–30°	
Parameter 2	100–200 mm	100–332 mm
Parameter 3	150 m–250 mm	/

These parameter ranges are designed reasonably considering avoiding excessive simulation conditions and be able to cover optimal result interval.

5. Underwater Vehicle Drag-Reduction Design Simulation

The general design strategy of the buoyancy block in this research is to reduce the drag from the upstream surface by introducing chamfer and curved surface that can guide the fluid flows smoother. Here, in this section, X-direction refers to the direction of surge motion, and Z-direction to the heave direction. And the complete process of the design strategy is shown in Figure 15.

Firstly, a CFD simulation is conducted for the design parameter 1 of the buoyancy block model of the underwater vehicle to observe the optimal results of parameter 1. With the underwater vehicle's speed around 1 knot and 0.5 m/s, the results obtained from the simulation are presented in Table 11.

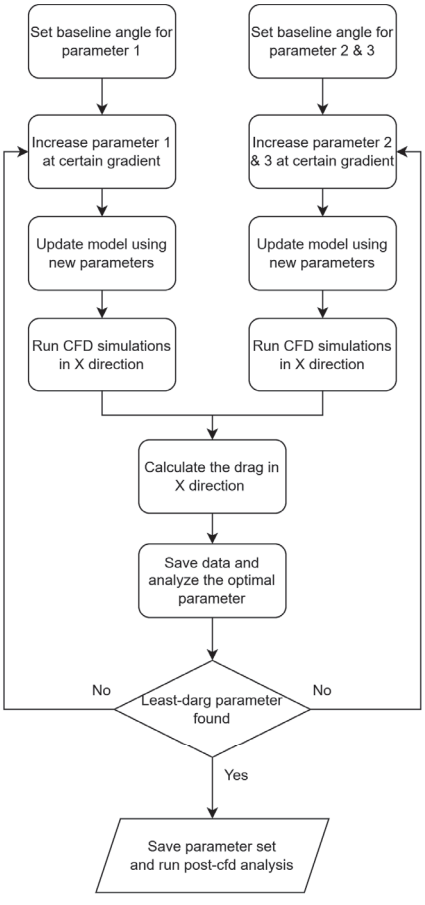

Figure 15. Flowchart of the design strategy.

Table 11. Simulation results of parameter 1 gradient under 0.5 m/s.

Parm1 (°)	Drag-X (N)	Drag-Z (N)
0 (Baseline)	249.4229	0.8633
5	235.1088	1.8906
10	220.8655	5.1278
15	203.1876	10.7220
20	179.0679	31.8028
25	165.0464	22.261
26	168.0316	15.3322
27	163.5313	7.929
28	163.5312	7.9326
29	166.7049	−8.6101
30	169.7156	−16.599

Using mathematical software tools, the results are fitted and analyzed. Figure 16 shows the fitting plot of the drag in the X direction. To aid in visualizing the optimization outcomes, polynomials are employed for fitting within the figure. As parameter 1 is set to 27.5°, the drag in the X direction of the buoyancy block achieves the lowest value. This phenomenon occurs due to the inclination angle of the buoyancy block's windward surface, which induces the formation of water streamlines along the windward surface.

Consequently, this reduces the impact force and stabilizes the streamlines in the upper region, thereby mitigating drag in the X direction.

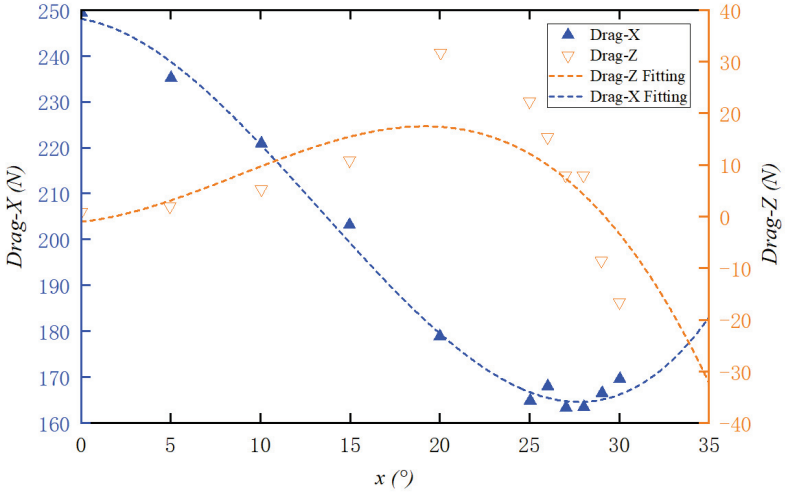

Figure 16. Fitting curve of simulation results of parameter 1.

The pressure distribution contour, velocity streamline, and comparison of the drag-reduced models are shown in Figure 17. When adjusting parameter 1, the angle of approach, the optimization results are best when the angle is between 20 and 25°. If the angle is too large, it will produce undesired forces in the Z direction, leading to counter-optimization results for the underwater vehicle in both directions. The conclusions are consistent with the aforementioned fitting results. In summary, it is concluded that when performing convex shape or concave shape design, the optimal result for the resistance of the buoyancy block's windward surface is achieved when parameter 1 is around 27.5°, within the given parameter range.

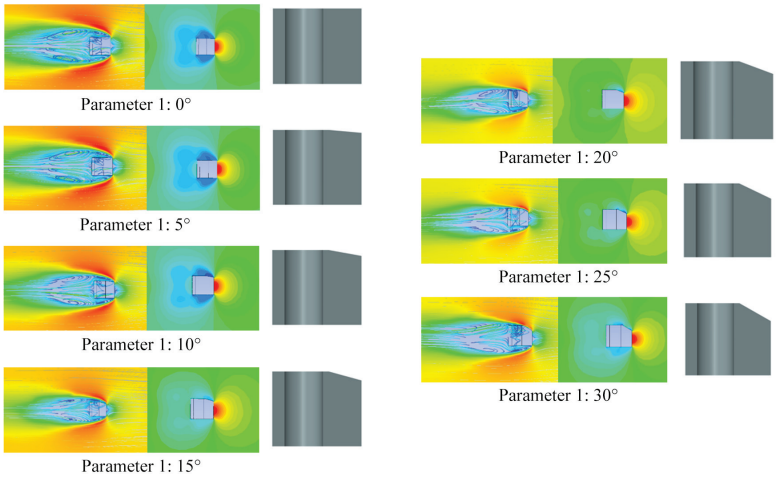

Figure 17. Partial pressure maps, velocity flow field diagrams, and comparison of optimization models.

After the determination of parameter 1, further simulations is conducted combining the concave design parameter 2, which is the approach length, and also parameter 3, which

is the approach radius. With the premise that the optimal result of 27.5° has already been used for parameter 1, the simulation results for concave design are presented in Table 12.

Table 12. Simulation results combining parameters 2 and 3.

Parm1 (°)	Parm2 (mm)	Parm3 (mm)	Drag_X (N)	Drag_Z (N)
27.5	0 (Baseline)	0 (Baseline)	163.5313	7.929
27.5	100	100	176.2649	118.1247
27.5	100	150	180.1904	120.8813
27.5	100	200	187.2354	126.9848
27.5	100	250	192.7954	125.1602
27.5	150	100	171.6083	111.8356
27.5	150	150	176.0831	114.4418
27.5	150	200	182.5689	116.6661
27.5	150	250	189.7901	117.7527

The combined fitting result for parameter 2 and 3 is shown in Figure 18. Polynomial fitting is used for demonstrating the variation trend, and the results were unexpected. The combined optimization of parameters 2 and 3 always showed an increasing trend in the drag in the X direction within the given range, which did not achieve the purpose of drag-reduction design.

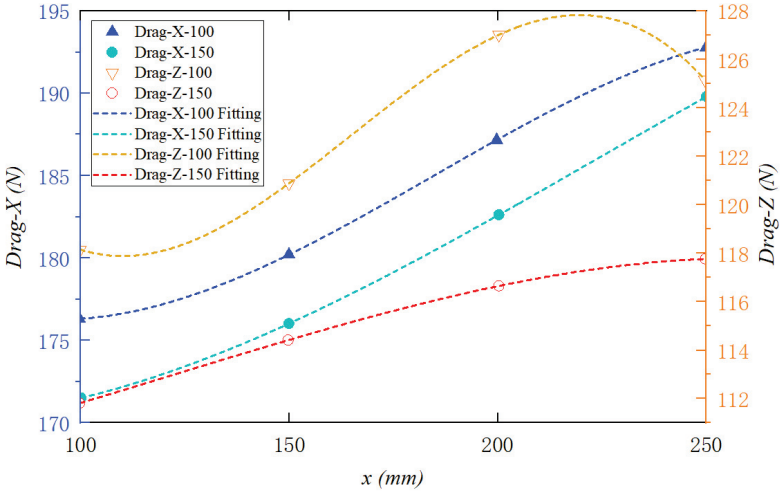

Figure 18. Fitting curve of simulation results of concave design.

The obtained pressure contour and velocity streamline are as Figure 19 shows. It can be observed that during the concave design process, the pressure at the bottom of the buoyancy block gradually increases with the optimization parameters. Additionally, due to the high-speed movement of the fluid along the surface of the vehicle, a larger separation is formed at the rear of the vehicle. Clearly, the concave design scheme has provided results in the opposite direction. The increasing separation acts on the rear of the buoyancy block, generating an oblique downward pull, which significantly increases the drag in both X and Z directions. This does not meet the purpose of this study.

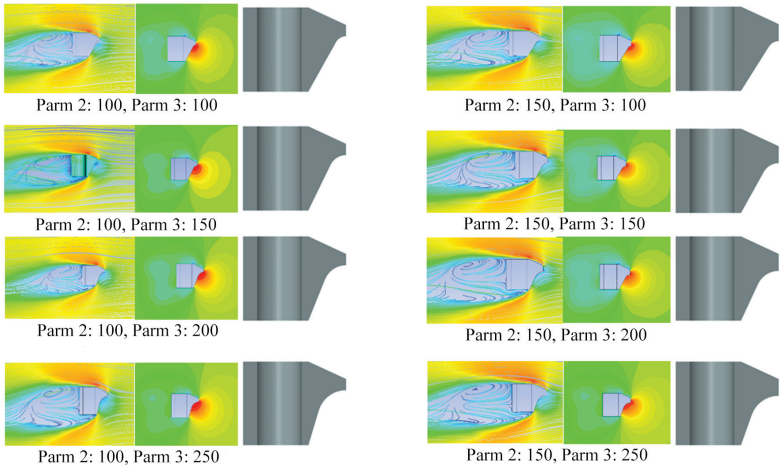

Figure 19. Pressure distribution contour, velocity streamline, and comparison of concave shape models.

In summary, under the condition of concave design, the shape optimization does not produce a positive effect. Due to the increased windward surface area, it leads to larger drag in X and Z directions. Thus, the concave design scheme should not be adopted.

For the convex design, with the premise that the optimal result of parameter 1 is 27.5°, the simulation results are as shown in Table 13.

Table 13. Simulation results of convex design.

Parm1 (°)	Parm2 (mm)	Drag_X (N)	Drag_Z (N)
27.5	0	143.7221	−129.0891
27.5	100	133.6255	−108.5722
27.5	150	128.4418	−95.4861
27.5	200	122.7489	−81.0143
27.5	250	119.3638	−71.6148
27.5	260	117.0644	−67.5918
27.5	270	117.9888	−67.8878
27.5	280	116.7907	−64.4911
27.5	290	114.5748	−58.5837
27.5	300	116.7188	−61.3501
27.5	310	115.9669	−58.5325
27.5	320	116.6530	−56.7416
27.5	332	116.7736	−53.8360

The convex design pressure distribution contour and velocity streamline are shown in Figure 20. In this case, the pressure points on the model decrease, leading to a balanced and stable flow velocity distribution, thereby reducing the generation of separations. This results in a significant decrease in resistance for the vehicle in both the X and Z directions. However, when parameter 2 reaches a threshold value, the separations generated at the model's tail gradually increase, leading to a reverse optimization outcome.

Figure 21 illustrates the fitting results of convex design simulations. When parameter 1 is set to 27.5°, an increase in parameter 2 leads to a quadratic distribution of resistance in the X direction, while resistance in the Z direction shows a linear trend. The growth in the Z direction is gradual, and the Z direction resistance gradually approaches zero within the parameter range. The irregular Z direction resistance generated due to water flow impact on the irregular exterior is mitigated through shape optimization. Moreover, the Z-direction resistance has minimal impact compared to the X direction. As depicted

in Figure 12, convex optimization reaches its minimum value around 290 mm. Hence, for parameter 2, 290 mm is selected as the final value.

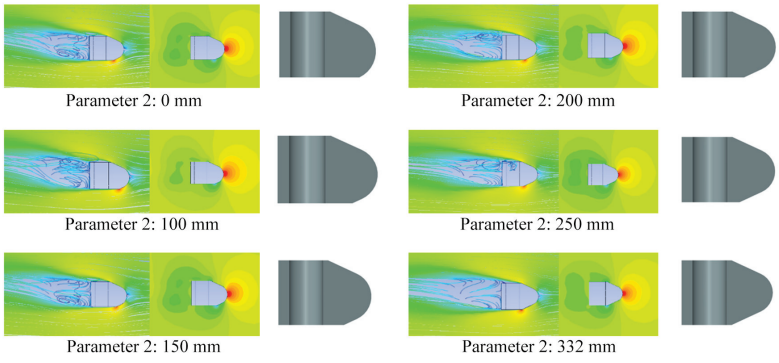

Figure 20. Pressure distribution contour, velocity streamline, and comparison of convex shape models.

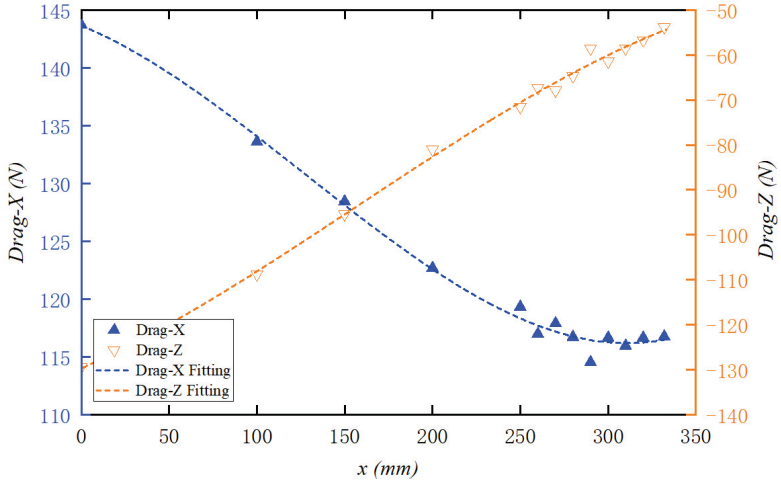

Figure 21. Fitting curve of simulation results of convex shape.

After obtaining our final simulation results, in order to verify the impact of different speeds on shape optimization and resistance, resistance experiments are conducted at different speeds for optimization parameter 1. The purpose was to confirm the independence of speed from the optimization results. The simulation results are presented in Table 14.

Table 14. Simulation results under 1 m/s.

Parm1 (°)	Parm2 (mm)	Drag_X (N)	Drag_Z (N)
5	290	940.0161	1.6734
10	290	883.9527	19.0173
15	290	813.0202	41.2795
20	290	717.9258	128.3172
25	290	658.5213	92.1224
30	290	673.7852	−55.7875

As Figure 22 shows, the final data were compared with the condition where the velocity is 0.5 m/s, as shown in Figure 15. It was observed that there was not a significant

difference in the resistance distribution at this velocity. The overall trend remained consistent. Consequently, the conclusion was drawn that at different velocities, there are no significant factors affecting the drag-reduction of the vehicle.

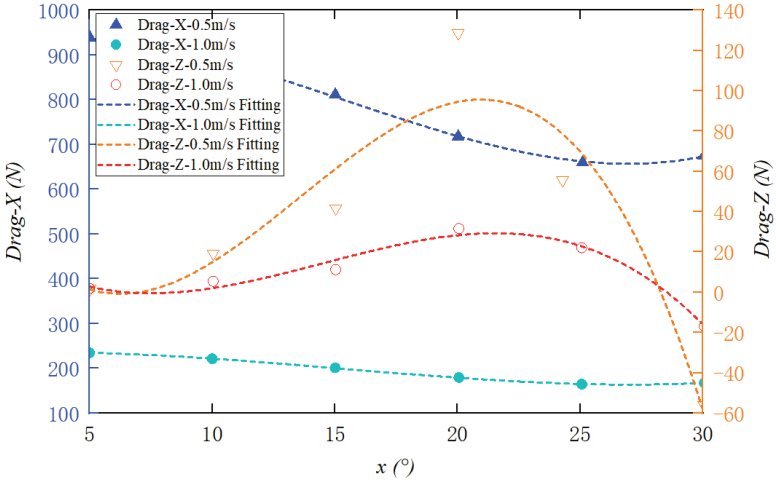

Figure 22. Fitting curve of simulation results under different velocities.

6. Result of Drag-Reduction Shape Design

Firstly, comparing the concave and convex design results by analyzing the velocity streamline of the these two strategy under their optimal parameter set, as Figure 23 shows. The concave strategy increase the flow velocity below the buoyancy block, but does not give much contribution to the reduction of the separations in the lower and rear area as the convex strategy.

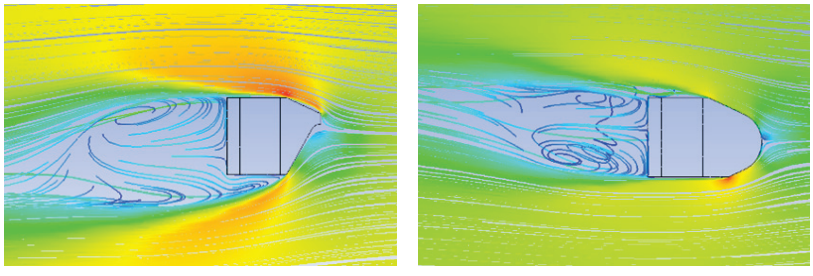

(**a**) (**b**)

Figure 23. Velocity streamline of concave and convex optimization. (**a**) Concave optimization; (**b**) convex optimization.

Following the shape optimization of the buoyancy block at the vehicle's front end, we have obtained optimized parameters that ensure the normal operation of the underwater vehicle in its current configuration. To assess the impact of locally optimizing the buoyancy block on the overall model, the partially designed model is re-integrated into the ROV model. The resulting comparison between the final model and the original model is shown in Figure 24.

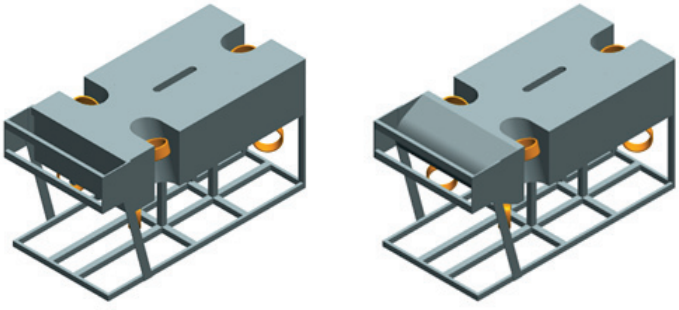

(**a**) (**b**)

Figure 24. Comparison of underwater vehicle model before and after drag-reduction design. (**a**) Original model; (**b**) final model.

Similarly, the optimized model of the ROV is simulated in the condition of velocity equals to 0.5 m/s. The obtained pressure contour and velocity streamline are as Figure 25 shows. A comparison between before and after optimization reveals that the optimized model has great characteristic to reduce pressure on the upstream side. The number of areas with high pressure decreases, leading to a more uniform distribution. Furthermore, the flow velocity field post-optimization indicates that the presence of streamlined surfaces results in the near elimination of separations at the rear of the vehicle. Consequently, with the absence of separations behind the vehicle, resistance in both the X and Z directions decreases.

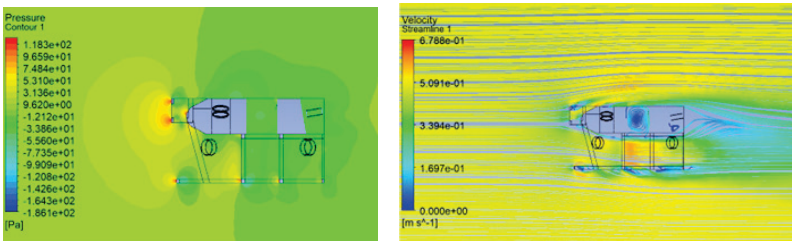

(**a**) (**b**)

Figure 25. Pressure distribution contour and velocity streamline of the final ROV model. (**a**) Pressure distribution; (**b**) velocity streamline.

And as Table 15 shows, The simulation numerical results indicate that after drag-reduction design, the resistance in the X direction has decreased by approximately 18%, while the resistance in the Z direction has decreased by approximately 32%. The localized results have a significant overall impact, leading to a notable reduction in drag on the underwater vehicle.

Table 15. Simulation resistance values before and after drag-reduction design

	Drag_X (N)	Drag_Z (N)
Pre	338.0139	56.4946
Post	276.0298	38.3697
Percentage	18.338%	32.083%

After analyzing the simulation results and contours before and after the optimization design, what can be found is that the major factors that influencing the drag performance of the ROV are the streamlined cross-section shape of its main structure which has big volume

proportion (e.g., buoyancy blocks), due to its open-frame design. By adopting convex shape design of the buoyancy block, the pressure at the front end are greatly reduced, and the volume of the separations at the rear end are also reduced, which decrease the drag from the tail.

7. Establishment and Validation of Underwater Physical Simulation Model

Since one of the objectives of the shape optimization of underwater vehicles is to enhance their mobility, it is essential to design a reasonable motion scheme to verify the improvement in the vehicle's mobility before and after optimization. In this paper, a physical simulation platform is constructed for underwater vehicles, which is based on ROS and built using C++ and Python languages. It integrates Gazebo and Rviz for data visualization operations. In terms of the establishment of the vehicle model, the platform provides a sufficient number of interfaces and offers two different types of underwater vehicles for the current simulation.

The simulation platform uses Gazebo for construction. Although Gazebo itself provides very few underwater-specific modules, the development of Gazebo packages can rely on a continuously improving platform. In addition, integration with ROS, developed by OSRF, has been ensured through the Gazebo/ROS package. The simulation environment is mainly divided into the following parts: ocean environment, underwater vehicle body, thruster model, and sensors. The overall operation process design of the simulation platform is shown in Figure 26. After the underwater vehicle obtains waypoint data and the current state, the heading angle error required by the vehicle at this moment is sent to the controller through a path-tracking algorithm. At this time, the controller calculates the error to obtain the total thrust required by the vehicle. The underwater vehicle thruster model is responsible for decoupling the total thrust required by the underwater vehicle to the relevant thrusters to achieve the independent control of each thruster. The modeling of the underwater vehicle body is mainly divided into three parts: physical model establishment, physical parameter setting, and hydrodynamic parameter estimation. At this time, the thruster thrust can move the vehicle through the body model of the underwater vehicle. The sensors carried by the vehicle will record the movement state at this time and capture and send the current state to the path-tracking algorithm to complete the next cycle.

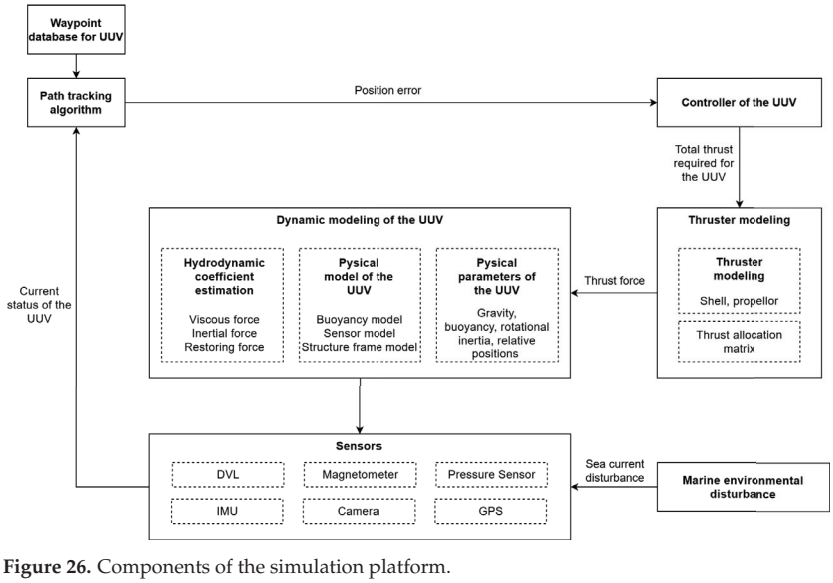

Figure 26. Components of the simulation platform.

Figure 27 shows the laboratory underwater vehicle reproduced in the simulation platform, which is a fully actuated vehicle composed of seven thrusters. The control in the vertical plane is driven by three motors, and the control in the horizontal plane is driven by four motors. The simulation model is constructed based on the solved kinematic and dynamic models of the underwater vehicle.

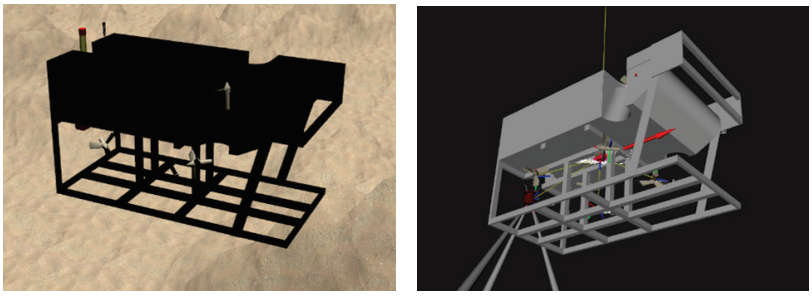

(**a**) (**b**)

Figure 27. Establishment of the ROV model in the physical simulation platform. (**a**) With map; (**b**) without map.

To facilitate intuitive observation of the model establishment and drag-reduction design, the primary movement objective of the vehicle in the simulation platform is to follow a predetermined trajectory within a two-dimensional plane. The simulation mainly consists of four components: the preset trajectory, the controller, the vehicle model parameters, and the effect presentation. Five coordinate points are selected within the two-dimensional plane and connected. The vehicle starts from a given position and traverses the five coordinate points, ensuring that the control parameters remain unchanged between the original model and the final model, i.e., a consistent controller and control strategy are determined. The model parameters of the vehicle before and after the drag-reduction design have been solved, as mentioned earlier. The dynamic and kinematic models of the vehicle before and after optimization are written into the simulation, and the results are shown in Figure 28.

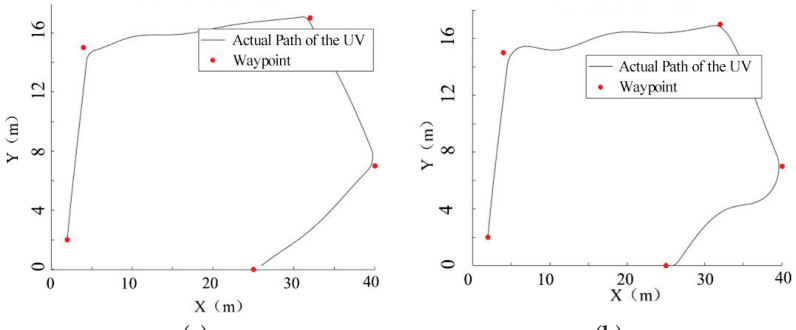

(**a**) (**b**)

Figure 28. Path following simulation of the underwater vehicle model before and after drag-reduction design. (**a**) Original model; (**b**) final model.

By examining the path tracking plot for the five given way-points, it can be observed that with all other variables remaining constant, the optimized model achieves better results with the specified control scheme. This allows the underwater vehicle to complete the set objectives more easily, with more accurate tracking of the established route. The vertical error of the vehicle from the preset trajectory is minimized at each navigation position, as shown in Figure 29. Since the vehicle needs to stably track the path, which involves

converging its vertical error from the trajectory onto the vehicle's path, the comparison of the vertical error from the optimized model before and after optimization with the preset trajectory indicates that the vehicle has acquired superior mobility capabilities after optimization. When tracking the trajectory, it can ensure that the vehicle better achieves the set objectives.

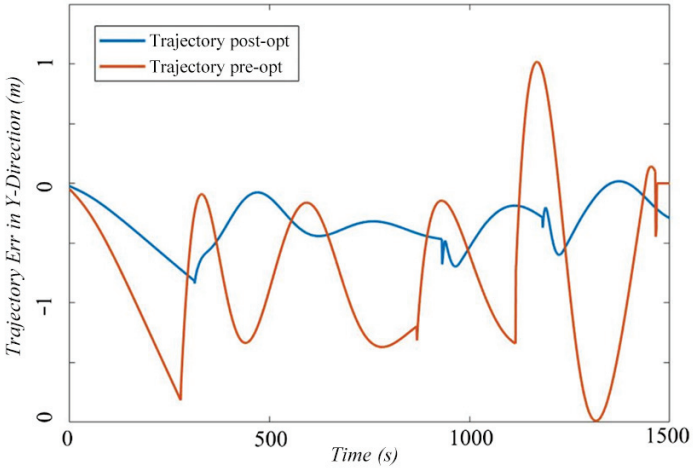

Figure 29. Vertical error between the model and the trajectory before and after drag-reduction design.

8. Conclusions

This work primarily focuses on modeling and drag-reduction design of a remotely operated underwater vehicle. By establishing the dynamic model of the vehicle, a comprehensive vehicle model that can represent the hydrodynamic characteristics of the vehicle is developed. CFD simulation methods are employed to determine the hydrodynamic parameters and analyze the fluid performance of underwater vehicle. Building upon this analysis, hypotheses concerning drag-reduction design are proposed, aiming to enhance the vehicle's shape without compromising its overall operational effectiveness. The paper presents two distinct types of design strategy, which are evaluated against baseline parameters to derive the target shape for the underwater vehicle. Results demonstrate a reduction in resistance by 18% in the X direction and 32% in the Z direction during vehicle movement. To further validate the efficacy of the design scheme, a independence verification is conducted across different velocities. Based on the analysis of the simulation results and contours before and after the drag-reduction design, it is evident that the primary factors influencing the drag performance of the UUV are related to the streamlined cross-section shape of its main structure, particularly the buoyancy blocks, due to the open-frame design. By adopting a convex shape for the buoyancy blocks, the pressure at the front end is significantly reduced, and the volume of separations at the rear end is minimized, thereby decreasing the drag from the tail. Moreover, the paper establishes an underwater physical simulation platform to verify the mobility of the vehicle both before and after the drag-reduction design. The findings confirm that the proposed design scheme effectively enhances the mobility of underwater vehicles. Due to the limitations of the simulations, physical experiments should be conducted in the following studies to validate the effectiveness of the design strategy. Also, flow influence from waves and vortexes that applied on underwater vehicles can be tested in real-world to measure the positive impact on motion stabilization control of the vehicles.

Author Contributions: Conceptualization, X.L.; methodology, X.L. and M.Z.; software, M.Z. and Y.S.; validation, X.L. and M.Z.; formal analysis, X.L. and M.Z.; investigation, X.L.; resources, M.Z.; data curation, X.L.; writing—original draft preparation, X.L. and D.Z.; writing—review and editing, X.W. and D.Z.; visualization, X.L. and M.Z.; supervision, X.W.; project administration, X.W.; funding acquisition, X.W. and X.L. All authors have read and agreed to the published version of the manuscript.

Funding: The work is supported by the Shenzhen Science and Technology Program (JSGG20211029095205007 and JCYJ20210324115812034), the Shenzhen Science and Technology Major Program (KJZD20231023100459001) and the Guangdong Provincial Key Laboratory of Intelligent Morphing Mechanisms and Adaptive Robotics Program (2023B1212010005).

Institutional Review Board Statement: Not applicable.

Informed Consent Statement: Not applicable.

Data Availability Statement: The original contributions presented in the study are included in the article, further inquiries can be directed to the corresponding author.

Acknowledgments: Authors would like to give special thanks to China Offshore Fugro Geosolutions (Shenzhen) Co., Ltd. for supporting experimental resources and sites.

Conflicts of Interest: Author Xuecheng Li was employed by the company China Offshore Fugro Geosolutions (Shenzhen) Co., Ltd. The remaining authors declare that the research was conducted in the absence of any commercial or financial relationships that could be construed as a potential conflict of interest.

References

1. Dalhatu, A.A.; de Azevedo, R.C.; Udebhulu, O.D.; De Tomi, G. Recent developments of remotely operated vehicle in the oil and gas industry. *Holos* **2021**, *3*, 1–18.
2. Kabanov, A.; Kramar, V.; Ermakov, I. Design and modeling of an experimental rov with six degrees of freedom. *Drones* **2021**, *5*, 113. [CrossRef]
3. Wu, Y.; Sima, C.; Zhu, Z. Key Development Directions of Marine Science and Technology. *Sci. Technol. Foresight* **2022**, *1*, 20–35.
4. Shen, K.; Yan, Y.; Yan, H. Research Status and Development Trend of Deep-sea Work Class ROV in China. *Control Inf. Technol.* **2020**, *3*, 7.
5. Zhang, K.; Yang, H.; Sun, T. Research on drag reduction structure design of ROV for high speed. *Ship Sci. Technol.* **2021**, *43*, 76–80.
6. Purzycki, M.; Komorowska, A.; Ilnicka, A.; Papież, J.; Szymańska, E. From ROVs to AUVs–Optimization and Analysis of Underwater Vehicles Design. In Proceedings of the 2022 45th Jubilee International Convention on Information, Communication and Electronic Technology (MIPRO), Opatija, Croatia, 23–27 May 2022; pp. 1517–1521.
7. Singh, A.P.; Paul, A.; Singh, Y.; Mukherjee, K. Mechanical design of a modular underwater rov for surveillance and cleaning purpose. In *Proceedings of the Recent Advances in Mechanical Engineering: Select Proceedings of ICRAME 2020*; Springer: Berlin/Heidelberg, Germany, 2021; pp. 779–793.
8. Fossen, T.I. *Handbook of Marine Craft Hydrodynamics and Motion Control*; John Wiley & Sons: Hoboken, NJ, USA, 2011.
9. Chin, C.; Lau, M. Modeling and testing of hydrodynamic damping model for a complex-shaped remotely-operated vehicle for control. *J. Mar. Sci. Appl.* **2012**, *11*, 150–163. [CrossRef]
10. Eidsvik, O.A. Identification of Hydrodynamic Parameters for Remotely Operated Vehicles. Master's Thesis, NTNU: Trondheim, Norway, 2015.
11. Yang, R.; Clement, B.; Mansour, A.; Li, M.; Wu, N. Modeling of a complex-shaped underwater vehicle for robust control scheme. *J. Intell. Robot. Syst.* **2015**, *80*, 491–506. [CrossRef]
12. Panda, J.P.; Mitra, A.; Warrior, H.V. A review on the hydrodynamic characteristics of autonomous underwater vehicles. *Proc. Inst. Mech. Eng. Part M J. Eng. Marit. Environ.* **2021**, *235*, 15–29. [CrossRef]
13. Avila, J.P.J.; Adamowski, J.C. Experimental evaluation of the hydrodynamic coefficients of a ROV through Morison's equation. *Ocean Eng.* **2011**, *38*, 2162–2170. [CrossRef]
14. Zarei, A.; Ashouri, A.; Hashemi, S.; Bushehri, S.F.; Izadpanah, E.; Amini, Y. Experimental and numerical study of hydrodynamic performance of remotely operated vehicle. *Ocean Eng.* **2020**, *212*, 107612. [CrossRef]
15. Ray, A.; Singh, S.; Seshadri, V. Evaluation of linear and nonlinear hydrodynamic coefficients of underwater vehicles using CFD. In Proceedings of the International Conference on Offshore Mechanics and Arctic Engineering, Honolulu, Hawaii, USA, 31 May–5 June 2009; Volume 43444, pp. 257–265.
16. Tang, S.; Ura, T.; Nakatani, T.; Thornton, B.; Jiang, T. Estimation of the hydrodynamic coefficients of the complex-shaped autonomous underwater vehicle TUNA-SAND. *J. Mar. Sci. Technol.* **2009**, *14*, 373–386. [CrossRef]
17. Jagadeesh, P.; Murali, K. RANS predictions of free surface effects on axisymmetric underwater body. *Eng. Appl. Comput. Fluid Mech.* **2010**, *4*, 301–313. [CrossRef]

18. Jinxin, Z.; Yumin, S.; Lei, J.; Jian, C. Hydrodynamic performance calculation and motion simulation of an AUV with appendages. In Proceedings of the 2011 International Conference on Electronic & Mechanical Engineering and Information Technology, Harbin, China, 12–14 August 2011; Volume 2, pp. 657–660.
19. Hou, X.; Guo, S.; Shi, L.; Xing, H.; Liu, Y.; Liu, H.; Hu, Y.; Xia, D.; Li, Z. Hydrodynamic analysis-based modeling and experimental verification of a new water-jet thruster for an amphibious spherical robot. *Sensors* **2019**, *19*, 259. [CrossRef]
20. Katsui, T.; Kajikawa, S.; Inoue, T. Numerical Investigation of Flow around a ROV with Crawler Based Driving System. In *Proceedings of the International Conference on Offshore Mechanics and Arctic Engineering*; American Society of Mechanical Engineers: New York, NY, USA, 2012; Volume 44946, pp. 23–30.
21. Hong, L.; Wang, X.; Zhang, D.; Xu, H. Numerical study on hydrodynamic coefficient estimation of an underactuated underwater vehicle. *J. Mar. Sci. Eng.* **2022**, *10*, 1049. [CrossRef]
22. Zhang, D.; Wang, X.; Zhao, M.; Hong, L.; Li, X. Numerical Investigation on Hydrodynamic Characteristics and Drag Influence of an Open-Frame Remotely Operated Underwater Vehicle. *J. Mar. Sci. Eng.* **2023**, *11*, 2143. [CrossRef]
23. Hong, L.; Wang, X.; Zhang, D.S. CFD-based hydrodynamic performance investigation of autonomous underwater vehicles: A survey. *Ocean. Eng.* **2024**, *305*, 117911. [CrossRef]
24. Baital, M.S.; Mangkusasmito, F.; Rahmawaty, M.A. Specification Design and Performances Using Computational Fluid Dynamics for Mini-Remotely Operated Underwater Vehicle. *Ultim. Comput. J. Sist. Komput.* **2022**, *14*, 20–27. [CrossRef]
25. Wang, Y.; Gao, T.; Pang, Y.; Tang, Y. Investigation and optimization of appendage influence on the hydrodynamic performance of AUVs. *J. Mar. Sci. Technol.* **2019**, *24*, 297–305. [CrossRef]
26. Ignacio, L.C.; Victor, R.R.; Del Rio, R.; Pascoal, A. Optimized design of an autonomous underwater vehicle, for exploration in the Caribbean Sea. *Ocean Eng.* **2019**, *187*, 106184. [CrossRef]
27. Lin, G.; Yang, Y.; He, Z.; Jiao, P. Hydrodynamic optimization in high-acceleration underwater motions using added-mass coefficient. *Ocean Eng.* **2022**, *263*, 112274. [CrossRef]
28. Moonesun, M.; Korol, Y.; Dalayeli, H. CFD analysis on the bare hull form of submarines for minimizing the resistance. *Int. J. Marit. Technol.* **2015**, *3*, 1–16.
29. Luo, W.; Guo, X.; Dai, J.; Rao, T. Hull optimization of an underwater vehicle based on dynamic surrogate model. *Ocean Eng.* **2021**, *230*, 109050. [CrossRef]
30. Lee, M.H.; Park, Y.D.; Park, H.G.; Park, W.C.; Hong, S.; Lee, K.S.; Chun, H.H. Hydrodynamic design of an underwater hull cleaning robot and its evaluation. *Int. J. Nav. Archit. Ocean. Eng.* **2012**, *4*, 335–352. [CrossRef]
31. Lin, Y.; Guo, J.; Li, H.; Wang, Z.; Chen, Y.; Huang, H. Improvement of hydrodynamic performance of the disk-shaped autonomous underwater helicopter by local shape modification. *Ocean Eng.* **2022**, *260*, 112056. [CrossRef]
32. Serani, A.; Scholcz, T.P.; Vanzi, V. A Scoping Review on Simulation-based Design Optimization in Marine Engineering: Trends, Best Practices, and Gaps. *Arch. Comput. Methods Eng.* **2024**, 1–29. [CrossRef]
33. Lin, Y.H.; Li, X.C. The investigation of a sliding mesh model for hydrodynamic analysis of a SUBOFF model in turbulent flow fields. *J. Mar. Sci. Eng.* **2020**, *8*, 744. [CrossRef]
34. Liu, H.L.; Huang, T.T. *Summary of DARPA Suboff Experimental Program Data*; Technical report; Naval Surface Warfare Center, Carderock Division: Bethesda, MD, USA, 1998.
35. Li, Q.; Cao, Y.; Li, B.; Ingram, D.M.; Kiprakis, A. Numerical modelling and experimental testing of the hydrodynamic characteristics for an open-frame remotely operated vehicle. *J. Mar. Sci. Eng.* **2020**, *8*, 688. [CrossRef]

Journal of
Marine Science and Engineering

MDPI

Article

Numerical Study of Discharge Coefficients for Side-Damaged Compartments

Siwen Tian [1], Fei Peng [1], Zhanzhi Wang [1,*] and Jingda Li [2]

[1] Department of Naval Architecture and Ocean Engineering, Naval University of Engineering, Wuhan 430033, China
[2] Unit 91991, Zhoushan 316100, China
* Correspondence: wzz200425@126.com

Abstract: Accurately evaluating the buoyancy and stability of damaged ships, particularly the flow rate of the water inflow through damaged openings, is of great significance for ship rescue and emergency repair. A three-dimensional simplified model of inflow for a ship's damaged side bulkheads is established using the shear stress transport *k-epsilon* and volume of fluid (VOF) models by STAR-CCM+. Moreover, the flow rates of water inflow through damaged openings with different shapes, characteristic sizes, and central depths are calculated. Furthermore, the corresponding discharge coefficients are obtained, and the relevant rules are summarized. It was found that the influence of water depth on the coefficient is minimal in these work conditions, but from the perspective of the damaged opening's characteristic dimensions and shape, the variation in the coefficient is more pronounced. Overall, the triangular opening has a higher coefficient than the circular opening, which in turn is higher than that of the square-damaged opening, and the coefficient decreases as the size of the opening increases. Lastly, empirical formulas for two different methods are provided. The research provides a reference for the rescue repair and buoyancy stability assessment of damaged ships.

Keywords: damaged ship; flooding; discharge coefficient; CFD

Citation: Tian, S.; Peng, F.; Wang, Z.; Li, J. Numerical Study of Discharge Coefficients for Side-Damaged Compartments. *J. Mar. Sci. Eng.* **2024**, *12*, 1502. https://doi.org/10.3390/jmse12091502

Academic Editors: Nastia Degiuli and Ivana Martić

Received: 11 July 2024
Revised: 26 August 2024
Accepted: 28 August 2024
Published: 1 September 2024

1. Introduction

Military ships are vulnerable to gunfire, torpedoes, anti-ship missiles, other ships, reefs, or sea structure impacts caused by hull damage; such damage can cause seawater to flow into cabins or liquid tanks to leak. If these leaks are not plugged in time, the ship's maneuverability, self-sustaining, and strike efficiency may be affected, leading to capsizing and loss of personnel. Civilian ships also face the same risks, including reef impacts, collisions, trade blocking, unrestricted submarine warfare, and other forms of tactical warfare, which greatly influence the safety of civilian ship transportation.

Evaluating the technical status of the ship after damage, especially the loss of buoyancy, is an important part of the repair work in damage control. In 1942, the U.S. aircraft carrier *USS Yorktown* (CV-5) was hit by Japanese aircraft in the Battle of Midway, resulting in a large amount of seawater rushing into the compartments. The ship's hull was damaged due to the commander's misjudgment of the ship's buoyancy and stability status. Moreover, the loss of control was missed; the CV-5 was attacked by a Japanese submarine and sank during the subsequent repair process. In 2018, the Norwegian frigate *KNM Helge Ingstad* (*F-313*) collided with a 62,000-ton tanker and ran aground, leading to serious injuries. The collision with a 62,000-ton tanker resulted in the ship running aground, causing a severe tear on the starboard side and a large amount of seawater rushing into the hold. The ship eventually capsized and sank. Thus, the importance of a timely and accurate assessment of the impact of breaching water ingress on a ship's buoyancy and stability is self-evident. Hence, estimating the rate of breaching water ingress and calculating the time of the ship's breaching water ingress are key issues in the assessment.

Theoretically, for viscous ideal fluid without considering the air compression effect, estimating the water inflow rate through the ship's damaged opening is equivalent to the thin-walled small hole constant outflow problem. As shown in Figure 1, to maintain a constant water level, the cross-sectional area, S_1, of a thin-walled container is required. The container wall is at a distance from the reference surface height, z; the cross-sectional area of a small orifice is S_2, the vertical distance from the orifice to the water surface is H, atmospheric pressure is p, gravitational acceleration is g, the density of the liquid is ρ, the water level decrease rate in the container is v_1, and the orifice outflow rate is v. The law of conservation of mass and Bernoulli's equation yield the following:

$$\begin{cases} \frac{{v_1}^2}{2} + \frac{p}{2} + g(z+H) = \frac{v^2}{2} + \frac{p}{\rho} + gz \\ S_1 v_1 = S_2 v \end{cases} \tag{1}$$

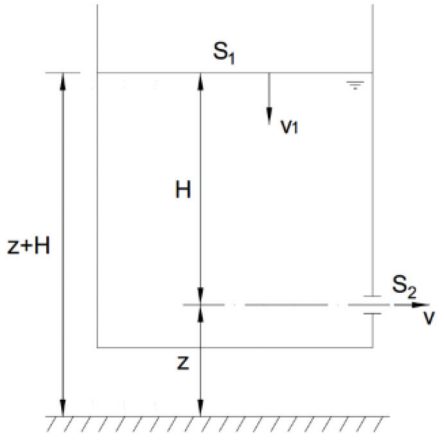

Figure 1. A thin-walled small opening with constant outflow.

Equation (1) can be simplified as follows:

$$v = \sqrt{\frac{2gH}{1 - \left(\frac{S_2}{S_1}\right)^2}} \tag{2}$$

Equation (2) represents the liquid outflow rate from the small, thin-walled orifice. In particular, when $S_2 \ll S_1$, Equation (2) can be simplified as follows:

$$v = \sqrt{2gH} \tag{3}$$

Equation (3) applies to seawater being poured into the compartments from the outboard side through the damaged opening but it does not apply to the diffusion of liquids or their discharge from the compartments to the outboard side.

This can lead to the theoretical formula used for calculating the flow rate through the opening, as follows:

$$Q = S_2 v \tag{4}$$

where Q is the volume flow rate through the opening.

A large opening with thin walls can be conceptually divided into numerous small openings, as the flow rate varies at different points across the damaged surface. The flow rate through the damaged opening is obtained by integrating the flow velocity over the area of these small openings. Its average over the area is the average outflow velocity of the opening [1].

However, in reality, during the flow process, the gravitational potential energy of the liquid does not completely convert into kinetic energy. Some of the energy is dissipated due to the internal friction between liquid molecules, the friction between the liquid and the wall surfaces, and the contraction effect of the outflow at the breach, resulting in the actual flow rate being less than the flow rate calculated theoretically. As a result, the discharge coefficient, C_d (also known as the flow rate coefficient), is introduced to correct the flow rate through the opening defined via Equation (4):

$$Q_0 = C_d \cdot Q \tag{5}$$

where Q_0 is the actual volume flow rate through the breach.

In the boundary conditions, C_d is affected by the shape, size, location, and central depth of the opening. Moreover, there is no theoretical formula to calculate the value of C_d in the industry; it is usually empirically taken between 0.5 and 0.9 according to different situations. Furthermore, a half-empirical dimensionless pressure loss factor k_L is also commonly used to obtain a semi-empirical dimensionless pressure loss coefficient [2], as follows:

$$C_d = \frac{1}{\sqrt{1 + k_L}} \tag{6}$$

The method of obtaining the value of C_d must be investigated to obtain a more accurate breakwater inlet flow rate in the buoyancy stability assessment of damaged vessels, especially when using numerical methods, such as the quasi-static method [3]. In the past, the discharge coefficient was usually experimentally obtained. Vassalos [4] found that a coefficient discharge of 0.6 is a good approximation for the damaged opening. Ruponen [5–7] conducted a series of experimental studies on the damaged opening inlet of a box barge. The author found that the discharge coefficient fluctuated between 0.72 and 0.83 for damaged opening sizes ranging from 0.02 m × 0.02 m to 0.1 m × 0.1 m with different types of inlets. Moreover, the discharge coefficient decreases with an increase in the damaged opening size. Sterning [8] investigated the discharge coefficients of a ship's cross-flooding duct through scale model experiments. The authors provided an essential dataset for the validation and further development of CFD approaches. Y. Li [9] conducted experimental studies on the discharge coefficient of petalled breaches and compared these results with the discharge coefficient of flat-edged damages. Wang [10] conducted a detailed experimental study of oil–water two-phase oil spill discharge coefficients for different damaged opening shapes, such as circular, square, elongated, and pentagonal. The design of the research program can be used as a reference for investigating the gas–liquid two-phase discharge coefficients.

With the vigorous development of CFD technology in recent years, parameters such as the mass flow rate of the damaged opening outflow can be directly obtained by numerical calculation, providing a new way to research discharge coefficients. Li [11] established a simplified two-dimensional single-chamber model using Fluent software and a *k-epsilon* turbulence model to simulate the discharge coefficients of ship breaches. The authors used the polynomial fitting method to provide the discharge coefficients and the relationship between the breaches and the aperture ratio, as follows:

$$C_d = 0.641 + 0.00952\frac{D}{h_c} \tag{7}$$

where D is the damaged opening size and h_c is the distance from the center of the damaged opening to the water surface. However, the investigation did not consider the impact of factors such as the shape of the damaged opening on the discharge coefficient. Li [12,13] used Fluent software based on the box barge model to explore the discharge coefficients of specific breaches of double-hulled oil tankers. The author set up 16 conditions from different inlet and outlet water flow modes, different fluid level heights, shapes and sizes, fluid mediums, flooding situations of long openings, lateral water inlets with structures,

commonly used damaged openings in the hull, double-hull bottom breakouts, and double-hull side breakouts, i.e., nine parameters were analyzed. The situations considered were comprehensive, but no detailed study was conducted on the individual angles. Hence, the results of each parameter were only provided for a single working condition.

Zhang [14] employed Fluent software to establish a simplified model of half-cylindrical compartments. The author employed a simplified model of a semi-cylindrical cabin to simulate the bottom-damaged opening of the ship, obtaining a discharge coefficient of approximately 0.65. Moreover, the author also noted that the irregular edge reduces the value of the inlet discharge coefficient. Furthermore, increasing the size of the damaged opening increases the inlet discharge coefficient slightly; however, it is set up with fewer working conditions (eight groups). The characteristic sizes of the damaged opening are small (0.0197–0.0394 m), and the depths of the water are also small (0.3 m and 0.5 m). Xue [15] used the shear stress transport *k-epsilon* and volume of fluid (VOF) models to analyze the attitude and resistance of a side-damaged frigate DTMB-5415. Wei [16,17] used the slip mesh method to develop numerical calculations for the discharge coefficients of square and circular flow holes of the SUBOFF submarine model with different drafts and sizes. However, the area of the flow holes was too small (0.004–0.016 m^2). In addition, the study's results could hardly be applied to the problem of valuing the discharge coefficients of the breaches of the damaged ship. Hu [18] used the VOF method to simulate the discharge coefficient of the circular drainage hole of the closed cavity and summarized the relevant laws. However, his research mainly focused on the drainage holes of aircraft, which are on the millimeter scale in diameter. Since the cabin damage and water ingress are not closed-cavity drainage models, his conclusions do not apply to ship damage issues, but his research methods can be used for reference.

There have been extensive investigations on discharge coefficients, but a universal empirical formula applicable to the ship breakout water intake problem has not yet been developed. In this paper, the discharge coefficient of the simplified model of the ship's side-damaged opening is calculated using the RANS method and VOF model, using commercial fluid numerical computation software STAR-CCM+ (version 2402). Moreover, the relationship between the water intake discharge coefficient and parameters, such as the shape of the damaged opening, the area, the characteristic size, and the depth of the center, is provided based on the idea of control variables. This 'law' can provide a certain reference basis for the assessment of the buoyancy state of a breached ship and for making decisions on damage control. Moreover, the research results can provide a reference basis for assessing the buoyancy and stability of damaged ships and for guiding decisions on damage management.

2. Computational Principles and Numerical Modeling

2.1. Principle of Discharge Coefficient Calculation

A CFD simulation of the damaged ship's damaged opening outflow process was conducted. The damaged opening mass flow rate was monitored and employed to calculate the average velocity of the damaged opening outflow. The results were compared with the theoretical velocity (hereinafter referred to as the average method) or with the theoretical velocity of the theoretical mass flow rate, which is obtained by dividing the area of the theoretical mass flow rate by the mass flow rate of the numerical calculation (hereinafter referred to as the integral method). Hence, the discharge coefficient is obtained.

(1) Averaging:

The mass flow rate of the damaged opening, obtained by numerical calculation, is M_0 (unit: kg/s), the cross-sectional area of the damaged opening is S_2 (unit: m^2), and the density of the liquid is ρ (unit: kg/m^3). The average flow rate of the damaged opening outflow v_0 (unit: m/s) is as follows:

$$v_0 = \frac{M_0}{\rho S_2} \tag{8}$$

The discharge coefficient can be obtained by considering the theoretical flow rate at the center of the damaged opening as the average theoretical flow rate, v, as follows:

$$C_d = \frac{v_0}{v} \tag{9}$$

(2) Integral method:

The theoretical mass flow rate M (unit: kg/s) is obtained by dividing the area of the theoretical flow rate, v, with the liquid density, ρ, in the damaged opening cross-section, as follows:

$$M = \int_{S_2} \rho v ds \tag{10}$$

The discharge coefficient is as follows:

$$C_d = \frac{M_0}{M} \tag{11}$$

The discharge coefficients obtained from the two methods are consistent [19].

2.2. Control Equations

The three-dimensional incompressible viscous fluid transient equations of motion are used as the theoretical basis. Moreover, the fluid density and the viscosity coefficient are assumed to be constants.

The mass conservation equation (the continuity equation) can be expressed as follows:

$$\frac{\partial u}{\partial x} + \frac{\partial v}{\partial y} + \frac{\partial w}{\partial z} = 0 \tag{12}$$

where u, v, and w are the velocity components of the velocity vector, v, along the x, y, and z axes, respectively.

The equation of conservation of momentum (equation of motion) can be expressed as follows:

$$\rho \frac{dv}{dt} = \rho F - grad p + \mu \nabla^2 v \tag{13}$$

where f is the mass force, p is the pressure, and μ is the hydrodynamic viscosity.

2.3. Turbulence Modeling

Navier–Stokes (N-S) equations can be expressed as follows:

$$\begin{cases} \frac{\partial(\rho u)}{\partial t} + \nabla(\rho u V) = -\frac{\partial p}{\partial x} + \frac{\partial \tau_{xx}}{\partial x} + \frac{\partial \tau_{yx}}{\partial y} + \frac{\partial \tau_{zx}}{\partial z} + \rho f_x \\ \frac{\partial(\rho u)}{\partial t} + \nabla(\rho v V) = -\frac{\partial p}{\partial y} + \frac{\partial \tau_{xy}}{\partial x} + \frac{\partial \tau_{yy}}{\partial y} + \frac{\partial \tau_{zy}}{\partial z} + \rho f_y \\ \frac{\partial(\rho u)}{\partial t} + \nabla(\rho w V) = -\frac{\partial p}{\partial z} + \frac{\partial \tau_{xz}}{\partial x} + \frac{\partial \tau_{yz}}{\partial y} + \frac{\partial \tau_{zz}}{\partial z} + \rho f_z \end{cases} \tag{14}$$

where p is the pressure, $\tau_{xx}, \ldots\ldots, \tau_{zz}$ is the component of the viscous stress τ, and f_x, f_y, f_z denotes the force per unit mass in the x, y, and z directions, respectively.

Since it is very difficult to solve the N-S equations directly, the Reynolds-averaged Navier–Stokes (RANS) equations are used to perform simplified solution calculations by averaging the unsteady flow control equations over time and only considering large-scale time-averaged flows.

k-epsilon turbulence modeling equations can be expressed as follows:

$$\begin{cases} \frac{\partial(\rho k)}{\partial t} + \frac{\partial(\rho k u_i)}{\partial x_i} = \frac{\partial}{\partial x_j}\left[(\mu + \frac{\mu_i}{\sigma_k})\frac{\partial k}{\partial x_j}\right] + G_k + G_b - \rho\varepsilon - Y_m + S_k \\ \frac{\partial(\rho \varepsilon)}{\partial t} + \frac{\partial(\rho \varepsilon u_i)}{\partial x_i} = \frac{\partial}{\partial x_j}\left[(\mu + \frac{\mu_i}{\sigma_\varepsilon})\frac{\partial \varepsilon}{\partial x_j}\right] + C_{1\varepsilon}\frac{\varepsilon}{k}(G_k + C_{3\varepsilon}G_b) - C_{2\varepsilon}\rho\frac{\varepsilon^2}{k} + S_\varepsilon \end{cases} \tag{15}$$

where G_k, G_b are the turbulent kinetic energy terms generated by the velocity gradient and buoyancy, respectively. Parameters $i, j = 1, 2, 3$ denote the x, y, and z directions, respectively, Y_m is the pulsation expansion term, $C_{1\epsilon}$, $C_{2\varepsilon}$, $C_{3\varepsilon}$ is an empirical constant, σ_k, σ_ϵ is the Prandtl number corresponding to the turbulent kinetic energy k and dissipation rate ε, and S_k, S_ε is the user-defined source term.

2.4. Free Level Treatment

The Eulerian multiphase flow-volume of fluid (VOF) domain model can be expressed as follows:

$$\begin{cases} \frac{\partial}{\partial t} r\rho v + \nabla r\rho v = 0 \\ \frac{\partial}{\partial t}(1-r)\rho_a v + \nabla(1-r)\rho_a v = 0 \end{cases} \tag{16}$$

where r is the water volume fraction and ρ_a is the density of air. The VOF method can model stratified multiphase fluids with large-scale interfaces, where the interphase interface is determined by solving the volume fractions of water and air in each control cell.

The free surface is defined by the isosurface, where the water volume fraction is 0.5 (i.e., equal to the volume fraction of air).

3. Simplified Modeling and Design of Working Conditions

3.1. Basic Model

The main focus of this paper is the breakthrough law governing the water inlet discharge coefficient when the ship-side shell plate is damaged. Therefore, the model should meet the following requirements.

1. The breakthrough surface is vertical or nearly vertical to the horizontal plane, in line with the typical characteristics of the ship-side shell plate arrangement.
2. The breakthrough is completely located below the water line, enabling the seawater to pass through the entire breakthrough into the cabin.
3. The size of the damaged opening should not be too small or too large because the unsuitable damaged opening size makes the study lose its practical significance.
4. The damaged opening chamber must be open and spacious to avoid the impact of the jet stream on the bulkheads or other structures on the calculation.

A typical local model of a damaged ship is shown in Figure 2.

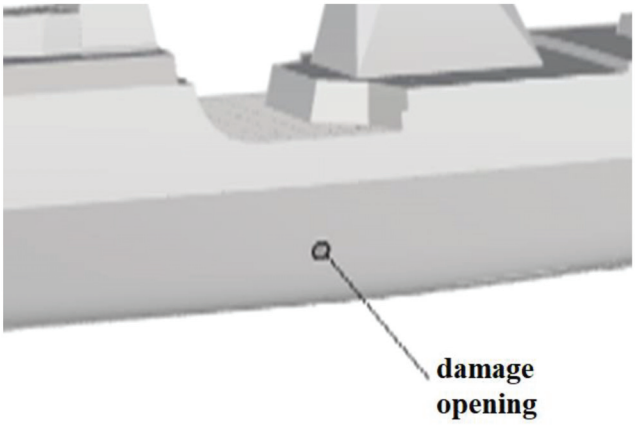

Figure 2. A local model of a typical damaged ship suitable for this study.

3.2. Simplified Model

Since most of the hull is irrelevant to the calculation, a simplified model can be intercepted from the relevant part of the damaged ship model to improve the speed and efficiency of modeling and calculation.

The simplified computational model is shown in Figure 3. The hexahedral computational domain is 10 m long, with a built-in bulkhead (red part) 10 mm thick to simulate the ship-side shell plate. The computational domain is divided into two parts. The first part is filled with seawater to simulate the marine environment, while the other represents the empty compartment. The upper part connects to the atmosphere to avoid the uneven air pressure affecting the computation. The middle part of the bulkhead is equipped with openings of various shapes, depths, and sizes to simulate various battle damage scenarios.

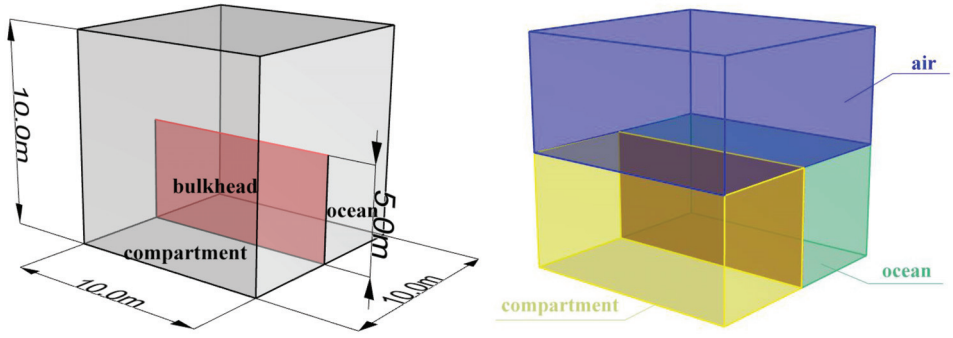

Figure 3. Simplified computational model.

3.3. Design of Working Conditions

We assumed that the ship was hit with an anti-ship weapon below the waterline on the side shell plate, resulting in a large amount of seawater rushing into the cabin. Thus, a total of 150 scenarios were designed based on common opening shapes, positions, and characteristic dimensions of damaged ships to investigate the relationship between the shape, depth, and size of the damaged opening and the discharge coefficient. Three different shapes of openings were designed: circular, square, and triangular. Five different central depths of the damaged openings were set, as follows: 1 m, 1.5 m, 2 m, 2.5 m, and 3 m. Ten different scenarios were set according to the parameters of the typical main guns of warships, torpedoes, and anti-ship missiles (Table 1) for the characteristic dimensions of the damage openings, as follows: 0.1 m, 0.2 m, 0.3 m, 0.4 m, 0.5 m, 0.6 m, 0.7 m, 0.8 m, 0.9 m, and 1 m The maximum value of the ratio of the characteristic size of the damaged opening to the thickness of the bulkhead was 0.01/0.05 = 0.2. Since this value is less than 2, the damaged opening can be considered to belong to the category of thin damaged openings. All working conditions are shown in Table 2.

Table 1. Parameters of typical anti-ship weapons.

Main Guns		Torpedoes		Anti-Ship Missiles	
Ship Classification	**Caliber (mm)**	**Type**	**Caliber (mm)**	**Type**	**Caliber (mm)**
Arleigh Burke	127	MK48	533	AGM-109	520
Ticonderoga	127	Sailfish	533	Hsiung Feng III	460
Sejong Daewang	127	Varunastra	533	AGM-84	340
Chilung	127	MK46	324	Type 12	350
Murasame	76	MU-90	324	P-J10	670

Table 2. All working conditions.

Type	Size (m)	Number in Different Depth of Damaged Opening Center				
		1.0 m	1.5 m	2.0 m	2.5 m	3.0 m
Circular	0.1	No. 1	No. 11	No. 21	No. 31	No. 41
Circular	0.2	No. 2	No. 12	No. 22	No. 32	No. 42
Circular	0.3	No. 3	No. 13	No. 23	No. 33	No. 43
Circular	.....	.....	.....	.....	.....	.....
Circular	1.0	No. 10	No. 20	No. 30	No. 40	No. 50
Square	0.1	No. 51	No. 61	No. 71	No. 81	No. 91
Square	0.2	No. 52	No. 62	No. 72	No. 82	No. 92
Square	0.3	No. 53	No. 63	No. 73	No. 83	No. 93
Square	.....	.....	.....	.....	.....	.....
Square	1.0	No. 60	No. 70	No. 80	No. 90	No. 100
Triangular	0.1	No. 101	No. 111	No. 121	No. 131	No. 141
Triangular	0.2	No. 102	No. 112	No. 122	No. 132	No. 142
Triangular	0.3	No. 103	No. 113	No. 123	No. 133	No. 143
Triangular	.....	.....	.....	.....	.....	.....
Triangular	1.0	No. 110	No. 120	No. 130	No. 140	No. 150

4. Numerical Simulation Points

The physical continuum model is multiphase and incorporates the volume of fluid (VOF) domain, *k-epsilon* turbulence, implicit unsteady state, VOF wave, and gravity. Two new phases were created in the multiphase-Eulerian phase, denoted as water and air. A liquid constant density was chosen to model the water, and a gaseous ideal gas was chosen to model the air. A new hydrostatic VOF wave was created in the VOF wave, and the point on the water level was made to be in the plane at the top of the divider.

The solver time step is set at 0.01 s, with the stopping criterion being the maximum physical time of 1 s, i.e., the program calculates in intervals of 0.01 s until it stops at 1 s.

Boundary Condition Settings and Post-Processing

The top of the computational domain was set as a pressure outlet to ensure that the pressure in the computational domain remained stable. The back wall of the pool represents the velocity inlet (the light red portion in Figure 4), while the remainder of the surface represents the wall.

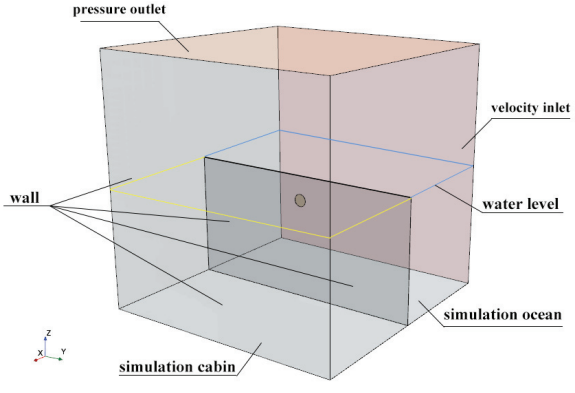

Figure 4. No. 5 (circular-damaged opening, depth of 1 m, diameter of 0.5 m).

A new mass flow monitor report on the damaged opening and a mass flow (kg/s) − time (s) plot were created based on the corresponding monitor. Moreover, a longitudinal profile was created through the damaged opening in the derived parts, and a

scalar scene was created. Lastly, the longitudinal profile displays a color mapping plot of the water volume fraction.

5. Mesh Division and Irrelevance Test

The mesh delineation quality greatly impacts CFD calculations. In general, the finer the mesh, the more accurate the calculation. However, the calculation time decreases with coarser mesh, but at the expense of accuracy.

The cut body mesh cell generator was selected for this calculation model. The base size of 1.0 m, target surface size of 100%, minimum surface size of 10%, very slow volume growth rate, and maximum mesh cell size of 100% were set. In addition to mesh encryption for the divider, the jet region, and the free liquid surface, the divider surface was encrypted with a target surface size of 10% (0.1 m). The minimum surface size was 1% (0.01 m), the surface of the inner wall of the damaged opening was encrypted with a target size of 1% (0.01 m), the jet region was encrypted with a customized isotropic encryption of 10% (0.1 m), and the free liquid surface region was encrypted with a customized Z-direction encryption of 10% (0.1 m).

The mesh of the damaged opening area, particularly the mesh of the opening wall, was a key factor affecting the flow rate of the calculation results. The encryption parameters of the mesh surface and the mesh-independence verification were carried out for the opening wall of the damaged opening. The smaller the characteristic size of the damaged opening, the more the flow phenomenon was affected by the friction of the opening wall. Therefore, the smaller the damaged opening, the smaller the encryption size of the opening wall mesh. Encryption parameter A is defined as follows:

$$\mathrm{A} = \frac{\text{Absolute valute of the encrypted surface size of the breach mesh surface(m)}}{\text{Feature size of the breach(m)}} \times 100\% \quad (17)$$

Parameter A decides the absolute value of the encrypted target surface size of the mesh surface of the damaged opening according to the feature size of the damaged opening. Cases 101–110 (triangular-damaged opening, depth of damaged opening center 1 m) are taken as examples to verify the mesh irrelevance. Parameter A is set to A = 5%, 1%, 0.5%, 0.1%, and 0.05% (Table 3) for the calculation. The results are shown in Figures 5 and 6.

Table 3. Verification of the mesh case for the working conditions.

Feature Size (m)		0.1	0.2	0.3	0.4	0.5	0.6	0.7	0.8	0.9	1
A = 5%	Absolute value of target surface size/mm	5	10	15	20	25	30	35	40	45	50
	mesh count	750k	720k	700k	700k	690k	690k	690k	690k	690k	690k
A = 1%	Absolute value of target surface size/mm	1	2	3	4	5	6	7	8	9	1
	mesh count	920k	890k	820k	850k	890k	790k	800k	810k	830k	840k
A = 0.5%	Absolute value of target surface size/mm	0.5	1	1.5	2	2.5	3	3.5	4	4.5	5
	mesh count	1150k	1100k	970k	1050k	1140k	930k	970k	1000k	1040k	1090k
A = 0.1%	Absolute value of target surface size/mm	0.1	0.2	0.3	0.4	0.5	0.6	0.7	0.8	0.9	1
	mesh count	3490k	2900k	3850k	2510k	2940k	3310k	2120k	2310k	2510k	2730k
A = 0.05%	Absolute value of target surface size/mm	0.05	0.1	0.15	0.2	0.25	0.3	0.35	0.4	0.45	05
	mesh count	8150k	6010k	8830k	4990k	6200k	7140k	3900k	4280k	4800k	5280k

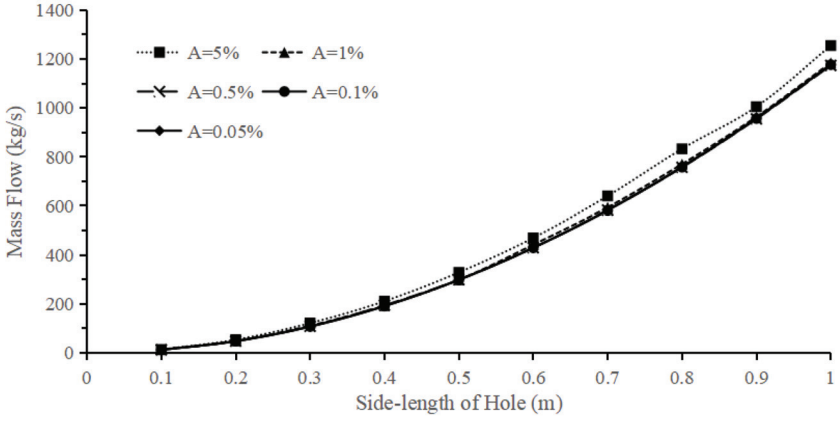

Figure 5. Mass flow rate with different encryption parameters.

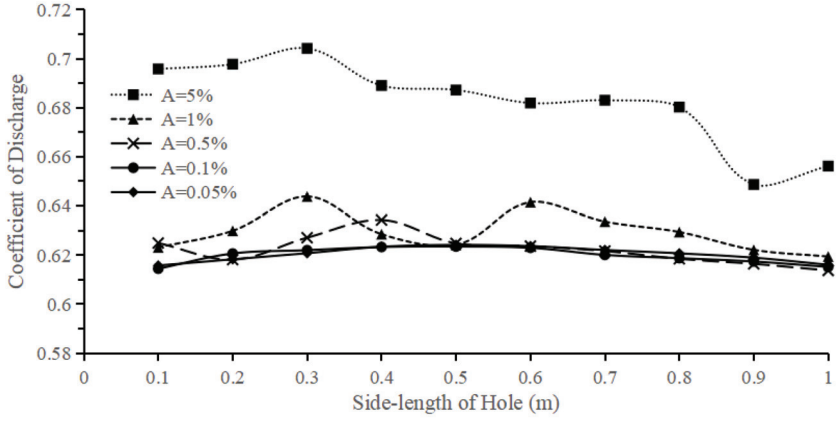

Figure 6. Discharge coefficients for different encryption parameters.

The number of finite elements increases as parameter A decreases, as follows: A = 5%, 1%, 0.5%, 0.1%, and 0.05%. Although the calculated mass flow rate at A = 1% is not very different from that at A = 0.05%, the discharge coefficient still fluctuates considerably, only stabilizing when the mesh encryption is encrypted to A = 0.1% (a minor difference from A = 0.05%. Since the difference between the calculation results is very small, it is ruminated that the encryption method of A = 0.1% has converged. Hence, the calculation accuracy and mesh independence requirements are satisfied. Therefore, A = 0.1% is used for the calculation to reduce the calculation volume and time.

The mesh quality is checked, and a representative case is selected for different damaged opening shapes, sizes, and central depths. Case 1 (circular-damaged opening, central depth of the damaged opening of 1 m, and damaged opening diameter of 0.1 m), Case 75 (square-damaged opening, central depth of the damaged opening of 2 m, and damaged opening edge length of 0.5 m), and Case 150 (triangular-damaged opening, central depth of the damaged opening of 3 m, and damaged opening edge length of 1 m) are taken. The mesh quality information is shown in Table 4. Some details about the mesh are shown in Figure 7.

Table 4. Mesh quality information.

Condition	Total Number of Divided Meshes	Percentage of Better Quality Meshes
1	3,699,176	99.537%
75	3,313,313	99.909%
150	2,728,580	99.768%

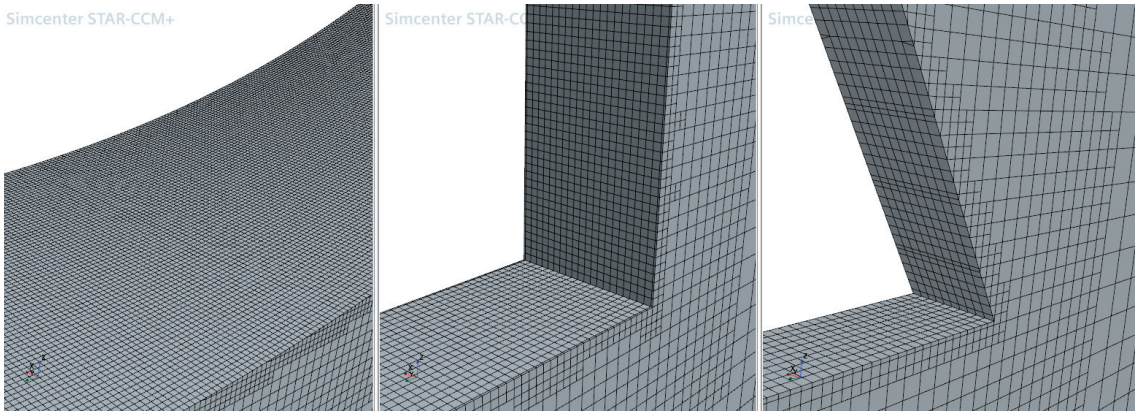

Figure 7. Local mesh details of condition nos. 1, 75, and 150.

The credibility of the time step taken as 0.01 s is also verified by taking the time steps of 0.005 s, 0.01 s, and 0.02 s, and calculating encryption parameter A = 0.05% of working conditions 101–110. The results are shown in Table 5 and Figures 8 and 9.

A difference between the calculation results when the time step is 0.01 s and 0.02 s can be observed. However, the results are negligible compared to those obtained with a time step of 0.005 s. Therefore, a time step of 0.01 s is more reasonable.

Table 5. Calculation results of the validation conditions.

No.	Characteristic Size of the Damaged Opening (m)	t = 0.02 s		t = 0.01 s		t = 0.005 s	
		Mass Flow (kg/s)	C_d	Mass Flow (kg/s)	C_d	Mass Flow (kg/s)	C_d
1	0.1	12.0625	0.631	11.7499	0.614	11.7493	0.614
2	0.2	47.4681	0.621	47.4725	0.621	47.4775	0.621
3	0.3	106.887	0.621	107.049	0.622	107.038	0.622
4	0.4	190.75	0.623	190.705	0.623	190.726	0.623
5	0.5	298.143	0.624	298.068	0.623	298.043	0.623
6	0.6	429.153	0.623	428.857	0.623	428.832	0.623
7	0.7	581.992	0.621	581.018	0.620	581.016	0.620
8	0.8	757.61	0.619	757.265	0.619	757.531	0.619
9	0.9	956.957	0.618	956.298	0.617	956.265	0.617
10	1.0	1178.24	0.616	1176.44	0.615	1176.29	0.615

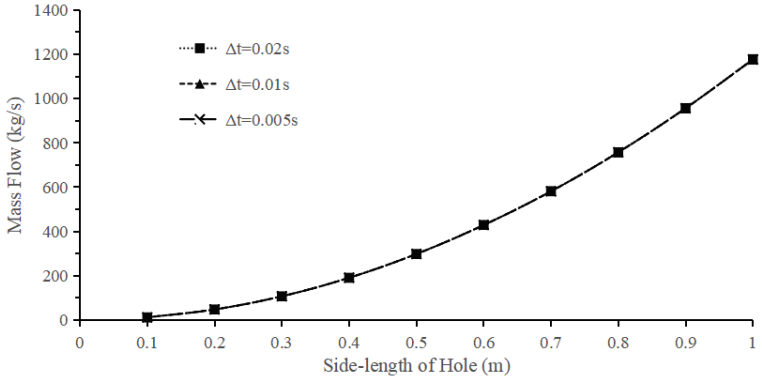

Figure 8. Damaged opening mass flow rate at different time steps.

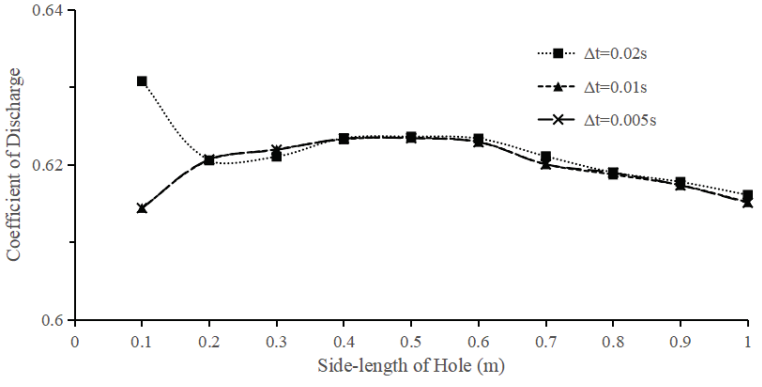

Figure 9. Discharge coefficients at different time steps.

6. Simulation

Condition nos. 1, 75, and 150 are taken as examples; these three typical working conditions, respectively, represent different shapes, central depths, and feature sizes of damaged openings. The flow rate–time plot of the damaged opening inlet is shown in Figure 10, the residuals are shown in Figure 11, and the longitudinal section along with the opening's export section visualization view of the damaged opening outlet is shown in Figures 12–20.

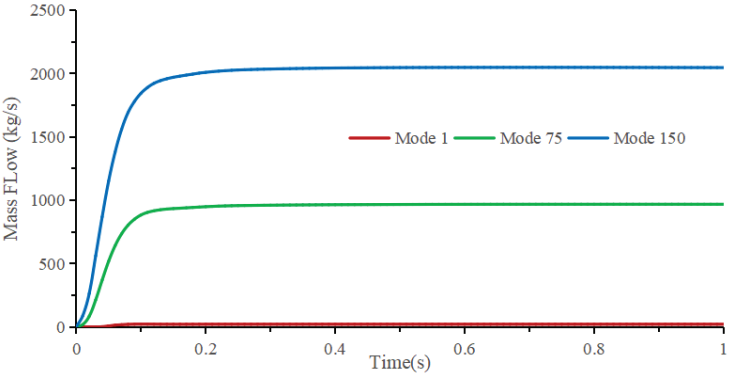

Figure 10. Flow rate–time plots of the damaged opening inlet water for three operating conditions.

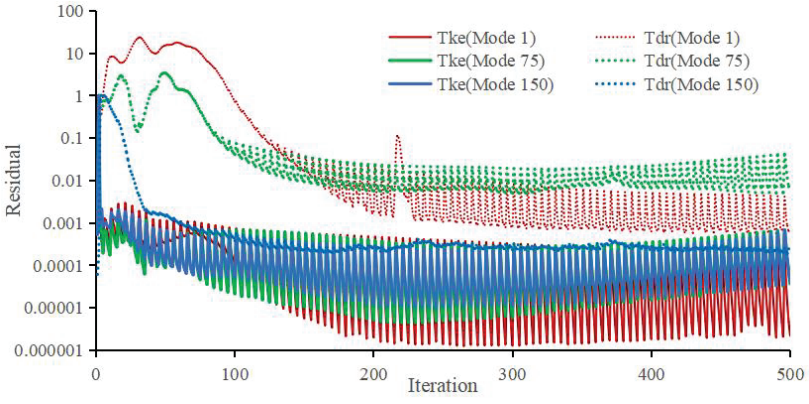

Figure 11. Residual analysis of the three conditions.

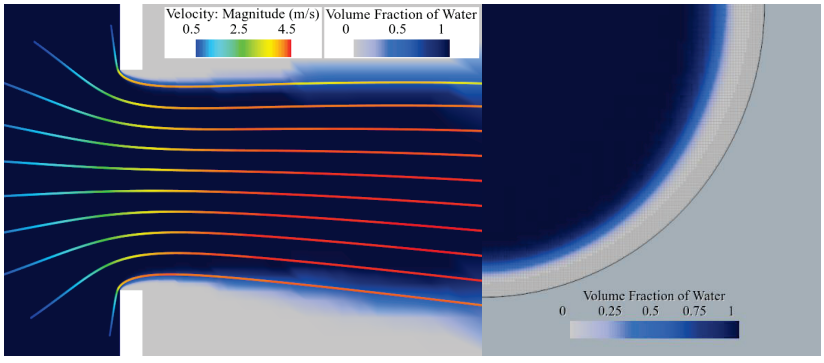

Figure 12. Visualization of the streamline and water volume fraction of the damaged opening outflow (using work condition no. 1 as the representative of the circular, small-size, and shallow-water-depth damaged opening; solution time = 1 s).

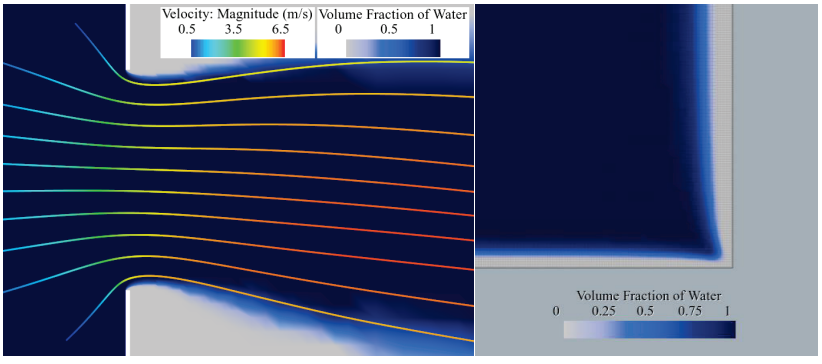

Figure 13. Visualization of the streamline and water volume fraction of the damaged opening outflow (using work condition no. 75 as the representative of the square, medium-size, and medium-water-depth damaged opening; solution time = 1 s).

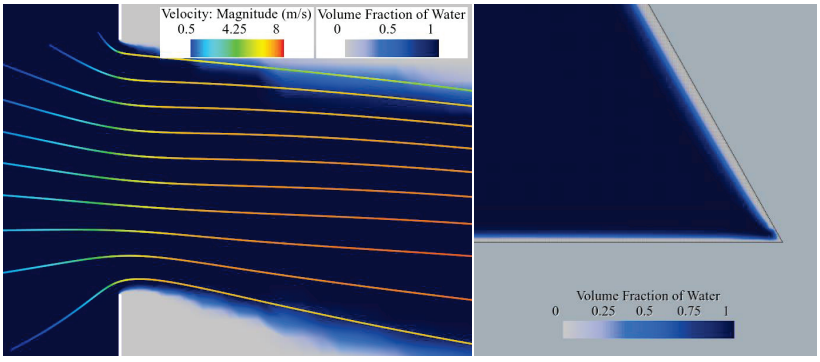

Figure 14. Visualization of the streamline and water volume fraction of the damaged opening outflow (using work condition no. 150 as the representative of the triangular, large-size, and deep-water-depth damaged opening; solution time = 1 s).

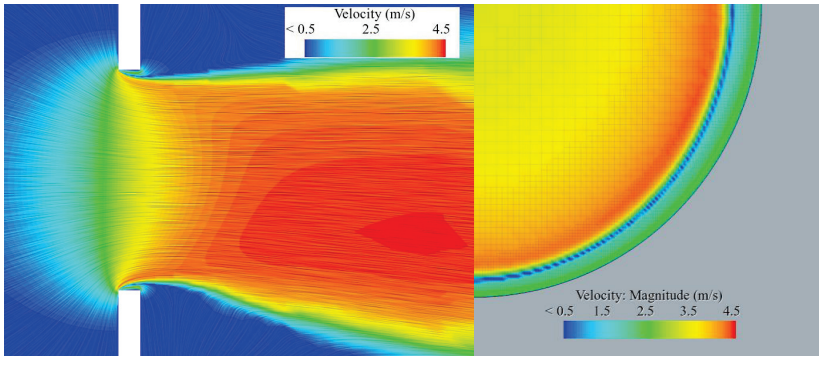

Figure 15. Visualization of the velocity distribution of the damaged opening outflow (using work condition no. 1 as the representative of the circular, small-size, and shallow-water-depth damaged opening; solution time = 1 s).

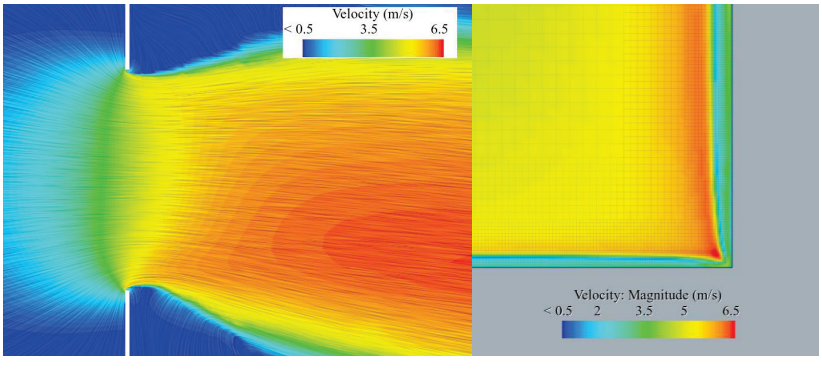

Figure 16. Visualization of the velocity distribution of the damaged opening outflow (using work condition no. 75 as the representative of the square, medium-size, and medium-water-depth damaged opening; solution time = 1 s).

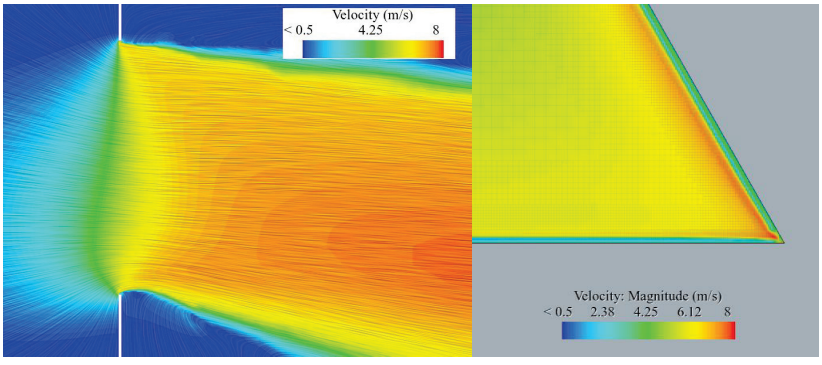

Figure 17. Visualization of the velocity distribution of the damaged opening outflow (using work condition no. 150 as the representative of the triangular, large-size, and deep-water-depth damaged opening; solution time = 1 s).

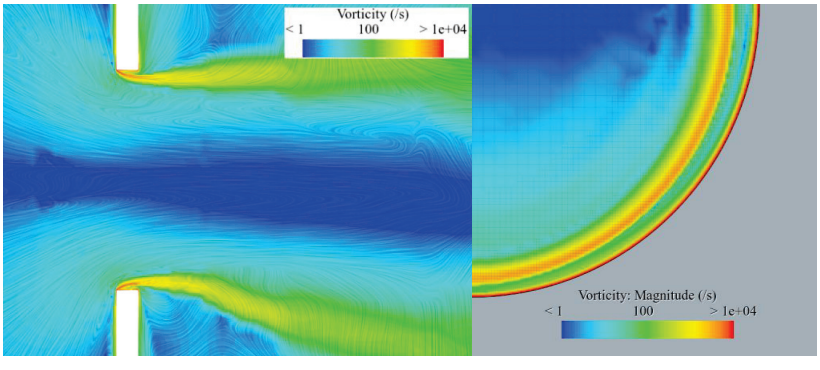

Figure 18. Visualization of the vorticity distribution of the damaged opening outflow (using work condition no. 1 as the representative of the circular, small-size, and shallow-water-depth damaged opening; solution time = 1 s).

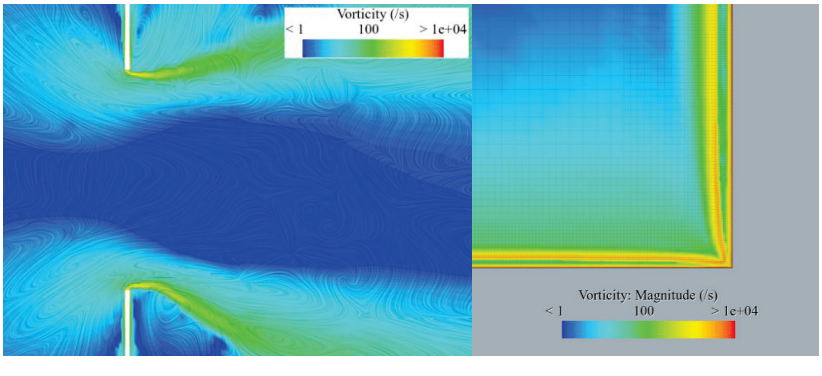

Figure 19. Visualization of the vorticity distribution of the damaged opening outflow (using work condition no. 75 as the representative of the square, medium-size, and medium-water-depth damaged opening; solution time = 1 s).

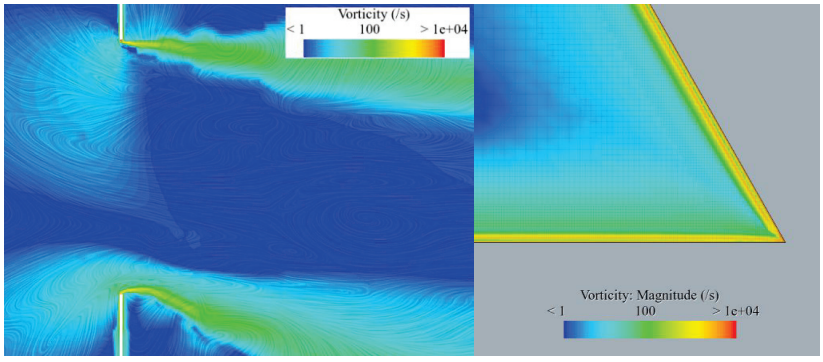

Figure 20. Visualization of the vorticity distribution of the damaged opening outflow (using work condition no. 150 as the representative of the triangular, large-size, and deep-water-depth damaged opening; solution time = 1 s).

Obviously, when the water flows out of the opening, a significant contraction occurs. The water jet does not spray tightly against the wall but is separated by a certain distance. This causes the cross-sectional area of the water jet to be smaller than the area of the opening, which is an important factor in the reduction of the flow rate.

As can be seen from the figures, the velocity at the center of the water jet is close to the theoretical value, but the velocity does not reach the value at the breach itself. Instead, it reaches the theoretical value at a certain distance away from the breach. This is clearly not caused by gravity, as there has not been a significant change in the Z-coordinate of the fluid at this point. Additionally, due to friction with the air, the velocity at the edge of the water jet must be lower than at the center of the jet, as shown in the figures.

Combining the velocity and volume fraction figures, vortices are mainly concentrated on the VOF separation interface of the fluid, especially near the outer edge of the opening where the vortices are the most intense. The motion of the vortices leads to the dissipation of energy, which is also an important factor in the reduction of the flow rate.

The results of the calculations are summarized in Tables 6–8.

Table 6. Results of the circular-damaged opening.

Feature Size (m)	Central Depth = 1 m		Central Depth = 1.5 m		Central Depth = 2 m		Central Depth = 2.5 m		Central Depth = 3 m	
	Mass Flow (kg/s)	C_d	Mass Flow (kg/s)	C_d	Mass Flow (kg/s)	C_d	Mass Flow (kg/s)	C_d	Mass Flow (kg/s)	C_d
0.1	21.0423	0.607	25.7237	0.606	29.6843	0.605	33.1695	0.605	36.3102	0.604
0.2	84.9736	0.612	104.002	0.612	120.019	0.612	134.113	0.611	146.833	0.611
0.3	191.866	0.615	234.961	0.615	271.194	0.614	303.076	0.614	331.845	0.614
0.4	340.639	0.614	417.515	0.614	482.060	0.614	538.815	0.614	590.004	0.614
0.5	531.413	0.613	652.102	0.614	753.108	0.614	841.911	0.614	921.874	0.614
0.6	762.600	0.611	937.116	0.613	1082.85	0.613	1210.43	0.613	1325.47	0.613
0.7	1029.91	0.606	1267.53	0.609	1465.09	0.61	1638.22	0.61	1793.45	0.609
0.8	1337.63	0.603	1649.34	0.607	1907.15	0.608	2132.20	0.607	2334.33	0.607
0.9	1681.33	0.598	2077.22	0.604	2402.71	0.605	2686.44	0.605	2940.79	0.604
1	2042.68	0.589	2549.51	0.6	2949.95	0.601	3298.05	0.601	3609.84	0.601

Table 7. Results of the square-damaged opening.

Feature Size (m)	Central Depth = 1 m		Central Depth = 1.5 m		Central Depth = 2 m		Central Depth = 2.5 m		Central Depth = 3 m	
	Mass Flow (kg/s)	C_d	Mass Flow (kg/s)	C_d	Mass Flow (kg/s)	C_d	Mass Flow (kg/s)	C_d	Mass Flow (kg/s)	C_d
0.1	27.0993	0.614	33.1543	0.613	38.2832	0.613	42.7587	0.612	46.8080	0.612
0.2	109.280	0.619	133.767	0.618	154.410	0.618	172.566	0.618	188.909	0.617
0.3	246.704	0.621	302.272	0.621	349.012	0.621	390.068	0.621	427.234	0.621
0.4	437.600	0.619	536.720	0.620	619.837	0.620	693.003	0.620	758.784	0.620
0.5	682.197	0.618	837.909	0.620	968.037	0.620	1082.39	0.620	1185.02	0.620
0.6	977.003	0.615	1202.27	0.617	1389.44	0.618	1553.49	0.618	1700.87	0.618
0.7	1316.88	0.609	1623.77	0.613	1877.54	0.614	2100.19	0.614	2299.20	0.613
0.8	1709.89	0.605	2113.09	0.610	2444.56	0.612	2733.25	0.616	2991.76	0.611
0.9	2142.21	0.599	2655.29	0.606	3073.29	0.607	3435.82	0.607	3760.66	0.607
1	2616.39	0.592	3253.41	0.601	3766.78	0.603	4211.06	0.603	4608.45	0.602

Table 8. Results of the triangular-damaged opening.

Feature Size (m)	Central Depth = 1 m		Central Depth = 1.5 m		Central Depth = 2 m		Central Depth = 2.5 m		Central Depth = 3 m	
	Mass Flow (kg/s)	C_d	Mass Flow (kg/s)	C_d	Mass Flow (kg/s)	C_d	Mass Flow (kg/s)	C_d	Mass Flow (kg/s)	C_d
0.1	11.7499	0.614	1176.44	0.614	16.5797	0.613	18.5307	0.613	20.2856	0.613
0.2	47.4725	0.621	14.3713	0.620	67.0424	0.620	74.9126	0.619	82.0587	0.619
0.3	107.049	0.622	58.0955	0.622	151.219	0.621	168.908	0.621	184.936	0.620
0.4	190.705	0.623	131.047	0.623	269.551	0.623	301.280	0.623	329.866	0.622
0.5	298.068	0.624	233.539	0.624	421.496	0.623	471.291	0.624	515.780	0.623
0.6	428.857	0.623	365.076	0.624	606.969	0.623	678.444	0.623	742.886	0.623
0.7	581.018	0.620	525.731	0.621	822.979	0.621	920.329	0.621	1007.48	0.621
0.8	757.265	0.619	712.717	0.620	1074.34	0.621	1201.32	0.621	1315.01	0.620
0.9	956.298	0.617	929.729	0.620	1358.08	0.620	1518.17	0.620	1661.83	0.619
1	1176.44	0.615	1175.69	0.618	1672.80	0.619	1870.24	0.619	2046.65	0.618

7. Analysis of Results and Summarization of Patterns

7.1. Influence of the Feature Size and Central Depth of Damaged Openings on Inlet Discharge Coefficients

The calculation results are shown in Figure 21.

The discharge coefficient of the damaged opening first increases with the characteristic size and then decreases as the size further increases. However, when the depth of the damaged opening exceeds 1 m, the overall change in the discharge coefficient is not significant. Finally, the difference between the maximum and the minimum value is approximately 0.01.

For the same shape of the damaged opening, a central depth of the damaged opening of 1 m and a characteristic discharge coefficient size higher than 0.3 m result in a more rapid flow than the other four groups. In contrast, the remaining four groups have no significant difference. Thus, it can be concluded that further increasing the water depth (once) after the central depth of the damaged opening reaches 1.5 m will no longer significantly impact the discharge coefficient.

This phenomenon may be related to the Reynolds number of the damaged opening. When the central depth of the damaged opening is 1 m, the damaged opening of the flow velocity is small. Thus, the Reynolds number is small and may be near the turning point. Consequently, the flow phenomenon in the damaged opening switches from laminar to turbulent. When the damaged opening size reaches 1.5 m, the flow velocity of the damaged opening is sufficient to transition from laminar to turbulent flow. Thus, the central depth of

the damaged opening continues to increase, which will not lead to significant changes in the discharge coefficient.

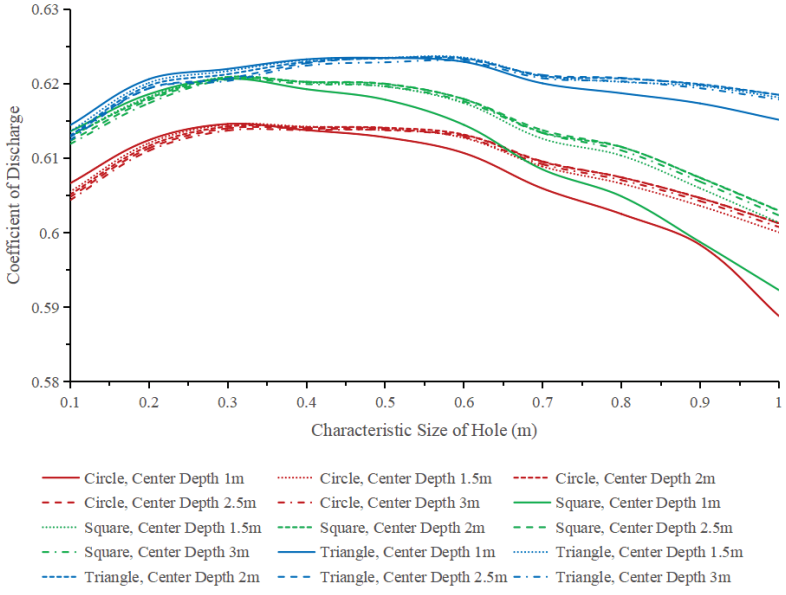

Figure 21. Discharge coefficient variations with feature sizes of damaged openings.

7.2. Influence of Shape and Area of Damaged Openings on Inlet Discharge Coefficients

To investigate the influence of the shape of the damaged opening on the inlet discharge coefficient, the area of the damaged opening must be consistent. A meaningful discussion about discharge coefficients can occur under the condition of identical outlet surface areas. The calculation results are shown in Figure 22.

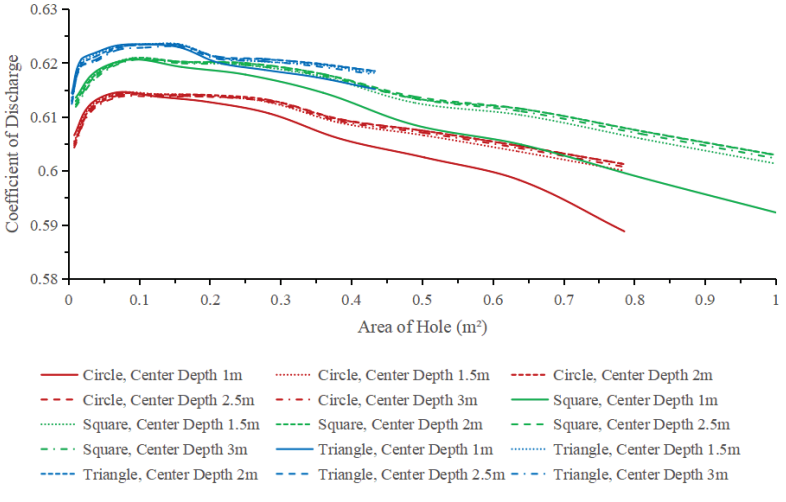

Figure 22. Discharge coefficient variations with the damaged opening area.

The discharge coefficient of the triangular-damaged opening is greater than that of the square- and circular-damaged openings for the same area and central depth of the damaged opening.

Moreover, the discharge coefficient of the damaged opening first increases with the area and gradually decreases with the continued increase of the area after rapidly reaching an extreme point.

It can be presumed that, for the same area and central depth of the regular polygon damaged opening, the closer its geometry is to the circle (i.e., the more sides), the smaller the discharge coefficient is, i.e., the closer to the discharge coefficient of the circular-damaged opening. However, according to Figure 22, the discharge coefficients of the three shapes of breaches are not translation relationships. Furthermore, it is reasonable to assume that the more sides of the circle that are connected to a regular polygon breach, the smaller the discharge coefficient becomes, moving closer to the discharge coefficient of the external circular-damaged opening. This specific rule will be investigated in the future.

In addition, the more sides there are in the circle, the smaller the discharge coefficient is, and the closer it is to the discharge coefficient of the externally connected circle-damaged opening. In addition, for the discharge coefficient with the area of the rule of law, when the damaged opening area is small, the Reynolds number is located in the vicinity of the turning point. The damaged opening flow state is between laminar and turbulent, and the Reynolds number with the damaged opening area also increases. Consequently, the damaged opening flow state completely transforms into turbulence, changing the rule of law.

7.3. Fitting Empirical Equations for Discharge Coefficients

Fitting empirical formulas can provide a convenient basis for the selection of flow coefficients when calculating the water inflow through damaged ships using methods such as the quasi-static method or potential flow method. First, the Π theorem, also known as Bridgman's theorem, is prepared for use in fitting. The Π theorem is a commonly used fundamental theorem of dimensional analysis in fluid mechanics and also serves as the theoretical basis for the method of dimensional analysis.

The main factors affecting the flow velocity of the damaged opening, v, are the head height (depth of the damaged opening center), H, the area of the damaged opening, S, the density of seawater, ρ, the coefficient of dynamic viscosity of seawater, μ, and the acceleration of gravity, g. The implicit function is constructed as follows:

$$f(v, H, S, \rho, \mu, g) = 0 \tag{18}$$

Parameters S, v, or ρ are chosen as the fundamental quantities, which, according to the Π theorem, form three dimensionless quantities, as follows:

$$\begin{cases} \Pi_1 = \frac{H}{S^{a1} v^{b1} \rho^{c1}} \\ \Pi_2 = \frac{\mu}{S^{a2} v^{b2} \rho^{c2}} \\ \Pi_3 = \frac{g}{S^{a3} v^{b3} \rho^{c3}} \end{cases} \tag{19}$$

where a_i, b_i, c_i $(i = 1, 2, 3)$ are the coefficients that need to be determined. The coefficients to be determined from the magnitude analysis that form three dimensionless quantities are as follows:

$$\begin{cases} \Pi_1 = \frac{H}{\sqrt{S}} \\ \Pi_2 = \frac{\mu}{\rho v \sqrt{S}} \\ \Pi_3 = \frac{g\sqrt{S}}{v^2} \end{cases} \tag{20}$$

Let $= kd^2$, where k is denoted as the equivalence coefficient, d is the damaged opening characteristic length, and $\sqrt{S}$ is denoted as the damaged opening equivalent characteristic length. Then, we have the following:

$$\prod_2 = \frac{\mu}{\rho v\sqrt{S}} = \mathrm{Re}^{-1} \tag{21}$$

where Re is the Reynolds number of the damaged opening.

According to the Π theorem, we have the following:

$$F(\prod_1, \prod_2, \prod_3) = 0 \tag{22}$$

Then, we have the following:

$$\prod_3 = \Phi(\prod_1, \prod_2) \tag{23}$$

Parameters Π_1, Π_2, Π_3 are substituted into Equation (23) to obtain an expression for the damaged opening flow rate, v, as follows:

$$v = \varphi(\frac{H}{\sqrt{S}}, \mathrm{Re})\sqrt{2gH} \tag{24}$$

where φ is the function to be determined. Then, the damaged opening discharge coefficient is characterized by the following relation:

$$C_d = \frac{v}{\sqrt{2gH}} = \varphi(\frac{H}{\sqrt{S}}, \mathrm{Re}) \tag{25}$$

The nonlinear polynomial fitting method is used as follows:

$$\begin{cases} C_d = ax^3 + by^3 + cx^2 + dxy^2 + ex^2 + fy^2 + gxy + hx + iy + j \\ x = \frac{H}{\sqrt{S}} \\ y = \mathrm{Re} \end{cases} \tag{26}$$

where $a, b, c, d, e, f, g, h, i, j$ are the coefficients to be determined. Since it is difficult to obtain the Reynolds number directly under battlefield conditions, it is approximated with reference to the following numerical calculations:

$$\mathrm{Re} \approx \frac{0.6\rho\sqrt{2gHS}}{\mu} \tag{27}$$

Combining the constants, Equation (22) transforms into the following:

$$\begin{cases} C_d = ax^3 + by^3 + cx^2y + dxy^2 + ex^2 + fy^2 + gxy + hx + iy + j \\ x = \frac{H}{\sqrt{S}} \\ y = \sqrt{HS} \end{cases} \tag{28}$$

Mathematical software was used to analyze the numerical calculation results as follows:

$$\begin{cases} C_d = 10^{-6}x^3 + 0.01y^3 - 0.0003x^2y - 0.03y^2 + 0.006xy - 0.0005x + 0.002y + j \\ x = \frac{H}{\sqrt{S}} \\ y = \sqrt{HS} \end{cases} \tag{29}$$

When the damaged opening is circular-damaged, $j = 0.610$, at which point the fitting coefficient is $R^2 = 0.8012$; when the damaged opening is square-damaged, $j = 0.615$, at which point the fit coefficient is $R^2 = 0.7948$; when the damaged opening is triangular-damaged, $j = 0.621$, at which point the fit coefficient is $R^2 = 0.9880$.

The results comparisons between the fitting formulae and the numerical calculations are shown in Tables 9–11.

Table 9. Results comparison of the circular-damaged opening.

Feature Size (m)	Central Depth = 1 m		Central Depth = 1.5 m		Central Depth = 2 m		Central Depth = 2.5 m		Central Depth = 3 m	
	C_d	Δ	C_d	Δ	C_d	Δ	C_d	Δ	C_d	Δ
0.1	0.608	0.001	0.608	0.002	0.608	0.003	0.608	0.003	0.610	0.006
0.2	0.611	−0.001	0.612	0.000	0.612	0.000	0.611	0.000	0.609	−0.002
0.3	0.612	−0.003	0.613	−0.002	0.614	0.000	0.615	0.001	0.615	0.001
0.4	0.611	−0.003	0.613	−0.001	0.614	0.000	0.616	0.002	0.617	0.003
0.5	0.610	−0.003	0.611	−0.003	0.613	−0.001	0.614	0.000	0.616	0.002
0.6	0.609	−0.002	0.609	−0.004	0.611	−0.002	0.612	−0.001	0.614	0.001
0.7	0.607	0.001	0.607	−0.002	0.608	−0.002	0.610	0.000	0.611	0.002
0.8	0.605	0.002	0.604	−0.003	0.605	−0.003	0.606	−0.001	0.608	0.001
0.9	0.603	0.005	0.602	−0.002	0.602	−0.003	0.603	−0.002	0.605	0.001
1	0.600	0.011	0.599	−0.001	0.599	−0.002	0.600	−0.001	0.603	0.002

Table 10. Results comparison of square-damaged opening.

Feature Size (m)	Central Depth = 1 m		Central Depth = 1.5 m		Central Depth = 2 m		Central Depth = 2.5 m		Central Depth = 3 m	
	C_d	Δ	C_d	Δ	C_d	Δ	C_d	Δ	C_d	Δ
0.1	0.614	0.000	0.613	0.000	0.613	0.000	0.612	0.000	0.611	−0.001
0.2	0.616	−0.003	0.617	−0.001	0.618	0.000	0.618	0.000	0.616	−0.001
0.3	0.617	−0.004	0.618	−0.003	0.619	−0.002	0.621	0.000	0.621	0.000
0.4	0.616	−0.003	0.617	−0.003	0.619	−0.001	0.620	0.000	0.621	0.001
0.5	0.614	−0.004	0.615	−0.005	0.617	−0.003	0.618	−0.002	0.620	0.000
0.6	0.612	−0.003	0.613	−0.004	0.614	−0.004	0.615	−0.003	0.617	−0.001
0.7	0.610	0.001	0.610	−0.003	0.610	−0.004	0.612	−0.002	0.614	0.001
0.8	0.608	0.003	0.607	−0.003	0.607	−0.005	0.608	−0.008	0.610	−0.001
0.9	0.605	0.006	0.603	−0.003	0.604	−0.003	0.605	−0.002	0.607	0.000
1	0.602	0.010	0.600	−0.001	0.600	−0.003	0.602	−0.001	0.605	0.003

Table 11. Results comparison of the triangular-damaged opening.

Feature Size (m)	Central Depth = 1 m		Central Depth = 1.5 m		Central Depth = 2 m		Central Depth = 2.5 m		Central Depth = 3 m	
	C_d	Δ	C_d	Δ	C_d	Δ	C_d	Δ	C_d	Δ
0.1	0.618	0.004	0.620	0.006	0.625	0.012	0.635	0.022	0.653	0.040
0.2	0.621	0.000	0.621	0.001	0.620	0.000	0.619	0.000	0.616	−0.003
0.3	0.622	0.000	0.623	0.001	0.624	0.003	0.623	0.002	0.622	0.002
0.4	0.623	0.000	0.624	0.001	0.625	0.002	0.626	0.003	0.626	0.004
0.5	0.622	−0.002	0.624	0.000	0.625	0.002	0.627	0.003	0.627	0.004
0.6	0.622	−0.001	0.623	−0.001	0.625	0.002	0.626	0.003	0.628	0.005
0.7	0.621	0.001	0.622	0.001	0.624	0.003	0.625	0.004	0.627	0.006
0.8	0.620	0.001	0.621	0.001	0.622	0.001	0.623	0.002	0.625	0.005
0.9	0.618	0.001	0.619	−0.001	0.620	0.000	0.621	0.001	0.623	0.004
1	0.617	0.002	0.617	−0.001	0.618	−0.001	0.619	0.000	0.621	0.003

In addition, Figures 21 and 22 show that the discharge coefficients are slightly affected by depth for breaches with water depths of 1.5 m and greater at the center of the damaged opening. Therefore, another empirical fitting formula can be given based on the characteristic dimensions of the damaged opening, as follows:

$$\begin{cases} C_d = -0.0666d^2 + 0.0524d + 0.6035, d < 1.5m \\ C_d = -0.0502d^2 + 0.0469d + 0.6029, d \geq 1.5m \end{cases}, \text{circular hole} \quad (30)$$

$$\begin{cases} C_d = -0.0637d^2 + 0.0431d + 0.6117, d < 1.5m \\ C_d = -0.0543d^2 + 0.0452d + 0.6103, d \geq 1.5m \end{cases}, \text{square hole} \quad (31)$$

$$\begin{cases} C_d = -0.0389d^2 + 0.0403d + 0.6127, d < 1.5m \\ C_d = -0.0353d^2 + 0.0412d + 0.6112, d \geq 1.5m \end{cases}, \text{triangular hole} \quad (32)$$

This formula is more concise, but the error is greater than the above formula.

8. Conclusions

This study presents a computational investigation into the discharge coefficients of water inflow through a damaged opening through the ship-side shell plate, using Computational Fluid Dynamics (CFD) software STAR-CCM+ (version 2402). This research is grounded on a simplified model and employs the Reynolds-averaged Navier–Stokes (RANS) methodology, coupled with the volume of fluid (VOF) technique and the control variable approach. The model parameters include characteristic dimensions ranging from 0.1 to 1 m and a central depth varying between 1 and 3 m, including three types of damaged opening shapes: circular, square, and triangular. This study delves into the variation patterns of the discharge coefficients revealed; the main findings are summarized as follows.

1. The calculations determined the patterns of influence that the central depth, characteristic dimensions, and shapes of the damaged openings have on the discharge coefficient of water ingress through a ship's side damaged by anti-ship weapons. Regarding the central depth of the damaged opening, within the water depth range of 1 m to 3 m, the influence of water depth on the discharge coefficient is minimal, with a maximum difference of only 0.003 (about 0.5%). But from the perspective of the damaged opening's characteristic dimensions and shapes, the variations in discharge coefficients are more pronounced. Overall, the triangular-damaged opening has a higher coefficient than the circular-damaged opening, which in turn is higher than that of the square-damaged opening; the coefficient decreases as the size of the damaged opening increases.
2. Based on the results of the numerical calculations, two sets of semi-empirical formulas for the discharge coefficient of ship-side damage are provided using the Π theorem and polynomial fitting method, respectively; the fitting effects are good. These formulas can serve as a reference for determining discharge coefficients in the time-domain simulation of ship-damaged opening scenarios using the quasi-static method and for the expedited evaluation of buoyancy stability.

It is important to recognize that the underlying factors contributing to the variability in the discharge coefficient remain to be elucidated. Therefore, future studies should focus on dissecting the specific mechanisms driving these variations to advance our understanding and refine the predictive models. Additionally, this outcome can be utilized to conduct time-domain simulation research on water ingress in ship compartments using the potential flow method or quasi-static method; this will further enhance the understanding of buoyancy stability and motion changes during ship compartment flooding.

Author Contributions: Methodology—Z.W. Numerical simulation and writing—S.T., supervision and validation—F.P., data curation—J.L. All authors have read and agreed to the published version of the manuscript.

Funding: This research received no external funding.

Institutional Review Board Statement: Not applicable.

Informed Consent Statement: Not applicable.

Data Availability Statement: Data are contained within the article.

Conflicts of Interest: The authors declare no conflicts of interest.

References

1. Xia, G.; Yang, D. *Naval Hydrodynamics*; Huazhong University of Science and Technology Press: Wuhan, China, 2018.
2. Ruponen, P. Progressive Flooding of a Damaged Passenger Ship. Ph.D. Dissertation, Helsinki University of Technology, Department of Mechanical EnginBering, Helsinki, Finland, 2007.
3. Ruponen, P. Adaptive time step in simulation of progressive flooding. *Ocean. Eng.* **2014**, *78*, 35–44. [CrossRef]

4. Dracos, V.; Osman, T.; Maciej, P. Dynamic Stability Assessment of Damaged Passenger/Ro-Ro Ships and Proposal of Rational Survival Criteria. *Mar. Technol.* **1997**, *34*, 241–266.
5. Ruponen, P. *Model Tests for the Progressive Flooding of a Boxed-Shaped Barge*; Helsinki University of Technology: Helsinki, Finland, 2006.
6. Ruponen, P.; Sundell, T.; Larmela, M. Validation of a simulation method for progressive flooding. *Int. Shipbuild. Prog.* **2007**, *54*, 305–321.
7. Ruponen, P.; Kurvinen, P.; Saisto, I.; Harras, J. Experimental and numerical study on progressive flooding in full-scale. *Int. J. Marit. Eng.* **2010**, *152*, A197–A208.
8. Stening, M.; Jarvela, J.; Ruponen, P.; Jalonen, R. Determination of Discharge Coefficients for a Cross-flooding Duct. *Ocean. Eng.* **2011**, *38*, 570–578. [CrossRef]
9. Li, Y.; Sobey, A.J.; Tan, M. Investigation into the effects of petalling on coefficient of discharge during compartment flooding. *J. Fluids Struct.* **2014**, *45*, 66–78. [CrossRef]
10. Wang, X.; Li, A.; Sobey, A.J.; Tan, M. Investigation into the effects of two immiscible fluids on coefficient of discharge during Compartment Flooding. *Ocean. Eng.* **2016**, *111*, 254–266. [CrossRef]
11. Li, A.; Jin, L.; Tian, A.; Han, Y. Simulation of Warship's Crevasse Flow Coeffcient. *Ship Sci. Technol.* **2010**, *4*, 105–108.
12. Li, Y. *On the Flow Process of the Damaged Ship Based on the CFD Simulation*; Harbin Engineering University: Harbin, China, 2016.
13. Li, Y.; Duan, W.; Jin, Y.; Guan, C.; Wen, Y. Flooding Process of Damaged Ship Based on CFD. *Shipbuild. China* **2016**, *6*, 149–163.
14. Zhang, S.; Gu, J.; Wu, J.; Chen, Z. CFD Simulation of Coefficient of Discharge. *Ship Sci. Technol.* **2019**, *10*, 59–62.
15. Xue, W.; Gao, Z.; Xu, S. Numerical Study on Attitude and Resistance of a Side-Damaged Ship during Steady Flooding. *J. Mar. Sci. Eng.* **2022**, *10*, 1440. [CrossRef]
16. Wei, K.; Gao, X.; Ma, P. Study of discharge coefficient of Square Water Hole Based on CFD. *J. Nav. Univ. Eng.* **2022**, *2*, 43–48.
17. Wei, K.; Gao, X.; Ma, P. Analysis of Overflow Characteristics of Circular Water Hole of Submarine. *Ship Sci. Technol.* **2022**, *7*, 12–17.
18. Hu, R.; Zhang, T.; Lu, Y.; Xu, C. Study on Discharge Coefficients of Drain Orifices in Closed Cavities. *Appl. Math. Mech.* **2023**, *1*, 61–69.
19. Li, J.; Zhao, Z. *Hydraulics*; Hohai University Press: Nanjing, China, 2001.

MDPI AG
Grosspeteranlage 5
4052 Basel
Switzerland
Tel.: +41 61 683 77 34

Journal of Marine Science and Engineering Editorial Office
E-mail: jmse@mdpi.com
www.mdpi.com/journal/jmse

Academic Open
Access Publishing

mdpi.com

ISBN 978-3-7258-2888-3